MODELLING THE LONG-TERM CYCLIC BEHAVIOUR OF PORTO SILTY-SAND STABILISED WITH CEMENT

ANTONIO FABRIZIO PANICO

Dissertação submetida para satisfação parcial dos requisitos do grau de

DOUTOR EM ENGENHARIA CIVIL

Orientador: Professor Doutor António Joaquim Pereira Viana da Fonseca

Co-Orientador: Professor Doutor Jean Vaunat

DEZEMBRO DE 2018

PROGRAMA DOUTORAL EM ENGENHARIA CIVIL 2018

DEPARTAMENTO DE ENGENHARIA CIVIL

Tel. +351-22-508 1901

Fax +351-22-508 2139

✉ prodec@fe.up.pt

Editado por

FACULDADE DE ENGENHARIA DA UNIVERSIDADE DO PORTO

Rua Dr. Roberto Frias

4200-465 PORTO

Portugal

Tel. +351-22-508 1400

Fax +351-22-508 1440

✉ feup@fe.up.pt

🌍 http://www.fe.up.pt

To my cousin Mimmo, in loving memory

ACKNOWLEDGEMENTS

I would like to thank many people who have helped me in this work.

My special thanks to my supervisor, Prof. Viana da Fonseca, for always believing in me and always providing scientific and human support; for being an example of perseverance, dedication, resilience, and enthusiasm.

To my co-supervisor Prof. Jean Vaunat, for guiding me in the elaboration of the constitutive model and for allowing me to spend a fundamental period in UPC. Thank you for your great competence, patience, and hospitality.

To Sara Rios, for always being present with suggestions, discussions, and friendship.

To the Professors and Researchers of the Civil Engineering Department at FEUP, from whom I had the opportunity to learn, in the classes of the PRODEC programme and in everyday interaction: Cristiana Ferreira, Prof. Matos Fernandes, Prof. Silva Cardoso, Prof. Couto Marques, Prof. Rui Calçada, Prof. Raimundo Delgado, Prof. Xavier Romão, Prof. Topa Gomes.

To Professor Rui Gomes from IST, for being a friend and an example of academic and human integrity.

To the staff of the Geotechnical Laboratory of FEUP, for the great professional competence and for the wisdom, patience, and companionship: Armando Pinto, Daniela Coelho, and Cláudia Pinto.

To the colleagues and friends with whom I worked and learned in the LabGeo: Marisa Soares, Miguel Amaral, Jubert Pineda, Nuno Raposo, Helena Dias, Davide Besenzon, Malgorzata Kijanka, André Domingues, Saul Guedes, Amanda dalla Rosa. Thank you for the happy moments spent together and for always being there in difficult times.

To the colleagues and friends of FEUP office: Daniela, Julieth, Sofia, Candido, Maxim, Lucy, Fernando, Carlos, Omar, Francisco. For being such a wonderful company and for always being willing to help.

To the colleagues and friends of UPC, for making me feel at home: Natalia, Victor, Matteo, Guillem, Olga, Francesca.

To my Portuguese friends, for making Porto and Portugal a place that I can call home: Mónica, Diana, Miguel, Marlene, Yunior, Pedro, Hugo, Mariska, Diana, Tiago, Filipa, Pedro, Nathalie, Adriana, Mariza, Angela, Ana Luis, André.

To my Italian friends, for moulding the person that I am and for always inspiring my actions: Sara, Miriam, Nino, Libera, Giuseppe, Antonio, Gabriele, Joy, Iolanda, Francesco, Desi, Rui, Giuseppe, Antonio, Alessandro, Claudio, Pietro, Graziano.

To little Chloe, Gabriel, and Anna, for the smiles.

To my cousins, the ones I always knew, the ones that arrived later, and the ones who are gone, for their support, optimism, and love.

To my grandparents, who still carry me on their shoulder.

To my sister Carla, for knowing me better than myself and always showing me how to stay human.

To my parents Silvana and Rocco, for everything I am and will ever be.

The present thesis had the financial support of the Portuguese Science and Technology Foundation (FCT) through SFRH/BD/92810/2013 scholarship, which is co-funded by the Portuguese Ministry of Science and Technology (MCTES).

ABSTRACT

Cyclic loading is an important action that can affect a wide variety of geotechnical structures. The repetition of low-to-medium intensity stress over a great number of cycles can lead to loss of serviceability due to accumulation of permanent strain and/or degradation of resilient moduli. This phenomenon can interest the foundation layers of structures and infrastructures subjected to periodic or variables loads (e.g. wind, sea waves, variable overloads, traffic loads, and earthquakes). Short-term cyclic loading in uncemented soil has been widely studied; nevertheless, few studies on the cyclic behaviour of soil-cement mixtures are found in literature, particularly with a high number of cycles. An extensive experimental study is presented, aimed at analysing the long-term permanent strain response of an artificially bounded granular material, contributing to the understanding of the behaviour of this material under cyclic loading conditions. The soil studied is a well-graded silty-sand remoulded from the highly weathered to decomposed horizons of Porto granitic rock masses. Nine different types of specimen were moulded mixing the soil with three different percentages of Portland cement and compacting the mixture to three different initial void ratio. Uncemented specimens were also tested for reference. The experimental programme included drained and undrained long-duration cyclic triaxial tests (with 1 million loading cycles), performed under stress-controlled conditions using an automatic hydraulic system equipped with high-precision internal strain and stress gauges. The very high number of loading cycles reached during the tests allowed observing novel trends of strain accumulation not detectable with the commonly performed tests with moderate number of load cycles.

Modelling the pre-yield behaviour of soils using isotropic hardening models is a difficult task. One-surface elasto-plastic models can predict the post-yield behaviour but fail to reproduce the pre-yield behaviour of soils, even if a non-linear elastic law is adopted. Moreover, the difference in stiffness between loading and unloading is not well reproduced. Complexity is increased when natural cement is present in soils or artificial cement is added to the granular materials, as the level of cementation influences the characteristics of the specific composite mixture. Models based on bounding surface plasticity are able to reproduce the experimentally observed smooth transition from purely elastic to fully plastic state. The original model proposed in the present thesis represents the extension of an existing model for cemented soil, reformulated in a two-surface bounding plasticity framework. Such framework introduces a kinematic hardening yield surface in the stress space moving inside an outer surface accounting for the stress history of the material. This approach allows the reproduction of the sudden change in stiffness modulus upon stress reversal and the accumulation of plastic strain for small stress amplitudes.

The model was implemented with a numerical method in order to obtain an approximate solution to the constitutive equations, since no closed-form solution is available. An explicit algorithm with two different iterative integration method are presented: a 2nd order Modified Euler algorithm and a 5th order Runge-Kutta-England algorithm, with error control. For the presented cyclic test, the first method is the more suitable, because of the smaller amount of calculations required at each integration interval and due to the small amplitude of the stress cycles applied.

The model implementation was validated in specific conditions in which a closed-form solution could be found. The model was calibrated against monotonic triaxial tests performed on the same type of soil, and the model performance was assessed against the cyclic triaxial tests presented in this study.

KEYWORDS: soil–cement, long-duration cyclic tests, modelling

RESUMO

O carregamento cíclico é uma ação importante que pode afetar um vasto leque de estruturas geotécnicas. A repetição de tensões de nível baixo a moderado durante um grande número de ciclos de carga pode afetar a durabilidade da estrutura por causa da acumulação de deformações permanente e/ou degradação dos módulos de rigidez. Este fenómeno pode interessar camadas de fundação de estruturas e infraestruturas sujeitas a carregamento periódico ou variável (tais como vento, ondas marinhas, sobrecargas variáveis, sobrecargas geradas pelo trânsito e sismos). O carregamento cíclico de curta duração em solos não cimentados tem sido largamente estudado. Porém, encontram-se poucos estudos sobre o comportamento cíclico de solos cimentados, nomeadamente em condições de longa duração. Este estudo apresenta um programa experimental completo, focado na análise da acumulação de deformações a longo prazo de um solo granular artificialmente cimentado, com o objetivo de contribuir à definição do comportamento deste solo em condições cíclicas. O solo objeto de estudo é uma areia siltosa bem graduada, reconstituída em laboratório a partir de horizontes completamente alterados do granito do Porto. Nove distintos tipos de provetes foram moldados misturando o solo com quatro diferentes teores de cimento Portland (incluindo provetes não cimentados) e compactando em duas diferentes compacidades iniciais. O programa experimental foi constituído por um vasto conjunto de ensaios triaxiais cíclicos de longa duração (um milhão de ciclos), drenados ou não drenados, efetuados em carga controlada e usando instrumentação interna de alta precisão. O alto número de ciclos atingido permitiu a observação de específicos padrões de acumulação, não observáveis em ensaios com pequeno ou moderado número de ciclos de carga.

A modelação do comportamento constitutivo antes do ponto de cedência plástica é uma tarefa complexa se um modelo com endurecimento isotrópico é adotado. Modelos constitutivos com apenas uma superfície de cedência não conseguem reproduzir de forma fiável o comportamento do solo dentro do seu domínio puramente elástico (antes da cedência), ou a repentina variação em rigidez observada entre a fase de carga e descarga de um ciclo. A adição de cementação ao solo aumenta a complexidade do problema, sendo que o nível de cimentação influencia a resposta de cada mistura. Os modelos baseados na *bounding surface plasticity* são aptos a reproduzir a transição progressiva de um comportamento puramente elástico até a completa plastificação. Nesta tese é proposto um modelo constitutivo original, baseado na extensão de um modelo para solos cimentados existente, adaptado à nova configuração de duas superfícies da *bounding plasticity*. O modelo apresenta uma superfície de cedência com endurecimento cinemático que se desloca dentro de uma superfície externa de referência que tem em conta da história de tensões do material. Este modelo permite a reprodução da resposta cíclica em ciclos de pequena amplitude observada nos ensaios laboratoriais.

O modelo foi implementado numericamente com intuito a obter uma solução aproximada das equações constitutivas. Um algoritmo explícito foi usado, com dois métodos iterativos de integração: o algoritmo de Euler modificado de segunda ordem e o algoritmo de Runge-Kutta-England de quinta ordem, ambos com controlo do erro. O primeiro método mostrou-se o mais adequado pelos ensaios efetuados, já que requer menos cálculos a cada intervalo de integração e dada a pequena amplitude dos ciclos aplicados.

A implementação do modelo foi validada por comparação com casos específicos em que uma solução em forma fechada foi encontrada. O modelo foi calibrado usando ensaios triaxiais monotónicos e o seu desempenho avaliado comparando com os ensaios cíclicos apresentados.

PALAVRAS-CHAVE: solo-cimento, ensaios cíclicos de longa duração, modelação

TABLE OF CONTENTS

LIST OF FIGURES

LIST OF TABLES

SYMBOLS

Scalar quantities are indicated in italic; vectors in bold italic; matrices or tensors in bold characters.

Latin letters

A_c	cross section area
$\mathbf{A}_{RK}$	Runge-Kutta matrix
$\boldsymbol{A}_w$	vector of the weights for a RK method of order d
$\boldsymbol{a}_w$	vector of the weights for a RK method of order $d-1$
b	equivalent distance between the model surfaces
b_{max}	maximum value of b
$\bar{b}$	amount of bonding at a certain strain level
b_0	initial amount of bonding
b_1	parameter regulating the amount of bond damage with respect to the volumetric strain
b_2	parameter regulating the amount of bond damage with respect to the distortional strain
B	interpolating parameter for the kinematic hardening modulus
$\mathbf{C}^{ep}$	elasto-plastic compliance tensor
$\mathbf{C}^{e}$	elastic compliance tensor
$\mathbf{C}^{p}$	plastic compliance tensor
C	cement content by weight
C_c	curvature coefficient
C_{iv}	cement content by volume
C_u	uniformity coefficient
c	cohesion
c'	effective cohesion
d	order of the RK method
D_{50}	effective diameter
$\mathbf{D}^{e}$	elastic stiffness tensor
$\mathbf{D}^{ep}$	elasto-plastic stiffness tensor
D_s	specimen diameter
E	Young's modulus
E_0	small-strain Young's modulus
E_{ss}	local truncation error estimate
E_{UCS}	initial tangent modulus calculated in UCT test
$\mathbf{e}$	deviatoric strain tensor
e	void ratio
e_i	initial void ratio
f	yield surface
f_{ref}	bounding (or reference) surface
F_r	ultimate vertical load in UCT tests
G	shear modulus
G_0	small-strain shear modulus
G_s	specific gravity
g	plastic potential function
H	hardening modulus
H'	kinematic hardening modulus
H_0	isotropic hardening modulus
H_b	bonding hardening modulus
H_s	specimen height
$\boldsymbol{h}$	hardening parameters vector
h	hardening parameter
$\mathbf{J}$	Jacobian matrix

K'	bulk modulus
k	generic evaluation in a RK method
K'_0	small strain bulk modulus
K_d	gain of the derivative term in PID controllers
K_i	gain of the integral term in PID controllers
K_p	gain of the proportional term in PID controllers
L_{LVDT}	initial distance between LVDT pivots
$LVDT_i$	initial reading of a LVDT
$LVDT_t$	reading of a LVDT at a given time
M	slope of the critical state line in the stress plane
m	Yu flow rule parameter
M_0	small strain longitudinal modulus
N	specific volume of the NCL at $p' = 1$kPa
n	porosity
n/C_{iv}^x	adjusted porosity/cement ratio
$\bar{n}$	yield surface shape parameter in CASM model (stress-state coefficient)
n_{cyc}	number of cycles
$\boldsymbol{n_f}$	normal vector to the yield surface
$\boldsymbol{n_g}$	normal vector to the plastic potential surface
n_t	number of trapezia for approximate solution of definite integrals
p'	mean effective stress
p'_0	size of the outer surface
p'_{0i}	initial size of the outer surface
p'_{0unc}	size of the outer surface for uncemented soils
p'_{0unc_i}	initial size of the outer surface for uncemented soils
p'_α	p'-coordinate of the apex of the yield surface in the stress plane
p'_{av}	average value of the effective mean stress
p'_c	excess isotropic strength: difference between the isotropic yield stress of a cemented soil and the isotropic yield stress of an equivalent uncemented soil
p'_e	equivalent pressure: pressure corresponding to a point on the normal compression line having the same void ratio as the tested specimen used for normalising the stress paths
p'_{IB}	normalising pressure for cemented soils
p'_{ref}	reference pressure value conventionally assumed equal to 1 kPa
$\Delta p'_{ss}$	sub-increment effective mean stress
p'_t	isotropic tensile strength
p'_{ti}	initial isotropic tensile strength
p'_Y	p'-coordinate of the yield point
q	deviatoric stress
q_α	q-coordinate of the apex of the yield surface in the stress plane
q_{BS}	deviatoric stress on the bounding surface determined in TX tests on medium to loose soil
q_{cr}	critical state deviatoric stress
q_{cyc}	cyclic deviatoric stress amplitude $(q_{max} - q_{min})$
q_{max}	maximum value of the deviatoric cyclic stress
q_{min}	minimum value of the deviatoric cyclic stress
q_{peak}	deviatoric peak stress determined in TX tests on dense soil
Δq_{ss}	sub-increment deviatoric stress
q_u	ultimate deviatoric stress
q_{UCS}	unconfined compression strength (UCS) determined in UCT tests
q_Y	q-coordinate of the yield point
R	size ratio between surfaces
R^2	coefficient of determination

r	yield surface shape parameter in CASM model (spacing ratio)
S	scalar multiplier of vector $\boldsymbol{\beta}$ in translation rule
$\mathbf{s}$	deviatoric stress tensor
s	slope of the effective stress path
$\bar{s}$	number of evaluations of the compliance matrix in a substep of a RK method
$SSTOL$	convergence tolerance for the plastic strain over a substep
T	dimensionless time
ΔT	dimensionless time increment
t	time
u	pore water pressure
v	specific volume
v_i	initial specific volume
V_i	initial volume
V_P	compression waves velocity
V_S	shear waves velocity
x	adjusting exponent in porosity/cement ratio (Consoli et al., 2007)
w	water (or moisture) content
w_L	liquid limit
w_{opt}	optimum water content
w_P	plastic limit
$YTOL$	convergence tolerance for the yield surface over a substep

Greek letters

$\boldsymbol{\alpha}$	coordinate vector of the apex of the yield surface, (p'_α, q_α)
$\dot{\boldsymbol{\alpha}}$	translation vector
α_H	kinematic over total hardening modulus ratio
α_t	parameter controlling tensile strength
$\boldsymbol{\beta}$	vector joining conjugate points on the yield surface and reference surface
$\boldsymbol{\beta}_{norm}$	normal component of vector $\boldsymbol{\beta}$ to the stress increment vector
$\boldsymbol{\beta}_{par}$	parallel component of vector $\boldsymbol{\beta}$ to the stress increment vector
β	correction factor for ΔT in stress point algorithms
$\beta_{p'}$	p' coordinate of vector $\boldsymbol{\beta}$
β_q	q coordinate of vector $\boldsymbol{\beta}$
Γ	specific volume of the CSL at $p' = 1$kPa
γ	unit weight
γ_c	cyclic strain
γ_d	dry unit weight
$\gamma_{d,max}$	maximum dry unit weight
δ_{ij}	Kronecker delta
$\boldsymbol{\varepsilon}$	strain vector
$\boldsymbol{\varepsilon}^e$	elastic strain vector
$\Delta\boldsymbol{\varepsilon}^e_{ss}$	elastic strain increment over a substep
$\boldsymbol{\varepsilon}^p$	plastic strain vector
$\Delta\boldsymbol{\varepsilon}^p_{ss}$	plastic strain increment over a substep
ε_3	axial (vertical) strain corresponding to 30% of the ultimate load in UCT tests
ε_a	axial (vertical) strain
$\varepsilon_{a\ cum}$	accumulated axial strain
$\varepsilon_{a\ cum}^{norm}$	normalised accumulated axial strain
ε_{cyc}	cyclic strain amplitude
$\varepsilon_{cum,n}$	accumulated strain at a certain cycle

ε_r	radial strain
$\varepsilon_{r\,cum}$	accumulated radial strain
ε_s	distortional (shear) strain
$\varepsilon_{s\,cum}$	accumulated distortional (shear) strain
ε_v	volumetric strain
$\varepsilon_{v\,cum}$	accumulated volumetric strain
ζ	Normalizing parameter for outward normal vector to the yield surface
η'	effective stress ratio
$\eta^{*\prime}$	effective stress ratio referred to the apex of the cemented reference surface
η'_α	effective stress ratio referred to the apex of the yielding surface
η'_U	effective stress ratio of the intersection point between the reference surface and the direction of the stress increment vector
θ	Lode's angle
θ_β	angle between vector $\boldsymbol{\beta}$ and the outward normal vector $\boldsymbol{n_f}$
κ	slope of an unloading-reloading line in the $(\ln p', v)$ plane
$\dot{\Lambda}$	plastic multiplier
λ	slope of the NCL and CSL in the $(\ln p', v)$ plane
μ	reducing factor for component of vector $\boldsymbol{\beta}$ normal to the stress increment vector
ν	Poisson's ratio
ξ	size parameter for plastic potential definition
ρ	unit mass
$\boldsymbol{\sigma}'$	effective stress vector
σ'_a	axial (vertical) effective stress
σ'_c	effective confining pressure
σ'_{ci}	initial effective confining pressure
σ'_r	radial effective stress
$\Delta\boldsymbol{\sigma}'_s$	elasto-plastic part of the stress path
$\Delta\boldsymbol{\sigma}'_{ss}$	sub-increment stress vector
σ'_y	isotropic yield stress
$\boldsymbol{\sigma}'_Y$	yield point stress, (p'_Y, q_Y)
$\hat{\boldsymbol{\sigma}}'$	direction of the stress increment vector
$\dot{\boldsymbol{\sigma}}'_\perp$	direction perpendicular to the stress increment vector
τ	shear stress
ϕ'	effective angle of internal friction
X	damage variable
Ψ	dilatancy
ψ	interpolating parameter for the kinematic hardening modulus
$\bar{\psi}$	state parameter
ω	shear-dependence parameter for hardening law

Abbreviations

ASTM	American Society for Testing and Materials
BP	back pressure
BS	bounding surface
CEN	European Committee for Standardization
CASM	clay and sand model
CSSM	critical state soil mechanics
CP	cell pressure
CSL	critical state line
D	drained test

DSS	direct simple shear test
FEUP	Faculty of Engineering of the University of Porto
IB	intact boundary surface
IC	isotropic compression test
IDMEC	Institute of Mechanical Engineering and Industrial Management of the University of Porto
LabGeo	Geotechnical Laboratory of FEUP
LNEC	Portuguese National Laboratory for Civil Engineering (Laboratório Nacional de Engenharia Civil)
LDT	local deformation transducer
LVDT	linear variable differential transformer
MCC	modified Cam clay
ME	modified Euler algorithm
NCL	normal compression line
OCC	original Cam clay
OCR	overconsolidation ratio
P	longitudinal (prime) seismic waves
PID	proportional–integral–derivative controller
PN	pore pressure
RK	Runge-Kutta algorithm
RKE	Runge-Kutta-England algorithm
S	shear (second) seismic waves
SBS	state boundary surface
TC	cyclic triaxial test
TX	(monotonic) triaxial test
U	undrained test
UCS	uniaxial compression strength
UCT	uniaxial compression test
UPC	Technical University of Catalonia

Chapter 1.

INTRODUCTION

1.1. GENERAL

Strain accumulation due to low-amplitude repeated loads is a major issue in a vast variety of geotechnical infrastructures and structures such as embankments, foundation layers of wind turbines or storage tanks. In the past, the study of strain accumulation has been pursued through empirical laws. Such methodology is not very reliable, as the results do not have a general validity. As reported by Wichtmann et al. (2005), there is a need for a systematic study on cyclic loading, since the present studies have been relying on experimental tests with insufficient number of loading cycles and the empirical laws inferred are not complete or contradictory.

A theoretical approach can be followed through a constitutive model based on a critical state soil mechanics framework. One-surface models cannot reproduce the complex behaviour of soils under repeated loading conditions (Yu, 2006). Some authors tried to improve classic models by introducing in the theoretical framework some law relating material stiffness with the number of cycles, obtaining a semi-empirical approach (e.g. Wichtmann et al., 2010; Ni et al., 2015) which are able to infer the accumulation of permanent strain at the end of each loading cycle, but not to reproduce accurately the evolution of strain within the cycle and consequently the stress-strain hysteretic loop observed in experimental data.

For this reason, more complex theories were developed within the framework of elastoplasticity. Models based on generalized plasticity (e.g. Tonni et al., 2006; Fu et al., 2014), bounding surface plasticity (e.g. Dafalias & Herrman, 1982; Bardet, 1986; Yu et al, 2007; Kan et al., 2014) and kinematic hardening plasticity (e.g. Oka et al., 1999) proved to be capable of reproducing the experimentally observed smooth transition from elastic to fully plastic state and the hysteretic loop in cyclic loading.

In the framework of bonding surface plasticity, the classic single yield surface approach is replaced by a two surface option, with a smaller yield surface laying inside a larger bounding surface. The two surfaces are related by a mapping rule, associating each point of the internal surface with a corresponding point of the external surface, which in turns regulates the hardening modulus. Bardet (1986) used a radial mapping rule and an associated flow rule to model the cyclic behaviour of sands; Yu et al. (2007a), with a similar mapping rule and a non-associated flow rule, proposed a model intended for both sandy and clayey soils (CASM-c).

In the above-mentioned models, hardening is isotropic, meaning that the yield and bounding surface share a common origin and the yield surface expands or contracts without moving. In the kinematic hardening plasticity framework, the yield surface translates in the stress space following a translation

rule that is usually proportional to the increment of plastic strain (Prager, 1955). In Oka et al. (1999) a nonlinear kinematic hardening rule is proposed, in which a term dependent of the accumulated plastic strain is added to the linear Prager term. In this way, the Authors establish a history-dependent hardening rule, which can be reduced to the linear formulation by choosing particular parameters.

Other authors have combined the bounding surface model with a kinematic hardening approach, obtaining a moving yield surface and a hardening modulus dependent on the distance between inner and bounding surface (e.g. Al-Tabbaa & Muir Wood, 1989; Stallebrass & Taylor, 1997; Gajo & Muir Wood, 1999; Grammatikopoulou et al., 2006; Corti et al., 2016).

All the reported models have the common characteristic of being calibrated and tested using experimental data from monotonic tests or cyclic tests with a small number of loading cycles (typically less than 1000). Thus, despite the great amount of advanced constitutive models developed in many different approaches, there is still a lack in the modelling of low-intensity long-term cyclic phenomena with hundreds of thousands of loading cycles and low deviatoric stress.

1.2. MOTIVATION AND OBJECTIVES OF THE RESEARCH

Scientific literature presents many studies on the cyclic behaviour on unbounded soils and on the monotonic or static behaviour of cemented soils. Studies on the cyclic behaviour of cemented soils are less frequent. The studies found are either oriented at the experimental study of the mixture or at the definition of a theoretical constitutive model. Experimental studies are usually characterized by the following drawbacks:

- the presented experimental plans are either incomplete or not consistent;
- the number of loading cycles involved in the study is usually low;
- experimental results are not modelled or are modelled only through simple empirical models.

On the other hand, theoretical works on constitutive modelling present often the following pitfalls:

- they are calibrated against a scarce amount of laboratory tests;
- the performance of the proposed model is assessed against a very small number of loading cycles, thus they are oriented at the short-term modelling and not at reproducing the long-term behaviour of the material;
- the models are aimed at either reproducing the progressive plasticisation observed in cyclic tests or at the destructuration observed in cemented soils, but the two effects are rarely reproduced simultaneously.

Furthermore, the two typology of studies presented are often separated. Combining the experimental and the modelling studies in an integrated approach, with the two aspects interacting and influencing each other, would be certainly beneficial.

For these reasons, the need for the present study arose, with the following main objects:

- performing a complete and consistent long-term experimental study, with the same type of test repeated on the soil in cemented and uncemented conditions and under cyclic load conditions;
- the key parameters of this study (degree of cementation, initial compaction, initial confinement and cyclic loads) span a great range of values, in order to give a complete mechanical characterization of the material and, in the same time, to serve as a solid base for the successive definition of an original constitutive model and for its calibration and testing;

- defining a new constitutive model, based on the behaviour observed in the laboratory tests and capable of account for the long-term behaviour of the soil and for its loss of structure due to the accumulated deformation.

The main challenges of the present work are to perform a large set of cyclic tests with a much higher duration than the current practice and to merge the experimental and theoretical approach in a single framework.

1.3. THESIS LAYOUT

This doctoral thesis is organized in nine chapters. After a brief introduction, Chapter 2 describes the main characteristics of the behaviour of cemented soils and presents the state of the art of the tests performed over such mixture in static and cyclic conditions. Particular emphasis is dedicated to the tests performed by other authors on artificially cemented Porto residual soil. Finally, the state of the art of soil modelling is presented.

Chapter 3 presents a review of some advanced constitutive models able to represent the characteristic features of a cemented soil in monotonic and cyclic conditions, such as the degradation of the bonds, the accumulation of permanent deformation with cycles, and the hysteretic cyclic stress-strain loops. Attention is focused on those constitutive models that represent the theoretical base for the definition of the new constitutive model proposed in the present research.

Chapter 4 and Chapter 5 describe the laboratory tests performed, presenting the detailed description of the equipment used, procedures followed and results obtained for each typology of test. In Chapter 4, the dynamic tests and UCS tests are presented, whilst Chapter 5 is focused on the set of long-term cyclic drained and undrained triaxial tests performed over uncemented and cemented soil specimens with different degree of compaction and cement content.

Chapter 6 introduces the theoretical bases for the definition of the proposed constitutive model, defined in the frame of bounding surface plasticity and equipped with a mixed isotropic/kinematic hardening law and a destructuration law. The aim of such model is to account for the cyclic accumulation of permanent strain and the loss of structure in the cemented bonds. Once the model is defined, some analytical solution in simplified hypotheses are derived, in order to validate the model by comparing the analytical solutions with the numerical output of the model.

Chapter 7 presents the numerical implementation of the model through two explicit methods for the numerical resolution of differential equations. Such methods are implemented for the case of drained and undrained stress paths in stress-driven and strain-driven triaxial tests. The advantages and disadvantages of the methods are illustrated.

In Chapter 8, the model performance is investigated through a series of simulated tests. Then, the model is calibrated and its performance is checked against the experimental data available. The principal positive outcomes and drawbacks of the model are analysed. A tentative modification of the drawbacks of the model is attempted by implementing some modifications to the original formulation of the model.

In Chapter 9, the main conclusions of this study are resumed and some possible future developments are outlined.

Chapter 2.

MONOTONIC AND CYCLIC BEHAVIOUR OF UNCEMENTED AND CEMENTED SOILS

2.1. INTRODUCTION

The improvement of soil by the addition of hydraulic cement as an alternative to traditional techniques in geotechnical engineering is a very interesting solution. Due to the growing constraints imposed by environmental issues, the use of large amounts of soil has been conditioned. Moreover, the costs of transport of such quantities have increased more and more over the years. Another problem related to untreated soils is the degradation of subgrades in highway-pavement and railway-track support systems, giving rise to high maintenance costs and reduced serviceability. The main causes of deterioration are the accumulation of plastic deformation and the resilient cyclic deformation leading to pavement cracking by fatigue.

Soil and granular materials stabilization with hydraulic cements is an interesting solution as stiffness and strength are highly improved by the treatment. It is especially attractive where high traffic loads with considerable number of passages are expected and high mechanical properties of subgrade soils are required. Furthermore, such a mixture allows reducing the amount of natural soil to be used, with environmental and economic savings. Many authors have studied the cyclic behaviour of soils and soft rocks (e.g.: Barksdale, 1972; Paute et al., 1996; Gomes Correia, 2004; Dawson et al., 2005; Werkmeister et al., 2005; Wichtmann et al., 2005; Puppala et al., 2009); others have studied soil-cement mixtures under monotonic and static conditions (e.g.: Clough et al., 1981; Leroueil & Vaughan, 1990; Leroueil & High, 2003; Consoli et al., 2010; Rios et al., 2012, 2014; Viana da Fonseca et al., 2014). It is interesting to note that although European Committee for Standardization (CEN) has already concluded a standard on "Cyclic load triaxial test for unbound mixtures" (CEN, 2004) there is still a lack in the equivalent for hydraulic bound mixtures.

The addition of cement in small quantities (2 to 7% of total weight) transforms the constitutive behaviour of the soil. This develops interparticular bonds, becoming a structured soil, giving rise to specific characteristics, such as tensile strength and real effective cohesion. Recently many authors adopted the term microstructured soil, to distinguish this phenomenon of bond at interparticular contacts with the macroscopic arrangement of the soil. Microstructure is a common characteristic in a great variety of natural soils and soft rocks. Natural cementation arises from many causes (such as solution and deposition of silica, carbonates or hydroxides, from cold welding at interparticular contacts under high pressure, from recrystallization of minerals during weathering) and interests a wide variety of soils (soft clays, stiff clays, granular and residual soils, weathered rocks) (Leroueil & Hight, 2003). Studies of the

properties of such materials showed that, despite of their variable and complex origins, the effects of natural or artificial cementation may be described in a simple and general way (Leroueil & Vaughan, 1990).

Classic constitutive models such as the critical state soil mechanics approaches, take into account the concepts of initial porosity and its subsequent modification by stress history, but do not include the effects of cementation, which was considered a characteristic only typical of rocks. More recent constitutive models are based on the classic ones (namely the Modified Cam-Clay model) and add new features in order to take into account the evolution of bonding with damage caused by monotonic or cyclic loading (degradation effect). All these models reduce to the classic ones when the bonding is zero.

2.2. BEHAVIOUR OF CEMENTED SOIL UNDER MONOTONIC LOADING CONDITIONS

In the following section, the principal features of the behaviour of cemented (or bonded) soils will be recalled. In literature, different definitions are found referring to similar, yet not coincident concepts as structure, fabric and bonding. In the present work, the definitions expressed hereinafter are adopted.

The term structure was introduced for clays by Mitchell (1976), as being the combination of fabric and bonding. Fabric can be described as the arrangement and distribution of the particles comprising the soil (Cuccovillo & Coop, 1997). Bonding (or cementation) refers to all the forces linking the particles among them. For a fine soil, such forces can originate from chemical interactions among particles or from interparticular cementing. For a coarse-grained soil, bonding can only take the form of interparticular cementing since interparticular forces are insignificant. Cementation has been recognised in many different soils, such as soft clays, stiff clays, granular soils, residual soils, weak and weathered rocks (Leroueil & Vaughan, 1990). This characteristic is originated from many natural causes or it can be artificially induced. Normally it is more complicated to study naturally cemented materials, because it is sometimes difficult to obtain the corresponding unbonded specimens of the same material and because of the variations in the properties of the intact samples, which prevent the preparation of many copies of identical specimens. For artificially cemented specimens the level of cementation and the homogeneity of the specimens are assured. Regardless the diverse nature of the cementation, the properties of a cemented soil can be described in a general and congruent way, as shown by Leroueil & Hight (2003).

Fig. 2.1 shows the main differences between a non-bonded soil as described by critical state soil mechanics (figures (a) and (c)) and a cemented soil (figures (b) and (d)). At the same void ratio, cemented soil has higher isotropic yield stress, undrained shear strength and stiffness than the corresponding non-bonded soil.

2.2.1. ISOTROPIC COMPRESSION

Isotropic compression tests carried out by many authors over different types of soil show that cemented soils can reach a region in the isotropic compression plane that is not permitted for the same reconstituted soil. The apparent isotropic yield stress of the cemented soil is higher than the value normally associated with its void ratio. As seen in Fig. 2.1b, this value increases from point L to Y. Beyond this value, the curve shows a steeper inclination than the normal compression line for uncemented soil and, for higher values of the mean effective stress (p') the two lines eventually coincide, meaning that the bonds are completely destroyed. Cuccovillo & Coop (1993) tested artificially cemented sands, varying the amount of cement added to the soil. The results of the isotropic compression tests (reported by Cuccovillo & Coop, 1999) showed an increase of the isotropic yield pressure. Nevertheless, depending on the level of

cementation, two different behaviour were observed. Strongly cemented soils reached states outside the intrinsic normal compression line (NCL) defined by the uncemented soil, while the weakly bonded soil yielded before reaching the NCL (Fig. 2.2).

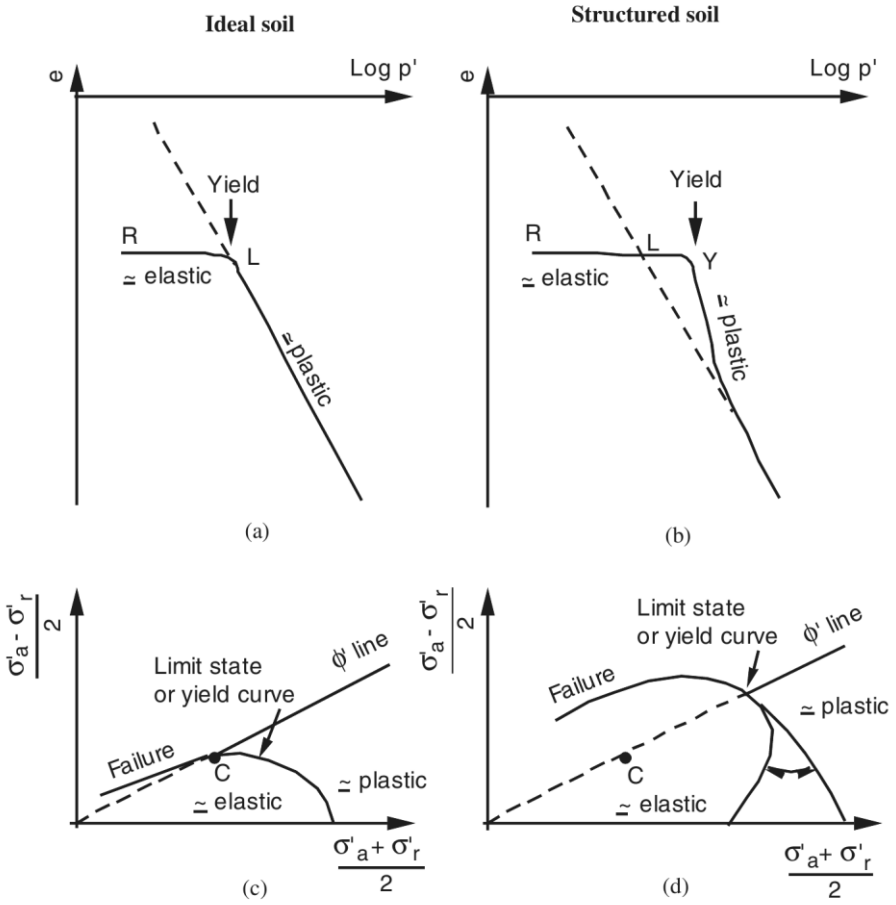

Fig. 2.1 - Schematic behaviour of ideal and bonded soils (Leroueil & Hight, 2003)

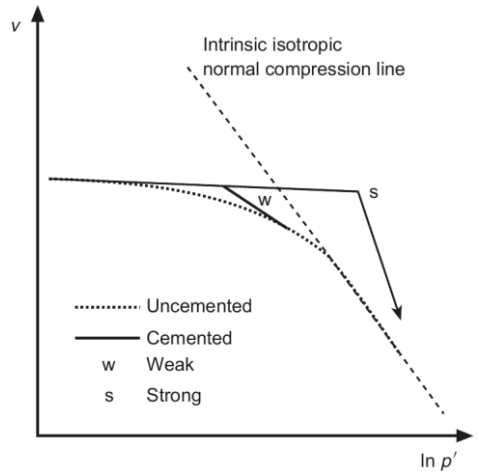

Fig. 2.2 - Schematic comparison of the isotropic compression of weakly and strongly cemented carbonate sand (Cuccovillo & Coop, 1999)

Cuccovillo & Coop (1999) extended the concept of normalisation used in the critical state soil mechanics framework for reconstituted material to structured soils. According to the classic concept of normalisation, the stresses are normalised by the equivalent mean effective stress on the NCL or the CLS (i.e. the mean effective stress with same specific volume of the initial state). For weakly cemented soils, the normalisation is the same, since the NCL of the uncemented soil is the same as the cemented soil. For strongly cemented soils, the stress in isotropic compression can overcome the NCL of the uncemented soils. Therefore, the intrinsic NCL is no longer the boundary surface of the soil. Instead, a bilinear boundary surface is observed (Fig. 2.3): for intact soils, the stress reaches higher stresses before isotropic yield stress is reached. As stress continue to increase, structure is progressively damaged and the stress path follows a line steeper than the NCL for the uncemented soil. When the soil structure is completely damaged (for isotropic stresses higher than point C), the boundary surface converge with the unbonded NCL.

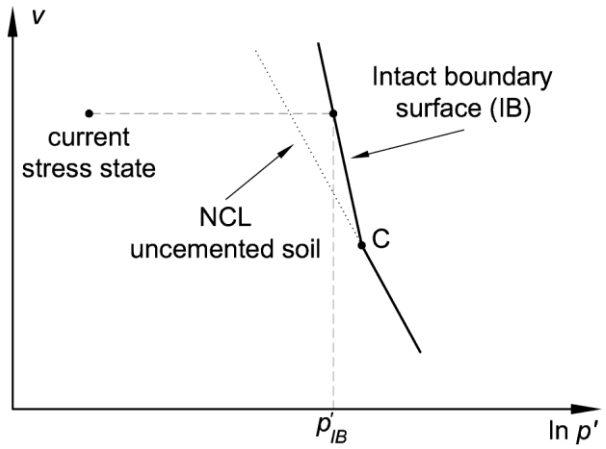

Fig. 2.3 – Isotropic compression for strongly cemented soils and definition of normalising parameter (after Cuccovillo & Coop, 1999)

This bi-linear boundary is called intact boundary surface (IB). The authors suggest that for strongly cemented soils, it should be used for normalisation instead of the CSL or the NCL, i.e. parameter p'_{IB} shown in figure shall be used as a normalising parameter. Such normalisation allows to trace the state boundary surface (SBS) of soils with different levels of cementation and to separate regions inside this surface of different behaviour, as explained in detail in the next section.

2.2.2. Peak strength and state boundary surface

The peak strength envelope of different soils reflect their cementation. Fig. 2.4 shows the peak strengths envelopes obtained by Rios (2011) from triaxial tests on artificially cemented specimens of Porto silty-sand with two specific levels of cementations (represented by black and white dots). In the same image, results retrieved from uncemented specimens are reported for comparison.

The image shows that the addition of cement leads to increment in the cohesion intercept (c') (corresponding to an increase in tensile strength), while the peak friction angle remains almost constant.

Fig. 2.5 shows the peak strength envelopes for cemented specimens subjected to small to high confinement pressures. For low confining pressures, two levels of cementations were studied, while for medium-to-high confining pressures all the specimens present the same level of cementation (represented by white dots in figure). In tests with low confining pressures, isotropic yield was not

reached during isotropic compression and the soil did not suffer great damage prior to shearing. For higher confining pressures, the soil was consolidated isotropically well above the isotropic yield stress and the soil bonding was partly damaged before the shearing loading was applied.

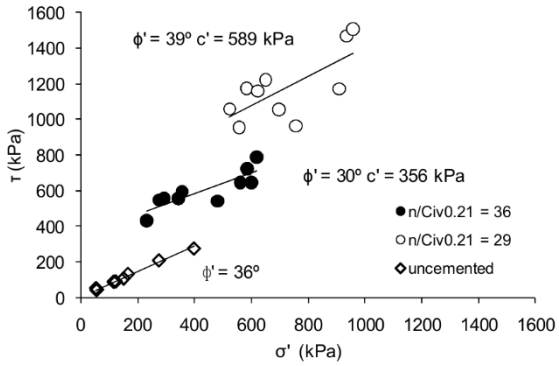

Fig. 2.4 – Stresses obtained in peak conditions on uncemented and cemented specimens of residual soil from Porto granite (Rios, 2011)

Following the framework of Cuccovillo & Coop (1999), more confined specimens suffer more damage during isotropic consolidation. Therefore, during triaxial shearing, equally cemented specimens subjected to different consolidation pressures show different patterns of behaviour. In low-to-medium consolidated specimens, the shear peak points are above the ultimate envelope, while for high consolidation levels, the peak and ultimate envelopes tend to coincide.

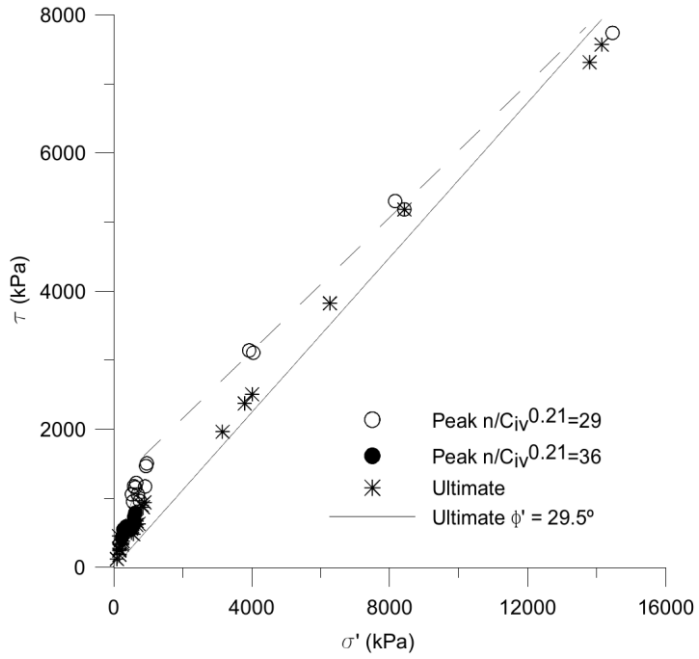

Fig. 2.5 – Peak strength points and envelopes for cemented specimens (Rios, 2011)

Using the normalisation described in the precedent section (Cuccovillo & Coop, 1999) it is possible to obtain a unique state boundary and yield surface for cemented soils, extending the normalisation usually applied to the uncemented soils, while using the usual normalisation (against NCL or CSL) multiple SBSs are found for differently consolidated cemented soils. This implies that cementation shall be treated as an intrinsic property of the soil. In Fig. 2.6 the framework obtained by the authors is shown.

The outer intact SBS refers to an intact specimen of the more strongly cemented soil, that is, an intact samples sheared from states located on the portion of the IB convergent with the NCL (i.e. isotropic stresses less than point C in Fig. 2.3). This surface limits the possible states that could be reached by the cemented soil. Uncemented (or reconstituted) specimens sheared from a state on the NCL follow a path that describes an intrinsic SBS. Such surface is the limit surface for the same soil in uncemented conditions or, alternatively, for a cemented specimen from which the cementation was completely removed. This is the case of a cemented specimen, isotropically consolidated to a value for which the intact boundary surface has converged with the NCL (i.e. beyond point C). For intermediate cases, bonding is partly damaged and the corresponding stress path is included in the area between the outer SBS and the intrinsic SBS. In the image, the yield surface is shown, which was determined as the locus of the points where the onset of plastic strain takes place during monotonic tests. The authors state that the yield surface is the boundary between two distinct regions inside the SBS, with different shear behaviours for the intact soil. Inside the yield surface, shear behaviour is controlled by bonding, thus soil resistance is cohesive. No volumetric plastic strain is expected in this area and soil stiffness is enhanced by bonding. Outside this surface, the behaviour is frictional and controlled by a progressive mechanism of bond degradation and particle breakage. The soil shows compressive volumetric plastic strain.

Besides the different SBS, an important difference between cemented and uncemented soil behaviour is that the yield surface for a weakly cemented (or uncemented) soil occupies a significantly much smaller portion (or no portion) of the permissible states in the normalised stress plane. Hence, the behaviour is mainly frictional and soil stiffness is lower. Volumetric strain is characterised by dilation on the dry side of the critical state, or compression on the wet side of the critical state, following the usual framework of critical state soil mechanics.

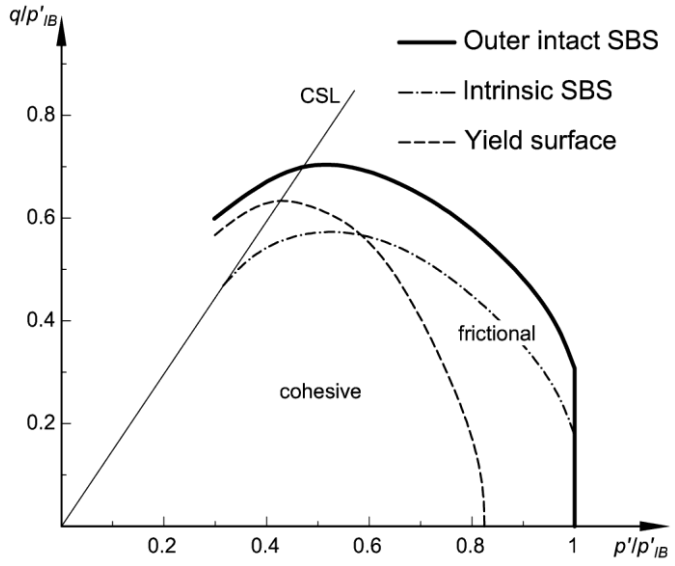

Fig. 2.6 – Normalised stress plane (after Cuccovillo & Coop, 1999)

2.2.3. SMALL-STRAIN STIFFNESS

The effect of cementation is also observed in the stiffness properties in the small strain domain. The value of small-strain stiffness Young's (E_0) and shear (G_0) moduli obtained by Amaral (2012) (Fig. 2.7) through low energy dynamic tests (using seismic waves propagation techniques), show that, for

specimens with the same degree of compaction, the moduli grow with increasing cement content, evidencing the influence of bonding in small strain stiffness.

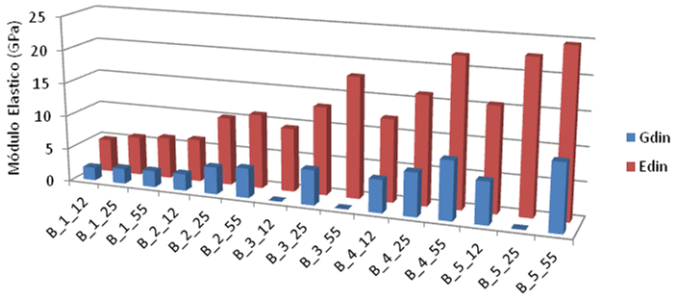

Fig. 2.7 – Influence of cement content on the small-strain stiffness moduli. The first number after letter "B" refers to the cement content by weight (C) while the second one refers to the degree of compaction (number of blows per layer during Proctor compaction) (Amaral, 2012)

The behaviour of cemented soil subjected to large strain shows that cemented soils are subjected to considerable softening after yielding. For this reason, the stress point at large strain for a cemented soil does not lie on the yield surface, as schematized in Fig. 2.1c (point C), but inside, as schematized in Fig. 2.1d. This is because the yield surface of the uncemented soil expands as an effect of cementation, increasing the yielding stress. After yielding has been reached, the bonds start to damage (indeed, bond damage is a progressive process but it mostly occurs after yielding), causing a decrease in deviatoric stress. When the bonds are destroyed, the stress level stabilises and no further softening is observed. Rios (2011) has confirmed this behaviour in a series of drained and undrained triaxial tests on cemented Porto silty-sand (Fig. 2.8).

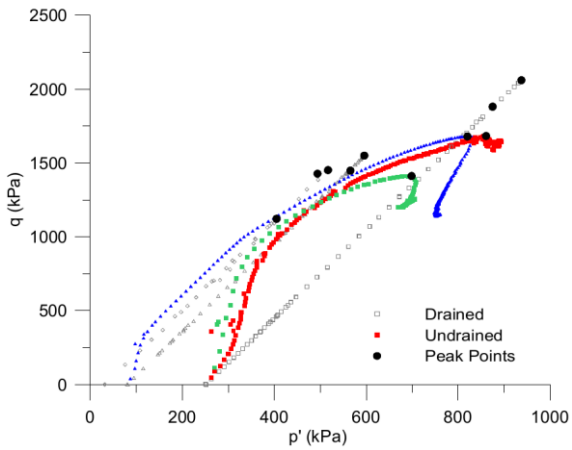

Fig. 2.8 – Results of triaxial compression tests over cemented Porto silty-sand specimens (Rios, 2011)

The stress-paths reported in the figure show that the stress state reaches the yield curve and subsequently (for large deformations) it decreases (softening) and ultimately stops inside the yield envelope, in a position that corresponds to the elastic domain of the corresponding intact specimen.

2.3. BEHAVIOUR OF SOIL UNDER LONG-TERM CYCLIC LOADING

Strain accumulation due to low-amplitude repeated loads is a major issue in a vast variety of geotechnical infrastructures and structures such as embankments, foundation layers of wind turbines or storage tanks, as reported by Wichtmann & Triantafyllidis (2012) (Fig. 2.9).

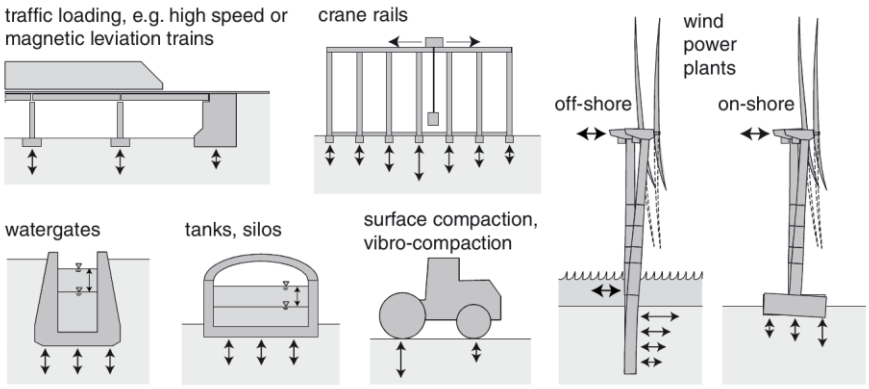

Fig. 2.9 – Sources of cyclic loading of soils (Wichtmann & Triantafyllidis, 2012)

The same authors define long-term cyclic loading (or high-cyclic or polycyclic loading) the repeated loading involving a large number of cycles ($n_{cyc} > 10^3$) with a relative small strain amplitude ($\varepsilon_{cyc} < 10^{-3}$). If the load cycles are applied at a low amplitude and with a low frequency, the inertial forces are negligible and the cyclic loading is considered quasi-static. If the frequency is large, inertial forces are relevant and the loading is dynamic. Often, the transition from a quasi-static to a dynamic loading is considered to be at a frequency around 5 Hz.

According to Pasten et al. (2014), the long-term response of geomaterials subjected to repetitive loading can be characterized by either ratcheting or shakedown behaviour. Ratcheting is defined as the sustained long-term accumulation of shear strain during repetitive loading; conversely, shakedown is a stable deformation state reached by the soil when strain accumulation decreases with the number of cycles and the plastic strain increment per cycle becomes null.

As reported by Sharma (2004), the cyclic tests can be classified as "one-way" or "two-way" tests depending on whether or not there is any principal stress reversal during cyclic loading. The term "one-way" refers to cycling in which the deviator stress is always positive and "two-way" implies that the deviator stress changes sign. Mao & Fahey (2003) refer to symmetric cyclic tests those tests in which the deviatoric cyclic stress is applied around a nil average value; otherwise, the test is referred to as non-symmetric.

A cyclic loading can be stress-driven or strain-driven, depending on the boundary conditions imposed (Fig. 2.10). For a stress-driven cyclic loading, a cyclic stress is prescribed on the surface of the soil element. Such configuration produces closed stress loops in the stress plane, and not perfectly closed strain loops in the strain plane, hence, to accumulation of plastic strain. Conversely, a strain-driven cyclic loading (with cyclic strain imposed on the boundary of the soil element) leads to perfectly closed strain loops and variation of the stress state. Finally, a simultaneous accumulation of stress and strain in mixed boundary value problems is also possible. In such situation, only some components of the stress and strain vectors are prescribed and others are free to change according to a constitutive law.

Conventional drained cyclic triaxial test is an example of stress-driven cyclic loading. In this kind of test, vertical stress varies cyclically between an upper and a lower value and the horizontal stress is held

constant (through the imposed effective confining pressure). In this case (Fig. 2.11), for granular unbonded soils granular a gradual strain accumulation is observed in each cycle, in the shear and volumetric component, as reported by Pasten et al. (2014).

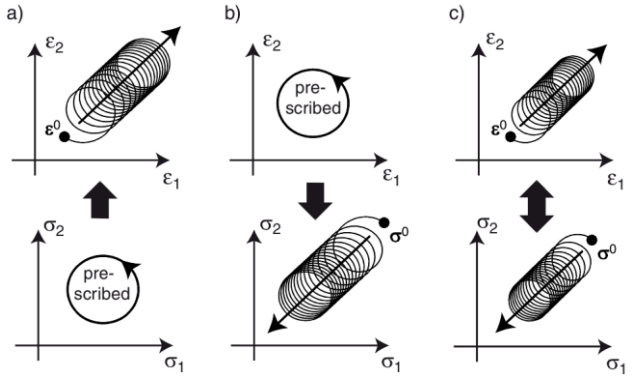

Fig. 2.10 – Accumulation of stress or strain (Wichtmann & Triantafyllidis, 2012)

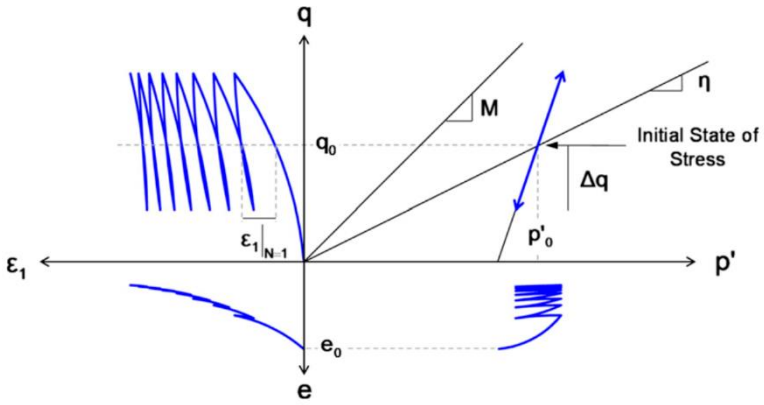

Fig. 2.11 – Behaviour of a granular material subjected to drained cyclic triaxial loading (Pasten et al., 2014)

Undrained cyclic triaxial test is usually performed as a mixed boundary problem, with an imposed component of stress, which typically is the deviatoric stress, and an imposed component of strain, which is the volumetric strain (equal to zero). In such case, as the change in volume is prevented, the pore water pressure can increase and decrease and, consequently, the mean effective stress progressively changes with increasing number of load cycles. Similarly, the unrestrained component of the strain vector (deviatoric strain) is free to change and an accumulation of this component during the cyclic loading is observed.

Extensive research has been performed on uncemented and cemented soils in undrained and drained cyclic loading conditions. In general, the conceptual frameworks built to explain the soil response subjected to small-strain repetitive loading are conceived as an extension of the framework used to explain the consider that the soil behaviour observed during monotonic tests can be used to describe the behaviour during cyclic tests. In other words, the cyclic tests executed, even when performed in stress states far from ultimate conditions, were planned and analysed bearing in mind the patterns of behaviour and the boundary surfaces observed for large-strain monotonic tests carried out under various confining pressures and up to ultimate shearing conditions.

2.3.1. RESPONSE OF UNCEMENTED SOIL UNDER CYCLIC LOADING

The study of the long-term response of unbonded and bonded geomaterials subjected to repetitive loading is a complex task, due to the large number of variables involved. A relevant study on the permanent deformation due to high-cyclic loading was performed at Ruhr University (Wichtmann et al., 2005; Poblete et al., 2011) on uncemented reconstituted granular soil. A set of drained cyclic triaxial tests with one thousand cycles was performed with different stress amplitudes, initial relative densities, average mean pressures and average stress ratios. The authors point out some relevant variables affecting the response of uncemented soil under conventional cyclic triaxial loading, namely:

- amplitude of the stress loops;
- average mean stress;
- average stress ratio;
- average void ratio.

The authors performed a series of drained tests with same average effective confining pressure and varying the deviatoric stress amplitude. The results show that the strain amplitude increases for increasing stress amplitude, as expected. Moreover, the accumulation curves showed that higher cyclic stress amplitudes cause larger accumulation rates. The results (reported in semilogarithmic scale in Fig. 2.12) show that accumulated strain increased almost proportionally with the logarithm of the number of cycles up to 10000 cycles and then a higher rate of accumulation is observed.

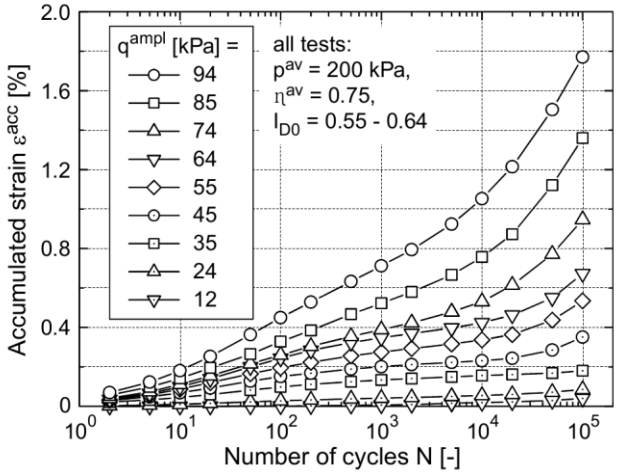

Fig. 2.12 – Accumulation curves in drained triaxial tests with different stress amplitudes (Wichtmann et al., 2005)

In early studies on cyclic loading, average stress was not taken into account as a key parameter for the interpretation of the soil response. Many studies were performed on dry or saturated sand specimens in drained conditions, submitted to cyclic simple shear tests (e.g. Silver & Seed, 1971; Youd, 1972; Cuellar et al., 1977; Sawicki & Swidzinski, 1989). Results showed none or little influence of the confining pressure (or applied vertical load, in the case of simple shear tests) on the accumulated strain and strain amplitudes observed in the tests. Further studies were performed in cyclic triaxial compression (e.g. Allen Marr & Christian, 1981; Wichtmann et al., 2005) and extension (Wichtmann et al., 2007) tests. All these studies reveals that mean effective stress has an important influence on the accumulation of permanent strain and on the evolution of the cyclic stiffness moduli. In particular, the accumulated strain at a certain number of cycles decreases for increasing values of mean effective stress (Fig. 2.13). Such result is hardly explainable with a classic elasto-plastic approach; on the other hand, such outcome fits in a bounding surface plasticity framework, illustrated in the following sections.

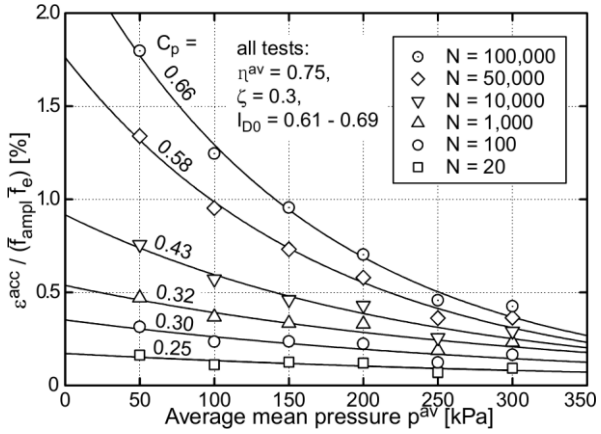

Fig. 2.13 – Accumulation curves in drained triaxial tests with different average mean pressures (Wichtmann et al., 2005)

This framework is also able to explain the effect of the average stress ratio. As the same authors show, accumulated axial strain increases for increasing values of the average stress ratio. Thus, accumulated strain has an inverse correlation with average mean stress and a direct correlation with the average stress ratio.

Many authors agree on the importance of the initial void ratio (or the correspondent relative density for sands) on the accumulated strain. As expected, the authors report an increased accumulated axial and/or volumetric strain in specimens with higher initial void ratios (i.e. looser soils) under simple shear (e.g. Silver & Seed, 1971; Youd, 1972; Sawicki & Swidzinski, 1989) and triaxial (e.g. Allen Marr & Christian, 1981; Wichtmann et al., 2005, 2007) tests.

Finally, the loading frequency does not have effects on accumulated strain for values less than 2 Hz (Sawicki & Swidzinski, 1989; Wichtmann et al., 2005)

Qadimi & Coop (2007) stressed the importance of the initial state of a soil in the isotropic compression plane (v - ln p') for its cyclic behaviour, and, in particular, where that state is located relative to the locations of the normal compression line (NCL) and the critical state line (CSL) of the soil. This approach was aimed at extending the critical state frameworks (where density and stress levels cannot be considered separately) to cyclic loading. The authors stress the importance of performing cyclic tests at high confining pressures to create a complete framework.

Lekarp & Dawson (1998) performed an experimental study on five type of granular soils (four well graded and one poorly graded) performing hollow cylinder tests and triaxial cyclic tests up to 80000 cycles. Triaxial tests were performed by varying both vertical stress and confining pressure, following the indication of the European Standard (CEN, 2004). Thus, different stress path from the conventional triaxial test were explored. The authors observed that accumulated permanent strain increased with maximum q/p stress ratio and the length of the stress path.

2.3.2. RESPONSE OF CEMENTED SOIL UNDER CYCLIC LOADING

The response of cemented soil and soft rocks subjected to cyclic loading has been less studied comparatively to the great amount of works on cyclic behaviour of uncemented soils. Many studies on the cyclic behaviour of uncemented soils were focused on the liquefaction phenomenon. Clough et al. (1989) performed a series of cyclic tests on naturally and artificially cemented sands. The authors showed that only the weakest naturally cemented sands were potentially subjected to liquefaction, and

this phenomenon is not likely to occur in strongly naturally cemented or in artificially cemented granular materials. Thus, such phenomenon is not of interest in the present research, as the tested material is either strongly cemented or uncemented but tested in drained conditions (where liquefaction is not expected).

Morgan & Williams (1970) present one of the first studies on cyclic behaviour of artificially cemented sand with hundreds of thousands (up to 732000) loading cycles. The study had the practical aim of investigate the material used as base layers in transportation infrastructures According to the local practice, small quantities of cement were added to the medium, poorly graded sand studied, corresponding to a percentage of 2% in weight. The testing programme consisted in a set of constant stress ratio cyclic triaxial tests (Fig. 2.14). The authors stress the importance of complementing the experimental research on the cyclic behaviour of cemented specimens with equivalent monotonic and static tests and with cyclic tests performed over uncemented specimens. Thus, prior to the realization of the cyclic programme, the authors investigate the effect of cement curing by performing a series of unconfined compression tests (UCT) on cemented specimens with different age. Results showed an increase of unconfined compression strength with the curing time and a stabilization after approximately 20 days. Then, Mohr-Coulomb envelope was determined through conventional monotonic tests. An increase in the apparent cohesion is observed with respect to the uncemented material, while the friction angle remains approximately constant. Mohr-Coulomb envelope was used as the reference envelope to define the stress applied in cyclic tests, which were expressed as a percentage of the expected static strength of the material. Two alternative criteria can be followed in the determination of the ultimate strength for the material. The stress on the ultimate envelope corresponding to the same maximum horizontal stress applied during cyclic loading is an option. Alternatively, the strength corresponding to the same stress ratio applied in the cyclic loading can be considered. This last value corresponds to the intersection between the ultimate envelope and the extension of the cyclic stress path. The authors suggests that the second criterion should be used as a normalising parameter. The long-term cyclic tests were performed with a frequency of approximately 0.4 Hz. The specimens were tested with an initial age of 7 days. Due to the long duration of the tests, the strength of the specimen increased considerably during the test, adding complexity to the analysis. The authors conclude that cyclic failure can be brittle or caused by incremental strain. If failure happens, it is likely to happen in the early cycles, otherwise cyclic loading continues indefinitely without causing failure. The authors found that a lower limit value of the normalised applied deviatoric stress exists for which failure does not occur. An upper limit is found beyond which all specimens fail. As for the accumulation of axial strain, the authors found that a stabilization is observed after a certain number of cycles, but this is due to the increasing strength of the bonds during loading caused by cure. The authors further refer that in similar tests on uncemented material no sign of stabilization in the axial strain accumulation was observed. Comparison with uncemented specimens shows that the effect of cementation is the increase of stiffness and the gain on tensile strength.

Nnadi & Mitchell (1991) present a similar study on a well-graded sand with higher confining stress. The aim of the research is to study the response of cemented tailings backfill materials. Portland cement was added in percentages of 3 or 5% in weight and a confining pressure of 50 or 100 kPa was imposed in cyclic triaxial and plane strain tests. The results are presented in terms of a so-called stress ratio, which is the applied axial cyclic stress divided by the cyclic stress at failure in a static test under the same cell pressure. Similarly, also the axial strain was normalised by the axial strain corresponding to a stress equal to 95% of the stress at failure. Cyclic tests reached 6000 cycles. In opposition to Morgan & Williams (1970) results, no failure is observed for stress ratios in the range 0-1. The accumulated axial strain with the number of cycles presents a logarithmic trend of accumulation in this range. Some tests were performed with stress ratios higher than one, i.e. with cyclic stress higher than the ultimate static

stress. Such loading conditions, which would be impossible in monotonic conditions, are withstood by the soil in cyclic loading due to the transient nature of the load. Nevertheless, failure for incremental strain is observed in such tests within few loading cycles. Comparing the results of the two studies, one may conclude that specimens with 3% or more of cement content present a strong structure and do not fail inside the boundary surface, while percentages of 2% do not guarantee such outcome. Such comparison is limited by the different nature of the sands studied.

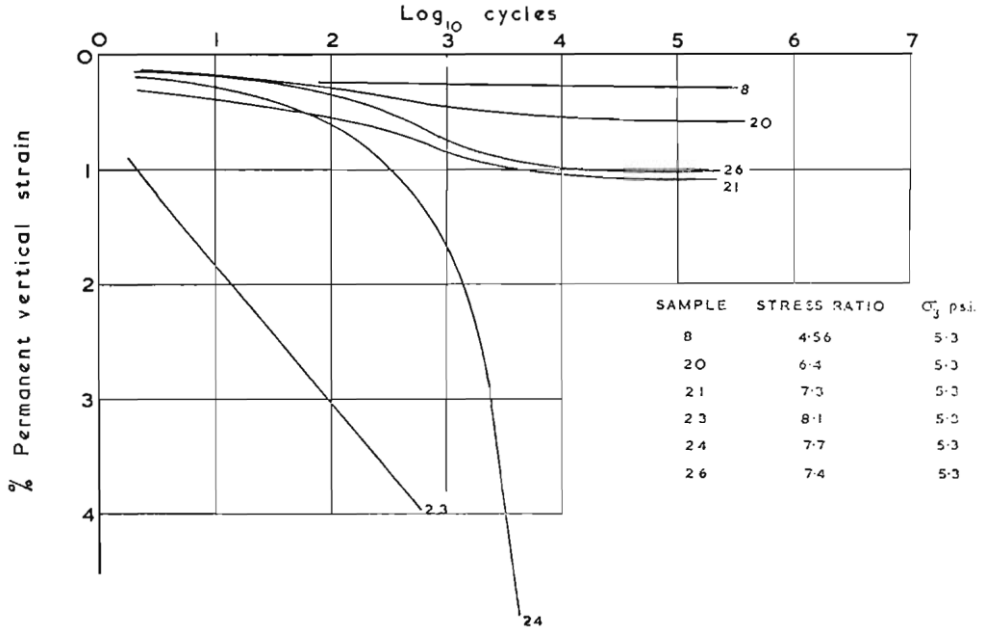

Fig. 2.14 – Accumulated vertical strain vs. number of cycles (Morgan & Williams, 1970)

Comprehensive cyclic test programmes were performed in the University of Sydney and in the University of Western Australia. Naturally cemented (Carter et al., 1988; Airey & Fahey, 1991) and artificially cemented (Zhao et Airey, 1992; Zhao et al., 1992; Yeoh & Airey, 1994, 1998; Sharma & Fahey, 2003a, 2003b; Sharma, 2004) calcareous soils were investigated in cyclic triaxial tests with thousands of loading cycles. A review of these studies is reported in Carter et al. (1999). The main objective of this research was the investigation of the cyclic strength characteristics (i.e. determination of the number of cycles to failure under given stress conditions). These authors present their findings in terms of cycles to failure vs. a so-called shear stress level, *S*. Such parameter (its specific formulation varied from one research to another) is a ratio of the maximum cyclic deviator stress imposed to the peak deviator stress obtained in an equivalent monotonic triaxial test. Since the studies were focused on cyclic failure, the applied *S* was rather high (0.7 to 0.9) and the results showed a good correlation with the number of cycles to failure. The high values of shear stress levels have an influence on the rate of accumulation of axial strain. In the first cycles, the accumulation is slow and progressively increasing; after a certain number of cycles, the rate of accumulation stabilizes at a constant rate (greater than the initial rate); when the specimen is approaching failure, the rate increases rapidly.

Yeoh & Airey (1994) present the curves of accumulated axial strain vs. the number of cycles in undrained cyclic tests on artificially cemented material. The curves show an initial linear trend in a bi-logarithmic representation, followed by a change in trend and a new trend with a higher rate of accumulation. The threshold between the two behaviour depends on the stress level applied. In tests with stress levels close to failure (e.g. 0.9), the switch between trends occurs within a hundred loading cycles. For long-term test conditions (S = 0.5) the change occurs after tens to hundreds of thousands of

loading cycles. A similar result is obtained for the same soil in drained conditions in Yeoh & Airey (1998). This result highlight the importance of performing a very high number of loading cycles in low-stress cyclic tests.

Pore pressure variation in undrained tests presents some patterns of behaviour recognized by different authors (Airey & Fahey, 1991; Yeoh & Airey, 1994; Sharma, 2004). During cyclic loading, pore pressure tends to increase in the first part of the test, corresponding to a reduction of mean effective stress, as typical of uncemented soils. Then, a peak is reached and a reversal in the sense of pore pressure generation is observe, with the pore pressure showing a decrease typical of a dilative soil. The peak points shown in Fig. 2.15 are referred to the results of Yeoh & Airey (1994). They approximately correspond to the threshold points in the axial strain accumulation shown by the same authors.

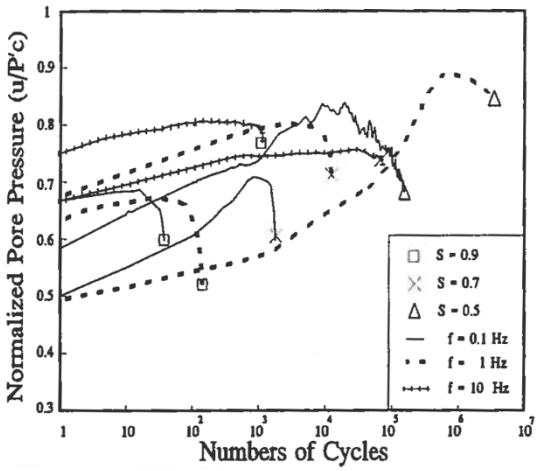

Fig. 2.15 – Pore pressure variation during cyclic loading (Yeoh & Airey, 1994)

The authors explain this reversal as the fact that the soil is approaching failure, as the sudden change in behaviour is sign of the progressive damage of cementation. Yeoh & Airey (1998) performed a similar study on the same artificially cemented soil in drained conditions. The accumulated axial strain results show a behaviour consistent with the undrained tests, while the accumulated volumetric strain shows a continuous positive increase (corresponding to a compressive behaviour) with the number of cycles. As the authors point out, this result contradicts the behaviour observed in undrained conditions in their precedent study, with a peak and a reversal in the sense of pore pressure accumulation.

2.4. MODELLING SOIL BEHAVIOUR UNDER CYCLIC LOADING

According to Lekarp & Dawson (1998), the main objective of research into long-term behaviour should be to establish a constitutive relationship allowing an accurate prediction of the amount of permanent strain at any number of cycles at any stress level. Many attempts have been made in the past to model the cyclic behaviour of uncemented and uncemented soils. Such models have the aim of extrapolating a general law with base on the experimental evidence retrieved in laboratory or in situ and on the case history. Following different approaches, the aim is to predict the evolution of the permanent strain and/or the variation of stiffness moduli as a function of the number of loading cycles, stress conditions and levels of cementation. This aim was pursued with an empirical or a theoretical approach, or with a mix of the precedent two.

Empirical modelling is the simplest approach, as they require a reduced computational effort. Typically, these models compute the variable of interest (stiffness modulus or one or more components of the

accumulated strain vector) at the end of a certain number of cycles. The relationship is inferred by fitting experimental data with a suitable mathematical law. This approach can give fast responses, especially when a very large number of cycles are involved. Nevertheless, the law is not related to a real physical framework. Additionally, the law is typically not general, being dependent on the boundary conditions applied. It is also very difficult to model more complex conditions, such as irregular cyclic stresses or different draining conditions.

Theoretical models are based on a physical (although simplified) representation of the studied material. They calculate the state of stress and strain in the medium in each stage of a loading-unloading cycle. In this aspect, their framework is not far from the theoretical models used for modelling monotonic loading. In fact, cyclic loading can be regarded as a series of alternate loading and unloading monotonic stress paths. Theoretical models can be divided in discrete element models and continuum constitutive models, depending on the type of physical model applied to the soil.

Discrete element models consider the soil as an assembly of particles with their mutual transmitted stresses. This approach is referred to as a micro-scale modelling of the soil. Although this approach is physically accurate, at present its application is cumbersome, as the computational cost associated to the representation of a large amount of particles and their mutual interactions is too high. Current results of discrete element analyses are more useful qualitatively than quantitatively. Muir Wood (2007) points out four main reasons for this:

- the number of particles that must be modelled for a realistic analysis is very large, and the duration of the analysis is consequently long.
- the model should be set up in three-dimensions, as two-dimensional analyses miss some key features of the soil behaviour. Obviously, this increases even more the complexity of the model.
- the majority of numerical analyses have made use of circular discs or spherical particles; thus, the real angular shape of the particles is not correctly modelled and the consequent interlocking effect is neglected.
- particle crushing has not yet been modelled satisfactorily.

For these reasons, continuum constitutive models (macro-scale models) are still the most widespread theoretical approach to soil modelling and are often simply referred to as constitutive models. In the following, some notable examples of empirical models and constitutive models are presented.

2.4.1. EMPIRICAL MODELLING

Empirical modelling is the simplest approach for modelling uncemented and cemented soil behaviour under repeated loading. This approach was the first to be used, as it allows modelling the behaviour of the soil without complex theoretical background and time-consuming calculations. Nevertheless, it is often too simplistic to represent a general framework for a soil, as it lacks of a physical background. Thus, empirical models are normally valid in the specific conditions of the tests performed.

This approach is usually based on a set of experimental data and it is aimed at modelling the permanent strain and/or stiffness variation with the number of cycles. According to Pasten et al. (2013), empirical models for cyclic loading can be divided as follows:

- models that describe one component of the accumulated strain as a function of the first load cycle, the number of cycles, the static state of stress, and the initial density;
- models that predict one component of the accumulated strain at a certain number of cycles as a function of the state of stress, the initial void ratio, and the static shear strength;

- models that predict the complete evolution of strain accumulation (i.e., magnitude and direction) as a function of the number of cycles, the state of stress, and the initial density.

The first two categories refer to simpler models, while the third includes models that are more sophisticated.

2.4.1.1. EMPIRICAL MODELS FOR UNCEMENTED SOILS

There are many examples of empirical models for unbounded soils under cyclic loading. The vast majority of the research carried out on loose soils in cyclic conditions involved cyclic triaxial tests or cyclic simple shear tests with a number of cycles that is normally not very high (usually n_{cyc} < 1000). The obtained data are used to model some fatigue-related characteristic, typically the accumulation of permanent axial strain or the degradation of stiffness with cycles. In general, all the models recognize an increase of the accumulated strain (ε_{acc}) with cycle numbers and a decrease of the strain accumulation rate ($\dot{\varepsilon}_{acc}$) with cycles.

According to Allotey & El Naggar (2005), under the conditions of uniform stress-controlled two-way cyclic loading, cyclic strain can be expressed by:

$$\gamma_c = f(D, S) \tag{2.1}$$

In which *S* represents the cyclic stress ratio and *D* is a fatigue damage function, which is an increasing function of the stress ratio and the number of cycles:

$$D = D(n_{cyc}, S) \tag{2.2}$$

Within this framework, many models were presented for different type of soils (granular soils, clays, tropical soils, subgrades for railway constructions, etc.).

Sawicki & Swidzinski (1989) developed a cyclic model where the volumetric strain is a function of the logarithm of an equivalent number of cycles:

$$\Phi = c_1 \ln(1 + c_2 z) \tag{2.3}$$

Where Φ is a variable dependent on the volumetric strain and the initial compaction, z is dependent on the number of cycles normalized by the cyclic strain amplitude, and c_1 and c_2 are constants. The authors recognized that all their experimental results in direct simple shear (DSS) tests align along this normalized relation, in a curve that they defined common compaction curve. Following research with triaxial compression tests and a greater number of cycles (Wichtmann et al., 2005) did not confirm this curve.

Lekarp & Dawson (1998), proposed a model for predicting the accumulated axial (vertical) strain ($\varepsilon_{a\ cum}$) at a given number of cycles ($\overline{n_{cyc}}$):

$$\frac{\varepsilon_{a\ cum}(\overline{n_{cyc}})}{L} = a\left(\frac{q}{p}\right)_{max}^{b} \tag{2.4}$$

Where *L* is the length of the stress path, $(q/p)_{max}$ is the maximum stress ratio reached in the test and a and b are material constants. A specific set of parameters shall be used for a given number of cycles. The model conceived for number of cycles greater than 100.

Allen Marr & Christian (1981) proposed a model for the assessment of axial or volumetric accumulated strain (ε_{cum}), as a function of the average stress ratio η_{ave} and an equivalent number of cycles n_{cyc_eq}:

$$\varepsilon_{cum} = \eta_{ave}\ C\ {n_{cyc\_eq}}^{D} \tag{2.5}$$

The values of constants C and D depend on whether ε_{cum} is referred to axial or volumetric strain.

A more complex approach was formulated by Niemunis et al. (2004) and used in Wichtmann et al. (2005) to model the long-term cyclic tests discussed in 2.3.1. The rate of the strain accumulation vector is given by a series of scalar functions, each of which representing one of the factors influencing cyclic loading behaviour:

$$\dot{\boldsymbol{\varepsilon}}_{cum} = f_p f_Y f_e f_\pi f_{ampl}\left(\dot{f}_N^A + \dot{f}_N^B\right)\boldsymbol{m} \tag{2.6}$$

Where f_{ampl} represents the effect of amplitude, shape and polarization of the strain loops; f_p is a function of average mean stress; f_Y accounts for the average stress ratio; f_e is a function of the average void ratio; f_Y includes the effects of polarization changes; $\dot{f}_N^A$ and $\dot{f}_N^B$ account for the effect of cyclic preloading (history) and the number of cycles. Vector $\boldsymbol{m}$ is the cyclic flow rule, describing the relative magnitude of volumetric and deviatoric strains. These functions include all the factors affecting cyclic behaviour, as determined in the experimental study and discussed earlier. The functions include one or more material constants, which shall be determined for the particular soil studied. Nine constants shall be determined in total. The authors perform a calibration of such constants basing on the performed tests, but they do not test the performance of the calibrated model against other experimental results. Thus, the model suitability to predict the accumulated strain in new tests is not assessed.

2.4.1.2. EMPIRICAL MODELS FOR CEMENTED SOILS

Fewer studies have been published dealing with cemented soils, than the corresponding studies on uncemented soils. As referred earlier, vast experimental programmes were performed in the University of Sydney and in the University of Western Australia. The key parameters of these studies was shear stress level S, which is a ratio of an equivalent deviatoric stress to the maximum cyclic deviator stress obtained in an equivalent monotonic triaxial test:

$$S = \frac{q_{eq}}{q_{peak}} \tag{2.7}$$

The definition of the equivalent deviatoric stress changes in different studies. Following an equivalent damage criterion, Carter et al. (1999) suggest:

$$q_{eq} = \frac{q_{cyc}}{\left(1 - \frac{q_{mean}}{q_{peak}}\right)} \tag{2.8}$$

Where q_{cyc} and q_{mean} are cyclic deviatoric stress amplitude and mean deviatoric stress. Sharma & Fahey (2003a), proposed a more complex expression for S, which takes into account not only the peak deviatoric stress, but also the effective confining pressure and the maximum effective stress ratio obtained in a monotonic test.

Yeoh & Airey (1994, 1998) adopted expression (2.7) with $q_{eq} = q_{cyc}$. They found a linear relation between S and the logarithm of the number of cycles at failure. Yeoh & Airey (1998) studied the degradation of the shear modulus with the number of cycles. Cyclic shear modulus (G_{cyc}) was normalized against a dynamic shear modulus (G_{max}), which is the modulus measured from ultrasonic wave-tests at the same confining pressure. The ratio of the moduli shows a logarithmic decrease with the number of cycles:

$$\frac{G_{cyc}}{G_{max}} = a + b \log n_{cyc} \tag{2.9}$$

Constants a and b depend on the stress level and the loading frequency.

Sharma & Fahey (2003b) studied the degradation of stiffness in a cemented calcareous soil, namely, a remoulded calcareous soil artificially cemented using a technique called CIPS. Using this process, the natural cementation of the soil was recreated in a controlled way avoiding any variability and granting the reproducibility of the tests. Cemented and uncemented specimens were submitted to undrained cyclic triaxial tests. Internal submersible strain gauges were directly applied on the specimen in order to measure small strain during the loading cycles. The tests had different confining pressures, cyclic stress levels, and number of cycles. In Fig. 2.16, the definition of the elastic moduli is reported. The initial tangent modulus is indicated with the subscript "0", while the modulus of each loop is defined as the slope of the line joining the vertices of the hysteresis loop of each cycle.

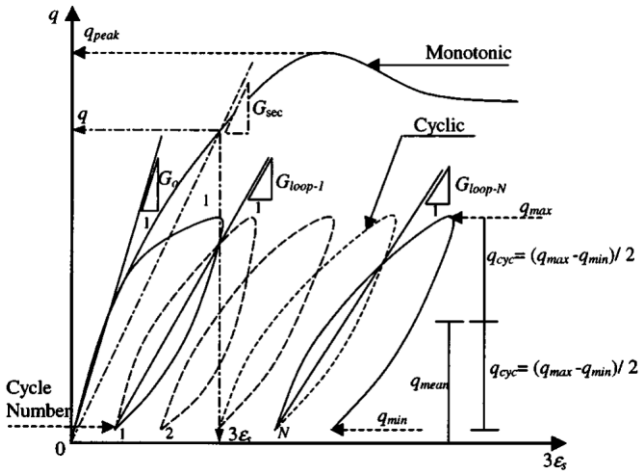

Fig. 2.16 – Definition of the elastic moduli (Sharma & Fahey, 2003b)

The results of the tests show an increment of the accumulated permanent strain and a degradation of the cyclic modulus with increasing number of cycles. Bonding increased the stiffness of the sample, namely the value of the initial stiffness modulus and the size of elastic range. The authors showed that the rate of degradation is faster for increasing cyclic stress level and confining pressure. Bond degradation with cycles leads to a decrease in stiffness and a reduction of the elastic range. Stiffness degradation was also observed in uncemented specimens: this is due to the decrease in confining pressure during cyclic loading, which is a result of the particular rearrangement (dilatancy) of the soil. Hence, the degradation of the cemented soil is due to the combined effect of the bonding damage and the soil dilatancy caused by the permanent strain accumulation. Basing on the results, the following relation between the stiffness degradation and the number of cycles was proposed:

$$\frac{G_{loop-N}}{G_{loop-1}} = 1 - \alpha(N-1) \tag{2.10}$$

in which α depends on stress level S, while the shear modulus of the first loop (G_{loop-1}) depends on S and on the initial tangent modulus G_0.

2.4.2. CONSTITUTIVE MODELLING

2.4.2.1. CLASSIC ELASTO-PLASTIC MODELS WITHIN THE FRAMEWORK OF CRITICAL STATE SOIL MECHANICS

Historically, the first and simplest constitutive model used was the rigid plastic model. This kind of approach aims at establishing a failure criterion and neglects the deformation prior to failure. During the 19th century and until the first half of the 20th century, the development of new models for soils followed

closely the advances in models for metals. The basics of elastic model were established. The combination of this framework with a failure criterion led to the development of elastic-perfectly plastic models (e.g. Mohr-Coulomb model). An enhancement of this framework is the elastic-hardening plastic framework. In this case, the onset of plastic deformation does not necessarily coincides with failure, as the yielding surface can evolve following a hardening rule. This can be isotropic, kinematic, or mixed. According to Muir Wood (2004), there are four main features of the hardening plastic models, three of which are in common to the elastic-perfectly plastic models.

1) Elastic relations: constitutive behaviour (stress-strain dependence) of the soil in perfectly elastic domain. These relations can be linear or non-linear, depending on the response of the studied material.
2) Yield criterion: it defines a surface (yield surface) in the stress space that represents the limit between the elastic region and elastic-plastic behaviour.
3) Flow rule: it describes the increment of plastic strain through the definition of a relation between dilatancy (i.e. the ratio of the incremental volumetric to distortional plastic strain) and stress. Alternatively, flow rule can be defined as the outward normal to an additional surface, the plastic potential. Flow rule can be associative, if the direction of incremental strain is normal to the yield surface (i.e. plastic potential and yield surface coincide), or non-associative otherwise.
4) Hardening rule: it links the change in size and/or position of the yield surface with the magnitude of the plastic strain and hence provides a link between the yield surface and the flow rule expressions. Depending on the way it modifies the yield surface, hardening rule can be isotropic (if yield surface expands or shrinks), kinematic (if yield surface translates) or mixed (if the two precedent effect are present simultaneously).

This fundamental framework is described more extensively in Annex 1.

Soil is a multiphase material that presents specific characteristics not common with metals, for example the volumetric strain observed during shearing and the principle of effective stress. Basing on these considerations, critical state soil mechanics (CSSM) was established (Roscoe et al., 1958; Schofield & Wroth, 1968). This framework, originally developed for cohesive soils, is able to fit different experimentally observed features of soil behaviour in a simple framework based on isotropically hardening elasto-plasticity. The name of the framework is due to the fact that, at failure, soil reaches a terminal state, called the critical state, at which the applied stress is constant, soil has a constant volume, and only deformation in shape is observed. The first model conceived in this framework is Cam-clay model, in its original (OCC – Schofield & Wroth, 1968) and modified version (MCC – Roscoe & Burland, 1968). They both present an isotropic hardening rule and an associative flow rule. MCC model will be presented in detail in next chapter. Even if this model was conceived for cohesive soils, its framework is the basis for the development of more complex models.

After MCC model, a large production of models arose with the aim of extending the framework of CSSM to granular soils. Yield surface and flow rule used in MCC were not suitable for sandy soils, which, unlike clays, show a clearly non-associative flow rule. Nova & Muir Wood (1979) presented one of the first models for granular soils, in which a piecewise yield surface is presented, corresponding to the regions of stress space with opposite tendencies in volumetric strain (dilatant and compressive, respectively). A specific flow rule is presented for each of the two regions: the dilatant region present a non-associative flow and the compressive region present an associated flow rule. Even if accurate for the prediction of the behaviour of granular soils under monotonic loading conditions, the definition of two different yield surfaces creates numerical problems at the point of passage between the two parts, since an outward normal is not defined here. Hence, a smooth surface is preferable. Many other models were conceived for sands and clays. Yu (1998) proposed a single framework that could be adapted to

both types. It is the so-called Clay and Sand (CASM) model. It presents two shape parameters capable of adapting the shape of the yield surface to experimental results. This model will be reviewed in the next chapter.

All the models described so far are based on isotropic hardening. While they are suitable to model the behaviour of unbonded soils in monotonic conditions, they cannot reproduce two fundamental aspects examined in the present work: cementation and cyclic loading. Cementation transforms the soil into a completely new material, providing it with some features typical of soft rocks rather than a mere cohesive soil. Cyclic load cannot be modelled through an isotropic hardening rule, since the cyclic loading would cause an expansion of the yield surface in the first loading cycle, and the following cycles would be entirely located inside the purely elastic domain, with no further accumulation of plastic strain. The experimentally observed stress-strain hysteretic loops cannot possibly be reproduced with such framework. A kinematic hardening rule is necessary instead.

For such a reason many authors have developed new constitutive models, adding extra features to the classic ones in order to deal with this increased complexity. The new advanced constitutive models were developed in a hierarchical approach (Desai et al., 1986; Muir Wood, 2004). This means new features are added to a precedent, less sophisticated model, to reproduce these more complex characteristics. The added features do not alter the previous framework of the model, which can be restored by setting specific parameters for the additional characteristics.

2.4.2.2. MODELLING CYCLIC LOADING

The description of the constitutive behaviour of the soil has historically been based on the elasto-plastic model with isotropic hardening and in the framework of critical state theory. In such approach a yield locus is defined, which delimits a region of the stress space where the soil behaviour is either linear elastic or nonlinear elastic. When the stress state intercepts the yield locus, this surface expands (or shrinks) isotropically generating plastic strain increments. Although such approach is suitable to model the behaviour of the soil at large strain and under monotonic loading paths, it fails to model the small-strain behaviour inside the locus, particularly when repeated loading actions are applied. Such small-strain domain has been studied more and more accurately with the development of local strain sensors, showing a hysteretic soil response with a clear kinematic hardening.

It is clear that classic isotropic hardening models cannot predict, even qualitatively, such features, as pointed out by many authors (e.g. Mroz et al., 1979; Dafalias & Herrmann, 1982; Jardine, 1992, 1995; Muir Wood, 2004; Yu et al., 2007a). Thus, new models were developed based on kinematic hardening. As reported by Yu (2006), even kinematic or mixed hardening cannot reproduce the advanced features described, if a single yield surface is considered. Thus, two alternative approaches were proposed: multi-surface plasticity and bounding surface plasticity.

Multi-surface plasticity was introduced by Mroz (1967) and Iwan (1967) for metals and later adapted to geomaterials. In this framework, several nested surfaces of constant plastic modulus are defined in the stress space instead of the single surface previously described. When the soil element is sheared, the stress point moves in the purely elastic domain until it touches the inner surface (Fig. 2.17). Then, as loading continues, the point keeps on moving dragging the surface along with it, while the larger surfaces remain fixed. During this phase, soil response is elasto-plastic with the plastic modulus associated to the first surface. As loading keep increasing, stress point touches in sequence the successive surfaces that are all dragged along with it. Plastic modulus changes accordingly to the larger surface in contact with the stress point. Every time a new surface is activated, hardening modulus changes accordingly. Thus,

a smooth transition in stiffness is observed in the stress-strain diagram, as the non-linear curve is approximated with several small linear curves of decreasing stiffness. When the load inverts and unloading begins, the process is inverted: loading is initially purely elastic and an increasingly plastic behaviour is reproduced, as the surfaces are successively intercepted. A translation rule shall be defined in the stress space to define the direction of translation of the generic surface f_i. Mroz (1967) translation rule is defined to ensure that all the surfaces touch at a common normal without intersecting. To obtain this, the direction of the translation vector is defined as the direction of the vector joining the current stress point on surface f_i with the conjugate point on the next surface, f_{i+1}. Conjugate points are points on the surfaces with the same direction of outward normal. With such rule, the surfaces successively approach at a common normal without intersecting.

Multi-surface plasticity represents a better approximation of the constitutive behaviour of the soil. Nevertheless, the piecewise linear definition of the stress-strain behaviour fails to reproduce a smooth transition in soil stiffness. This problem is solved with bounding surface plasticity.

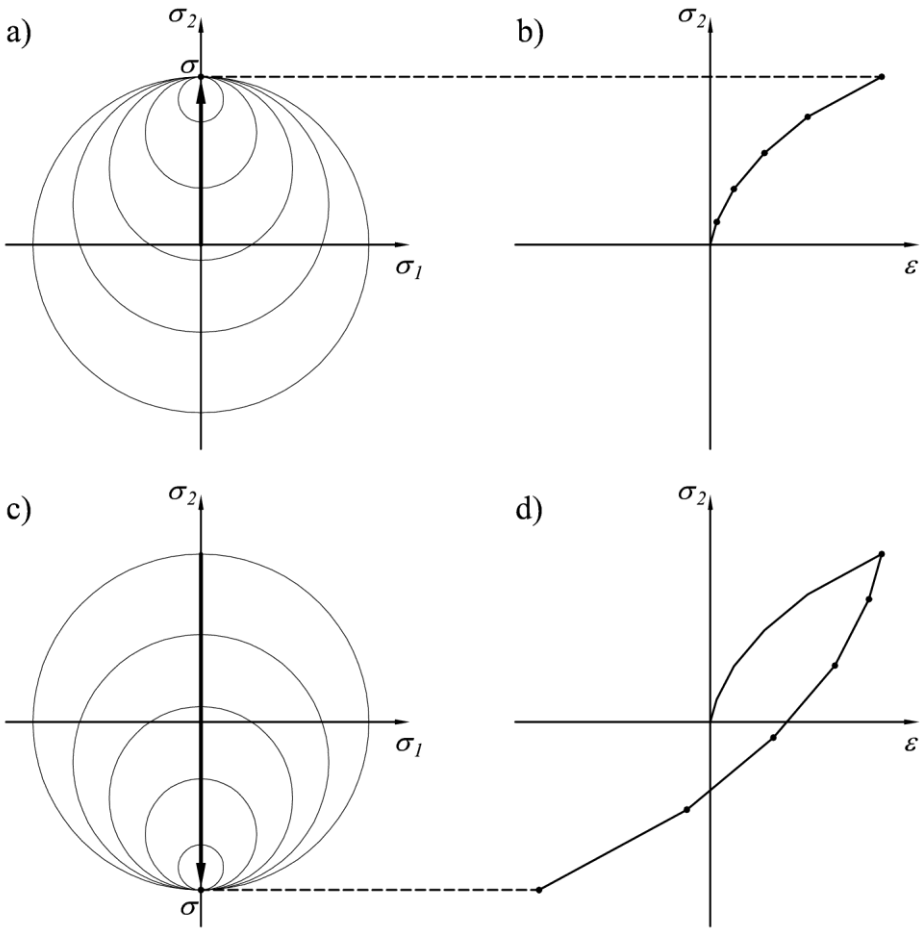

Fig. 2.17 – Multi-surface plasticity: representation of the stress plane and stress-strain plane during loading (a and b) and during unloading (c and d) (Mroz, 1967)

Bounding surface plasticity was introduced by Dafalias & Popov (1975) and Krieg (1975). This approach (Fig. 2.18) includes one kinematically-hardening yield surface inside a larger surface, referred to as bounding surface (BS) (some authors use alternative denominations such as reference surface or limit surface). Soil stiffness is no longer piecewise and linear. Instead, stiffness is dependent on a

distance vector $\boldsymbol{\delta}$ between the actual stress point on the yield surface and the bounding surface. This last feature is key for interpreting the behaviour of the soil inside the BS: in fact, rather than the applied stress, the fundamental parameter is the ratio between the applied stress and the corresponding stress on the bounding surface. The framework represents a generalization of the multi-surface approach with infinite surfaces. In bounding surface, a continuous field of plastic moduli is defined in the stress space, corresponding to the infinite possible positions that the yield surface can occupy. Thus, each position of the yield surface corresponds to a specific plastic modulus, which varies smoothly in the loading path.

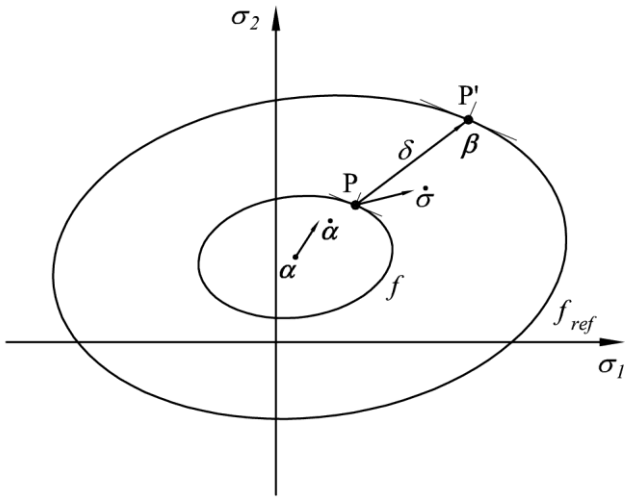

Fig. 2.18 – Bounding surface plasticity: representation of yield surface (f) and bounding surface (f_{ref})

The new approach is capable to model the complex behaviour observed in small-strain scale and non-monotonic loading programmes, while still being able to model large-strain, monotonic response as the classical models. Thus, the new framework is more general than the one-surface option, as it is applicable to a wider range of loading paths and strain levels. A vast variety of constitutive models were presented, for different soils and stress configurations (e.g. Mroz et al., 1978; Dafalias & Herrmann, 1982; Bardet, 1986; Al-Tabbaa & Muir Wood, 1989; Manzari & Dafalias, 1997; Gajo & Muir Wood, 1999a, 1999b; Wang & Xie, 2014; Corti et al., 2016). The definition of translation rule and distance $\boldsymbol{\delta}$ between surfaces is specific to each model. In the scheme of Fig. 2.18, Mroz (1967) translation rule is represented. Yield surface centre ($\boldsymbol{\alpha}$) translates along a vector $\dot{\boldsymbol{\alpha}}$ parallel to vector $\boldsymbol{\beta}$, which is the vector joining conjugate points P and P'. This translation rule originally conceived for multi-surface plasticity was often adopted in bounding surface models. Distance $\boldsymbol{\delta}$ is considered in this case coincident with vector $\boldsymbol{\beta}$, but other definitions could be adopted. Hashigushi (1985) suggested that distance $\boldsymbol{\delta}$ should be defined as a scalar quantity represented by the component of vector $\boldsymbol{\beta}$ projected onto the direction of the outward normal to the yield surface in the current stress point.

In the next chapter, a particular bounding surface model is analysed (Al-Tabbaa & Muir Wood, 1989). It is interesting as it represents a hierarchical extension of the classic monotonic modified Cam-clay. Another interesting framework was proposed by Jardine (1992, 1995). It is particularly interesting as it analyses the physical reality underlying the model. In this framework, the current effective stress point is surrounded by two kinematic-hardening (i.e. moving along with the stress point) non-intersecting sub-yield surfaces (called Y1 and Y2, respectively), moving inside a larger isotropic surface, called initial bounding surface (Jardine, 1992) or Y3 surface (Jardine, 1995). These surfaces divide the formerly known "elastic" domain in three zones. Zone I (inside the smaller sub-yield surface Y1) presents a linear elastic behaviour. Zone II (between Y1 and the bigger sub-yield surfaces Y2) is non-linear elastic with

recoverable strain. Zone III (between Y2 and the initial bounding surface or Y3) where incremental plastic strain develops and stiffness moduli decrease with an increasing rate as the stress point approaches the initial BS. Jardine (1995) states that, when Y3 is plotted in a stress space normalised by an equivalent pressure p'_e (i.e. the pressure corresponding to a point on the normal compression line having the same void ratio as the tested specimen), Y3 represents the bounding surface which cannot be crossed by undrained monotonic or cyclic tests. Shibuya & Hight (1987) showed that undrained monotonically loading triaxial tests performed from a normally compressed state define sections of the initial BS. Jardine (1995) concluded that only a drained test can go beyond the initial BS, which starts to isotropically expand (or shrink, depending on where the surface is intercepted) with a significant loss in stiffness and large plastic strain development. Jardine (1992) suggested that the initial sizes of the sub-yield and bounding surfaces increase for cemented soils and depending on the degree of cementation. Jardine (1995) points out that the general pre-failure response depends on many variables concerning the soil nature (e.g. density, bonding, preparation method, stress history, overconsolidation ratio) and the applied loads (e.g. effective stress path trajectory, drainage conditions, and distance from the bounding surface).

The aim of the present research is to study the long-term behaviour of artificially cemented soil mixtures subjected to repeated actions under service load levels, and different confining pressures (constant within each test). As explained, in the framework of bounding plasticity the small-strain behaviour of the soil depends on the distance between the applied stress and the bounding surface, rather than on the applied stress itself. As explained in detail in the following sections, the applied stress levels were calculated so that the stress state intercepts both the sub-yield surfaces and reach zone III of Jardine (1992, 1995) model. On the other hand, the relative minimum distance between the stress level and the bounding surface shall be equal for all the tests, so a comparison between specimens with different characteristics can be performed. As the size of the bounding surface is different for specimens with different compactions and cementation levels, an indexation through a proper parameter was performed. The information about the size and position of the bounding surface was retrieved from the work of Rios (2011) and Rios et al. (2012, 2014), who have performed monotonic triaxial tests with a strain level up to 30% of axial strain, corresponding to critical state conditions.

2.4.2.3. MODELLING CEMENTATION

Modelling the constitutive behaviour of these soils is a difficult task, as cementation modifies the response of the soil at small and large strain. Advanced constitutive models were developed to deal with this increased complexity. Such model were developed from the usual elasto-plasticity with isotropic hardening, and in the framework of critical state soil mechanics. To this common framework, extra features were added to represent the increased strength and stiffness due to cementation, and the progressive loss of bonding associated with the development of plastic strain. Gens & Nova (1993) proposed a framework for bonded soils and weak rocks (and the relative implementation in an elasto-plastic model), focused on the destructuration process of a bonded material during yielding. The model is based on the usual modified Cam-clay model for unbounded soil, equipped with a bonding variable taking into account the level of cementation and a destructuration law, which regulates the loss of bonding with the progressive accumulated strain. The framework is described in detail in Chapter 3.

Rouinia & Muir Wood (2000) model is a bounding surface model with a destructuration law. It is conceived as an extension of Al-Tabbaa & Muir Wood (1989) model for structured natural cohesive soils. Following the framework of bounding surface plasticity, a kinematically hardening yield surface separating elastic and elastic-plastic domain is dragged along with the stress path. The bounding surface

is referred to as structure surface because it contains information about the magnitude and anisotropy of soil structure (cementation). As plastic strain occurs, destructuration is induced in the material. Such behaviour is represented by the shrinkage of the structure surface in the direction of a third surface, the so-called reference surface. Such surface represents the behaviour of the completely destructured soil and corresponds to the bounding surface of Al-Tabbaa and Muir Wood (1989) model. As volumetric deformation occurs, the three surfaces change in size as an effect of isotropic hardening. As usual, kinematic stiffness is related to the distance between yield and structure surface. As indicated by Gens and Nova (1993), damage is associated to incremental plastic strain and it is not affected by the purely elastic properties of the material. A destructuration law regulates the rate of destructuration with plastic strain increment.

Vaunat & Gens (2003) model (also described in Gens et al., 2007) combines the framework proposed for structured soils and soft rocks into a conceptual and mathematical framework developed to reproduce the soil/rock transition of bonded materials. This model considers the structured soil as two materials working in parallel: a granular matrix modelled through an elastic-plastic constitutive law, typical of soils, and the bonds, modelled through a damage elastic law typical of quasi-brittle materials (Fig. 2.19). This assumption implies that the external load will be distributed between the soil matrix and the bonds according to the constitutive law of each material. The authors do not specify a particular constitutive law for soil matrix. As they recommend, any constitutive law can be used as long as it is suitable to represent the desired features with a designed level of complexity. An elastic damage law is associated to the bonds and their loss of rigidity changes the distribution of the external load accordingly.

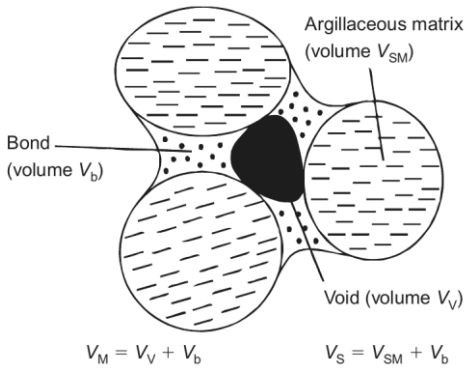

Fig. 2.19 – Conceptual scheme underlying the model (Gens et al., 2007)

Bonds are described as a quasi-brittle material and their behaviour is modelled through an elastic-damage law. The model proposed by Carol et al. (2001) has been selected. This model assumes a linear elastic behaviour of the material; during loading the cross sectional area implied in the definition of stress is reduced due to the development of micro-cracks. Damage is defined as the ratio between micro-cracks area and overall area. A specific relation links the damage with the work of the external loads to the soil element. External stress will distribute between bond and matrix according to the respective rigidity. Stress partitioning is based on the proposal of Cordebois & Sidoroff (1982), who used the energy equivalence principle that establishes the equilibrium between the energy of the composite material and the sum of energies for all components. During the process of loading, bond damage occurs. This mechanism is accompanied by a destructuration of the material and a progressive transfer of load from bonds to soil matrix.

These approaches were both originally conceived for cohesive material. CASM-n model (Yu et al., 2007b) represents an extension of the CASM model (Yu, 1998) to bonded soils, using a framework similar to that described in Gens & Nova (1993). The same yield surface used in CASM model is

enlarged by the effect of cementation, in order to represent the increased isotropic yield stress and tensile strength. Plastic strain causes a destructuration of the material, which in turn results in a reduction of the surface, which tends towards the uncemented surface adopted in the original CASM formulation. Rowe (1962, 1963) flow rule is adopted, which is non-associative. The tensile strength conferred by cementation is accounted in the flow rule as a cohesion term. The model can be applied to granular and cohesive soils, since it inherits the property of the original CASM model to adapt the shape of the yield surface to the specific material through a set of shape parameters.

2.5. ARTIFICIALLY CEMENTED PORTO SILTY-SAND BEHAVIOUR UNDER MONOTONIC AND CYCLIC LOADING CONDITIONS

The state of the art research on the soil studied in the present thesis is reported in this specific section, including monotonic and cyclic experimental studies performed on uncemented and cemented soil, and the constitutive modelling performed on the monotonic loading.

The behaviour of the mixture composed of residual soil of Porto granite and cement in saturated condition and monotonic loading was extensively studied by Rios (2011), and Rios et al. (2012, 2014). The tests performed by the authors included uniaxial compression tests (UCT), indirect tensile tests and static triaxial tests under low to high confining pressure.

The mixtures studied had different cement contents (C) and initial void ratios (e_i), thus, the necessity of an indexation arose. Such indexation had to include the two competing factors (cement content and initial void ratio) into a single parameter that could be directly related to the growing characteristics of strength and stiffness of the mixture. The classic water/cement ratio used for concrete does not apply to soil/cement mixtures: in the case of concrete, the material is cured in saturated conditions, so the initial void ratio does not influence the final mechanical characteristics. In soil-cement mixtures, the water does not fill all the voids in the material when the specimen is being moulded so the initial void ratio influences the mechanical properties of the material. Consoli et al. (2007) proposed an index based on the ratio of porosity to the volumetric cement content adjusted by an exponent, called porosity/cement ratio (n/C_{iv}^{x}). Through a vast set of uniaxial compression tests (UCT) performed on the same material with different cement contents and void ratios, the authors have shown an exponential correlation between unconfined compression strength and the ratio. The adjusting exponent x depends on the type of soil and it is defined as the value that allows the best correlation coefficient in the data. The authors extended this methodology to other results obtained from triaxial compression tests (Consoli et al., 2009) confirming the adequacy of the ratio. Other authors studied the ratio and agreed that, at least for compression tests, the value of exponent x does not depend on the test performed but it is constant for a particular soil, with a value ranging between 0 and 1 (Viana da Fonseca et al., 2009a, 2014; Rios, 2011).

Rios (2011) and Rios et al. (2012) have applied this framework to artificially cemented Porto residual soil. The authors preliminarily determined the optimum water content (w_{opt}) and the maximum dry unit weight ($\gamma_{d,max}$) of the mixture through Modified Proctor test, obtaining the results reported in Table 2.1.

Table 2.1 – Optimum values obtained in Modified Proctor test (Rios, 2011)

w_{opt} (%)	$\gamma_{d,max}$ (kN/m³)
12	18.7

Through a set of UCT tests, the authors then determined the adjusting exponent for the particular mixture, obtaining a value of 0.21. Thus the porosity/cement ratio used in successive analyses was $n/C_{iv}^{0.21}$.

Once the ratio has been defined, Rios (2011) and Rios et al. (2014) performed an extensive set of monotonic triaxial compression tests and isotropic compression tests on uncemented and cemented specimens with various cement contents, initial void ratios, confining pressures and draining conditions. The uncemented specimens were prepared with initial void ratios of 0.60 or 0.75; the cemented specimens were prepared with four moulding points: 2 or 4% in cement content was used to mould specimens with ratio ($n/C_{iv}^{0.21}$) of 36; 5 or 7% in cement content (C) was used to mould specimens with ratio of 29. The initial void ratios were chosen accordingly to these parameters and ranged between 0.58 and 0.75.

These mixtures were produced in various copies and submitted to various confining pressures: low-pressure tests were performed with effective confining pressures (σ_c') ranging from 30 to 250 kPa and high pressure tests with σ_c' ranging from 10000 to 43000 kPa. Each mixture was tested in drained and undrained conditions. For all the specimens (cemented and uncemented) the moulding water content was equal to the optimum value of 12% obtained from Modified Proctor test.

The results obtained give a complete characterization of each mixture: from isotropic tests, the isotropic yield stress (p_0') and the normal compression line (NCL) were determined; from monotonic triaxial tests, the ultimate deviatoric stress (q_u) and the critical state deviatoric stress (q_{cr}) shear stress were derived, as well as the critical state line (CSL) and the dilatancy (Ψ) of each mixture. Moreover, plotting the stress paths of each test on the ($p' - q$) plane it is possible to trace the boundary surface of each mixture in the stress space. The results are showed in Fig. 2.20, where the author normalised the axes dividing the values by the equivalent pressure of the uncemented soil (p_e').

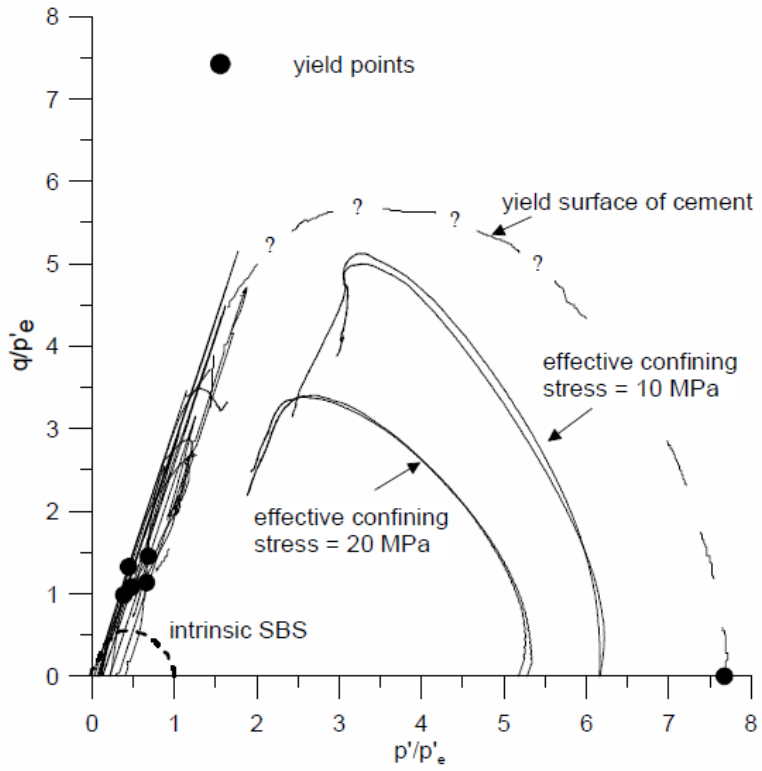

Fig. 2.20 - Normalised results for the yield surface (Rios, 2011)

2.5.1. SOIL BEHAVIOUR UNDER ISOTROPIC COMPRESSION TESTS

Rios et al. (2012) present a set of isotropic compression tests performed over uncemented specimens and cemented specimens with different initial void ratio and cement contents but two unique adjusted porosity/cement ratios equal to 36 and 29 (see the scheme in Fig. 2.21). The initial void ratios of the specimen tested ranged the interval 0.6÷0.8. The compression curves of the cemented silty-sand specimens are initially flat, reflective of the stiffness of the cement, but at a certain stress the slope of the curves increases markedly. Such threshold, which can be identified with the isotropic yield stress, is dependent on the adjusted porosity/cement ratio and not on the cementation of the specimen. For increasing stress, the slope progressively reduces until a point where for each adjusted porosity/cement ratio the compression curves for the different cement contents eventually converge to a unique compression line, parallel but not coincident with the normal compression line (NCL) of the uncemented soil. The authors propose that for the particular soil examined, there is a family of parallel NCLs for the cemented soil parallel to the NCL of the uncemented soil, each line representing a contour of dosage, and the lower the adjusted porosity/cement ratio, the further away the cemented NCL from the uncemented NCL. The authors explain this result with the fact that artificial cement, unlike natural (weaker) cementing agents, promote the creation of strong bonds that are not completely destroyed even at large stresses. Amaral (2012) studied the same cemented soil in the same laboratory and with the same interval of void ratios and with an adjusted ratio equal to 41, obtaining a third NCL coherent with the scheme of Rios et al. (2012). The third NCL is parallel to the precedent ones and located between the NCL of the uncemented specimens and the NCL of the ratio equal to 36.

The results of Rios et al. (2012) and Amaral (2012) can be interpreted with the framework proposed by Cuccovillo & Coop (1993, 1999). These authors proposed a model of cemented soils that distinguished between weakly and strongly cemented soils. When isotropically compressed, the first type of soil yields before reaching the NCL, while the second type reached states outside the intrinsic NCL defined by the uncemented soil. The fundamental difference here is that the intrinsic NCL is not unique as proposed by Cuccovillo & Coop (1999) but it is different for cemented and uncemented soils and its position depends on the porosity/cement ratio. It is worth noting that Cuccovillo & Coop (1999) model is only referred to naturally cemented soils. Apart from this difference, all the cemented specimens studied by Rios et al. (2012) exhibit the behaviour of a strongly cemented soil, each one with a specific intrinsic NCL. As explained by Cuccovillo & Coop (1999) (and confirmed by the experimental curves shown in Fig. 2.21), the isotropic yield stress of strongly cemented specimens is not always located on the corresponding intrinsic NCL. The isotropic yield locus (i.e. the locus of all the isotropic yield stresses) of cemented soil is no longer coincident with the intrinsic NCL but it has a bilinear shape, as shown in Fig. 2.22. The authors refer to it as the intact isotropic boundary (intact IB). The offset between the isotropic boundary of an intact cemented soil and the corresponding intrinsic NCL reduces as the specific volume decreases, until the two boundaries become coincident. For uncemented soils, the usual framework holds, with the NCL defining the isotropic boundary of the soil.

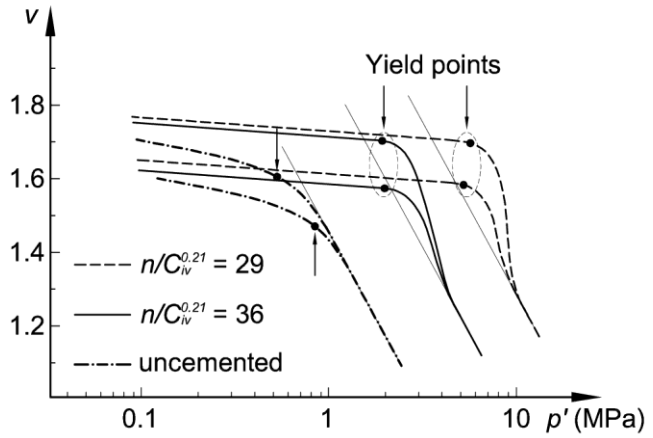

Fig. 2.21 - Scheme of the isotropic compression curves presented by Rios et al. (2012)

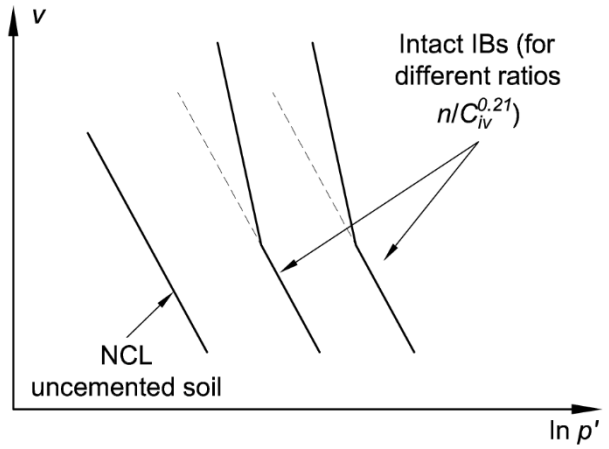

Fig. 2.22 – Interpretation of the isotropic compression curves presented by Rios et al. (2012) in the framework of strongly cemented soil (Cuccovillo & Coop, 1993, 1999)

Thus, the isotropic yield stress of cemented specimens may not coincide with its intrinsic NCL. As one can see from Fig. 2.21, the isotropic yield stresses of the cemented specimens are outside the respective NCL, in the steeper part of the isotropic yield locus (due to the relatively high initial void ratio of the specimens tested). Conversely, the uncemented specimens show the behaviour usually observed in remoulded soils, with an initial elastic behaviour followed by progressive softening and a second trend coincident with the normal compression line (which is never crossed). In this case, the isotropic yield stress varies considerably with the initial specific volume of the specimen.

2.5.2. SOIL BEHAVIOUR UNDER TRIAXIAL COMPRESSION TESTS

Rios et al. (2014) studied the shearing behaviour of the same soil, through a set of drained and undrained monotonic compression triaxial tests. The tests were performed over uncemented specimens and cemented specimens with adjusted ratio $n/C_{iv}^{0.21}$ equal to 36 and 29 (in continuity with Rios et al., 2012). The initial void ratios ranged in the interval from 0.60 to 0.75, except for one specimen with e_i = 1.2. All the tests were performed at a constant cell pressure and divided in two groups: low-to-medium-pressure tests (drained or undrained; with an isotropic confining pressure equal to 30, 80, or 250 kPa) and high-pressure tests (all undrained; confined at 10 MPa or 20 MPa).

The results of the uncemented drained tests of the first group in the $(q - \varepsilon_a)$ plane show a clear elastic behaviour up to a peak of the deviatoric stress, after which softening is observed. Such peak is more evident in the less confined specimens, which also show a dilative behaviour. In the case of cemented specimens, the elastic domain is extended and the peak deviatoric stress is higher; the peak is sharper as the following softening is more evident than in the uncemented specimens. The volumetric behaviour is clearly dilatant. It is important to highlight that cemented specimens with different cement contents at given values of adjusted ratio and effective cell pressure have similar peak deviator stress and axial strain. The results of the undrained tests at low pressure confirmed the role of the adjusted ratio: the cemented specimens with an adjusted porosity/cement ratio of 36 have similar shape of the deviatoric stress vs. axial strain curves, clearly distinct from the specimens with ratio equal to 29. The first group of tests shows strain hardening with no defined peak, while the second group reaches a higher value of deviatoric stress followed by softening. The tests at high pressures were performed on one uncemented specimen and four cemented specimens, all with ratio equal to 29. The uncemented specimen shows a compressive behaviour, with strain hardening and increase of pore water pressure to a stable state. The cemented specimens showed a mild strain softening after peak, probably due to the bond damage during shearing.

As for the ultimate envelope, the results show that there is a unique failure envelope for all the specimens irrespective of their porosity/cement ratio, passing through the origin. However, the adjusted porosity/cement ratio influences the peak angle of friction and cohesion intercept, with the peak envelope for the index equal to 29 higher than that for the ratio equal to 36 (confirming the results of the deviatoric stress vs. axial strain plane). Basing on these results and extending the approach of the critical state soil mechanics to the cemented soils, the authors attempted to define a critical state line (CSL) for the cemented soil (only the specimens with ratio equal to 29 were analysed). Similarly to the results of the NCL, also in this case it seems that a CSL for the cemented soil can be identified in the isotropic plane $(\ln p' - v)$. This line is parallel to the corresponding CLS for uncemented soil, and shifted towards higher values of the intercept with the axes. Moreover, the distance between the NCL and the respective CSL appears to be similar for the cemented and uncemented soil.

Finally, the authors normalised the effective stress paths of the triaxial tests by dividing the deviatoric and mean effective stress by an equivalent pressure p'_e. Such pressure is the mean effective stress on the NCL, calculated with the same specific volume as the specific volume of the tested specimen after consolidation. As shown in the precedent section, there is a specific NCL for each porosity/cement ratio and a NCL for uncemented specimens. Thus, the equivalent pressure is different for uncemented specimens and cemented specimens with different porosity/cement ratio. For the uncemented specimens, a unique state boundary surface (SBS) was determined in the normalised stress plane, as expected (Fig. 2.23). As one can see, the high pressure undrained test begins at a normalised mean effective stress equal to 1 and define a unique state boundary surface on what is traditionally called the "wet side of critical", that ends at a normalised deviatoric stress around 0.5. The undrained low-pressure tests all plot on the left side of the high-pressure test (in the zone traditionally called "dry side of critical"). Despite their trajectory being reduced, the envelope of all the tests define a bounding surface also in this case (indicated with a traced line). As for the cemented specimens, four undrained high-pressure triaxial tests (all with $n/C_{iv}^{0.21}$ = 29) are presented (Fig. 2.23), two of which performed with an initial isotropic consolidation of 10 MPa and two with an isotropic consolidation of 20 MPa. Due to the high level of isotropic consolidation reached in these tests, all the specimens passed the steeper yielding locus of Cuccovillo & Coop (1993, 1999) model (Fig. 2.22) and reached a state on the NCL determined for the corresponding ratio. The normalised stress paths for the tests carried out at same initial isotropic pressure have similar plots irrespectively of the cement contents, defining a unique state boundary surface on what is traditionally called the "wet side of critical", starting from the corresponding NCL.

Specimens with different initial confining pressure present different SBS: the less confined specimens (10 MPa) reached a maximum normalised deviatoric stress around 0.8, while the more confined (20 MPa) reached 0.6. It is interesting to note that these maximum values, as well as in the uncemented case, are reached at a corresponding normalised effective mean stress approximately equal to 0.5. This difference in the maximum normalised deviatoric stress is consistent with the framework of Cuccovillo & Coop (1999): the more confined specimens have suffered more bond degradation during isotropic compression than the less confined specimens; thus, the normalised stress path of the first group of tests reached lower values of normalised deviatoric stress than the second group. Nevertheless, all the four normalised stress paths tend towards the same critical state line, which is represented by a single point in the normalised stress plane. The undrained tests (with ratio of 29 and 36) performed at low stresses (which showed a dilatant response) all plot on the left side of the normalised CSL and also define a bounding surface, which is not complete due to the similar initial normalised effective confining pressure of the tests and to the short extension of their effective stress paths.

As explained above, according to Jardine (1995) and Shibuya & Hight (1987), these normalised surfaces represent (for each equivalent pressure) the initial bounding surface from the model of Jardine (1992).

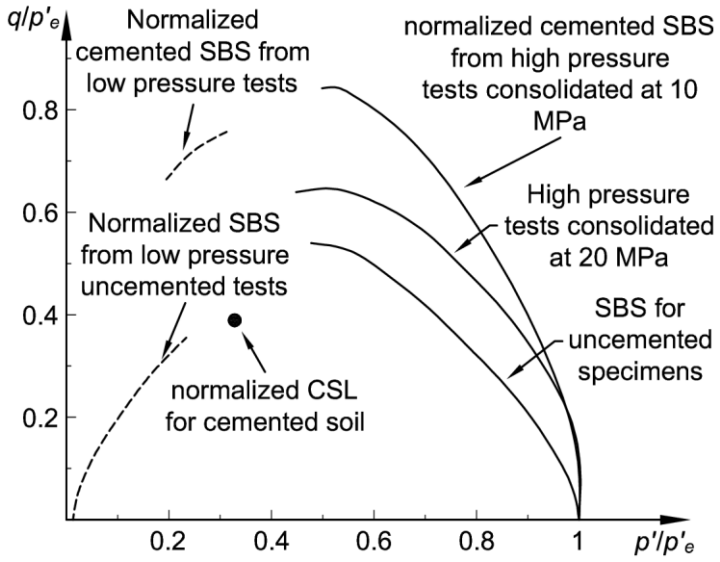

Fig. 2.23 – Scheme of the normalised state boundary surfaces for the cemented and uncemented soil presented by Rios et al. (2014)

Results from Rios et al. (2012, 2014) prove that some of the features of the critical state soil mechanics normally associated to unbonded soil can be applied also to the cemented silty-sand studied. For example the existence of straight normal compression line and unique critical state line; the existence of a unique state boundary surface (for each porosity/cement ratio); the subdivision of the stress space in a "dry" or dilative and a "wet" or compressive side. The adjusted porosity/cement ratio $n/C_{iv}^{0.21}$, rather than the cement content, proved to be the key parameter for the evaluation of the monotonic properties in isotropic and triaxial loading of the present cemented soil, at least in the interval of void ratios investigated. Decreasing values of the ratios (i.e. increasing compaction and/or cementation) lead to an expansion of the state boundary surface, in both the ($\ln p' - v$) isotropic plane and ($p' - q$) stress plane. Thus, a specific normalised bounding surface exists for uncemented specimens and for cemented specimens with a specific porosity/cement ratio.

2.5.3. CONSTITUTIVE MODELLING IN MONOTONIC LOADING CONDITIONS

Isotropic compression tests and monotonic triaxial tests reported in Rios et al. (2012, 2014) were modelled in Rios et al. (2016) using CASM-n model (Yu et al., 2007b). The calibration process followed a staged approach, starting from the simplest case of the isotropic compression test on uncemented soil, and proceeding towards increasingly complex load paths (triaxial) and cementation conditions (from uncemented to cemented soils). In each stage, the authors calibrated the specific parameters referring to the particular conditions analysed. In the initial stage (isotropic loading and uncemented soil), only parameters referred to the definition of the CSL and NCL of the uncemented soil in the isotropic compression plane are defined. Then, triaxial compression tests on uncemented soils are considered in order to calibrate the parameters relative to the shape of the yield surface and the critical state parameters (Fig. 2.24). Finally, isotropic (Fig. 2.25) and triaxial (Fig. 2.26) tests performed on cemented soil are considered, in order to calibrate the parameters relative to the initial amount of bonding and the destructuration law.

The performance of the calibrated model has been assessed by comparing the model output with the experimental results of drained and undrained triaxial tests on cemented specimens (Fig. 2.27). The agreement is generally good. Nevertheless, an abrupt change in stiffness is observed in correspondence to soil yielding. This leads to considerable divergence from the experimental results, especially in what concerns the undrained stress paths. This outcome is typical of the type of model used, which is an isotropically hardening, one surface model. As referred in the previous sections, this type of model presents a large purely elastic domain, which is unable to reproduce a smooth change in stiffness and an early development of plastic strain, even if a non-linear elastic constitutive model is considered (as in the present case). In Chapter 8, the same tests are modelled with a bounding surface plasticity model, and the differences between the two approaches are highlighted.

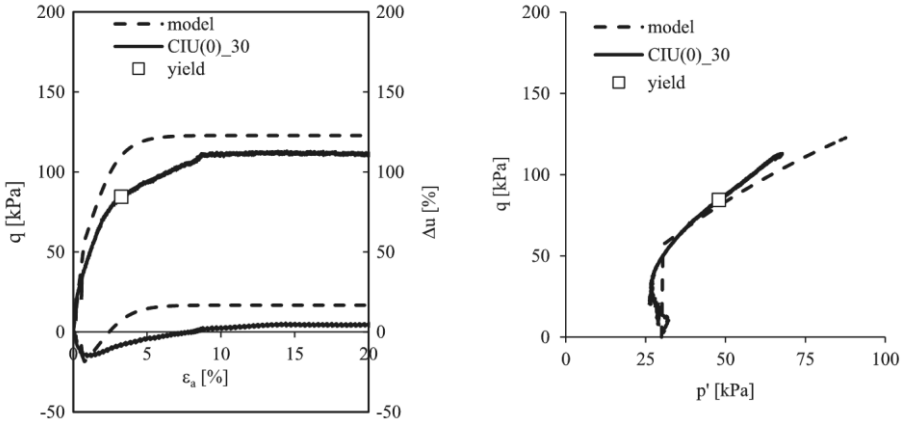

Fig. 2.24 – Performance of the model on undrained triaxial tests on uncemented specimens (Rios et al., 2016)

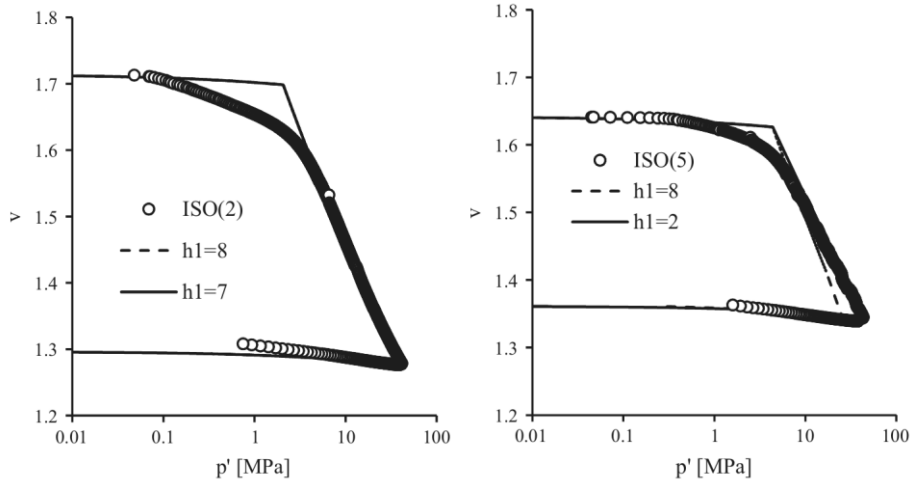

Fig. 2.25 – Model calibration on isotropic tests on cemented specimens (Rios et al., 2016)

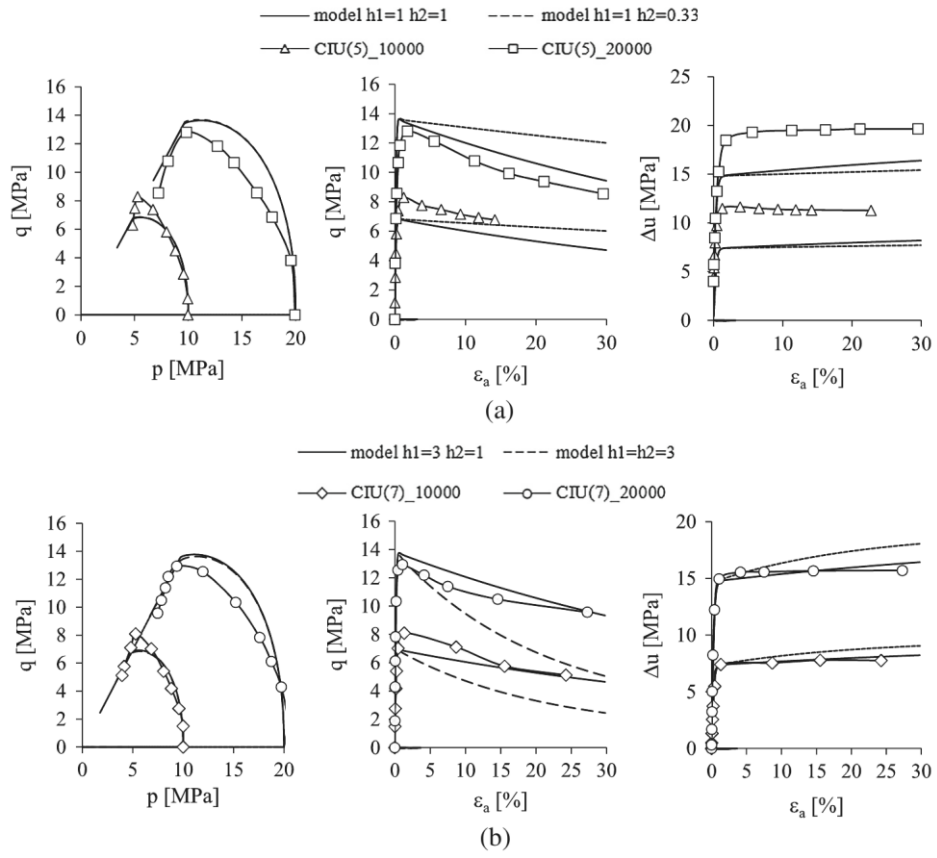

Fig. 2.26 – Model calibration on triaxial tests on cemented specimens (Rios et al., 2016)

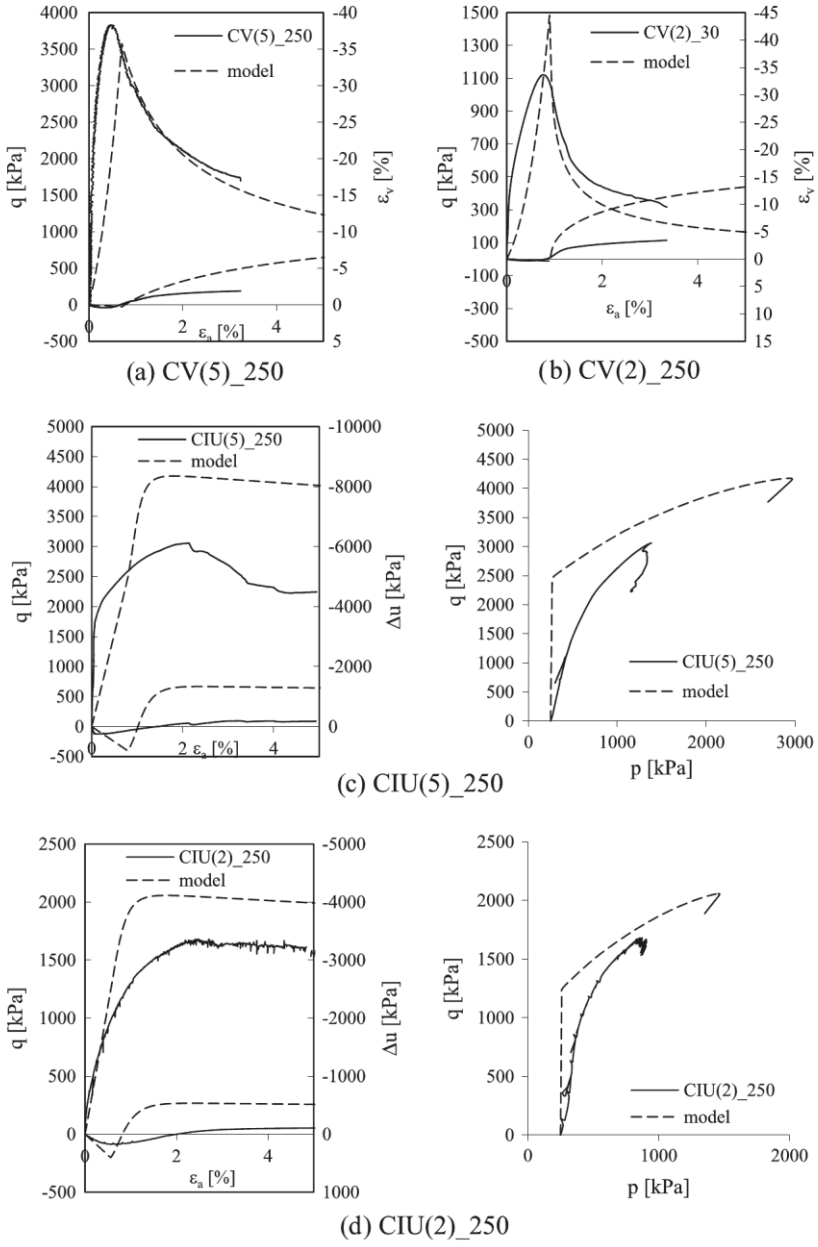

Fig. 2.27 – Model performance on drained (a, b) and undrained (c, d) triaxial tests on cemented specimens (Rios et al., 2016)

2.5.4. CYCLIC TESTS PERFORMED ON CEMENTED PORTO SILTY SAND

The first long-term cyclic triaxial tests on cemented Porto silty-sand were performed by Rios (2011) as a complement of the precedent tests carried out in monotonic conditions. Three types of tests were performed, using the same moulding conditions used for monotonic tests reported in sections 2.5.1-2.5.2. The tests were conducted at a frequency of 1 Hz and the deviatoric stress imposed was always positive, as the equipment used was not able to impose tensile stress. For this reason, the cyclic loading was preceded by anisotropic consolidation.

Due to the great amount of data registered, only selected cycles were analysed. Following the European Standard (CEN, 2004), the cycles were selected in groups of 10 consecutive cycles and the average value of the resilient modulus calculated for each cycle was considered. This process is necessary because the value of the modulus has high variability in each cycle, due to the high rigidity of the specimens that leads to very small deformations within a single cycle. The resilient modulus of each cycle was calculated as the slope of the line joining the edges of the hysteresis loop of the cycle.

The test types called 1 and 2 where conceived adapting the European Standard for cyclic testing of unbounded granular soil (CEN, 2004), since a corresponding European Standard for bonded materials does not exist. In the tests of type 1, two specimens were moulded with 2 and 5% of cement, respectively. The aim was to define values of the material resilient modulus for different stress levels. For this purpose, a cyclic conditioning was first applied in order to stabilize the cyclic permanent deformations and subsequently attain a resilient behaviour. This conditioning was performed by applying a large number of cycles (20000) at a significant stress level. The results of the conditioning phase (Fig. 2.28) show that, for the less cemented specimen, the accumulated strain rate decreases with the number of cycles, with a logarithmic accumulation. The accumulated strain tends to stabilize towards the end of the conditioning, although due to the logarithmic nature of the accumulation, it is possible that the strain continues to accumulate at a very small rate. The more cemented specimen does not show appreciable strain throughout the conditioning. After the completion of this phase, several test stages of 5000 cycles were applied with different stress levels. The two specimens were tested undrained. The results showed that the resilient modulus decreased during the conditioning phase and after each stage, proving the destructuration of the bonds. As expected, the level of destructuration was higher in the weaker 2% specimen, which in the end of the test showed a behaviour similar to the unbounded material.

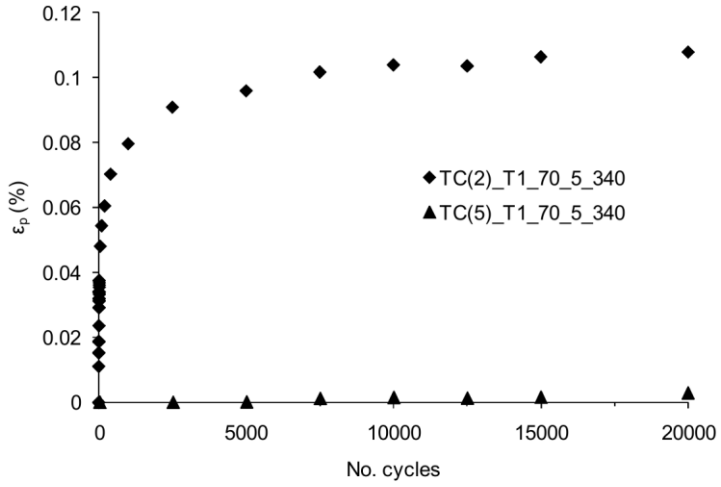

Fig. 2.28 – Conditioning phase for type 1 tests (Rios, 2011)

Type 2 tests were proposed in the European standard to evaluate the maximum stress levels that should not be exceeded to avoid the development of excessive permanent deformations. This procedure consists in applying several stress levels in stages of 10000 cycles without prior conditioning to evaluate permanent deformations of the material for a particular stress level. This type of test was performed in specimens with 2 and 5% of cement content in undrained conditions and 7% in drained and undrained conditions. The results showed that, for the specimen with 2% of cement content, accumulated vertical strain rate rapidly decreases, while the accumulated vertical strain has a logarithmic increase with the number of cycles (Fig. 2.29). From the comparison between tests carried out on specimens with 7% in

drained and undrained conditions, it appears that the resilient modulus is higher in undrained conditions. Conversely, the permanent deformation is higher in drained conditions.

Another specimen with 7% of cement was moulded with a different initial void ratio and tested drained, in order to compare two different void ratios keeping the other parameters constant. The results showed that the resilient modulus is higher for the denser specimen, proving the significant effect of initial void ratio. The evolution of the permanent deformation for tests cemented with 5 and 7% was difficult to interpret due to scatter derived from the low strain level. For this reason, Rios (2011) concluded that it is not always possible to adapt the European Standard to cemented soils and that new testing criteria should be found.

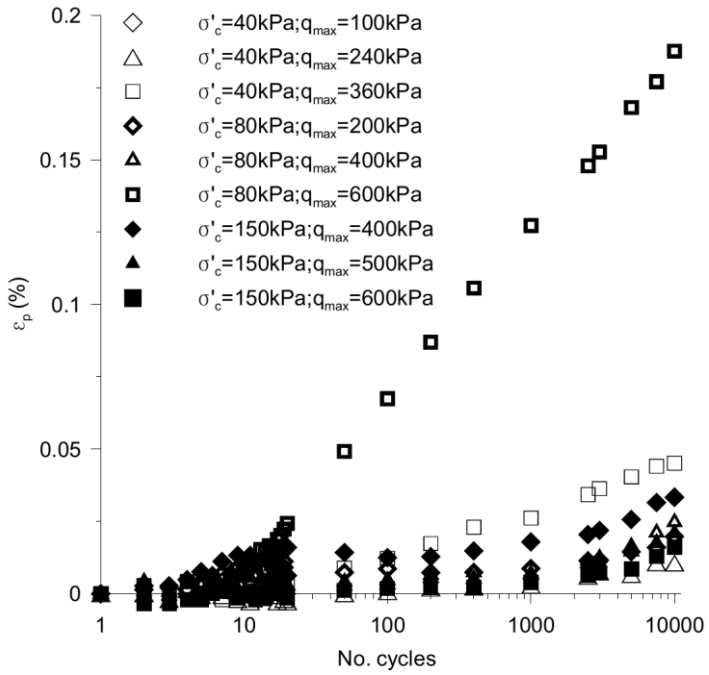

Fig. 2.29 – Accumulated vertical strain for type 2 test on specimen TC(2)_T2 (Rios, 2011)

Type 3 tests are not indicated in the European Standard and they were performed with the aim of studying the fatigue response of the soil. For this reason, these tests were carried out with a large number of cycles at a low stress level. Three specimens were moulded with C = 5% and two different initial void ratios: two specimens with a higher void ratio and one specimen with a lower void ratio. The two tests on the less compacted specimens were performed as follows: one undrained test divided in two stages of loading of 250000 cycles each (Fig. 2.30); one drained test including two stages with 500000 cycles each (Fig. 2.31). The two tests showed that the rate of permanent strain decreased with cycles but did not reach zero, which means that a continuous accumulation of permanent strain is observed. A change in the trend of vertical accumulation is observed for undrained tests after 1000 cycles and for drained tests after 10000 cycles. This result seems in accordance with the results obtained by Wichtmann et al. (2005), which also showed a change in the trend of accumulation in an uncemented soil after a high number of cycles. This important result shows the need for long-duration cyclic tests and the inadequacy of the present European Standard, which prescribes tests up to 20000 cycles. The resilient modulus remained relatively constant throughout each test. The drained test on the more compacted specimen did not show vertical strain accumulation, because the applied stress level was not adequate to produce an appreciable accumulated strain.

Type 3 tests are novel since they are not prescribed in European Standard and because of the very few literature reporting tests at a so high number of cycles. The results showed that is important to investigate the behaviour of cemented soil at such a high number of cycles since the accumulated permanent strain continues to evolve in cemented soils even after a great number of cycles and despite the low stress ratio applied.

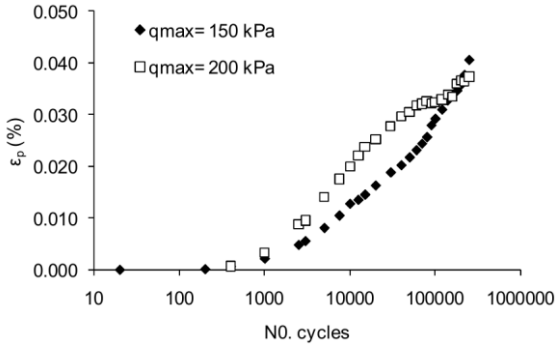

Fig. 2.30 – Accumulated vertical strain for type 3 undrained test (Rios, 2011)

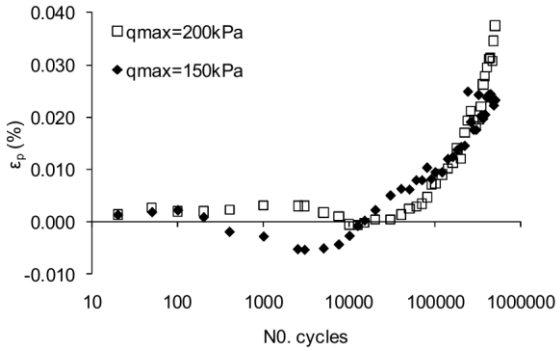

Fig. 2.31 – Accumulated vertical strain for type 3 drained test (Rios, 2011)

2.6. CONCLUSIONS

This chapter recalled the main research performed over uncemented soils in cyclic conditions, and cemented soils in monotonic and cyclic conditions.

Cemented soils shows a specific set of features that are not common to uncemented soils. Strength and stiffness are increased with respect to the corresponding uncemented material; boundary surface expands in isotropic and shear stress planes, thus, cemented soil can reach states in the stress space that are not permitted for the uncemented soil. The existing research proves that, even with some specificities, natural and artificial cementation respond to a common congruent framework. The main difference is that, while the former can be completely removed from the soil by the application of adequate stress and/or strain, the second remains an internal bias of the soil even at high stress levels and/or high stress repetition. This is because the bonds associated to natural cementation are weaker than the soil particles, while artificial bonds are stronger and resist even when particles are crushing.

Extensive research on cyclic loading conditions was found in literature, especially focused on uncemented soils. Of this, not many studies with a number of cycles beyond 1000 cycles were found. In fact, many studies were focused on the cyclic resistance of the soil, thus, tests were carried out with the aim of reaching cyclic failure within a reasonable amount of cycles rather than assess the long-term

behaviour of the soil under small-stress cyclic loading. Wichtmann et al. (2005) showed that the trend of accumulation of vertical strain with the number of cycles has a knee around 10000 cycles, confirming the importance of testing programmes with thousands of cycles, which is not very common in practice. This aspect is observed also in cemented soils, where the initial rate of destructuration is very low and it increases sensibly after thousands of cycles, leading to incremental strain accumulation. Additionally, the results on volumetric strain accumulation show a reversal in the sense of accumulation from a compressive to a dilative behaviour. The reversal point is found at a high number of cycles. It is observed that the lower is the applied stress, the higher is the number of cycles at which such switch occurs.

Modelling soil behaviour in monotonic and cyclic conditions has followed two approaches: empirical approach and constitutive modelling. Empirical approach is the simplest method; it is based on experimental results and is aimed at finding a mathematical law to predict the value of one or more strain component at a certain stage of the test. For cyclic conditions, the key variable is usually the number of cycles. Empirical relations are established between this independent variable and the accumulated strain and/or stiffness modulus. These relations are often limited to a small number of cycles and they do not have a general applicability. More advanced empirical models have a broader validity, but they increase in complexity, as the number of constant parameters to be calibrated is usually high. It is also important to note that the results of different empirical models often conflict with each other. Many relations were found for uncemented soils. Nevertheless, empirical models for cemented soils are few and more focused on stiffness degradation than strain accumulation.

A more general framework of the soil response is obtained through constitutive modelling. The flexibility of this approach allows the definition of models with increasing complexity, by the addition of more complex features on the simpler framework of existing models. With this hierarchical approach, models can be easily extended to other soil types and non-monotonic stress conditions, and specific features (e.g. cementation) can be incorporated in existing models without losing the original formulation. Thus, the basic elasto-plastic models based on Critical State concept have evolved to the bounding plasticity framework, with a kinematic hardening law in addition to the usual isotropic hardening concept. This framework is able to reproduce the soil behaviour observed in experimental tests. The accumulation of permanent strain in low-stress cyclic conditions and the smooth transition in stiffness from an elastic state to failure can be modelled only using this advanced framework and not with the simpler models. In the same way, cementation is a feature only reproducible with a specific extension of the basic formulation. The two aspects (bounding plasticity and cementation) can be combined in a single framework. This has been done in the past. Many models were developed including one or the two features combined. Nevertheless, the performance of these models has not been tested against long-term tests. Thus, the suitability of the existing models to reproduce long-term behaviour is not known.

In the final section of this chapter, the attention is focused on the soil studied in the present thesis. The material was extensively studied in uncemented and cemented conditions, in isotropic compression tests and monotonic drained and undrained tests. The outcome of this research shows the congruence between the soil behaviour and the general behaviour described by many authors for naturally cemented and other artificially cemented soils. Some specificities are present; cemented Porto silty-sand does not seem to recover a state of complete destructuration even if very high stress levels are applied. This is due to the strength of the artificial bonds that cannot be removed completely and alter permanently the structure of the soil. Nevertheless, the majority of the features generally recognized for cemented soils are observed in cemented Porto silty-sand. The constitutive modelling of the soil with a single surface model showed a good agreement but highlighted some known downsizes of this type of models.

Some cyclic triaxial test was performed on cemented Porto silty-sand. Three type of tests were executed. The first two types are based on an adaptation of the European Standard for uncemented soils. The results showed that this Standard is not always applicable to cemented soils, because of the low intensity of the stress and the low number of the loading cycles prescribed. The third type of tests is the most innovative and shows novel trends in the strain accumulation vs. number of cycles. Due to the very high number of cycles and the low stress imposed, this kind of tests is suitable to investigate the long-term behaviour of the material in the small-strain domain. This configuration of test is very hard to find in literature, because the majority of the cyclic tests on cemented soil show either a low number of loading cycles or are designed to assess the cyclic resistance of the soil. Thus, they are intended to induce a large accumulated strain and failure in a reasonable amount of time (i.e. number of cycles). In this logic, tests with a high number of cycles represent a by-product, rather than a planned outcome. Only two tests of type 3 were performed, thus a further research is necessary.

Chapter 3.

ADVANCED ELASTO-PLASTIC CONSTITUTIVE MODELS: FROM CAM-CLAY TO BOUNDING PLASTICITY

Advanced constitutive models were developed from the classic elasto-plastic framework. Different models were developed for specific purposes and were specialized on a specific feature that was not possible to reproduce correctly with the simpler framework (e.g.: soil liquefaction, ageing effects, wet-drainage cycles, effect of temperature, response of soils under cyclic loading, effect of cementation, etc.). In the present work, models for cyclic loading and models for cemented soils are of interest and attention is focused only on these two types of advanced models.

Strain accumulation due to low-amplitude repeated loads is a major issue in a vast variety of geotechnical infrastructures and structures such as roadways and railways platform embankments, foundation layers of wind turbines or storage tanks. In the past, the study of strain accumulation has been pursued through empirical laws. Such methodology is simple, but the results do not have a general validity, being dependent on the initial state of the specimen tested and on the test conditions. As reported by Wichtmann et al. (2005), there is a need for a systematic study on cyclic loading, since the present studies have been relying on experimental tests with insufficient number of loading cycles and the empirical laws inferred are not complete or contradictory.

A theoretical approach can be followed through a constitutive model based on a critical state soil mechanics framework. One-surface models cannot reproduce the complex behaviour of soils under repeated loading conditions (Yu, 2006). Some authors implemented a mixed approach, combining classic constitutive models with one or more empirical laws relating the progressive stiffness degradation and/or strain accumulation with the number of cycles. A theorethical framework is used to derive the complete stress-strain response of the soil at the first loading cycle (or at selected loading cycles); the empirical relations extend this result to the subsequent (or intermediate) cycles. In this way, a semi-empirical approach is obtained (e.g. Wichtmann et al., 2010; Pasten, 2013; Ni et al., 2015), which has the advantage of being able to infer the accumulation of permanent strain at the end of each loading cycle using a simple framework and a reduced computational time. Nevertheless, these models cannot reproduce the stress-strain hysteretic loop at each loading cycle.

Fully theorethical approach were developed within the framework of elastoplasticity. Models based on generalized plasticity (e.g. Tonni et al., 2006; Fu et al., 2014), bounding surface plasticity (e.g. Dafalias & Herrman, 1982; Bardet, 1986; Yu et al, 2007; Kan et al., 2014) and kinematic hardening plasticity

(e.g. Oka et al., 1999) proved to be capable of reproducing the experimentally observed smooth transition from elastic to fully plastic state and the hysteretic loop in cyclic loading.

In the framework of bonding surface plasticity, the classic single yield surface approach is replaced by a two surface option, with a smaller yield surface laying inside a larger bounding surface. The two surfaces are related by a mapping rule, associating each point of the internal surface with a corresponding point of the external surface, which in turns regulates the hardening modulus. Bardet (1986) used a radial mapping rule and an associated flow rule to model the cyclic behaviour of sands; Yu et al. (2007a), with a similar mapping rule and a non-associated flow rule, proposed a model intended for both sandy and clayey soils (CASM-c).

In the above-mentioned models, hardening is isotropic, meaning that the yield and bounding surface share a common origin and the yield surface expands or contracts without moving. In the kinematic hardening plasticity framework, the yield surface translates in the stress space following a translation rule that is usually proportional to the increment of plastic strain (Prager, 1955). In Oka et al. (1999) a nonlinear kinematic hardening rule is proposed, in which a term dependent of the accumulated plastic strain is added to the linear Prager term. In this way, the authors establish a history-dependent hardening rule, which can be reduced to the linear formulation by choosing particular parameters.

Other authors have combined the bounding surface model with a kinematic hardening approach, obtaining a moving yield surface and a hardening modulus dependent on the distance between inner and bounding surface (e.g. Al-Tabbaa & Muir Wood, 1989; Stallebrass & Taylor, 1997; Gajo & Muir Wood, 1999; Grammatikopoulou et al., 2006; Corti et al., 2016).

As referred in the precedent chapter, the behaviour of cemented soils has been modelled by defining a bonding variable that increases the dimension of the boundary surface. Such variable decreases monotonically following an energetic or accumulated plastic strain criterion, defined in a destructuration or damage law. Gens & Nova (1993) approach is described in detail in the present chapter, as it describes the general structure of this framework, which has been implemented in many successive models for different types of soils.

This chapter presents a review of the evolution of the constitutive models from the simpler framework to the more sophisticated ones, suitable for cemented soils and cyclic loading. As shown in the following sections, such progressive increasing of complexity was always pursued in a modular manner, in order to preserve the structure of the previous frameworks and adding extra features that can be deactivated by selecting specific parameters.

3.1. BASIC DEFINITIONS FOR STRESS AND STRAIN INVARIANTS

The basic definition and terminology adopted hereafter are specified in detail in Annex 1. In the same annex, the general framework of the elastic-hardening plastic model, which underlies the models described hereafter, is described.

Here the definitions for the stress in axisymmetric conditions are recalled:

$$p' = \frac{\sigma'_a + 2\sigma'_r}{3} \tag{3.1}$$

$$q = \sigma'_a - \sigma'_r \tag{3.2}$$

Subscripts *a* and *r* refer to the stress in vertical (parallel to the axis of a cylindrical specimen) and horizontal (radial) directions, respectively.

The vector of strain increment is composed by the volumetric and distortional components, which are defined as follows:

$$\begin{aligned} \varepsilon_v &= \varepsilon_a + 2\varepsilon_r \\ \varepsilon_s &= \frac{2}{3}(\varepsilon_a - \varepsilon_r) \end{aligned} \tag{3.3}$$

3.2. MODIFIED CAM CLAY MODEL (ROSCOE AND BURLAND, 1968)

Modified Cam clay (MCC) model represents the basis for the models presented in this paper. For this reason, a brief review is reported. Yield surface has the expression:

$$f = p'(p' - p'_0) + \left(\frac{q}{M}\right)^2 \tag{3.4}$$

or, alternatively:

$$f = (2p' - p'_0)^2 + \left(\frac{2q}{M}\right)^2 - p'^2_0 \tag{3.5}$$

which describes an ellipse in the stress plane (p', q), centered on the axis p' and passing through the origin of the coordinate system (Fig. 3.1).

The shape of the ellipse is controlled by M and its size is controlled by p'_0, that represents the hardening parameter (h).

In the principal stress space, its shape is reported in Fig. 3.2.

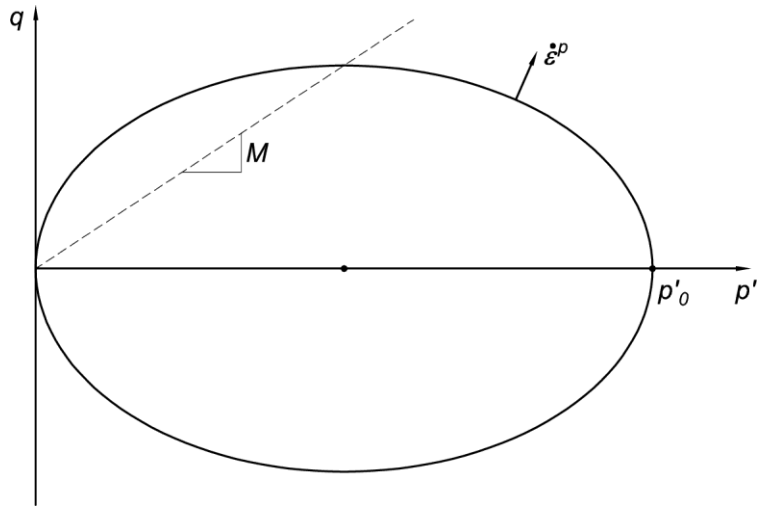

Fig. 3.1 – Cam clay model

The cross section of the yield surface in the deviatoric plane is a circle, because parameter M does not depend on Lode's angle θ.

The model uses an associated flow rule, thus $g \equiv f$ and the flow rule is:

$$\frac{\dot{\varepsilon}_v^p}{\dot{\varepsilon}_s^p} = \frac{\partial g/\partial p'}{\partial g/\partial q} = \frac{\partial f/\partial p'}{\partial f/\partial q} = \frac{M^2 - \eta'^2}{2\eta'} \tag{3.6}$$

where the dot superscript indicates an infinitesimal increment of the variable and η' is the effective stress ratio q/p'.

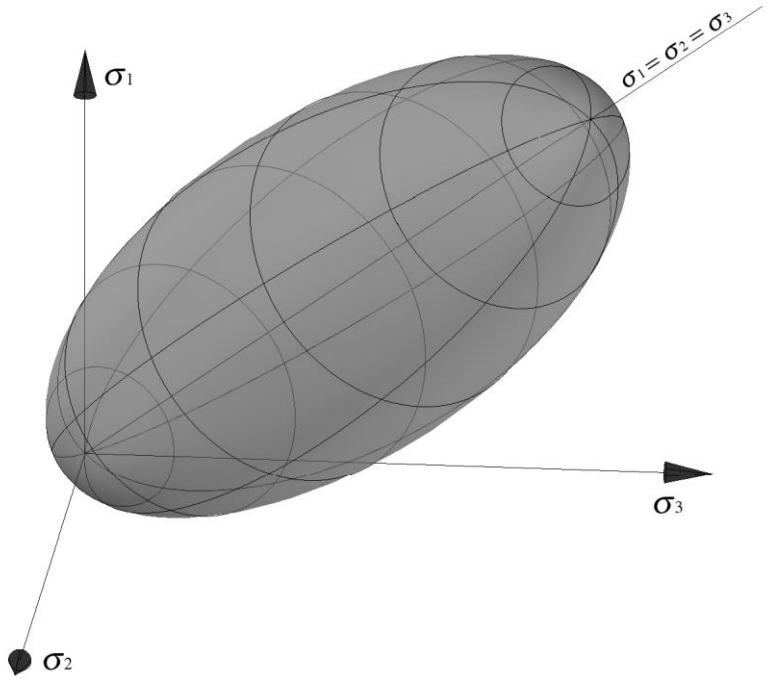

Fig. 3.2 - Cam-clay yield surface in the principal stress space

Hardening rule is isotropic and depending only on the volumetric strain increment:

$$\frac{\dot{p}_0'}{p_0'} = \frac{v_i}{(\lambda - \kappa)} \dot{\varepsilon}_v^p \tag{3.7}$$

In this relationship, v_i is the initial specific volume, λ is the slope of the normal compression line (NCL) in the $(\ln p', v)$ plane and κ is the slope of an unloading-reloading line in the same plane (Fig. 3.3). The usual convention of positive volumetric compression is adopted.

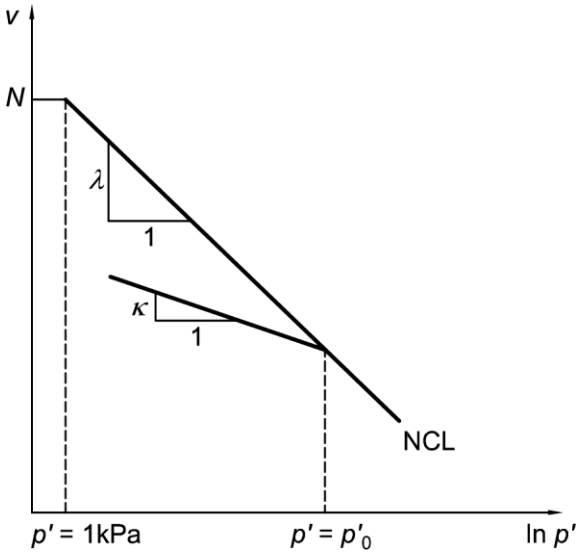

Fig. 3.3 - Normal compression line and unloading-reloading line in semilogarithmic isotropic plane

As described in detail in Annex 1, constitutive relations are determined by replacing yield surface and hardening rule expressions in Prager's consistency condition (1949):

$$df = \frac{\partial f}{\partial p'}\dot{p}' + \frac{\partial f}{\partial q}\dot{q} + \frac{\partial f}{\partial p_0'}\dot{p}_0' = 0 \tag{3.8}$$

Combining this expression with (3.4) and (3.7), the constitutive relations between plastic strain and stress increments are derived:

$$\begin{pmatrix} \dot{\varepsilon}_v^p \\ \dot{\varepsilon}_s^p \end{pmatrix} = \frac{\lambda - \kappa}{v_i p'(M^2 + \eta^2)} \begin{pmatrix} M^2 - \eta'^2 & 2\eta' \\ 2\eta' & \dfrac{4\eta'^2}{M^2 - \eta'^2} \end{pmatrix} \begin{pmatrix} \dot{p}' \\ \dot{q} \end{pmatrix} \tag{3.9}$$

Hardening modulus is determined as follows:

$$H = -\frac{\partial f}{\partial p_0'}\frac{\partial p_0'}{\partial \varepsilon_v^p}\frac{\partial g}{\partial p'} = p'\frac{v_i p_0'}{\lambda - \kappa}(2p' - p_0') \tag{3.10}$$

A non-linear law describes the elastic stress-strain relationship:

$$\begin{pmatrix} \dot{\varepsilon}_v^e \\ \dot{\varepsilon}_s^e \end{pmatrix} = \begin{pmatrix} \dfrac{\kappa}{v_i p'} & 0 \\ 0 & \dfrac{1}{3G} \end{pmatrix} \begin{pmatrix} \dot{p}' \\ \dot{q} \end{pmatrix} \tag{3.11}$$

which is a function of the bulk (K') and shear (G) moduli expressed below

$$\begin{aligned} K' &= \frac{v_i p'}{\kappa} \\ G &= \frac{3(1-2\nu)}{2(1+\nu)}K' \end{aligned} \tag{3.12}$$

where ν is Poisson's ratio.

By combining the elastic and plastic parcels of the strain increment, and inverting the relations, the complete constitutive relations are determined:

$$\begin{pmatrix} \dot{p}' \\ \dot{q} \end{pmatrix} = \left[\begin{pmatrix} K' & 0 \\ 0 & 3G \end{pmatrix} - \frac{\begin{pmatrix} K'^2(2p' - p_0')^2 & \dfrac{6GK'q(2p' - p_0')}{M^2} \\ \dfrac{6GK'q(2p' - p_0')}{M^2} & \dfrac{36G^2q^2}{M^4} \end{pmatrix}}{K'(2p' - p_0')^2 + \dfrac{12Gq^2}{M^4} + \dfrac{v_i\, p' p_0'(2p' - p_0')}{\lambda - \kappa}} \right] \begin{pmatrix} \dot{\varepsilon}_v^p \\ \dot{\varepsilon}_s^p \end{pmatrix} \tag{3.13}$$

Cam clay model requires the experimental determination of four soil parameters: λ, κ, M, ν. In addition, a reference point on the normal compression line is required (N).

3.3. AL-TABBAA AND MUIR WOOD MODEL (1989)

This section presents a brief description of the model, the full detail of the features are presented in Al-Tabbaa (1987), Al-Tabbaa & Muir Wood (1989) and Muir Wood (2004).

Bubble model was conceived as an extension of modified Cam clay model and the original formulation can be recovered by selecting specific parameters. Bubble model is formulated for axisymmetric conditions in the (p', q) effective stress plane.

3.3.1. YIELD SURFACE

An elliptical surface is defined in the stress plane and passing through its origin, called reference or outer or bounding surface (f_{ref} in Fig. 3.4). Inside this surface, the yield surface (the so-called bubble) is defined (f). This smaller surface presents the same shape of the reference surface and it is dragged along with the stress path. As the yield surface translates in the stress plane, plastic strain is developed (kinematic hardening). Each point P of the yield surface is associated with a conjugate point P' on the reference surface, defining the distance b between surfaces. This distance is in turn related to the stiffness of the soil. The two surfaces change in size whenever the bubble moves in translation, causing an isotropic hardening along with the kinematic hardening.

The outer surface has the expression of MCC surface, while the inner yield surface has the following expression:

$$f = \frac{(q - q_\alpha)^2}{M^2} + (p' - p'_\alpha)^2 - R^2 p_0'^2 \tag{3.14}$$

where p'_0 represents the size of the outer surface; M is the slope of the critical state line in the stress plane; R is the ratio of the sizes of the surfaces and (p'_α, q_α) are the coordinates of the centre of the bubble.

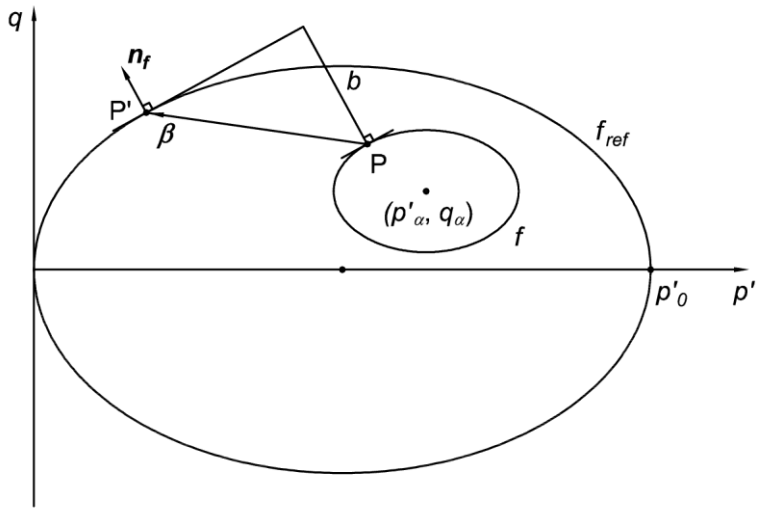

Fig. 3.4 – Al-Tabbaa & Muir Wood (1989) model

3.3.2. TRANSLATION RULE AND HARDENING MODULUS

Translation rule, indicating the direction in which the bubble translates, is defined in order to guarantee that the two surfaces meet without intersecting. For this reason, translation is always parallel to a vector $\boldsymbol{\beta}$, joining the current stress point on the yield surface with the corresponding conjugated point on the outer surface (conjugate points have the same direction of the outward normal $\boldsymbol{n_f}$ - Fig. 3.4):

$$\begin{pmatrix} \dot{p}'_\alpha \\ \dot{q}_\alpha \end{pmatrix} = \frac{\dot{p}'_0}{p'_0} \begin{pmatrix} p'_\alpha \\ q_\alpha \end{pmatrix} + S\boldsymbol{\beta} \tag{3.15}$$

The first term of the right-hand member refers to the change in the centre coordinates due to the expansion (or contraction) of the yield and reference surface and the second term is the assumed

translation along vector $\boldsymbol{\beta}$. Term S is a scaling parameter defining the magnitude of the translation. Its value is determined geometrically by considering that the stress point must remain onto the yield surface during the surface translation. Coordinate increments $(\dot{p}'_\alpha, \dot{q}_\alpha)$ are hardening parameters (whose definition is reported in Annex 1) and constitute the hardening parameter vector, together with size increment $\dot{p}'_0$:

$$\boldsymbol{h} = \begin{pmatrix} \dot{p}'_0 \\ \dot{p}'_\alpha \\ \dot{q}_\alpha \end{pmatrix} \tag{3.16}$$

The isotropic component of the vector maintains the same formulation of Cam clay model reported in (3.7). When yield and reference surface are in contact, hardening modulus is calculated as usual by combining the hardening rules and the yield surface expression in Prager's consistency condition (1949) (the general procedure is reported in Annex 1). In this case, the procedure shall include the three components of the hardening vector:

$$df = \frac{\partial f}{\partial p'}\dot{p}' + \frac{\partial f}{\partial q}\dot{q} + \frac{\partial f}{\partial p'_0}\dot{p}'_0 + \frac{\partial f}{\partial p'_\alpha}\dot{p}'_\alpha + \frac{\partial f}{\partial q_\alpha}\dot{q}_\alpha = 0 \tag{3.17}$$

Resulting in the following hardening modulus:

$$H_0 = \frac{v_i}{(\lambda - \kappa)}(p' - p'_\alpha)\left[p'(p' - p'_\alpha) + \frac{q(q - q_\alpha)}{M^2}\right] \tag{3.18}$$

The authors point out that, when the surfaces are not in contact, soil response is stiffer and the hardening modulus shall be higher. Thus, when the surfaces are not in contact, the hardening modulus is defined as:

$$H = H_0 + H' \tag{3.19}$$

where H_0 is the hardening modulus when the surfaces are in contact, and H' is a positive component arbitrarily defined, which is present only when the surfaces are not in contact and tends to zero as the yield surface approaches the outer surface. The definition of H' is not related to the consistency condition and shall be determined in order to fit the experimental behaviour of the particular soil studied. Al-Tabbaa & Muir Wood (1989) define this component as a function of the distance *b*:

$$H' = \frac{v_i}{\lambda - \kappa} B \left(\frac{b}{b_{max}}\right)^{\psi} p_0'^3 \tag{3.20}$$

As shown in Fig. 3.4, distance *b* is the scalar component of vector $\boldsymbol{\beta}$ in the direction of the normal to the yield surface $\boldsymbol{n_f}$ (Hashiguchi, 1985). Parameters λ and κ are the slope of the normal compression line and an unloading-reloading line in the isotropic compression plane (as in MCC model). Parameters ψ and *B* control the rate of change of the hardening modulus with the change of distance b. Parameter *B* is not present in Al-Tabbaa & Muir Wood (1989) but was introduced in a later implementation of the model by Rouainia & Muir Wood (2001) in order to improve the model flexibility.

Term b_{max} represents the maximum value that distance *b* can assume. The maximum distance between surfaces is reached when the reference and yield surface are in contact, and the stress point is located onto the point of the bubble opposite to the contact point. In addition, vectors $\boldsymbol{\beta}$ and $\boldsymbol{n_f}$ should be parallel, in order to maximize the scalar product. This situation corresponds to one of the two possible configurations shown in Fig. 3.5. The value of parameter *M* determines which of the two possible values is maximum. If $M > 1$, the maximum distance is in the direction parallel to axis q, otherwise it is in the direction parallel to axis p'. Since the model was originally conceived for fine soils that typically show

$M < 1$, Al-Tabbaa & Muir Wood (1989) assume that the maximum distance is in the direction parallel to axis p':

$$b_{max} = (1 - R)p'_0 \tag{3.21}$$

This is not generally true as it depends on the particular soil studied.

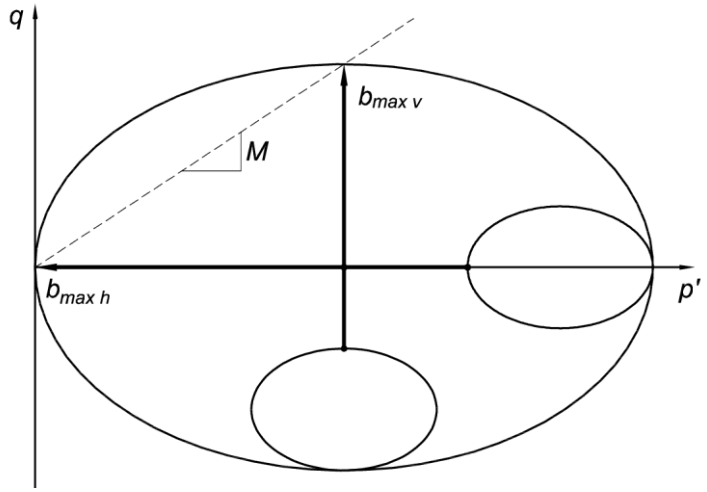

Fig. 3.5 – Possible maximum values of distance b

3.3.3. CONSTITUTIVE RELATIONS

The elastic relations are the same as in MCC model (equations (3.11)) and the flow rule is associated. Thus, the complete constitutive relations are:

$$\begin{pmatrix} \dot{\varepsilon}_v \\ \dot{\varepsilon}_s \end{pmatrix} = \left[\begin{pmatrix} \frac{\kappa}{v_i p'} & 0 \\ 0 & \frac{1}{3G} \end{pmatrix} + \frac{1}{H} \begin{pmatrix} (p' - p'_\alpha)^2 & (p' - p'_\alpha)\frac{q - q_\alpha}{M^2} \\ (p' - p'_\alpha)\frac{q - q_\alpha}{M^2} & \left(\frac{q - q_\alpha}{M^2}\right)^2 \end{pmatrix} \right] \begin{pmatrix} \dot{p'} \\ \dot{q} \end{pmatrix} \tag{3.22}$$

Model parameters are defined in Table 3.1. The matrices in square brackets correspond to the matrices of elastic $\boldsymbol{C}^e$ and plastic $\boldsymbol{C}^p$ compliance, respectively.

3.3.4. FAILURE

Failure is likely to occur when the hardening modulus H is nil or negative, because in such case the soil behaviour is unstable and cannot sustain an increase in the applied load. Since the modulus is the sum of two independent parcels, different situations can arise. In MCC model, hardening modulus is isotropic and it can be positive or negative depending whether the stress state intersects the yielding surface at a stress ratio η' greater or less than M. In the first case, H is negative (softening) and the soil can no longer sustain the stress, which reduces, causing instable behaviour and volumetric dilatancy. If H is positive, the soil compacts and the stress increases in elasto-plastic conditions (stable behaviour). In both cases, the stress state tends to approach the CSL and H tends to zero. In the present model, the isotropic parcel of hardening modulus can be positive or negative, while kinematic modulus H' is always positive. Soil stability depends on whether the sum of the two components is positive or negative.

Failure is not likely to occur when the bubble is far from the Cam clay, because in such situation kinematic modulus H' is typically greater in absolute value than the isotropic modulus H_0. Thus, although H_0 is negative, the overall hardening modulus H is positive. A positive hardening modulus corresponds to a stable elasto-plastic behaviour, thus failure is not expected in this case. When the bubble approaches the outer surface, distance b reduces and, consequently, modulus H' (still positive) tends to zero. Conversely, isotropic modulus H_0 does not vary considerably during bubble translation. If the stress state intersects the yield surface in the dilatant domain, H_0 is negative and remains negative throughout the translation path. As the kinematic modulus progressively decreases, the total hardening modulus H can be assume a negative value before the surfaces are in contact. For this reason, failure can occur when the surfaces are not in contact (i.e. inside the reference surface). This is likely to occur in the dilatant domain of critical state ($\eta' > M$, Fig. 3.6). This represents an improvement of the double surface approach with respect to MCC model. In fact, it is well known that in this domain MCC model overestimates the peak deviator stress envelope experimentally observed (Hvorslev surface). In MCC model, failure in dilatant domain occurs when the stress point intersects the yield surface, which is coincident with the reference surface of the present framework. In bounding plasticity surface approach, failure occurs at lower stresses, in better accordance with the experimental evidence.

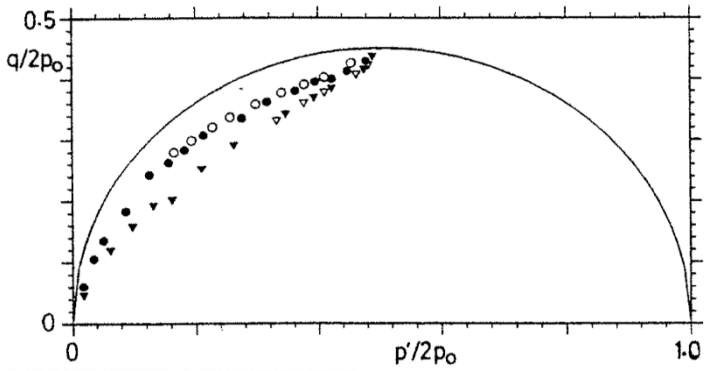

Fig. 3.6 - Failure points predicted by the model for dry side of critical state (Al-Tabbaa & Muir Wood, 1989)

The model requires the calibration of eight parameters: five are the same as MCC model and three are new parameters, as shown in Table 3.1. The model can be calibrated through triaxial or oedometer tests.

The model performance was assessed by comparing the model output with cyclic tests performed on a clayey soil (Fig. 3.7). The output shows the capability of this model to represent the cyclic hysteretic loops observed in the stress-strain plane. Volumetric and deviatoric strain are correctly reproduced in loading and unloading. The loops show a progressive change in stiffness, without the abrupt change observed in elasto-plastic models. Nevertheless, only few cycles are reproduced. Thus, the long-term performance of the model is not known.

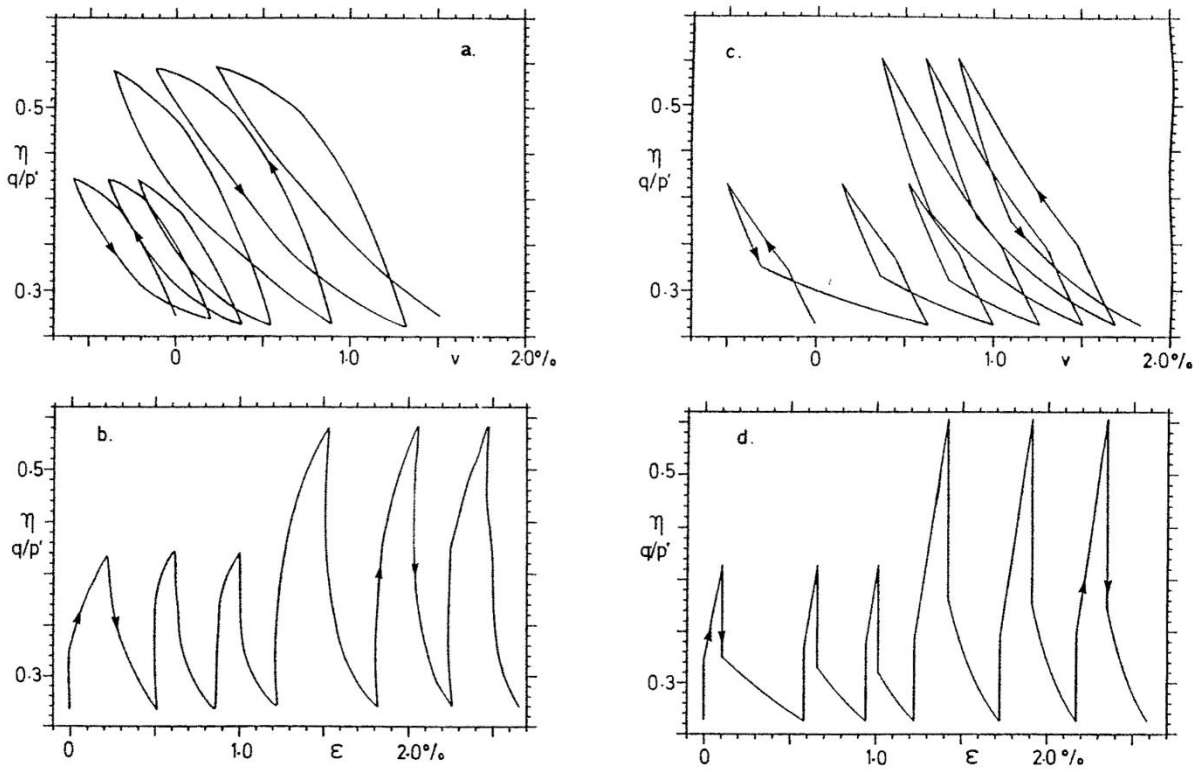

Fig. 3.7 – Performance of the calibrated model in cyclic loading: experimental observation (a, b) and model output (c, d) (Al-Tabbaa & Muir Wood, 1989)

Table 3.1 – Model parameters

	Elastic behaviour
κ (*)	slope of the isotropic unloading/reloading line
G (*)	elastic shear modulus
	Critical state
N (*)	parameter defining the position of the normal consolidation line (necessary to calculate $p_0^{'}$)
λ (*)	slope of the normal consolidation line
M (*)	stress ratio at critical state
	Yield surface
R	ratio of the sizes of yield and outer surfaces
	Hardening modulus
ψ	exponent of the interpolation function regulating kinematic hardening
B	linear parameter of the interpolation function regulating kinematic hardening

Symbol (*) identifies the parameters also required in Modified Cam-clay model

3.4. CASM MODEL (YU, 1998)

Clay and Sand model (CASM) was proposed by Yu (1998). This model (described in detail in Yu, 2006) has the advantage of being suitable for both clays and sands.

CASM is an elastic-plastic strain hardening model based on the concept of state parameter (in the present work indicated as $\bar{\psi}$), defined as the difference between the actual specific volume (or void ratio) and the specific volume (or void ratio) at the critical state for the same mean effective stress (Been & Jefferies, 1985):

$$\bar{\psi} = v + \lambda \ln p' - \Gamma \tag{3.23}$$

where v is the specific volume and the remaining parameters are illustrated in Fig. 3.8. State parameter is nil at the critical state, positive on the compressive (wet) side and negative on the dilatant (dry) side.

Early critical state models proved to be more suitable for clays and silts than for granular materials (Gens & Potts, 1988). Successive attempts to extend the original critical state framework to granular soils resulted in an increased complexity of the yield surface formulation and an increased number of material constants. To avoid this drawback, the state parameter concept was introduced with the aim of replacing the overconsolidation ratio (OCR), normally used for representing the state of fine soils, with a variable more suitable for granular soils. While OCR refers only to the stress state, state parameter depends on stress state and soil density, incorporating two key factors of the soil state. Experimental research confirmed that the state parameter is suitable to describe much of the behaviour of granular materials over a wide range of stresses and densities (Been & Jefferies, 1985). State parameter concept can be easily extended to clays and silts, thus, it is a more general variable than OCR.

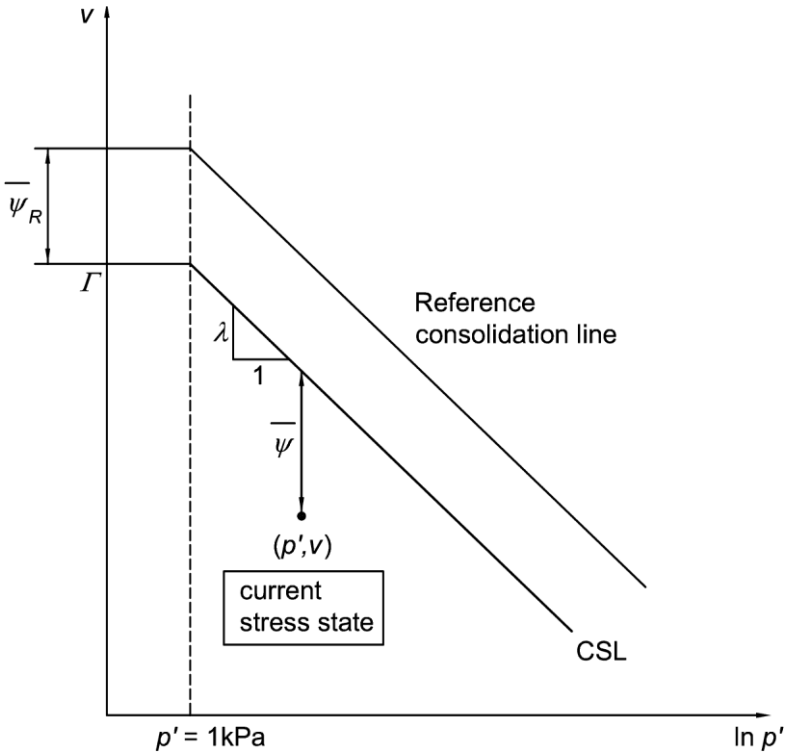

Fig. 3.8 – Definition of state parameter

3.4.1. YIELD SURFACE

Yield surface *f* presents the following expression:

$$f = \left(\frac{q}{Mp'}\right)^{\bar{n}} + \frac{\bar{\psi}}{\bar{\psi}_R} - 1 \tag{3.24}$$

In the above expression, $\bar{n}$ is a material constant called stress-state coefficient. It regulates the shape of the yield surface.

Term $\bar{\psi}_R$ is a positive reference state parameter, which denotes the vertical distance between the critical state line (CSL) and a reference compression line, assumed parallel to the CSL (Fig. 3.8). It is expressed as follows:

$$\bar{\psi}_R = (\lambda - \kappa) \ln r \tag{3.25}$$

Where r is a parameter called spacing ratio, varying with material type, controlling the location of the intersection between the CSL and the yield surface.

Yu (1998) states that for clays, normal compression line (NCL) should be used as the reference consolidation line. This assumption can be extended to sands, although the correct determination of the NCL is sometimes not straightforward. In these assumptions, referring to the scheme of Fig. 3.8 and with geometrical considerations, the expression of the yield surface (3.24) can be rewritten as follows:

$$f = \left(\frac{q}{Mp'}\right)^{\bar{n}} + \frac{1}{\ln r} \ln \frac{p'}{p'_0} \tag{3.26}$$

The expression is represented in Fig. 3.9 in the normalized stress plane.

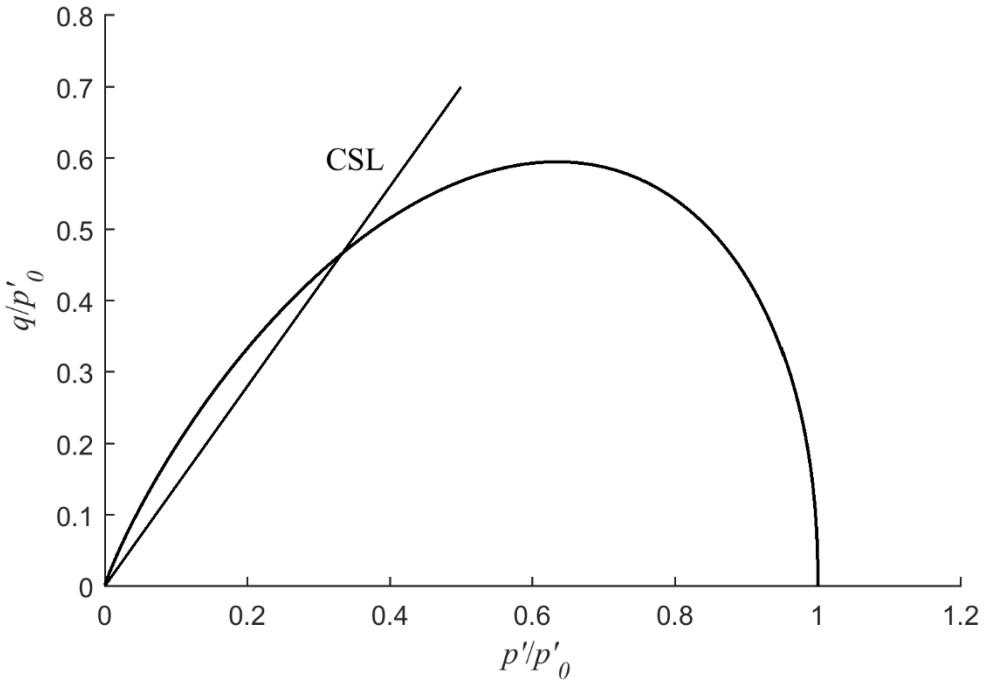

Fig. 3.9 – Yield surface for CASM model

The expression of the yield surface is very flexible and can be easily adapted to different type of soils by selecting two suitable values of the shape parameters $\bar{n}$ and r. In Fig. 3.10, parameter r is maintained constant and different values of $\bar{n}$ are adopted. As shown in figure, yield surface intersects the critical state line in a point with mean effective stress p' equal to (p'_0/r); the intersection does not necessarily

occur at the maximum deviatoric stress. This feature is typically observed in granular material: when tested in undrained conditions with a high initial confinement, this type of soil commonly shows a peak and a reduction of the deviatoric stress even if the volumetric behaviour is compressive. This behaviour cannot be correctly reproduced by a model for clays (as MCC model), where no softening is foreseen before reaching the critical state during compressive behaviour.

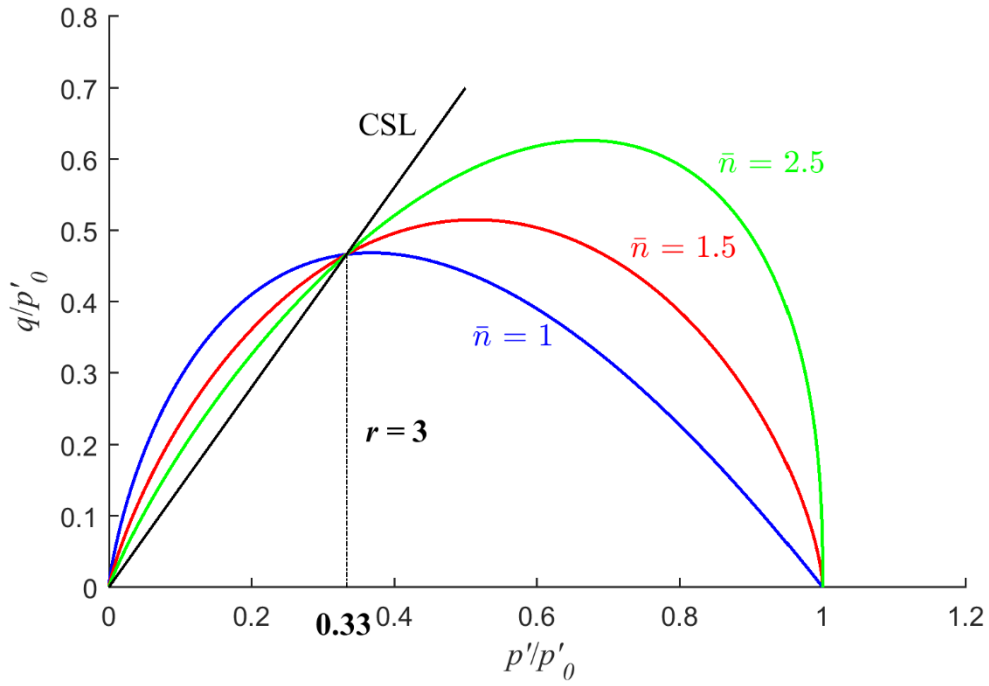

Fig. 3.10 – Effect of parameter $\bar{n}$ on CASM yield surface

If only parameter r is varied, the intersection between CSL and surface changes accordingly. The parameter has an influence on the point of the surface with maximum deviatoric stress. In Fig. 3.11, it can be observed that the maximum deviatoric stress reached by the surface increases for decreasing values of r. On the other hand, the mean effective stress at which peak stress is observed remains unchanged. In fact, this value only depends on parameter $\bar{n}$:

$$p'_{qmax} = \frac{p'_0}{\sqrt[\bar{n}]{\exp(1)}} \tag{3.27}$$

In the above expression, $\exp(1)$ is the base of natural logarithm. The maximum deviatoric stress is:

$$q_{max} = \frac{M p'_0}{\sqrt[\bar{n}]{\exp(1)\bar{n}\ln r}} \tag{3.28}$$

By selecting specific shape parameters, CASM yield surface can be adapted to reproduce the shape of other models. For instance, original Cam clay model (Schofield & Wroth, 1968) is obtained by selecting:

$$\begin{gathered} \bar{n} = 1 \\ r = \exp(1) \approx 2.72 \end{gathered} \tag{3.29}$$

Modified Cam clay is approximately recovered by selecting:

$$r = 2$$
$$\bar{n} = \frac{1}{\ln r} \approx 1.44 \tag{3.30}$$

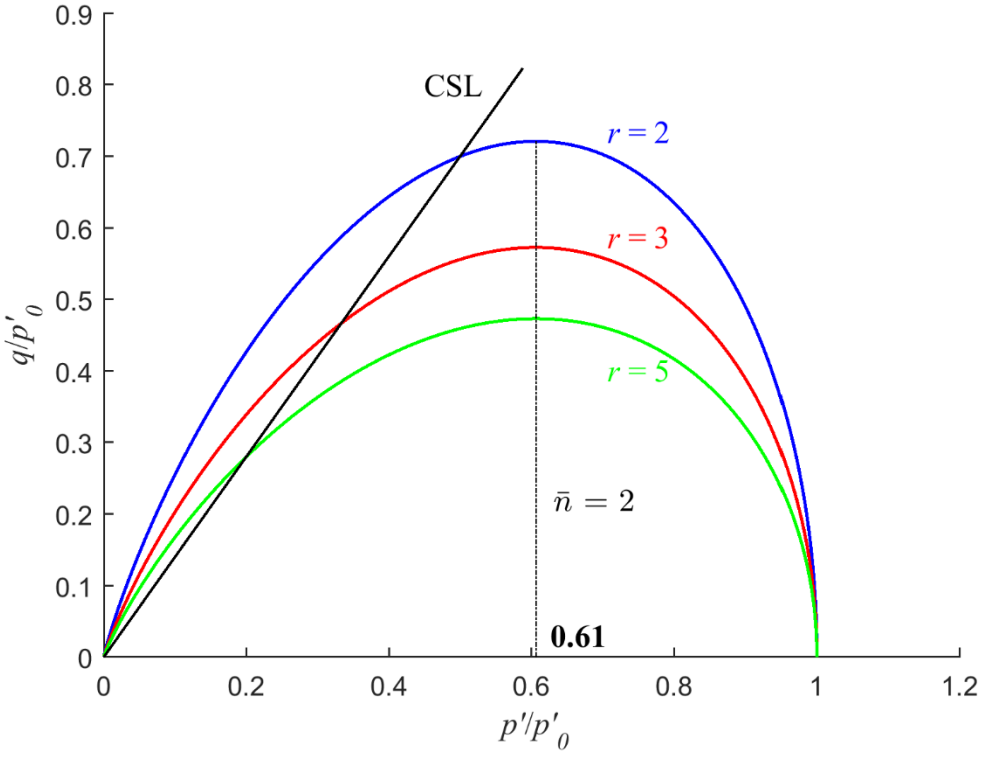

Fig. 3.11 – Effect of parameter r on CASM yield surface

3.4.2. FLOW RULE

The model adopts a non-associated flow rule. Plastic potential function depends on Rowe's stress-dilatancy relationship (Rowe, 1962, 1972), expressed as follows:

$$\frac{\dot{\varepsilon}_v^p}{\dot{\varepsilon}_s^p} = \frac{9(M - \eta')}{9 + 3M - 2M\eta'} \tag{3.31}$$

where η' is the effective stress ratio q/p', and ε_v^p, ε_s^p are the volumetric and deviatoric plastic strain increments, respectively.

Plastic potential function can be obtained by the integration of equation (3.31), resulting in:

$$g = 3M \ln\frac{p'}{\xi} + (3 + 2M)\ln(2\eta' + 3) - (3 - M)\ln(3 - \eta') \tag{3.32}$$

where ξ is a size parameter controlling the size of the plastic potential in the current stress state. The complete integration procedure is reported in Annex 3.

This function (reported in Fig. 3.12, along with CASM yield surface) ensures that the behaviour of the soil is dilative for $\eta' > M$, and contractive otherwise. At critical state, volumetric plastic strain increment is zero, as expected. On the other hand, the flow rule does not correctly reproduce the plastic strain increment in an isotropic stress path ($\eta' = 0$). In fact, in such case Rowe flow rule predicts deviatoric

and volumetric plastic strain increments, while the experimental evidence suggests that only volumetric plastic strain is generated in the isotropic plane.

An alternative flow rule is proposed by Yu (2006) (Fig. 3.12). This flow rule is based on a plastic potential whose shape is similar to CASM yield surface but with no volumetric strain increments at critical states. The stress-dilatancy relation in this case is:

$$\frac{\dot{\varepsilon}_v^p}{\dot{\varepsilon}_s^p} = \frac{M^n - \eta'^n}{m\,\eta'^{n-1}} \tag{3.33}$$

where m is an additional model parameter that allows adjusting the ratio of volumetric and distortional strain increments to experimental results. The plastic potential function (see Annex 3) is:

$$g = \ln\frac{p'}{\xi} + \frac{m}{n(m-1)}\ln\left[1 + (m-1)\left(\frac{\eta'}{M}\right)^n\right] \tag{3.34}$$

for $m \neq 1$ and:

$$g = \ln\frac{p'}{\xi} + \frac{1}{n}\left(\frac{\eta'}{M}\right)^n \tag{3.35}$$

for $m = 1$.

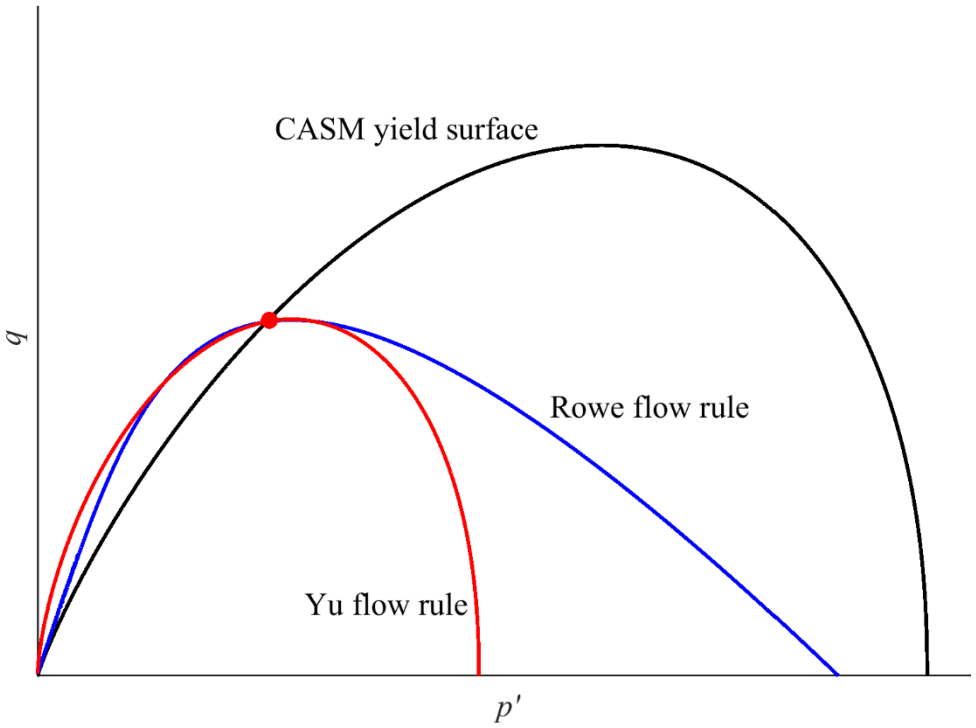

Fig. 3.12 – Shape of Rowe and Yu flow rules

The figure shows a generic stress state on the yield surface and the two proposed flow rules. One can see that Yu plastic potential surface intersects the horizontal axis at a perpendicular angle. Thus, the generated plastic strain (perpendicular to the plastic potential by definition) in an isotropic stress path are expected to be purely volumetric.

3.4.3. HARDENING MODULUS AND ELASTIC BEHAVIOUR

As in MCC model, the hardening rule depends solely on the variation of the size of the surface (equation (3.7)). Hence, hardening modulus has a similar expression as in (3.10) but adapted to the present yield surface and flow rule:

$$H = -\frac{\partial f}{\partial p_0'}\frac{\partial p_0'}{\partial \varepsilon_v^p}\frac{\partial g}{\partial p'} = \frac{1}{\ln r}\frac{v_i}{\lambda - \kappa}\frac{\partial g}{\partial p'} \tag{3.36}$$

$\partial g/\partial p'$ is the first derivative in p' of the selected flow rule.

Elastic behaviour follows the non-linear law of Cam clay model (equation (3.11)).

3.4.4. MODEL PERFORMANCE

The model was tested against clays and sands to assess its performance. In the case of clays, a comparison with the output of MCC model was performed, showing a better fit of the present model to the experimental data. Conversely to MCC model, CASM is capable to not overestimate the peak strength of very overconsolidated clays (Fig. 3.13(a)). The development of volumetric strain (or pore water pressure) during triaxial loading showed a better fit than MCC in overconsolidated and normally consolidated samples of the same material.

The model was tested against very loose, loose, medium dense and dense sand with good results. In particular, the undrained behaviour of very loose sands is well reproduced, with a peak strength followed by sudden strain softening (example in Fig. 3.13(b)).

3.5. GENS & NOVA FRAMEWORK FOR BONDED SOILS (1993)

Many authors have shown that the behaviour of soft rocks such as marl, tuff or calcarenite can be described by introducing only a few additional parameters into the original mathematical structure of models for remoulded or intact uncemented soils. Gens & Nova (1993) proposed a constitutive model for bonded soils and weak rocks able to reproduce the destructuration process of a bonded material during yielding. The model is developed in the framework of hardening plasticity for unbounded soil enhanced with conceptual features taking into account the level of bonding and the destructuration law, which is a measure of the damage. This model is conceived for monotonic loading and it is not suitable to model soil response under cyclic loading.

3.5.1. EFFECT OF BONDING

The value of bonding is defined in terms of the difference in specific volume Δv between the normal consolidation line (NCL) for the unbounded material and the state boundary line for a particular value of p'. In the (p', q) plane, yield surface is enlarged with respect to the corresponding uncemented soil, as an effect of bonding. In the isotropic compression plane, NCL translates towards higher values of the intercepts with the axes, expanding the domain of the permissible states. As shown in Fig. 3.14b, bonding causes an expansion of the yield surface towards the positive direction of the p' axis (corresponding to a higher isotropic yield stress) and towards the negative direction (tensile strength).

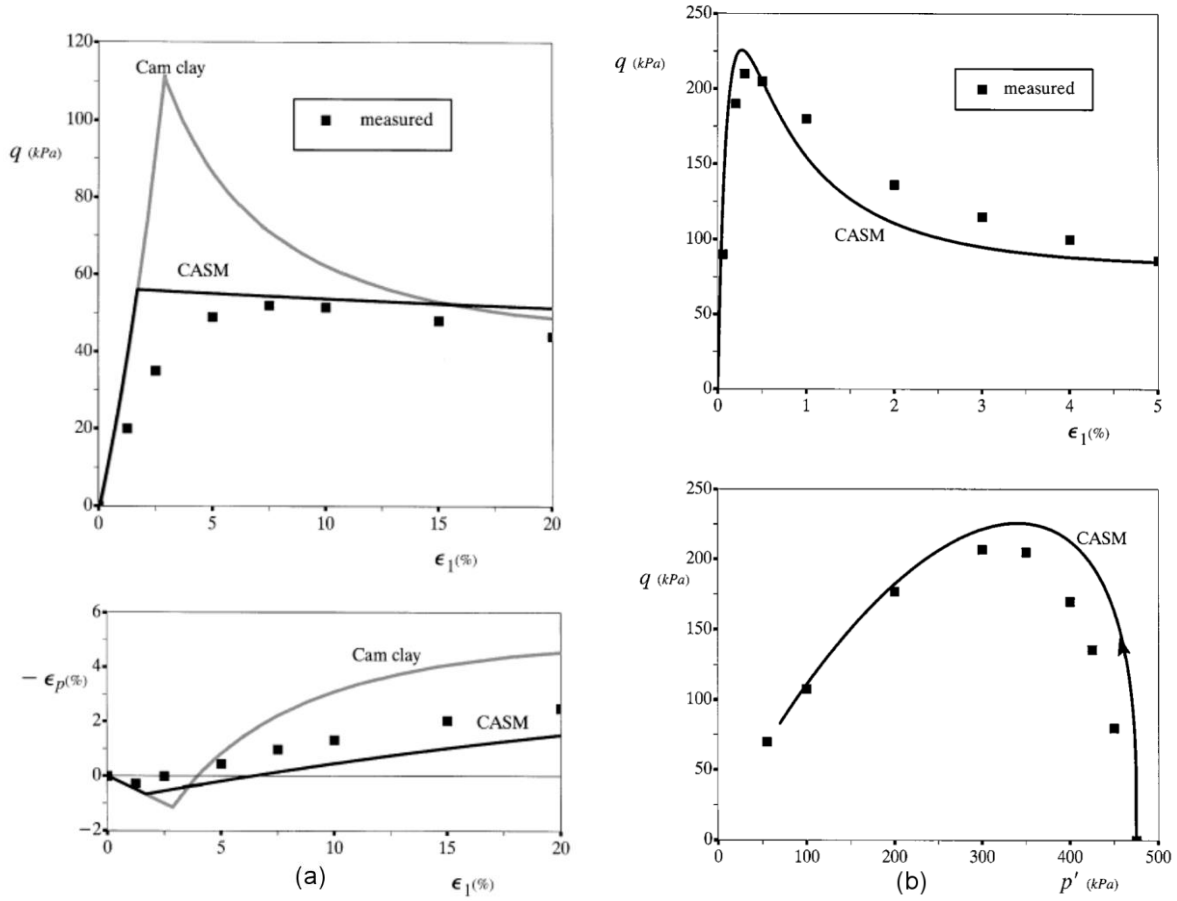

Fig. 3.13 – (a) Performance of CASM model with clayey soil (comparison with MCC model); (b) Performance of CASM model on very loose sand (Yu, 1998)

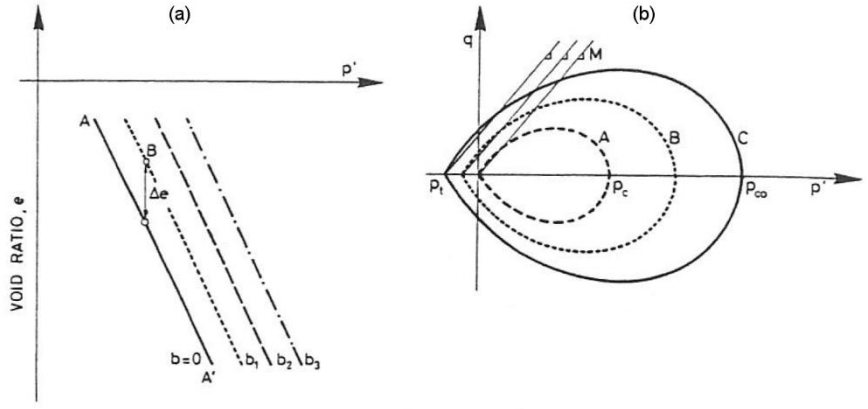

Fig. 3.14 – Behaviour of soil with various degrees of bonding: (a) isotropic plane and (b) yield surfaces (Gens & Nova, 1993)

The yield surface of the bonded soil is controlled by two parameters: p_{co} that reflects the yield stress of the bonded soil under isotropic compression; and p_t, related to the tensile strength (the two quantities are intended as effective stresses). For increasing bonding, both parameters increase. These parameters are linked with bonding as follows:

$$\frac{p_{co}}{p_c} = f(b) \tag{3.37}$$

$$\frac{p_t}{p_c} = f_t(b) \tag{3.38}$$

where p_c is the effective isotropic yield stress for unbonded soil and b is a non-dimensional variable that represents the amount of bonding. If b is nil, the properties of an unbonded soil are recovered, with p_{co} equal to p_c and p_t equal to zero.

3.5.2. BOND DEGRADATION

The evolution of yielding process is controlled by the unbonded plastic hardening and by bond degradation represented by their hardening moduli, H_s and H_d:

$$H = H_s - H_d \tag{3.39}$$

H_s is the usual isotropic hardening modulus (simply noted as H in MCC model), associated solely to the unbonded soil matrix. It can assume positive or negative values and it regulates the expansion or reduction (softening) of the yield surface as for the unbonded soil. As in MCC model, isotropic hardening depends on the parameter regulating the size of the yield surface (equation (3.7)). In the present framework, such parameter (here noted as p_c) has the following general formulation:

$$\dot{p}_c = \frac{\partial p_c}{\partial \varepsilon_v^p}\dot{\varepsilon}_v^p + \frac{\partial p_c}{\partial \varepsilon_s^p}\dot{\varepsilon}_s^p = 0 \tag{3.40}$$

In MCC model, p_c only depends on the volumetric plastic strain increment:

$$\frac{\partial p_c}{\partial \varepsilon_s^p} = 0 \tag{3.41}$$

In Gens & Nova (1993) framework, the hardening parameter can depend on one or both components of the plastic strain vector. This choice depends on the type of soil to be modelled. In fact, condition (3.41) is valid for fine soils (thus, it is suitable for MCC model) where no volumetric strain is expected at critical state; conversely, in the case of sands, dilation is observed in post-critical states. Thus, for granular soils, parameter p_c shall be dependent on both components of plastic strain.

Term H_d is relative to the progressive loss of bonding during loading. In particular, it regulates the shrinkage of the yield surface due to bond degradation; thus, its value is always positive (the negative sign in (3.39) makes its contribution always negative). The level of bonding in the soil is expressed by the bonding variable b. This variable has an initial positive value b_0 and decreases monotonically with the increasing degradation of bonding. Degradation is controlled by a damage variable h:

$$b = b(h) \tag{3.42}$$

Such variable is in turn a function of the plastic strain vector $\boldsymbol{\varepsilon}^p$:

$$h = h(\boldsymbol{\varepsilon}^p) \tag{3.43}$$

Function h is a monotonically increasing function and b is a decreasing function, as shown in Fig. 3.15.

In axisymmetric conditions, this leads to

$$h = h(\varepsilon_v^p, \varepsilon_s^p) \tag{3.44}$$

where ε_v^p and ε_s^p are the plastic volumetric and shear strain, respectively.

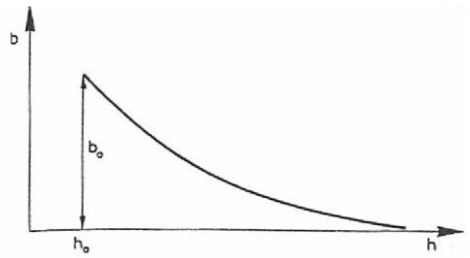

Fig. 3.15 – Relation between bonding and damage (Gens & Nova, 1993)

As previously showed, H_s is a function of the stress state; thus, there is a locus in the stress space where it is equal to zero (in MCC model, it coincides with the CSL). This locus divides the space into two regions: one for high confinement pressures, where $H_s > 0$ (Fig. 3.16a), and the other for low pressures, where the modulus is negative (Fig. 3.16b). If the soil yields in the first region, two situations can occur: if $H_s > H_d$ (case reported in figure), the yield surface expands until the soils fails at $H = 0$. If $H_s < H_d$ (i.e. the strengthening due to hardening is inferior to degradation due to debonding), H is negative and the yield surface shrinks (softening). For low confining pressures, the soil yields in the region where $H_s < 0$. In this case, total modulus H is the sum of two negative terms and softening is expected in any region of the domain.

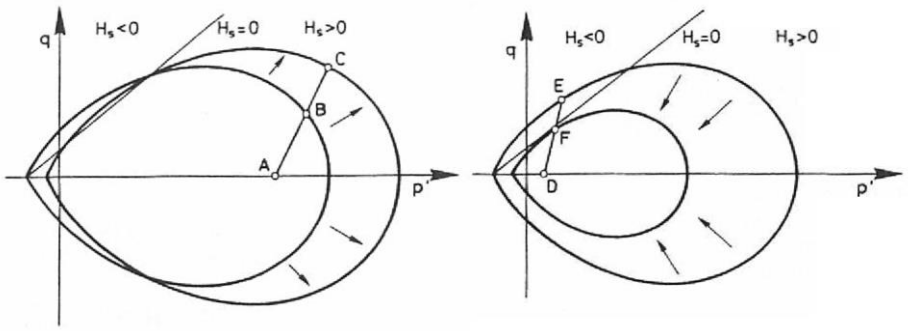

(a) (b)

Fig. 3.16 – Evolution of the yield surface in the $H_s > 0$ region (with $H_s > H_d$) (a) and in the $H_s < 0$ region (b) (Gens & Nova, 1993)

The authors state that a soil can be considered rigorously linear elastic only up to axial strains of the order of 10^{-5}. This implies that non-elastic behaviour is observed well before the stress state approaches the yield surface. The authors assume that elasticity is valid in first approximation. Nevertheless, the model is not suitable to reproduce more complicated behaviour, such as small-strain cyclic loading. In models based on kinematic hardening, additional yield surfaces are considered inside the outer surface, in order to incorporate this feature of the soil behaviour.

3.5.3. IMPLEMENTATION OF THE MODEL

The authors implemented an existing model for unbonded soils in the proposed framework for bonded soils. The model developed by Nova (1988) was adopted as reference surface for the unbonded material. In the new framework, the original yield function assumes the following form:

$$f \equiv 3(\gamma - 3)\beta ln\frac{p'^*}{p_{co}} + \eta^{*2}\left(\frac{3}{2}(\gamma - 1) - \frac{2}{9}\gamma\eta^*\right) = 0 \tag{3.45}$$

where

$$p'^{*} = p' + p_t$$
$$\eta^{*} = q/p'^{*} \tag{3.46}$$

γ is a constitutive parameter related to the value of η^{*}, and β is a parameter related to the shape of f. The plastic potential function g has the following expression:

$$g \equiv 9(\gamma - 3) ln \frac{p'^{*}}{p_{co}} + \eta^{*2} \left(\frac{3}{2}(\gamma - 1) - \frac{2}{9}\gamma\eta^{*} \right) = 0 \tag{3.47}$$

Functions f and g coincide only if $\beta = 3$. Thus, flow rule is associated only for this particular value of the parameter; otherwise, it is non-associated. This feature gives an increased flexibility to the model.

Functions (3.37) and (3.38) are defined as follows:

$$f(b) = p_{co}/p_c = 1 + b \tag{3.48}$$

$$f_t(b) = p_t/p_c = \alpha_t b \tag{3.49}$$

The relation that links bond degradation with damage is:

$$b = b_0 e^{-(h - h_0)} \tag{3.50}$$

Damage variable h is in turn a function of volumetric and shear plastic strain increments:

$$\dot{h} = h_1 \left| \dot{\varepsilon}_s^p \right| + h_2 \left| \dot{\varepsilon}_v^p \right| \tag{3.51}$$

The absolute values guarantee that function h is monotonically increasing regardless the sign of the plastic strains.

Hardening parameter p_c depends on volumetric and shear plastic strain:

$$p_c = (p_c)_i \exp \left(\frac{\varepsilon_v^p + \xi (3/2 (\varepsilon_s^p)^2)^{1/2}}{B_p} \right) \tag{3.52}$$

ξ and B_p are model parameters and $(p_c)_i$ is the value of p_c when plastic strain is zero.

Finally, the behaviour inside the yield locus is expressed by a non-linear elastic relation:

$$\dot{\varepsilon}_v^e = \kappa \frac{\dot{p}'}{p'}$$
$$\dot{\varepsilon}_s^e = L\dot{\eta} \tag{3.53}$$

In this framework, the unbonded and bonded components of the soil behaviour are modelled separately and are independent from each other. This allows the inclusion of existing models for unbonded soils in the present formulation. The application of a model is immediate if the yield surface can be written in the form $f(p', \eta) = 0$ by applying the same change of variables as in (3.45). Thus, results obtained for the same soil in unbonded and bonded conditions can be incorporated in a single congruent approach, reducing the calibration effort.

3.5.4. MODEL PERFORMANCE

The model was tested in isotropic and triaxial stress conditions, in order to show qualitatively its performance. Different levels of bonding were applied to simulated isotropic tests, including unbonded soil. All the tests had the same initial value of p_c. The consolidation curves (Fig. 3.17) show a translation of the isotropic yield stress to increasing values for increasing bonding. The curves show a progressive degradation with the development of plastic strain and a tendency to converge towards the consolidation curve for the unbonded material for high levels of applied stress. The rate of degradation is higher in

tests with higher levels of bonding. This behaviour is in agreement with the framework for bonded soil described in Chapter 2 (Fig. 2.1 and Fig. 2.2).

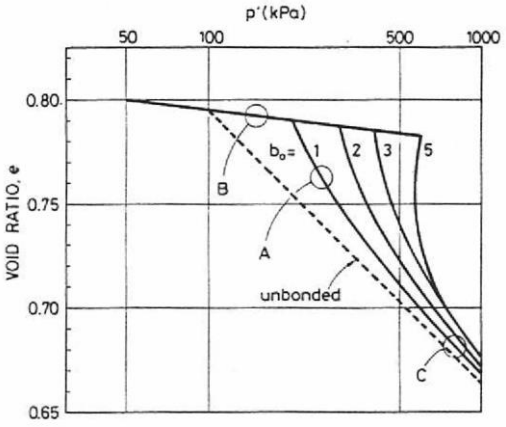

Fig. 3.17 – Simulated isotropic consolidation curves for different degrees of bonding (Gens & Nova, 1993)

Simulated drained triaxial tests were performed with the same level of bonding and different confining pressures. The results (Fig. 3.18) showed the different behaviour between tests with different confinement. High confined tests show volumetric compression and strain hardening. Low confined tests show dilatancy and a brittle behaviour, with a sharp peak in deviatoric stress followed by softening. In all the tests, bond degradation occurs in a gradual manner.

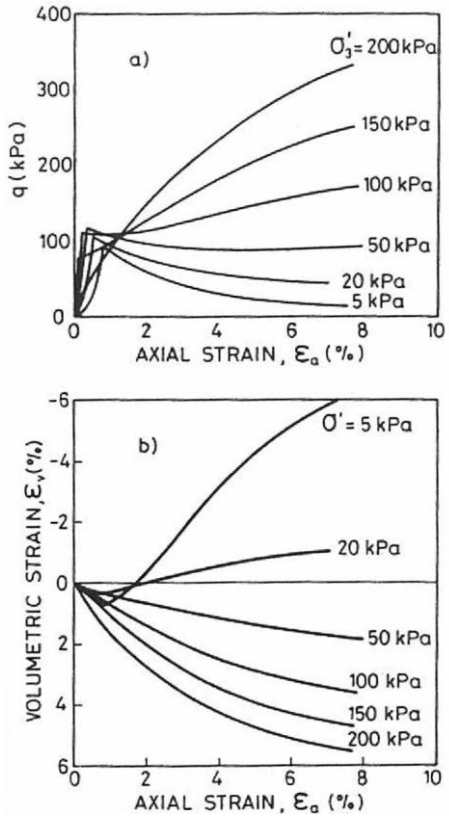

Fig. 3.18 – Simulated triaxial compression test results: (a) deviatoric stress vs. axial strain and (b) volumetric vs. axial strain (Gens & Nova, 1993)

3.6. CONCLUSIONS

The present chapter described the mathematical formulation of some advanced constitutive models based on the elastic hardening-plastic framework. The evolution of the framework from the Cam clay model to more sophisticated models has been shown. More complex models have been developed with base on the existing ones in an increasing complexity and potentially universal way. The structure of the simpler models was incorporated in the more sophisticated ones. More complex models are conceived in a form that allows to restore the precedent formulation by selecting specific values for the parameters regulating the new features.

Cam clay model is an isotropically hardening model conceived for clays, based on the critical state concept. It is equipped with the fundamental features of an elasto-plastic model: yield surface, hardening rule, flow rule, and elastic law. In this model, hardening is isotropic and flow rule is associated. In order to model different type of soils under different state of stress, more complex models need to be used. The new models should include new features following three parallel lines of evolution: the possibility of model different type of soils; the possibility to include cyclic loading; and the possibility to model bonded soils.

The first feature was implemented in clay and sand model (CASM). In such model, the yield surface can be adapted to various type of soils through the calibration of two specific shape parameters. This feature, in combination with a non-associated flow rule, enhances the variety of soils that can be modelled by the soil.

Bounding surface plasticity permits to model the hysteretic response observed in soils subjected to cyclic loading by combining a mapping rule and a kinematically hardening smaller yield surface. In this way, the purely elastic domain is restrained to a small area and plastic strain is observed during loading and unloading phases. Soil stiffness variation with strain is smooth and there is not the abrupt variation observed in one-surface models.

Cementation is reproduced in an effective framework that can be easily applied to existing models for granular soils. A structure variable is defined and a damage law is defined governing the progressive destructuration of the soil, related to the accumulation of plastic strain.

In Chapter 6, the features described herein are tentatively combined to define a new framework able to describe the cyclic behaviour of the cemented soil studied in the present study.

Chapter 4.

EXPERIMENTAL PROGRAMME: ASSESSING THE LEVEL OF BONDING

A vast experimental programme was conducted on a series of compacted specimens of Porto residual silty-sand in uncemented and artificially cemented conditions, using the materials, equipment, and procedure described hereafter. In order to maximize the amount of data retrieved from each specimen, different types of non-destructive tests were performed before conducting the specimen to failure. After the moulding, cemented specimens were submitted to a series of dynamic tests in order to assess the gain in stiffness with time. After 28 days period of curing (planned in view of the short-term curing period of this cement), the specimens were submitted to long-term cyclic triaxial test. As discussed in the following chapters, the deviatoric cyclic stress imposed to the specimens was small comparing to the ultimate load in corresponding monotonic conditions. Thus, the imposed load did not conduct the specimen to failure, even with the large number of cycles imposed. This is coherent with the aim of studying the soil behaviour in the so-called small-strain domain described in Chapter 2. For this reason, the cemented specimen could be retrieved from the triaxial cell without evident damages and submitted to additional tests. More specifically, a further dynamic test was performed in order to assess the difference in stiffness before and after the test. Finally, the specimen was conducted to failure through an unconfined compression test (UCT). The timeline of the testing programme for a specimen is reported in Fig. 4.1. For uncemented specimens, dynamic tests were not performed, since their characteristics do not evolve in time.

In the present chapter, the moulding process, and the dynamic and UCT tests are described. Particular attention is focused on the characteristics of cementation of the specimens: initial level of bonding; the gain of bonding with the curing, the destructuration caused by cyclic stress, and the final strength of the cemented soil. Cyclic triaxial tests, which represent the most important part of the present research, are presented separately in Chapter 5.

4.1. MATERIALS STUDIED

4.1.1. PORTO RESIDUAL SILTY-SAND

Porto residual soil is a remoulded well-graded silty sand originated by the weathering of Porto granite, the most common rock in the north-western region of Portugal. The soil was studied in detail in its natural and remoulded state in static and monotonic loading conditions (Viana da Fonseca, 1996, 2003; Viana da Fonseca et al., 2006, 2013b; Rios, 2011; Amaral, 2012). As shown by Viana da Fonseca (2003),

this soil in its natural state has some variability in the grain distribution curve, even if extracted in the same site (Fig. 4.2).

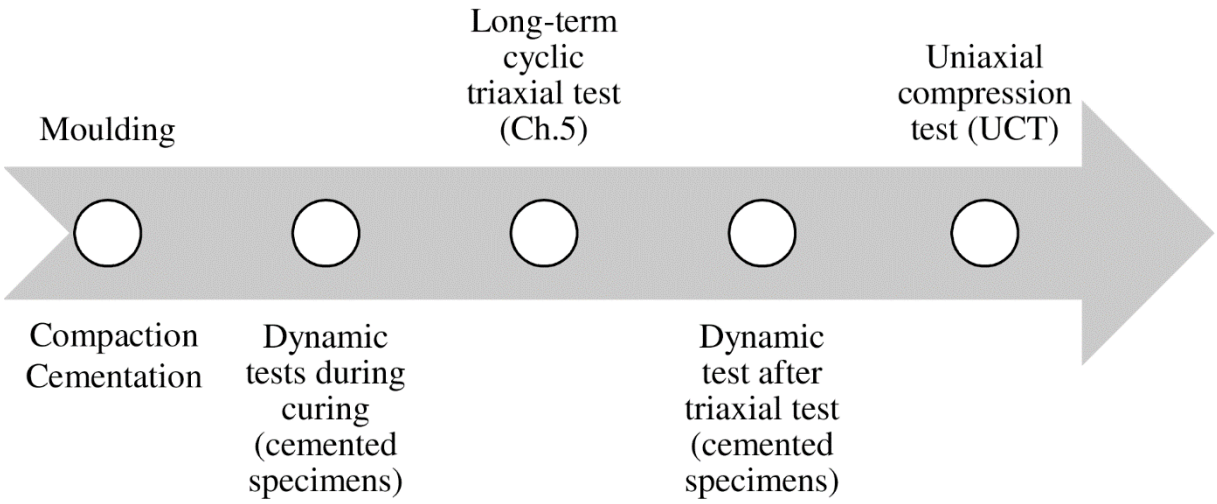

Fig. 4.1 – Timeline of the experimental programme on a single specimen

Because of this non homogeneity (typical of residual soils), other authors (Rios, 2011; Amaral, 2012) who have studied this soil in remoulded conditions, decided to correct the soil grain distribution curve in order to obtain a consistent research work and to meet the Portuguese specifications for soil-cement mixtures. In the particular case of the extracted site, the amount of fines had to be reduced from the natural 40% to 30%. Such correction was applied also in the present research, in order to have a consistent research work. Due to the great amount of soil required for the laboratory tests, the correction was performed over different batches of soil, obtaining slightly different corrected curves. Some corrected grain distribution curves used are shown in Fig. 4.3.

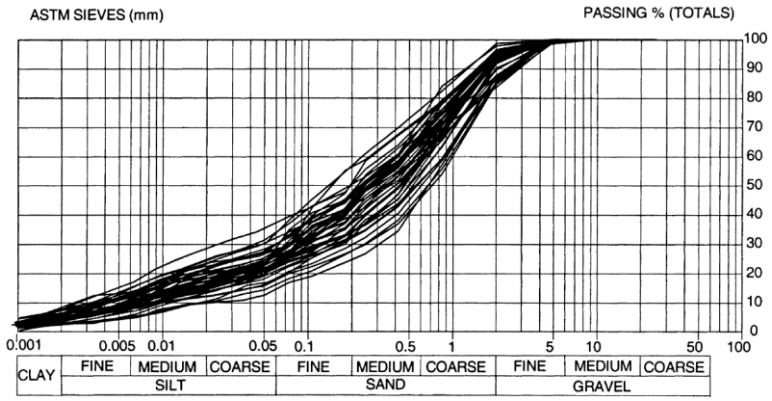

Fig. 4.2 - Grain size distribution curves of Porto silty-sand (Viana da Fonseca, 2003)

This soil is classified as a silty sand (SM) according to the unified classification system (ASTM, 1998a), being a very well graded soil. The results of the physical identification tests are shown in Table 4.1.

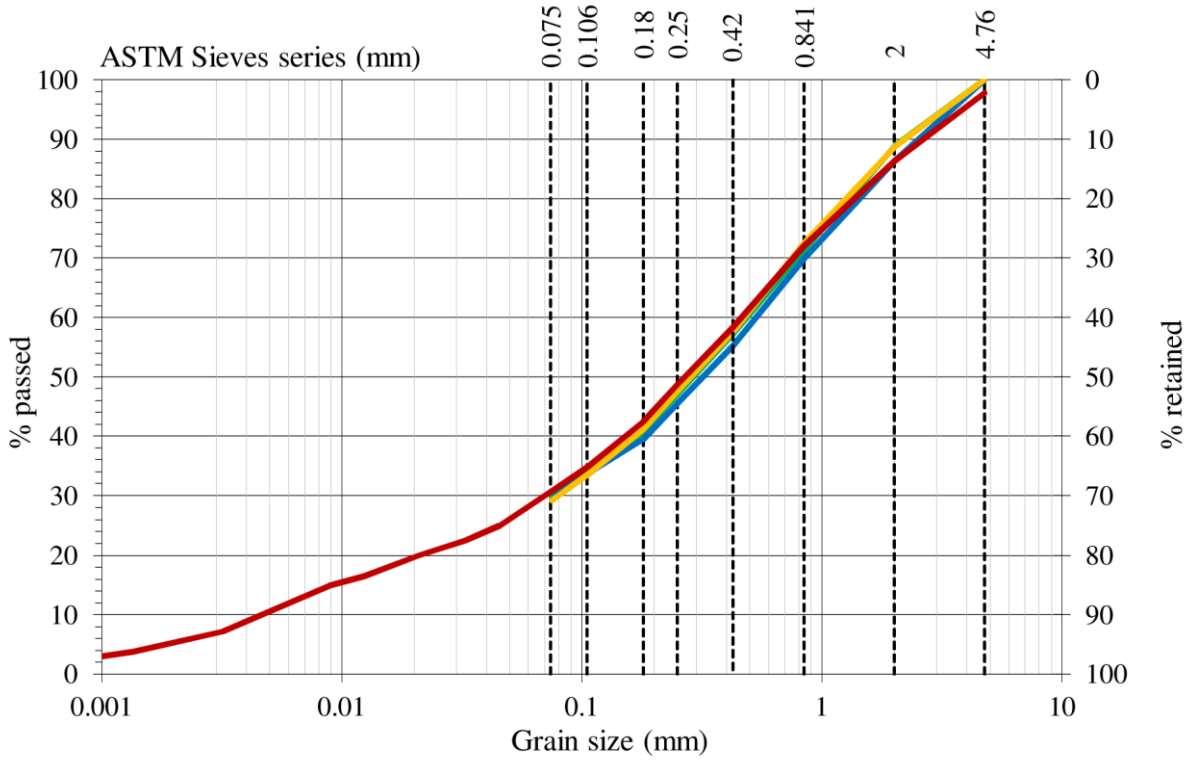

Fig. 4.3 – Some corrected grain size distribution curves for the studied soil

Table 4.1 - Physical parameters of the soil

G_s	D_{50} (mm)	C_u	C_c	w_L (%)	w_P (%)
2.72	0.25	113	2.72	34	31

where

- G_s is the specific gravity;
- C_u is the uniformity coefficient;
- D_{50} is the effective diameter, i.e. the largest particle size in the smallest 50%;
- C_c is the curvature coefficient;
- w_L is the liquid limit;
- w_P is the plastic limit.

From the difference between these two limits, a plastic index equal to 3 is obtained, which makes the soil non-plastic.

4.1.2. CEMENT

Portland cement of high initial strength was used as the cementing agent of these mixtures. The cement used is denominated as CEM I 52,5 R in European Standard EN 197-1 (CEN, 2000). This type of cement has a rapid increase of strength and reaches nominal strength within 28 days.

This cement presents more than 95% of clinker and its mechanical characteristics, determined by the manufacturer in accordance with EN 196-1 (CEN, 1994), are shown in Table 4.2. The unit mass of this cement is 3.1 g/cm^3 (Rios, 2011).

Table 4.2 - Mechanical characteristics

Compression Strength (MPa) (EN 197-1)	
Initial Strength	Final Strength
2 days	28 days
≥ 30	≥ 52.5

4.2. PREPARATION OF THE SPECIMENS

Coop & Atkinson (1993) report that an important effect of cementing is a reduction in specific volume resulting from the increase in fines content. This reduction influences the stress-strain behaviour and the peak strength of the soil. Therefore, the authors conclude that comparisons between the behaviour of cemented and uncemented soils should be carried out on samples with the same grading. For this reason, the cemented specimens were prepared with a soil from which it was previously removed an amount of fines equal to the weight of cement to be introduced (Fig. 4.4 and Fig. 4.5). The higher the cement content in a specimen, the higher was the amount of fines removed from the base material. This procedure ensures that the grain size distribution is the same for all the cemented and uncemented specimens tested.

The day before the moulding, a small amount of soil was weighted before and after a period of approximately 12 hours in the oven with the purpose of evaluating the hygroscopic water content of the soil and consequently the exact volume of water to be added to the mixture to assure the target moisture content. The needed amount of soil, cement and tap water were collected. Soil and cement were mixed (Fig. 4.6) until a uniform consistency was obtained. Water was then added continuing the mixing process until a homogeneous paste was created (Fig. 4.7).

Fig. 4.4 - Specimen preparation: sieving the soil in order to remove the fine fraction

Fig. 4.5 - Specimen preparation: weighing removed fine fraction

Fig. 4.6 - Specimen preparation: mixing soil and cement

The amount of cement for each mixture was calculated basing on the mass of dry soil and the target moisture content. The target water content of all the samples was 12%; this value was retrieved from Standard and Modified Proctor tests performed over a mixture of 3% of cement (Rios, 2011). These tests showed that a water content of approximately 12% is the optimum moisture content to obtain the highest unit weight.

After mixing sufficient material for one specimen, the mixture was divided in three parts and stored in three closed containers (Fig. 4.8) to avoid moisture loss before subsequent compaction. Two small portions of the mixture were taken for moisture content determination (Fig. 4.9).

Next, compaction was performed using the method proposed by Ladd (1978) and adopted by many authors (Consoli et al., 2007; Viana da Fonseca et al., 2010; Rios, 2011). The correct weight of soil-cement mixture was placed into a cylindrical stainless steel lubricated mould (Fig. 4.10), and statically compacted in three layers to reach the specified dry density (Fig. 4.11). The top of each layer was slightly

scarified to ensure continuity between the layers. The sample was extracted (with a hand operated vertical extruder) from the mould 12 hours after this process in order to prevent swelling (Fig. 4.12).

Fig. 4.7 - Specimen preparation: adding water to the soil-cement mixture

Fig. 4.8 – Specimen preparation: fractioning the mixture

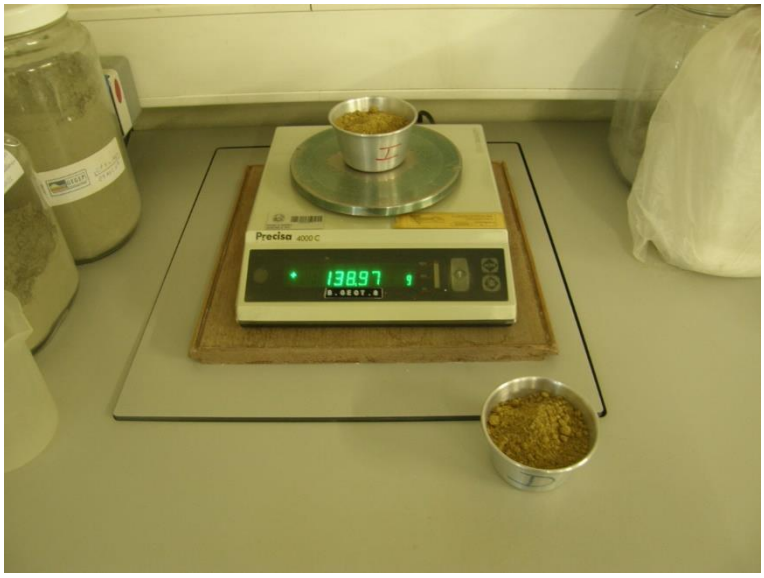

Fig. 4.9 – Specimen preparation: moisture content determination

Fig. 4.10 – Specimen preparation: pouring the mixture into the mould

The physical parameters of the specimen were carefully evaluated in order to control the quality of the moulding process. The water content was determined during the moulding process as specified earlier (Fig. 4.9). After extraction, the specimen was weighted with a high precision scale and its dimensions (diameter and height) measured with a Vernier calliper (Fig. 4.13).

The specimen was considered suitable for testing if the following tolerances were met:

- Dry unit weight (γ_d) within ±1% of target value;
- Moisture content (w) within ±0.5% of the target value;
- Diameter(D_s) within ±1 mm;
- Height (H_s) within ±2 mm.

Fig. 4.11 – Specimen preparation: static compaction

Fig. 4.12 – Specimen extrusion

The specimen was then placed in a plastic bag in order to avoid significant variation of moisture content (Fig. 4.14) and cured in a humid chamber at 23°C ±2°C and a relative humidity above 95% for 28 days. The gain of strength is very fast in the first 7 days of curing and then becomes slower, as shown in the dynamic tests presented in paragraph 4.3. Still, it was decided to wait for a curing period of 28 days, to assume that the gain in cementation for the following two weeks of curing (the period of the triaxial test of one million of cycles), would be negligible.

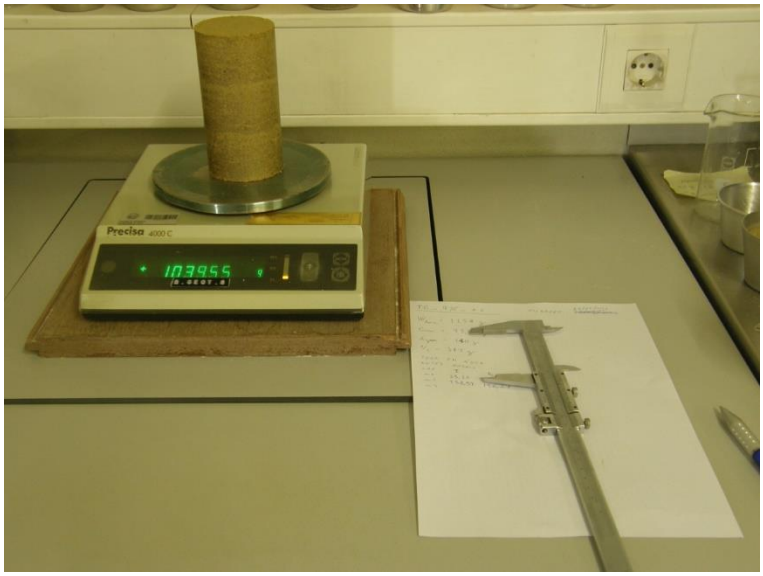

Fig. 4.13 – Weight and dimensions measurement

Fig. 4.14 – Specimen prepared to be stored in humid chamber

4.3. DYNAMIC TESTS

4.3.1. INTRODUCTION

Low energy dynamic tests were performed on the same cemented specimens submitted to cyclic triaxial tests, in order to measure the evolution of the extremely low strain (up to the order of 10^{-5}) stiffness parameters (elastic moduli) during the curing time of 28 days preceding the execution of the cyclic triaxial test. An additional dynamic test was performed on the cemented specimens after the cyclic tests, in order to assess the variation in stiffness due to the test. Uncemented specimens were not submitted to dynamic tests before cyclic triaxial test since their stiffness parameters do not essentially evolve in time. Moreover, it was not possible to test them after cyclic loading because the percolation of water destroyed their integrity after confining pressure was removed at the end of the cyclic triaxial test.

4.3.2. TESTING PROGRAMME

After compaction, the specimen was left one day in the moulding cylinder that was kept in the humid chamber. The first dynamic test was performed right after demoulding. Specimens were kept in the humid chamber, inside a plastic bag to avoid loss of humidity during curing time. Specimens were tested more frequently in the first days after demoulding, when the variation of the stiffness parameters is higher. If one indicates as “day 0” the day of compaction, readings were performed at days 1, 2, 5, 9, 14, 21 and 23. At day 23, the specimen was submerged in a water tank in order to facilitate its saturation, in preparation for the subsequent triaxial test. At day 26, the specimen was removed from the tank, submitted to a further dynamic test and then mounted in the triaxial cell. The results of this last dynamic test were different from the previous ones because of the higher water content (suction effects).

At day 40, after the cyclic triaxial test has been performed (see Chapter 5), the specimen was removed from the cell and the last dynamic test was performed, before submitting the same specimen to unconfined compression test (paragraph 4.4).

4.3.3. EQUIPMENT

The instrumentation used for the dynamic tests consists in an ultrasonic equipment called Pundit Lab®, manufactured by Proceq® (Fig. 4.15). Two couples of piezoelectric ultrasonic transducers by Olympus-Panametrics® were used: a pair for longitudinal ("P") wave, with a nominal frequency of 50 kHz; a pair for shear ("S") wave velocities measurement (nominal frequency of 82 kHz) (Fig. 4.16). For each couple, one transducer is used as transmitter and the other one as receiver.

They are both connected to Pundit Lab®, which is capable of generating a pulse wave, reading the response wave and sending the results to a computer for data analysis. A thin layer of coupling ultrasonic gel was used to improve coupling between the transducers and the specimen.

4.3.4. DATA PROCESSING AND RESULTS

Fig. 4.17 shows a typical output of a longitudinal wave displayed in the software Punditlink®, provided with the instrumentation. Knowing the time of wave's first arrival and the space between the transducers (the height of the specimen), it is possible to calculate the compression (longitudinal) and shear (transversal) wave velocity (V_P and V_S respectively).

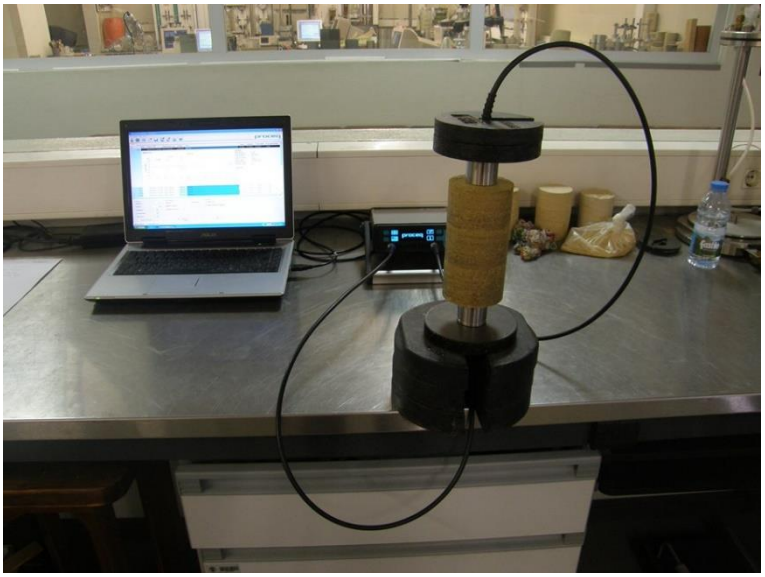

Fig. 4.15 - Equipment for dynamic test: Pundit Lab® is visible behind the specimen

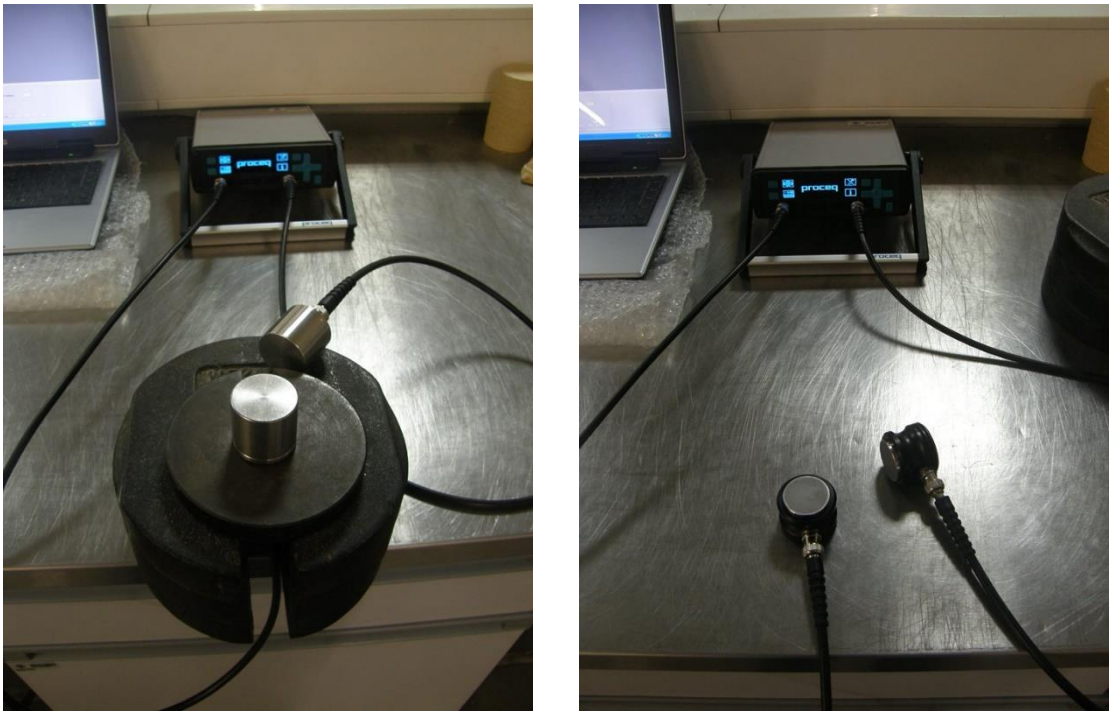

(a) (b)

Fig. 4.16 – Ultrasonic transducers manufactured by Olympus-Panametrics® for (a) longitudinal ("P") and (b) shear ("S") wave velocities measurement

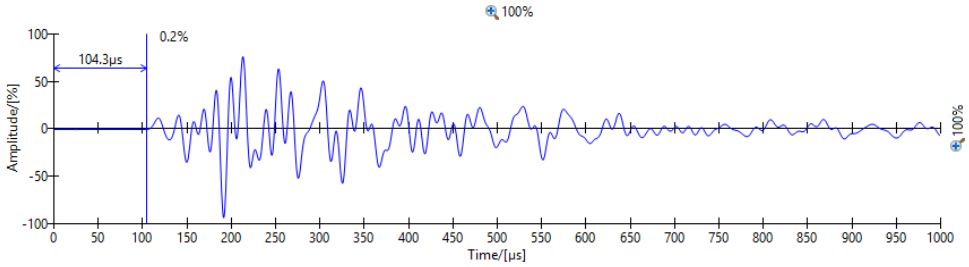

Fig. 4.17 – Reading of a longitudinal ("P") wave displayed with Punditlink®. Time of first arrival is shown.

The determination of the elastic parameters is performed according to the following equations:

$$M_0 = \rho V_P^2 \tag{4.1}$$

$$G_0 = \rho V_S^2 \tag{4.2}$$

$$\nu_0 = \frac{\left(\frac{V_P}{V_S}\right)^2 - 2}{2\left(\frac{V_P}{V_S}\right)^2 - 2} \tag{4.3}$$

$$E_0 = 2G_0(1 + \nu_0) \tag{4.4}$$

where:

- ρ is the mass density (unit mass) of the specimen;
- E_0 is Young's modulus;
- G_0 is the shear modulus;
- ν_0 is Poisson's ratio;
- M_0 is the longitudinal modulus.

The subscript "0" refers to the value of these parameters in the small-strain domain, corresponding to strains of the order of up to 10^{-5}. In order to determine the unit mass ρ, the specimens were weighted and the geometrical dimensions were measured before each test.

In the following figures, an example of data processing is showed, with the evolution of the parameters throughout the curing period, for a specimen with 7% of cement content. Results before submerging the specimen and after submerging the specimen in water are shown in the graphs. The "diamond" data point at day 26 refers to the measurement performed before submitting the specimen to the cyclic triaxial test; the second point (40 days) refers to the specimen after the end of the cyclic triaxial test.

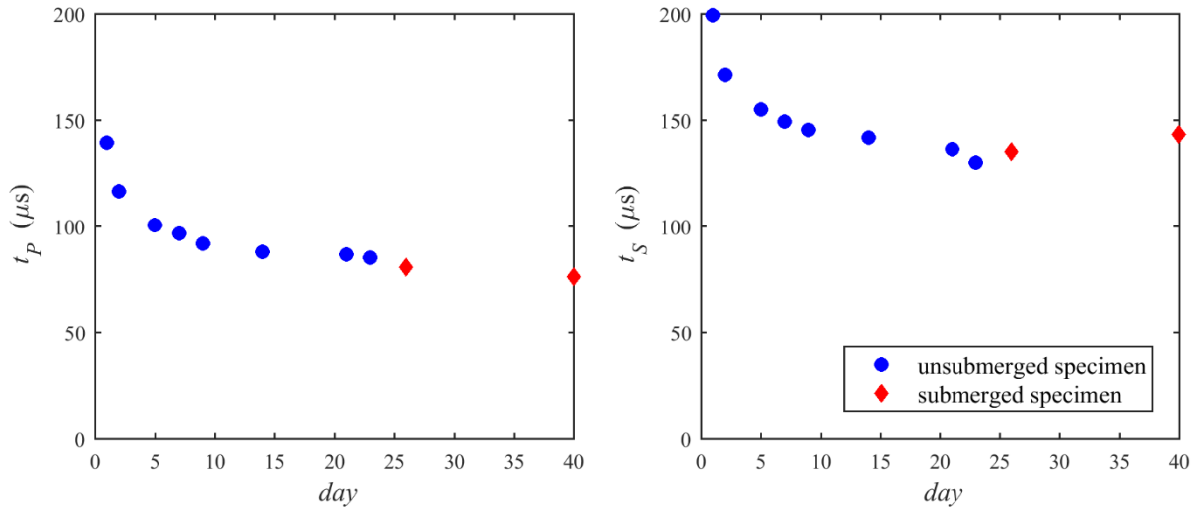

Fig. 4.18 – Arrival times for longitudinal and shear waves vs. days of curing

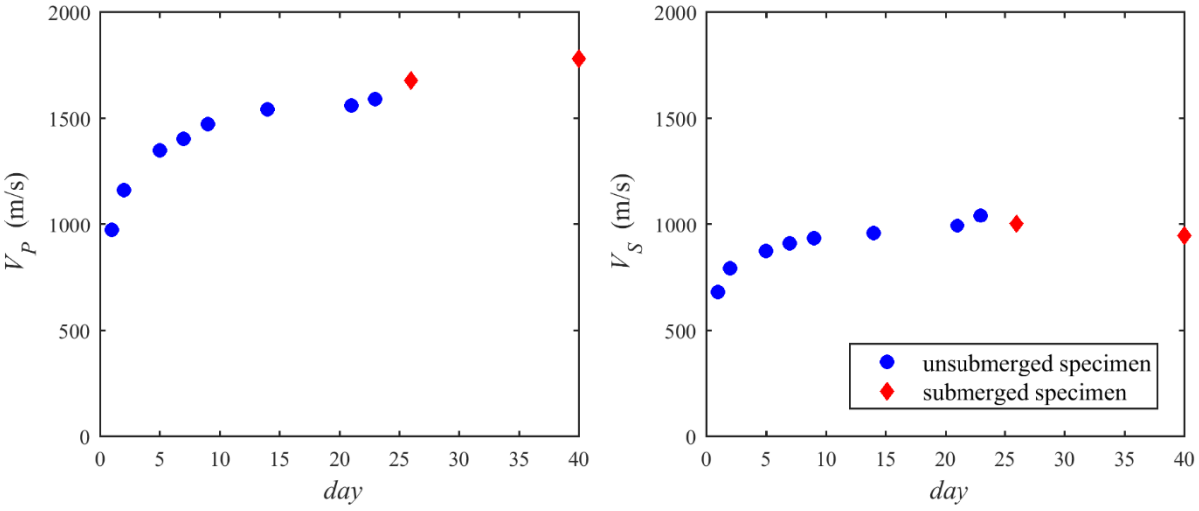

Fig. 4.19 – Longitudinal and shear wave velocity vs. days of curing

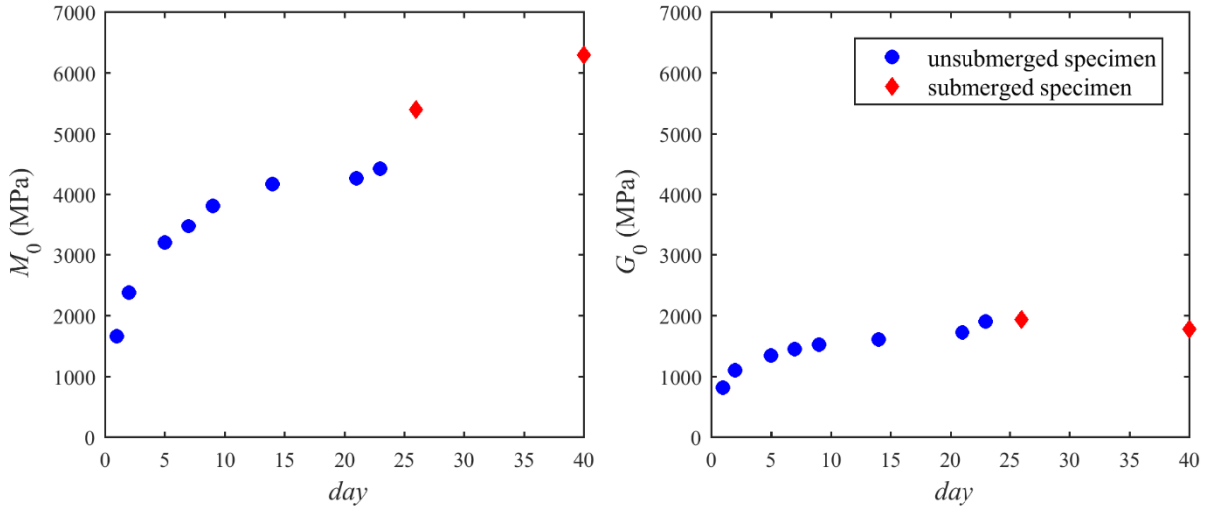

Fig. 4.20 - Longitudinal and shear moduli vs. days of curing

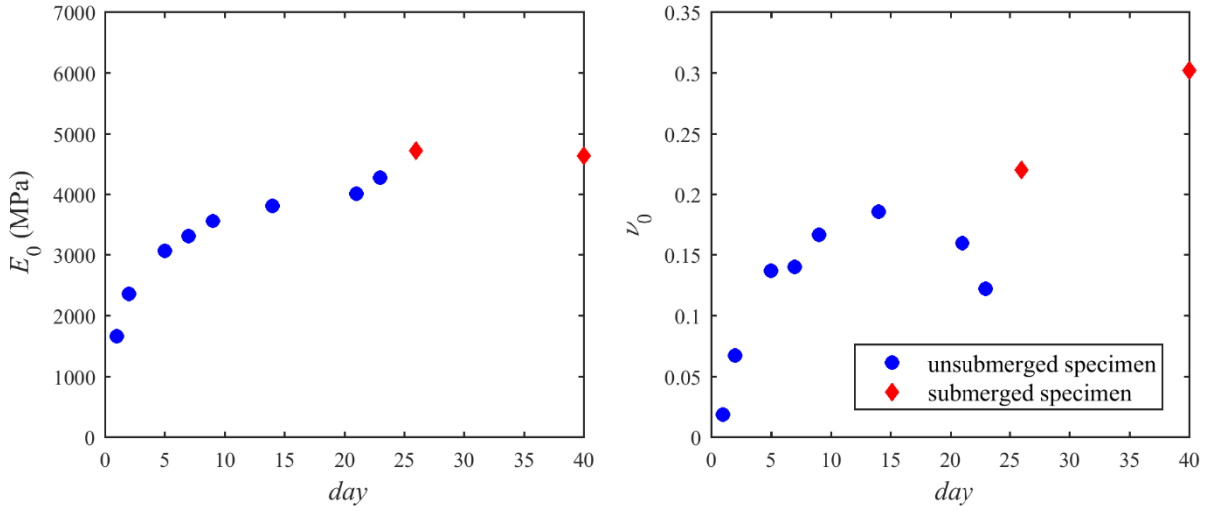

Fig. 4.21 – Young's modulus and Poisson's ratio vs. days of curing

One can see that the stiffness parameters related to the distorsional component of strain have a logarithmic increment with time and tend to remain stable during the duration of the cyclic triaxial test (days 28-40). The distortional values (the pure value, G_0, and the hybrid, E_0) present a slight decrease during the cyclic test. This can be possibly due to the progressive loss of bonding (cementation) due to the cyclic load applied. On the other hand, the longitudinal modulus M_0 increases. It is possible that this behaviour is due to the prevalence of the water phase in the voids, after saturation and breakage of bonds. Poisson's ratio ranges between 0.14 and 0.20 (the first two very low values are erroneous since the precision of V_P is cumbersome), which are typical values for stiff soils in unsaturated conditions. This value increases for the submerged specimen, even though it does not reach the typical value for a complete saturated soil (0.50). This is due to the rather high permeability of the specimens, which are capable of draining a part of water right after being retired from water, losing complete saturation. It is still notorious that the value of ν after the saturation, by increasing the back pressure in the triaxial cell, does not reach the reference value of 0.5, which is a proof that the cemented skeleton particulate system prevails over the pore water.

Table 4.3 –Stiffness moduli obtained through wave velocity measurement

Test name	G_0 (MPa) at 23 days	ν_0 at 23 days	G_0 (MPa) at 26 days	ν_0 at 26 days	G_0 (MPa) at 40 days	ν_0 at 40 days
TC_7%_29	2290	0	-	-	-	-
TC_5%_36	1438	0.05	-	-	-	-
TC_3%_36	1456	0.13	-	-	-	-
TC_3%_e1	1078	0.15	-	-	-	-
TC_5%_e1	1429	0.17	-	-	1650	0.41
TC_7%_e1	1912	0.12	1938	0.22	1786	0.30
TC_3%_e2	1454	0.12	1500	0.14	2255	0.31
TC_5%_e2	2241	0.16	2282	0.19	831	0.36
TC_7%_e2	2433	0.13	2586	0.22	2800	0.29

In Table 4.3, the results obtained for all the tests are presented. The values obtained at the end of the curing period and before submerging the specimen, after submerging the specimen, and after the completion of triaxial test are reported. It is interesting to note (Fig. 4.22) the exponential relation between the stiffness of the unsubmerged specimens and the adjusted porosity/cement ratio $n/C_{iv}^{0.21}$ introduced in Chapter 2. A similar trend is found in UCT tests between the unconfined compression strength and the same ratio (paragraph 4.4).

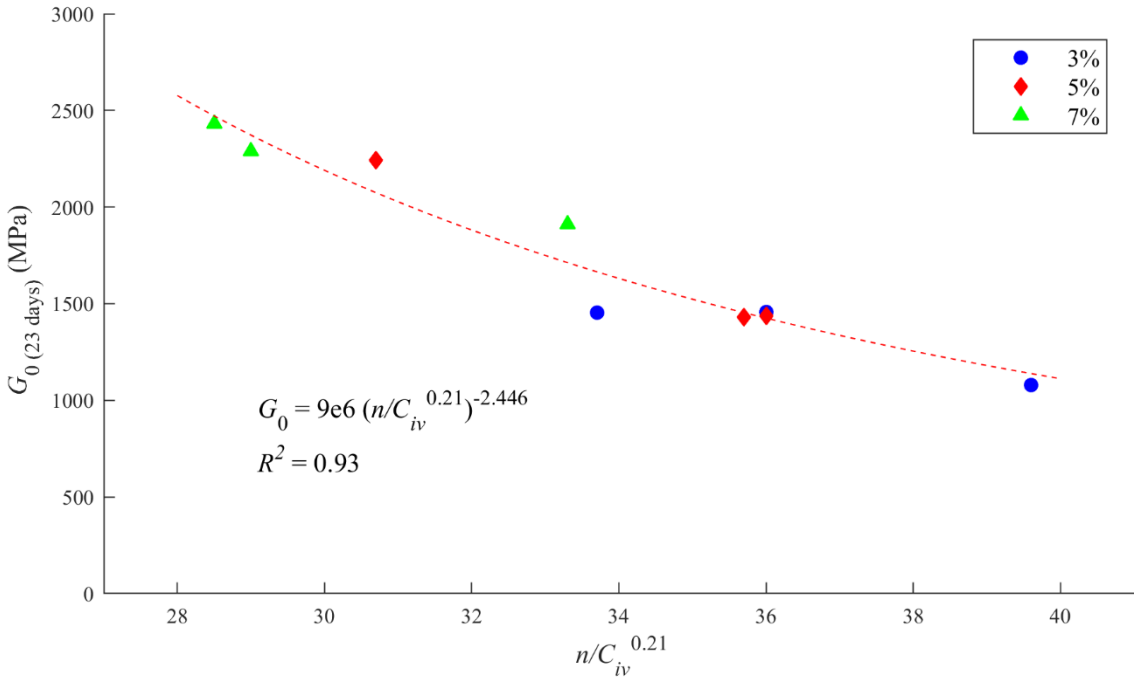

Fig. 4.22 - Relation between porosity/cement ratio and Young's modulus at 23 days of curing

4.4. UNCONFINED COMPRESSION TEST (UCT)

Unconfined compression tests (UCT) were performed on the specimens after dynamic tests and cyclic triaxial test. After the end of triaxial test, water pressure was released and the specimen was removed from the triaxial cell and the last dynamic test was performed. UCT test was performed immediately after this test. Consequently, the degree of saturation of the specimen was high at the moment of the test. This minimized the effect of suction on the uniaxial compression strength.

4.4.1. APPARATUS AND PROCEDURE

The aim of the UCT is to determine the unconfined compressive strength (UCS) and the modulus of elasticity of the specimens, after they were submitted to cyclic triaxial test. Cemented and uncemented specimens had different behaviours after the end of the cyclic test; therefore, two different procedures were adopted for the two cases.

After the end of the triaxial test, the cemented specimens were removed from the triaxial cell and their surface dried with a cloth. Then, the specimen was weighted and a dynamic test was performed. This process was done as fast as possible in order to avoid excessive drainage of the water retained in the specimen. The specimen was tested in a strain-controlled compression testing machine (manufactured by Clockhouse®) equipped with a vertical press capable of applying a maximum load of 100 kN and a load cell with maximum load capacity of 20 kN (Fig. 4.23). During the test, the instrumentation was connected to a computer for automatic data acquisition by using the software Triax®.

Fig. 4.23 - Equipment used for unconfined compression test

European Standard EN 13286-41 (CEN, 2003a) specifies that the load should be applied in a continuous and uniform manner so that rupture occurs between 30 to 60 seconds from the beginning of loading. Nevertheless, this limit would require an unpractical high rate of deformation. Thus, the specimen was

tested at a constant axial displacement rate of 1 mm/min, according to Portuguese Standard (LNEC, 1972). This rate also complies for all specimens with ASTM Standard 2938 for unconfined compressive strength of intact rock core specimens (ASTM, 1995), which specifies that the strain rate should produce the failure of the specimen in an interval between 2 and 15 minutes.

The axial strain was measured with two Local Deformation Transducers (LDT) (Fig. 4.24) manufactured by University of Tokyo (Goto et al., 1991) pivoted onto the lateral surface of specimen, diametrically opposed to each other and at a vertical distance approximately equal to 3/4 of the height of the specimen.

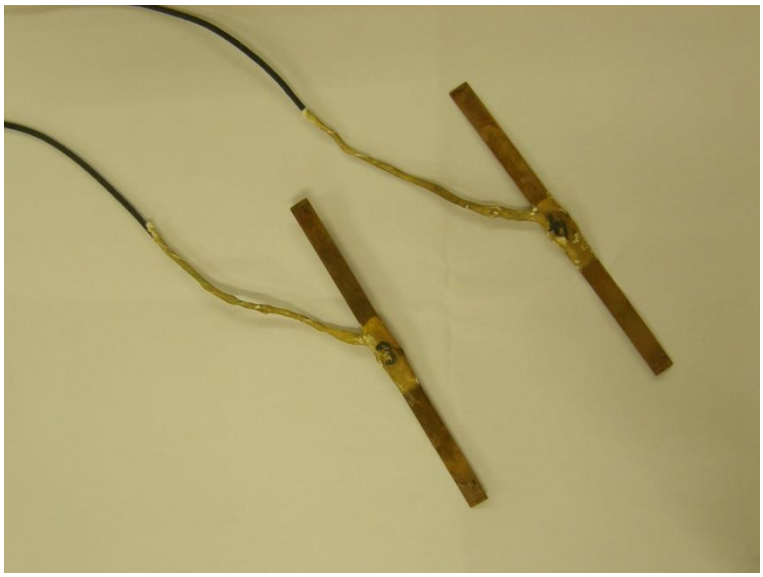

Fig. 4.24 - Two local Deformation Transducers used during unconfined compression tests

Data acquisition was performed by the electronic system at a frequency of one acquisition per second, in order to obtain a good definition of the load-strain curve.

4.4.2. DATA PROCESSING AND RESULTS

The interpretation of the recorded data was performed according to the requirements of the European Standards (CEN, 2003a; CEN, 2003b). Fig. 4.25 shows an example of output presenting the relation between the axial load F measured by the load cell and the axial strain ε_a. The axial strain calculated by each LDT at a given time is defined as:

$$\varepsilon_a = \frac{LDT_t - LDT_i}{L_{LDT}} \tag{4.5}$$

where LDT_t is the reading of the LDT at a given time, LDT_i is the initial reading of the same LDT, and L_{LDT} is the distance at which the pivots are attached to the specimen. The resulting axial strain is obtained as the average value of the readings of the two LDTs.

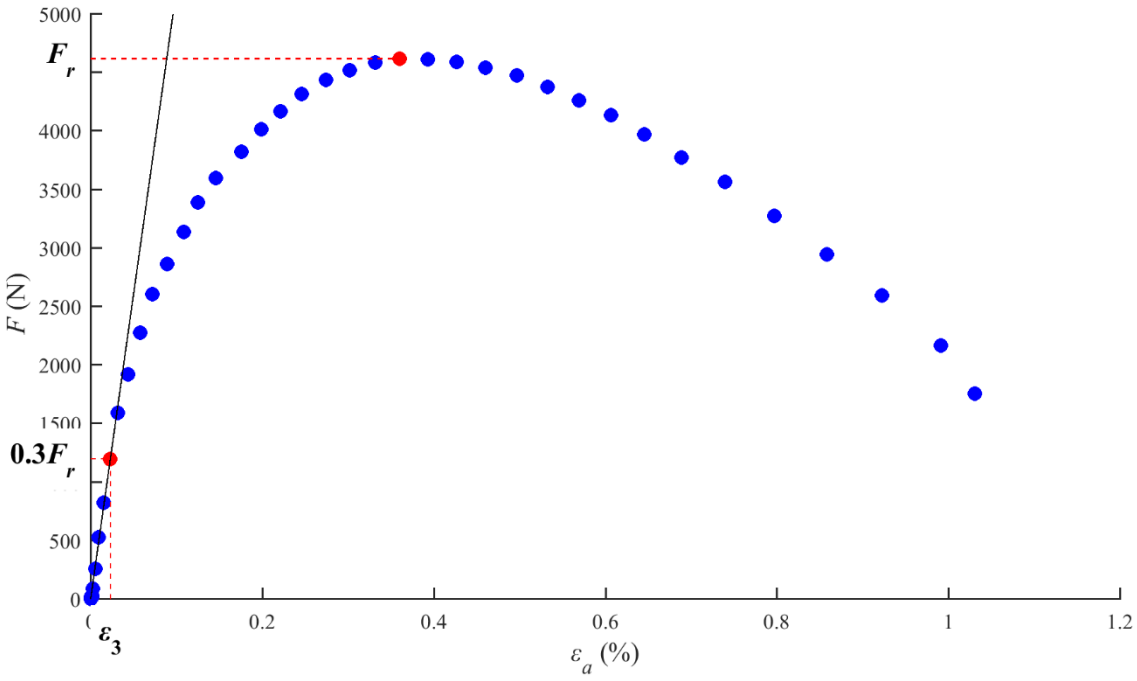

Fig. 4.25 – Example of graph load vs. axial strain for a uniaxial compression test

In Fig. 4.25, the point corresponding to the ultimate load F_r and the point corresponding to a load equal to $0.3F_r$ are highlighted. The expressions for the unconfined compressive strength q_{UCS} and the modulus of elasticity E_{UCS} are the following:

$$q_{UCS} = \frac{F_r}{A_c} \tag{4.6}$$

$$E_{UCS} = \frac{1.2F_r}{\pi D_s^2 \varepsilon_3} \tag{4.7}$$

where:

- F_r is the ultimate load;
- A_c is the cross section area of the specimen;
- D_s is the diameter of the specimen;
- ε_3 is the axial strain corresponding to a load of $0.3F_r$ (Fig. 4.25).

Modulus E_{UCS} corresponds graphically to the slope of the continuous line reported in Fig. 4.25, passing through the origin of the stress-strain plain, and the point of strain ε_3 and load $0.3F_r$. Although this definition corresponds to a secant modulus, E_{UCS} is a good approximation of the tangent modulus relative to the initial slope of the stress-strain curve (because it is defined between two points situated in the initial, linear domain of the stress-strain curve).

In the case of tests on uncemented soil, it was impossible to remove the specimen from the triaxial chamber without destroying it, because of its low cohesion due to saturation. Thus, the UCT was performed in the same triaxial cell used for cyclic test. After the end of the cyclic triaxial test, cell pressure and back pressure were relieved and the water in the cell removed. The axial actuator of the triaxial apparatus (described in Chapter 5) was controlled in displacement in order to impose the same rate imposed to the cemented specimens (1 mm/min); the internal drainage line was open during the test (in both the ends of the specimen) in order to avoid pore water pressure increase. As expected, uncemented specimens showed very small (yet not nil) values of strength and stiffness. The observed

strength and stiffness in these specimens are most likely due to the confinement provided by the membrane used during the triaxial test, rather than to real properties of the material. During the test, the typical barrelling deformation was observed in the specimens, thus, the membrane was subjected to a deformation that in turn caused an elastic reaction, which provided an erroneous confinement. For this reason, the real strength and stiffness for these specimens will be considered nil.

The results of all the specimens are reported in Table 4.4 and plotted in the graphs that are presented herein.

Table 4.4 – Results of unconfined compression tests

Test name	$n/C_{iv}^{0.21}$	C (%)	e_i	E_{UCS} (MPa)	q_{UCS} (kPa)
UCT_0%_e1	-	0	0.75	1.4	20
UCT_3%_e1	39.6	3	0.75	856	737
UCT_5%_e1	35.7	5	0.75	1280	1162
UCT_7%_e1	33.3	7	0.75	2330	1633
UCT_0%_e2	-	0	0.60	1.9	137
UCT_3%_e2	33.7	3	0.60	1450	1628
UCT_5%_e2	30.7	5	0.60	1850	1362
UCT_7%_e2	28.5	7	0.60	5270	3159

Fig. 4.26 and Fig. 4.27 show the relation between the values of UCS and stiffness modulus, respectively, and the cement content.

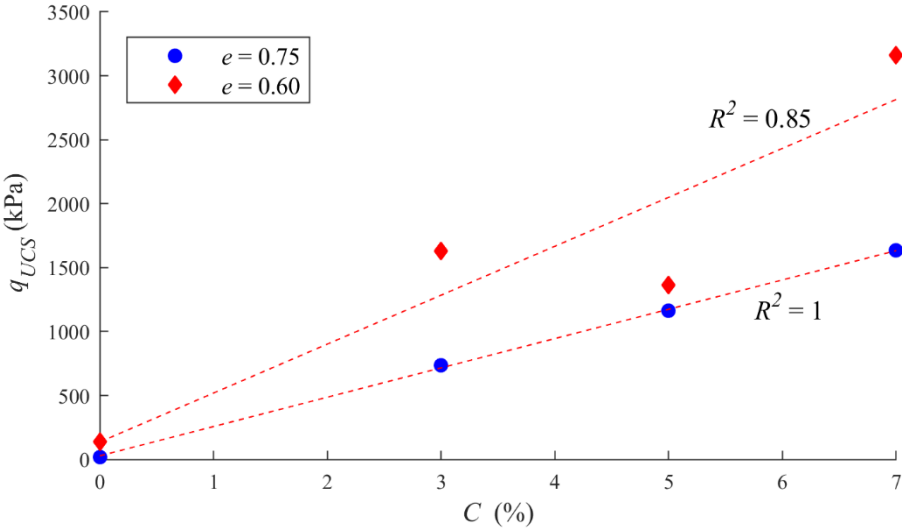

Fig. 4.26 – Results of UCT plotted against cement content: unconfined strength vs. cement content

As expected, the variation is linear in both cases with a high value of the correlation coefficient, especially for the specimens with higher initial void ratio (0.75). For the more compacted specimens (0.60) the results show an increase in strength and modulus of elasticity with respect to the specimen with same cement content. The linear correlation of this second group of specimens has a lower value

of the correlation coefficient, probably because of inhomogeneity in the compaction of the specimens or because of the different damage suffered during the cyclic test.

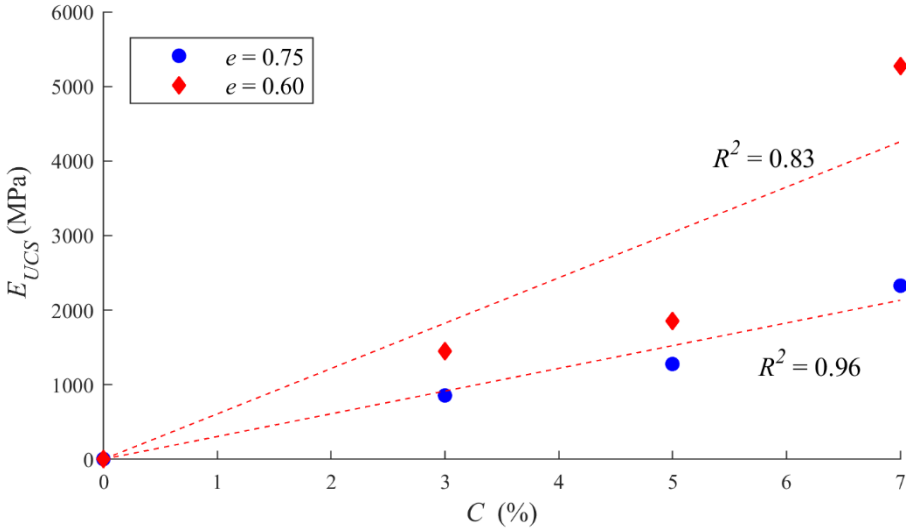

Fig. 4.27 – Results of UCT plotted against cement content: modulus of elasticity vs. cement content

4.5. CONCLUSIONS: CURING AND DESTRUCTURATION OF CEMENTED SPECIMENS

The tests performed before and after cyclic tests (dynamic tests and UCT) allowed to better understand the evolution of the bonding parameters of cemented soil during curing and after the cyclic loading. As pointed out in the former paragraphs, porosity/cement ratio ($n/C_{iv}^{0.21}$) proved to be a good indexing parameter for mixtures characterized by multiple different initial parameters, permitting to summarize the results in a simpler representation and highlighting interesting trends.

In Fig. 4.28, the correlation between compression strength and the ratio $n/C_{iv}^{0.21}$ is shown for cemented specimens. Such correlation has the form of a power law:

$$q_{UCT} = 9.6\text{e}9\left(\frac{n}{C_{iv}^{0.21}}\right)^{-4.449} \tag{4.8}$$

It is interesting to compare this relation, obtained for specimens with 40 days of cure and already submitted to cyclic test, with the relation obtained by Rios (2011) for the same cemented soil with 7 days of cure and reported in Fig. 4.29.

One can see that the constant coefficient of the power law has increased (from $4\text{e}10^9$ to $1\text{e}10^{10}$) while the exponent of the adjusted ratio is similar in the two cases (-4.296 and -4.449), as should be expected in the simple framework proposed by Consoli et al. (2007). This means that the curve has translated vertically without modifying its shape, suggesting that the increase in strength due to the longer curing time is greater than the decrease due to damage during cyclic test. This result is reasonable since the stress imposed during cycling loading is a low percentage of the strength of the specimen. Only the test UCT_5%_e2 showed a strength significantly smaller than what was expected from the relation above; thus, it was excluded from the figure. Probably this is a sign of greater damage suffered during the cyclic triaxial test and this indicates that the UCT test is a simple technique to assess the conditions of the specimens after the cyclic test.

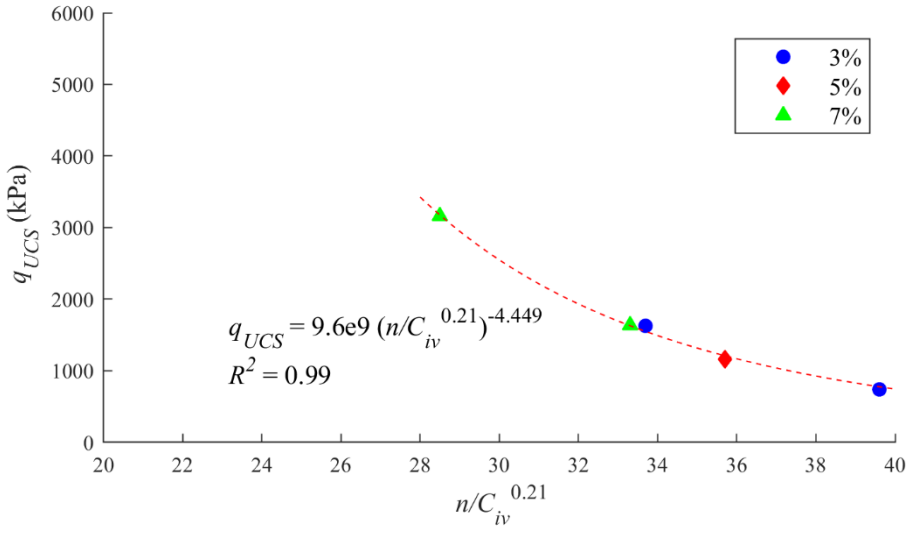

Fig. 4.28 - Relation between unconfined compression strength and porosity/cement ratio after 40 days of cure

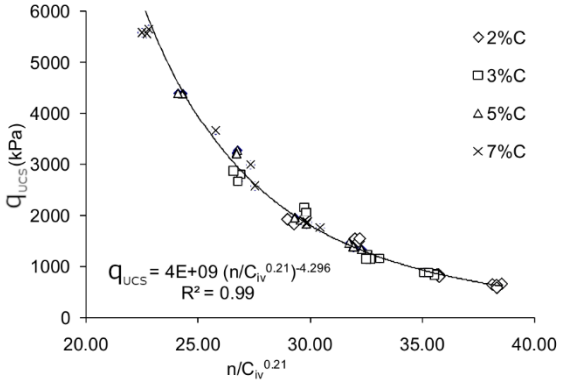

Fig. 4.29 - Relation between unconfined compression strength and porosity/cement ratio after 7 days of cure (Rios, 2011)

A similar trend is observed in a corresponding graph, representing the relation between the modulus of elasticity E_{UCS} and the same adjusted ratio (Fig. 4.30). It should be noted that a similar power law was observed also in dynamic tests, in the relation between dynamic Young's modulus and the adjusted porosity/cement ratio (Fig. 4.22). Being non-destructive tests, dynamic tests also permit to study the evolution of the stiffness parameters before (with 26 days of cure) and after the triaxial cyclic tests. In such conditions, the curing process has ended and the gain in stiffness with time is nil (as shown in paragraph 4.3). Thus, the evolution of the stiffness moduli before and after the triaxial test is only a consequence of destructuration by fatigue and not of the curing time. Table 4.5 reports a comparison between the small-strain shear modulus (G_0) measured before and after the cyclic test. Modulus G_0 is shown instead of Young's modulus because it only depends on shear waves velocities (as expressed in equation (4.2)) that are not affected by the different degree of saturation of the specimen.

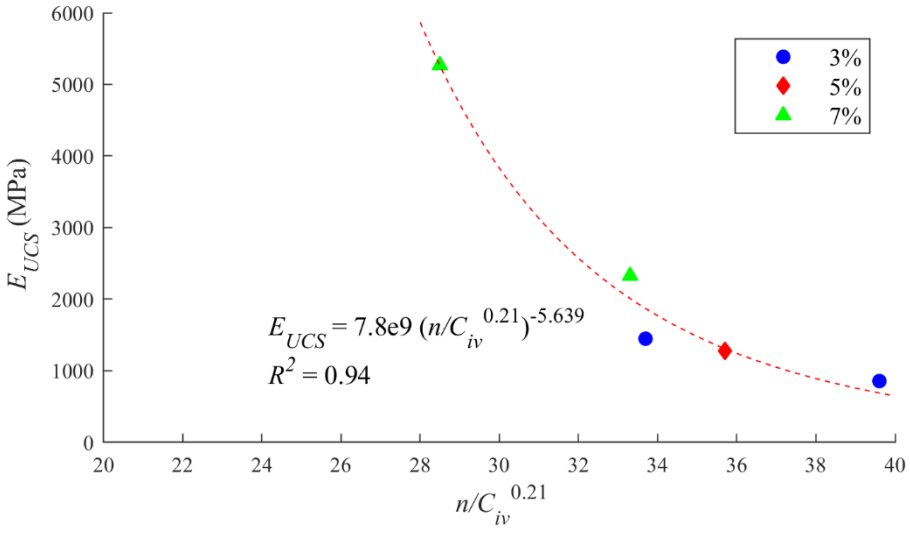

Fig. 4.30 - Relation between modulus of elasticity and porosity/cement ratio after 40 days of cure

Table 4.5 – Dynamic shear modulus before and after cyclic test

Test name	G_0 before test (MPa)	G_0 after test (MPa)	Variation (%)
TC_5%_e1	1429	1650	15
TC_7%_e1	1912	1786	-7
TC_3%_e2	1454	2255	55
TC_5%_e2	2241	831	-63
TC_7%_e2	2433	2800	15

As the results show, the specimens with 7% of cement suffer a small variation in the shear modulus. This is probably due to the high level of cementation that forms a continuous rigid skeleton preventing material degradation during cyclic loading. The other results are more difficult to interpret: in general, it is noted a slight increase of the shear modulus. The only exception is specimen TC_5%_e2 that shows a major drop of rigidity. This is in agreement with the low value of UCS strength, confirming an important degradation of structure during cyclic test.

Chapter 5.

LONG-TERM STRESS-DRIVEN CYCLIC TRIAXIAL TESTS

5.1. INTRODUCTION

Cementation is an intrinsic characteristic of a wide variety of soils, as highlighted in Chapter 2. Regardless the origin or the nature of the cementing agent and soil involved, all cemented soils share a well-established framework that differs from an unbonded granular soil behaviour.

This chapter presents an extensive experimental study performed over Porto residual soil, a well-graded silty-sand remoulded in laboratory and artificially cemented with Portland cement, presented in Chapter 4. The study includes a large set of drained and undrained cyclic triaxial tests with a very high number of loading cycles (1 million) performed over specimens with different cement contents and void ratios. Attention is focused on the long-term accumulation behaviour of axial and volumetric permanent strain (for drained tests) or pore pressure variation (for undrained tests) under low intensity cyclic stress. The high number of loading cycles and the inclusion of the volumetric component in the analysis are two novelties that are not considered in the majority of the studies dealing with the cyclic properties of cemented or uncemented soils.

5.2. EXPERIMENTAL PROGRAMME

The experimental programme included 24 drained and 3 undrained isotropically consolidated cyclic triaxial tests performed over cylindrical specimens of equal dimensions (diameter D_s and height H_s) and moulded in nine different mixtures (moulding points), each one with a specific combination of initial void ratio and cement content. The physical properties of the nine mixtures are reported in Table 5.1. Eight of these mixtures were used to mould the specimens for drained tests (mixtures n. 1 to 8 in table): three specimens were moulded for each mixture and tested with a specific combination of confining pressure and deviatoric stress, for a total of 24 drained tests. Specimens corresponding to moulding points n.3 and n.8 were moulded in four identical samples: three samples were submitted to drained cyclic tests; one sample was submitted to an undrained cyclic test. Finally, mixture n.9 was moulded in a single specimen tested undrained. Thus, a total of three undrained cyclic triaxial tests were performed (with mixtures 5%_e1, 7%_e2, and 3%_e3). As shown in Table 5.1, the specimens have three different initial void ratios (e_i) and four different cement contents (C), including uncemented specimens. The water content used during moulding is the same for all the specimens (12%) and equal to the optimum

water content determined by Proctor tests, corresponding to a maximum dry unit weight of 18.9 kN/m^3 (Rios, 2011).

Table 5.1 – Testing programme – moulding conditions

Mixture number	Mixture denomination	D_s (mm)	H_s (mm)	e_i	C (%)	γ_d (kN/m^3)	w (%)	Number and type of tests performed
1	0%_e1	71	136	0.75	0	15.5	12	3 TC-D
2	3%_e1	71	136	0.75	3	15.6	12	3 TC-D
3	5%_e1	71	136	0.75	5	15.7	12	3 TC-D + 1 TC-U
4	7%_e1	71	136	0.75	7	15.7	12	3 TC-D
5	0%_e2	71	136	0.60	0	17.0	12	3 TC-D
6	3%_e2	71	136	0.60	3	17.1	12	3 TC-D
7	5%_e2	71	136	0.60	5	17.1	12	3 TC-D
8	7%_e2	71	136	0.60	7	17.2	12	3 TC-D + 1 TC-U
9	3%_e3	71	136	0.65	3	16.5	12	1 TC-U

Note: TC-D - drained cyclic triaxial test; TC-U - undrained cyclic triaxial test

The eight mixtures for the drained tests are divided into two groups (denominated as “e1” and “e2”), each one characterized by a single value of initial void ratio (0.75 and 0.60, respectively). Each group is formed by an uncemented specimen of soil and 3 other specimens with different cement contents (3, 5 and 7% in weight of the dry uncemented soil). Three different levels of effective confining pressure were chosen for the three specimens of each mixture, as specified in detail in the next section, in order to study the influence of different confinement levels on the behaviour of the mixtures.

The three undrained tests were performed on one specimen moulded with a mixture from group “e1” (e_i = 0.75), and one specimen with a mixture from “e2” (e_i = 0.60). The third undrained test was performed with a specimen with initial void ratio of 0.65. This mixture belongs to a third group, “e3”. The isotropic consolidation applied to the undrained specimens before cyclic loading is equal to the effective confining pressure of the less confined group of drained tests, as detailed in the next section.

As explained in detail in the following section, the applied cyclic stress in each test was calculated in order to be lower than the corresponding elastic limit of the specimen tested. For this reason, the deviatoric stress applied ranged between 10 and 20% of the yielding deviatoric stress of each mixture, referred to the same mixture tested in a triaxial test performed under the same boundary conditions (drained or undrained conditions, constant cell pressure) and with a monotonically increasing axial deformation. The designed number of cycles for each test is one million cycles. However, this limit was not attained in all the tests due to technical difficulties. Nevertheless, only tests with at least 600000 cycles were accepted.

In Table 5.2 the full experimental plan of 24 drained and 3 undrained triaxial cyclic tests is reported.

5.3. STRESS LEVELS

The stress levels to be applied in the tests were defined with the objective of studying the soil, under different confining pressures, inside the small-strain domain as defined by Jardine (1992, 1995), and

with a constant relative distance from the outer surface. Such distance depends on the porosity/cement ratio of the specimen, which regulates the size of the boundary surface itself (Rios et al., 2012, 2014). It is assumed that the normalized cemented surfaces for cemented specimens with different porosity/cement ratios $n/C_{iv}^{0.21}$ (Consoli et al., 2007; Rios et al., 2012 – defined in section 2.5) are similar among them.

Table 5.2 – Testing programme – Definition of cyclic triaxial tests

		DRAINED			UNDRAINED
		Confining pressure			Initial confining pressure
Initial void ratio	*C*(%)	Low (s1)	Medium (s2)	High (s3)	Low (s1U)
e1 = 0.75	0	TC_0%_e1_s1	TC_0%_e1_s2	TC_0%_e1_s3	
	3	TC_3%_e1_s1	TC_3%_e1_s2	TC_3%_e1_s3	
	5	TC_5%_e1_s1	TC_5%_e1_s2	TC_5%_e1_s3	TC_5%_e1_s1U
	7	TC_7%_e1_s1	TC_7%_e1_s2	TC_7%_e1_s3	
e2 = 0.60	0	TC_0%_e2_s1	TC_0%_e2_s2	TC_0%_e2_s3	
	3	TC_3%_e2_s1	TC_3%_e2_s2	TC_3%_e2_s3	
	5	TC_5%_e2_s1	TC_5%_e2_s2	TC_5%_e2_s3	
	7	TC_7%_e2_s1	TC_7%_e2_s2	TC_7%_e2_s3	TC_7%_e2_s1U
e3 = 0.65	3				TC_3%_e3_s1U

In the present paper, the deviatoric and mean effective stress are defined as follows:

$$q = \sigma_a - \sigma_r \tag{5.1}$$

$$p' = \frac{\sigma'_a + 2\sigma'_r}{3} \tag{5.2}$$

5.3.1. EFFECTIVE CONFINING PRESSURE

To avoid intersections with the bounding surface, the effective confining pressure (σ'_c) of each test shall be less than the corresponding isotropic yield stress (σ'_y) of the tested specimen. Hence, σ'_y shall be determined for the nine tested mixtures. For uncemented specimens, σ'_y is retrieved from the uncemented normal compression line (NCL) (Rios et al., 2012 – see Chapter 2). For the cemented specimens, a specific NCL exists for each $n/C_{iv}^{0.21}$ (see Fig. 2.21). For the range of initial void ratios investigated in the present paper (e_i = 0.6-0.75), σ'_y is very similar for the same porosity/cement ratio, despite the different initial void ratios. In Fig. 2.21, yield points of specimens with different e_i and same $n/C_{iv}^{0.21}$ are grouped in circles. From Rios et al. (2012) and Amaral (2012), isotropic yield stresses corresponding to $n/C_{iv}^{0.21}$ equal to 29, 36, and 41 were graphically determined (Table 5.3).

Some of the tested specimens were moulded with different porosity/cement ratios. Thus, a regression law relating the known values of $n/C_{iv}^{0.21}$ and σ'_y was determined, in order to retrieve by interpolation the unknown isotropic yield stresses. Since in the isotropic compression plane the isotropic stress is

usually expressed in logarithmic scale, a logarithmic regression law is established between the ratio and the yield stress (Fig. 5.1).

Table 5.3 - Isotropic yield stresses determined from the results of Rios et al. (2012) and Amaral (2012)

Adjusted porosity/cement ratio, $n/C_{iv}^{0.21}$	Isotropic yield stress, σ'_y (kPa)
41	1500
36	3000
29	4000

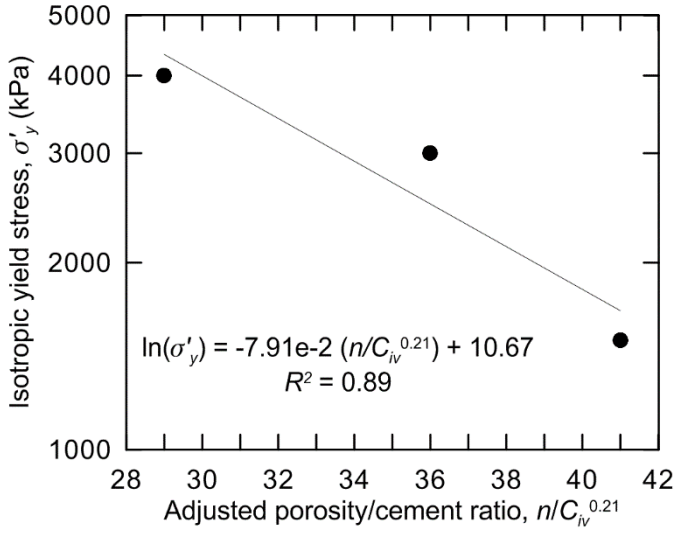

Fig. 5.1 – Regression law between isotropic yield stress and adjusted porosity/cement ratio

Isotropic yield stress was directly determined for six mixtures, and it was inferred from the regression law for the remaining three (Table 5.4). For each cyclic test, it shall be $\sigma'_c < \sigma'_y$.

Each specimen submitted to drained triaxial test was moulded in three copies subjected to three different levels of effective confining pressure (Table 5.5). The first set of tests (s1) with the lowest confinement was performed with an effective confining pressure of 40 kPa for all the eight drained tests. The three undrained tests (Table 5.6) were isotropically consolidated to the same pressure. The monotonic triaxial tests performed by Rios et al. (2014) on similar specimens confined at 30 and 80 kPa showed a dilatant behaviour with a peak deviatoric stress.

As for the second (s2 - intermediate confinement) and third (s3 - high confinement) sets (all drained tests), the value of σ'_c for each test was selected so that ratio σ'_c/σ'_y is constant for all the tests in the same set.

This criterion is intended to extend to cyclic tests the approach proposed for monotonic tests by Cuccovillo & Coop (1999) and adopted by Rios et al. (2012, 2014), in which the concept of normalization is applied to cemented soils. In this sense, σ'_y is intended as a normalizing parameter, similarly to the previously defined p'_e parameter (Fig. 2.23). The two parameters are not coincident; nevertheless, for the present mixtures, their difference is smaller than the uncertainty in their determination.

Table 5.4 - Isotropic yield stresses determined from regression law or directly determined from the data of Rios et al. (2012) and Amaral (2012)

Specimen	Adjusted porosity/cement ratio, $n/C_{iv}^{0.21}$	Isotropic yield stress, σ_y' (kPa)
0%_e1	-	300
3%_e1	40	1500
5%_e1	36	3000
7%_e1	33	3137 (*)
0%_e2	-	800
3%_e2	34	3028 (*)
5%_e2	31	3948 (*)
7%_e2	29	4000
3%_e3	36	3000

* value determined from regression law

Table 5.5 - Stress levels (drained tests)

e_i	C (%)	s1			s2			s3		
		σ_c' (kPa)	q_{cyc} (kPa)	σ_c'/σ_y'	σ_c' (kPa)	q_{cyc} (kPa)	σ_c'/σ_y'	σ_c' (kPa)	q_{cyc} (kPa)	σ_c'/σ_y'
0.75	0	40	10-19	1/7.5	100	17-26	1/3	151	14-29	1/2
	3	40	93-158	1/38	500	78-140	1/3	717	53-110	1/2
	5	40	156-279	1/75	991	95-238	1/3	1500	107-271	1/2
	7	40	206-375	1/78	1033	165-310	1/3	1569	102-251	1/2
0.60	0	40	17-27	1/20	266	36-88	1/3	403	43-87	1/2
	3	40	200-368	1/76	1003	162-286	1/3	1515	101-238	1/2
	5	40	319-577	1/99	1303	100-254	1/3	1649	125-327	1/2.4
	7	40	321-581	1/120	1585	208-390	1/3	1649	174-361	1/2.9

Table 5.6 - Stress levels (undrained tests)

e_i	C (%)	s1U		
		σ_c' (kPa)	q_{cyc} (kPa)	σ_c'/σ_y'
0.75	5	40	100-200	1/38
0.60	7	40	250-500	1/75
0.65	3	40	100-200	1/7.5

As stated, the research is aimed at studying the cyclic behaviour under different confining pressures inside the small-strain domain. In the hypothesis that the critical state framework influences not only the large-strain and ultimate behaviour of the soil, but also the small-strain cyclic behaviour (Qadimi & Coop, 2007), the confinement of the first set of tests (s1 – low confinement) was selected in order to study the dry or dilatant domain of the stress space. The subsequent sets are aimed at studying the wet or contractive domain of the stress space (s3), and an intermediate zone between the former two (s2). The individuation of the dry side of the critical state from the results of the monotonic tests is straightforward. It is more difficult to individuate for each mixture the wet side and the transition zone between these two regions (i.e. a confining pressure such that less confined specimens submitted to monotonic triaxial test show dilative behaviour, and more confined specimens show contractive behaviour). In order to establish a criterion, the normalized state boundary surfaces (SBS) of Fig. 2.23 have been used as a reference to determine the stress levels of each test (the uncemented surface and the cemented surface for tests consolidated at 10 MPa). Since the left part of each surface was retrieved from tests showing a dilatant unstable behaviour and the right part is associated to contractive stable behaviour, it is concluded that the transition between the two regions is located around the limit between the two surfaces. In Fig. 5.2 (referred to cemented specimens), this point is indicated as point T (final point of the high-pressure undrained stress paths). Since the tests of the second and third groups are all drained, a straight line is traced from point T with an inclination of 3:1 (coincident with the trajectory of a monotonic drained triaxial test). This line intersects the normalized p'/σ'_y axis at a value close to 0.33. Performing the same procedure with the uncemented normalized SBS, a similar outcome is obtained. All the monotonic triaxial tests performed by Rios et al. (2014) with $\sigma'_c < 0.33p'_e$ showed a dilative behaviour, while tests with $\sigma'_c > 0.33p'_e$ showed a contractive behaviour. This is not sufficient to state that $0.33p'_e$ is the boundary between dilatant and compressive behaviour, but this value can be used as a guideline in the planning of the tests.

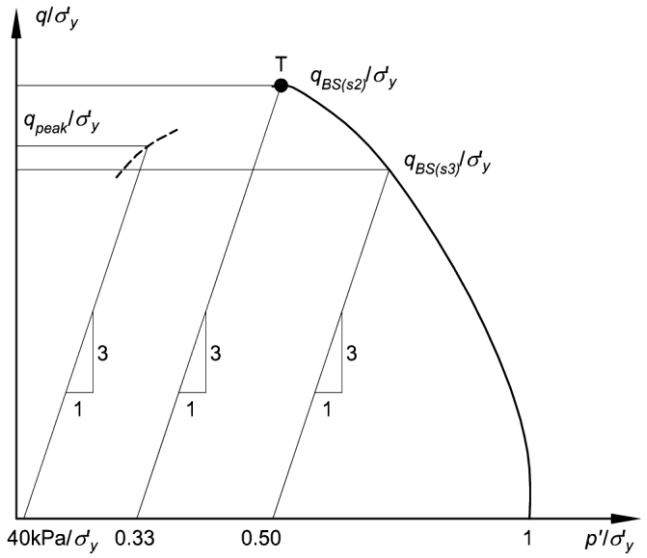

Fig. 5.2 – Possible boundary between dry and wet side of the normalized bounding surface for cemented soils and determination of q_{peak} and q_{BS} for drained tests

Thus, for the second set of tests, the effective confining pressure was set equal to 1/3 of the corresponding isotropic yield stress:

$$\sigma'_{c(s2)} = 0.33\sigma'_y \tag{5.3}$$

For the third set of tests, a higher effective confining pressure is required (still inferior to the corresponding σ'_y). A value equal to $0.5\sigma'_y$ has been selected.

$$\sigma'_{c(s3)} = 0.5\sigma'_y \tag{5.4}$$

This confining pressure could not be applied to tests TC_5%_e2_s3 and TC_7%_e2_s3, because the limit pressure of the triaxial apparatus would be exceeded. For both tests, the maximum allowable cell pressure was applied, obtaining ratios σ'_c/σ'_y of 1/2.4 and 1/2.9, respectively.

5.3.2. DEVIATORIC CYCLIC STRESS

Deviatoric cyclic stress q_{cyc} was applied in a sinusoidal form in the time domain, varying between an upper (q_{max}) and a lower limit (q_{min}). As explained in the precedent section, these limits shall respect the requirement of not intercepting the bounding surface (BS) of the tested specimen.

Following the framework of bounding surface plasticity (illustrated in Chapter 3), the relative distance δ between the applied stress and the bounding surface should be equal in all tests. Distance δ is defined in a specific way in different models. In all of them, δ is relative to the size of the bounding surface, i.e. it is a distance measured in the normalized stress space. Moreover, soil stiffness only depends on distance δ. Therefore, if all the cyclic tests are performed with the same distance δ, the same amount of accumulated strain with number of cycles should be observed in all the tests. Such hypothesis shall be verified hereinafter.

In the present research, δ is defined as the distance between the applied stress state and the BS, measured along a monotonic stress path correspondent to the same drainage and confinement conditions of the cyclic test performed. For drained tests, the distance was measured along a monotonic drained trajectory with same effective confining pressure as the drained cyclic test performed. For undrained tests, the distance was measured along a corresponding monotonic undrained trajectory (retrieved from Rios et al., 2014).

The applied deviatoric cyclic stress was selected as a percentage of the corresponding deviatoric stress on the respective normalized BS. Maximum value q_{max} was selected as the 20% of the corresponding deviatoric stress q_{BS} on the respective normalized BS (for each drainage condition, soil compaction, porosity/cement ratio, and confinement). The minimum value q_{min} was selected as the 10% of the same stress (i.e. $q_{min} = 0.5q_{max}$), for the practical purpose of avoiding loss of contact between the triaxial cell piston and the specimen top cap during cyclic loading. Due to the precision of the apparatus used for the tests, the real deviatoric stress imposed was not always exactly coincident with the calculated value; the variations are in any case small.

For the low confined tests (s1), the bounding surface is coincident with the deviatoric peak stress envelope determined in the monotonic triaxial tests. Thus, it seemed reasonable in the first set of tests (s1), to define $q_{max} = 0.2q_{peak}$ (the deviatoric peak stress is different for each test and, consistently, different values of cyclic deviatoric stress are imposed in each test). The peak stresses for the undrained tests were retrieved from the corresponding monotonic tests (Rios et al., 2014). For the drained tests, a straight line inclined at 3:1 was traced in the normalized stress space starting from a mean effective stress equal to 40 kPa/σ'_y up to the normalized (uncemented or cemented) BS (Fig. 5.2). The value of q_{peak}/σ'_y is determined as the intersection with the peak strength envelope. Multiplying by the corresponding σ'_y, the value of q_{peak} for the particular mixture tested is determined. The suitability of this method was validated by comparing the calculated peaks with real results from drained monotonic triaxial tests (Rios et al., 2014) performed under similar confining pressure (30 and 80 kPa) and similar soil-cement mixtures.

For the second (s2) and third (s3) sets of tests, the same graphical construction was used starting from the respective normalized confining pressures (0.33 and 0.5, respectively – Fig. 5.2). The corresponding normalized deviatoric stresses on the BS were determined (q_{BS}/σ'_y). The cyclic stress is determined as:

$$q_{cyc} = q_{max} - q_{min} = (0.20 - 0.10)q_{BS} \quad (5.5)$$

Thus, each test has a specific interval of applied deviatoric stress (Table 5.5 and Table 5.6), depending on the corresponding isotropic yield stress of the mixture and the applied confining pressure. The above expression states that the minimum deviatoric load should be one half of the maximum. From Table 5.5 and Table 5.6, one can see that this ratio is not always exactly reproduced in practice. This was due to the precision of the testing equipment used, which prevented to impose the exact value required. Nevertheless, the differences are always small.

The frequency of application of the loading cycles was 1 cycle per second. As reported in many experimental works based on cyclic triaxial tests conducted on the same mixtures in similar conditions (Rios, 2011; Amaral, 2012; Viana da Fonseca et al., 2013), this frequency guarantees that the specimens submitted to drained tests are effectively fully drained during the tests. Pore pressure was measured continuously during each test to confirm the draining conditions (refer to section 5.4.2 for the detailed description of the drainage set up and pressure measurement system).

5.4. EQUIPMENT

All the tests were performed in the Geotechnical Laboratory of FEUP (LabGeo-FEUP) in a dynamic frame with actuators for static and cyclic loading and dedicated hardware and software, load cells and internal transducers. The apparatus was developed by the Institute of Mechanical Engineering and Industrial Management (IDMEC) of the University of Porto, under specifications of LabGeo-FEUP. It mainly consists of a hydraulic unit, triaxial cell and measurement devices (Fig. 5.3). A pressure regulation system is responsible for pressurizing the water used during the test.

5.4.1. HYDRAULIC UNIT

5.4.1.1. UNIT DESCRIPTION

The hydraulic unit is responsible for pressurizing the oil circuit that allows the actuation of the servo actuator. It is based on a variable displacement axial piston pump and it is controlled through a computer. The unit can induce axial loads through a vertical actuator capable to act in cyclic conditions up to 5 Hz and until a maximum load of 10 kN. The loading frame consists of a base, two columns threaded on top and a traverse equipped with a set of screwing nuts for height adjustment.

The system is controlled via the dedicated software Dynatester®, operating in Windows XP®. It is configured according to the hardware specificities of the system and it can impose various combinations of loading or displacement (e.g. ramp, constant and sinusoidal).

5.4.1.2. PID CONTROLLER TUNING

The software controls the process through an electronic feedback control system, which compares the output of the hydraulic unit with the control signal. The difference is considered an error signal, which is corrected in order to adjust the output of the unit to a value closer to the control signal. The used control system is called proportional–integral–derivative controller (PID controller), which is found in

large numbers in all industries (Astrom & Hagglund, 1995). This type of controller must be tuned, i.e. three parameters (the gains of the proportional, integral and derivative terms - K_p, K_i, and K_d, respectively) must be adjusted in order to regulate the velocity at which the system responds to an error (i.e. a discrepancy between the target input value of loading and/or displacement and the corresponding measured value).

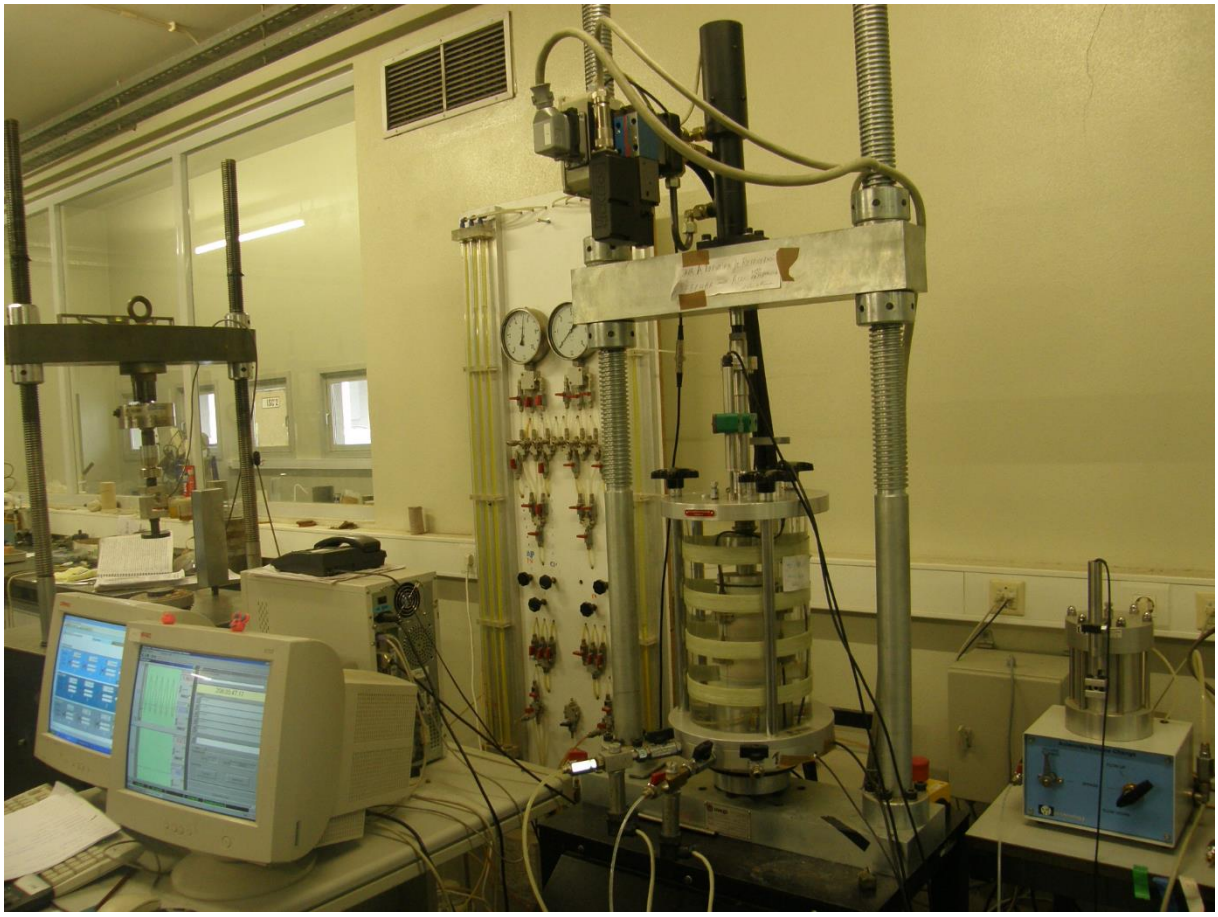

Fig. 5.3 - Cyclic triaxial apparatus used for experimental programme

The tuning process has an extreme practical importance. If one or more gains of the PID controller are set incorrectly (too high or too low), the controlled process input can be unstable, i.e., its output diverges rapidly and in an uncontrolled manner from the selected input, leading to the damage of the specimen and possible mechanical damage of the system components. Although all modern PID controllers have some capability for automatic tuning (Astrom & Hagglund, 1995), this is not the case of the used system. Thus, a manual tuning was performed. The process is rather complex because the most suitable set of gains is not only dependent on the characteristics of the system, but also on the particular test conditions and specimen characteristics (specimen stiffness, magnitude of the stress levels applied and frequency of the applied cycles). Thus, a specific set of gain shall be selected for each test. Through the experience gained in the trial and error process applied to the vast set of tests performed, some guidelines in the choice of the gains are herein outlined. Limiting the analysis to the cyclic triaxial tests performed and to the type of soil studied in the present work, the main factors affecting the values of the PID controller parameters of the used system seem to be the following:

- level of cementation and density of the specimen;
- confining pressure;

- cyclic deviatoric stress amplitude;
- loading frequency.

As said, a specific set of parameters should be found for each test, but this would require an unacceptable amount of time, given the long curing time of cemented specimens. From the experience gathered in laboratory, the main difference in response was observed between uncemented and cemented specimens, and a smaller difference between the less cemented specimens and the more cemented ones. Thus, the indicative values reported in Table 5.7 were followed for the first-attempt tuning in the performed tests.

Table 5.7 – Indicative initial values for the PID controller gains

Specimen type	K_p	K_i	K_d
uncemented	4÷5	0.1÷0.2	0.5÷1
less cemented (C = 2÷4%)	3÷4	0.005	0.5÷1
more cemented (C = 5÷7%)	2÷3	0.005÷0.007	0.5÷1

The above values should be regarded merely as a first guess, not exempt from potential fallacies. As one can see from the table, the values of K_p and K_i decrease with the increasing level of cementation, while gain K_d seems to not be influenced by the level of cementation, at least for the studied specimens.

5.4.2. TRIAXIAL CELL AND MEASUREMENT DEVICES

The cell (the complete setup is illustrated schematically in Fig. 5.4) is made of a stainless metal, with an acrylic plastic transparent cylindrical body. The cell is reinforced with rings of bonded fiberglass for withstanding pressures up to 1700 kN/m^2. In order to guarantee the continuity of the loading action (forward and reverse), the frame piston is attached to the actuator through a connection.

Measurement items include:

- an internal submergible load cell;
- three pressure gauges, measuring the confining pressure inside the cell and the pore pressures at the top and bottom of the specimen;
- three linear variable displacement transducers (LVDTs) directly attached to the specimen, enabling the accurate measurement of axial deformation (n.16 in Fig. 5.4);
- two external LVDTs, one installed at the top of the triaxial cell (n.4 in Fig. 5.4); and one integrated in the servo actuator;
- a volume gauge (LVDT type) with a capacity of 100 cm^3, measuring the volumetric deformation of the specimen.

Pressure regulation is performed through the motorized air compressor system of LabGeo (Fig. 5.5) or using two digital pressure/volume controllers (manufactured by GDS Instruments© - Fig. 5.6). These instruments are equipped with a programmable step-motor moving a piston that acts directly on water without any air/water interface. They are especially useful during saturation and consolidation, since it is possible to program a linear and slow variation of pressure during these stages. During cyclic loading, air compressor system was preferred as it guarantees a faster response to the imposed pressure variations.

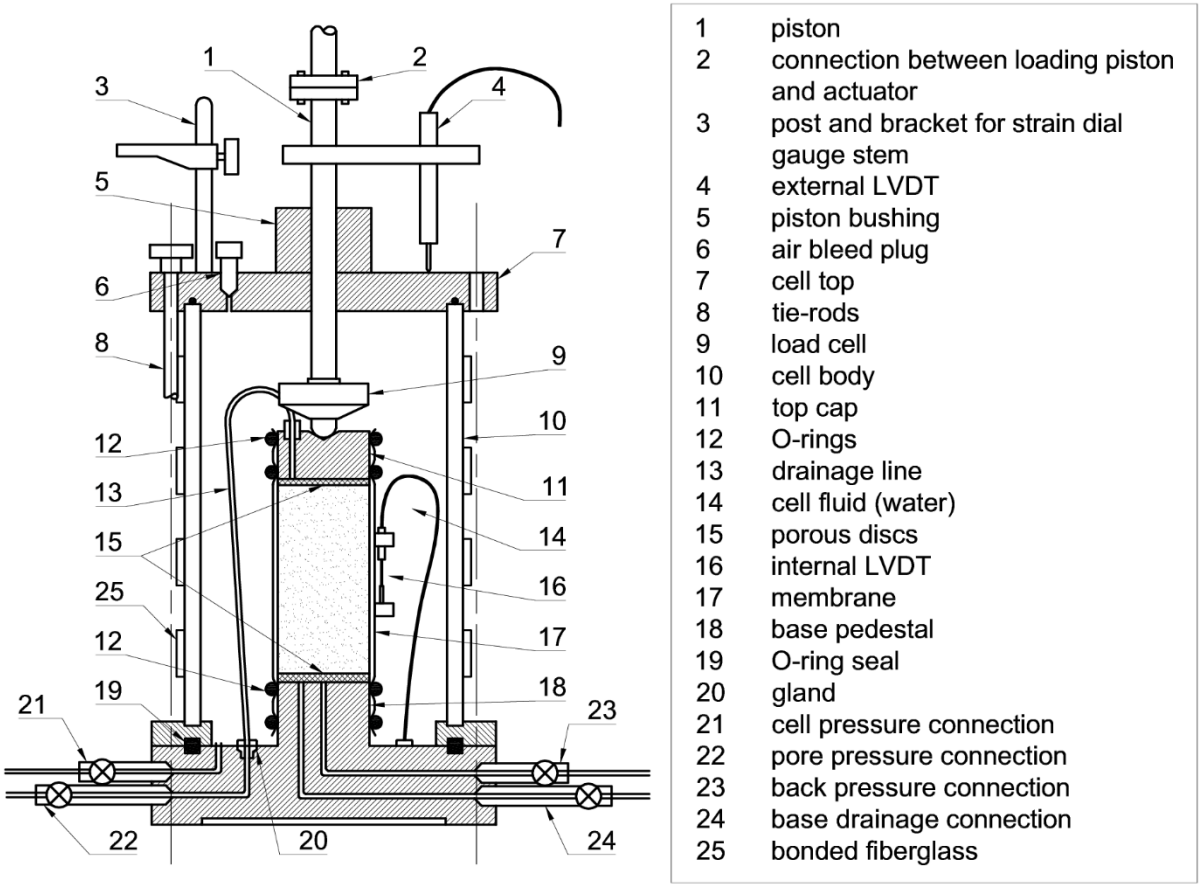

Fig. 5.4 - Details of the triaxial cell used for cyclic tests

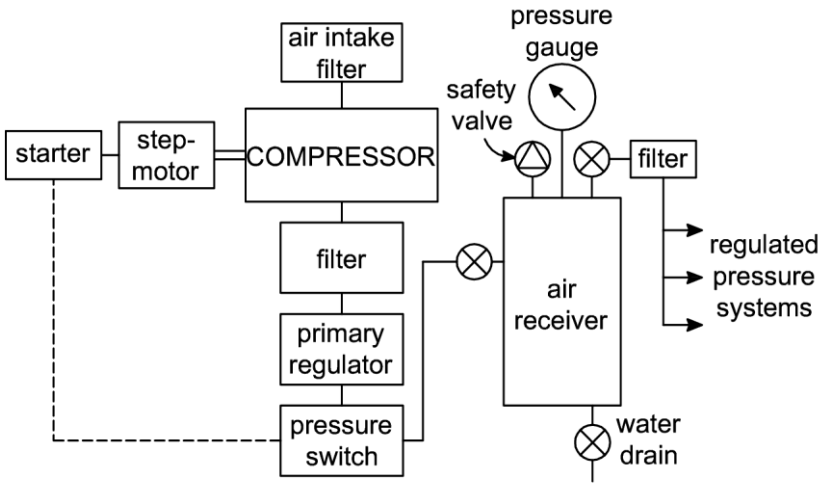

Fig. 5.5 - Scheme of the motorized air compressor system of LabGeo-FEUP

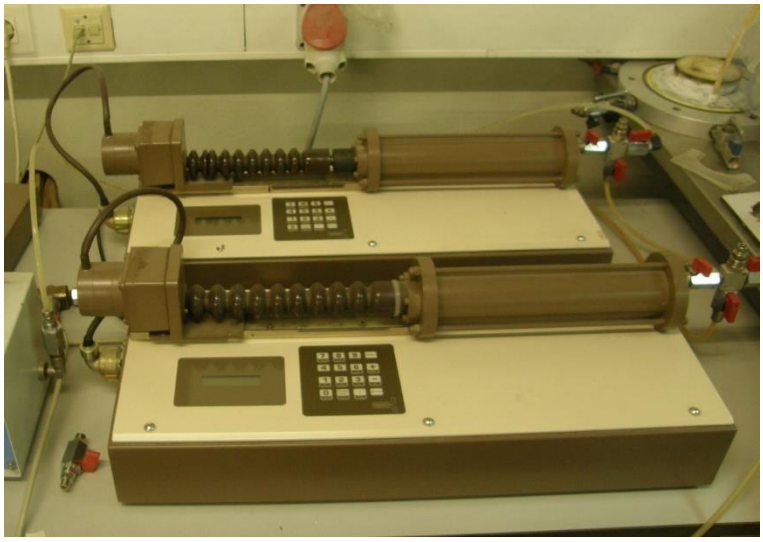

Fig. 5.6 - Digital pressure/volume controllers

5.4.3. AXIAL DISPLACEMENT MEASUREMENT

The measurement of the axial displacement was performed through the three internal LVDTs and confirmed by the measurement of the external LVDTs. The three internal LVDTs are all equal (10 mm range D5W submersible LVDT displacement transducers manufactured by RDP Electronics®) and each of them is equipped with an amplifier (manufactured on-purpose by RDP Electronics®) to amplify the signal generated into a form suitable for the monitoring system used. The gain of each amplifier (i.e. the output/input voltage ratio) was manually adjusted in order to achieve the best representation of the signal generated by the transducers.

The three internal LVDTs were individually calibrated before the start of the testing programme in the same monitoring system used to perform the tests, using a proper LVDT calibration device equipped with a micrometre. The validity of the calibration was checked before the beginning of each test. In Fig. 5.7 an example of calibration is reported. In the vertical axis, the value measured by the calibration device is reported (in millimetres); while in the horizontal axis the corresponding value read by the electronic system is indicated (in Volts). The calibration was started with the pin almost completely inserted into the transducer; a value of 10 mm was assigned at this position (equal to the nominal range of the instrument). Then, the pin was slowly pulled out of the transducer for a distance of 2mm, the position was maintained, and a value of 8 mm was registered at this position. The process was repeated and readings were registered at each millimetre, until the position corresponding to 0 mm was registered in the system. As shown in the figure, in the calibration interval the relation between the displacement measured by the calibration device and the corresponding reading of the LVDT is linear. Thus, the range of linear behaviour of the three internal LVDTs has an extension of at least 10 mm. At the beginning of each tests, each LVDT was pivoted in a position such that the corresponding measure (displayed by the computerized monitoring system) was around 5 mm, at the middle of the linearity range (corresponding to a value around 0 V in the system). Thus, each LVDT had a linear span of measurement of 5 mm in each direction (extension or contraction). Due to the low level of the imposed axial stress, during the entire cyclic test the maximum axial deformation was in the order of the decimals of millimetres, much smaller than the maximum allowed deformation of 5 mm.

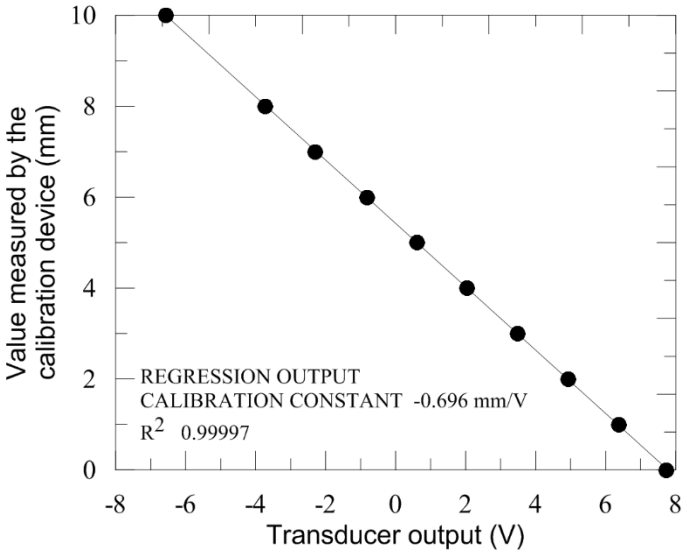

Fig. 5.7 – Example of calibration on an internal LVDT

The output of the three internal LVDTs was accurately controlled after each test, eliminating the outliers detected through the comparison of the three outputs.

The two external LVDTs have a range of measurement of 50 mm. Due to their position, the external LVDTs were much more prone to bedding errors, thus, the measurement of axial strain was performed through the internal LVDTs and the external LVDTs were used as a confirmation of this more precise measurement. An example of output is given in Fig. 5.8. The output of the three internal and the two external axial LVDTs for selected cycles is reported in the vertical axis, while the time is reported in the horizontal axis, in logarithmic scale (the time starts at the arbitrary value of 1 s to avoid problems with the representation of 0 on a logarithmic scale). The initial value of the vertical axis is set equal to 0 for all the gauges, in order to facilitate the comparison. In the reality, all the internal LVDTs started from an initial value around 4÷6 mm (close to the middle point of the linear range of measurement). The two external LVDTs (with range equal to 50 mm) were initially positioned around 15÷20 mm.

One can see that the three internal LVDTs have similar readings (of the order of the decimals of millimetres, inside the linear range of measurement), while the external LVDTs present higher values, but a similar shape of the displacement with time. All the LVDTs show a bedding error in the first cycle, which is more evident for the external LVDTs. This bedding error was carefully removed from all the measurements, in all the tests. In the comparison of the internal and external LVDTs output, it should be noted that the reading of the latter is referred to the whole height of the specimen, while the internal LVDTs measure the deformation of the central third of the specimen. Nevertheless, the strain measured by the external LVDTs is slightly higher than the corresponding strain measured by the internal LVDTs. It is interesting to note that the LVDT installed in the actuator (more distanced from the specimen) presents higher readings than the LVDT installed on the cell top cap.

Due to the small strain level reached in the cyclic tests, the shape of the specimen at the end of each test was not altered considerably, i.e. no barrelling and/or shear bands and/or cracks were visible on the specimens. Moreover, the membrane did not show wrinkles. Thus, the arrangement of the internal LVDTs pivoted on the specimen did not suffered significant alteration (such as slippage, loss of verticality and/or misalignments, exit from the linear range of measurement) that could lead to a degradation of the measurement.

The processing of the raw data is further detailed in section 5.6.

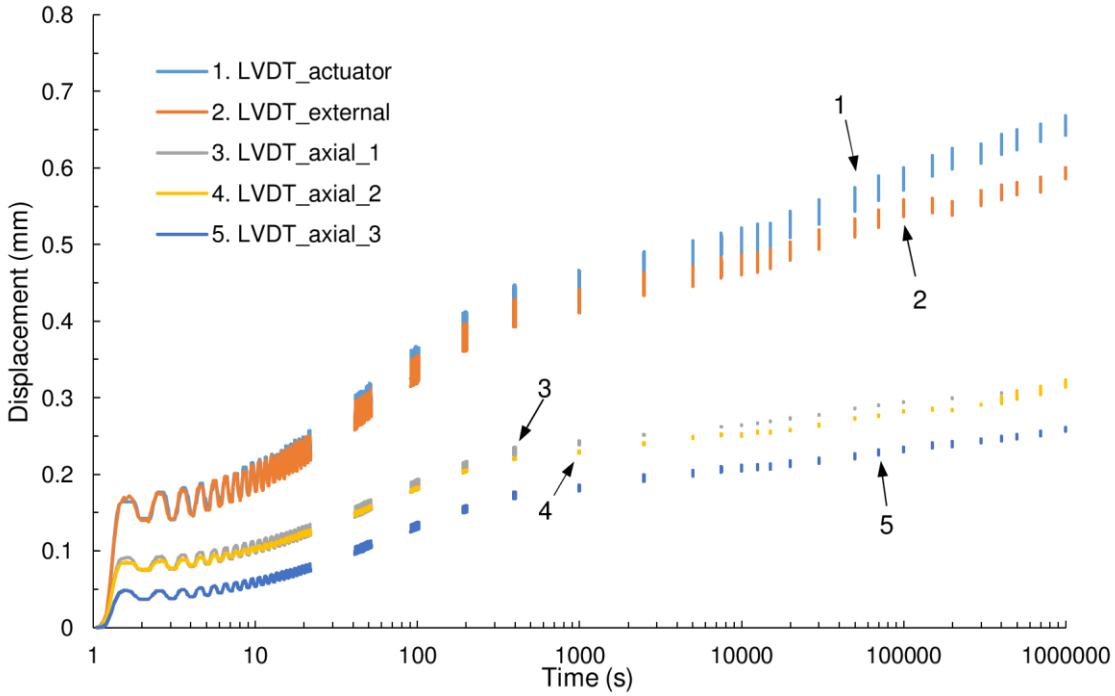

Fig. 5.8 – Output of the three internal, external, and integrated axial LVDTs for the test TC_0%_e1_s1 (time in logarithmic scale)

5.4.4. VOLUMETRIC VARIATION MEASUREMENT

The measurement of the volumetric variation was performed using a volume gauge manufactured by VJ Tech® (Fig. 5.9) with a capacity of 100 cm^3. The gauge operates through a LVDT similar to those used for the measurement of axial strain. Such LVDT measures the difference in the level of water inside a cylindrical tank. Since the cross section of the tank is constant, a variation in the water level corresponds to a consequent variation of the volume of water contained in the tank. Also for this instrument, the calibration was performed before the beginning of the testing program in the same apparatus where the tests were subsequently performed; the correctness of the calibration was verified before each test. The calibration was performed using a graduated cylinder. The volume of the water flowing out of the gauge was measured with such instrument and the corresponding reading was inserted in the system at selected intervals. The relation between the measured and the read values showed a linear response throughout the 100 cm^3 range of the instrument; thus, the volume gauge has a valid range of measurement corresponding to 100 cm^3.

During each drained test, after the saturation of the specimen the volume gauge and the connecting system were carefully purged from air and connected to the back pressure connection of the triaxial cell (n. 23 in Fig. 5.4). During the subsequent phases of isotropic compression and cyclic shearing, the volume gauge measured the volume change of the specimen by measuring the quantity of water flowing in and out of the specimen. The volume gauge was initially positioned at around 50 cm^3, at the middle of the measuring range. Such position ensured almost 50 cm^3 of range in both directions (compression and dilation). Such span is sufficient for a correct measurement of the volumetric deformation, since the maximum volumetric deformation measured at the end of each test was less than 5 cm^3.

Fig. 5.9 – Volume gauge

5.5. TESTING PROCEDURE

As reported in many manuals (e.g. Bishop & Henkel, 1957; Head, 1982; Lade, 2016), triaxial tests are typically divided in the following phases:

- Specimen saturation
- Specimen consolidation (isotropic or anisotropic)
- Shearing phase (monotonic and/or cyclic)

After the curing period in the humid chamber, each cemented specimen was submerged in a water tank in order to ease the successive saturation process in the cell; then, it was positioned in the triaxial cell. The uncemented specimens were not submerged outside the triaxial cell because water would destroy their integrity, so they were directly positioned in the cell the day after demoulding (with a water content equal to the moulding humidity of 12%) and saturated as specified in the following. From this point on, the process followed the same steps for uncemented and cemented specimens.

The specimen (cemented or uncemented) positioned onto the base pedestal was separated from the specimen cap and base by rigid porous discs and filter-paper discs. A rubber membrane was fitted around the specimen and sealed at both ends with four O-rings. The specimen was equipped with three axial strain gauges (LVDT type) directly installed onto its lateral surface (Fig. 5.10). The cell body was closed, filled with distilled tap water and the piston was connected to the hydraulic actuator.

The saturation of the specimens was performed in two stages. At first, by percolating de-aired water upwards through the specimen with a cell pressure of 25 kPa and a back pressure at the bottom of 15 kPa, leaving the upper end of the specimen open to the atmospheric pressure. This stage lasted until the volume of the percolated water was at least twice the volume of the voids of the specimen. Then, the specimen was isolated from the exterior and the back pressure at the bottom of the specimen was increased in a controlled manner along with the cell pressure, so that the air in the voids was dissolved. All specimens were saturated using a constant rate of increase of pressure of 30 kPa/h (using the two

aforementioned digital pressure/volume controllers) and maintaining a differential of 10 kPa between the cell pressure and the back pressure.

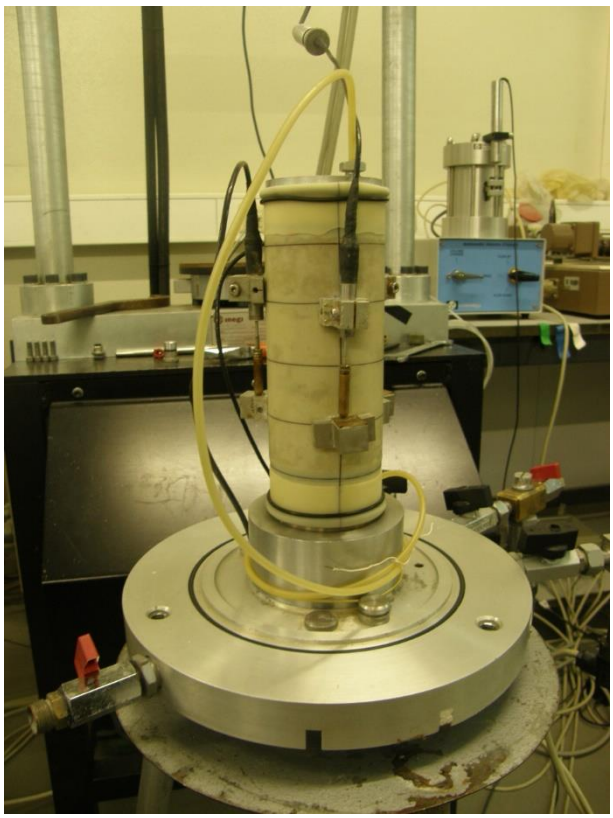

Fig. 5.10 – Test preparation: detail of the internal LVDTs arrangement

The final back pressure was assumed equal to 500 kPa, as the experience in LabGeo-FEUP assures the complete saturation with this value (Rios, 2011; Amaral, 2012; Viana da Fonseca et al., 2013a). A manual check of the *B* pore pressure parameter value (Skempton, 1954) was performed for all the specimens. Although high values of this parameter were measured in all the tests, this control is not sufficient by itself to assure complete saturation (Viana da Fonseca, 1996). In fact, as reported by many authors, for structured specimens the reading of the parameter *B* is not always reliable. Nevertheless, complete saturation for the imposed back pressure was verified many times in earlier works (conducted on the same material and in the same conditions) through compression (P) wave velocity measurements using ceramic piezoelectric transducers (bender/extender elements) installed directly in the top cap and base of the triaxial cell, and embedded in the specimen (Viana da Fonseca & Coutinho, 2008; Viana da Fonseca et al., 2009b; Ferreira et al., 2011; Rios, 2011; Amaral, 2012; Viana da Fonseca et al., 2013a). Following the literature, the specimen is fully saturated when compression wave velocity is approximately 1500 m/s. In the mentioned works, it was shown that this velocity is always reached for specimens subjected to the adopted back pressure of 500 kPa.

The specimen was then allowed to consolidate isotropically until the target effective consolidation pressure of the specific test was reached. The top cap drainage of the specimen (equipped with a pressure transducer, able to read the variations of pore water pressure throughout the test) was kept closed as during the precedent phase and the water was allowed to drain through the bottom drain, linked to the volume gauge. A check on the volume variation through the volumetric transducer was performed at the end of the consolidation in order to assure that the consolidation process was completed.

The actuator was then started using the dedicated software and the ram was slowly put in contact with the top cap and displaced until the load measured by the load cell reached the minimum value of the designed deviatoric cyclic load (q_{min}). This value was maintained constant until the excess pore water pressure was dissipated (the volume of water flowing out the specimen through the bottom drain was checked), then the sinusoidal cyclic loading initiated with a loading frequency of 1 Hz. As reported above, this frequency assures that the loading process is fully drained in all the drained tests. This was confirmed by the pore pressure measurement performed by the pressure transducer connected to the specimen top cap (since its drainage remained closed during the test, the top cap is the zone of the specimen farer from the drainage and more prone to pore pressure build up). For undrained specimens, the drainage valve connected to the bottom end of the specimen was closed after the application of q_{min} and before the start of the cyclic loading and the pore pressure variation was measured by the two pressure transducers connected to both ends of the specimen.

5.6. DATA PROCESSING

In order to obtain a good definition of the cyclic response of the soil in the stress-strain plane, the data acquisition frequency was set equal to 20 Hz, i.e. the monitoring system was set to save 20 points for each loading-unloading cycle. Due to the long duration of the tests, the corresponding output files contain a considerable amount of data. In order to reduce the amount of data to be analysed, European Standard EN 13286-7 (CEN, 2004) suggests to consider a reduced set of cycles. As suggested by the standard, readings are taken continuously during the first 20 cycles, and then at the following cycles:

$$n_{cyc} = (1\text{- } 20, 50, 100, 200, 400, 1000, 2500, 5000, 7500, 10000, 20000) \quad (5.6)$$

At each selected cycle, the readings are taken for 10 consecutive cycles (e.g. at cycle 50, all cycles between 40 and 50 were selected). After 20000 cycles, the standard does not give any indication, so the following cycles were selected at intervals of 20000 cycles (i.e. 39900-40000, 59990-60000…). The selected cycles were extracted from the output file using a MATLAB© script specifically developed for this purpose. The same code is also able to perform the subsequent data elaboration and to present the results.

Fig. 5.11 shows a scheme of a typical response in the stress–strain plain, where the characteristic hysteretic loops can be observed. The accumulated (axial or volumetric) strain at a certain cycle ($\varepsilon_{cum,n}$) is defined as the strain at the end of that cycle. Axial and volumetric accumulated strain are directly measured through the internal LVDTs and the volume gauge. From $\varepsilon_{a\ cum}$ and $\varepsilon_{v\ cum}$, one can derive the value of permanent distortional (deviatoric) deformation ($\varepsilon_{s\ cum}$) using the usual relations:

$$\varepsilon_{s\ cum} = \frac{2}{3}(\varepsilon_{a\ cum} - \varepsilon_{r\ cum}) \quad (5.7)$$

$$\varepsilon_{v\ cum} = \varepsilon_{a\ cum} + 2\ \varepsilon_{r\ cum} \quad (5.8)$$

where $\varepsilon_{r\ cum}$ is the accumulated radial strain.

Replacing equation (5.8) into (5.7) one obtains:

$$\varepsilon_{s\ cum} = \varepsilon_{a\ cum} - \frac{1}{3}\varepsilon_{v\ cum} \quad (5.9)$$

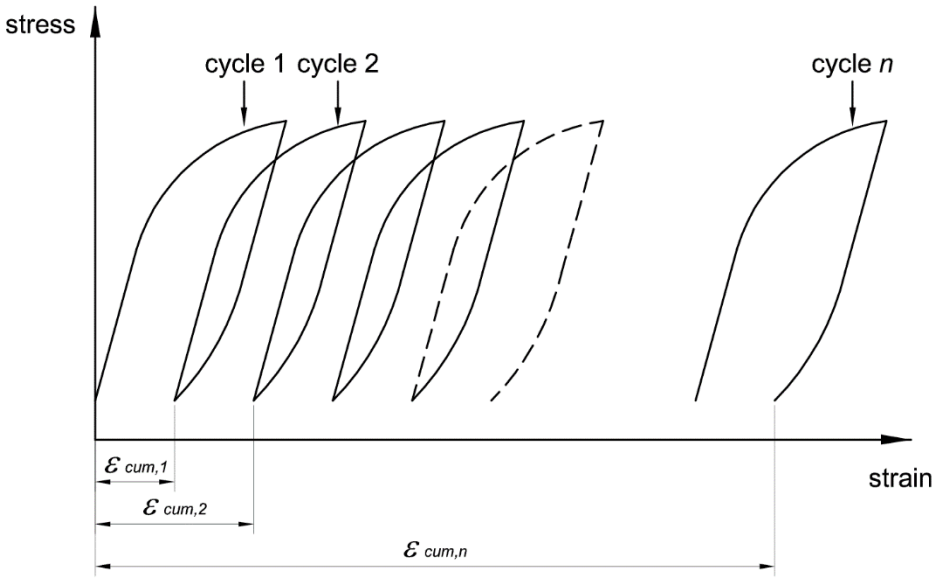

Fig. 5.11 - Definition of accumulated permanent strain

For undrained tests, this implies:

$$\varepsilon_{v\,cum} = 0\,;\ \varepsilon_{s\,cum} = \varepsilon_{a\,cum} \tag{5.10}$$

During the tests, axial deformation is measured by a redundant number of devices, as explained in the precedent sections: three internal LVDTs, one external LVDT on the cell cap and one transducer integrated in the actuator. The axial deformation at a given time is computed as follows:

$$\varepsilon_a = \frac{LVDT_t - LVDT_i}{L_{LVDT}} \tag{5.11}$$

Where $LVDT_t$ is the reading of the LVDT at a given time and $LVDT_i$ is the initial reading of the same LVDT. Term L_{LVDT} has a specific definition depending on the type of LVDT considered: for internal LVDTs, L_{LVDT} is the distance at which the pivots of the transducer are glued onto the specimen; for the external LVDTs, it is equal to the initial height of the specimen.

The best representation of the deformation is given by the internal LVDTs, since the external transducers are affected by the compliance of the loading piston, cell top and other parts of the apparatus. Thus, the measurement of the internal LVDTs was considered in the subsequent analysis of the results, using the external measurement as an extra check to confirm the quality of the internal measure. Since three internal LVDTs were used in the tests, the average of the three measurements was considered.

For the volumetric strain calculation, a similar formula is applied for the volume gauge:

$$\varepsilon_v = \frac{LVDT_t - LVDT_i}{V_i} \tag{5.12}$$

where $LVDT_t$ and $LVDT_i$ have the same meaning of the precedent formula, referred to the volumetric transducer; V_i is the initial volume of the specimen, obtained measuring the initial height (H_s) and diameter (D_s) of the specimen.

The validity of expressions (5.11) and (5.12) (that are defined for infinitesimal strain) is guaranteed by the small strain levels attained during the triaxial tests (<1%), as it can be seen in the results presented in the following section.

5.7. RESULTS AND DISCUSSION

The great amount of data retrieved during the 11 days long cyclic loading was recorded in a large text file. As mentioned in the precedent section, the file was managed using a MATLAB© script specifically developed for this purpose; the same script performs the subsequent data elaboration and presents the results in graphic and numeric format.

During cyclic loading, a series of hysteretic loops is observed in the stress-strain plane. An example referring to test TC_0%_e1_s1 is shown in Fig. 5.12, where the cycles selected with the criteria explained earlier are plotted in the deviatoric stress vs. axial strain plane. Six cycles (labelled with a letter from A to F) are extracted from this figure and plotted separately in Fig. 5.13. The loops are not perfectly closed (this can be observed clearly in cycle A, while in cycles B to F is not readily recognisable because of the very small amount of accumulated strain), leading to the development of permanent axial strain during each cycle. The evolution of the hysteretic loops with the number of cycles shows a progressive increase in stiffness with cycles, leading to a decreasing rate of strain accumulation. This behaviour is referred to as cyclic hardening (Dafalias & Popov, 1975). A similar output is observed for the drained tests in the mean effective stress vs. volumetric strain plane (test TC_7%_e2_s3 in Fig. 5.14); for undrained tests, the loops are observed in the effective stress path trajectory ($p' - q$ stress plane), as an effect of the pore pressure variation (see example in Fig. 5.15). Also in this case the loops are not closed, leading to volumetric strain accumulation (in drained tests) or accumulation of extra-pore pressure (in the undrained tests). In the undrained case, the recorded loops in the stress plane do not seem to evolve with the number of cycles (Fig. 5.16). In the case of the volumetric strain vs. mean effective stress results (drained tests), it was not possible to visualize the single loops, since their definition is not optimal, due to the low strain level compared to the sensibility of the measuring gauge. Nevertheless, the long-term tendency is correctly reproduced.

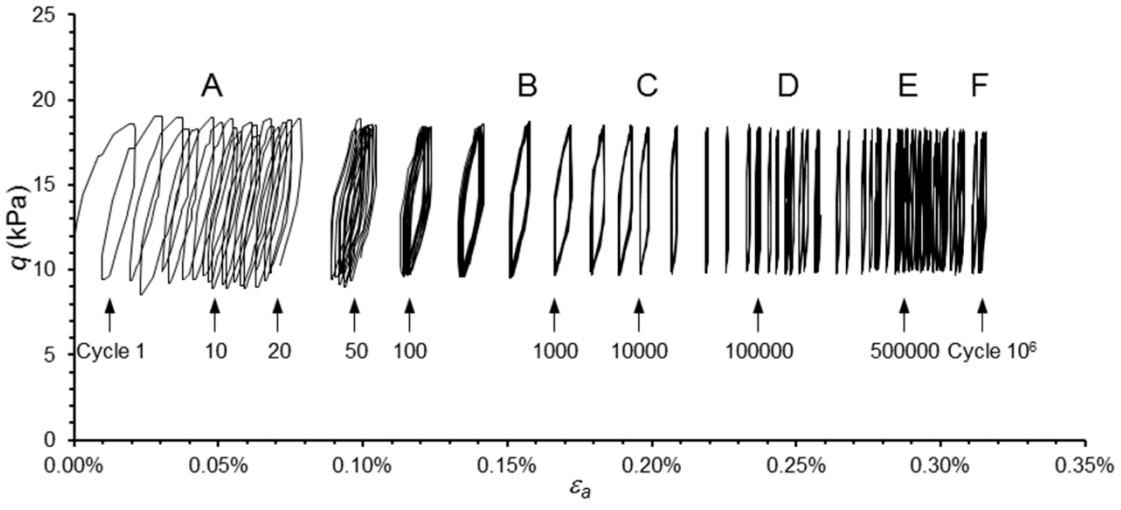

Fig. 5.12 – Hysteretic deviatoric stress- axial strain loops for test TC_0%_e1_s1 (selected cycles)

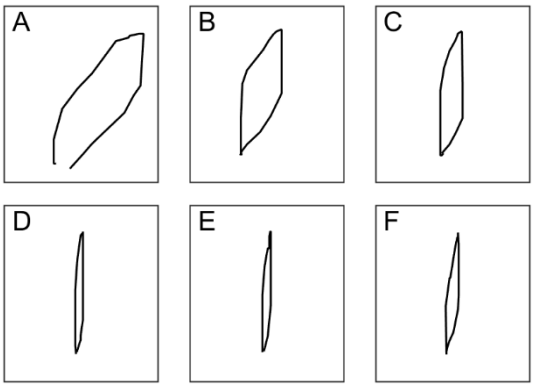

Fig. 5.13 – Evolution of hysteretic loops with number of cycles for test TC_0%_e1_s1

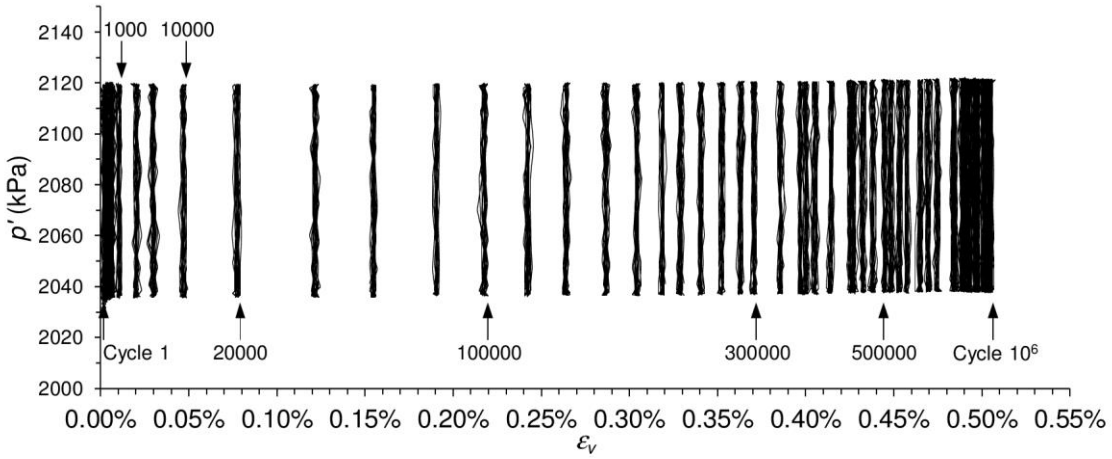

Fig. 5.14 – Hysteretic mean effective stress - volumetric strain loops for test TC_7%_e2_s3 (selected cycles)

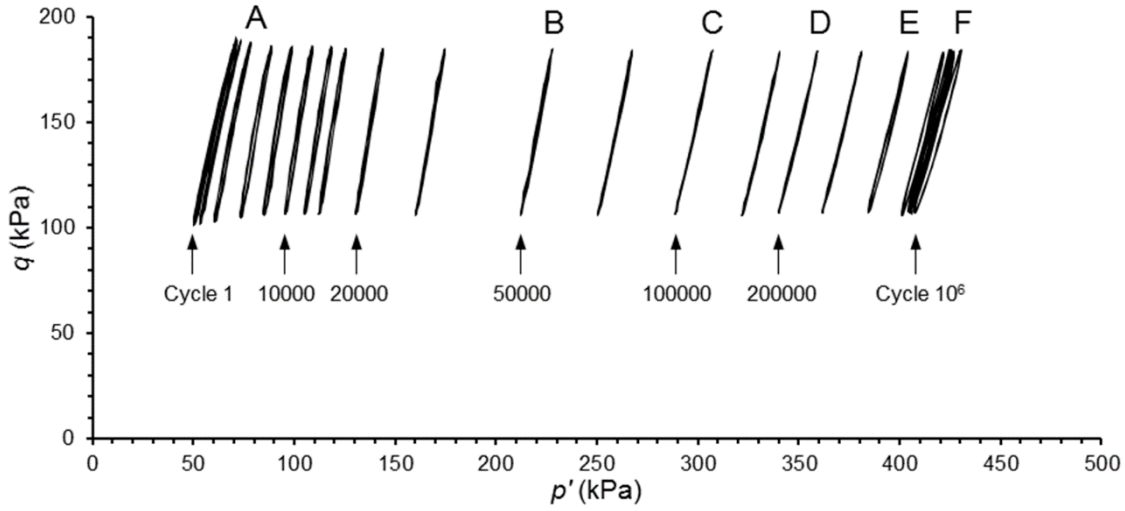

Fig. 5.15 – Hysteretic loops in the effective stress plane for test TC_3%_e3_s1U (selected cycles)

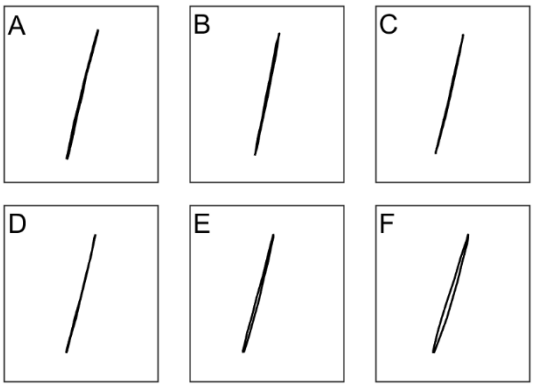

Fig. 5.16 – Evolution of hysteretic loops with number of cycles for test TC_3%_e3_s1U

5.8. DRAINED TESTS

5.8.1. LOW CONFINED TESTS

The first set of tests ("s1") is the set with lower effective confining pressure (40 kPa). The results are shown in Fig. 5.17 and Fig. 5.18 (Panico & Viana da Fonseca, 2016b).

The results are shown in a semi-logarithmic scale. This representation was preferred because it is more suitable to represent the first cycles, which present the higher rate of accumulation. Moreover, semi-logarithmic scale eases the recognition of particular trends of accumulation.

For axial strain, the results of the uncemented and cemented specimens were plotted in two distinct vertical axes, as the accumulated strain is very different in the two cases. The final accumulated strain is similar for the two uncemented specimens (around 0.35%), and much lower for cemented specimens. Although some dispersion is inevitable at such small strain levels, axial strain accumulation is similar for all the cemented specimens, and around 0.04%. This result shows that the adjusted porosity/cement ratio, previously used as indexing parameters in UCT and monotonic triaxial tests, can be used also in cyclic triaxial tests. In fact, the stress levels applied in the tests were defined in a normalized stress space, based on a parameter derived from that ratio (Fig. 5.1). Since the applied stress was determined in this normalized space as a fraction of the corresponding ultimate stress, it is expectable that the amount of accumulation is similar for the cemented specimens with different initial compaction and cementation. The ratio is not applicable to uncemented specimens, whose stress levels where derived in a non-normalized stress space. This is a possible cause for the different response of the uncemented specimens. Another possible explanation of the different response between uncemented and cemented specimens is the different stiffness of the two classes of soils in the small-strain domain, due to cementation. The cemented specimens are stiffer and less prone to strain accumulation even if the applied stress is the same fraction of the corresponding ultimate load for all the specimens.

The study of the trends of accumulation of axial strain leads to interesting considerations. In cemented specimens, the accumulated axial strain increases with a slow rate for the first 10000 cycles and increases significantly after that. A double logarithmic trend is observed (i.e. a logarithmic trend with two different inclinations): a first part with a constant slope (which is linear in the semi-logarithmic representation) and a second part (after approximately 10000 cycles) more inclined than the first part of the test. For uncemented specimens, a similar behaviour is observed but with opposite trends: also in this case, a double logarithmic rate of accumulation is observed, but the slope of the first part is higher than the slope of the second part of the test (the switch occurs around 1000 cycles).

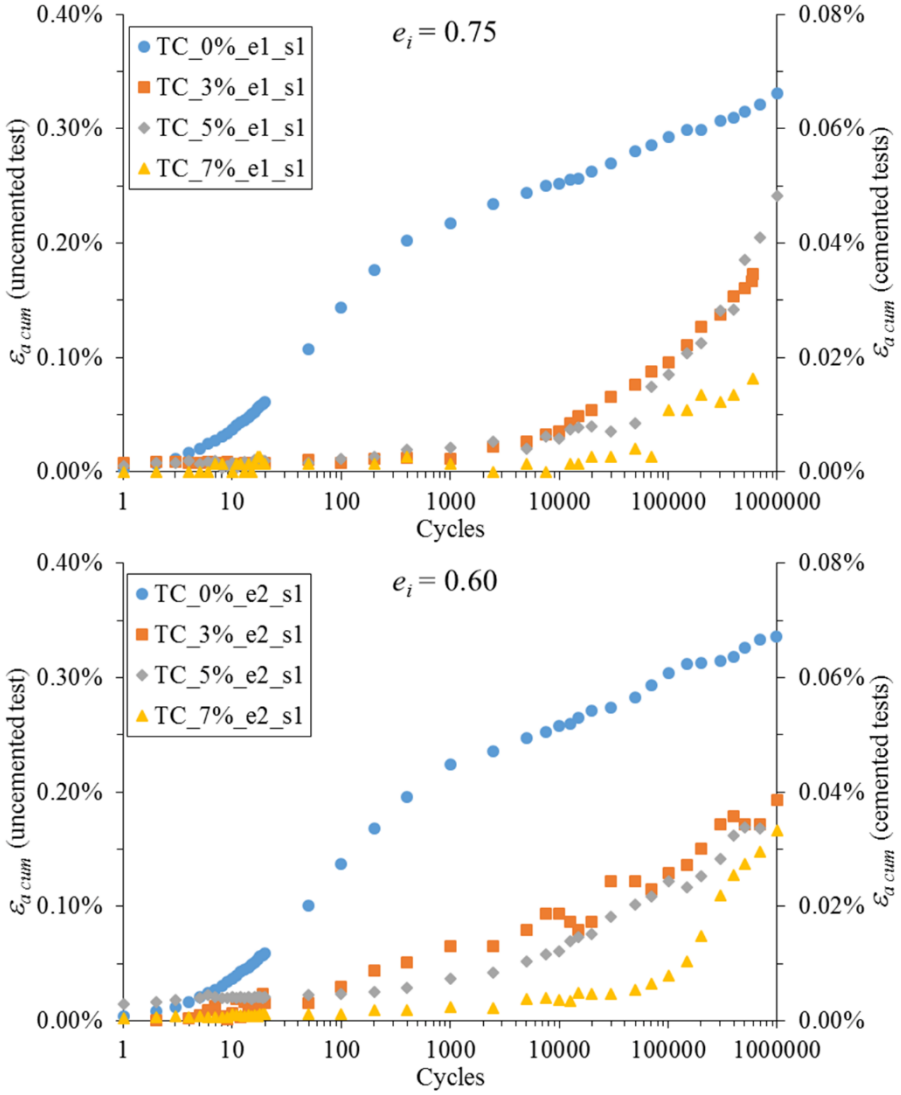

Fig. 5.17 – Accumulated axial permanent strain with cycles (first set of tests)

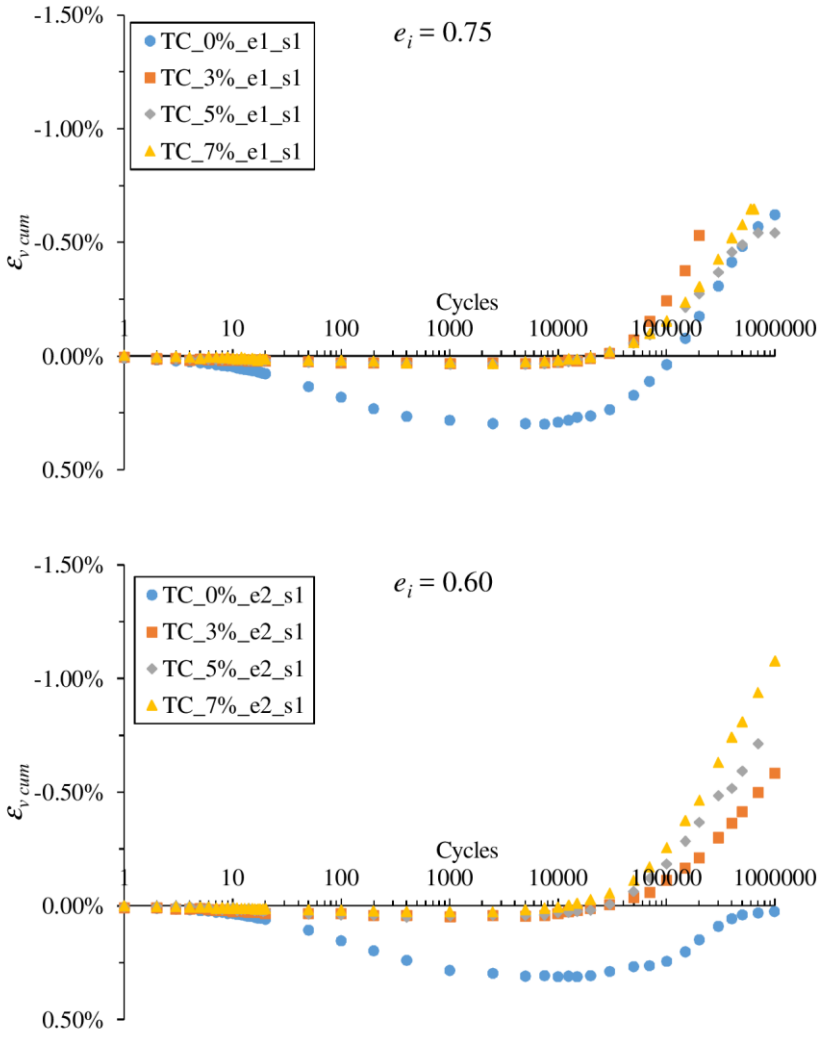

Fig. 5.18 – Accumulated volumetric permanent strain with cycles (first set of tests)

This different behaviour evidences the influence of cementation: as expected, specimens with higher cement contents suffer lower accumulated strain during cycling loading. Nevertheless, cementation makes the soil stiffer but more brittle: while the bonds are mostly intact, the soil fabric remains nearly undisturbed and the rate of accumulation is low; after the development of progressive damage in the bonds due to repeated loading, the weakened structure of the mixture loses the capacity to prevent deformation and the rate of accumulated strain increases. On the other hand, the uncemented specimens show a very different behaviour. As the particles are relatively free to rearrange, the rate of accumulation is higher in the first part of the test (this stage corresponds to a volumetric compaction of the soil). When the rearrangement has modified the structure of the granular matrix compacting the soil, the rate of accumulation decreases.

The trend of accumulation of the volumetric strain is more complex. The accumulation is positive (compression) in the first 10000 cycles (close to zero for cemented specimens) and then it becomes negative, showing a dilatant behaviour. Dilatancy is expected in this case as this behaviour is typically observed in monotonic drained tests on dense (low confined) soils. It is unsure what causes the change between the first compressive part and the second dilatant part. This is a possible effect of the

rearrangement in the soil fabric, which corresponds to the change in the accumulation of the permanent strain rate previously observed in the axial strain. Moreover, it must be pointed out that an initial compressive behaviour is also observed in the initial stages of monotonic tests performed on dense soils.

The graphs in Fig. 5.19 display the volumetric vs. axial accumulated strain; one can observed that they are similar to the corresponding graph referred to a monotonic drained test (even though the levels of strain involved are much smaller in this case). In any case, the volumetric response of a soil during cyclic loading should be further investigated, as in the literature on soil response under cyclic loading such aspect is neglected.

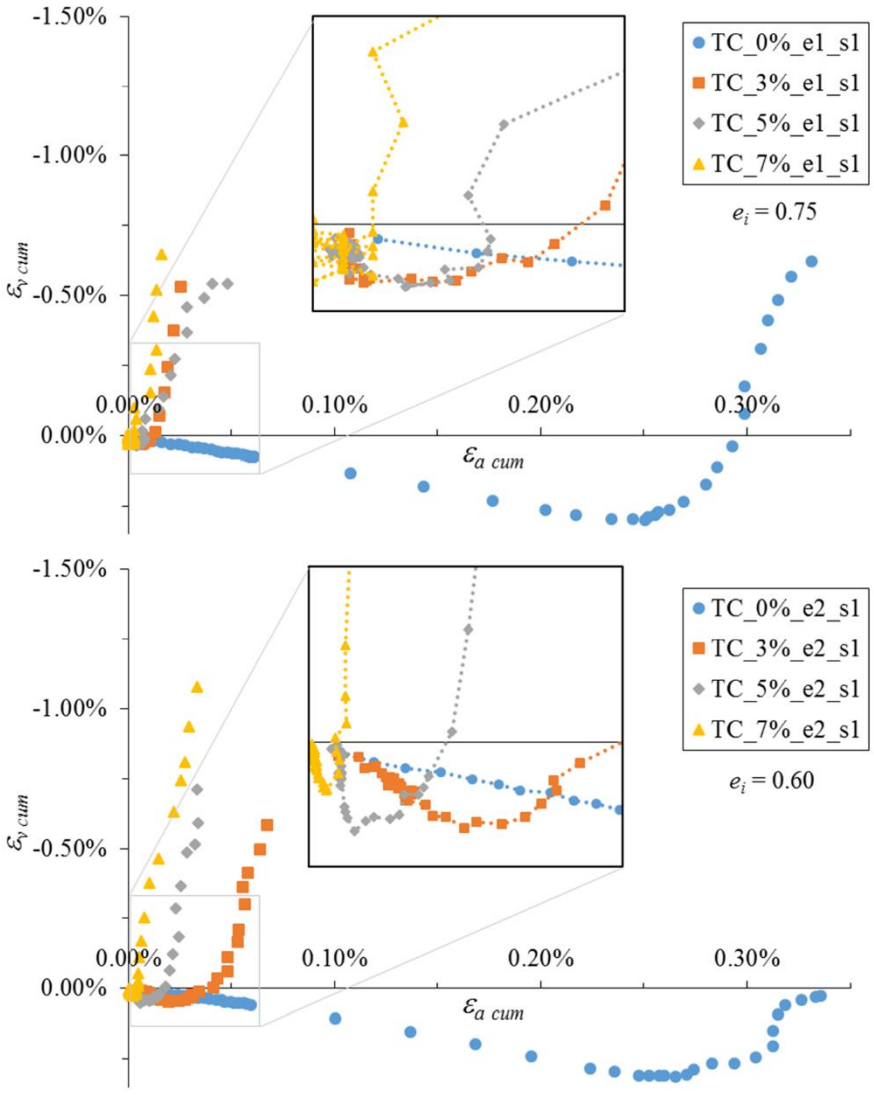

Fig. 5.19 – Accumulated volumetric vs. axial strain (first set of tests)

5.8.2. MEDIUM CONFINED TESTS

In this group of tests, the effective confining pressure was set as 1/3 of the isotropic yield stress (σ'_y) of each specimen. Thus, all the specimens were consolidated to a ratio σ'_y/σ'_c of 3, which implies that each test had a different effective confining pressure, conversely to the precedent set. The aim pursued in the definition of this ratio was to perform a set of tests in a domain close to the limit between a dilative

volumetric behaviour and the compressive behaviour. The value of the ratio was retrieved from the data referring to the monotonic tests (Rios et al., 2014) and using a graphic method. This value is equal for all the specimens of this group because the elastic envelopes presented for uncemented and cemented specimens are different in size but have similar shape. Hence, in the normalized stress plane $(p'/\sigma'_y, q/\sigma'_y)$ they all coincide.

The results relative to the accumulation of axial strain (Fig. 5.20 – Panico & Viana da Fonseca, 2016a) show similarities and differences with respect to the precedent set. The accumulation trend is logarithmic with a double trend; for uncemented specimens, the trend of the first part of the test presents a higher rate of accumulation than the second part; for cemented specimens the rate is lower in the first part, higher after destructuration. The two uncemented specimens suffer an accumulation at 10^6 cycles approximately equal to 0.3% (similar to the uncemented specimens of the first group), which is higher than the corresponding accumulation in cemented specimens. The accumulated axial strain in the cemented specimens at the end of the tests presents a higher scatter than the precedent set of tests, where almost all the tests converged towards 0.04%. In the present set, the specimens of group e1 (e_i = 0.75) present final axial accumulations between 0.04 and 0.06%, specimens e2 present accumulations between 0.08-0.10%.

It is important to remember that the ultimate deviatoric stress, which was the base for the definition of the stress applied during the cyclic tests, was determined on a bounding surface, which limit is not as well defined as the sharp peak states corresponding to lower confined states (and used in the precedent group). Moreover, the isotropic yield stress that were the base for the normalization of the bounding surfaces were in some case not known directly but retrieved as an interpolation of the available ultimate stresses for other mixtures. Thus, the applied stress can be in some cases slightly different from the target percentages, hence the increased sparsity.

The accumulation of volumetric strain (Fig. 5.21) shows interesting results. The accumulation is compressive in the first 10000 cycles as in the precedent case. Then, some tests follow a dilatant behaviour typical of a dense sand with an inversion in the sense of accumulation (e.g. tests TC_0%_e1_s2 and TC_3%_e2_s2).

Other specimens show a different behaviour, with a double inversion in the rate of volumetric strain accumulation. After the initial compression, a first inversion is observed, followed by the development of negative volumetric permanent strain (dilatant behaviour); then, a second inversion is observed and the volume strain accumulation recovers the positive tendency of the first cycles (e.g. tests TC_3%_e1_s2, TC_5%_e2_s2, and TC_7%_e2_s2). In the hypothesis (already formulated in the precedent section) that the cyclic response of a cemented soil can be compared to that of a granular material in monotonic conditions, one can conclude that the behaviour of the soil in this set of tests reflects an intermediate state between that of a dense, dilatant material, and a loose, compressive condition. Such conclusion seems to be supported by the volumetric vs. axial accumulation graphs shown in Fig. 5.22.

At least in the first 100000 cycles, the accumulated volumetric strain of the cemented specimens is much smaller than the uncemented specimens, and increases at a higher rate afterwards. As explained in the precedent section, this is possibly due to the role of bonding and destructuration on the soil behaviour. While in the first part of the cyclic loading cementation prevents the accumulation of plastic strain, in the long run the damage of the interparticular bonds leads to a sudden increase of the accumulation (brittle behaviour), with high rates of accumulation.

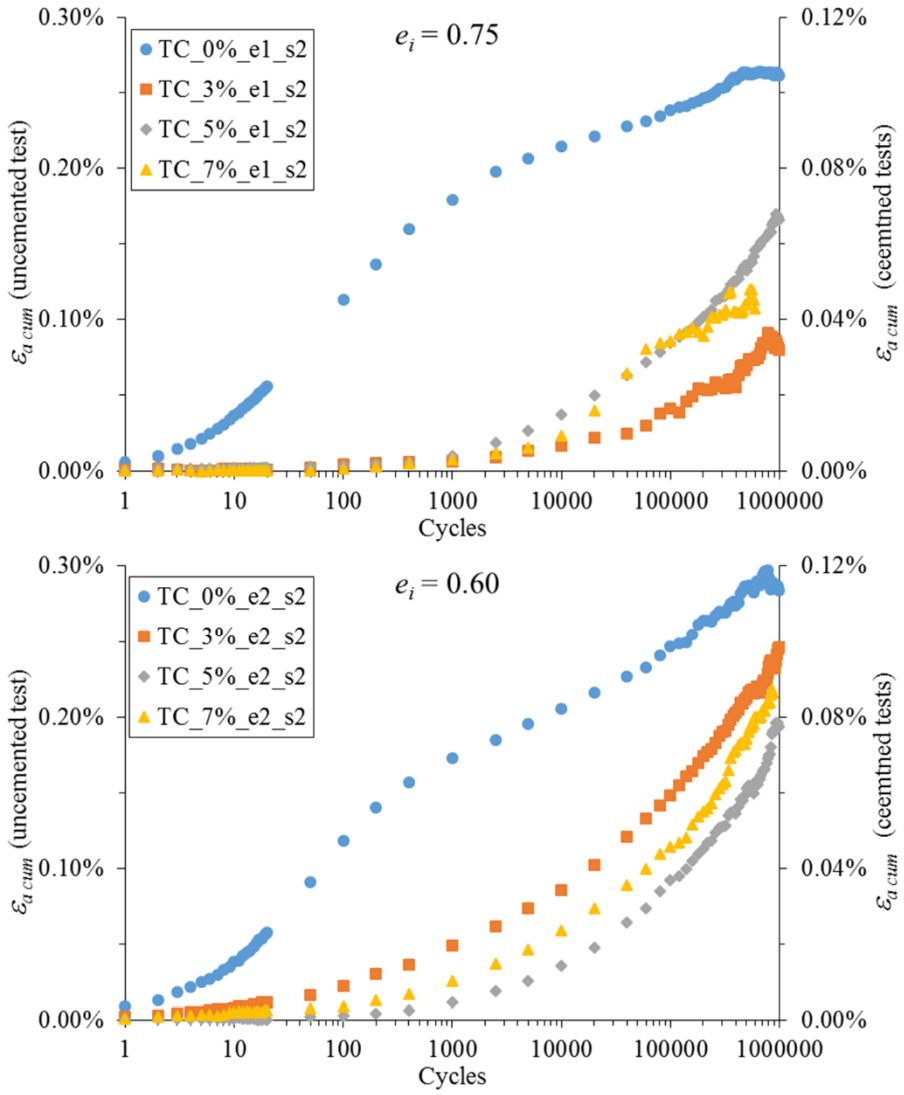

Fig. 5.20 - Accumulated axial permanent strain vs. number of cycles (second set of tests) (Panico & Viana da Fonseca, 2016a)

These results emphasise the importance of an experimental plan with such high number of cycles: phenomena as the double inversion of volumetric accumulation or the change of the rate of axial accumulation are only observable after hundreds of thousands of loading cycles and cannot be detected with a conventional cyclic testing plan with only hundreds or even thousands of cycles. This conclusion has been already highlighted in earlier studies (Viana da Fonseca et al., 2013a) being at present confirmed. An example of the importance of long-term tests is the volumetric behaviour of tests TC_3%_e1_s2 and TC_7%_e1_s2 (Fig. 5.21). The two tests follow the same accumulation path up to around 100000 cycles, and only after this high number of cycles they diverge, following opposite paths of accumulation (the former towards compression, the latter towards dilation).

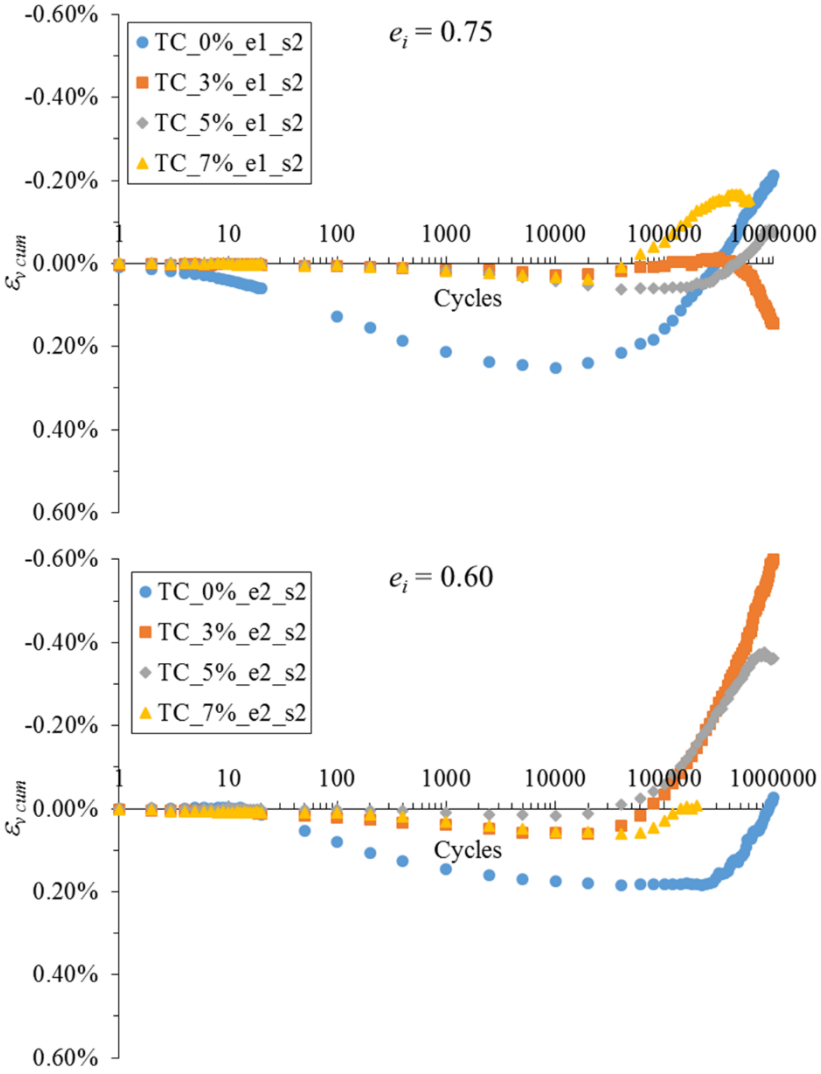

Fig. 5.21 - Accumulated volumetric permanent strain vs. number of cycles (second set of tests) (Panico & Viana da Fonseca, 2016a)

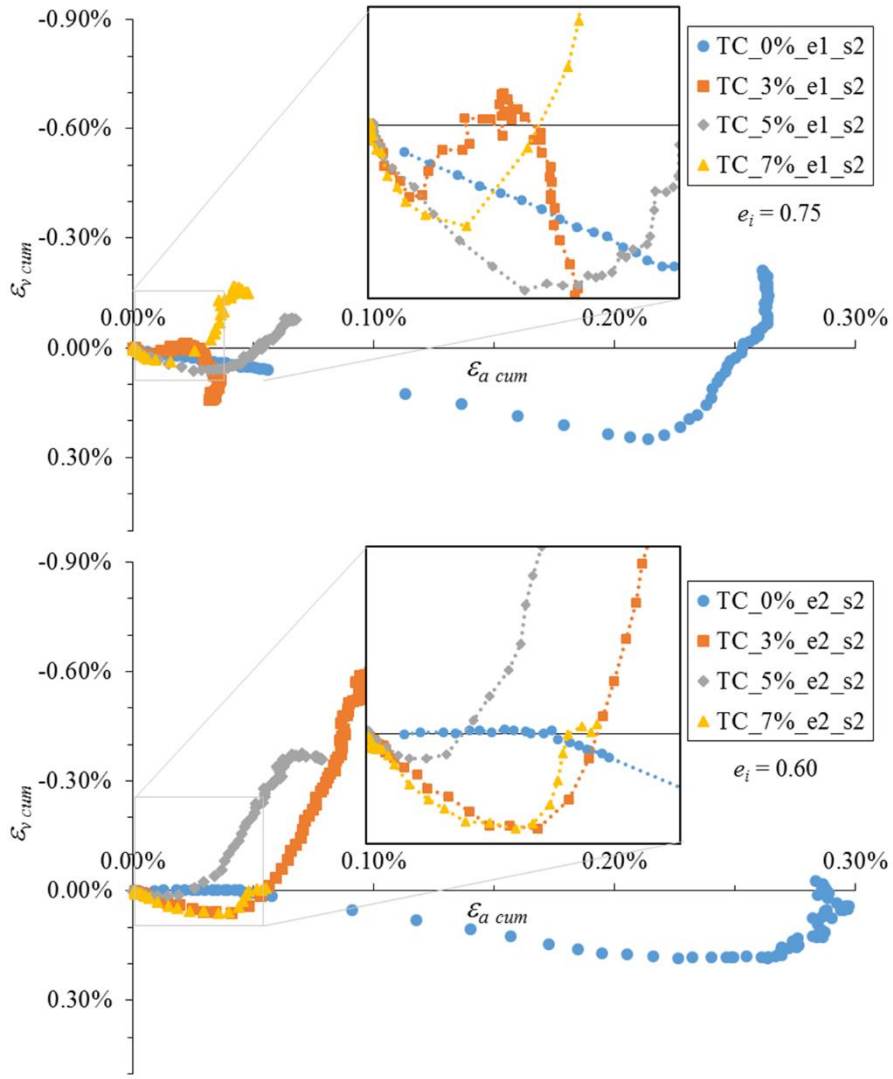

Fig. 5.22 – Accumulated volumetric vs. axial strain (second set of tests)

5.8.3. HIGH CONFINED TESTS

These tests were performed with an effective confining stress equal to half the isotropic yield stress of each specimen ($\sigma'_y/\sigma'_c = 2$). In these conditions, the soil is expected to be in a loose state and exhibit a compressive behaviour when sheared drained. The selected value of the ratio arose from a compromise between the need of performing the test in a domain of compressive volumetric response and the necessity to maintain a minimum distance between the stress path and the bounding surface. Referring to the scheme in Fig. 5.2, if a higher normalized effective confining pressure is selected, the corresponding deviatoric stress on the bounding surface would be smaller. Hence, the target deviatoric cyclic stress (which is a fraction of the former) would decrease accordingly. A test with high confinement and small deviatoric stress would result in extremely small deformation that would be difficult to measure accurately during the test.

As in the previous tests, a double logarithmic trend of axial strain accumulation is observed (Fig. 5.23). For the cemented specimens, the rate of axial accumulation in the first part of the test is lower than the rate in the second part. For the uncemented specimens, test TC_0%_e1_s3 shows a behaviour similar to

the cemented specimens, with a cyclic softening in the second part of the test; while test TC_0%_e2_s3 presents a second branch less inclined than the first part, similarly to the uncemented specimens of the low and medium confined tests. The axial accumulation at the end of the test is higher in uncemented tests than in the cemented tests, as observed in the precedent groups. Nevertheless, in this case the difference of final axial accumulation between uncemented and cemented specimens is less marked than the precedent cases. The uncemented specimens present final accumulations between 0.15 and 0.20% (it was around 0.35% in the uncemented specimens of the precedent groups); the cemented tests reach final accumulated strain between 0.05 and 0.10%. In general, final accumulated strain seems to decrease in more confined uncemented specimens; conversely, cemented specimens appear to develop higher accumulated axial strain with increasing confinement (see examples in Fig. 5.24).

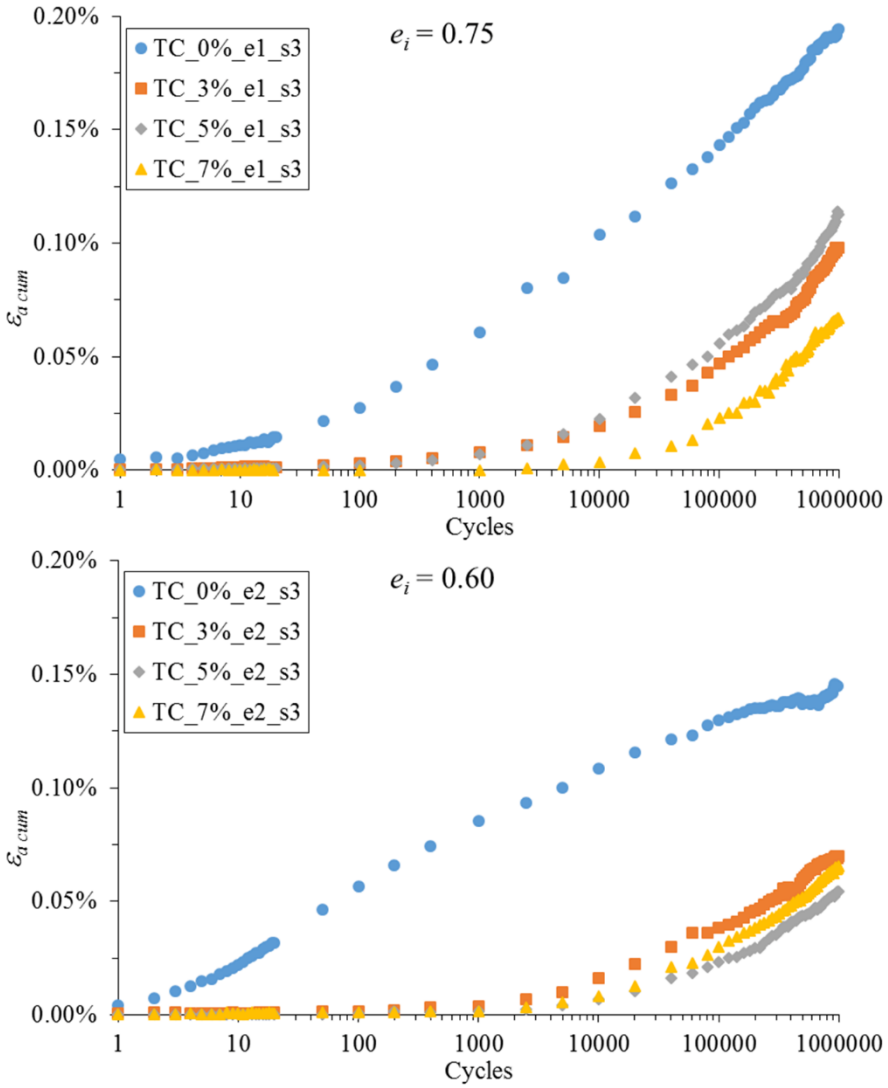

Fig. 5.23 - Accumulated axial permanent strain vs. number of cycles (third set of tests)

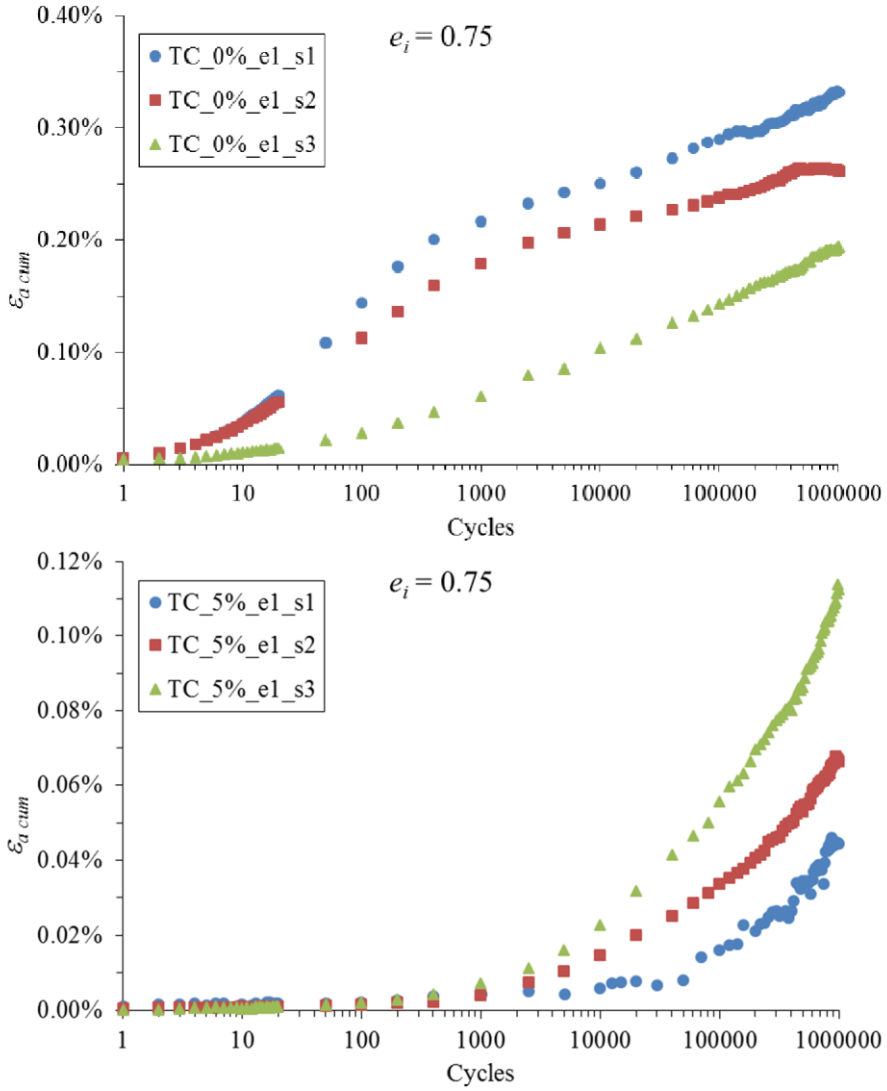

Fig. 5.24 – Example of comparison of accumulated axial strain of identical specimens under the three different loading conditions: uncemented specimen 0%_e1 and cemented specimen 5%_e1

A possible explanation of this behaviour is that the increase of effective confining pressure has a stiffening effect on the granular matrix, as it increases the number of the interparticular contacts and the forces acting between them (i.e. it ameliorates the soil fabric), thus contrasting the shearing stress caused by the deviatoric load. On the other hand, in cemented soils, the effect of the confining pressure contributes to the process of progressive damage of the cementitious bonds: the work done by the external stress is partly absorbed by the bonds, resulting in damage, partly by the granular matrix, resulting in permanent strain. As explained by Vaunat & Gens (2003), as the damage increases, the load is progressively transferred from the bonds to the soil, causing a progressive increase in the accumulated strain rate. Some scatter is present in the results – especially in cemented soils – due to the uncertainties associated to these type of tests in such small strain levels, and in the difficulty of retrieving the exact isotropic yield stress for each specimen.

The results relative to the volumetric strain show that the criterion followed in the design of the tests was not completely accomplished (Fig. 5.25 and Fig. 5.26). The volumetric behaviour is not purely compressive in all the tests; in some tests the volumetric accumulation presents a mixed behaviour between compression and dilation (e.g. tests TC_7%_e1_s3 and TC_3%_e2_s3) or even dilatancy (the

uncemented tests). In some tests, a clear compressive tendency is observed (TC_3%_e1_s3 and TC_7%_e2_s3).

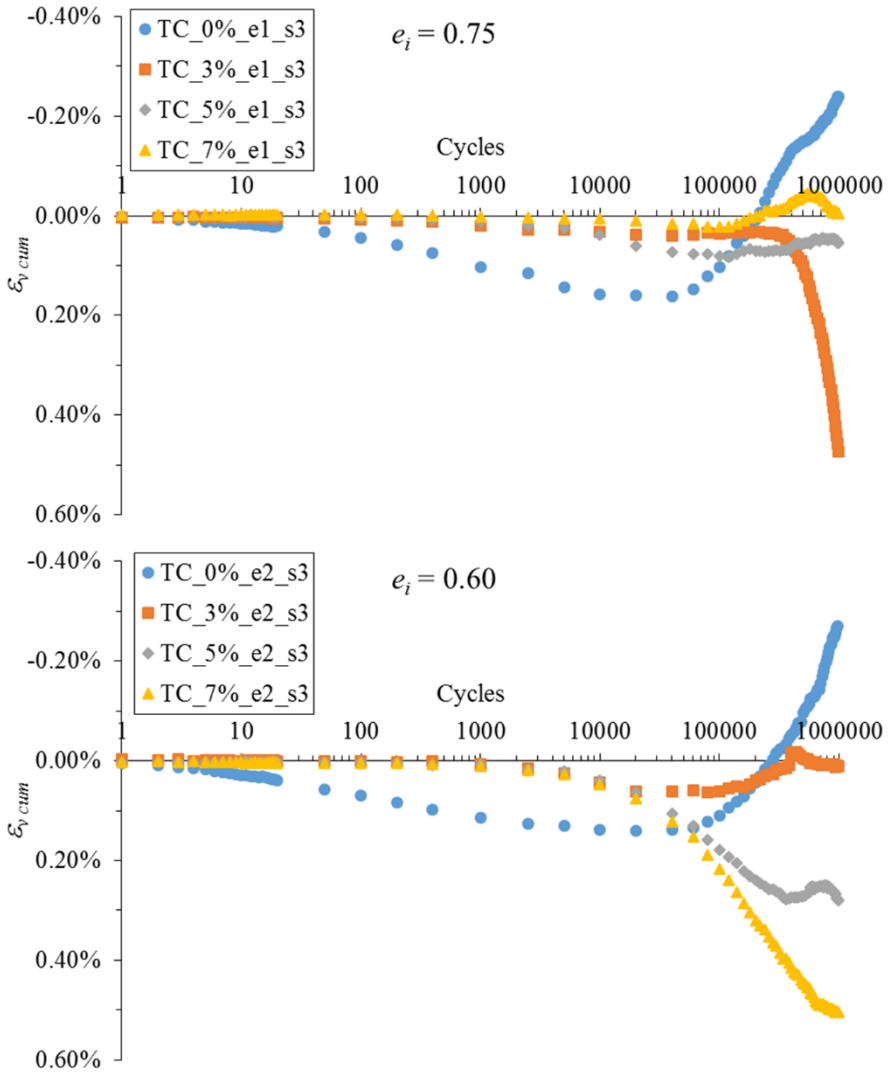

Fig. 5.25 - Accumulated volumetric permanent strain vs. number of cycles (third set of tests)

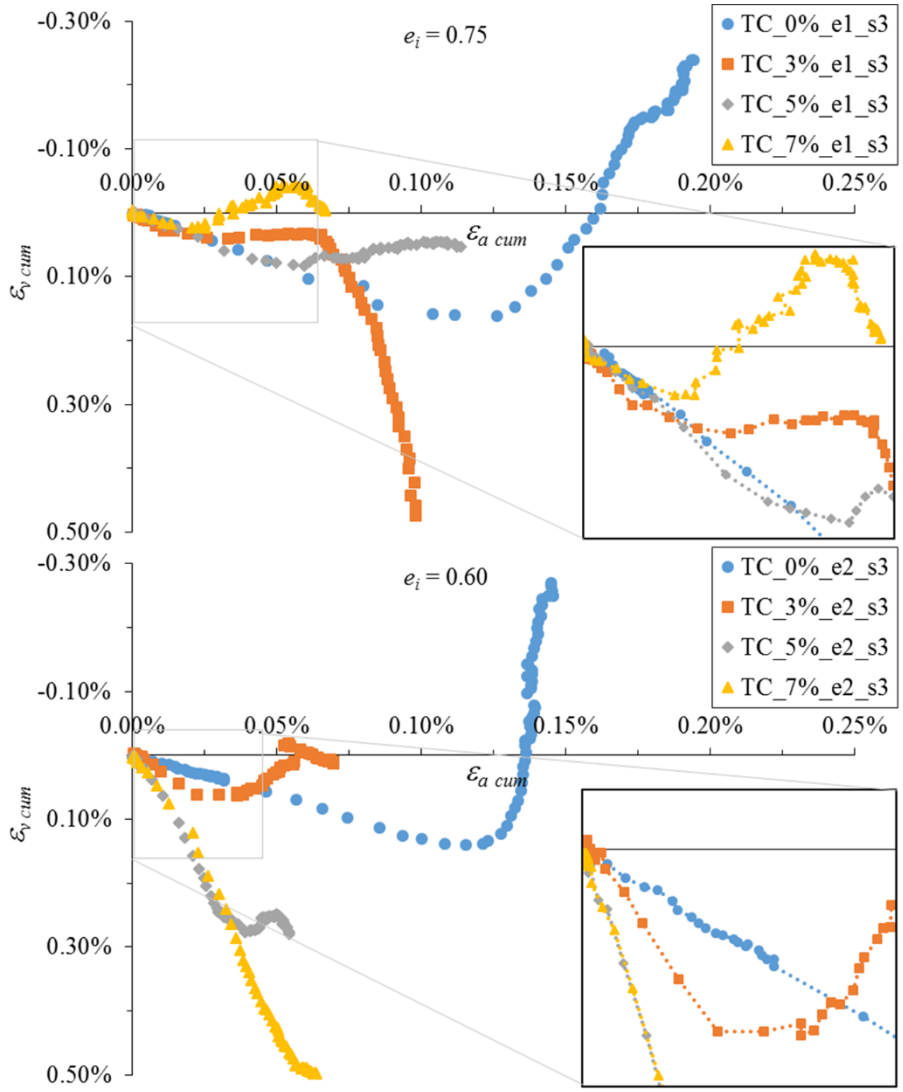

Fig. 5.26 – Accumulated volumetric vs. axial strain (third set of tests)

Two possible reasons for this behaviour can be outlined:

- The chosen effective confining pressure ($\sigma'_c = 0.50\sigma'_p$) is not sufficient for the test to be clearly in the wet side of the critical state;
- It is possible that the unloading part of the cyclic loading behaves differently from the loading part. As seen in Fig. 5.14, cyclic tests show hysteretic loops in the stress plane with a loading and an unloading part. The volumetric strain increment observed during the unloading part of each cycle is negative, thus if this negative increment is greater in absolute value than the positive incremental volumetric strain observed in the loading part of the cycle, the resulting accumulated strain at the end of the cycle is negative.

Nevertheless, for all the tests of the present group, when compared with the corresponding specimens of the precedent sets, a shift towards compression is observed, i.e. the dilatancy (where present) is less marked than in the precedent tests (see examples in Fig. 5.27).

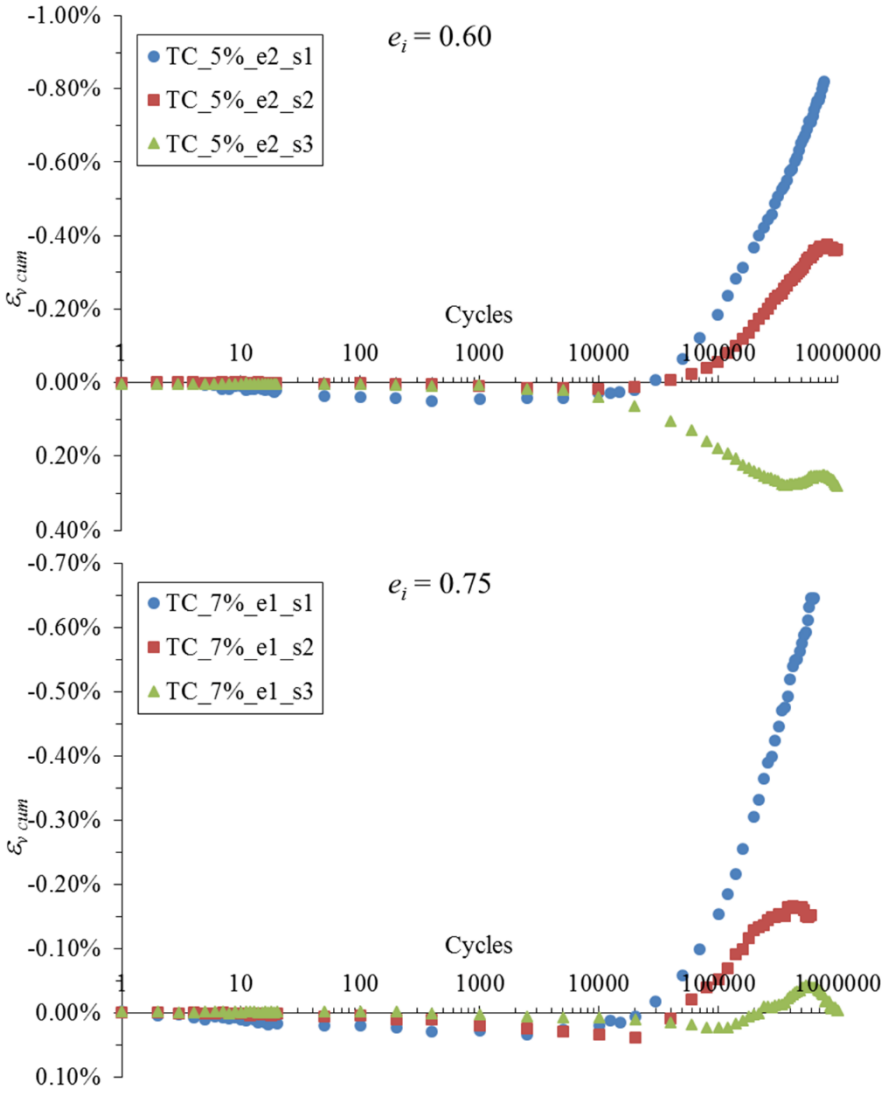

Fig. 5.27 – Example of comparison of the accumulated volumetric strain of identical specimens under the three different loading conditions: 5%_e2 and 7%_e1

The uncemented specimens (Fig. 5.28) confirm this trend. The only exception is test TC_0%_e2_s3, which shows a more dilative behaviour than the less confined specimens do. In this case, it is possible that an error in the measurement of the volumetric strain occurred.

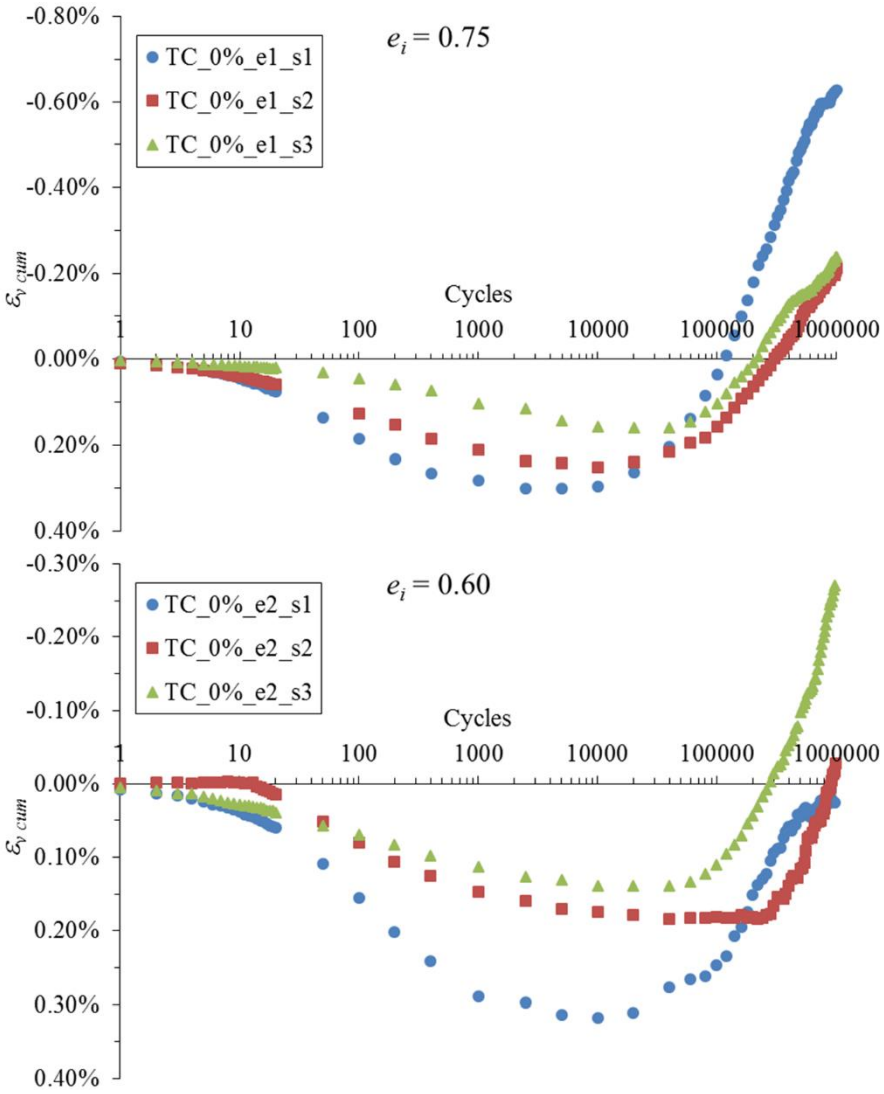

Fig. 5.28 – Comparison of the accumulated volumetric strain of uncemented specimens under the three different loading conditions: specimen 0%_e1 and 0%_e2

5.9. UNDRAINED TESTS

The three undrained tests were performed with an initial effective confinement of 40 kPa, which is equal to the confinement of the first set of drained tests. Thus, the three specimens are expected to follow a dilatant behaviour similar to the less confined drained tests.

The results of this set of tests (Viana da Fonseca et al., 2013a) are reported in Fig. 5.29 and Fig. 5.32.

The accumulation of axial deformation shows also in this case a logarithmic trend with two distinguished rate of accumulations: a first part with lower accumulation and a second part with a higher ratio. The transition between the two trends occurs around 10000 cycles in all the tests.

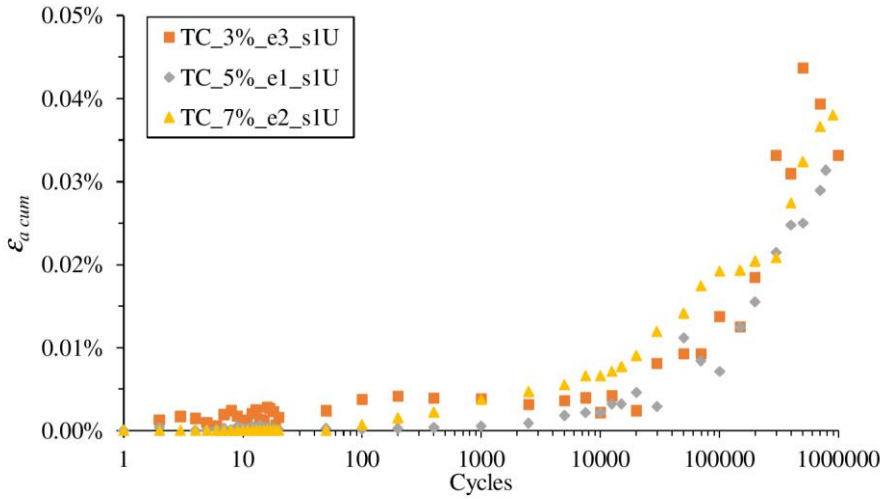

Fig. 5.29 - Accumulated axial permanent strain vs. number of cycles (undrained tests)

It is interesting to compare the undrained tests with the corresponding drained tests. Tests with 5 and 7% of cement content are directly comparable with the corresponding drained tests (belonging to the first set of drained tests). The comparison (Fig. 5.30) shows that the results are nearly coincident in the two cases, suggesting that the accumulation of axial deformation is independent on the drainage conditions.

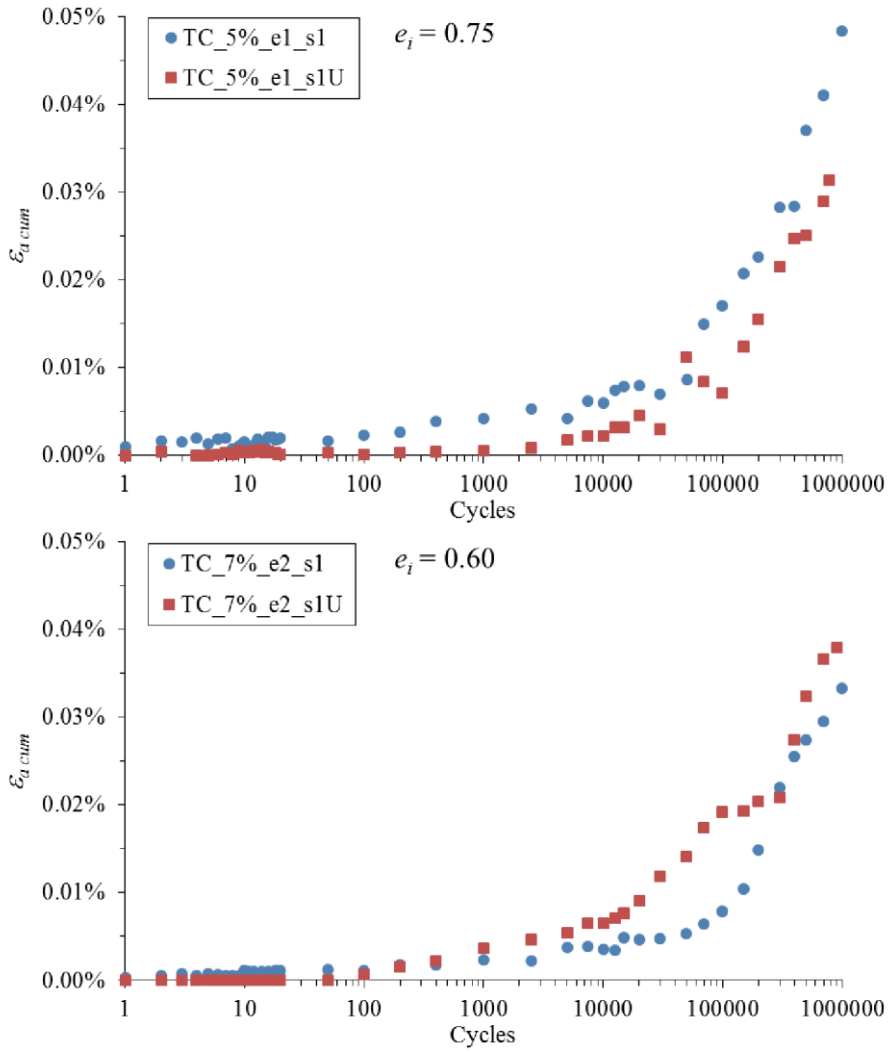

Fig. 5.30 – Comparison between drained and undrained tests performed on equal specimens with same initial effective confining pressure

Test TC_3%_e3_s1U has no direct correspondence with any drained tests, as its initial void ratio (0.65) is intermediate between the two more similar drained tests, TC_3%_e1_s1 and TC_3%_e1_s2 with initial void ratio of 0.75 and 0.60, respectively (see Fig. 5.17). The comparison between the three tests (Fig. 5.31) shows also in this case a correspondence in the accumulation of axial strain, regardless of the drainage condition.

In Fig. 5.32, the variation of pore pressure for the three tests is plotted against the number of cycles. The variation is negative for the three tests, confirming the dilatant tendency of the material in these conditions, as shown in the accumulated volumetric strain of the first set of drained tests.

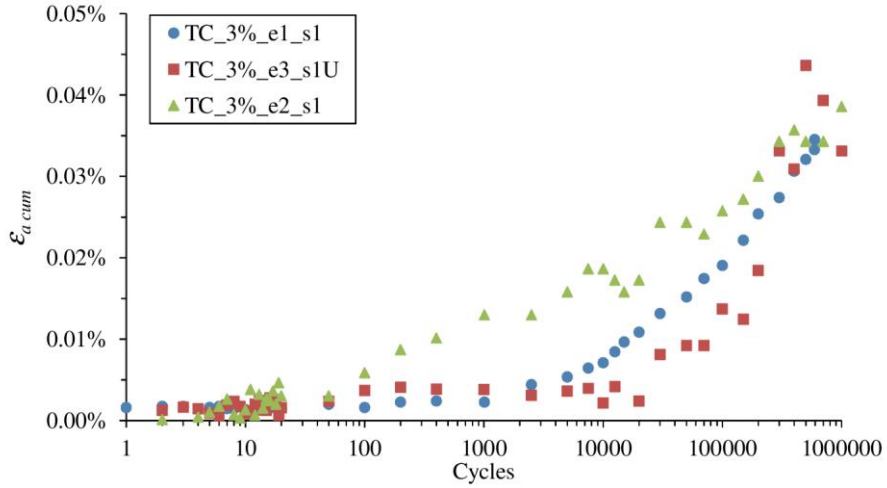

Fig. 5.31 – Comparison between drained and undrained tests performed on specimens with same cement content and initial effective confining pressure

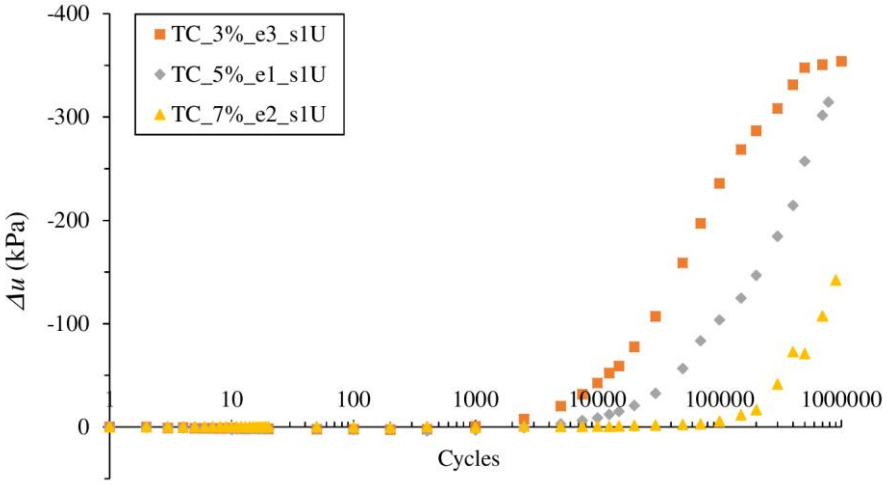

Fig. 5.32 – Pore pressure variation vs. number of cycles (undrained tests)

The role of the structure is very clear in the results. No variation in pore pressure is observed in the first 1000 cycles; then, when the progressive damage in the structure increases the particles rearrange and an increasing variation in pore pressure can be observed. This variation is higher for the less cemented specimens and decreases for more cemented specimens. The variation seems to stabilize for the 3% specimen while it continues with a logarithmic trend for the remaining specimens. The accumulation process starts around 1000 cycles for specimens with 3 and 5% of cement content and around 100000 cycles for the specimen with 7%. It is interesting to note that the value of the adjusted porosity/cement ratio presented in the precedent sections is the same for the first two tests (36) and is inferior (29 – corresponding to an increased level of structure) for the third, more resistant, one. This confirms the suitability of such ratio as an indexing parameter for the cyclic properties of these mixtures.

5.10. CONCLUSIONS

An extensive long-term cyclic triaxial tests programme was conducted over 27 specimens of artificially cemented silty-sand, moulded in distinct state conditions: 9 different moulding points including four different cementation levels (including uncemented specimens) and three different initial void ratios. Three specimens were submitted to undrained tests, while the others were tested drained. For each state condition, three specimens for drained test were moulded in the same conditions and submitted to three different confining pressures, in a total of 24 drained cyclic triaxial tests. All the 27 cyclic triaxial tests reached up to 1 million loading cycles, performed with a constant total confining pressure and with a controlled deviatoric cyclic stress, applied in a sinusoidal form. The applied cyclic stress was selected to guarantee that the tests were performed within the small-strain domain of the material, and at the same relative distance from the corresponding ultimate stress; the three confining pressures of the drained tests were selected in order to study three different zones of the elastic envelope (dilatant, compressive, intermediate). The small values of deviatoric stress ensured that the accumulation of permanent strain was due solely to the fatigue and not to progressive plastic yielding.

The results of the axial strain accumulation in drained conditions show that the accumulation rate decreases with the number of cycles, but does not stabilize despite the great number of loading cycles and the low intensity of deviatoric stress applied. The undrained tests confirmed this tendency.

In all the tests, the trend of accumulation of the axial strain with respect to the number of cycles is logarithmic. An inflection point is observed at a certain number of cycles (different for uncemented and cemented specimens) after which the rate of accumulation – still logarithmic – changes: it becomes higher for the cemented specimens and lower for the uncemented specimens. The final value of the accumulation shows a distinct behaviour between cemented (drained and undrained) and uncemented specimens, with the former group exhibiting a smaller accumulation than the latter. The results relative to axial accumulation evidence the role of cementation: the cemented material becomes stiffer than the uncemented soil (for the same relative distance from the ultimate state) but more brittle due to the progressive degradation of the particle bonds with the accumulation of permanent strain. Drained tests performed with different confining pressures show that an increase of confining pressure, which is associated to a more ductile response in uncemented soils, has a negative effect on cemented soils since it accelerates the destructuration process.

The volumetric strain accumulation shows a more complex behaviour. Many precedent studies published on uncemented and cemented soils under cyclic loading present only the axial strain accumulation, neglecting the volumetric strain accumulation; thus, it is difficult to perform a comparison. The combination of the results of axial and volumetric strain accumulation shows some similarities with the behaviour of a monotonically compressed soil. An initial compression is observed in all the specimens; then, the accumulation trend switches to a dilatant behaviour, which is more evident in less confined specimens (as observed in monotonic tests) and less pronounced in specimens confined at higher stress. In some tests, a double switch is observed, with a double change in the sign of accumulation rate with the number of loading cycles.

Consistently, the undrained, low confined tests show a negative pore pressure variation, which corresponds to a dilatant tendency. The variation trend is similar to the trend observed in the volumetric strain accumulation in drained tests: an initial part with small to nil variation in pore pressure is followed by a sudden increase in negative variation, confirming the increased stiffness and fragility caused by the cementation.

Chapter 6.

DEVELOPMENT OF A NOVEL ELASTO-PLASTIC CONSTITUTIVE MODEL

Kinematic hardening models were developed to add extra features to the framework of the isotropic hardening critical state models, by adding an anisotropic component of hardening. Decoupling isotropic and anisotropic hardening implied the definition of two separate surfaces. One outer surface is defined, also called "bounding" or "consolidation" surface (Mróz et al., 1979), accounting for the degree of consolidation of the soil and reflecting its isotropic behaviour. An internal yield surface delimits the elastic domain; this surface translates in the domain enclosed by the outer surface. Bounding surface plasticity models enhances this two-surface framework with law that links each point on the internal surface with a corresponding point on the outer surface, creating a correspondence between the soil response and the relative position of the surfaces. This framework is very flexible as it incorporates the consolidation history of the soil (or any factor of hardening like structure) and the non-linear behaviour at low stress levels.

In the present chapter, a new constitutive model is proposed based on this framework. The model is first presented in the form for uncemented specimens. Then, a framework for accounting the effect of cementation and the destructuration caused by the accumulation of plastic strain is added. In this way, it is expected that the model will be suitable to model the small-strain cyclic behaviour and the large-strain monotonic behaviour of the studied cemented soil.

6.1. MODEL FOR UNCEMENTED SOILS

6.1.1. YIELD AND REFERENCE SURFACES

The model combines different features of existing models (described in Chapter 3) in a new formulation developed in the framework of bounding plasticity. For the outer reference surface, the expression of CASM model (Yu, 1998) was selected:

$$f_{ref} = \left(\frac{|q|}{Mp'}\right)^{\bar{n}} + \frac{1}{\ln r}\ln\frac{p'}{p'_0} \tag{6.1}$$

Where M is the slope of the critical state line in the stress plane and $\bar{n}$ and r are parameters regulating the shape of the surface.

As in Al Tabbaa & Muir Wood (1989) model, the yield surface has same shape of the reference surface and a smaller size:

$$f = \left(\frac{|q - q_\alpha|}{M(p' - p'_\alpha)}\right)^{\bar{n}} + \frac{1}{\ln r}\ln\frac{p' - p'_\alpha}{Rp'_0} \tag{6.2}$$

This expression represents a kinematic hardening surface of apex $\boldsymbol{\alpha} = (p'_\alpha, q_\alpha)$ and horizontal axis (Rp'_0), as shown in Fig. 6.1. Parameter R represents the ratio of the sizes of the reference and yield surfaces.

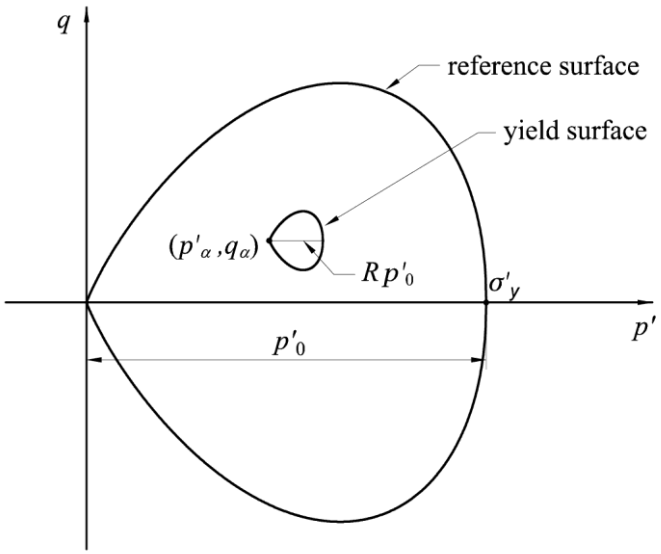

Fig. 6.1 – Yield and reference surface for uncemented conditions in the (*p'*, *q*) plane

6.1.2. HARDENING MODULUS

Consistency condition (Prager, 1955) requires that:

$$df = \frac{\partial f}{\partial p'}\dot{p}' + \frac{\partial f}{\partial q}\dot{q} + \frac{\partial f}{\partial \Lambda}\dot{\Lambda} = 0 \tag{6.3}$$

where $\dot{\Lambda}$ is the plastic multiplier, which is a scalar positive value. From the former expression and knowing that:

$$H = -\frac{\partial f}{\partial \Lambda} \tag{6.4}$$

the value of $\dot{\Lambda}$ is determined as

$$\dot{\Lambda} = \left(\frac{\partial f}{\partial p'}\dot{p}' + \frac{\partial f}{\partial q}\dot{q}\right)/H \tag{6.5}$$

where H is the hardening modulus. The derivative in (6.4) depends on the hardening parameters $(p'_\alpha, q_\alpha, p'_0)$:

$$H = -\frac{\partial f}{\partial \Lambda} = -\left(\frac{\partial f}{\partial p'_0}\frac{\partial p'_0}{\partial \Lambda} + \frac{\partial f}{\partial p'_\alpha}\frac{\partial p'_\alpha}{\partial \Lambda} + \frac{\partial f}{\partial q_\alpha}\frac{\partial q_\alpha}{\partial \Lambda}\right) \tag{6.6}$$

In the above expression, two components can be highlighted: isotropic (H_0) and kinematic (H') hardening moduli, expressed as follows:

$$H_0 = -\frac{\partial f}{\partial p'_0}\frac{\partial p'_0}{\partial \Lambda} \tag{6.7}$$

$$H' = -\left(\frac{\partial f}{\partial p'_\alpha}\frac{\partial p'_\alpha}{\partial \Lambda} + \frac{\partial f}{\partial q_\alpha}\frac{\partial q_\alpha}{\partial \Lambda}\right) \tag{6.8}$$

Maintaining the usual definition adopted in critical state models, isotropic hardening only depends on the incremental volumetric plastic strain, as described by the following expression:

$$\frac{\partial p'_0}{\partial \varepsilon_v^p} = \frac{v_i}{\lambda - \kappa} p'_0 \tag{6.9}$$

Some authors (e.g. Nova & Muir Wood, 1979; Gens & Nova, 1993; Yu, 2006) suggest that the hardening parameter p'_0 can be regarded as a function of both plastic strain components:

$$dp'_0 = \frac{\partial p'_0}{\partial \varepsilon_v^p}\dot{\varepsilon}_v^p + \frac{\partial p'_0}{\partial \varepsilon_s^p}\dot{\varepsilon}_s^p \tag{6.10}$$

This would better represent the observed experimental behaviour that cannot be predicted by a merely volumetric hardening law. For example, in laboratory monotonic tests a change in stress state is often observed after the critical state has been reached. To represent such a behaviour, shear-dependent hardening laws have been proposed. Yu (2006) suggested:

$$dp'_0 = \frac{v_i}{\lambda - \kappa} p'_0\, \dot{\varepsilon}_v^p + \omega \frac{v_i}{\lambda - \kappa} p'_0\, \dot{\varepsilon}_s^p = \frac{v_i}{\lambda - \kappa} p'_0 \left(\dot{\varepsilon}_v^p + \omega\, \dot{\varepsilon}_s^p\right) \tag{6.11}$$

in which the derivatives of p'_0 with respect to the strain increments are identical except for a coefficient ω, which shall be determined experimentally.

The soil studied in the present work did not show shear-dependent behaviour when sheared monotonically up to critical state (Rios et al., 2014). Thus, there is no need to seek for a more sophisticated incremental law for p'_0 and expression (6.9) holds its validity.

Consequently, the expression of the isotropic hardening modulus becomes:

$$H_0 = -\frac{\partial f}{\partial p'_0}\frac{\partial p'_0}{\partial \varepsilon_v^p}\frac{\partial g}{\partial p'} = -\frac{\partial f}{\partial p'_0}\frac{v_i}{\lambda - \kappa}\, p'_0\, \frac{\partial g}{\partial p'} \tag{6.12}$$

where g is the plastic potential function.

Kinematic hardening modulus does not derive from the consistency condition and it is defined according to the experimental behaviour of the soil. The expression adopted is similar to Rouainia & Muir Wood (2001) expression:

$$H' = \frac{v_i}{\lambda - \kappa}\left(B\frac{b}{b_{max}}\right)^{\psi} p_0'^3 \tag{6.13}$$

Conversely to the original formulation, the scaling parameter B is located into parentheses, under the exponent ψ. This difference is due to the different soils studied in the two models. In the present case, the stiff behaviour of the granular soil led to the need of a high value of the hardening modulus. Using the original expression (3.20), very high values of parameter B are necessary for the correct reproduction of the experimental results, leading to numerical problems. Hence, the above modification was implemented, where B can assume lower values, since it is elevated to the exponent ψ, which is usually much greater than the unity.

Distance b is defined as the component of vector $\boldsymbol{\beta}$ in the direction of the normal to the yield surface (Hashiguchi, 1985). Vector $\boldsymbol{\beta}$ joins the current stress point on the yield surface with the corresponding conjugate point on the outer surface. Conjugate points are defined as points with the same direction of

the outward normal. By comparing the expressions of the yield and reference surface [(6.1) and (6.2)] it is:

$$\boldsymbol{\beta} = \begin{pmatrix} \dfrac{p' - p'_\alpha}{R} - p' \\ \dfrac{q - q_\alpha}{R} - q \end{pmatrix} \tag{6.14}$$

Thus, distance b is the result of the scalar product of this vector with the normal vector to the yield surface:

$$\boldsymbol{n_f} = \begin{pmatrix} \dfrac{\partial f}{\partial p'} \\ \dfrac{\partial f}{\partial q} \end{pmatrix} \tag{6.15}$$

normalised by its length, as follows:

$$b = \boldsymbol{\beta} \cdot \frac{\boldsymbol{n_f}}{\|\boldsymbol{n_f}\|} \tag{6.16}$$

The first derivatives of the yield surface are reported in Annex 2.

The maximum distance b_{max} is the maximum value that b can assume. From geometrical considerations, it is clear that this maximum is reached when the two surfaces are at contact at one point and the stress point is located on the opposite side of the yield surface. In particular, one of the two configurations showed in Fig. 6.2.

The maximum distance is one of the two distances shown in figure, depending on the shape parameters of the surface. In particular, if

$$M > \frac{1}{2}\sqrt[n]{\exp(1)\, n \ln(r)} \tag{6.17}$$

maximum distance is the distance measured along the q-axis direction (b_q in figure); otherwise it is the distance along the p'-axis direction, $b_{p'}$ (term $\exp(1)$ indicates the base of the natural logarithm).

Hence, the maximum distance depends on the model parameters that are not known a priori and should be defined as follows:

$$b_{max} = \max(b_q, b_{p'}) = \max\left((1-R)\frac{2Mp'_0}{\sqrt[n]{\exp(1)\, n \ln(r)}}, (1-R)p'_0 \right) \tag{6.18}$$

In both cases, the expression depends linearly on the size of the surfaces (represented by p'_0).

Normalisation of distance b by its maximum value b_{max} is fundamental for a good performance of the model. In fact, if the kinematic hardening modulus were depending only on b, in a case in which the surfaces decreased in size during cyclic loading, b would decrease as well, causing in turn a diminution of modulus H'. Such behaviour corresponds to a softening of the material whenever the stress state is located on the dry side of the surface. The experimental data presented in the earlier chapters show that a hardening of the material is possible also in dense (i.e. low confined) specimens. On the other hand, with the normalisation a more adequate behaviour is reproduced. In fact, when the surfaces shrink, both b and b_{max} decrease. The resulting ratio (b/b_{max}) can increase or decrease depending on how fast the two parcels change. As reported above, b_{max} depends linearly on p'_0. Distance b is the result of a scalar product and thus depends on three factors: 1) magnitude of vector $\boldsymbol{\beta}$ (which in turn depends on p'_0); 2)

magnitude of normalized vector $\boldsymbol{n_f}$, which is equal to the unity by definition; 3) the angle θ_β formed by these two vectors. Distance b will thus increase for increasing magnitude of $\boldsymbol{\beta}$ and/or for decreasing values of angle θ_β. If during the cycling process the surfaces are shrinking and the angle is progressively increasing, distance b (equal to the scalar product of the two vectors) is decreasing to a rate inferior to p'_0, while b_{max} is decreasing proportionally to p'_0. Thus, the ratio b/b_{max} is increasing and, consequently, the hardening modulus increases.

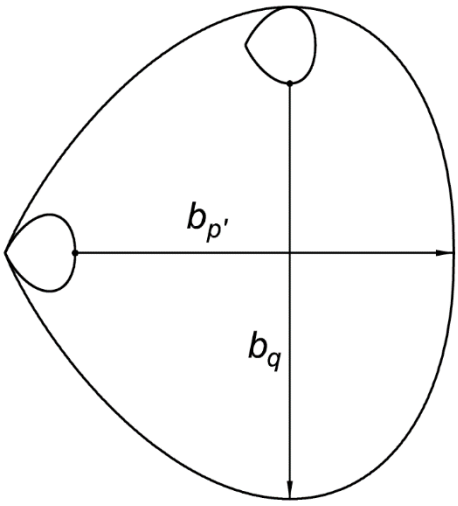

Fig. 6.2 – Possible maximum distances between surfaces

On the other hand, if the surfaces are expanding (p'_0 is increasing) and the angle θ_β is increasing, distance b could be increasing less than b_{max}. In this case, there would be softening (and possibly instability) even with the two surfaces expanding, which is opposite to the experimental evidence. This issue will be further addressed in Chapter 8.

6.1.3. TRANSLATION RULE

Translation rule indicates the direction in which the apex $\boldsymbol{\alpha}$ of the yield surface translates in the stress plane. Translation is always parallel to vector $\boldsymbol{\beta}$, thus the incremental translation vector ($\dot{\boldsymbol{\alpha}}$) is defined as follows:

$$\dot{\boldsymbol{\alpha}} = \begin{pmatrix} \dot{p}'_\alpha \\ \dot{q}_\alpha \end{pmatrix} = S\boldsymbol{\beta} \tag{6.19}$$

where S is a positive scalar regulating the length of the vector. Expression (6.8) can be rewritten as:

$$H'\dot{\Lambda} = -\left(\frac{\partial f}{\partial p'_\alpha}\dot{p}'_\alpha + \frac{\partial f}{\partial q_\alpha}\dot{q}_\alpha\right) \tag{6.20}$$

Replacing equations (6.19) and (6.5) in this expression and rearranging the terms, one can find the value of the scalar S:

$$S = -\frac{\dfrac{\dfrac{\partial f}{\partial p'}\,\dot{p}' + \dfrac{\partial f}{\partial q}\,\dot{q}}{H}\,H'}{\dfrac{\partial f}{\partial p'_\alpha}\left(\dfrac{p'-p'_\alpha}{R} - p'\right) + \dfrac{\partial f}{\partial q_\alpha}\left(\dfrac{q-q_\alpha}{R} - q\right)} = -\frac{\dfrac{\partial f}{\partial p'}\,\dot{p}' + \dfrac{\partial f}{\partial q}\,\dot{q}}{\dfrac{\partial f}{\partial p'_\alpha}\beta_{p'} + \dfrac{\partial f}{\partial q_\alpha}\beta_q}\,\frac{H'}{H} \tag{6.21}$$

Where $\beta_{p'}$ and β_q are the components of vector $\boldsymbol{\beta}$ in the stress plane.

6.1.4. CONSTITUTIVE RELATIONS

The vector of plastic strain increment is calculated from the vector of stress increment through the matrix of plastic compliance $\mathbf{C}^p$, whose elements are calculated as follows:

$$C^P_{rsij} = \frac{1}{H}\frac{\partial g}{\partial \sigma'_{rs}}\frac{\partial f}{\partial \sigma'_{ij}} \tag{6.22}$$

The elastic response is governed by the matrix of elastic compliance $\mathbf{C}^e$. Thus, the complete elasto-plastic constitutive relations become:

$$\begin{pmatrix}\dot{\varepsilon}_v \\ \\ \dot{\varepsilon}_s\end{pmatrix} = (\mathbf{C}^e + \mathbf{C}^p)\,\dot{\boldsymbol{\sigma}}' = \left(\begin{pmatrix}\frac{1}{K'} & 0 \\ 0 & \frac{1}{3G}\end{pmatrix} + \frac{1}{H}\begin{pmatrix}\frac{\partial g}{\partial p'}\frac{\partial f}{\partial p'} & \frac{\partial g}{\partial p'}\frac{\partial f}{\partial q} \\ \\ \frac{\partial g}{\partial q}\frac{\partial f}{\partial p'} & \frac{\partial g}{\partial q}\frac{\partial f}{\partial q}\end{pmatrix}\right)\begin{pmatrix}\dot{p}' \\ \\ \dot{q}\end{pmatrix} \tag{6.23}$$

It is worth noting that in a stress-driven drained axisymmetric loading path, the elastic and plastic parcels of the incremental strain can be separated and computed independently. This is convenient in the numerical implementation of the model since the elastic part of the constitutive equations can be integrated in closed form and thus it can be excluded from the iterative process that is needed for the numerical solution of the plastic equations.

6.1.5. PURELY ELASTIC BEHAVIOUR

As shown in the precedent section, the elastic constitutive relations are expressed as follows:

$$\begin{pmatrix}\dot{\varepsilon}^e_v \\ \\ \dot{\varepsilon}^e_s\end{pmatrix} = \begin{pmatrix}1/K' & 0 \\ 0 & 1/3G\end{pmatrix}\begin{pmatrix}\dot{p}' \\ \\ \dot{q}\end{pmatrix} \tag{6.24}$$

Where K' and G are the bulk and shear modulus, respectively. In the vast majority of the existing constitutive models, bulk modulus K' depends linearly on the mean stress, following the well-known expression derived from the results of an isotropic compression test:

$$K' = \frac{v_i}{k}p' \tag{6.25}$$

As for the shear modulus, two options can be followed. For an isotropic elastic material, four elastic constants can be defined (K', G, E, and ν) of which only two are independent (Zytynski et al., 1978). The first option is to select a constant value of Poisson's ratio, ν; then, the value of G can be deduced from the classic Hook's relations:

$$G = \frac{3(1-2\nu)}{2(1+\nu)}K' = \frac{3(1-2\nu)}{2(1+\nu)}\frac{v_i}{k}p' \tag{6.26}$$

In this formulation, the shear and bulk moduli are dependent on the mean effective stress. This approach leads to two main pitfalls: on one hand, the values of the elastic moduli calculated in this way are normally lower than the values retrieved from laboratory tests. This aspect was confirmed in the present formulation by implementing the model in a numerical formulation (as illustrated in Chapter 7) and using it to reproduce the stress-strain hysteretic behaviour observed in the cyclic triaxial tests. The results of the simulations show that, using the moduli calculated with the precedent relations, the inclination of

the loops is lower than the observed one. Additionally, the values of G calculated using expression (6.26) are much lower than the values derived in UCS tests and monotonic triaxial compression tests.

Moreover, it is demonstrated (Zytynski et al., 1978) that such formulation is not conservative, since energy can be extracted from the system when a closed loading-unloading stress path is considered. Such energy is proportional to the area enclosed in the stress loop. In the tests considered in the present work, this problem does not arise since in all the cyclic triaxial tests performed, the stress point in the $(p' - q)$ plane follows the same path during loading and unloading; thus, the area enclosed in the cyclic stress path is nil and no energy is extracted from the system. In any case, to avoid problems with possible future applications of the model, this approach is discarded.

An alternative approach for the definition of the elastic moduli is to assume that G is constant and derive its value from laboratory tests. The main issue with this approach is that Poisson's ratio is not constant and can assume negative values, which is physically incorrect.

It is worth noting that the usual definitions used for the elastic moduli were derived for one-surface, isotropic-hardening models, which present a large elastic domain. In such models, it is necessary to find a law to model the non-linear behaviour clearly observed inside the large yield locus; for this reason, non-linear relations were derived. In the present model, the yield surface encloses a relatively small area in the stress plane; the region between the yield and reference surfaces, which in classic models is defined as elastic domain, is elasto-plastic in the present two-surface formulation. Thus, the non-linearity formerly modelled as "non-linear elasticity" is here non-linearity due to progressive elasto-plastic yielding. The area enclosed in the kinematic-hardening yield surface can be identified with the area defined as the linear elastic region (Jardine, 1992), or first yield envelope (Malandraki & Toll, 1996). In this small-strain domain, the elastic moduli can be regarded as constant and they can be identified with the moduli for very small strain (K_0', G_0).

Jardine (1995) presented an extensive study on the linear elastic region for various materials and highlighted the importance of dynamic methods (resonant column test or geophysical methods) in the definition of the small-strain moduli. The same author states that the small-strain moduli vary with the stress level at which the soil is subjected. Amaral et al. (2012) presented the results of two isotropic tests performed over specimens of reconstituted uncemented residual Porto silty-sand in a triaxial chamber equipped with bender elements. At each mean stress level, the specimen was allowed to consolidate isotropically; then, the shear wave velocity was measured and the dynamic shear modulus was calculated. Results showed a logarithmic increase of the shear modulus with the increase in p'. In particular, the logarithmic trend is gentle for low stress values and it changes its inclination (to a steeper logarithmic rate) after the mean effective stress exceeds the isotropic yield stress p_0' of the specimen. Thus, for values of p' less than p_0', the value of the shear modulus is almost constant. For this reason, the shear modulus is considered constant inside the bounding surface. If one considers also Poisson's ratio ν constant, the small-strain bulk modulus is in turn a constant value.

For cemented specimens, small-strain moduli (still considered constant) depend on the level of cementation. The values adopted will be determined in Chapter 8.

6.1.6. Plastic potential: Rowe and Yu flow rules

Rowe flow rule (3.31) is still valid but is referred to the apex of the yield surface:

$$\frac{\dot{\varepsilon}_v^p}{\dot{\varepsilon}_s^p} = \frac{9(M - |\eta_\alpha'|)}{9 + 3M - 2M|\eta_\alpha'|}\ \mathrm{sgn}(\eta_\alpha') \tag{6.27}$$

In which η'_α is the effective stress ratio referred to the apex of the bubble:

$$\eta'_\alpha = \frac{q - q_\alpha}{p' - p'_\alpha} \tag{6.28}$$

and sgn( ) indicates the signum function, used to guarantee that the flow rule is symmetrical with respect to the horizontal axis of the yield surface.

In this formulation, the classic Rowe relation applied to a single-surface critical state model (i.e. centred in the origin of the stress plane) is translated to the apex of the bubble, and its formulation referred to the compression semi-plane is mirrored with respect to the horizontal axis of the yield surface (see the corresponding plastic potential surfaces in Fig. 6.3). Muir Wood (1990) suggested that, for a single surface, isotropically hardening framework, the shape of Rowe plastic potential surface in the tensile semi-plane ($q < 0$) is different from the shape in the compression semi-plane ($q > 0$) (i.e. the surface is not symmetric with respect to the p' axis). Hence, one could conclude that expression (6.27) is not correct, because it does not reproduce the same plastic potential surface referred to the origin of the axes in a kinematic hardening framework, but uses only the upper part of that formulation and mirrors it with respect to the horizontal axis of the bubble.

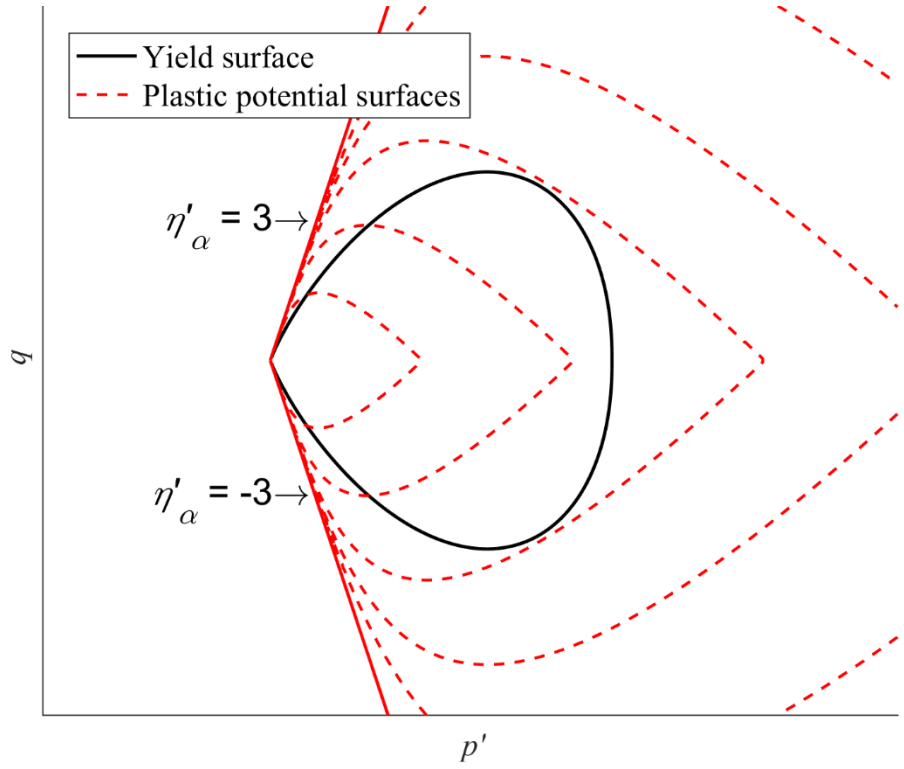

Fig. 6.3 – Rowe flow rule in the stress plane

Nevertheless, the asymmetry of the plastic potential indicated by Muir Wood (1990) is due to the fact that Rowe flow rule formulation is derived from a relation dependent on the ratio of the major over the minor principal stress (Rowe, 1962). In the compression semi-plane, the major principal stress is vertical and the minor is the horizontal (σ'_1/σ'_3), while in the tensile semi-plane the order is inverted. Thus, Rowe's ratio is also inverted (σ'_3/σ'_1) and the resulting formulation in the tensile semi-plane is different from the formulation in the compressive semi-plane.

In the case of a kinematically hardening yield surface translating in the compressive stress semi-plane ($q > 0$), the major principal state is always the vertical (axial) stress, whether the deviatoric stress is

increasing or decreasing (i.e. whether the stress state intersects the yield surface in its upper or lower part). Hence, the formulation of Rowe's ratio remains unchanged in the two cases. Thus, it is correct to use the same shape of the plastic potential derived for compression also in the semi-plane below the horizontal axis of the yield surface (i.e. $q < q_\alpha$) and in the compression semi plane ($q > 0$) simply by mirroring it with respect to the horizontal axis ($q = q_\alpha$) of the yield surface. The correctness of this hypothesis shall be checked by assessing the model performance in reproducing the behaviour of the cyclic tests conducted, in which loading-unloading cycles in the positive semi-plane were imposed to the soil.

Consequently, if the stress is applied in the tensile semi-plane ($q < 0$), Rowe flow rule referred to the kinematic hardening yield surface would have the same expression (with origin translated to the apex of the surface) of Rowe flow rule expression in the tensile plane in the case of isotropic yield surface. This expression would still be symmetric with respect to the horizontal axis of the kinematic yield surface. In the present study, no tests were performed with tensile deviatoric stress. Hence, this expression will not be implemented in the present model. Nevertheless, it can be readily implemented in future developments of the model.

Integrating relation (6.27) (following the procedure reported in Annex 3), the plastic potential function is determined:

$$g = 3M \ln \frac{p' - p'_\alpha}{\xi} + (3 + 2M) \ln(2|\eta'_\alpha| + 3) - (3 - M) \ln(3 - |\eta'_\alpha|) \tag{6.29}$$

whose first derivatives in in p' and q are reported in Annex 2.

As highlighted in Chapter 3, this surface has an angular point at $\eta'_\alpha = 0$, which causes numerical problems in the definition of the outward normal vector in this point.

A similar approach can be applied to Yu (2006) flow rule (equation (3.33)) obtaining:

$$\frac{\dot{\varepsilon}_v^p}{\dot{\varepsilon}_s^p} = \frac{M^{\bar{n}} - {\eta'_\alpha}^{\bar{n}}}{m\, {\eta'_\alpha}^{\bar{n}-1}} \operatorname{sgn}(\eta'_\alpha) \tag{6.30}$$

Integrating this equation (similarly to the one-surface case reported in Annex 3), two possible solutions are found. If parameter $m \neq 1$, it is:

$$g = \ln \frac{p' - p'_\alpha}{\xi} + \frac{m}{\bar{n}(m-1)} \ln \left[1 + (m-1) \left(\frac{|\eta'_\alpha|}{M} \right)^{\bar{n}} \right] \tag{6.31}$$

Otherwise, for $m = 1$:

$$g = \ln \frac{p' - p'_\alpha}{\xi} + \frac{1}{\bar{n}} \left(\frac{|\eta'_\alpha|}{M} \right)^{\bar{n}} \tag{6.32}$$

The same first derivatives of g in p' and q are associated to expressions (6.31) and (6.32) (reported in Annex 2).

It is important to study the domain of existence of both flow rules. In fact, while in the usual one-surface models the conditions of existence are easily satisfied, in the case of a plastic potential associated to a kinematic hardening yield surface the stress point can cross the boundary of the existence domain and reach a non-permitted state.

In the formulation for one surface models, Rowe flow rule is satisfied for $\eta' < 3$ (see Fig. A.4 in Annex 3). For a conventional monotonic triaxial stress path, this condition is always satisfied. In the case of a kinematic hardening yield surface, the condition is:

$$|\eta'_\alpha| < 3 \tag{6.33}$$

This condition in the stress plane is represented by two lines inclined at a slope of 3:1 and passing through the apex of the yield surface (Fig. 6.3). Being referred to the apex of a moving surface, the limit line is possibly crossed (for example during the unloading phase of a drained cyclic triaxial test). For this reason, when the model is implemented in a computer code, the script shall include a check on this condition at each stress increment in the elastoplastic domain.

If Yu flow rule is considered and $m \geq 1$ is adopted, the plastic potential is defined on the entire stress plane (Fig. 6.4). In this case, no checks are required on the existence domain. If $m < 1$, the condition of existence is:

$$|\eta'_\alpha| < M \sqrt[\bar{n}]{\frac{1}{1-m}} \tag{6.34}$$

This condition is represented by two lines passing through the yield surface apex (Fig. 6.5). Again, the condition shall always be checked during the test.

It is important to note that the domain of existence in this case depends on the value of the model parameters. In fact, the slope of the boundary lines decreases for decreasing values of m. Therefore, the domain of the permitted states restrains as this parameter decreases. During model calibration, this issue represents a limitation to the possible values that parameter m can assume.

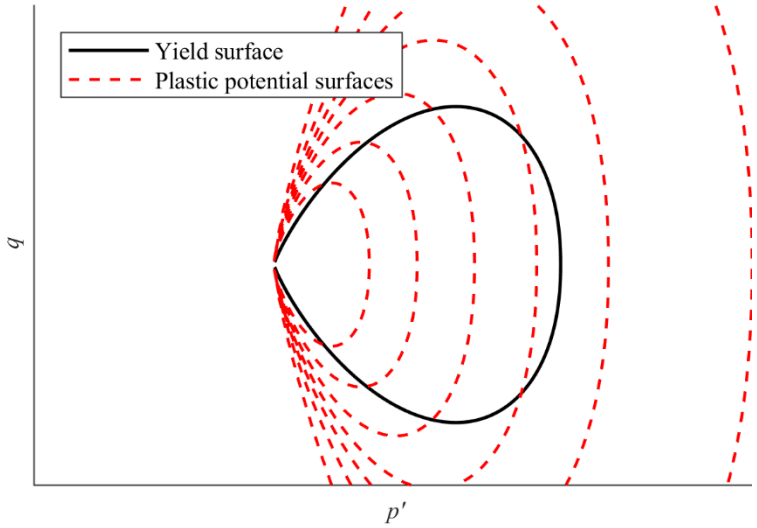

Fig. 6.4 –Yu flow rule with $m \geq 1$

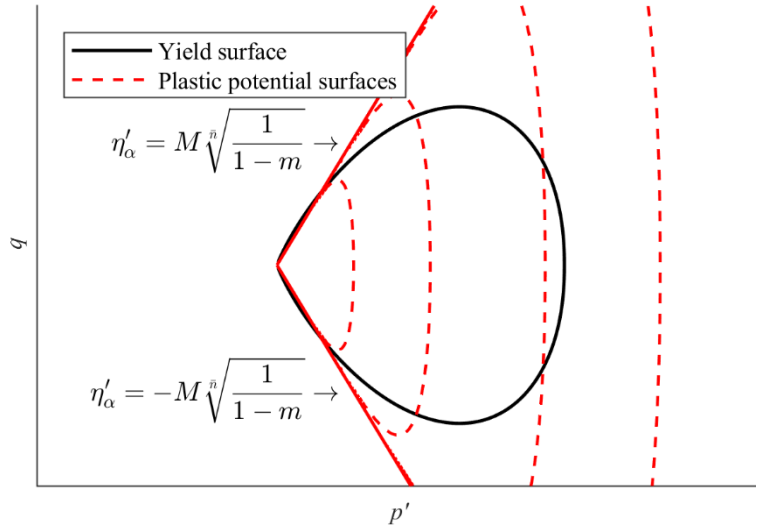

Fig. 6.5 – Domain of existence of Yu flow rule with $m < 1$ in the stress plane

6.2. MODEL FOR CEMENTED SOILS

This model is an expansion of the former one to include tensile resistance and a destructuration law (Panico et al., 2018).

6.2.1. YIELD AND REFERENCE SURFACES

Reference surface is similar to the uncemented model but with a tensile strength p'_t, as shown in Fig. 6.6. Moreover, due to the increasing value of the isotropic yield stress σ'_y , the surface expands also in the positive direction of the p' axis of an additional parcel p'_c. Thus, the new surface is similar to the uncemented case but expanded in both the tension and compression directions, which is expressed in the following equation:

$$f_{ref} = \left(\frac{|q|}{M(p' + p'_t)}\right)^{\bar{n}} + \frac{1}{\ln r}\ln\frac{p' + p'_t}{p'_0} \tag{6.35}$$

The tensile strength p'_t is expressed as a positive value in the above expression.

Horizontal axis p'_0 is dependent not only on the level of cementation but also on the level of compaction of the uncemented soil, i.e. on the horizontal axis of an equally compacted specimen of the same soil in uncemented conditions (hereafter noted as p'_{0unc}). During cyclic loading, the accumulation of plastic strain causes an incremental damage to the bonded structure of the soil; such destructuration of the cement bonds leads to a shrinkage of the surfaces, i.e. the value of p'_0 tends towards that of $p'_{0\mathrm{unc}}$ (which in turn can change due to densification or dilatancy of the granular soil matrix). As the cementitious bonds are progressively destructured during loading, the cemented surface shrinks and tends to coincide with the uncemented surface.

The expression of the yield surface is:

$$f = \left(\frac{|q - q_\alpha|}{M(p' - p'_\alpha)}\right)^{\bar{n}} + \frac{1}{\ln r}\ln\frac{p' - p'_\alpha}{Rp'_0} \tag{6.36}$$

Tensile strength does not appear in this expression because it is implicitly accounted for in the position of the apex and in the increased dimension of the horizontal axis Rp'_0.

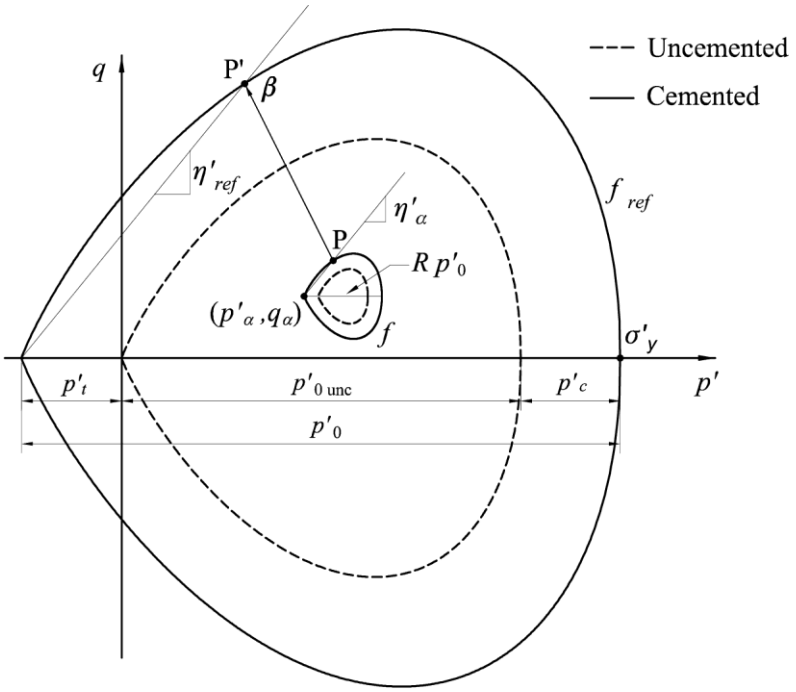

Fig. 6.6 – Yield and reference surface for cemented conditions in the (*p'*, *q*) plane

6.2.2. BONDING AND DAMAGE LAW

In order to define the initial magnitude and the rate of destructuration of the new defined surfaces, a non-dimensional variable $\bar{b}$ shall be introduced, representing the amount of bonding at a certain strain level. Following Gens & Nova (1993) framework, the expression of p'_0 is:

$$p'_0 = p'_{0unc}\left(1 + \bar{b}\right) \tag{6.37}$$

and the tensile strength is:

$$p'_t = \alpha_t\, \bar{b} \tag{6.38}$$

Where α_t is an additional model parameter that can be determined from the initial value of the tensile strength. While p'_0 depends on p'_{0unc}, p'_t is only dependent on the level of bonding. If p'_t were also dependent on p'_{0unc}, a test in which the contribution of soil matrix densification were predominant over a small loss of structure would result in an increase of tensile strength with increasing deformation. With the adopted formulation, the value of p'_t is certainly monotonically decreasing from an initial value and tending towards zero for large deformation.

Bonding variable $\bar{b}$ shall be associated to an initial value b_0 (referred to the undamaged material) and shall be dependent on a damage variable X, which measures the level of destructuration of the soil with the progressive accumulation of plastic strain:

$$\bar{b} = b_0\, e^{-X} \tag{6.39}$$

The degree of bonding is b_0 for $X = 0$ (undamaged state) and decreases monotonically towards zero as the damage variable increases. Parameter b_0 depends on the cement content and soil compaction; it can be determined experimentally from the values of isotropic yield stress derived from isotropic tests

performed on the cemented specimens (Rios et al., 2012). This process will be described in detail in the following sections.

Substituting (6.39) into (6.37) and (6.38), one obtains:

$$p'_0 = p'_{0unc}\,(1 + b_0\, e^{-X}) \tag{6.40}$$

$$p'_t = \alpha_t\, b_0\, e^{-X} \tag{6.41}$$

In the last expression, α_t and b_0 are two constant parameters that can be unified in a single parameter, corresponding to the tensile strength of the undamaged material, p'_{ti}. This modification has the advantage that the initial value of tensile strength is directly related to the results of the unconfined compression tests, as explained in the following sections. Thus, the expression of the tensile strength can be reformulated as follows:

$$p'_t = p'_{ti}\, e^{-X} \tag{6.42}$$

Damage variable X is formulated in order to increase monotonically and linearly with the accumulation of volumetric and deviatoric plastic strain:

$$X = b_1 \int d\left|\varepsilon_v^p\right| + b_2 \int d\left|\varepsilon_s^p\right| \tag{6.43}$$

or, in incremental form:

$$\dot{X} = b_1\left|\dot{\varepsilon}_v^p\right| + b_2\left|\dot{\varepsilon}_s^p\right| \tag{6.44}$$

Where b_1 and b_2 are two adjusting parameters that shall be calibrated from experimental results. In the above expression, the plastic strain increments are in absolute value: in this way, the damage increases with the accumulation of plastic strain whether its sign is positive or negative (in either case the effect is damage level increase).

6.2.3. HARDENING MODULUS

Similarly to the uncemented model, the consistency condition is formulated and the hardening modulus is derived. The hardening parameters are the same as in the uncemented case:

$$f = f(p', q, p'_0, p'_\alpha, q_\alpha) \tag{6.45}$$

In this case, p'_0 depends in turn from the length of the axis of the uncemented surface and from the bonding variables in the following form:

$$p'_0 = p'_0\left(p'_{0unc}(\varepsilon_v^p(\Lambda)), X(\left|\varepsilon_v^p\right|(\Lambda), \left|\varepsilon_s^p\right|(\Lambda))\right) \tag{6.46}$$

while the coordinates of the centre are dependent on the plastic multiplier as in the precedent case:

$$\begin{aligned} p'_\alpha &= p'_\alpha(\Lambda) \\ q_\alpha &= q_\alpha(\Lambda) \end{aligned} \tag{6.47}$$

Substituting expressions (6.46) and (6.47) in (6.45) and deriving with respect to the plastic multiplier, one obtains:

$$\begin{aligned} H = -\frac{\partial f}{\partial \Lambda} = -\frac{\partial f}{\partial p'_0}\left[\frac{\partial p'_0}{\partial p'_{0unc}}\left(\frac{\partial p'_{0unc}}{\partial \varepsilon_v^p}\frac{\partial \varepsilon_v^p}{\partial \Lambda}\right) + \frac{\partial p'_0}{\partial X}\left(\frac{\partial X}{\partial\left|\varepsilon_v^p\right|}\frac{\partial\left|\varepsilon_v^p\right|}{\partial \Lambda} + \frac{\partial X}{\partial\left|\varepsilon_s^p\right|}\frac{\partial\left|\varepsilon_s^p\right|}{\partial \Lambda}\right)\right] - \\ - \left(\frac{\partial f}{\partial p'_\alpha}\frac{\partial p'_\alpha}{\partial \Lambda} + \frac{\partial f}{\partial q_\alpha}\frac{\partial q_\alpha}{\partial \Lambda}\right) \end{aligned} \tag{6.48}$$

In this expression, three terms can be highlighted: an isotropic (H_0) and a kinematic (H') term, as in the former case, and a bonding hardening modulus (H_b), which is always negative and which is associated to the loss of structure of the soil. Remembering that, in the framework of elastoplasticity, is:

$$\frac{\partial \boldsymbol{\varepsilon}^p}{\partial \Lambda} = \frac{\partial g}{\partial \boldsymbol{\sigma}'} \tag{6.49}$$

the three aforementioned terms can be expressed as:

$$H_0 = -\frac{\partial f}{\partial p_0'}\frac{\partial p_0'}{\partial p_{0unc}'}\frac{\partial p_{0unc}'}{\partial \varepsilon_v^p}\frac{\partial g}{\partial p'} \tag{6.50}$$

$$H' = \frac{v_i}{\lambda - \kappa}\left(B\frac{b}{b_{max}}\right)^{\psi} p_0'^3 \tag{6.51}$$

$$H_b = -\frac{\partial f}{\partial p_0'}\frac{\partial p_0'}{\partial X}\left(\frac{\partial X}{\partial\left|\varepsilon_v^p\right|}\left|\frac{\partial g}{\partial p'}\right| + \frac{\partial X}{\partial\left|\varepsilon_s^p\right|}\left|\frac{\partial g}{\partial q}\right|\right) \tag{6.52}$$

The kinematic hardening modulus is identical to the uncemented case. The derivatives are calculated as follows:

$$\frac{\partial f}{\partial p_0'} = -\frac{1}{p_0'\ln(r)} \tag{6.53}$$

$$\frac{\partial p_0'}{\partial p_{0unc}'} = 1 + b_0\, e^{-X} = \frac{p_0'}{p_{0unc}'} \tag{6.54}$$

$$\frac{\partial p_{0unc}'}{\partial \varepsilon_v^p} = \frac{v_i}{\lambda - \kappa} p_{0unc}' \tag{6.55}$$

$$\frac{\partial p_0'}{\partial X} = -p_{0unc}'\, b_0\, e^{-X} \tag{6.56}$$

$$\frac{\partial X}{\partial\left|\varepsilon_v^p\right|} = b_1 \tag{6.57}$$

$$\frac{\partial X}{\partial\left|\varepsilon_s^p\right|} = b_2 \tag{6.58}$$

The derivatives of the yield function and plastic potential with respect to the stress variables are the same of the uncemented case and reported in Annex 2. The expressions for the isotropic and bonding hardening moduli can be rewritten as follows:

$$H_0 = \frac{1}{\ln(r)}\frac{v_i}{\lambda - \kappa}\frac{\partial g}{\partial p'} \tag{6.59}$$

$$H_b = \frac{\partial f}{\partial p_0'} p_{0unc}'\, b_0\, e^{-X}\left(b_1\left|\frac{\partial g}{\partial p'}\right| + b_2\left|\frac{\partial g}{\partial q}\right|\right) \tag{6.60}$$

Tensile strength p_t' does not appear in the definition of the hardening moduli, but it is present in the expression of vector $\boldsymbol{\beta}$:

$$\boldsymbol{\beta} = \begin{pmatrix} \dfrac{p' - p_\alpha'}{R} - (p' + p_t') \\ \\ \dfrac{q - q_\alpha}{R} - q \end{pmatrix} \tag{6.61}$$

and, consequently, in the definition of scalar S:

$$S = -\frac{\frac{\frac{\partial f}{\partial p'}\dot{p}' + \frac{\partial f}{\partial q}\dot{q}}{H}H'}{\frac{\partial f}{\partial p'_\alpha}\left(\frac{p'-p'_\alpha}{R} - (p'+p'_t)\right) + \frac{\partial f}{\partial q_\alpha}\left(\frac{q-q_\alpha}{R} - q\right)} \tag{6.62}$$

All the remaining definition referred to translation rule, constitutive equations, and plastic potential remain the same described in paragraphs 6.1.3 to 6.1.6.

It is clear that, by selecting:

$$b_0 = 0 \tag{6.63}$$

$$p'_{ti} = 0 \tag{6.64}$$

the model for cemented soils reduces to the model for uncemented soils described in section 6.1. This is coherent with the hierarchical approach (Desai et al., 1986) described in Chapter 2, which prescribes to preserve the original formulation of a model when additional features are added.

6.2.4. PLASTIC POTENTIAL

As referred by Yu et al. (2007b), the presence of bonding tends to generate a cohesion c in the soil, intended in the broad sense of tensile strength. While this tensile strength (as a cohesion intercept) causes the increase of the size of the yield surface, it also inhibits the dilation of soil. In terms of energy, this occurs because the total work done by the stress at the boundary of an element is partly dissipated in friction and partly in disrupting the structure of the soil, which in this case is mainly due to the interparticular bonding (Cuccovillo & Coop, 1999). Hence, stress-dilatancy relationship is dependent on c, as shown in Fig. 6.7. For increasing values of c, the stress-dilatancy graph shifts towards reduced values of dilatancy for a given stress ratio. Conversely, for increasing values of mean effective stress, the dilatancy increases for a given stress ratio. Thus, the two terms are concurrent, as c tends to reduce or prevent dilatancy, while p' tends to enhance its effect.

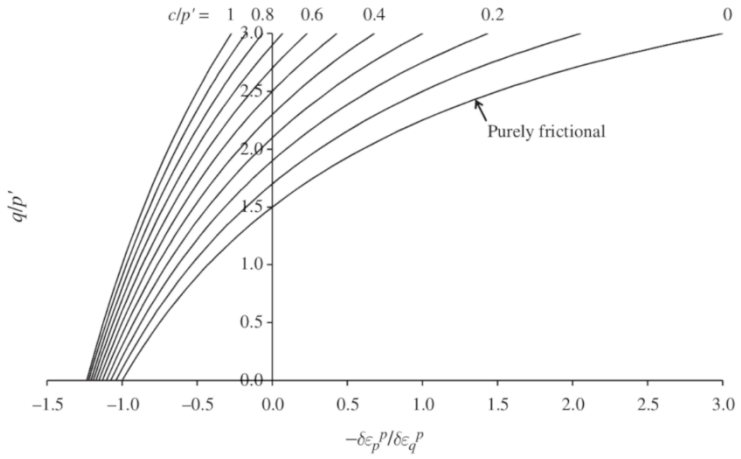

Fig. 6.7 – Effect of adding the cohesion component to the stress—dilatancy relationship (Yu et al., 2007b)

Basing on these assumptions, Yu et al. (2007b) reformulate Rowe's dilatancy rule including term c. The authors showed that this parameter, being equal to twice the intercept of the yield surface with the q-axis, is directly related to tensile strength p'_t. In a single-surface model, this implies that the origin of

Rowe plastic potential surface is shifted horizontally to converge with the apex of the yield surface of coordinates $(0, -p'_t)$. Equation (3.31) becomes:

$$\frac{\dot{\varepsilon}_v^p}{\dot{\varepsilon}_s^p} = \frac{9(M - \eta^{*\prime})}{9 + 3M - 2M\eta^{*\prime}} \tag{6.65}$$

Where $\eta^{*\prime} = q/(p' + p'_t)$ is the effective stress ratio referred to the apex of the large isotropic yield surface.

This formulation is readily adaptable to the present two-surface model simply considering that the yield surface of the one surface models corresponds to the reference surface of the bounding plasticity framework. Flow rule is still centred in the apex of the kinematic yield surface since the apex of the yield surface is conjugate with the apex of the reference surface, which incorporates tensile strength. Thus, the expression does not suffer modifications from the formulation for uncemented soils (6.27).

For the same reasons, the formulation of Yu flow rule is the same of the uncemented conditions (expression (6.30)).

6.3. MODEL PARAMETERS

The required parameters can be grouped in four categories:

- basic CASM parameters, typical of critical state models (e.g. elastic law, critical state parameters);
- advanced CASM parameters, controlling the shape of the yield surface;
- kinematic hardening parameters, defining the size of the yield surface and the kinematic hardening modulus;
- bond damage parameters, controlling the rate of bonding damage with strain.

The four categories are grouped in Table 6.1.

Additionally, the initial values of five state variables shall be set, corresponding to the initial size of the uncemented reference surface, p'_{0unc_i}, the initial amount of bonding, b_0 and p'_{ti} , and the initial position of the yield surface, $p'_{\alpha i}$ and $q_{\alpha i}$.

Different strategies for calibration may be adopted. Following the work of Rios et al. (2016), a staged approach is pursued:

1. Definition of a procedure for initialization of the CASM state variable (p'_{0unc_i});
2. calibration of the basic CASM parameters for the uncemented (reference) material;
3. calibration of the advanced CASM parameters for the uncemented material;
4. definition of a criterion for the initial position of the yield surface;
5. calibration of the kinematic hardening parameters;
6. definition of a procedure for initialization of the bonding state variables, b_0 and p'_{ti}, for cemented materials;
7. calibration of the parameters regulating bond damage.

This procedure is applied in order to keep separate different tasks that may require each a different amount and type of data. The calibration procedure is illustrated in Chapter 8.

Table 6.1 - Model parameters

Basic CASM parameters	
K_0'	small-strain bulk modulus
ν	Poisson's ratio
κ	slope of an unloading-reloading line in the $(\ln p', v)$ plane
N	specific volume of the NCL at $p' = 1\text{kPa}$
λ	slope of the NCL and CSL in the $(\ln p', v)$ plane
M	slope of the critical state line in the stress plane
Advanced CASM parameters	
$\bar{n}$	yield surface shape parameter (stress-state coefficient)
r	yield surface shape parameter (spacing ratio)
Kinematic hardening parameters	
R	surfaces size ratio
B	interpolating parameter for the kinematic hardening modulus
ψ	interpolating parameter for the kinematic hardening modulus
Bond damage parameters	
b_1	parameter regulating the amount of bond damage with volumetric strain
b_2	parameter regulating the amount of bond damage with distortional strain

6.4. TRANSLATION OF THE YIELD SURFACE

In this paragraph, some important features of the translation of the yield surface during the application of a loading path are reported. These characteristics must be acknowledged because they will be used in the subsequent paragraphs, where simplified conditions are sought for the analytical study of the model behaviour. For simplicity, the case in which the stress path is linear in the stress plane is considered. When a loading path is applied, yield surface is dragged along with the stress state whenever yielding occurs. Regardless the initial relative position between the surface apex and the stress point, it was observed that the yield surface tends to shift during the load application, so that vector $\boldsymbol{\beta}$ (joining yield point and its conjugate point on the reference surface) becomes parallel to the stress increment $\dot{\boldsymbol{\sigma}}'$. This means that, if the surface is initially in a position for which $\boldsymbol{\beta}$ is not parallel to $\dot{\boldsymbol{\sigma}}'$, after a conveniently long stress path, the surface tends to occupy a relative position that makes vector $\boldsymbol{\beta}$ parallel to the stress increment. This implies that the point at which the stress path intersects the yield surface changes accordingly to fulfil this condition.

As shown in Fig. 6.8, if one indicates with Y the yield point and with U the conjugate point on the reference surface, the yield surface will tend to occupy a position that satisfies the following:

$$\dot{\boldsymbol{\alpha}} \cdot \dot{\boldsymbol{\sigma}}' = 0 \tag{6.66}$$

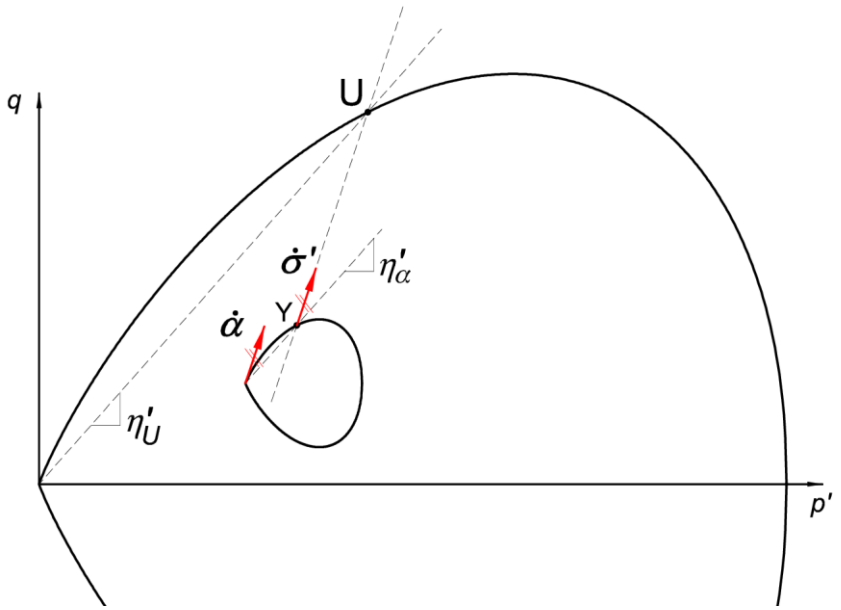

Fig. 6.8 – Configuration with translation vector parallel to stress increment vector

In this condition, one can see that vector $\boldsymbol{\beta}$, joining points Y and U, is parallel to vector $\dot{\boldsymbol{\sigma}}'$ which, in turn, is parallel to the translation vector $\dot{\boldsymbol{\alpha}}$. If condition (6.66) is not satisfied, the relative position of the yield surface with respect to the stress point changes and point Y changes accordingly. One can note that, in such conditions, point U is the intersection between the reference surface and the extension of the stress increment vector. To determine the initial position of the bubble that satisfied condition (6.66), one can determine point U as the extension of the stress path on the reference surface, calculate η'_U, and calculate the initial coordinates of the apex that gives:

$$\eta'_\alpha = \eta'_U \tag{6.67}$$

In a cyclic test with linear stress path, it is geometrically observed that, if condition (6.66) is respected during loading, it is respected also during the unloading phase.

6.4.1. TRANSLATION OF THE YIELD SURFACE IN THE CASE OF PURELY KINEMATIC HARDENING

The reason of this behaviour is easily understandable in the hypothesis that kinematic hardening modulus is the only non-nil term of the hardening modulus (i.e. $H_0 = H_b = 0$). In this case, equation (6.62) becomes:

$$S = -\frac{\frac{\partial f}{\partial p'}\,\dot{p}' + \frac{\partial f}{\partial q}\,\dot{q}}{\frac{\partial f}{\partial p'_\alpha}\,\beta_{p'} + \frac{\partial f}{\partial q_\alpha}\,\beta_q} \tag{6.68}$$

where $\beta_{p'}$ and β_q are the components of vector $\boldsymbol{\beta}$. For the selected yield surface it is:

$$\begin{aligned} \frac{\partial f}{\partial p'_\alpha} &= -\frac{\partial f}{\partial p'} \\ \frac{\partial f}{\partial q_\alpha} &= -\frac{\partial f}{\partial q} \end{aligned} \tag{6.69}$$

Thus, the precedent relation becomes:

$$S = \frac{\frac{\partial f}{\partial p'}\,\dot{p}' + \frac{\partial f}{\partial q}\,\dot{q}}{\frac{\partial f}{\partial p'}\beta_{p'} + \frac{\partial f}{\partial q}\,\beta_q} = \frac{\frac{\partial f}{\partial p'} + \frac{\partial f}{\partial q}\,\frac{\dot{q}}{\dot{p}'}}{\frac{\partial f}{\partial p'} + \frac{\partial f}{\partial q}\,\frac{\beta_q}{\beta_{p'}}}\,\frac{\dot{p}'}{\beta_{p'}} \tag{6.70}$$

Replacing *S* in the first of the (6.19) one obtains:

$$\dot{p}'_\alpha = \frac{\frac{\partial f}{\partial p'} + \frac{\partial f}{\partial q}\,\frac{\dot{q}}{\dot{p}'}}{\frac{\partial f}{\partial p'} + \frac{\partial f}{\partial q}\,\frac{\beta_q}{\beta_{p'}}}\,\dot{p}' \tag{6.71}$$

with a similar process and using the second of the (6.19), one obtains:

$$\dot{q}_\alpha = \frac{\frac{\partial f}{\partial p'}\,\frac{\dot{p}'}{\dot{q}} + \frac{\partial f}{\partial q}}{\frac{\partial f}{\partial p'}\,\frac{\beta_{p'}}{\beta_q} + \frac{\partial f}{\partial q}}\,\dot{q} \tag{6.72}$$

In the case in which:

$$\frac{\dot{q}}{\dot{p}'} = \frac{\beta_q}{\beta_{p'}} \tag{6.73}$$

one obtains:

$$\begin{aligned} \dot{p}'_\alpha &= \dot{p}' \\ \dot{q}_\alpha &= \dot{q} \end{aligned} \tag{6.74}$$

That is, if vector $\boldsymbol{\beta}$ is parallel to $\dot{\boldsymbol{\sigma}}'$ (condition (6.73)), the translation vector $\dot{\boldsymbol{\alpha}}$ is equal in direction and length to $\dot{\boldsymbol{\sigma}}'$ (i.e. the incremental displacement vector is parallel to the incremental stress vector). In these conditions and with a linear stress path (such as a drained triaxial stress path), the displacement of the bubble is a straight line and its length is equal to the length of the elasto-plastic (post-yield) part of the stress path. The effective stress ratio relative to the apex of the yield surface (η'_α) remains constant during the loading process; thus, the derivatives of yield and plastic potential functions ($\partial f/\partial \boldsymbol{\sigma}'$ and $\partial g/\partial \boldsymbol{\sigma}'$, which only depend on η'_α - see Annex 2) are in turn constant, making the integration of the constitutive relations easier. It is also important to note that for cyclic loading, the translation path of the yield surface is the same for each loading-unloading cycle; hence, the accumulation of plastic strain is linear with the number of cycles.

If vector $\boldsymbol{\beta}$ is not parallel to the stress increment, e.g. $\dot{q}/\dot{p}' < \beta_q/\beta_{p'}$, the situation showed in Fig. 6.9 occurs.

Vector $\boldsymbol{\beta}$ can be decomposed in the normal and parallel components to the stress increment ($\boldsymbol{\beta}_{norm}$ and $\boldsymbol{\beta}_{par}$, respectively). During loading, the normal component causes the bubble to shift in a position with a lower value of η'_α, causing a rotation of vector $\boldsymbol{\beta}$ towards the direction of $\dot{\boldsymbol{\sigma}}'$. In the case in which $\dot{q}/\dot{p}' > \beta_q/\beta_{p'}$, the translation would cause ratio η'_α to increase, and vector $\boldsymbol{\beta}$ would rotate towards the direction of $\dot{\boldsymbol{\sigma}}'$ as well. In both cases, the normal component $\boldsymbol{\beta}_{norm}$ would progressively reduce and $\boldsymbol{\beta}$ would tend to coincide with $\boldsymbol{\beta}_{par}$.

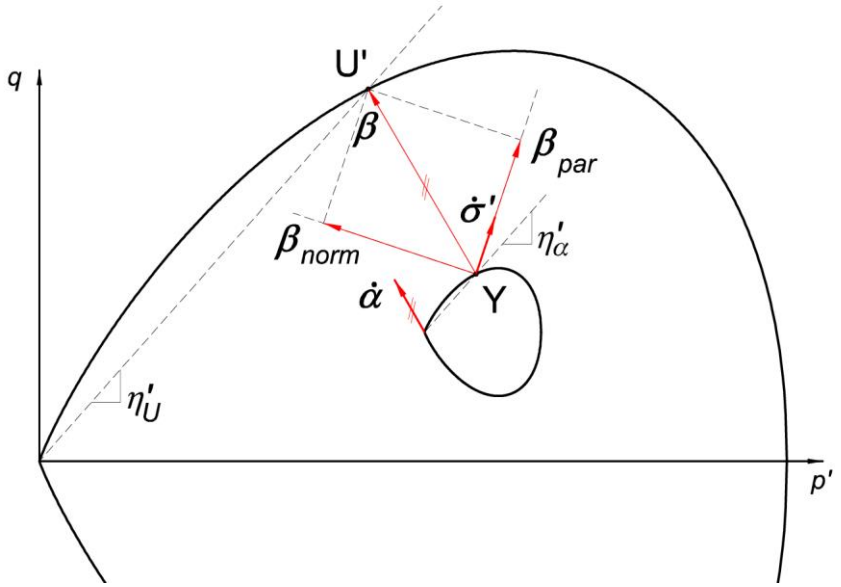

Fig. 6.9 – Displacement of the yield surface when vectors are not parallel

6.4.2. TRANSLATION OF THE YIELD SURFACE WITH ISOTROPIC HARDENING

In the case of $H_0 \neq 0$ and $H_b = 0$, the above considerations are still valid with some modifications.

Relation (6.70) becomes:

$$S = \alpha_H \frac{\frac{\partial f}{\partial p'} + \frac{\partial f}{\partial q}\frac{\dot{q}}{\dot{p}'}}{\frac{\partial f}{\partial p'} + \frac{\partial f}{\partial q}\frac{\beta_q}{\beta_{p'}}} \frac{\dot{p}'}{\beta_{p'}} \tag{6.75}$$

where

$$\alpha_H = \frac{H'}{H' + H_0} \tag{6.76}$$

This ratio is equal to 1 if isotropic hardening modulus is nil, greater than 1 for negative values of isotropic modulus H_0 (i.e. the stress point intersects the yield surface at a stress ratio $|\eta'_\alpha| > M$, where dilatancy is expected), and less than 1 for positive values of H_0 ($|\eta'_\alpha| < M$, compressive behaviour). When stress increment and vector $\boldsymbol{\beta}$ are parallel, it is:

$$\begin{pmatrix} \dot{p}'_\alpha \\ \dot{q}_\alpha \end{pmatrix} = \alpha_H \begin{pmatrix} \dot{p}' \\ \dot{q} \end{pmatrix} \tag{6.77}$$

Translation vector is still parallel to the stress increment, but its length is greater or less accordingly to the value of α_H (thus, depending on whether dilatant or compressive side of yield surface is intersected). The difference in length of the two vectors causes the yield surface (and consequently the reference surface) to shrink or expand accordingly to the sign of the isotropic hardening modulus. Ratio α_H only influences the length of the translation vector but not its direction. The behaviour observed in the precedent section is still valid: if condition (6.66) is met, the displacement of the apex is parallel to the stress path. If the initial position does not respect the condition, the yield surface will shift towards a condition of parallelism between $\boldsymbol{\beta}$ and $\dot{\boldsymbol{\sigma}}'$, accordingly to the scheme of Fig. 6.9. In this case, if a cyclic triaxial stress path is applied, the accumulation of plastic strain does not increase linearly with the

number of cycles, because the length of the elasto-plastic part of the stress path changes with the number of cycles.

Finally, if no components of the hardening modulus are nil, ratio α_H becomes:

$$\alpha_H = \frac{H'}{H' + H_0 + H_b} \tag{6.78}$$

As H_b is always negative, in this case α_H will be less than one at $|\eta'_\alpha| = M$ (where $H_0 = 0$). The ratio will be equal to 1 in a position where $H_0 = -H_b$, thus in a point where $|\eta'_\alpha| < M$, and H_0 is positive. In a domain where $H_0 > H_b$, α_H is greater than one and the surface expands. The same behaviour of the precedent case is still valid with this minor modification. In Chapter 8, the present considerations are validated by simulated tests performed with a numerical implementation of the model.

6.5. ANALYTICAL SOLUTIONS FOR SIMPLIFIED HYPOTHESES

In order to validate the model and to have a better understanding of its features, some simplified cases have been studied and analytically solved. For sake of simplicity, all the cases are applied to the model for uncemented soils.

Three stress paths were studied in the hypothesis that the isotropic hardening is nil. This assumption implies that the surfaces do not change in size, simplifying the integration of the constitutive relations. If the size of the surfaces is constant, equation (6.9) loses its significance. Thus, as no hardening rule is defined, it is impossible to derive the plastic multiplier and hence the constitutive relations. Nevertheless, the present simplified hypotheses are only aimed at testing in a simple way the validity of the model implementation. Thus, it is assumed that the constitutive relations still hold and the value $H_0 = 0$ is simply replaced in them. For the reasons explained, this leads to the incoherent result of having constant size of the surfaces with development of volumetric plastic strain. Nevertheless, this process allows the comparison between the results of the analytical solutions, and the outcome of the numerical implementation, obtaining a partial validation of the latter. A monotonic isotropic stress path, a constant p' cyclic stress path, and a drained triaxial cyclic stress path were studied.

Finally, a monotonic stress path with constant effective stress ratio ($\eta' = \bar{\eta}'$ = constant) was studied in the case of kinematic and isotropic hardening. As shown in the subsequent sections, the particular case of constant effective stress path allows for simplifications in the calculation process. Although a complete analytical solution could not be found, some partial results were found and compared with the numerical results.

6.5.1. SOLUTIONS FOR PURELY KINEMATIC HARDENING

The studied stress paths refer to an isotropic monotonic stress path, a constant p' cyclic stress path, and a drained cyclic triaxial stress path.

As said, two simplified hypotheses were applied to the resolution of these cases. The isotropic hardening modulus (H_0) is set to be nil: this implies that only the kinematic modulus (H') acts, leading to a simple translation of the yield surface without change in size. Bearing in mind the considerations of the precedent paragraph, the initial position of the yield surface was selected so that the yielding point Y on the yield surface is the conjugate of point U on the reference surface (see the scheme in Fig. 6.8). Point U is the intersection point between the extension of the stress path (which is linear in the three cases) and the reference surface. In the single surface framework (e.g. CASM model), point U would ideally

be the yielding point of a test executed with same stress path and in conditions of monotonic compressive loading.

According to the behaviour described in the precedent section, in these conditions the relative position of the yielding point Y with respect to the apex of the surface is constant while the yield surface translates along with the stress point. This is because the surfaces do not change in size and the translation of the yield surface is parallel to the stress path. In the case of cyclic loading, upon stress reversal a new yielding point is individuated in the lower part of the yield surface, which remains also constant during unloading (as will explained in detail in the subsequent sections). The model response is the same in each loading-unloading cycle, leading to a linear accumulation of plastic strain.

These simplified conditions make the integration of the governing equations straightforward. The analyses are presented in the subsequent sections and detailed in Annex 4.

6.5.1.1. ISOTROPIC MONOTONIC LOADING

In this case, the initial positions of the surfaces and the stress increment are shown in Fig. 6.10. An associative flow rule has been considered, even though the implementation of Yu flow rule would have been equally possible. Rowe flow rule is not recommended in this case as it presents a singularity point in the isotropic compression plane (as explained in 6.1.6.).

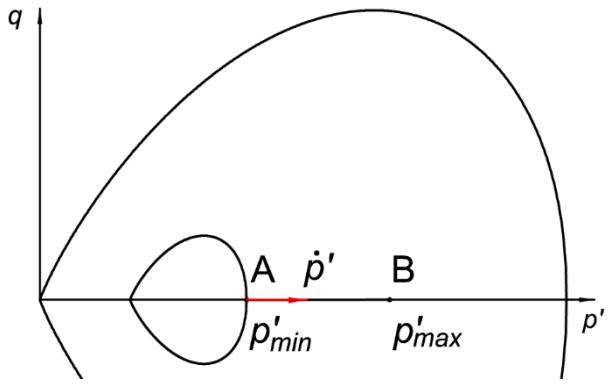

Fig. 6.10 – Loading during isotropic compression

It was not possible to reproduce a cyclic loading-unloading stress path because during the unloading part, the stress point would coincide with the apex of the bubble, which represents a singularity for the first derivatives of the yield function. Therefore, a monotonically increasing isotropic load is considered between points A and B, whose corresponding effective mean stresses are p'_{min} and p'_{max}, respectively.

The elastic part of the volumetric strain is:

$$\Delta\varepsilon^{e}_{vAB} = \frac{1}{K'}\,(p'_{max} - p'_{min}) \tag{6.79}$$

To compute the plastic strain, one has to distinguish the case in which parameter ψ is different from 1 and the case where it is equal to 1, because the integration of the constitutive equations is different in the two cases. In the first case it is:

$$\Delta\varepsilon^{p}_{vAB} = -\frac{\lambda-\kappa}{v_i}\,B^{\psi}\,\frac{(b_{max})^{\psi}}{B^{\psi}R^{2}p_0'^{5}\,(\ln r)^{2}(1-\psi)}\left[(p'_0 - p'_{max})^{1-\psi} - (p'_0 - p'_{min})^{1-\psi}\right] \tag{6.80}$$

In the second it is:

$$\Delta\varepsilon_{vAB}^{p} = -\frac{\lambda-\kappa}{v_i}\frac{b_{max}}{BR^2 {p'_0}^5 (\ln r)^2}\ln\frac{p'_0-p'_{max}}{p'_0-p'_{min}} \tag{6.81}$$

Maximum distance b_{max} between the surfaces is defined in expression (6.18).

The sum of elastic and plastic parts gives the total volumetric strain. The integrations of the constitutive equations are reported in detail in Annex 4.

In Fig. 6.11, a comparison between the analytical solution and the numerical implementation output is presented. The parameters and stresses adopted in the simulation are summarized in Table 6.2. The good agreement between the two approaches is evident. It is interesting to note the sudden increase in volumetric strain as the isotropic stress approaches the isotropic yield stress (300 kPa) and the distance between the two surfaces tends towards zero. When the two surfaces are in contact, indefinite volumetric strains are predicted, as the total plastic modulus is nil (isotropic and kinematic hardening moduli are both nil). The rate of increase of the volumetric strain depends on parameters B and ψ.

Table 6.2 - Model parameters and stress levels for isotropic loading simulation

Model parameters	
M	1.4
$\bar{n}$	10
r	2
R	0.06
B	1.5
ψ	8
Stress levels	
p'_{min}	40 kPa
p'_{max}	250 kPa
p'_0	300 kPa

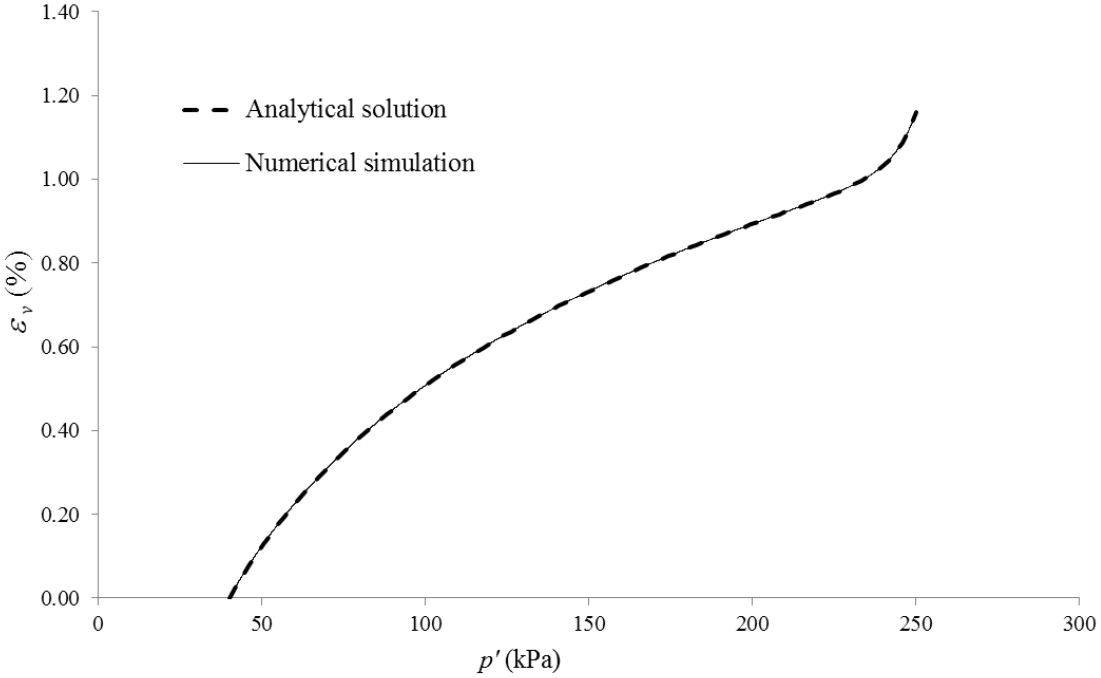

Fig. 6.11 – Comparison between analytical and numerical results for monotonic isotropic loading

6.5.1.2. CONSTANT p' CYCLIC STRESS PATH

This case was studied for a cyclic loading between the values of q_{min} and q_{max}. For simplicity, the stress path was set in order to intersect the yield surface in its top and bottom points (points Y_{load} and Y_{unl} in Fig. 6.12). Rowe flow rule has been considered.

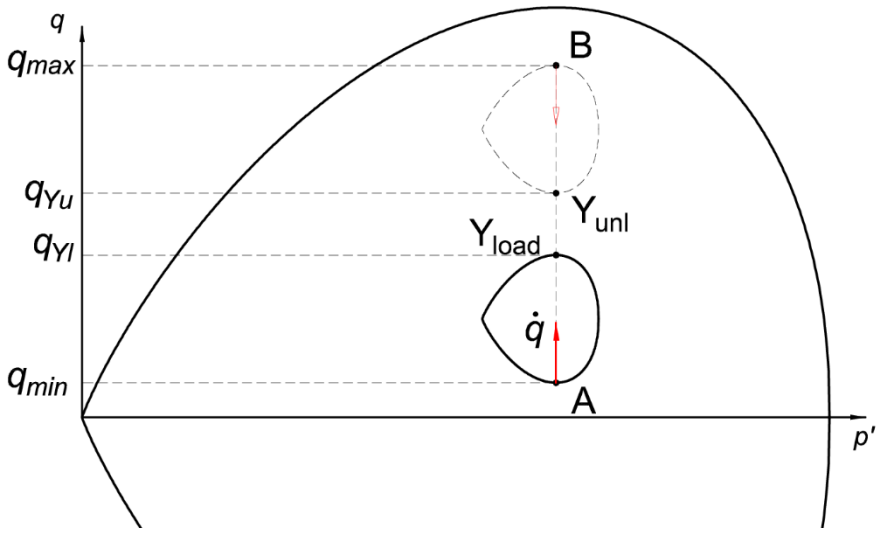

Fig. 6.12 – Constant p' cyclic loading

As referred earlier, during the cyclic loading, the coordinates of the yield points Y_{load} and Y_{unl} will remain constant in each cycle. Since the two surfaces do not change in size, vector $\boldsymbol{\beta}$ linking yield point and its conjugate point on the reference surface is always vertical and thus is parallel to the stress path. Yield

surface is thus dragged vertically at each loading and unloading stress path. The process is constant at each cycle, thus the accumulated strain increases linearly with the number of cycles.

The loading path is delimited between q_{min} and q_{max}; stresses q_{Yl} and q_{Yu} correspond to the yielding points during loading and unloading, respectively. During loading, the stress path is elastic in the interval between q_{min} and q_{Yl} and elasto-plastic between q_{Yl} and q_{max}. Conversely, during unloading it is elastic between q_{max} and q_{Yu} and elasto-plastic between q_{Yu} and q_{min}.

The constitutive relations are integrated on a loading-unloading cycle (see Annex 4) and the results multiplied by the number of cycles. The accumulated volumetric strain at the end of n_{cyc} cycles is thus determined (for $\psi \neq 1$):

$$\varepsilon_{v\,cum} = n_{cyc}\, C_p \left[\left(\frac{Mp'_0}{\sqrt[\bar{n}]{\exp(1)\cdot\bar{n}\cdot\ln r}} - q_{max} \right)^{1-\psi} - \left(\frac{Mp'_0}{\sqrt[\bar{n}]{\exp(1)\cdot\bar{n}\cdot\ln r}} - q_{Yl} \right)^{1-\psi} + \right. \\ \left. + \left(\frac{Mp'_0}{\sqrt[\bar{n}]{\exp(1)\cdot\bar{n}\cdot\ln r}} + q_{min} \right)^{1-\psi} - \left(\frac{Mp'_0}{\sqrt[\bar{n}]{\exp(1)\cdot\bar{n}\cdot\ln r}} + q_{Yu} \right)^{1-\psi} \right] \tag{6.82}$$

coefficient C_p is a constant dependent on the model parameters and on the derivatives of f and g calculated in Y_{load}:

$$C_p = -\frac{\lambda-\kappa}{v_i} \frac{\left(\frac{\partial g}{\partial p'}\right)_{Y_l} \left(\frac{\partial f}{\partial q}\right)_{Y_l}}{p_0'^3(1-\psi)} \left(\frac{b_{max}}{B}\right)^{\psi} \tag{6.83}$$

The maximum distance between the surfaces b_{max} is defined in expression (6.18).

If $\psi = 1$, the resulting expression is:

$$\varepsilon_{v\,cum} = n_{cyc}\, C_p \left(\ln \frac{Mp'_0 - \sqrt[\bar{n}]{\exp(1)\cdot\bar{n}\cdot\ln r}\, q_{max}}{Mp'_0 - \sqrt[\bar{n}]{\exp(1)\cdot\bar{n}\cdot\ln r}\, q_{Yl}} + \right. \\ \left. + \ln \frac{Mp'_0 + \sqrt[\bar{n}]{\exp(1)\cdot\bar{n}\cdot\ln r}\, q_{min}}{Mp'_0 + \sqrt[\bar{n}]{\exp(1)\cdot\bar{n}\cdot\ln r}\, q_{Yu}} \right) \tag{6.84}$$

and

$$C_p = -\frac{\lambda-\kappa}{v_i} \frac{\left(\frac{\partial g}{\partial p'}\right)_{Y_l} \left(\frac{\partial f}{\partial q}\right)_{Y_l}}{p_0'^3} \frac{b_{max}}{B} \tag{6.85}$$

The total accumulated strain coincides with the strain generated in the plastic part, because the strain of the elastic part is nil at the end of each cycle since the initial and final stresses coincide. Using the flow rule, one can compute the distortional plastic strain and, consequently, the axial plastic strain, as shown in Annex 4.

In Fig. 6.13, a comparison between analytical and numerical solutions is presented for 5000 cycles and for the parameters summarized in Table 6.3. Also in this case, a good agreement is obtained. As expected, the accumulation increases linearly with the number of cycles.

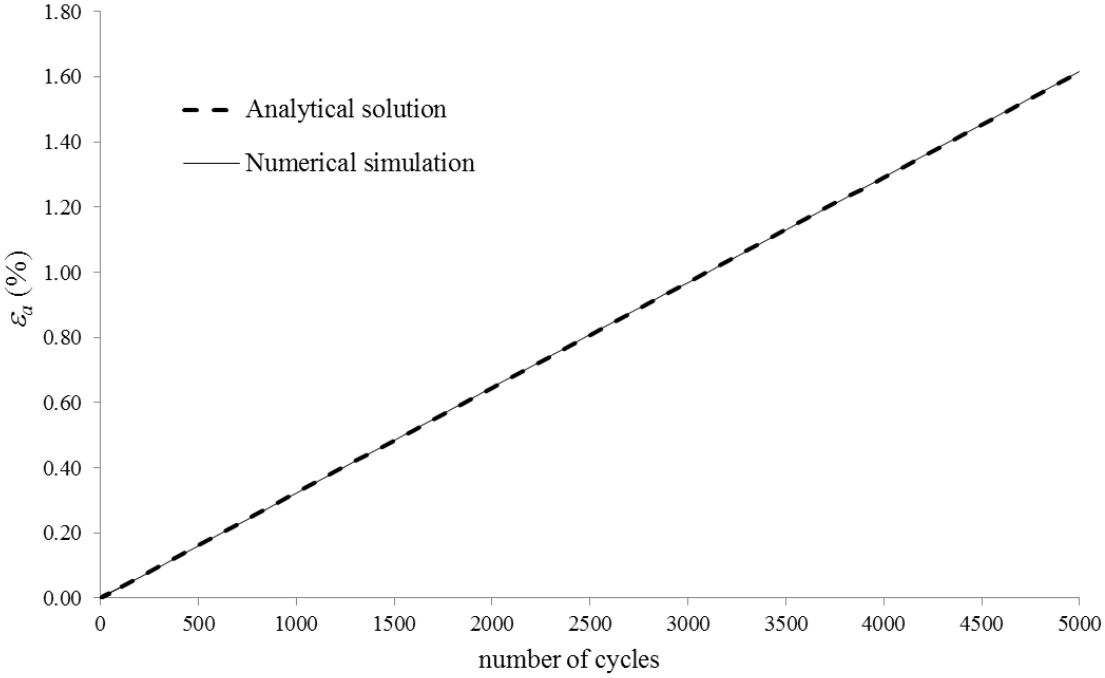

Fig. 6.13 – Comparison between analytical and numerical results for constant p' cyclic loading

Table 6.3 - Model parameters and stress levels for constant p' cyclic loading simulation

Model parameters	
M	1.4
$\bar{n}$	10
r	2
R	0.01
B	1.8
ψ	10
Stress levels	
q_{min}	10 kPa
q_{max}	100 kPa
p'_0	300 kPa

6.5.1.3. DRAINED CYCLIC TRIAXIAL STRESS PATH

This configuration is shown in Fig. 6.14. The slope of the effective stress path is the slope of vector $\dot{\boldsymbol{\sigma}}'$ (effective stress increment vector):

$$s = \dot{q}/\dot{p}' \tag{6.86}$$

In conventional drained compression triaxial tests, the stress path is a straight line of constant slope $s = 3$. The position of the yield surface was selected so that the yielding point Y on the yield surface is the conjugate of point U on the reference surface, as explained earlier. As shown in Fig. 6.14, the cyclic

stress path varies between the points (p'_{min}, q_{min}) and (p'_{max}, q_{max}). During loading, Points Y and U have coordinates (p'_{Yload}, q_{Yload}) and (p'_{Uload}, q_{Uload}), respectively. During unloading, the intersection points are on the lower part of the surfaces. Their coordinates are identified by the subscript "unl", to distinguish them from the precedent ones.

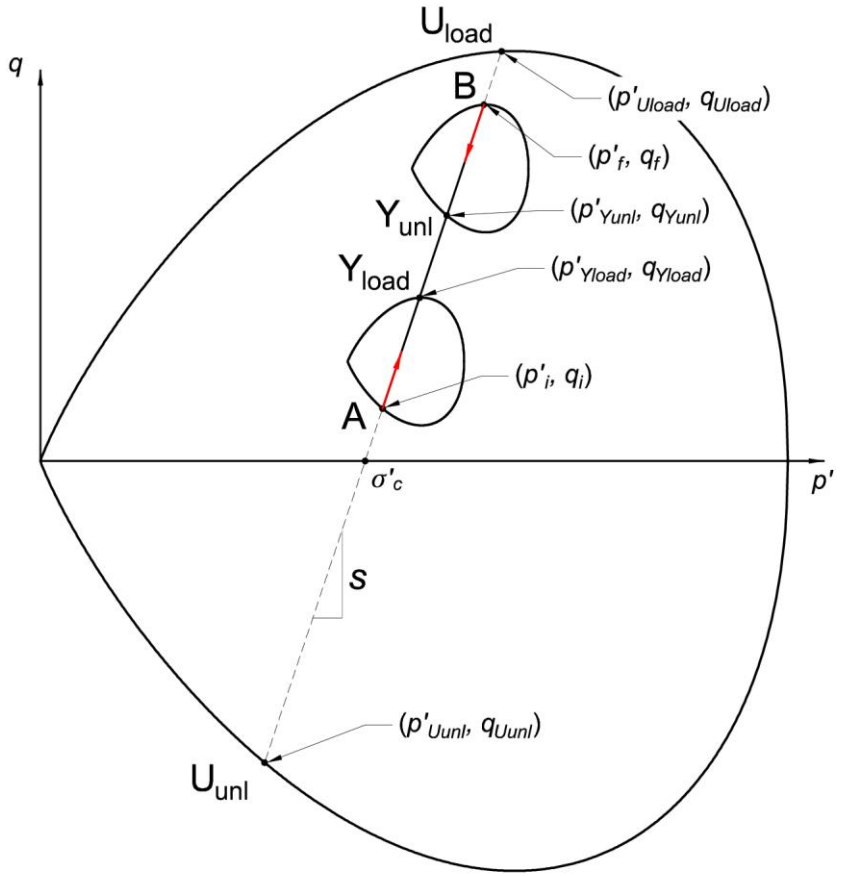

Fig. 6.14 – Drained stress path with a constant slope

The accumulated volumetric plastic strain at the end of n_{cyc} cycles is:

$$\varepsilon_v = n_{cyc}\, C_{TX}\, \Gamma(\mathrm{Y}_{load}, \mathrm{Y}_{unl}, \mathrm{U}_{load}, \mathrm{U}_{unl}, \mathrm{A}, \mathrm{B}, s, \sigma'_c) \tag{6.87}$$

where C_{TX} is a constant depending on the model parameters and Γ is a function depending on the coordinates of Y and U, on the stress path, and on the initial and final stress points. The expression of Γ and the complete calculations performed (including the integration of the constitutive equations) are reported in Annex 4. The accumulated distortional strain is computed through the flow rule.

Also in this case, a comparison between analytical and numerical solution was performed with good results, as shown in the figure below, which reports the accumulation of axial strain with the number of cycles. Axial strain was derived from volumetric and distortional strain using the usual expressions.

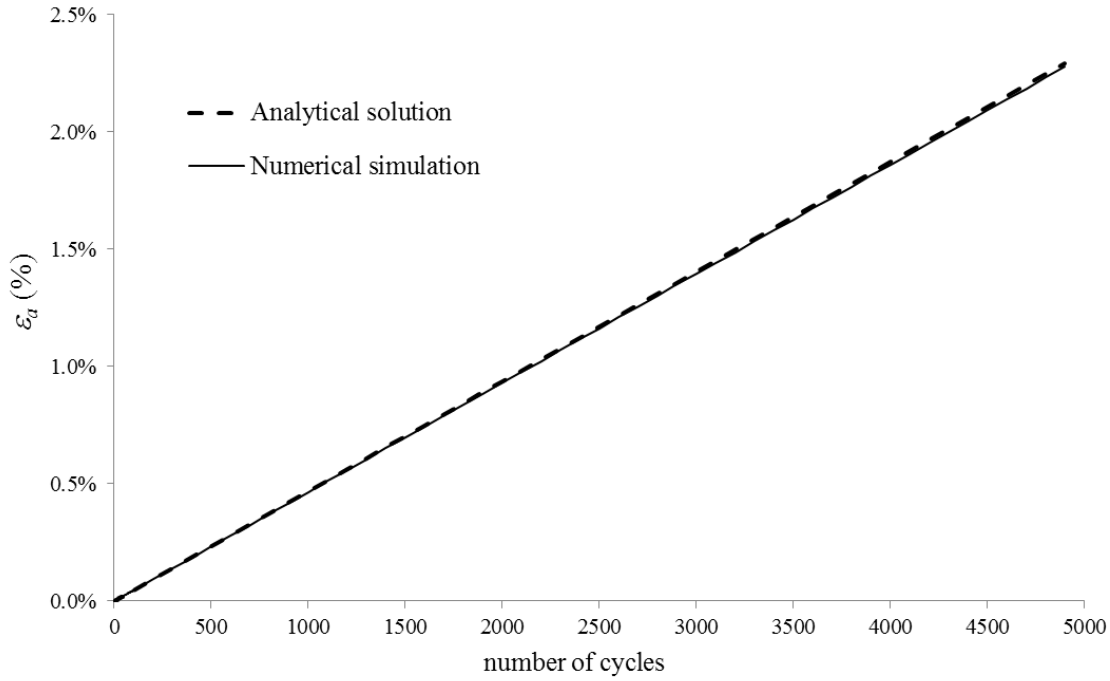

Fig. 6.15 – Comparison between numerical and analytical solution for constant slope stress path

The simulation shown in figure is referred to the parameters reported in the table below.

Table 6.4 - Model parameters and stress levels for cyclic triaxial loading simulation

Model parameters	
M	1.4
$\bar{n}$	10
r	2
R	0.01
B	5.8
ψ	35
Stress levels	
p'_{min}	103 kPa
q_{min}	10 kPa
p'_{max}	117 kPa
q_{max}	50 kPa
σ'_c	100 kPa
p'_0	300 kPa

6.5.2. SOLUTIONS FOR MIXED HARDENING

6.5.2.1. SOLUTION FOR THE GENERAL CASE

When both the hardening moduli are not nil, the displacement of the bubble is not a straight line parallel to the stress path, thus the integration of the differential equations (6.23) is no longer straightforward as in the precedent case. Moreover, the hardening parameter p_0' is a variable dependent on the stress vector $\boldsymbol{\sigma}'$ and on the vector $\boldsymbol{\alpha}$ of the apex coordinates, making the integration of the equations very difficult. The complete process that should be followed is resumed in Box 6.1.

Box 6.1 – Integration procedure

1. Write the expression of the stress path as a relationship between q and p' (and between $\dot{q}$ and $\dot{p}'$):
$$q = q(p')$$
$$\dot{q} = \dot{q}(\dot{p}')$$
2. Solve the system of differential equations (6.19) (translation rule) obtaining the translation of the apex of the bubble as function of the stress state:
$$p'_\alpha = p'_\alpha(p')$$
$$q_\alpha = q_\alpha(p')$$
3. Replace this expressions in the equation of the yield surface (6.2), obtaining the size of the bubble as a function of the stress path:
$$p'_0 = p'_0(p')$$
4. Replace the relations found in 1, 2, and 3 in the constitutive equations (6.23)
5. Integrate equations (6.23) to find the accumulated plastic strains in the stress path *AB*:
$$\varepsilon_{v\,AB}^{p} = \int_{p'_A}^{p'_B} f_v(p')\,\dot{p}$$
$$\varepsilon_{s\,AB}^{p} = \int_{p'_A}^{p'_B} f_s(p')\,\dot{p}$$

In practice, due to the non-linearity of the problem and the complexity of the translation rule and yield surface, it is very difficult to find even a partial solution for the problem. Even if the calculation is performed over a linear stress path as a TX-CID stress path, the expressions in step 2 cannot be integrated. Constant effective stress ratio stress path allows the partial resolution of the problem.

6.5.2.2. CONSTANT EFFECTIVE STRESS RATIO MONOTONIC STRESS PATH

Constant effective stress ratio path is a particular configuration that allows to simplify the problem. The stress path is defined as:

$$\frac{q}{p'} = \bar{\eta} = const \tag{6.88}$$

Such path is a straight line passing through the origin of the axes in the plane $(p' - q)$. In such configuration, the directions of vectors $\boldsymbol{\beta}$ and $\boldsymbol{n_f}$ (and consequently the first derivatives of the yield surface and plastic potential) are constant during loading, even if yield and reference surfaces change in size. As shown in Fig. 6.16, as the reference surface expands (or contracts) during loading, intersection points between the stress path and the successive surfaces ($U_1 \ldots U_2$) are all conjugate (i.e. the points have the same direction of the outward normal). This is due to the particular configuration of the stress

path, which passes through the origin of the stress plane. In other stress paths, the successive ultimate points on the reference surface are not conjugate, thus, the directions of vectors $\boldsymbol{\beta}$ and $\boldsymbol{n}_f$ are not constant during loading.

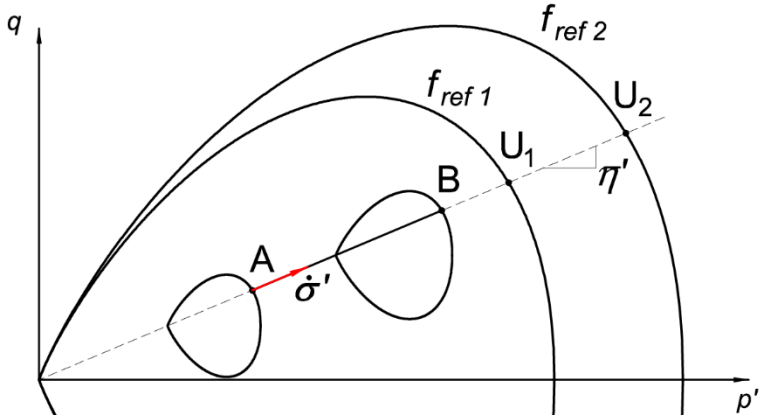

Fig. 6.16 – Constant effective stress ratio path

As usual, the initial position of the yield surface is selected such that translation vector $\boldsymbol{\beta}$ is parallel to the stress increment $\dot{\boldsymbol{\sigma}}'$. When the yield surface changes in size and position, the successive yield points (Y', Y"…) will be all conjugate among them and with the corresponding points (U', U"…) on the reference surface. Thus, vector $\boldsymbol{\beta}$ will be parallel to the stress increment throughout the loading process, resulting in a linear translation path. This leads to significant simplifications in the calculation. It is important to note that only a monotonically increasing loading can be studied, since the unloading part of a constant η' stress path would intersect the yield surface in its apex, where first derivatives of the yield function are not defined. The detailed resolution of the loading stress path between A and B is reported in detail in Annex 4.

In the described configuration of stress path and initial position of the yield surface, the translation rule equations (6.19) reduce to one equation. In fact, it is only necessary to determine one of the two coordinates of the apex of the bubble (for example p'_α) and the second one is determined for the linearity of the translation path ($q_\alpha = \bar{\eta} p'_\alpha$). Moreover, all the variables (partial derivatives, vectors, hardening moduli) are only dependent on p' and p'_0. As shown in 6.4.2, in these conditions translation rule reduces to:

$$\dot{p}'_\alpha = \frac{H'}{H}\dot{p}' \tag{6.89}$$

As the hardening moduli only depends on p' and p'_0, in the above expression it is convenient to replace $\dot{p}'_\alpha$ with $\dot{p}'_0$, by rearranging and differentiating the equation of the yield surface (6.2). The differential equation becomes:

$$\dot{p}'_0 = \frac{1}{R\, k_M}\frac{H_0}{H}\dot{p}' \tag{6.90}$$

where k_M is a constant dependent on the yield surface parameters and reported in Annex 4. By solving this equation and replacing in (6.2), all the hardening parameters are determined as functions of the stress state.

Although it was impossible to find the general solution for equation (6.90), two particular cases were solved for two specific values of parameter ψ, namely 1 and 4.

For $\psi = 1$, the solution is:

$$p' = k_M p'_0 - (k_M p'_{0i} - p'_{\mathrm{A}}) \exp\left[\frac{1}{4} R k_M \frac{k_{H'}}{k_{H_0}} (p'^4_{0i} - p'^4_0)\right] - k_M (1 - \\ - R) \exp\left(-\frac{1}{4} R k_M \frac{k_{H'}}{k_{H_0}} p'^4_0\right) \int_{p'_{0i}}^{p'_0} \exp\left(\frac{1}{4} R k_M \frac{k_{H'}}{k_{H_0}} p'^4_0\right) dp'_0 \tag{6.91}$$

where $k_{H'}$ and k_{H_0} are two constants reported in Annex 4 and p'_{0i} and p'_{A} are the values of p'_0 and p' at the beginning of the elasto-plastic part of the loading path. The definite integral on the right-hand member of (6.91) does not have an analytical solution. Thus, an approximate computation was performed through the trapezium rule. Following such numerical method, the above equation is rewritten in an approximate form as follows:

$$p' \cong k_M p'_0 - (k_M p'_{0i} - p'_{\mathrm{A}}) \exp\left[\frac{1}{4} R k_M \frac{k_{H'}}{k_{H_0}} (p'^4_{0i} - p'^4_0)\right] - \\ - k_M (1 - R) \Delta p'_0 \left[\frac{1}{2} + \frac{1}{2} \exp\left[\frac{1}{4} R k_M \frac{k_{H'}}{k_{H_0}} (p'^4_{0i} - p'^4_0)\right] + \right. \\ \left. + \sum_{k=2}^{n_t - 1} \exp\left[\frac{1}{4} R k_M \frac{k_{H'}}{k_{H_0}} (p'^4_{0k} - p'^4_0)\right]\right] \tag{6.92}$$

The integral domain was divided into n_t trapezia of height $\Delta p'_0$.

Note that it is not possible to invert the function and explicit p'_0 as a function of p'. Thus, one cannot integrate equations (6.23) as indicated in the algorithm reported in Box 6.1. Nevertheless, the analytical relation between the stress path and the change in size of the surfaces has been found and it can be compared against the numerical results from the model. Moreover, using the yield surface one can also define the relation between stress path and the translation of the yield surface. The evolution of the yield surface during loading is thus completely determined in size and position.

The validity of the solution has been verified by comparing the analytical solution with the numerical implementation of the model (which is described in detail in Chapter 7). In Fig. 6.17, two cases are shown, referring to the compressive ($\bar{\eta}$ = 0.46) and dilatant domain ($\bar{\eta}$ = 1.45) of the yield surface (usually referred to as dry and wet side in critical state models). The graphs reports the relation between the stress variable p' and p'_0. As stated above, variables q, p'_α, and q_α are directly related to the former two.

In the case of the dilatant domain, the instability causes the specimen to fail when the total hardening modulus reaches 0. The parameters used in the two cases are reported in Table 6.5.

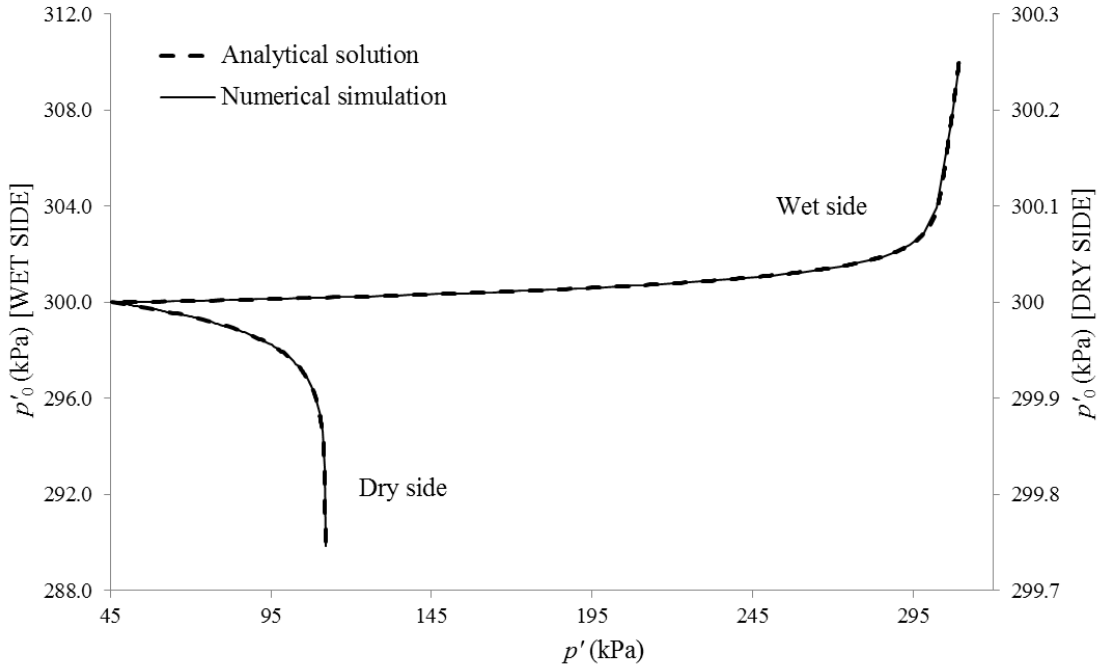

Fig. 6.17 – Relation between stress level and size of the surfaces. Comparison between analytical and numerical solutions for two cases referred to ψ = 1

Table 6.5 - Model parameters and stress levels for constant effective stress ratio stress path and ψ = 1

Parameter	Compressive domain	Dilatant domain
M	1.4	1.4
$\bar{n}$	10	10
r	2	2
R	0.02	0.02
B	0.001	0.1
ψ	1	1
p'_{min}	45 kPa	45 kPa
p'_{max}	309 kPa	112 kPa
p'_{0i}	300 kPa	300 kPa
$\bar{\eta}$	0.46	1.45

For $\psi = 4$, equation (6.90) has two different solutions whether the stress point is on the compressive or dilatant side. In both cases, the solutions are implicit functions of p' and p'_0, as reported in Annex 4. Also in this case, two comparisons with the numerical model were performed (Fig. 6.18) showing a good agreement between the solutions.

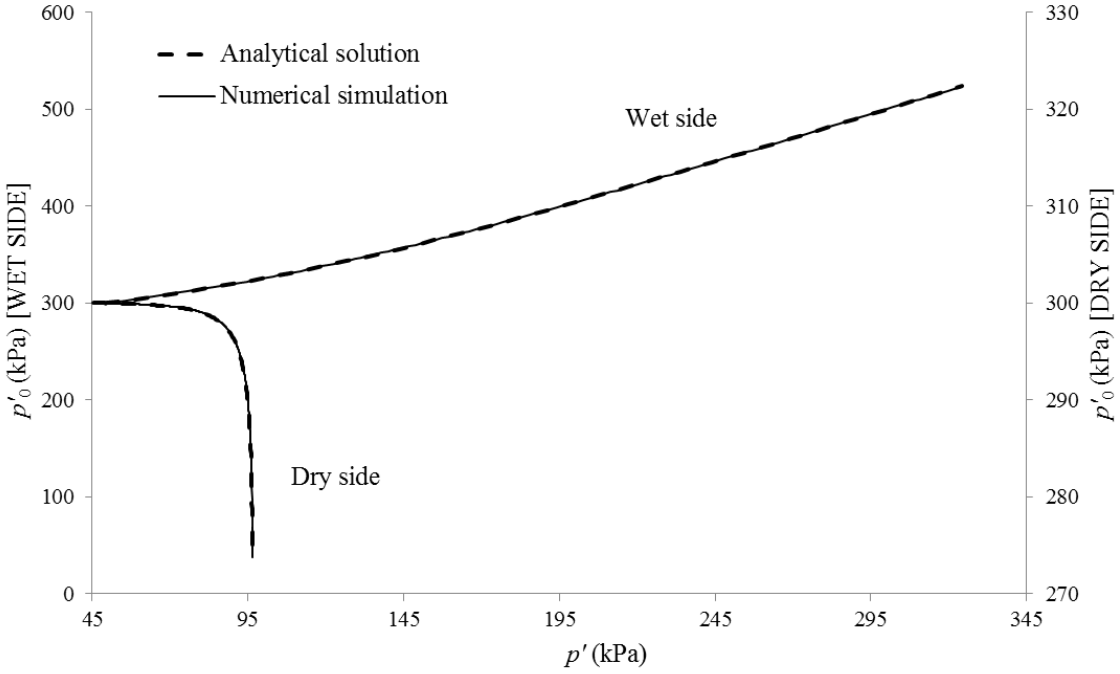

Fig. 6.18 – Relation between stress level and size of the surfaces. Comparison between analytical and numerical solutions for two cases referred to ψ = 4

The parameters used in the two cases are reported in the table below.

Table 6.6 - Model parameters and stress levels for constant effective stress ratio stress path and ψ = 4

Parameter	Compressive domain	Dilatant domain
M	1.4	1.4
$\bar{n}$	10	10
r	2	2
R	0.02	0.02
B	0.1	10
ψ	4	4
p'_{min}	45 kPa	45 kPa
p'_{max}	324 kPa	96 kPa
p'_{0i}	300 kPa	300 kPa
$\bar{\eta}$	0.46	1.45

6.6. CONCLUSIONS

A novel constitutive model for cemented soils based on bounding surface plasticity was presented and its main features were described, as in Panico et al. (2018). The model is conceived as the extension and combination of precedent models in a single framework for granular soils capable of reproducing cyclic behaviour and soil cementation.

The model is firstly introduced in its uncemented version, to highlight the characteristics related to the bounding surface plasticity; then, the cemented framework is presented. The model is implemented following the principles of hierarchical modelling (Desai et al., 1986), in which new characteristics are added without altering the precedent simpler framework. Thus, the level of complexity of the model can be adjusted to the particular problem, activating or deactivating single features without preventing the functionality of the others.

The number of parameters required for the model is rather high; for this reasons the parameters to be calibrated are divided in subsets of smaller dimensions, each referred to a particular feature of the model (critical state behaviour, bounding plasticity, cementation...). The successive calibration (reported in Chapter 8) is performed in a staged approach, starting from a configuration with a single subset of parameters active, and activating subsequently the other features with their related parameters.

Particular attention is focused on the translation characteristics of the yield surface. It is shown that the yield surface tends to occupy a position that makes its translation parallel to the stress increment vector. If such condition is not respected, the yield surface progressively shift to a position (relative to the stress state) such that the parallelism between the two vectors is recovered. This characteristic is very important for subsequent analyses, because it is used to obtain particular conditions in which the integration of the constitutive equations is simpler, and thus to obtain a closed-form solution for these particular cases.

Although a general closed-form solution for the model was not found, some partial analytical solutions under particular conditions of loading and with simplified model features were derived and checked against the numerical implementation of the model (described in Chapter 7) for validation. The solutions are referred to the uncemented model. The first set of solutions was determined in the hypothesis that only kinematic hardening is active without isotropic hardening, i.e. the yield surface translates in the stress plane without changing in size. Moreover, the initial position of the yield surface was selected such that the condition of parallelism between stress path and translation vector is respected. In such situation, the yield surface and plastic potential derivatives are constant; thus, the governing equations can be integrated. The same situation occurs also in the case of mixed hardening model in a constant stress ratio stress path. All the tests confirmed the concordance between analytical and numerical solutions, contributing to the model validation. A model pitfall that emerged from this analysis is the impossibility to perform constant stress cyclic tests (including cyclic isotropic tests), because the stress path during the unloading path would intersect the yield surface in its apex, where the first derivatives of the surface are not defined. The local change of the yield surface formulation in the zone near the apex with a more suitable formulation is necessary if this type of stress path shall be applied.

Chapter 7.

NUMERICAL IMPLEMENTATION OF THE MODEL

The constitutive relations of the model described in the former chapter cannot be integrated to obtain a closed-form solution. Thus, an approximate solution shall be found through the discretization of the stress or strain increments in a number of small intervals and a numerical integration with an iterative algorithm over these intervals.

As reported by many authors (e.g. Gens & Potts, 1988), the incremental formulation of the constitutive equations for an elasto-plastic model are written as follows:

$$\begin{aligned} \dot{\boldsymbol{\sigma}}' &= \mathbf{D}^e \dot{\boldsymbol{\varepsilon}}^e = \mathbf{D}^e (\dot{\boldsymbol{\varepsilon}} - \dot{\boldsymbol{\varepsilon}}^p) \\ \dot{\boldsymbol{\sigma}}' &= \mathbf{D}^e \left(\dot{\boldsymbol{\varepsilon}} - \dot{\Lambda} \frac{\partial g}{\partial \boldsymbol{\sigma}'} \right) = \mathbf{D}^{ep} \dot{\boldsymbol{\varepsilon}} \end{aligned} \tag{7.1}$$

where $\mathbf{D}^e$ is the elastic stiffness tensor and $\mathbf{D}^{ep}$ is the elasto-plastic stiffness tensor. As already referred in Chapter 6, for critical state models, in the most general case the hardening parameters increments are linearly dependent on the plastic strain increments and on the current value of one or more hardening parameters:

$$\dot{\boldsymbol{h}} = \dot{\boldsymbol{h}}(\dot{\boldsymbol{\varepsilon}}^p, \boldsymbol{h}) \tag{7.2}$$

This is for example the case of Al-Tabbaa & Muir Wood (1989) model (described Chapter 3), where the translation of the yield surface (i.e. the incremental variation $\dot{\boldsymbol{\alpha}}$ of the coordinates of the centre of the surface) is dependent on the current size of the surface, p_0'. In the model presented in this thesis, the hardening parameters are independent from each other; thus, the above relation can be rewritten as follows:

$$\dot{\boldsymbol{h}} = \dot{\boldsymbol{h}}(\dot{\boldsymbol{\varepsilon}}^p) \tag{7.3}$$

Remembering that $\dot{\boldsymbol{\varepsilon}}^p$ is dependent on the plastic multiplier $\dot{\Lambda}$ through relation (6.49), it is:

$$\dot{\boldsymbol{h}} = \dot{\boldsymbol{h}}(\dot{\boldsymbol{\varepsilon}}^p(\Lambda)) = \frac{\partial \boldsymbol{h}}{\partial \boldsymbol{\varepsilon}^p} \frac{\partial \boldsymbol{\varepsilon}^p}{\partial \Lambda} \dot{\Lambda} = \frac{\partial \boldsymbol{h}}{\partial \boldsymbol{\varepsilon}^p} \frac{\partial g}{\partial \boldsymbol{\sigma}'} \dot{\Lambda} \tag{7.4}$$

Yield surface condition must be always satisfied:

$$f(\boldsymbol{\sigma}', \boldsymbol{h}) = 0 \tag{7.5}$$

As well as the consistency condition:

$$df = \frac{\partial f}{\partial \boldsymbol{\sigma}'}\dot{\boldsymbol{\sigma}}' + \frac{\partial f}{\partial \boldsymbol{h}}\dot{\boldsymbol{h}} = 0 \tag{7.6}$$

Substituting the second of the (7.1) and the (7.4) into the (7.6), one obtains the value of the plastic multiplier:

$$\dot{\Lambda} = \frac{\frac{\partial f}{\partial \boldsymbol{\sigma}'}\mathbf{D}^e\dot{\boldsymbol{\varepsilon}}}{-\frac{\partial f}{\partial \boldsymbol{h}}\frac{\partial \boldsymbol{h}}{\partial \boldsymbol{\varepsilon}^p}\frac{\partial g}{\partial \boldsymbol{\sigma}'} + \frac{\partial f}{\partial \boldsymbol{\sigma}'}\mathbf{D}^e\frac{\partial g}{\partial \boldsymbol{\sigma}'}} \tag{7.7}$$

The first term of the denominator is the hardening modulus H:

$$H = -\frac{\partial f}{\partial \boldsymbol{h}}\frac{\partial \boldsymbol{h}}{\partial \boldsymbol{\varepsilon}^p}\frac{\partial g}{\partial \boldsymbol{\sigma}'} \tag{7.8}$$

Combining expressions (7.1), (7.4), and (7.7), the constitutive equations are completely defined:

$$\begin{aligned}\dot{\boldsymbol{\sigma}}' &= \mathbf{D}^{ep}\dot{\boldsymbol{\varepsilon}} \\ \dot{\boldsymbol{h}} &= \mathbf{R}^{ep}\dot{\boldsymbol{\varepsilon}}\end{aligned} \tag{7.9}$$

Where

$$\begin{aligned}\mathbf{D}^{ep} &= \mathbf{D}^e - \frac{\mathbf{D}^e\frac{\partial g}{\partial \boldsymbol{\sigma}'}\frac{\partial f}{\partial \boldsymbol{\sigma}'}\mathbf{D}^e}{H + \frac{\partial f}{\partial \boldsymbol{\sigma}'}\mathbf{D}^e\frac{\partial g}{\partial \boldsymbol{\sigma}'}} \\ \mathbf{R}^{ep} &= \frac{\partial \boldsymbol{h}}{\partial \boldsymbol{\varepsilon}^p}\frac{\partial g}{\partial \boldsymbol{\sigma}'}\frac{\frac{\partial f}{\partial \boldsymbol{\sigma}'}\mathbf{D}^e}{H + \frac{\partial f}{\partial \boldsymbol{\sigma}'}\mathbf{D}^e\frac{\partial g}{\partial \boldsymbol{\sigma}'}}\end{aligned} \tag{7.10}$$

In order to find a numerical solution to the problem, a discretization is performed over these incremental equations in order to divide the problem in small finite intervals, on which an approximate solution can be found. The above equations are then rewritten as follows:

$$\begin{aligned}\Delta\boldsymbol{\sigma}_i' &= \mathbf{D}^{ep}\Delta\boldsymbol{\varepsilon}_i \\ \Delta\boldsymbol{h}_i &= \mathbf{R}^{ep}\Delta\boldsymbol{\varepsilon}_i\end{aligned} \tag{7.11}$$

Where the subscript i refers to the interval number and the infinitesimal increments of the strain and stress are substituted by the finite increments Δ. Due the non-linearity of the problem, the matrices are dependent on the current stress and strain levels and thus they are not constant over an increment. For this reason, the approximate solution strategy is not straightforward and different approaches exist. The solving algorithms are called stress point algorithms.

7.1. STRESS POINT ALGORITHMS

Equations (7.9) and the respective boundary conditions constitute a boundary value problem whose solution in closed form cannot be found. As stated in the precedent section, the problem is divided in a set of finite increments and an approximate solution for the differential equations is sought in each interval. Although the total strain variation is known in each interval, the manner in which it varies during the interval is not know: for this reason, a further assumption must be done and this assumption is different for each algorithm.

Stress point algorithms are divided in two families: explicit (or forward) and implicit (or backwards) algorithms. In the first case, the state of the system at the end of the increment is calculated as a function

of the state of the system at the beginning of the increment i; this means that the solving equation is explicit and is directly solvable. In implicit methods, the unknown variable at the end of the interval is a function of the same unknown at the beginning of the interval; thus the solving equation is implicit as the unknown quantity is present in both members of the equation and more sophisticated solution strategies must be implemented.

The simplest algorithms of the two families are the forward Euler scheme (explicit) and the backwards Euler scheme (implicit). The first method calculates the stress increments by calculating the matrices at the beginning of the interval, while the second estimates the solutions at the end of an interval (which is unknown) and then solves the resulting implicit equation. Explicit algorithms have the advantage of being non-iterative within an interval, while to solve implicit equations an iterative scheme in the interval is necessary. On the other hand, to ensure the precision of the explicit methods, the increment must be divided in a number of conveniently small substeps; in the more advanced algorithm, the size of each substep is automatically determined through an iterative process. Thus, iterations are still necessary if a good accuracy has to be ensured.

According to Potts & Zdravkovic (1999), the most used explicit algorithms belong to the class of the so-called substepping algorithm, while a broadly used implicit algorithm is the return algorithm. Substepping algorithms are explicit algorithms that respond to the need for a control of the accuracy: as written above, this aim can be fulfilled by dividing the interval in smaller subincrements. Many implementations of this type of algorithm exist (Wissman & Hauck, 1983; Sloan, 1987; Sloan, et al. 2001); the more sophisticated implementation present an automatic substepping iterative procedure with error control at the end of each substep.

Return algorithms (e.g. Borja & Lee, 1990; Borja, 1991) estimate the stress increment at the end of the interval. As this value is unknown, an implicit equation shall be solved. Most implementation perform a first iteration, in which the constitutive relations are considered purely elastic; a first try of the stress is calculated called elastic predictor; then, if this try value is found outside the yield surface, it is brought back to the yield surface through an iterative procedure.

Potts & Ganendra (1994) made a comparison between the two classes of algorithms. The performance of each one strongly depends on the particular problem treated. Substepping algorithm has the advantage that it is robust, it is easier to implement in a computer code, it requires less calculation time from the CPU, once it is implemented, it is easily adaptable to different constitutive models. Return algorithm is faster to converge but it needs complicated mathematics to be implemented and each model requires a very specific implementation. In addition, the model is more likely to fail to converge and requires more CPU time. For these reasons, the authors conclude that substepping algorithms should be preferred.

Based on these considerations, in the present work, two algorithms are used for the solution of the problem: the modified Euler (ME) method and the 5^h order Runge-Kutta (RK) method (Sloan, 1987). Both algorithms belong to the class of the explicit substepping algorithm. ME method is a second-order method, i.e. the real solution in the interval is approximate through a second-order curve; RK methods present various implementations with different orders (higher than quadratic): in the present case, a 5^{th} order implementation was implemented. For a given level of accuracy required, higher order methods require higher calculation time for obtaining convergence within a single interval with respect to lower order methods. In fact, the stiffness (or compliance) matrix shall be calculated twice at each iteration in the case of ME method, while it shall be calculated six times per iteration in the case of 5^{th} order RK method. On the other hand, a higher order method allows the subdivision of the problem in larger intervals with respect to lower order methods. Thus, the overall computation time can be higher of lower depending on the level of non-linearity of the problem studied and the boundary conditions imposed.

7.2. MODEL IMPLEMENTATION FOR STRESS-DRIVEN CYCLIC TESTS

The implementation of these methods followed a specific procedure for each type of stress or strain paths to be reproduced. In the present work, the model is intended to be used to reproduce stress-driven cyclic triaxial tests and strain-driven monotonic triaxial tests. Both the types include drained and undrained conditions. Thus, the constitutive equation (7.1) are rearranged and adapted to each of these four cases in order to find an optimal implementation in each case.

For the stress-driven case, the stress increment is imposed externally and it is known a priori, while the strain increment is unknown. Then, it seems reasonable to write the constitutive equation (7.1) in the following form:

$$\dot{\boldsymbol{\varepsilon}} = (\mathbf{C}^e + \mathbf{C}^p)\dot{\boldsymbol{\sigma}}' = \mathbf{C}^{ep}\,\dot{\boldsymbol{\sigma}}' \tag{7.12}$$

Where $\mathbf{C}^e$ is the matrix of plastic compliance and $\mathbf{C}^{ep}$ is the matrix of elasto-plastic compliance, which are the inverse matrices of $\mathbf{D}^e$ and $\mathbf{D}^{ep}$, respectively. Matrix $\mathbf{C}^p$ is the compliance matrix responsible for the plastic parcel of the total strain.

As in the precedent case, by substituting the (7.4) into the (7.6), one obtains the value of the plastic multiplier $\dot{\Lambda}$:

$$\dot{\Lambda} = \frac{\dfrac{\partial f}{\partial \boldsymbol{\sigma}'}\dot{\boldsymbol{\sigma}}'}{-\dfrac{\partial f}{\partial \boldsymbol{h}}\dfrac{\partial \boldsymbol{h}}{\partial \boldsymbol{\varepsilon}^p}\dfrac{\partial g}{\partial \boldsymbol{\sigma}'}} = \frac{\dfrac{\partial f}{\partial \boldsymbol{\sigma}'}}{H}\dot{\boldsymbol{\sigma}}' \tag{7.13}$$

where hardening modulus H is expressed in (7.8). Substituting the above relation in (6.49), one obtains:

$$\dot{\boldsymbol{\varepsilon}}^p = \frac{1}{H}\frac{\partial f}{\partial \boldsymbol{\sigma}'}\frac{\partial g}{\partial \boldsymbol{\sigma}'}\dot{\boldsymbol{\sigma}}' \tag{7.14}$$

Comparing this expression with (7.12), the compliance matrix results in:

$$\mathbf{C}^{ep} = \mathbf{C}^e + \mathbf{C}^p = \mathbf{C}^e + \frac{1}{H}\frac{\partial f}{\partial \boldsymbol{\sigma}'}\frac{\partial g}{\partial \boldsymbol{\sigma}'} \tag{7.15}$$

Once again, the discretization process leads to the following solving equations:

$$\begin{gathered}\Delta\boldsymbol{\varepsilon}_i = \Delta\boldsymbol{\varepsilon}_i^e + \Delta\boldsymbol{\varepsilon}_i^p = (\mathbf{C}^e + \mathbf{C}^p)\Delta\boldsymbol{\sigma}_i' \\ \Delta\boldsymbol{h}_i = \mathbf{Q}^{ep}\Delta\boldsymbol{\sigma}_i'\end{gathered} \tag{7.16}$$

where $\mathbf{Q}^{ep}$ is determined substituting (7.13) in (7.4):

$$\mathbf{Q}^{ep} = \frac{1}{H}\frac{\partial \boldsymbol{h}}{\partial \boldsymbol{\varepsilon}^p}\frac{\partial g}{\partial \boldsymbol{\sigma}'}\frac{\partial f}{\partial \boldsymbol{\sigma}'} \tag{7.17}$$

7.2.1. DRAINED CYCLIC TRIAXIAL STRESS PATH

In the case of a drained and stress-driven triaxial test, the implementation of the algorithm is particularly simple. In fact, in such case the stress conditions are defined overall the boundary surface of the specimen. A cyclic axial stress is acting on the top and bottom surfaces of the specimen varying between two defined upper and lower limits, while a constant confining pressure is acting on the entire surface of the specimen. These stress conditions result in the typical stress path observed in the $(p' - q)$ plane with the state of stress moving cyclically on a segment of a straight line with slope 3:1. Since the effective stress path is known a priori, the elastic and plastic parcels of the constitutive equations can be decoupled, solved separately and the results can be summed afterwards. The constitutive equations can be written in terms of volumetric and deviatoric parcels as follows:

$$\begin{pmatrix} \Delta\varepsilon_{vi} \\ \\ \Delta\varepsilon_{si} \end{pmatrix} = \begin{pmatrix} \Delta\varepsilon_{vi}^{e} + \Delta\varepsilon_{vi}^{p} \\ \\ \Delta\varepsilon_{si}^{e} + \Delta\varepsilon_{si}^{p} \end{pmatrix} = (\mathbf{C}^{e} + \mathbf{C}^{p}) \begin{pmatrix} \Delta p_i' \\ \\ \Delta q_i \end{pmatrix} \tag{7.18}$$

7.2.1.1. STRESS PATH DEFINITION AND MODEL INITIALIZATION

In the drained triaxial cyclic tests performed, a constant effective confining pressure σ_c' is imposed and the deviatoric stress varies between a minimum (q_{min}) and a maximum value (q_{max}). As referred above, in such situation the incremental stress ratio is constant: $\Delta q_i/\Delta p_i' = 3$. Thus, the stress path is completely defined in the (p', q) plane as a segment of a straight line, passing through point (σ_c', 0), inclined at a slope $s = 3$, and limited between q_{min} and q_{max}. If one indicates as A and B the points corresponding to the minimum and maximum deviatoric stress, a generic loading cycle starts in A, follows the straight path up to point B, and goes back to the starting point A. In each cycle, a loading and an unloading part can be determined, following the same path with opposite directions. In both cases, the loading path intersects the yield surface at some point. Thus, the stress path can be divided in a purely elastic and an elasto-plastic domain. This means that at each cycle, a yielding point can be individuated during loading and one during unloading.

If all the model parameters have already been selected (as shown in Chapter 8), the initialization the model requires the definition of five state parameters (see section 6.3):

- the initial coordinates of the apex, $p_{\alpha i}'$ and $q_{\alpha i}$
- the uncemented reference surface, p_{0unc_i}'
- the initial amount of bonding, b_0
- the initial tensile strength, p_{ti}'

The initial coordinates of the yield surface are set in order to satisfy condition (6.66), as will be explained in detail in the next chapter. Size $p_{0unc,i}'$ coincides with the isotropic yield stress of an uncemented soil having same properties and compaction of the cemented soil to be modelled. Thus, following the framework of critical state soil mechanics, its value is determined in the isotropic plane ($\ln p', v$) as the intersection of the normal compression line (NCL) with the unloading-reloading line passing through the initial specific volume v_i of the specimen. Thus, after parameters λ, κ, and N have been determined, the size is determined as follows:

$$p_{0unc\_i}' = e^{\frac{N - v_i}{\lambda - \kappa}} \tag{7.19}$$

The initial bonding b_0 and the initial tensile strength p_{ti}' are not directly related to the performed laboratory test. Thus, their values are determined indirectly by a geometric construction and using the results of the available laboratory tests. The position and size of the reference surface is known if the coordinates of at least two points of the surface are determined. Using the results of the isotropic compression tests (IC) and UCT tests, two points are determined, corresponding to the isotropic yield stress (σ_y') and to the unconfined compression strength (q_{UCS}) (see Fig. 7.1).

From IC tests on cemented specimens, the isotropic yield stress is retrieved. From UCT tests, the unconfined compression strength (q_{UCS}) is known for each mixture. It is supposed that this point lies on the reference surface, in the hypothesis that this surface coincide with the peak state envelope for unconfined soil. Supposing that the stress path of the UCT tests starts from the origin of the stress plane (0, 0) and that the stress path is drained (i.e. it is inclined with a slope of 3/1), the point corresponding to the unconfined compression strength has coordinates $(q_{UCT}/3, q_{UCT})$ in the (p', q) reference system. The derivation of these parameters from experimental tests is explained in detail in Chapter 8.

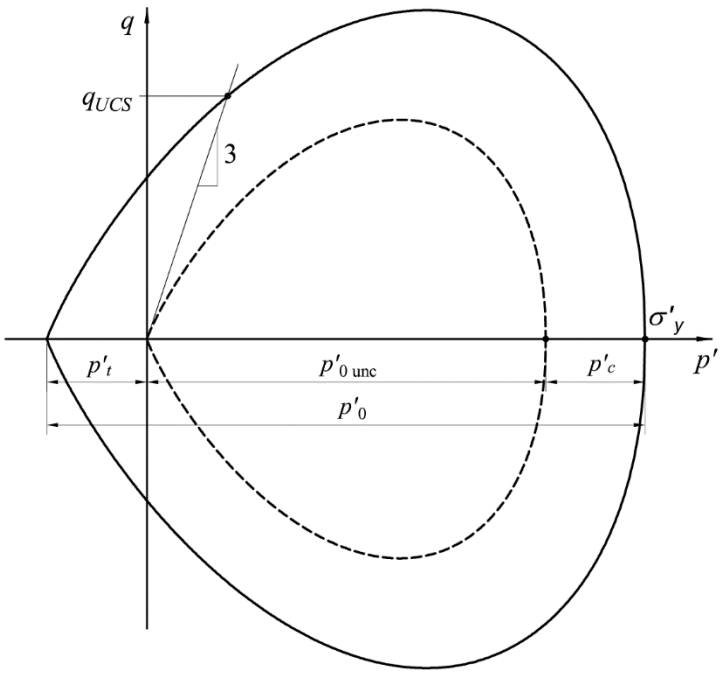

Fig. 7.1 – Initialization of bonding state parameters

The initial size of the reference surface (p'_{0i}) is by definition:

$$p'_{0i} = \sigma'_y + p'_{ti} \tag{7.20}$$

Substituting this expression and the coordinates of the point corresponding to the unconfined compression strength in the reference surface (6.35), one obtains:

$$\left(\frac{q_{UCS}}{M(q_{UCS}/3 + p'_{ti})}\right)^{\bar{n}} + \frac{1}{\ln r}\ln\frac{q_{UCS}/3 + p'_{ti}}{\sigma'_y + p'_{ti}} = 0 \tag{7.21}$$

In this expression, the only unknown is p'_{ti} (if the shape parameters have already been selected). Since it is not possible to find a closed-form solution for the expression, bisection method shall be used to solve iteratively the expression. Two points for the searching interval shall be selected (see Fig. 7.2.). They shall belong to the p' axis and shall be located inside and outside the reference surface, respectively. The internal point is the origin of the stress plane (0, 0), as it certainly lies inside the reference surface (for cemented soils). The external point shall be located on the negative part of the p' axis. As tentative value, a distance is selected on the negative p' axis equal to the value of q_{UCS}. There is no guarantee that this point lies outside the reference surface; thus, before starting the process, such value shall be substituted to p'_{ti} in (7.21), and the resulting value shall be negative. If this is not the case, the tentative value is multiplied by 2 and the check is performed again, until a negative value is obtained. Thus, this point and the origin of the axes become the boundaries of the interval on which the bisection method is applied. The convergence tolerance is set at 10^{-11}, which gives a good precision within a small computation time.

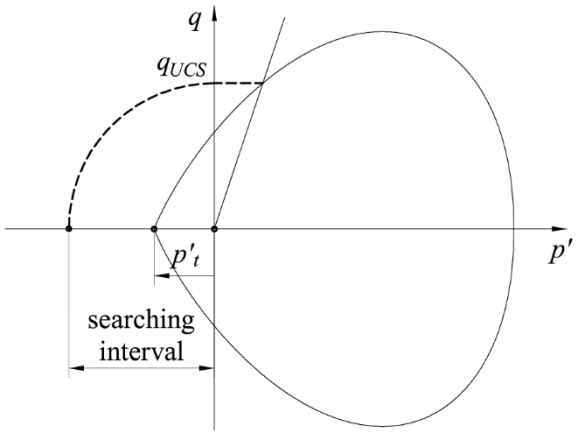

Fig. 7.2 – Searching interval for bisection method for tensile strength calculation

After the initial value of the tensile strength has been determined, the initial size of the reference surface is determined through expression (7.20). Then, inverting expression (6.40) and taking into account that in the initial undamaged state, the damage variable X is nil, one obtains the value of the initial degree of bonding:

$$b_0 = \frac{p'_{0i}}{p'_{0unc\_i}} - 1 \tag{7.22}$$

7.2.1.2. YIELD POINT CALCULATION

Once the initial position and size of the surfaces are set, the yielding point $\boldsymbol{\sigma}'_Y$ is calculated as the intersection between stress path and yield surface. The size of the yield surface (determined through parameter R) shall be adequately small in order to ensure that an intersection with the stress path exists, otherwise the process is purely elastic and no strain accumulation is produced. In this way, the stress path is divided between a purely elastic and an elasto-plastic part. The equations relative to the elastic part can be solved in closed form, as the constitutive relations (although not linear) can be integrated. Thus, there is no need to use an iterative method for this domain. In the second domain, both elastic and plastic strain are developed. This approximate calculation must be performed at each stress reversal (i.e. at the beginning of each loading path and at the beginning of each unloading path). Due to the particular formulation of the yield surface, it is not possible to determine the yielding point in a closed form. The drained stress path in a constant confined triaxial test has the following expression:

$$q = 3(p' - \sigma'_c) \tag{7.23}$$

where q ranges between q_A and q_B as explained earlier, and σ'_c is the effective confining pressure (which is constant throughout the test). The intersection between this stress path and the yield surface (6.2) produces an implicit expression that cannot be solved in closed form. Thus, an iterative method for finding an approximate solution shall be used, such as Newton-Raphson method or bisection method. To implement Newton-Raphson method, the coordinates of the unknown yield point $\boldsymbol{\sigma}'_Y$ in the i-nth iteration are written as:

$$p'_{Y(i)} = p'_{A(i)} + \alpha_{Y(i)}(p'_B - p'_A) = p'_{A(i)} + \alpha_{Y(i)}\Delta p'_{AB} \tag{7.24}$$

$$q_{Y(i)} = q_A + \alpha_{Y(i)}(q_B - q_A) = q_A + \alpha_{Y(i)}\Delta q_{AB} \tag{7.25}$$

Substituting these expressions in the expression of the yield surface, an implicit expression in the unknown α_Y is obtained:

$$f(\alpha_Y) = \left(\frac{|q_A + \alpha_Y(q_B - q_A) - q_\alpha|}{M(p'_A + \alpha_Y(p'_B - p'_A) - p'_\alpha)} \right)^{\bar{n}} + \frac{1}{\ln r} \ln \frac{p'_A + \alpha_Y(p'_B - p'_A) - p'_\alpha}{R p'_0} = 0 \tag{7.26}$$

Before starting the iterative process, one shall verify that points A and B are one inside and the other outside of the yield surface, that is:

$$f(\boldsymbol{\sigma}'_A) \cdot f(\boldsymbol{\sigma}'_B) < 0 \tag{7.27}$$

If this condition is verified, the yield point is located within the interval AB; otherwise, the stress path is purely elastic and no yielding is observed. The first attempt value for α_Y is obtained with a linear interpolation between the values of f in A and B:

$$\alpha_{Y(1)} = \frac{f(\boldsymbol{\sigma}'_A)}{f(\boldsymbol{\sigma}'_A) - f(\boldsymbol{\sigma}'_B)} \tag{7.28}$$

Applying the iterative method, better approximations of α_Y are calculated as follows:

$$\alpha_{Y(i+1)} = \alpha_{Y(i)} - \frac{f(\boldsymbol{\sigma}'_{Y(i)})}{\frac{\partial f}{\partial \alpha}} = \alpha_{Y(i)} - \frac{f(\boldsymbol{\sigma}'_{Y(i)})}{\left(\frac{\partial f}{\partial \boldsymbol{\sigma}'}\right)_i \frac{\partial \boldsymbol{\sigma}'}{\partial \alpha}} = \alpha_{Y(i)} - \frac{f(\boldsymbol{\sigma}'_{Y(i)})}{\left(\frac{\partial f}{\partial p'}\right)_i \Delta p'_{AB} + \left(\frac{\partial f}{\partial q}\right)_i \Delta q_{AB}} \tag{7.29}$$

The values of the yield function and its derivatives are calculated in the point found in the previous iteration. The iteration end when a set tolerance criterion is met, namely:

$$|f(\boldsymbol{\sigma}'_Y)| < 10^{-10} \tag{7.30}$$

As it gives a good precision with a reasonable computation time.

Although this method is known as having a fast convergence, a problem can raise in the unloading path BA. In such case, it is common to have:

$$p'_A \leq p'_\alpha \tag{7.31}$$

Thus, when calculating $f(\boldsymbol{\sigma}'_A)$, the argument of the logarithm is negative or nil and the function is not defined. This is because the expression of the yield function is defined on the semi-plane defined by effective mean stress higher than the p'-coordinate of the yield surface apex:

$$p' > p'_\alpha \tag{7.32}$$

Thus, during an unloading stress path, if the value of the yield surface in the final point $f(\boldsymbol{\sigma}'_A)$ is not defined, the stress interval BA is substituted by an interval BA*, where point A* has the following stress coordinates:

$$\boldsymbol{\sigma}'_{A^*} = \begin{pmatrix} p'_\alpha \\ \\ 3(p'_\alpha - \sigma'_c) \end{pmatrix} \tag{7.33}$$

That is, A* is a point laying on the stress path and with same p'-coordinate as the apex of the yield surface. Since $f(\boldsymbol{\sigma}'_{A^*})$ is still undefined, the first value of α_Y can be selected as the midpoint of this interval:

$$\alpha_{Y(1)} = 0.5 \tag{7.34}$$

The iteration process follows as described above, with the following additional check to be performed at the end of each iteration:

$$p'_{Y(i)} > p'_{\alpha} \tag{7.35}$$

Because of this problem and for the fact that the computation times are comparable, a simpler bisection method was implemented. The solving expression is written as:

$$\left(\frac{\left|3\left(p'_{Y(i)} - \sigma'_c\right) - q_{\alpha}\right|}{M\left(p'_{Y(i)} - p'_{\alpha}\right)}\right)^{\bar{n}} + \frac{1}{\ln r}\ln\frac{p'_{Y(i)} - p'_{\alpha}}{Rp'_0} = 0 \tag{7.36}$$

As in the former case, two initial tentative values for p'_Y are selected along the stress path, one inside and one outside the yield surface, and condition (7.27) shall be verified before starting the iterative process. At each iteration, the searching interval is bisected and the subinterval that satisfied condition (7.27) is selected for further processing, until a set tolerance is matched. For the loading part of the cycle, the initial interval is set between points A and B; for the unloading part, it is set between B and A or between points B and A* if point A exceeds the domain of existence of the yield surface. The advantage of bisection method is that, once the searching interval is set, the successive approximate solutions will always be included in that interval. Thus, it is sufficient to set an adequate interval in the beginning to be sure that the condition of existence of the yield surface will be always satisfied in the successive iterations, while in the precedent Newton-Raphson method such check shall be performed at each iteration. The convergence criterion is checked by substituting the result of a generic iteration $p'_{Y(i)}$ in expression (7.36) and applying criterion (7.30). At the end of the iterative process, the calculated value of p'_Y is substituted into the (7.23) to calculate q_Y.

It is worth noting that the determination of the yield point must be performed at the beginning of each loading and unloading part of the cyclic stress path, i.e. twice per each loading cycle.

7.2.1.3. PURELY ELASTIC BEHAVIOUR

After the yielding point has been calculated, the stress path is divided in the purely elastic part (the interval between the initial stress point and the yielding point) and an elasto-plastic part (from the yielding point to the final point of the stress interval). The elastic part is governed by the linear elastic constitutive relations illustrated in section 6.1.5:

$$\begin{pmatrix}\dot{\varepsilon}_v^e \\ \dot{\varepsilon}_s^e\end{pmatrix} = \begin{bmatrix}1/K'_0 & 0 \\ 0 & 1/3G_0\end{bmatrix}\begin{pmatrix}\dot{p}' \\ \dot{q}\end{pmatrix} \tag{7.37}$$

Since the stiffness moduli are constant, the elastic constitutive equation (7.37) are easily integrated:

$$\begin{aligned}\Delta\varepsilon_v^e &= \frac{1}{K'_0}\Delta p' \\ \Delta\varepsilon_s^e &= \frac{1}{3G_0}\Delta q\end{aligned} \tag{7.38}$$

7.2.1.4. MODIFIED EULER ALGORITHM

When the stress path intersects the yielding surface, the elasto-plastic part of the stress path begins. Since in this case the constitutive equations cannot be integrated in closed form, a numerical algorithm must be used. Modified Euler method is a simple, reliable, second order method for numerical resolution of differential equations commonly used in literature (e.g.: Sloan, 1987; Potts & Ganendra, 1994; Ding et al., 2015; Ghorbani et al., 2016). As aforementioned, the particular formulation of the problem allows the separation of the two contributions: the elastic part is again calculated with the integrated elastic

equations (7.38) and the plastic strain is calculated numerically through the Modified Euler algorithm. The elasto-plastic part of the stress path A-B-A is

$$\Delta\boldsymbol{\sigma}'_s = \boldsymbol{\sigma}'_B - \boldsymbol{\sigma}'_Y \tag{7.39}$$

for the loading part AB.

Following the algorithm, the elasto-plastic stress increment is divided into sub-increments $\Delta\boldsymbol{\sigma}'_{ss}$ as follows:

$$\Delta\boldsymbol{\sigma}'_{ss} = \Delta T \Delta\boldsymbol{\sigma}'_s \tag{7.40}$$

where ΔT is a reducing scalar factor that must be determined iteratively for each substep. The first tentative value of this factor is 1, i.e. the initial value of the sub-increment is set to be equal to the entire elasto-plastic part of the loading stress path. Factor ΔT is sometimes referred to as "dimensionless time" increment (Sloan, 1987), since it can be regarded as an increment of a time variable T, which is equal to 0 at the beginning of the elasto-plastic stress path, and equal to 1 at the end. Although this time variable is defined, it is important to stress the fact that the entire process is time-independent and "time" here is merely a parameter that identifies different states of the system.

Once the size of the substep is set, equations (7.16) are solved over this stress increment. As stated earlier, the elastic strain increments are calculated applying relations (7.38) to the substep:

$$\begin{pmatrix}\Delta\varepsilon_v^e \\ \\ \Delta\varepsilon_s^e\end{pmatrix} = \Delta\boldsymbol{\varepsilon}^e_{ss} = \mathbf{C}^e \Delta\boldsymbol{\sigma}'_{ss} = \begin{pmatrix}\dfrac{1}{K'_0}\Delta p'_{ss} \\ \\ \dfrac{1}{3G_0}\Delta q_{ss}\end{pmatrix} \tag{7.41}$$

The plastic strain increment is calculated through numerical integration using modified Euler method, following the scheme in Fig. 7.3. The plastic constitutive equations are solved in the hypothesis that the plastic compliance matrix calculated in the beginning of the increment ($\mathbf{C}_i^p$) is constant throughout the increment. This is generally not true, thus the same calculation is repeated a second time on the same stress increment using the plastic compliance matrix calculated at the end of the stress increment ($\mathbf{C}_f^p$) and in the same hypothesis of constant compliance matrix. The semi-difference of the two calculations represents the error *E* due to discretization.

The plastic constitutive equations are:

$$\begin{pmatrix}\Delta\varepsilon_v^p \\ \\ \Delta\varepsilon_s^p\end{pmatrix} = \Delta\boldsymbol{\varepsilon}^p_{ss} = \mathbf{C}^p \Delta\boldsymbol{\sigma}'_{ss} = \frac{1}{H_0 + H_b + H'}\begin{pmatrix}\dfrac{\partial f}{\partial p'}\dfrac{\partial g}{\partial p'} & \dfrac{\partial f}{\partial q}\dfrac{\partial g}{\partial p'} \\ \\ \dfrac{\partial f}{\partial p'}\dfrac{\partial g}{\partial q} & \dfrac{\partial f}{\partial q}\dfrac{\partial g}{\partial q}\end{pmatrix}\begin{pmatrix}\Delta p'_{ss} \\ \\ \Delta q_{ss}\end{pmatrix} \tag{7.42}$$

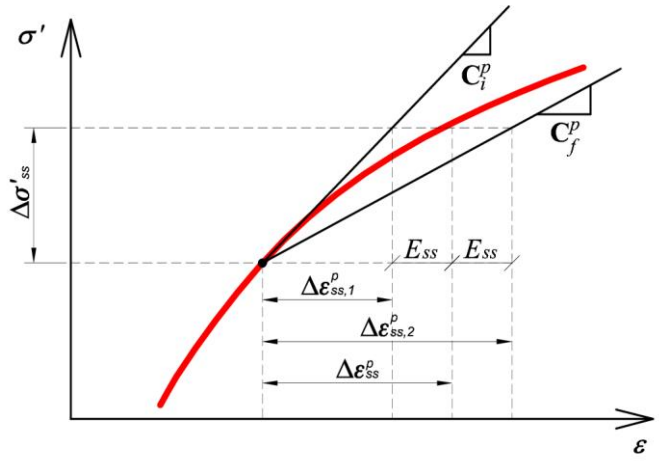

Fig. 7.3 – Modified Euler integration for substepping scheme

In the first calculation, the plastic compliance matrix is calculated in the initial point of the substep:

$$\begin{pmatrix}\Delta\varepsilon^p_{v,1}\\ \Delta\varepsilon^p_{s,1}\end{pmatrix} = \Delta\boldsymbol{\varepsilon}^p_{ss,1} = \mathbf{C}_i^p \Delta\boldsymbol{\sigma}'_{ss} = \\ = \frac{1}{H_{0,i} + H_{b,i} + H'_i}\begin{pmatrix}\left(\frac{\partial f}{\partial p'}\right)_i\left(\frac{\partial g}{\partial p'}\right)_i & \left(\frac{\partial f}{\partial q}\right)_i\left(\frac{\partial g}{\partial p'}\right)_i\\ \left(\frac{\partial f}{\partial p'}\right)_i\left(\frac{\partial g}{\partial q}\right)_i & \left(\frac{\partial f}{\partial q}\right)_i\left(\frac{\partial g}{\partial q}\right)_i\end{pmatrix}\begin{pmatrix}\Delta p'_{ss}\\ \Delta q_{ss}\end{pmatrix} \tag{7.43}$$

Where the components of the hardening modulus, H_0, H_b, and H', are calculated with expressions (6.59), (6.60), and (6.51):

$$H_{0,i} = \frac{1}{\ln(r)}\frac{v_i}{\lambda-\kappa}\left(\frac{\partial g}{\partial p'}\right)_i \tag{7.44}$$

$$H_{b,i} = \left(\frac{\partial f}{\partial p'_0}\right)_i p'_{0unc,i}\, b_0\, e^{-X_i}\left(b_1\left|\frac{\partial g}{\partial p'}\right|_i + b_2\left|\frac{\partial g}{\partial q}\right|_i\right) \tag{7.45}$$

$$H' = \frac{v_i}{\lambda-\kappa}\left(B\frac{b_i}{b_{max,i}}\right)^{\psi} p'^3_{0,i} \tag{7.46}$$

and the partial derivatives of the yield surface and plastic potential are reported in Annex 2. Subscript i indicates the initial point of the substep ($\boldsymbol{\sigma}'_i$), which for the first substep coincides with the yielding point $\boldsymbol{\sigma}'_Y$. The hardening parameters used in the above expression are referred to the size and position of the yield surface at the beginning of the substep ($p'_{0unc,i}$, $p'_{\alpha,i}$, $q_{\alpha,i}$, X_i).

Once the first values of the plastic strain increments have been calculated, the second equation of the (7.16) (hardening parameters) is solved using the stress state at the beginning of the substep and the plastic strain increments calculated in (7.43):

$$\Delta \boldsymbol{h}_1 = \begin{pmatrix} \Delta p'_{0unc,1} \\ \Delta p'_{\alpha,1} \\ \Delta q_{\alpha,1} \\ \Delta X_1 \end{pmatrix} \tag{7.47}$$

Discretizing expressions (6.55), (6.19), and (6.44) one obtains:

$$\Delta p'_{0unc,1} = \frac{v_i}{\lambda - \kappa} p'_{0unc,i}\, \Delta \varepsilon^p_{v,1} \tag{7.48}$$

$$\Delta \boldsymbol{\alpha}_1 = \begin{pmatrix} \Delta p'_{\alpha,1} \\ \Delta q_{\alpha,1} \end{pmatrix} = S_i \boldsymbol{\beta}_i = S_i \begin{pmatrix} \dfrac{p'_i - p'_{\alpha,i}}{R} - \left(p'_i + p'_{t,i}\right) \\ \dfrac{q_i - q_{\alpha,i}}{R} - q_i \end{pmatrix} \tag{7.49}$$

$$\Delta X_1 = b_1 \Delta \left|\varepsilon^p_{v,1}\right| + b_2 \Delta \left|\varepsilon^p_{s,1}\right| \tag{7.50}$$

where:

$$S_i = - \frac{\dfrac{\left(\dfrac{\partial f}{\partial p'}\right)_i \Delta p'_{ss} + \left(\dfrac{\partial f}{\partial q}\right)_i \Delta q_{ss}}{H_{0,i} + H'_i} H'_i}{\left(\dfrac{\partial f}{\partial p'_\alpha}\right)_i \left(\dfrac{p'_i - p'_{\alpha,i}}{R} - \left(p'_i + p'_{t,i}\right)\right) + \left(\dfrac{\partial f}{\partial q_\alpha}\right)_i \left(\dfrac{q_i - q_{\alpha,i}}{R} - q_i\right)} \tag{7.51}$$

In the precedent relations, $p'_{t,i}$ is the value of the tensile strength at the beginning of the substep and shall not be confused with the initial value of the tensile strength p'_{ti}. The two values only coincide in the first substep of the loading stress path of the first cycle, when the specimen is intact.

The stress state and hardening parameters are updated using the increments hereby calculated, in order to obtain the state of stress and yield surface at the end of the substep:

$$\begin{aligned} \boldsymbol{\sigma}'_f &= \boldsymbol{\sigma}'_i + \Delta \boldsymbol{\sigma}'_{ss} \\ p'_{0unc,f} &= p'_{0unc,i} + \Delta p'_{0unc,1} \\ p'_{\alpha,f} &= p'_{\alpha,i} + \Delta p'_{\alpha,1} \\ q_{\alpha,f} &= q_{\alpha,i} + \Delta q_{\alpha,1} \\ X_f &= X_i + \Delta X_1 \end{aligned} \tag{7.52}$$

and consequently:

$$\begin{aligned} p'_{0,f} &= p'_{0unc,f} \left(1 + b_0\, e^{-X_f}\right) \\ p'_{t,f} &= p'_{ti}\, e^{-X_f} \end{aligned} \tag{7.53}$$

These values are used to calculate the matrix of plastic compliance at the end of the substep and using it to obtain a second approximate solution of the constitutive equations:

$$\begin{pmatrix}\Delta\varepsilon_{v,2}^{p}\\ \\ \Delta\varepsilon_{s,2}^{p}\end{pmatrix}=\Delta\boldsymbol{\varepsilon}_{ss,2}^{p}=\mathbf{C}_{f}^{p}\Delta\boldsymbol{\sigma}_{ss}^{\prime}=$$
$$=\frac{1}{H_{0,f}+H_{b,f}+H_{f}^{\prime}}\begin{pmatrix}\left(\frac{\partial f}{\partial p^{\prime}}\right)_{f}\left(\frac{\partial g}{\partial p^{\prime}}\right)_{f} & \left(\frac{\partial f}{\partial q}\right)_{f}\left(\frac{\partial g}{\partial p^{\prime}}\right)_{f}\\ \left(\frac{\partial f}{\partial p^{\prime}}\right)_{f}\left(\frac{\partial g}{\partial q}\right)_{f} & \left(\frac{\partial f}{\partial q}\right)_{f}\left(\frac{\partial g}{\partial q}\right)_{f}\end{pmatrix}\begin{pmatrix}\Delta p_{ss}^{\prime}\\ \\ \Delta q_{ss}\end{pmatrix} \tag{7.54}$$

All the precedent calculations are repeated with the updated values of the stress point and hardening parameters. The new hardening parameters increments are calculated using the strain increment of equation (7.54):

$$\Delta p_{0unc,2}^{\prime}=\frac{v_i}{\lambda-\kappa}p_{0unc,f}^{\prime}\,\Delta\varepsilon_{v,2}^{p} \tag{7.55}$$

$$\Delta\boldsymbol{\alpha}_{2}=\begin{pmatrix}\Delta p_{\alpha,2}^{\prime}\\ \\ \Delta q_{\alpha,2}\end{pmatrix}=S_f\boldsymbol{\beta}_f \tag{7.56}$$

$$\Delta X_2=b_1\Delta\left|\varepsilon_{v,2}^{p}\right|+b_2\Delta\left|\varepsilon_{s,2}^{p}\right| \tag{7.57}$$

At the end of this iteration, the local truncation error estimate (i.e. the error caused by one iteration) is measured as the semi-difference of the two calculated values of the plastic strain. Since the strain vector in axisymmetric conditions is formed by two components, two errors are calculated separately for the two components, and the resulting error is the Euclidian norm of the vector formed by the errors in the two components

$$E_{ss}=\frac{\left\|\Delta\boldsymbol{\varepsilon}_{ss,2}^{p}-\Delta\boldsymbol{\varepsilon}_{ss,1}^{p}\right\|}{2}=\frac{1}{2}\sqrt{\left(\Delta\boldsymbol{\varepsilon}_{v,2}^{p}-\Delta\boldsymbol{\varepsilon}_{v,1}^{p}\right)^{2}+\left(\Delta\boldsymbol{\varepsilon}_{s,2}^{p}-\Delta\boldsymbol{\varepsilon}_{s,1}^{p}\right)^{2}} \tag{7.58}$$

This error shall be less than a set tolerance

$$E_{ss}\leq SSTOL \tag{7.59}$$

If this condition is not respected ($E_{ss}>SSTOL$), the size of the stress increment is reduced by reducing ΔT, and the process is repeated with a new error estimation until the tolerance criterion is satisfied. In the implementation presented by Sloan (1987), a relative error is considered, dividing the absolute error E_{ss} by the stress level at the end of the increment (in that case the method was implemented for strain driven conditions). Adapting this formulation to the present case, the relative error would be:

$$\frac{E_{ss}}{\left\|\boldsymbol{\varepsilon}_{i-1}^{p}+\Delta\boldsymbol{\varepsilon}_{ss}^{p}\right\|} \tag{7.60}$$

In the case of a long-term cyclic test, this relative measure of the error is inadequate because the total plastic strain at the denominator increases for increasing cycles. Thus, after a certain number of cycles, as the plastic strain accumulates, the denominator of the above expression increases. This leads to decreasing values of the relative error with increasing number of cycles, independently from the value of the absolute error estimate E_{ss}. For this reason, the absolute error (which is only dependent on the increment of the substep and not on the accumulated plastic strain) was preferred over the relative error. The value of the tolerance was set as:

$$SSTOL=10^{-10} \tag{7.61}$$

This value is much smaller than the one suggested by many authors (e.g. Sloan, 1987; Potts & Ganendra, 1994; Gens & Potts, 1988). However, conversely to precedent works, the error hereby used is absolute and not relative, thus it is possible that different measures of the tolerance arise. The above value was

determined iteratively through a heuristic approach: the model was implemented in a computer code (Annex 5) and a set of simulated tests was run with the same parameters and initial conditions and varying only the value of $SSTOL$. For each simulation, the corresponding output curve was plotted on the same graph for comparison. The selected value of $SSTOL$ is the value below which no further modifications of the output curve was noted.

In case the iteration does not converge ($E_{ss} > SSTOL$), a new value of ΔT is selected by multiplying the previous value by a reducing factor β:

$$\Delta T_{new} = \beta \Delta T \tag{7.62}$$

Since modified Euler method is a second-order method, the local error is proportional to the square of ΔT (in mathematical notation, the error estimate is $O(\Delta T^2)$). This means that, if ΔT is reduced by a factor β, the corresponding error E_{ss} will be reduced by a factor β^2.

$$E_{SSnew} = \beta^2 E_{ss} \tag{7.63}$$

Since it is required that:

$$E_{SSnew} \leq SSTOL \tag{7.64}$$

Substituting expression (7.63) into (7.64) and rearranging terms, it is:

$$\beta = \left(\frac{SSTOL}{E_{ss}}\right)^{1/2} \tag{7.65}$$

As this is an approximate procedure, a more conservative expression is used:

$$\beta = 0.8\left(\frac{SSTOL}{E_{ss}}\right)^{1/2} \tag{7.66}$$

in order to reduce the number of iterations that are rejected. Additionally, the following restrictions are imposed on the value of β:

$$0.1 \leq \beta \leq 2 \tag{7.67}$$

in order to avoid extreme variations in the size of the substep between two consecutive iterations (Potts & Zdravkovic, 1999).

After the tolerance criterion is satisfied, the position and size of the yield and reference surfaces are updated. The resulting strain and hardening parameters increments for the substep are calculated as the average value of the two aforementioned calculations. The variables at the end of the substep $(i + 1)$ are calculated adding the substep increment to the corresponding value of the variable at the beginning of the substep (i):

$$\begin{gathered}
\boldsymbol{\varepsilon}_{i+1}^{p} = \boldsymbol{\varepsilon}_{i}^{p} + \Delta\boldsymbol{\varepsilon}_{ss}^{p} = \boldsymbol{\varepsilon}_{i}^{p} + \frac{\Delta\boldsymbol{\varepsilon}_{ss,1}^{p} + \Delta\boldsymbol{\varepsilon}_{ss,2}^{p}}{2} \\
\boldsymbol{\varepsilon}_{i+1}^{e} = \boldsymbol{\varepsilon}_{i}^{e} + \Delta\boldsymbol{\varepsilon}_{ss}^{e} \\
\boldsymbol{\varepsilon}_{i+1} = \boldsymbol{\varepsilon}_{i+1}^{e} + \boldsymbol{\varepsilon}_{i+1}^{p} \\
p'_{0unc,i+1} = p'_{0unc,i} + \Delta p'_{0unc} = p'_{0unc,i} + \frac{\Delta p'_{0unc,1} + \Delta p'_{0unc,2}}{2} \\
p'_{\alpha,i+1} = p'_{\alpha,i} + \Delta p'_{\alpha} = p'_{\alpha,i} + \frac{\Delta p'_{\alpha,1} + \Delta p'_{\alpha,2}}{2} \\
q_{\alpha,i+1} = q_{\alpha,i} + \Delta q_{\alpha} = q_{\alpha,i} + \frac{\Delta q_{\alpha,1} + \Delta q_{\alpha,2}}{2} \\
X_{i+1} = X_{i} + \Delta X = X_{i} + \frac{\Delta X_{1} + \Delta X_{2}}{2}
\end{gathered} \tag{7.68}$$

leading to:

$$\begin{gathered}
p'_{0,i+1} = p'_{0unc,i+1}\,(1 + b_0\, e^{-X_{i+1}}) \\
p'_{t,i+1} = p'_{ti}\, e^{-X_{i+1}}
\end{gathered} \tag{7.69}$$

The dimensionless time is update as well:

$$T_{i+1} = T_i + \Delta T \tag{7.70}$$

The iteration process continues with the next substep in the same way described above, until the end of the loading vector is reached ($T = 1$). At each substep, the pseudo-time increment must be selected in order to satisfy:

$$T_{i+1} \leq 1 \tag{7.71}$$

If the condition is not respected, the increment for the next substep is recalculated as:

$$\Delta T = 1 - T_i \tag{7.72}$$

It is worth noting that the dimensionless time increment input value is taken equal to the unity in the first iteration of the first substep. For the subsequent steps, the first value of the new substep is equal to the last value of ΔT in the previous substep. Thus, since the last iteration of a substep is meant to converge, parameter β will be greater than the unity. In this way, ΔT is allowed to progressively increase from a substep to the following (if the soil is becoming stiffer) leading to a better adaptation of the algorithm to the problem and a shorter computation time. In this sense, the lower bound of parameter β expressed in (7.67) is meant to serve as a limitation between two successive iterations of the same substep, while the upper bound (2) certifies that the amplitude of the next substep does not increase too abruptly with respect to the former one.

Potts & Gens (1985) suggest that it is possible that (although the above condition is satisfied) the stress state at the end of the substep, combined with the hardening parameters leads to yield surface drift, i.e. the stress point is no longer on the yield surface at the end of the substep. This error can accumulate with subsequent substeps, leading to increasing errors. The authors provide a consistent and accurate method to deal with this problem. In the present implementation, due to the stress-driven formulation of the problem and the low non-linearity, the condition on the strain error (7.59) is normally sufficient to guarantee that the stress point remains on the yield surface during the loading. The only case in which surface drift can occur is the case in which the plastic response of the model is very stiff and the accumulated plastic strain at the end of a cycle is very small. In such case, the error estimate tends to zero and the tolerance is easily satisfied. This leads to the subdivision of the elasto-plastic interval in a

low number of large substeps and possible yield surface drift. To deal with this problem easily, it is sufficient to add a second convergence criterion on the yield surface f at the end of a substep (Potts & Zdravkovic, 1999):

$$|f(\boldsymbol{\sigma}'_{i+1}, \boldsymbol{h}_{i+1})| \leq YTOL \tag{7.73}$$

This condition is checked only after the strain error criterion is satisfied. As explained, if the hardening of the soil is not extremely high, the verification of condition (7.59) guarantees that this second requirement is also satisfied. In case of extremely high plastic modulus, in which the yield surface translates generating very small plastic strain at each increment (of the order of 10^{-6}), condition (7.73) can be the stricter condition. In such case, the substep is reduced by dividing the pseudo-time increment by 2 and the iteration is repeated. It was observed that:

$$YTOL = 10^{-1} \tag{7.74}$$

is an adequate tolerance to ensure precise results.

When the end of the loading path of a cycle is reached (point B), the increment stress vector is inverted and the unloading path begins. The process illustrated is repeated on path BA, calculating again the yielding point and identifying the purely elastic and the elasto-plastic parts of the unloading path. The elasto-plastic stress increment in the unloading case is:

$$\Delta\boldsymbol{\sigma}'_s = \boldsymbol{\sigma}'_A - \boldsymbol{\sigma}'_Y \tag{7.75}$$

All the steps described earlier are applied until point A is reached; at that point, a loading-unloading stress cycle is completed. The variables are updated and the procedure is repeated for the desired number of stress cycles.

Box 7.1 – Model implementation for stress-driven drained stress path and Modified Euler algorithm

1. Input of the model parameters including size and position of the yield surface; definition of the stress vector $(\boldsymbol{\sigma}'_B - \boldsymbol{\sigma}'_A)$
2. Calculation of the yielding point $\boldsymbol{\sigma}'_Y$ (intersection between stress path and yield surface)
3. Elastic domain$(\boldsymbol{\sigma}'_Y - \boldsymbol{\sigma}'_A)$: computation of elastic strain increment through integration of the elastic constitutive relations
$$\Delta\boldsymbol{\varepsilon}^e_i = \mathbf{C}^e \Delta\boldsymbol{\sigma}'_{YA}$$
4. Elastoplastic domain $(\boldsymbol{\sigma}'_B - \boldsymbol{\sigma}'_Y)$ through substepping algorithm:
   - An initial value for the load increment is set: $\Delta\boldsymbol{\sigma}'_{ss} = \Delta T(\boldsymbol{\sigma}'_B - \boldsymbol{\sigma}'_Y)$, with ΔT=1
   - Numerical integration of the constitutive equations is performed over the load increment with modified Euler method:
$$\Delta\boldsymbol{\varepsilon}^p_{ss,1} = \mathbf{C}^p_i \Delta\boldsymbol{\sigma}'_{ss}$$
$$\Delta\boldsymbol{\varepsilon}^p_{ss,2} = \mathbf{C}^p_f \Delta\boldsymbol{\sigma}'_{ss}$$
   - Two values of the plastic strain increments are computed using the matrix of plastic compliance at the beginning and at the end of the stress increment (see Fig. 7.3)
   - The error associated to the numerical integration is estimated as the semi-difference of the two computed strain increments. Since the strain increment is a two dimensional vector (with isotropic and deviatoric components), the error is the norm of the errors computed in each dimension:
$$E_{ss} = \frac{1}{2}\left\|\Delta\boldsymbol{\varepsilon}^p_{ss,2} - \Delta\boldsymbol{\varepsilon}^p_{ss,1}\right\|$$

- If the error E_{ss} is less than the user defined tolerance ($E_{ss} \leq SSTOL$) then the program proceeds to step 5; else, the load increment is reduced ($\Delta T_{new} < \Delta T$) and the iteration is repeated until the tolerance criterion is met

5. After the end of the iteration, the results of the substep are calculated:
   - Computation of the plastic strain increment as the average of the two increments calculated in the last iteration:

$$\Delta\boldsymbol{\varepsilon}_{ss}^{p} = \frac{1}{2}\left(\Delta\boldsymbol{\varepsilon}_{ss,1}^{p} + \Delta\boldsymbol{\varepsilon}_{ss,2}^{p}\right)$$

   - computation of the elastic strain increment for the substep $\Delta\boldsymbol{\varepsilon}_{ss}^{e}$ using the equations of point 3
   - hardening parameters $(p_0', p_\alpha', q_\alpha)$ are updated
6. Start next substep (repeat steps 4-5) until the end of the stress path $\boldsymbol{\sigma}_B'$ is reached
7. Computation of accumulated strain: $\Delta\boldsymbol{\varepsilon}_{ss} = \Delta\boldsymbol{\varepsilon}_{ss}^{e} + \Delta\boldsymbol{\varepsilon}_{ss}^{p}$
8. Repeat points 2 to 7 for the unloading part of the stress cycle $(\boldsymbol{\sigma}_A' - \boldsymbol{\sigma}_B')$
9. Repeat for n_{cyc} cycles
10. Write results to a .csv text file

7.2.1.5. RUNGE-KUTTA-ENGLAND ALGORITHM

Runge-Kutta (RK) integration scheme is very similar to the modified Euler (ME) method, being both substepping algorithms with error control. While the modified Euler method is a second-order method, the class of Runge-Kutta methods include higher order degrees of integration. In fact, it is possible to say that modified Euler method is a particular implementation of a second-order Runge-Kutta method.

In the modified Euler method, the matrix of plastic compliance was calculated at the beginning and at the end of the substep, and the plastic increment calculated using each of them had the same weight (1/2 each) on the determination of the result:

$$\Delta\boldsymbol{\varepsilon}_{ss}^{p} = \left(\frac{1}{2}\mathbf{C}_i^{p} + \frac{1}{2}\mathbf{C}_f^{p}\right)\Delta\boldsymbol{\sigma}_{ss}' \tag{7.76}$$

In the case of higher order methods, the matrix is still calculated at the opposite end of the sub-increment, but shall also be calculated in some intermediate points. For example, in a 3rd order method, the matrices will be calculated at the beginning, at the end, and at the middle point of the interval:

$$\Delta\boldsymbol{\varepsilon}_{ss}^{p} = \frac{1}{3}\sum_{k=1}^{3}\mathbf{C}_k^{p}\,\Delta\boldsymbol{\sigma}_{ss}' \tag{7.77}$$

Note that in the above formulation, the three matrices have the same weight in the determination of the result. It is understandable that each point can have a different weight on the determination of the result; the matrix calculated in the central point should have a greater weight than the matrices in the extreme points, since the central point is likely to be more representative of the result than the extreme points. These weights and the position of the points at which the compliance matrices are calculated (also called nodes) are not uniquely defined and differ by different authors. For example, in the above formulation the central matrix could have a weight equal to twice the weight of the extreme points (i.e. the three matrices would be multiplied by 1/4, 1/2, and 1/4, respectively). For higher-order methods, the range of possible implementations is wider. Furthermore, the nodes are not known a priori. In the ME method, the results of the first calculation were used to calculate a tentative end point of the interval (with a tentative strain increment and a tentative set of hardening parameters). This point was in turn the point in which the second matrix was calculated. In higher order methods, the nodes are progressively calculated starting from the node at the beginning of the interval and combining the already calculated

nodes with an interpolating law that is not predetermined. Thus, different implementations exist even for schemes of the same order; each implementation uses a specific set of nodes, weights, and interpolations. In the present work, the implementation presented by England (1969) has been implemented, hence the name Runge-Kutta-England (RKE). In a general way, it is possible to state that higher-order methods require more computation time to perform a single iteration (as the number of matrices to calculate is higher) but give a smaller error; thus, less iterations are needed for convergence and the size of the increment can be greater than lower-order methods. The total computational time depends on the type of problem that shall be solved.

The present implementation is a 5th order RKE method with error control, following the method described in Sloan (1987). The solving 5th order expressions are:

$$\begin{aligned} \boldsymbol{\varepsilon}_{i+1}^{p} &= \boldsymbol{\varepsilon}_{i}^{p} + \frac{1}{336}\left(14\Delta\boldsymbol{\varepsilon}_{1}^{p} + 35\Delta\boldsymbol{\varepsilon}_{4}^{p} + 162\Delta\boldsymbol{\varepsilon}_{5}^{p} + 125\Delta\boldsymbol{\varepsilon}_{6}^{p}\right) \\ \boldsymbol{h}_{i+1} &= \boldsymbol{h}_{i} + \frac{1}{6}(14\Delta\boldsymbol{h}_{1} + 35\Delta\boldsymbol{h}_{4} + 162\Delta\boldsymbol{h}_{5} + 125\Delta\boldsymbol{h}_{6}) \end{aligned} \tag{7.78}$$

The strain and hardening parameter increments shall be evaluated 6 times. It is important to note that the order of the method (d) is not always equal to the number of evaluations ($\bar{s}$). In fact, generally it is $\bar{s} \geq d$. In particular, it is necessary to perform six evaluations in order to produce a 5th Runge-Kutta type method (Butcher, 1965, apud England, 1969). To evaluate the six increments, the same constitutive relations of the precedent case are used:

$$\Delta\boldsymbol{\varepsilon}_{ss,k}^{p} = \mathbf{C}^{p}(\boldsymbol{\sigma}_{k}', \boldsymbol{h}_{k})\Delta\boldsymbol{\sigma}_{ss}' \tag{7.79}$$

$$\Delta p_{0unc,k}' = \frac{v_i}{\lambda - \kappa} p_{0unc,k}' \, \Delta\varepsilon_{v,k}^{p} \tag{7.80}$$

$$\Delta\boldsymbol{\alpha}_{k} = S_{k}\boldsymbol{\beta}_{k} \tag{7.81}$$

$$\Delta X_{k} = b_{1}\Delta\left|\varepsilon_{v,k}^{p}\right| + b_{2}\Delta\left|\varepsilon_{s,k}^{p}\right| \tag{7.82}$$

With $k = 1 \ldots 6$. The coordinates of the six nodes are:

$$\begin{aligned} &\boldsymbol{\sigma}_{1}' = \boldsymbol{\sigma}_{i}' \quad ; \quad \boldsymbol{\sigma}_{2}' = \boldsymbol{\sigma}_{i}' + \tfrac{1}{2}\Delta\boldsymbol{\sigma}_{ss}' \quad ; \quad \boldsymbol{\sigma}_{3}' = \boldsymbol{\sigma}_{i}' + \tfrac{1}{4}(\Delta\boldsymbol{\sigma}_{ss}' + \Delta\boldsymbol{\sigma}_{ss}') \\ &\boldsymbol{\sigma}_{4}' = \boldsymbol{\sigma}_{i}' - \Delta\boldsymbol{\sigma}_{ss}' + \mathbf{2}\Delta\boldsymbol{\sigma}_{ss}' \quad ; \quad \boldsymbol{\sigma}_{5}' = \boldsymbol{\sigma}_{i}' + \tfrac{1}{27}(7\Delta\boldsymbol{\sigma}_{ss}' + 10\Delta\boldsymbol{\sigma}_{ss}' + \Delta\boldsymbol{\sigma}_{ss}') \\ &\boldsymbol{\sigma}_{6}' = \boldsymbol{\sigma}_{i}' + \frac{1}{625}(28\Delta\boldsymbol{\sigma}_{ss}' - 125\Delta\boldsymbol{\sigma}_{ss}' + 546\Delta\boldsymbol{\sigma}_{ss}' + 54\Delta\boldsymbol{\sigma}_{ss}' - 378\Delta\boldsymbol{\sigma}_{ss}') \end{aligned} \tag{7.83}$$

$$\begin{aligned} &\boldsymbol{h}_{1} = \boldsymbol{h}_{i} \quad ; \quad \boldsymbol{h}_{2} = \boldsymbol{h}_{i} + \tfrac{1}{2}\Delta\boldsymbol{h}_{1} \quad ; \quad \boldsymbol{h}_{3} = \boldsymbol{h}_{i} + \tfrac{1}{4}(\Delta\boldsymbol{h}_{1} + \Delta\boldsymbol{h}_{2}) \\ &\boldsymbol{h}_{4} = \boldsymbol{h}_{i} - \Delta\boldsymbol{h}_{2} + \mathbf{2}\Delta\boldsymbol{h}_{3} \quad ; \quad \boldsymbol{h}_{5} = \boldsymbol{h}_{i} + \tfrac{1}{27}(7\Delta\boldsymbol{h}_{1} + 10\Delta\boldsymbol{h}_{2} + \Delta\boldsymbol{h}_{4}) \\ &\boldsymbol{h}_{6} = \boldsymbol{h}_{i} + \frac{1}{625}(28\Delta\boldsymbol{h}_{1} - 125\Delta\boldsymbol{h}_{2} + 546\Delta\boldsymbol{h}_{3} + 54\Delta\boldsymbol{h}_{4} - 378\Delta\boldsymbol{h}_{5}) \end{aligned} \tag{7.84}$$

As stated above, each node is calculated as an interpolation of the precedent nodes and their estimated increments. In the case of the stress vector, the increment is always $\Delta\boldsymbol{\sigma}_{ss}'$ as it is the defined stress increment for the substep. Thus, in the evaluation k, the plastic compliance matrix is calculated using the stress $\boldsymbol{\sigma}_{k}'$, and the hardening moduli corresponding to terms ($\boldsymbol{\varepsilon}_{k}^{p}$, $\boldsymbol{h}_{k}$) (from the (7.83)). Then, the increments $\Delta\boldsymbol{\varepsilon}_{k}^{p}$ and $\Delta\boldsymbol{h}_{k}$ are calculated using relations (7.79) to (7.82). Finally, the stress, strain and hardening moduli of the next evaluation ($\boldsymbol{\sigma}_{k+1}'$, $\boldsymbol{\varepsilon}_{k+1}^{p}$, $\boldsymbol{h}_{k+1}$) are calculated with the (7.83), using the values and the increments of the current and the precedent evaluations. The six computed values are used in (7.78) to calculate the variables at the end of the sub-increment.

In order to estimate the local truncation error, it is necessary to compare the results of the 5th order method with a similar 4th order method. The error estimate is the difference of the increments obtained with the two methods. The 4th order expressions are:

$$\begin{aligned} \boldsymbol{\varepsilon}_{i+1}^{p\ (4)} &= \boldsymbol{\varepsilon}_i^p + \frac{1}{6}\left(\Delta\boldsymbol{\varepsilon}_1^p + 4\Delta\boldsymbol{\varepsilon}_3^p + \Delta\boldsymbol{\varepsilon}_4^p\right) \\ \boldsymbol{h}_{i+1}{}^{(4)} &= \boldsymbol{h}_i + \frac{1}{6}(\Delta\boldsymbol{h}_1 + 4\Delta\boldsymbol{h}_3 + \Delta\boldsymbol{h}_4) \end{aligned} \tag{7.85}$$

Where the increments are the same as the precedent method. Subtracting the two solutions, the local truncation error estimate is:

$$E_{ss} = \left\| \boldsymbol{\varepsilon}_{i+1}^{p\ (5)} - \boldsymbol{\varepsilon}_{i+1}^{p\ (4)} \right\| = \frac{1}{336}\left\| -42\Delta\boldsymbol{\varepsilon}_1^p - 224\Delta\boldsymbol{\varepsilon}_3^p - 21\Delta\boldsymbol{\varepsilon}_4^p + 162\Delta\boldsymbol{\varepsilon}_5^p + 125\Delta\boldsymbol{\varepsilon}_6^p \right\| \tag{7.86}$$

In this case, the error estimate is $O(\Delta T^5)$. Thus, if the iteration does not converge, the correction factor β is:

$$\beta = 0.8\left(\frac{SSTOL}{E_{ss}}\right)^{1/5} \tag{7.87}$$

Hence, a faster convergence of a higher-order method. The rest of the process is the same described in the precedent sections.

7.2.1.6. General formulation of a Runge-Kutta algorithm

The general formulation of a RK algorithm of order d with $\bar{s}$ evaluations is described in England (1969). The solving equations, applied at the present case, are:

$$\boldsymbol{\varepsilon}_{i+1}^p = \boldsymbol{\varepsilon}_i^p + \sum_{k=1}^{\bar{s}} A_k \Delta\boldsymbol{\varepsilon}_k^p \tag{7.88}$$

$$\boldsymbol{h}_{i+1} = \boldsymbol{h}_i + \sum_{k=1}^{\bar{s}} A_k \Delta\boldsymbol{h}_k \tag{7.89}$$

where A_k is the generic element of the vector $\boldsymbol{A}_w$ of the weights of the nodes and:

$$\begin{aligned} \Delta\boldsymbol{\varepsilon}_k^p &= \mathbf{C}^p(\boldsymbol{\sigma}'_k, \boldsymbol{h}_k)\Delta\boldsymbol{\sigma}'_{ss} \\ \Delta\boldsymbol{h}_k &= \mathbf{Q}^{ep}(\boldsymbol{\sigma}'_k, \boldsymbol{h}_k)\Delta\boldsymbol{\sigma}'_{ss} \end{aligned} \tag{7.90}$$

That is, the matrices $\mathbf{C}_k^p$ and $\mathbf{Q}_k^{ep}$ are calculated in the $\bar{s}$ nodes $\left(\boldsymbol{\sigma}_k^{'}, \boldsymbol{h}_k\right)$, which are in turn determined progressively starting from the beginning of the sub-increment and with linear interpolations of the already determined nodes:

$$\begin{aligned} \boldsymbol{\sigma}'_k &= \boldsymbol{\sigma}'_i + \sum_{j=1}^{\bar{s}} a_{kj}\Delta\boldsymbol{\sigma}'_{ss} \\ \boldsymbol{h}_k &= \boldsymbol{h}_i + \sum_{j=1}^{\bar{s}} a_{kj}\Delta\boldsymbol{h}_k \end{aligned} \tag{7.91}$$

Where a_{kj} is the generic element of the so-called Runge-Kutta matrix $\mathbf{A}_{RK}$, which is a square matrix containing the interpolating factors for the determination of the nodes. For $j > k$, it is $a_{kj} = 0$, because each node shall depend only on the precedent. To estimate the local truncation error of a RK method of

order d, the corresponding method of order $(d-1)$ shall be implemented and the error shall be calculated as the difference between the solutions found with the higher-order and the lower-order methods. The lower-order method is implemented using the same Runge-Kutta matrix and a new vector of the weights $\boldsymbol{a}_w = (a_k)$. The local truncation error is:

$$E_{ss} = \left\| \sum_{k=1}^{\bar{s}} (A_k - a_k) \Delta \boldsymbol{\varepsilon}_k^p + O(\Delta T^d) \right\| \tag{7.92}$$

and, consequently:

$$\beta = 0.8 \left(\frac{SSTOL}{E_{ss}} \right)^{1/d} \tag{7.93}$$

This general formulation is particularly convenient when a method has to be implemented in a computer code, since the relations are the same. It is only sufficient to load the Runge-Kutta matrix and the vectors of the weights for the two solutions, and different methods can be implemented. In the case of the 5th order RKE method described in the precedent section, one shall specify the order $(d = 5)$ and the required evaluations $(\bar{s} = 6)$ and specify the required input variables as follows:

$$\mathbf{A}_{RK} = \begin{pmatrix} 0 & & & & & \\ 1/2 & 0 & & 0 & & \\ 1/4 & 1/4 & 0 & & & \\ 0 & -1 & 2 & 0 & & \\ 7/27 & 10/27 & 0 & 1/27 & 0 & \\ 28/625 & -125/625 & 546/625 & 54/625 & -378/625 & 0 \end{pmatrix}$$

$$\boldsymbol{A}_w = \begin{pmatrix} 1/24 \\ 0 \\ 0 \\ 5/48 \\ 27/56 \\ 125/336 \end{pmatrix} \quad \boldsymbol{a}_w = \begin{pmatrix} 1/6 \\ 0 \\ 2/3 \\ 1/6 \\ 0 \\ 0 \end{pmatrix} \tag{7.94}$$

As stated above, modified Euler method is a particular RK method with $d = \bar{s} = 2$. Thus, it can be implemented in the general framework with the following input:

$$\mathbf{A}_{RK} = \begin{pmatrix} 0 & 0 \\ 1 & 0 \end{pmatrix}$$

$$\boldsymbol{A}_w = \begin{pmatrix} 1/2 \\ 1/2 \end{pmatrix} \quad \boldsymbol{a}_w = \begin{pmatrix} 1 \\ 0 \end{pmatrix} \tag{7.95}$$

This general formulation is very convenient because it allows switching between different implementations by changing the set of the two vectors and the RK matrix, allowing for an improved generality in computer coding.

7.2.2. UNDRAINED CYCLIC TRIAXIAL STRESS PATH

In an undrained test, the variation of pore water pressure Δu leads to an unknown value of p'. Thus, while the total stress path is still inclined at a slope of 3:1 in the $p' - q$ plane, the drained stress path is

unknown a priori. Nevertheless, an additional boundary condition is defined, stating that volumetric strain shall be nil, which compensate the fact that the state of stress is only partially known.

When the stress state is in the purely elastic domain, the stress path is parallel to the q-axis in the $p' - q$ plane, i.e. the variation of effective mean stress is zero. This statement is evident considering that, when the soil is in the purely elastic state, the only possible strain is elastic. Thus, since the total volumetric strain is zero, also the elastic volumetric strain is nil. Substituting this value in the first of the elastic constitutive equations (7.37), it is $\dot{p}' = 0$ (regardless the definition of the bulk modulus K').

After yielding, when the stress point is in the elasto-plastic domain, although the total volumetric strain is still zero, elastic and plastic volumetric strain occur. Since their sum is nil, it is:

$$\dot{\varepsilon}_v = \dot{\varepsilon}_v^e + \dot{\varepsilon}_v^p = 0 \tag{7.96}$$

and, consequently:

$$\dot{\varepsilon}_v^p = -\dot{\varepsilon}_v^e \tag{7.97}$$

Rewriting the constitutive equations (7.12):

$$\begin{pmatrix} \dot{\varepsilon}_v \\ \dot{\varepsilon}_s \end{pmatrix} = \mathbf{C}^{ep} \begin{pmatrix} \dot{p}' \\ \dot{q} \end{pmatrix} = \begin{bmatrix} C_{11}^{ep} & C_{12}^{ep} \\ C_{21}^{ep} & C_{22}^{ep} \end{bmatrix} \begin{pmatrix} \dot{p}' \\ \dot{q} \end{pmatrix} = \begin{pmatrix} C_{11}^{ep}\dot{p}' + C_{12}^{ep}\dot{q} \\ C_{21}^{ep}\dot{p}' + C_{22}^{ep}\dot{q} \end{pmatrix} \tag{7.98}$$

Substituting $\dot{\varepsilon}_v = 0$ and rearranging the first equation, one obtains:

$$\dot{p}' = -\frac{C_{12}^{ep}}{C_{11}^{ep}}\dot{q} \tag{7.99}$$

Substituting this result into the second equation, it is:

$$\dot{\varepsilon}_s = -\frac{C_{12}^{ep}C_{21}^{ep}}{C_{11}^{ep}}\dot{q} + C_{22}^{ep}\dot{q} = \frac{C_{11}^{ep}C_{22}^{ep} - C_{12}^{ep}C_{21}^{ep}}{C_{11}^{ep}}\dot{q} = \frac{\det(\mathbf{C}^{ep})}{C_{11}^{ep}}\dot{q} \tag{7.100}$$

where $\det(\mathbf{C}^{ep})$ is the determinant of the stiffness matrix.

In this way, the unknown ($\dot{p}'$ and $\dot{\varepsilon}_s$) are written in terms of the driving stress $\dot{q}$. The pore-water pressure increment is defined as the difference between the increments in the total and the effective mean stress:

$$\dot{u} = \dot{p} - \dot{p}' \tag{7.101}$$

Remembering that the total stress path is a straight line inclined at 3:1 in the p'-q plane, one can write

$$\dot{p} = \frac{\dot{q}}{3} \tag{7.102}$$

and

$$\dot{u} = \left(\frac{1}{3} - \frac{\det(\mathbf{C}^{ep})}{C_{11}^{ep}}\right)\dot{q} \tag{7.103}$$

Writing the expression for a generic finite increment i, one obtains the following system of constitutive equations:

$$\begin{aligned} \Delta p_i' &= -\frac{C_{12}^{ep}}{C_{11}^{ep}}\Delta q_i \\ \Delta \varepsilon_{s,i} &= \frac{\det(\mathbf{C}^{ep})}{C_{11}^{ep}}\Delta q_i \end{aligned} \tag{7.104}$$

$$\Delta \boldsymbol{h}_i = \mathbf{Q}^{ep} \Delta \boldsymbol{\sigma}'_i$$

where the third relation has the same meaning explained in the drained case - expressions (7.16) and (7.17).

Consequently, pore water pressure variation is:

$$\Delta u_i = \left(\frac{1}{3} - \frac{\det(\mathbf{C}^{ep})}{C_{11}^{ep}} \right) \Delta q_i \tag{7.105}$$

As in the drained case, the matrices cannot be integrated along the stress path and an approximate solution through a numerical method shall be sought. Also in this case, a substepping algorithm has been adopted. The complete implementation of the undrained stress path follows the same procedure described for the drained case, except for some differences that will be described hereafter.

7.2.2.1. YIELD POINT

In this case, the purely elastic stress path follows a vertical line (constant p') in the $p' - q$ plane. The yield point is calculated as the intersection between this stress path and the yield surface. Since p'_Y is known (being equal to the effective mean stress at the beginning of the elastic path), the only unknown is q_Y and the solving equation has a closed-form solution:

$$\left(\frac{|q_Y - q_\alpha|}{M(p'_Y - p'_\alpha)} \right)^{\bar{n}} + \frac{1}{\ln r} \ln \frac{p'_Y - p'_\alpha}{R p'_0} = 0 \tag{7.106}$$

$$q_{Y\ \substack{load \\ unload}} = q_\alpha \pm M(p'_Y - p'_\alpha) \left(-\frac{1}{\ln r} \ln \frac{p'_Y - p'_\alpha}{R p'_0} \right)^{1/\bar{n}} \tag{7.107}$$

where the two solutions refer to the case of a loading and an unloading stress path, respectively.

7.2.2.2. EXPLICIT SUBSTEPPING ALGORITHM

The algorithm is applied similarly to the drained case, using the general formulation described in 7.2.1.6 with equations (7.104). In this case, the sub-increment is referred solely to the deviatoric stress:

$$\Delta q_{ss} = \Delta T \, \Delta q_s \tag{7.108}$$

In undrained conditions, elastic and plastic contributions cannot be decoupled. Thus, the matrix of elasto-plastic compliance should be calculated, by summing the elastic matrix $\mathbf{C}^e$ (reported in (7.37)) and the plastic matrix $\mathbf{C}^p$ (relation (7.43)). With the same notation used in 7.2.1.6, the equations become:

$$\begin{aligned} p'_{i+1} &= p'_i + \sum_{k=1}^{s} A_k \Delta p'_k \\ \varepsilon_{s,i+1} &= \varepsilon_{s,i} + \sum_{k=1}^{s} A_k \Delta \varepsilon_{s,k} \\ \boldsymbol{h}_{i+1} &= \boldsymbol{h}_i + \sum_{k=1}^{s} A_k \Delta \boldsymbol{h}_k \end{aligned} \tag{7.109}$$

and:

$$\begin{aligned}\Delta p'_k &= -\frac{C_{12}^{ep}(\boldsymbol{\sigma}'_k, \boldsymbol{h}_k)}{C_{11}^{ep}(\boldsymbol{\sigma}'_k, \boldsymbol{h}_k)}\Delta q_{ss} \\ \Delta \varepsilon_{s,k} &= \frac{\det(\mathbf{C}^{ep}(\boldsymbol{\sigma}'_k, \boldsymbol{h}_k))}{C_{11}^{ep}(\boldsymbol{\sigma}'_k, \boldsymbol{h}_k)}\Delta q_{ss} \\ \Delta \boldsymbol{h}_k &= \mathbf{Q}^{ep}(\boldsymbol{\sigma}'_k, \boldsymbol{h}_k)\Delta \boldsymbol{\sigma}'_{ss}\end{aligned} \tag{7.110}$$

The coordinates of the nodes are calculated as reported in (7.91) with a small difference for the two components of the state of stress:

$$\begin{aligned}p'_k &= p'_i + \sum_{j=1}^{s} a_{kj}\Delta p'_k \\ q_k &= q_i + \sum_{j=1}^{s} a_{kj}\Delta q_{ss}\end{aligned} \tag{7.111}$$

because in this case the deviatoric stress increment is a known input while the mean effective stress is an unknown with k estimates.

In order to compute the increments of the hardening parameters, the volumetric and deviatoric plastic strain increment shall be known - see relations (7.48) and (7.50). They can be calculated using equations (7.42), after the effective mean stress increment being determined.

7.3. MODEL IMPLEMENTATION FOR STRAIN-DRIVEN MONOTONIC TRIAXIAL TESTS

In this case, the constitutive equations in the form of the expressions (7.1) to (7.11) are used in this case. For axisymmetric conditions, the discretized constitutive equations [the first of (7.11)] become:

$$\begin{pmatrix}\Delta p'_i \\ \Delta q_i\end{pmatrix} = \mathbf{D}^{ep}\begin{pmatrix}\Delta \varepsilon_{vi} \\ \Delta \varepsilon_{si}\end{pmatrix} = \begin{bmatrix}D_{11}^{ep} & D_{12}^{ep} \\ D_{21}^{ep} & D_{22}^{ep}\end{bmatrix}\begin{pmatrix}\Delta \varepsilon_{vi} \\ \Delta \varepsilon_{si}\end{pmatrix} = \begin{pmatrix}D_{11}^{ep}\Delta \varepsilon_{vi} + D_{12}^{ep}\Delta \varepsilon_{si} \\ D_{21}^{ep}\Delta \varepsilon_{vi} + D_{22}^{ep}\Delta \varepsilon_{si}\end{pmatrix} \tag{7.112}$$

while the expression of the plastic multiplier (7.7) becomes:

$$\dot{\Lambda} = \frac{\frac{\partial f}{\partial p'}K'\dot{\varepsilon}_v + \frac{\partial f}{\partial q}3G\dot{\varepsilon}_s}{H + \frac{\partial f}{\partial p'}K'\frac{\partial g}{\partial p'} + \frac{\partial f}{\partial q}3G\frac{\partial g}{\partial q}} \tag{7.113}$$

Where the elastic stiffness matrix $\mathbf{D}^e$ is the inverse of the matrix of elastic compliance (7.37):

$$\mathbf{D}^e = \begin{bmatrix}K' & 0 \\ 0 & 3G\end{bmatrix} \tag{7.114}$$

Replacing expression (7.113) and (6.19) in (6.20), one can determine the value of the scalar S (already defined in (6.21) for the stress-driven case) in terms of strain increments:

$$S = -\frac{H'}{H + \frac{\partial f}{\partial p'}K'\frac{\partial g}{\partial p'} + \frac{\partial f}{\partial q}3G\frac{\partial g}{\partial q}}\frac{\frac{\partial f}{\partial p'}K'\dot{\varepsilon}_v + \frac{\partial f}{\partial q}3G\dot{\varepsilon}_s}{\frac{\partial f}{\partial p'_\alpha}\beta_{p'} + \frac{\partial f}{\partial q_\alpha}\beta_q} \tag{7.115}$$

Conversely to expression (6.21), this expression is determined for $H = 0$.

Conventional strain-driven triaxial tests are performed with a controlled axial (vertical) strain increment ($\Delta\varepsilon_a$), varying from 0 to a user-defined value, and a constant cell pressure ($\Delta\sigma_3 = 0$). From the basic relations reported in Annex 1, the above constitutive relations can be rewritten as follows:

$$\begin{pmatrix} \frac{\Delta\sigma'_{1i} + 2\Delta\sigma'_{3i}}{3} \\ \Delta\sigma'_{1i} - \Delta\sigma'_{3i} \end{pmatrix} = \begin{pmatrix} \left(D_{11}^{ep} - \frac{1}{3}D_{12}^{ep}\right)\Delta\varepsilon_{vi} + D_{12}^{ep}\Delta\varepsilon_{ai} \\ \left(D_{21}^{ep} - \frac{1}{3}D_{22}^{ep}\right)\Delta\varepsilon_{vi} + D_{22}^{ep}\Delta\varepsilon_{ai} \end{pmatrix} \tag{7.116}$$

Depending on the drainage conditions, different solutions are derived.

7.3.1. DRAINED TRIAXIAL STRESS PATH

The boundary conditions imposed in this case is:

$$\Delta u_i = 0 \tag{7.117}$$

which, combined with the constant cell pressure condition, results in:

$$\Delta\sigma'_{3i} = 0 \tag{7.118}$$

Substituting in the constitutive equation and rearranging them, one obtains the variation of the unknown variables as a function of the driving strain:

$$\begin{pmatrix} \Delta\sigma'_{1i} \\ \Delta\varepsilon_{vi} \end{pmatrix} = \frac{3}{9D_{11}^{ep} - 3D_{12}^{ep} - 3D_{21}^{ep} + D_{22}^{ep}} \begin{pmatrix} 3\,\det(\mathbf{D}^{ep}) \\ D_{22}^{ep} - 3D_{12}^{ep} \end{pmatrix} \Delta\varepsilon_{ai} \tag{7.119}$$

Consequently, the stress and strain components are determined:

$$\begin{aligned} \Delta p'_i &= \frac{\Delta\sigma'_{1i}}{3} \\ \Delta q_i &= \Delta\sigma'_{1i} \\ \Delta\varepsilon_{si} &= \Delta\varepsilon_{ai} - \frac{\Delta\varepsilon_{vi}}{3} \end{aligned} \tag{7.120}$$

Basing on these equations, the Modified Euler method was implemented on the strain path AB as described in section 7.2, with minor adjustments.

The yield point calculation and the computation of the purely elastic part is the same reported in sections 7.2.1.1 - 7.2.1.3. Since the purely elastic constitutive relations are linear, it is possible to use the matrix of elastic compliance and apply the constitutive relations between the initial and the yield stresses. It is important to check that the axial strain at the end of the purely elastic domain ε_{aY} (i.e. the strain corresponding to the yield stress) is less than the corresponding final elastic strain ε_{aB} for the particular test. This requirement is usually satisfied because of the reduced size of the yield surface.

As for the elasto-plastic domain, the Modified Euler method is applied as in paragraph 7.2.1.4, considering that the driving variable is the axial strain. Thus, the size of the elasto-plastic domain is given by:

$$\Delta\varepsilon_{as} = \varepsilon_{aB} - \varepsilon_{aY} \tag{7.121}$$

which is divided into sub-increments:

$$\Delta\varepsilon_{ass} = \Delta T\Delta\varepsilon_{as} \tag{7.122}$$

The method is implemented using the above constitutive relations and the hardening parameters increments are calculated using expressions (7.48) - (7.50) and (7.55) - (7.57). Scalar S is calculated discretizing expression (7.118). Local truncation error estimate is calculated as:

$$E_{ss} = \frac{\Delta\sigma'_{1,2} - \Delta\sigma'_{1,1}}{2} \tag{7.123}$$

In the present case, the relative error has shown to give a better control of the algorithm precision:

$$R_{ss} = \frac{E_{ss}}{\sigma'_{1,i-1} + \Delta\sigma'_{1,ss}} < SSTOL \tag{7.124}$$

The tolerance was set as $SSTOL = 10^{-9}$. As in the former case, this value was determined iteratively by running the same simulated test with different values of tolerance and comparing the corresponding output curves, until a tolerance that guaranteed a stable solution was determined. Also in this case, a convergence criterion on the yield surface is added, as reported in expressions (7.73) and (7.74).

7.3.2. UNDRAINED TRIAXIAL STRESS PATH

In this case, the variation of volumetric strain is nil. This implies than the distortional strain is equal to the axial strain, and the constitutive relations reduce to:

$$\begin{pmatrix} \Delta p'_i \\ \Delta q_i \end{pmatrix} = \begin{pmatrix} D_{12}^{ep} \\ D_{22}^{ep} \end{pmatrix} \Delta\varepsilon_{ai} \tag{7.125}$$

The method is applied as in the precedent cases and the relative error estimate is calculated as in the previous case. Pore pressure variation is calculated as the difference between the total and the effective mean stress increment:

$$\Delta u = \Delta q/3 - \Delta p'_i \tag{7.126}$$

7.4. CONCLUSIONS

The numerical implementation of the model was presented in this chapter. Implicit and explicit methods were described, and the main advantages and disadvantages highlighted.

In the present work, an explicit substepping algorithm was implemented using two different algorithms for the numerical integration of the constitutive equations: a second order modified Euler (ME) algorithm and a fifth order Runge-Kutta-England (RKE) algorithm. Following substepping algorithm, the problem is divided in a set of finite increments and an approximate solution for the system of differential equations is calculated in each interval along an incremental stress or strain path, using one of the two aforementioned integration methods. The two algorithms were implemented for stress-driven and for strain-driven triaxial stress paths in undrained and drained conditions. The constitutive equations were written in a suitable form for each of these boundary conditions in order to ease the implementation of the algorithm.

The comparison between the two integration methods showed that, for a given precision, the higher-order RKE method requires more calculations at each interval, but allows for a discretization in a smaller number of intervals (i.e. intervals with higher amplitude) with respect to the lower order ME method. Thus, RKE method is preferable in cases with high non-linearity and long stress paths. In the case of the stress-driven cyclic tests, ME method is preferable, because the maximum size of an interval is limited to the amplitude of the loading or unloading part of each cycles. With RKE method and the selected precision, a single interval would be greater than this amplitude. Thus, the increased computational time is not compensated by a faster progression of the algorithm. In the case of strain-driven monotonic tests, the performance of the two methods is comparable. For this reason, ME algorithm was used for

successive model implementation. Nevertheless, RKE method was often used during the analyses to validate the results obtained with the simpler method.

Chapter 8.

PERFORMANCE OF THE MODEL

In the present chapter, the performance of the model described in Chapter 6 and numerically implemented as illustrated in Chapter 7 is studied. In the first section, the model is validated by modelling a group of monotonic triaxial tests. These tests were used in a previous work to calibrate a single surface CASM model in cemented conditions. Through the comparison of the two models, the present implementation will be validated and its state variables initialized.

The following sections of the chapter explore the performance of the model in cyclic triaxial conditions. The model response is firstly assessed in the stress-strain plane, where the hysteretic loops generated by the model are analysed. Then, attention is focused on the model output in terms of accumulation curves, that is, the curves showing the accumulation of axial and volumetric strain with the number of loading cycles. This second analysis is less detailed but more concise than the previous one, as it envisages only the accumulated strain at the end of each cycle, without detailing the loading and unloading phase of each cycle. A complete parametric analysis is performed though various sets of simulated cyclic triaxial tests, in which one parameter is changed in turn, keeping the others fixed.

Finally, the model is calibrated against the long-term cyclic triaxial tests presented in Chapter 5 and some minor modifications of the model are presented, with the aim to address the issues raised during the calibration process with the original model.

8.1. MODEL INITIALIZATION AND VALIDATION THROUGH MONOTONIC TRIAXIAL TESTS

The numerical implementation of the model described in Chapter 7 is validated by calibrating it against monotonic drained and undrained triaxial tests results presented by Rios et al. (2014). As reported in 2.5.3, the tests were already modelled using CASM-n model (Yu et al., 2007b) in Rios et al. (2016). Since the present model is based on a CASM-n model with a similar damage law and a kinematic hardening extension, some of the parameters calibrated in Rios et al. (2016) are adopted in the present formulation. It is expected that the large-strain response (corresponding to the post-yield response in single-surface models or the response when the surfaces are in contact in view of the two-surface formulation) is the same in the two models, whereas it may be different in the small-strain behaviour (when the surfaces are not in contact). In fact, in a single surface approach like the CASM-n model, this domain is considered elastic, while in the present model the kinematic yield law produces plastic strain from an early stage of deformation. As explained in section 6.3, a staged approach is followed for the initialization of the five state variables and the calibration of the 13 model parameters reported in Table 6.1.

8.1.1. INITIALIZATION OF SURFACE SIZE IN UNCEMENTED SOIL

The initial value of the horizontal axis of the uncemented surface, p'_{0unc_i}, is calculated as the intersection between the normal compression line (NCL) of the uncemented soil and a swelling line passing through the point defining the initial state of the specimen (v_i, p'_i). The following well-known expression is used:

$$p'_{0unc\_i} = \exp\left(\frac{N - v_i - \kappa \ln p'_{ref}}{\lambda - \kappa}\right) \tag{8.1}$$

In this expression, initial specific volume v_i is known for each specimen and the reference pressure value p'_{ref} is conventionally assumed equal to 1 kPa, since all specimens are fully saturated (i.e. no suction is expected) before testing. For an uncemented soil, the value of p'_{0unc_i} corresponds to the value of the isotropic yield stress, σ'_y.

8.1.2. BASIC CASM PARAMETERS FOR UNCEMENTED SPECIMENS

Basic parameters are those shared with classical critical state models and were determined by Rios et al. (2016), from the experimental data collected in isotropic compression and triaxial compression tests performed by Rios et al. (2012, 2014). Parameters related to the slope and position of normal compression line and swelling lines are determined from isotropic compression tests. Parameters related to the slope and position of the critical state line (CSL) are determined from triaxial compression tests. Such tests reached elevated levels of axial strain, in order to define clearly the critical state (zero-dilatancy state) of the soil.

From these studies, the values reported in Table 8.1 were retrieved for this category of parameters. In addition to these parameters, the constant small-strain bulk modulus K'_{0unc} (defined in 6.1.5) of the uncemented soil shall be determined. This was determined with a heuristic process by comparing the initial slope of the stress-strain curves calculated in simulated monotonic triaxial tests with the experimental results.

Table 8.1 – Basic CASM model parameters

κ	N	λ	M	ν	K'_{0unc}
0.0097	2.35	0.112	1.4	0.3	9.75e4 kPa

Rios et al. (2016) adopted a flow rule based on Rowe's formulation [expression (3.31)]. In the present validation, such law is maintained, adapting it to the kinematic yield surface as illustrated in section 6.1.6.

8.1.3. ADVANCED CASM PARAMETERS

These parameters ($\bar{n}$ and r) define the shape of the yield and reference surface and were determined in Rios et al. (2016). The yielding points of the drained and undrained triaxial tests were determined graphically. Then, these points were normalised by the corresponding isotropic yield stress of each specimen (indicated as p'_{s0} in Fig. 8.1). The normalised yielding points were plotted in this normalised

space, along with the normalised stress paths of the undrained tests. Yielding points and normalised stress paths plotted together give a qualitative indication of the surface shape.

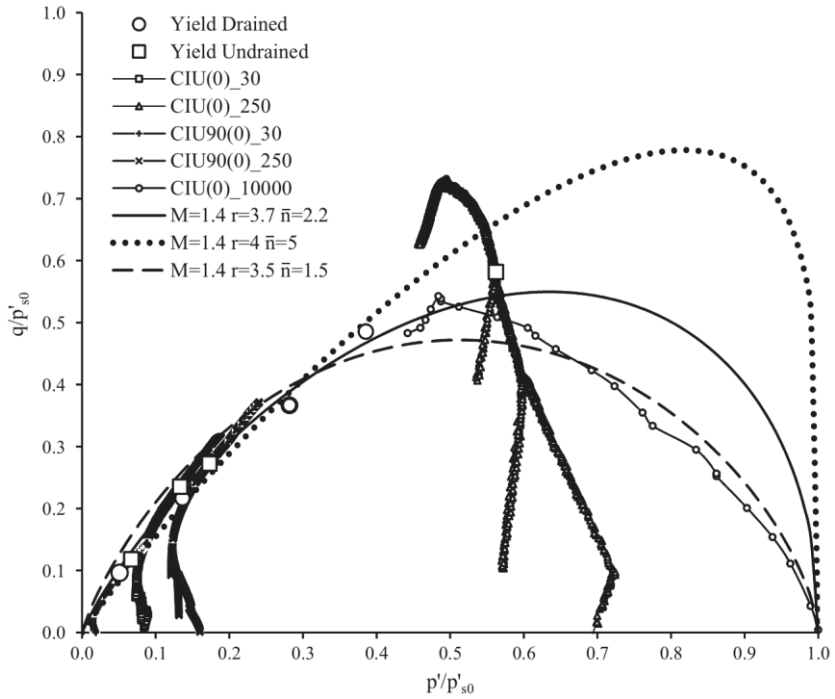

Fig. 8.1 – Normalised plot for the yield stress points of drained and undrained tests of uncemented specimens (Rios et al., 2016)

From the figure, it can be observed that the majority of the tests are on the dry side of the critical state, while two are on the wet side. In particular, one is normally consolidated, as it was isotropically compressed prior to shearing to a very high confining pressure (10 MPa), higher than the isotropic yield stress of the specimen relative to its initial state. The authors searched for the shape parameters that better fitted the normalised surface to the experimental data, retrieving the values reported in Table 8.2.

Table 8.2 – Advanced CASM model parameters

$\bar{n}$	r
2.2	3.7

For the reasons illustrated in the precedent sections, the surface defined as yield surface in the CASM-n model is considered coincident with the reference surface of the bounding surface framework. Additionally, it is supposed that the kinematic yield surface has the same shape of the outer surface.

8.1.4. KINEMATIC HARDENING PARAMETERS

These parameters control the size of the kinematic yield surface (through the ratio R of the surfaces sizes) and the interpolating function regulating the kinematic hardening modulus (B and ψ). Since these parameters are not related to one or more specific physical properties, their value was established by assigning tentative values and then comparing the results of the simulated test with the experimental results. Attention was focused on the stiffness in the region inside the reference surface (i.e. when the

surfaces are not in contact). If the computed stiffness is lower than the observed one, parameter B is increased; otherwise, its value is decreased and a new model output is generated. During this phase, the two remaining parameters R and ψ are maintained fixed. After a suitable value is found for B, the shape of the stress-strain curve in the model and experimental output are compared. As the kinematic surface approaches the external surface, kinematic hardening modulus decreases with a rate dependent on parameter ψ. If the rate of decrease in the simulated test is too fast (or too slow), parameter ψ is decreased (increased). In this process, R remains constant, while B shall be adjusted consequently. In fact, as shown in the expression of the hardening modulus (expression (6.13)), B is elevated to the exponent ψ. If ψ is updated from the precedent tentative value ψ_1 to a new value ψ_2, parameter B shall be updated from a value B_1 to B_2. A first estimation of the new tentative value B_2 can be calculated by noting that the initial value of H' shall remain equal to the value obtained with the precedent combination of parameters. Thus, B_2 is initially fixed in order to have:

$$B_2{}^{\psi_2} = B_1{}^{\psi_1} \tag{8.2}$$

A new simulation is performed with B_2 and ψ_2, and B_2 is adjusted if required (normally the correct value is not very different from the first value calculated with expression (8.2)).

After a reasonable adjustment is found for a specific test, the same parameters are applied to a different test in order to verify if the set is still valid. This verification can result in three outcomes. In the first case, the set of parameters is valid also for the second test and they do not need to be changed. In the second case, the adjustment is not perfect but it is at least qualitatively acceptable. In this case parameter R remains unchanged; parameters B and ψ are changed in order to seek for the best adjustment for the second test. Then, the average values of the parameters determined for the first and second tests are considered. If the adjustment between the model and the experimental results for the second test is not satisfactory, parameter R is changed. Maintaining a fixed value of R, a new couple of parameters B and ψ is determined using the same scheme illustrated above. The new parameters are applied at the precedent test, and their fitting is checked. If the outcome is negative, a third attempt value of R is selected and the interpolating parameters are determined for the first test. The process continues until a set of parameters suitable for the two tests is found. At this point the parameters are applied to a third test and the process is repeated as in the precedent case (R is maintained and B and ψ are changed in case of reasonable adjustment; the three parameters are changed in case of no adjustment). At the end of this iterative process, the values reported in table were obtained.

Table 8.3 – Kinematic hardening parameters

R	B	ψ
0.08	1e-6	1

8.1.5. Initial position of the yield surface

In paragraph 6.4, it is shown that the initial position of the yield surface does not have a great influence on the long-term cyclic response of the model, because it tends to shift to a particular position, for which the translation vector and the stress increment are parallel. In the case of a monotonic loading path, the short duration of the loading path does not allow the surface apex to reach this particular position, if it is initially positioned in a different configuration. Thus, for monotonic loading it is important to select an adequate initial position of the surface ($p'_{\alpha i}$, $q_{\alpha i}$), since it will result in an initial compressive or dilative tendency of the soil response. A possible criterion in this initialization can be found by analysing the stress path followed by the surface prior the start of the monotonic triaxial loading. Before the start

of the shearing phase of the test, all the specimens are isotropically consolidated from an initial unconfined state to a final isotropic compression, following a path similar to that reported in Fig. 6.10. Thus, it is reasonable to suppose that in all the tests the stress point is located in point A represented in the same figure. If the stress point at the beginning of the triaxial compression is indicated as (p_i', q_i), the initial values of the apex coordinates are:

$$\begin{aligned} p_{\alpha i}^{'} &= p_i^{'} - R p_{0i}^{'} \\ q_{\alpha i} &= q_i \end{aligned} \tag{8.3}$$

where p_{0i}' is the initial value of p_0'.

Since all the tests are isotropically consolidated at an effective confining pressure σ_c' and no further anisotropic consolidation is applied, the initial stress point is $(\sigma_c', 0)$. Thus:

$$\begin{aligned} p_{\alpha i}^{'} &= \sigma_c^{'} - R p_{0i}^{'} \\ q_{\alpha i} &= 0 \end{aligned} \tag{8.4}$$

8.1.6. PERFORMANCE OF THE MODEL FOR UNCEMENTED SPECIMENS

Once all the parameters for uncemented soils have been determined, the performance of the model for uncemented tests can be assessed. Three triaxial tests were selected, one drained and two undrained, respectively whose initial characteristics are reported in Table 8.4. The model output is plotted along with the respective experimental result in Fig. 8.2 and Fig. 8.4. Due to the different confining pressure, the undrained tests show a dilative and a compressive behaviour, respectively. In general, it can be observed a reasonable agreement between the model and the experimental results. It is interesting to compare these results with the corresponding results obtained in the single-surface CASM-n model used by Rios et al. (2016). One can see that in the large strain domain (i.e. the post-yield domain in CASM-n model or the domain in which the surfaces are in contact the present kinematic hardening model) the two models give similar results, confirming the validity of the present implementation. In the small-strain domain, Rios et al. (2016) state that the most difficult aspect to reproduce with a single-surface model is the non-linearity of this domain, especially the stress path of undrained tests, and a more complex elastic model would be needed. The present approach is capable of better reproducing the initial non-linear behaviour using a simple linear elastic law combined with kinematic hardening. In Rios et al. (2016) simulation of CIU(0)_30 test, a vertical effective stress path is observed starting from the beginning of the test up to around 60 kPa, corresponding to the elastic domain of the used model. With the present model, a non-linear behaviour is observed since the beginning of the test. Additionally, the change in behaviour from compressive to dilative behaviour is qualitatively reproduced, due to the shift of the yield surface during the loading process.

Table 8.4 – Initial state variables and index properties for uncemented triaxial tests

Name	Type	v_i	$\sigma_c^{'}$ (kPa)	p_{0unc_i}' (kPa)	$p_{\alpha i}^{'}$ (kPa)
CV90(0)_100	Drained	1.6	100	1558	-24.6
CIU(0)_30	Undrained	1.75	30	359.5	1.2
CIU(0)_250	Undrained	1.75	250	359.5	221.2

In Fig. 8.3, one can see the initial and final configuration of the surfaces and the path followed by the stress point and the apex of the bubble in the stress plane. Yield surface translation follows the behaviour illustrated in 6.4 and confirmed in 8.2.1 for cyclic loading: translation vector is not initially parallel to the effective stress increment, thus the apex coordinates adjust consequently as loading increases. The initial position of the yield surface make the behaviour elasto-plastic from the very beginning of the loading. The position selected is convenient because it results in an initial compressive behaviour of the soil in all the tests, regardless the initial confining pressure, in agreement with the observed experimental behaviour. As the strain increases, yield surface shifts to a position that makes the translation vector parallel to the stress increment. The volumetric strain increment changes accordingly and switches from the compressive to the dilative side. When the yield surface intersects the external reference surface at a common normal, the two surfaces shrink together (because the isotropic hardening modulus is negative) until the stress point reaches the critical stress ratio M (where isotropic hardening is nil). Fig. 8.5 shows the surface configuration for the two undrained tests of Fig. 8.4. In the less confined test, a negative pore pressure variation is observed, while in the more confined test such variation is positive. In both cases, the effective stress path tends to intercept the external surface at a stress ratio approximately equal to the critical state ratio. As expected, in the first test the final configuration of the surfaces shows a smaller size than the initial one, while in the second test an expansion of the surfaces is observed.

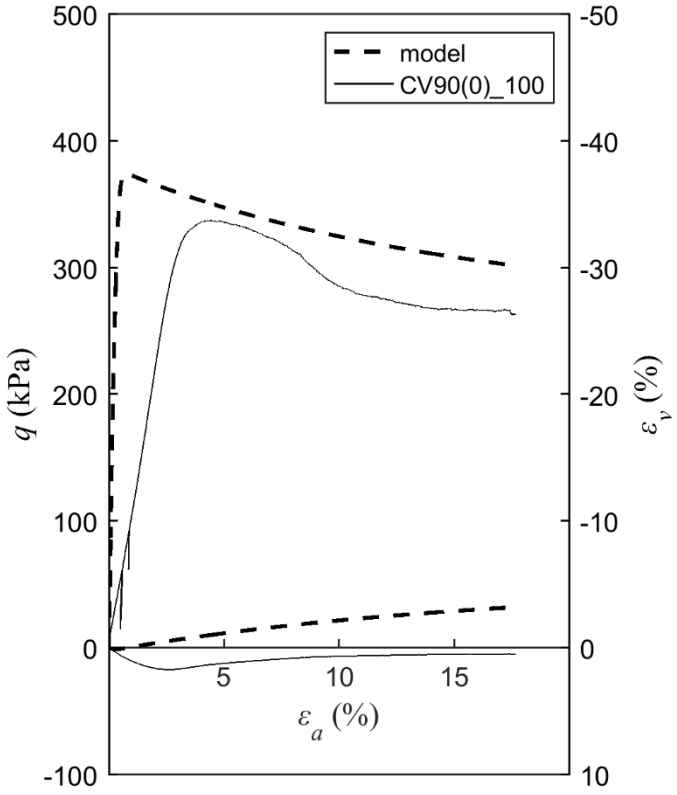

Fig. 8.2 – Performance of the calibrated model on drained triaxial tests and uncemented specimens

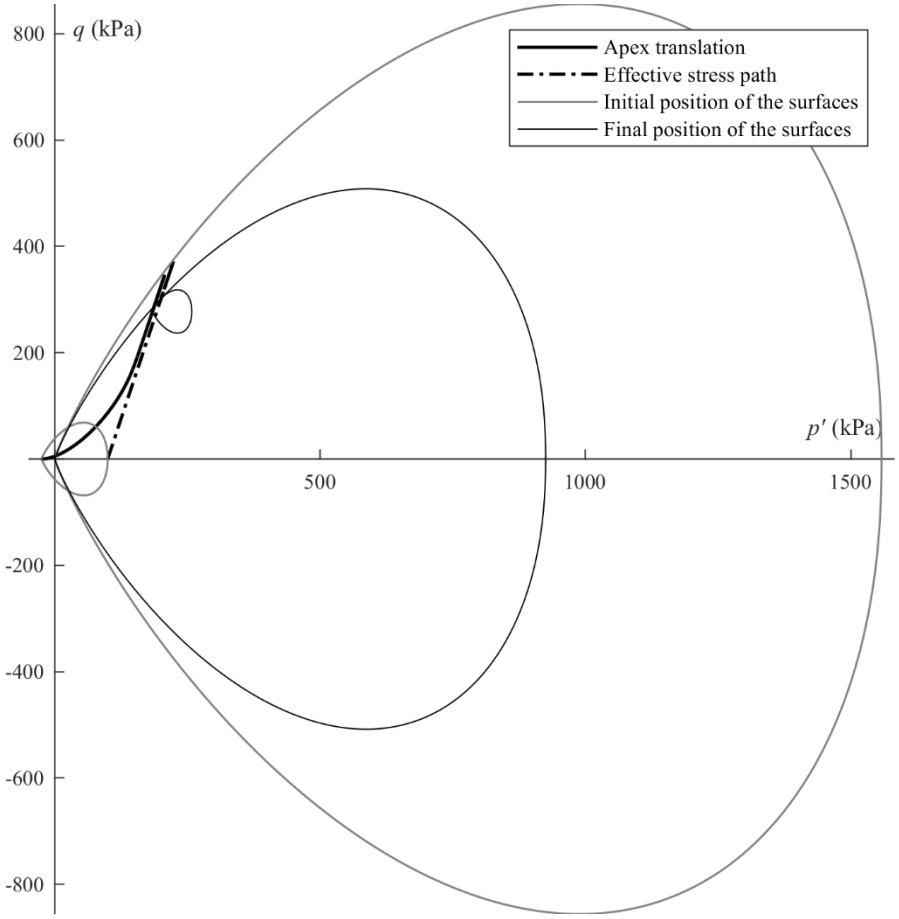

Fig. 8.3 – Kinematic and isotropic hardening in drained triaxial tests and uncemented specimens

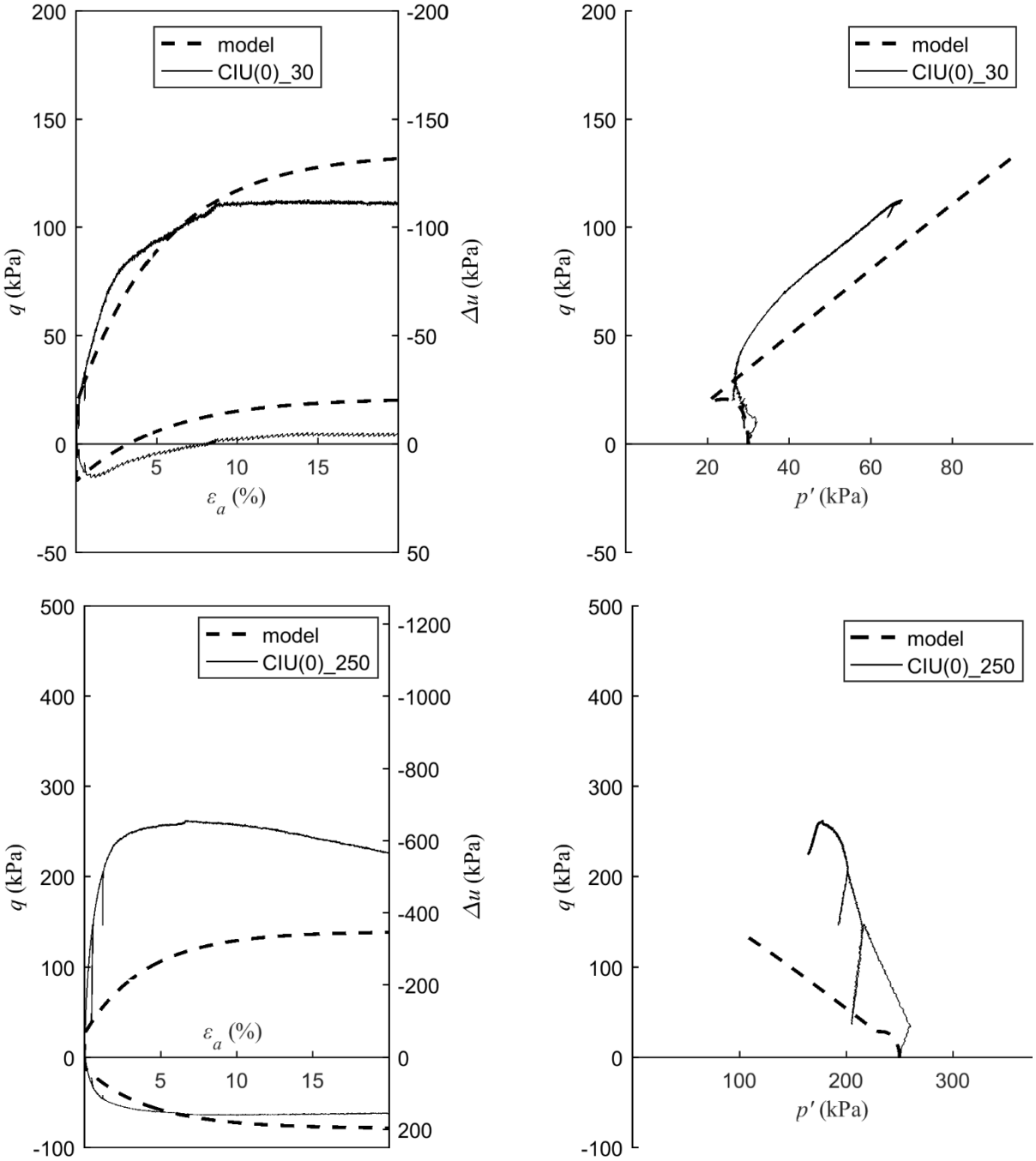

Fig. 8.4 – Performance of the calibrated model on undrained triaxial tests and uncemented specimens

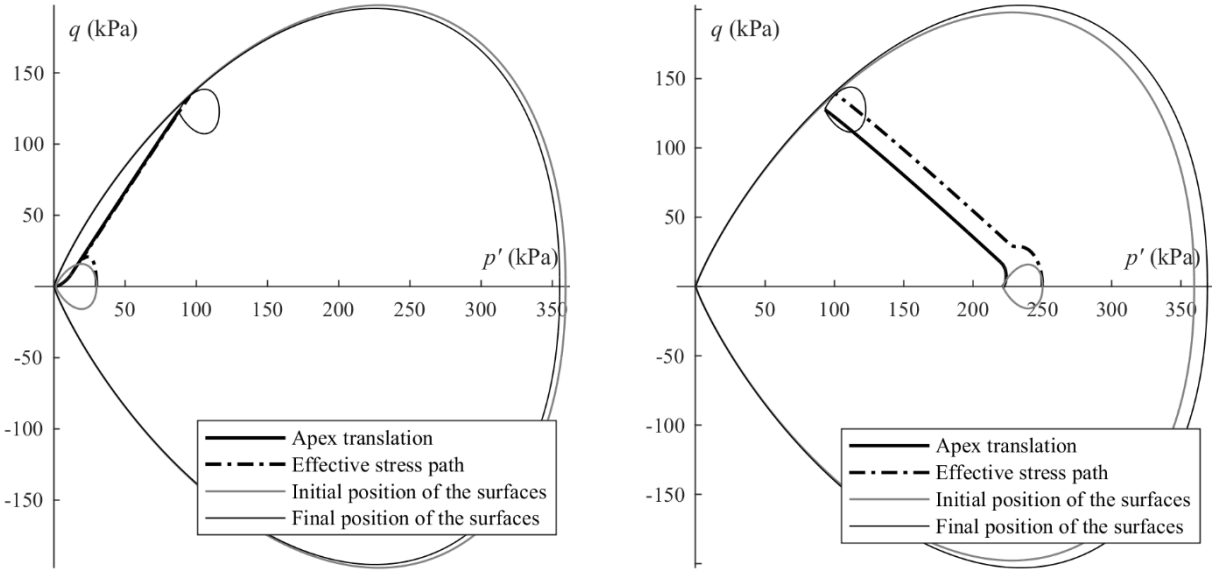

Fig. 8.5 – Kinematic and isotropic hardening in undrained triaxial tests and uncemented specimens

8.1.7. INITIALIZATION OF BONDING STATE PARAMETERS

In order to model the behaviour of cemented soils, the uncemented model is extended as illustrated in Chapter 6 in order to include the enhanced dimension of the surfaces and the tensile strength. These properties are regulated by two initial bonding state parameters and a destructuration law, as expressed in equations (6.40) to (6.43). The initial bonding parameters are the initial amount of bonding b_0 and the initial tensile strength p'_{ti}. In order to determine the position and size of the reference surface, at least two points of the surface should be known, as shown in section 7.2.1.1. In the hypothesis that the reference surface coincides with the yield surface of single-surface models, the point in which the surface intercepts the positive p' axis is the isotropic yield stress σ'_y determined in isotropic compression tests for cemented soil (Fig. 7.1). In Chapter 5 it was shown that such pressure depends on the level of cementation and compaction, or, more specifically, on the adjusted porosity/cement ratio $n/C_{iv}^{0.21}$ (Rios et al., 2012). Rios et al. (2016) confirmed this dependence and, using the results of several isotropic compression tests on cemented soil, presented a correlation between the ratio and the initial excess isotropic strength (i.e. the difference between the isotropic yield stress of the cemented specimen and the isotropic yield stress of an equivalent uncemented specimen), in the form of a power law:

$$p'_c = \sigma'_y - p'_{0unc\_i} = 9.95\text{e}9 \left(\frac{n}{C_{iv}^{0.21}} \right)^{-4.265} \tag{8.5}$$

With this law, the isotropic yield stress of the cemented specimens was calculated, after having calculated the isotropic yield stress of an equivalent uncemented specimen by using relation (8.1).

The second point pertaining to the reference surface is found using the results of the unconfined compression tests (UCT) reported in section 4.4, and specifically the law [expression (4.8)] relating the adjusted ratio and the unconfined compression strength (UCS) obtained from the experimental results in section 4.5.

As illustrated in section 7.2.1.1, knowing two points of the reference surface and through an iterative method, tensile strength p'_{ti} is determined. Consequently, initial surface size p'_{0i} and initial degree of bonding b_0 are calculated using expressions (7.20) and (7.22). This iterative process can be performed

only after the shape of the surface has been determined, that is, parameters M, r, and $\bar{n}$ shall be fixed before the iteration is performed.

Following Rios et al. (2016), the bulk modulus of cemented specimens is made dependent on bonding. The relation proposed by Yu et al. (2007b) is used in a slightly modified form:

$$K_0' = K_{0unc}' \left(1 + \sqrt{\frac{p_c'}{\sigma_c'}} \right) \tag{8.6}$$

In this expression, effective confining pressure σ_c' is considered instead of the generic mean effective stress p' in order to have a constant modulus for each test.

Rowe flow rule (1962, 1972) presents a different formulation for cemented soils, as explained in section 6.2.4. Nevertheless, Rios et al. (2016) apply the expression for uncemented soils also for cemented soils. This is because the experimental results show no decrease in the dilative tendency of the soil due to cementation. In the present paragraph, the same option was followed, in order to validate the new model by comparing the output with the results of the model implemented by Rios et al. (2016). Nevertheless, to avoid numerical problems, in the following sections the cemented formulation is adopted for Rowe (and Yu) flow rule. In fact, a bonded formulation for the yield (and reference) surface combined with a flow rule for uncemented soils leads to a domain of the yield surface (corresponding to relative values of stress ratio η_α' greater than a certain minimum value, in turn dependent on the level of bonding) in which the plastic potential is not defined. In the stress paths simulated in the present section, such zone is not intercepted by the stress point, thus, such problem does not causes numerical instability. Nonetheless, in a generic stress path this problem can arise; thus, a cemented formulation for the flow rule shall be adopted in order to guarantee a general stable response for the model.

8.1.8. CALIBRATION OF BOND DAMAGE PARAMETERS

The two remaining parameters (b_1 and b_2) regulate the accumulation of damage with increasing volumetric and distortional plastic strain, respectively, as shown in relation (6.44). For sake of simplicity, the same value is considered for both parameters.

The calibration process was performed by comparison with the experimental results. A first attempt value was selected equal to zero for both the parameters and the model output compared with the experimental results. Then, the parameter value was successively increased until a good agreement was attained. An example of such process is shown in Fig. 8.6. As one can see, the influence of the damage parameters is more relevant for large strain levels (especially after critical state has been reached), because the damage law increase linearly with the accumulation of plastic strain.

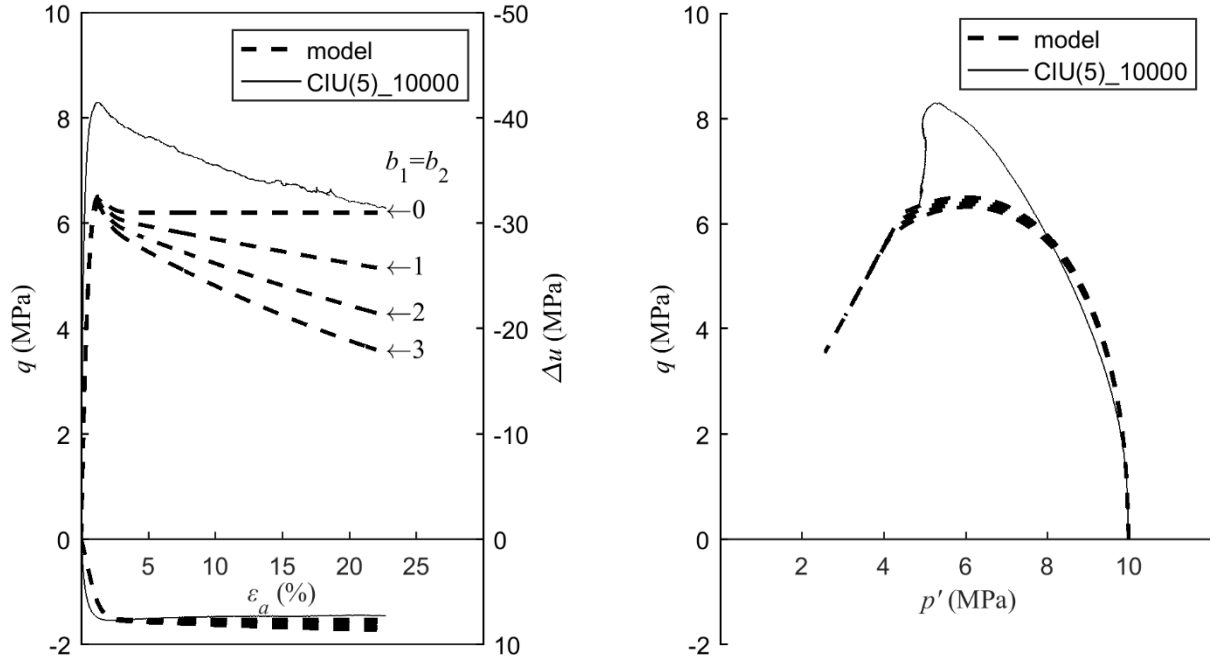

Fig. 8.6 – Example of calibration of bond damage parameters

At the end of the process, a value equal to 3 was selected as the best fitting value for the damage parameters, as reported in Table 8.5.

Table 8.5 – Bond damage parameters

b_1	b_2
3	3

8.1.9. PERFORMANCE OF THE CALIBRATED MODEL FOR CEMENTED SOIL

The calibrated model was validated by simulating a set of drained (D) and undrained (U) triaxial tests (Fig. 8.7 and Fig. 8.8). The initial conditions and state parameters of the simulated tests are reported in Table 8.6.

Table 8.6 – Initial state variables and index properties for cemented triaxial tests

Name	Type	v_i	C	$n/C_{iv}^{0.21}$	$\sigma_c'^{(1)}$ (kPa)	$p_{0i}'^{(2)}$ (kPa)	b_0	$p_{ti}'^{(3)}$ (kPa)	$p_{\alpha i}'^{(4)}$ (kPa)
CV(2)_30	D	1.61	2	36	30	4057	1.87	353	-295
CV(5)_250	D	1.58	5	29	250	8775	3.63	1117	-452
CIU(2)_250	U	1.60	2	36	250	4194	1.69	344	-85
CIU(5)_250	U	1.58	5	29	250	8775	3.96	1117	-452

(1) effective confining pressure; (2) initial size of the reference surface; (3) initial isotropic tensile strength; (4) p'-coordinate of the apex of the yield surface in the stress plane

Similarly to the uncemented tests results, also in this case a good agreement between the large-strain performances of the two models is observed; in the small strain domain, the present model is more

capable of representing the initial non-linearity than the corresponding single-surface model. Drained test CV(5)_250 shows practically the same output in the two implementation. The estimated peak strength in test CV(2)_30, although higher than the experimental result, is more accurate in the present implementation (around 1200 kPa) than in Rios et al. (2016) output (around 1500 kPa). This is because the dilative tendency of the test causes a shrinkage of the surfaces before they are in contact, while in a single-surface model the only surface remains unchanged until the stress point is in contact with it. Hence, the progressive yielding observed in two-surface model leads to more accurate results than the sudden yield in the single-surface approach (Panico et al., 2018).

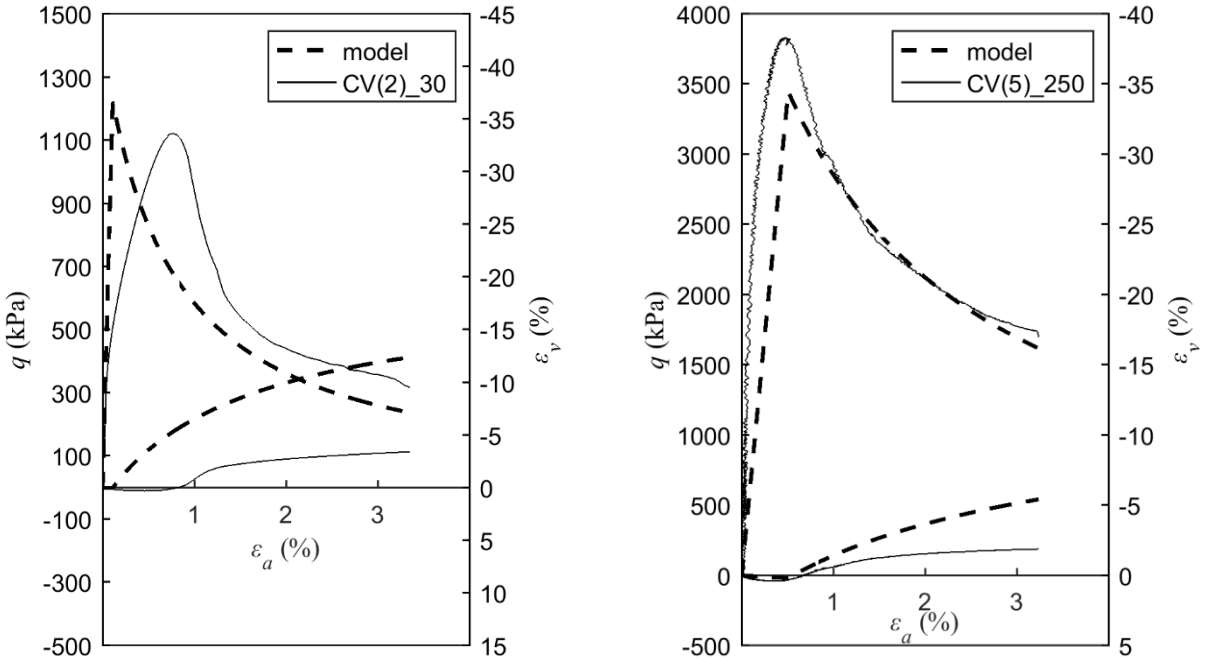

Fig. 8.7 – Performance of the calibrated model on drained triaxial tests and cemented specimens

The most evident improvement is observed in the undrained effective stress paths presented in Fig. 8.8. In this case, the non-linearity is well represented from an early stage of deformation, as well as the change in volumetric behaviour from a compressive tendency to dilation.

In Fig. 8.9, the initial and final configuration of the surfaces and the path followed by the yield surface are shown. As expected, as the deformation progresses, the reference surface shrinks as an effect of reduced tensile strength and isotropic yield stress. Yield surface approaches the outer surface and translates in contact with it afterwards, tending towards the critical state stress ratio. A further shrinkage is observed after this state is reached, because of the progressive loss of cementation due to the incremental distortional plastic strain. The large-strain results are in agreement with the results of the single-surface model (Panico et al., 2018).

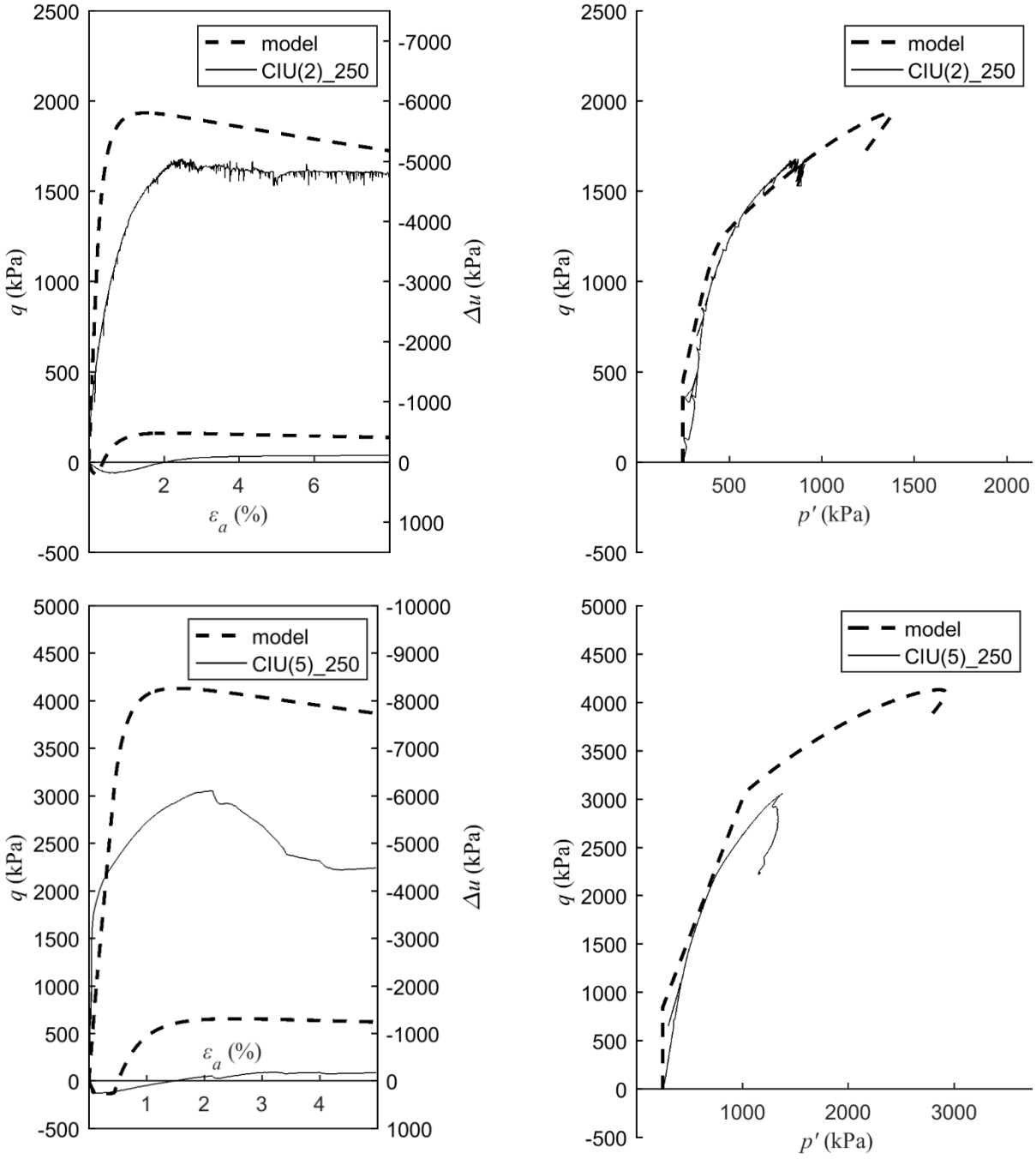

Fig. 8.8 – Performance of the calibrated model on undrained triaxial tests and cemented specimens

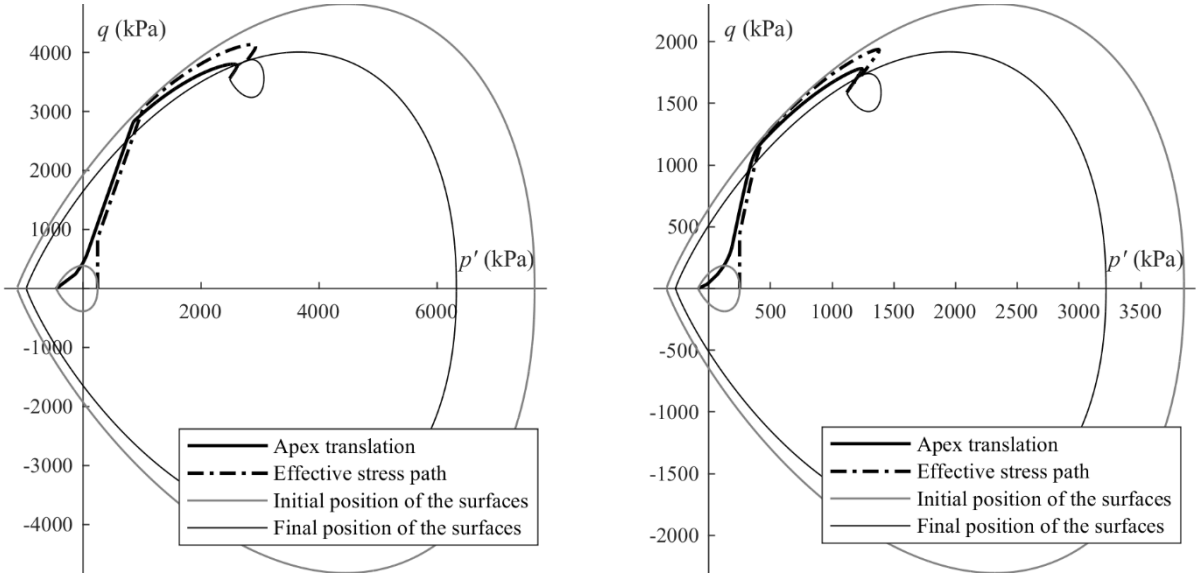

Fig. 8.9 – Kinematic and isotropic hardening in undrained triaxial tests CIU(2)_250 (left) and CIU(5)_250 (right)

The performed comparison between the proposed kinematic hardening model and an existing implementation of an isotropic hardening model showed the validity of the present implementation for modelling uncemented and cemented soil. The large-strain performance is very similar for the two models, while in the small-strain domain a better performance of the kinematic hardening approach is observed, due to the specific capacity of this framework to model non-linear behaviour since an early stage of deformation.

8.2. MODEL RESPONSE IN CYCLIC TRIAXIAL CONDITIONS

A series of simulated drained cyclic triaxial tests have been performed in order to assess the performance of the model and to study the influence of parameters R, B, ψ, and the damage parameters b_1 and b_2 on the model results. First, a series of tests was run with the same stress conditions and varying in turn each parameter. Then, with a selected set of parameters, various simulated tests were run with different values of confining pressure, in order to study the model response is the compressive and dilative domains. In all the simulations, Rowe flow rule was used.

The numerical algorithm presented in Chapter 7 was implemented in the commercial software MATLAB® (reported in Annex 5) by the discretization of the stress path in small stress increments and the application of an approximate integration method. Before presenting the results, some considerations on the initial position of the bubble surface are outlined.

8.2.1. INITIAL POSITION OF THE YIELD SURFACE

The relative position between initial stress point and initial apex of the bubble does not affect significantly the long-term cyclic response of the model. As referred in paragraph 6.4, regardless the initial coordinates of the apex, the position of the yield surface tends to adjust so that the direction of vector $\boldsymbol{\beta}$ is parallel to the stress increment vector $\dot{\boldsymbol{\sigma}}'$. This is equivalent to say that the direction of the stress increment vector intersects the yield and reference surface at conjugate points, as expressed mathematically in condition (6.66).

This behaviour was confirmed in the simulated tests performed with the numerical implementation. An example referred to an uncemented soil is shown in Fig. 8.10, in which the initial position of the yield surface does not satisfy condition (6.66). The yield surface apex shifts towards higher values of effective mean stress during the first cycle: p'_α is around 590 kPa at the beginning of the first cycle and it is around 640 kPa at the end of the same cycle. Then, the position of the apex stabilises (i.e. the displacement becomes linear and it is equally repeated in each of the successive cycles) when the condition of parallelism between the vectors is met. After this equilibrium is reached, the translation of the yield surface remains parallel to the stress path. The yield surface expand or shrinks in the successive cycles (depending on the value of the flow rule during loading and unloading), but the translation path remains in the same conditions of parallelism with the stress path.

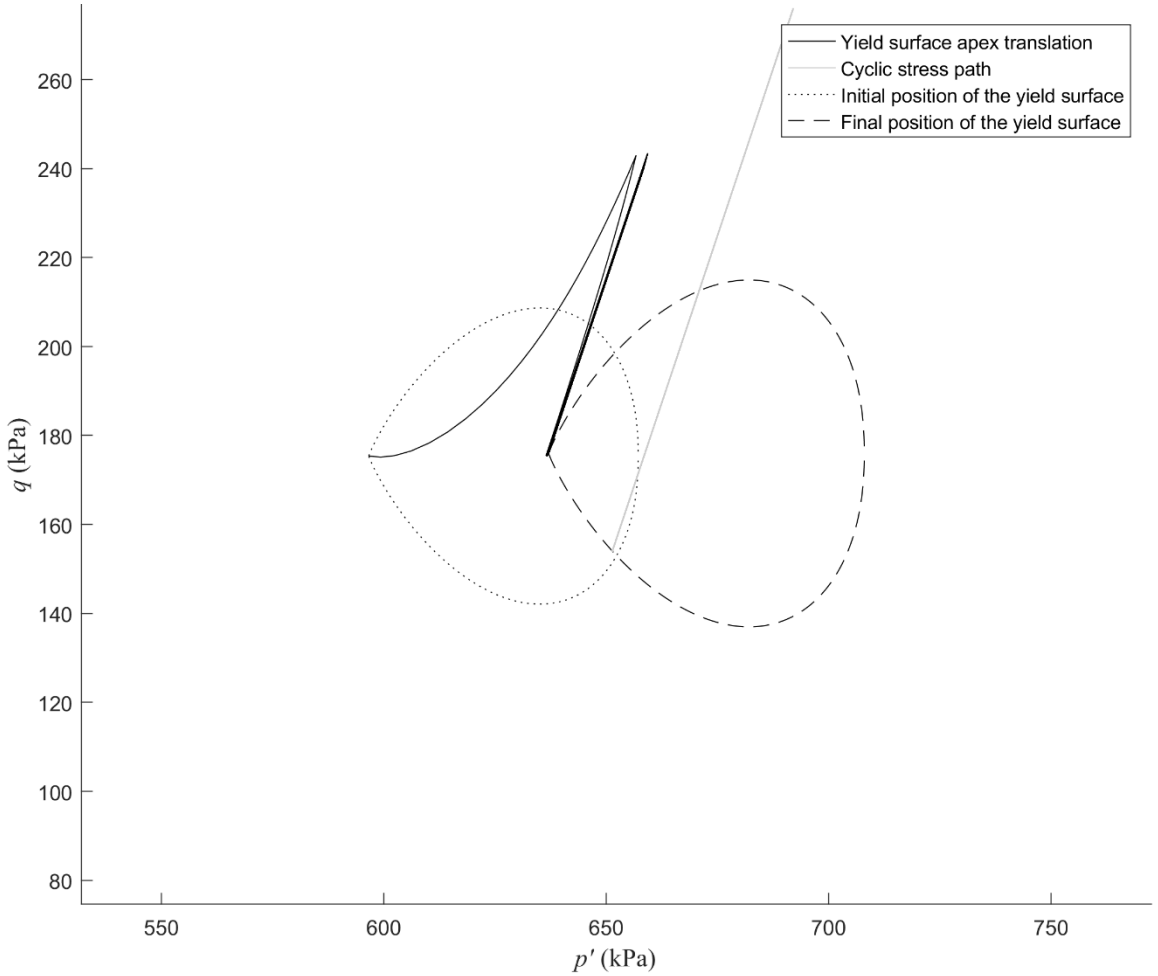

Fig. 8.10 – Initial shift of the yield surface in the first cycles and subsequent stabilisation (unbonded soil)

To confirm this result (analysed in paragraph 6.4.1), numerical simulations were performed where the initial coordinates of the apex satisfied the condition. In Fig. 8.11 an example is shown (also in this case an uncemented soil was considered). As expected, the translation of the bubble is linear and parallel to the stress increment and its length depends on the value of α_H (see paragraph 6.4.2). The difference in length between the translation path and the elasto-plastic part of the stress path causes the bubble to shrink or expand accordingly to the sign of the isotropic hardening modulus, but the displacement remains linear.

If the isotropic modulus is nil, the surfaces do not change in size and the length of the translation path is equal to the length of the elasto-plastic part of the stress path. The translation path is the same in each loading-unloading cycle, hence the plastic strain at the end each cycle is constant and the accumulated plastic strain increases linearly with the number of cycles.

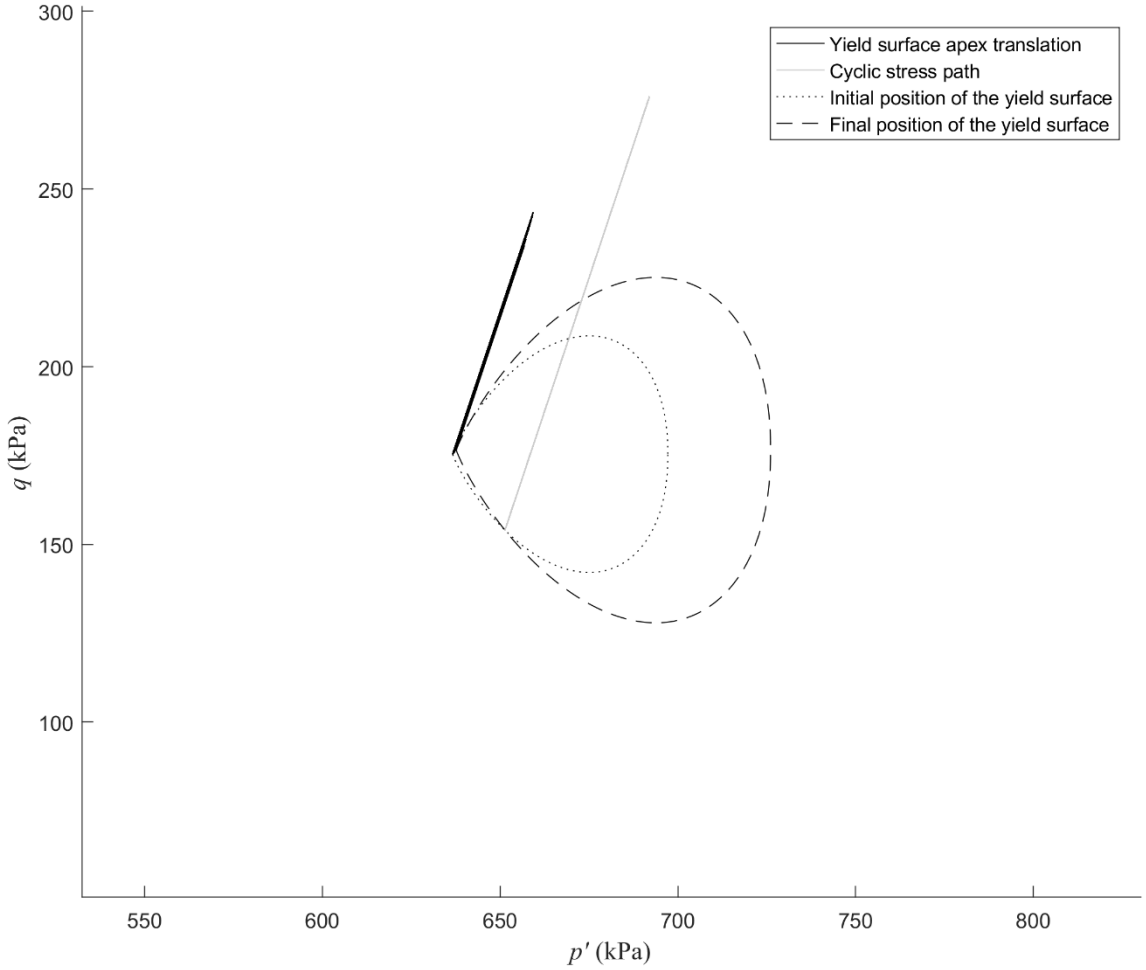

Fig. 8.11 – Model response when vector $\boldsymbol{\beta}$ is initially parallel to the stress path (unbonded soil)

In all the simulation performed, the shift of the yield surface to the referred position is always completed in the very first cycles (approximately the first 2-3 cycles). Thus, the initial position of the bubble has a limited influence on the results of a long-duration cyclic test with hundreds of thousands of cycles. For this reason, in the subsequent tests the initial position of the yield surface was always set in order to satisfy condition (6.66).

If the soil is cemented, the bonding hardening modulus is not nil. Still, the position of the yield surface tends towards a condition of parallelism between $\boldsymbol{\beta}$ and $\dot{\boldsymbol{\sigma}}'$, as explained in 6.4.2. Nevertheless, the progressive loss of bonding (namely the loss of tensile strength p_t') modifies the position of the reference surface apex at each cycle. Consistently, vector $\boldsymbol{\beta}$ changes slightly direction at each cycle and the yield surface shifts accordingly to restore parallelism with $\dot{\boldsymbol{\sigma}}'$.

8.2.2. MODEL RESPONSE IN THE STRESS-STRAIN PLANE

The model response shows the typical stress-strain loops observed in the experimental results. An example of the model output is reported in Fig. 8.12, where the first 20 cycles of a drained triaxial test are represented.

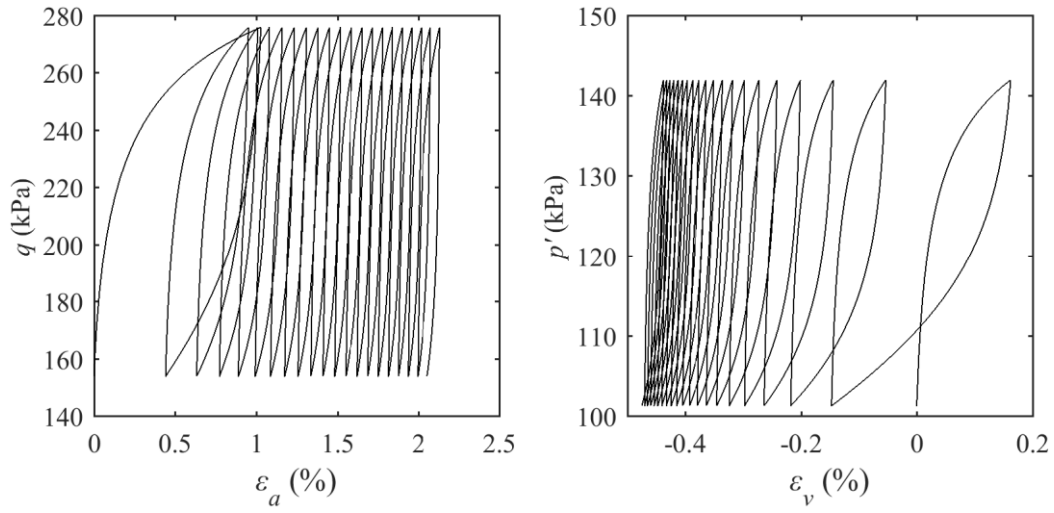

Fig. 8.12 – Example of model output. Stress-strain loops in the axial and volumetric components for a drained cyclic triaxial test simulation

The loops appear in the axial and volumetric stress-strain planes. In the axial response, the development of positive plastic strain during loading is greater than the negative plastic strain increment during unloading, leading to a positive overall accumulation at the end of each cycles. In the volumetric case in the example reported the opposite occurs: the negative plastic strain during unloading is prevalent and the overall accumulation is negative. The example is referred to a case in which the isotropic hardening modulus is positive during loading, and negative during unloading. If the isotropic modulus is negative also during loading, negative volumetric plastic strain is expected also during loading. Conversely, if the isotropic modulus is positive during loading and unloading, the volumetric strain increment will be positive in both cases. Finally, it is possible that the modulus is positive during loading and negative during unloading (as in the case of the image), but the first part is prevalent on the second. In this case, the overall accumulation at the end of each cycle will be compressive.

Thus, the overall accumulation of axial and volumetric strain with cycles is an effect of the separate contributions of the loading and unloading parts of each cycle, which can have equal or opposite sign. In the precedent example, if only the strain accumulation with the number of cycles was analysed, it would not be possible to know if the negative volumetric strain accumulation observed was the effect of the sum of the negative accumulations during the two phases of each cycles, or the result of the difference between a negative and a positive contribution.

The example shows a progressive stiffening of the soil with the number of cycles, i.e. the plastic strain increments at each loading and unloading part of each cycle are progressively decreasing. This effect, often called cyclic hardening (Dafalias & Popov, 1975), also observed in the experimental results (Chapter 5), is highlighted in Fig. 8.13. The total hardening modulus H of the simulated test is plotted against the deviatoric stress q. This variable was selected in the representation because q is the driving stress, but it would be equivalent to represent the hardening modulus against the effective mean stress p', or against a strain variable. The loading and unloading parts of the cyclic stress path are reported in

two separated graphs to avoid overlapping. The graphs are only referred to the elasto-plastic (post-yield) part of the loading or unloading path, as the hardening modulus is not defined inside the yield surface, where purely elastic behaviour is observed. It is important to note that, for the type of tests simulated in the present work, in which a stiff response of the soil is expected over thousands of cycles, the kinematic component of the hardening modulus is greatly dominant in respect to the isotropic components. Thus, the total and the kinematic modulus are almost coincident.

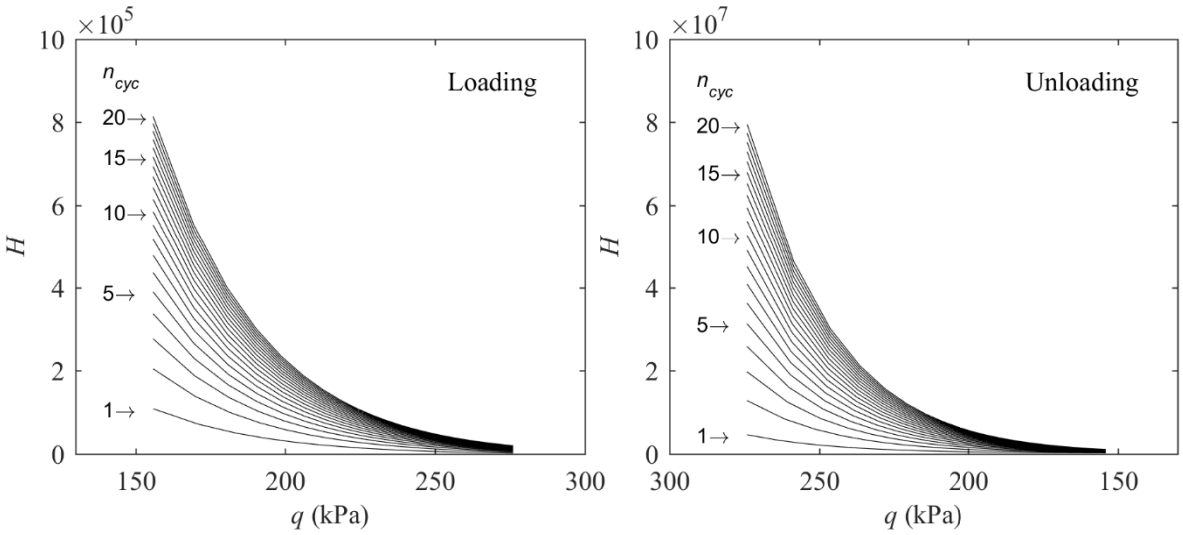

Fig. 8.13 – Variation of the total hardening modulus with the deviatoric stress for a drained cyclic triaxial test simulation

From the figure one can see that, at the beginning of each elasto-plastic loading or unloading path, the hardening modulus assumes a finite value. As the loading increases or decreases, the yield surface translates and distance b between the two surfaces changes, resulting in a change of the hardening modulus. In the presented example, the distance decreases within a loading or unloading path and, consequently, the hardening modulus decreases, resulting in the non-linear shape of the stress-strain loops previously observed. From the figure, one can observe that the hardening modulus increases with the number of cycles: for each cycle, the value of the modulus is greater than in the precedent cycle, with the $(H - q)$ curves having similar shape. In the presented example, the hardening modulus during the unloading is much greater than the hardening modulus during the loading phase of the same cycle (note that the scales are two orders of magnitude apart). It is not possible to represent the two graphs with the same vertical scale, because the great difference of hardening modulus during loading and unloading prevents a correct visualization of both families of curves in the same scale. To avoid this problem, the same graphs were plotted in a logarithmic vertical scale, as shown in Fig. 8.14.

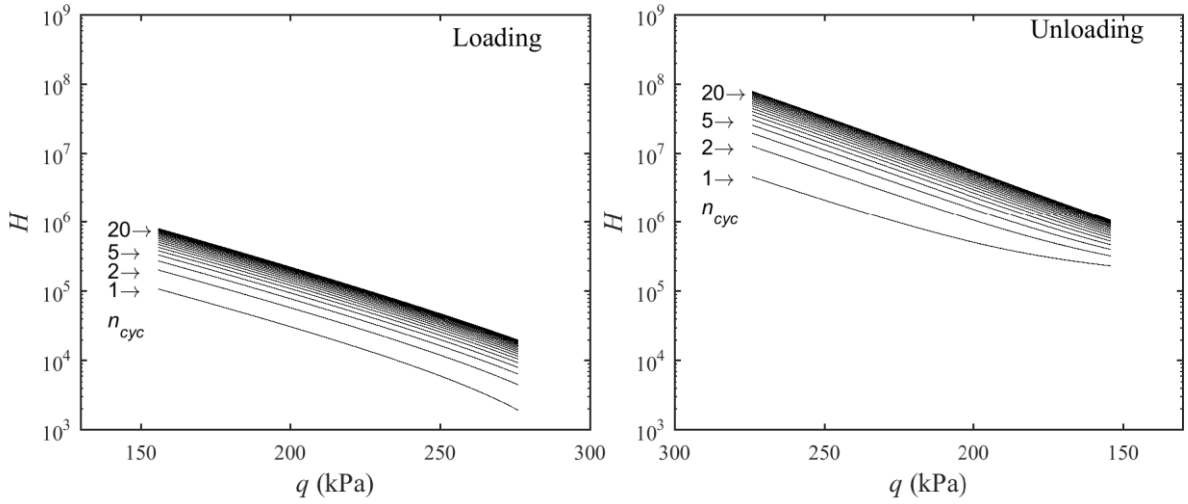

Fig. 8.14 – Variation of the total hardening modulus with the deviatoric stress for a drained cyclic triaxial test simulation (semi-logarithmic scale) and ψ = 30

In this representation, the difference between loading and unloading is clear, with a stiffness in the second part much higher than in the first. The reported example corresponds to a cyclic test in which distance b between the surfaces is greater during unloading than during loading, leading to a higher hardening modulus during unloading. This, in turn, causes the positive accumulation of the axial strain shown in Fig. 8.12. Volumetric strain is negative because it is influenced on the sign of the isotropic hardening modulus, rather than on the total hardening modulus. It is also worth noting that, in the semi-logarithmic representation, the $(H - q)$ curves are approximately linear, leading to the conclusion that the relation between H and q presents an exponential trend.

The shape of the $(H - q)$ curves is greatly dependent on the value of parameter ψ. This is the exponent of the normalised distance b, which in turn depends on the stress state. By varying the value of parameter ψ, the $(H - q)$ curves change in slope and position. In Fig. 8.14 the simulated test was performed with ψ = 30. In Fig. 8.15 and Fig. 8.16, the test was repeated in the exact same conditions, but with a value of ψ equal to 28 and 10, respectively. As one can see, the progressive decrease of parameter ψ causes the following effects on the curves $(H - q)$:

- the curves shift towards increasing values of hardening modulus;
- the slope of the curves decreases, i.e. the ratio of the final to the initial hardening modulus of a single loading (or unloading) elasto-plastic path is less marked;
- the ratio between the hardening modulus at the beginning of a generic loading path to the corresponding value in the precedent cycle decreases;
- the ratio between the hardening modulus at the beginning of a generic unloading phase to the corresponding value at the beginning of the loading part (in the same cycle) decreases.

All these effects express an increasingly linear response of the model for decreasing values of exponent ψ, as expected. For a sufficiently small value of these parameters, the hardening modulus does not evolve with the number of cycles, as shown in Fig. 8.16.

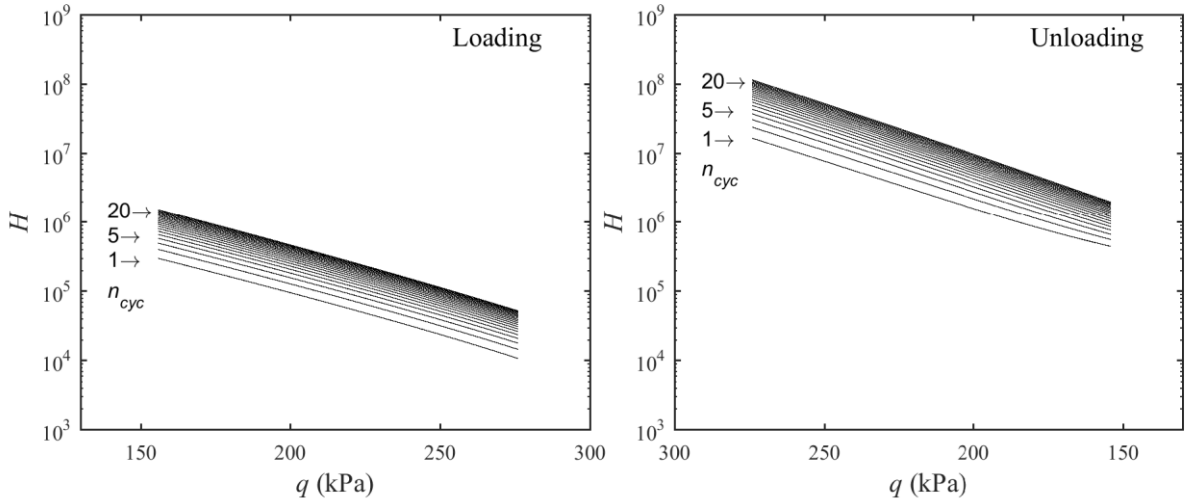

Fig. 8.15 – Variation of the total hardening modulus with the deviatoric stress for ψ = 28

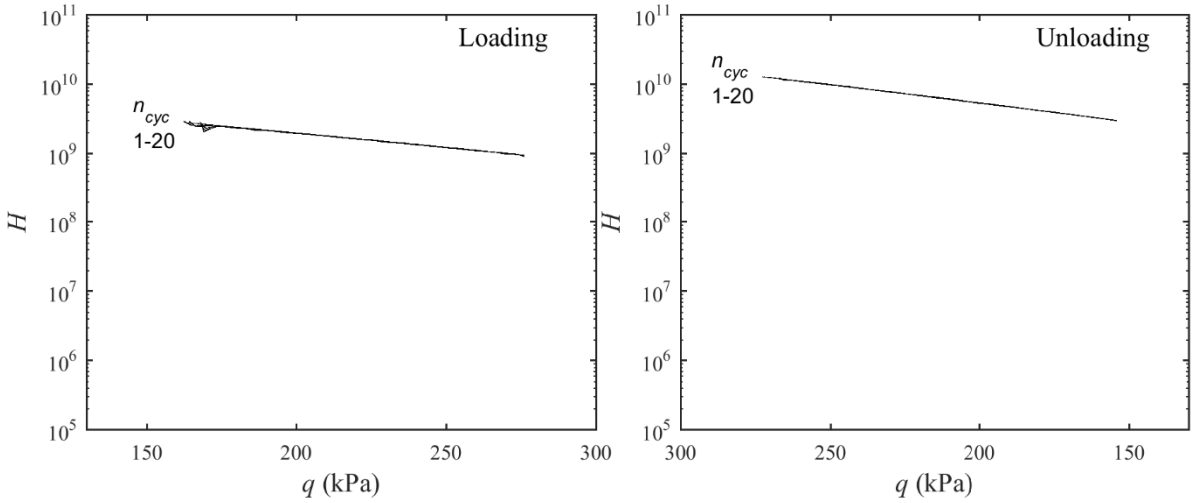

Fig. 8.16 – Variation of the total hardening modulus with the deviatoric stress for ψ = 10

Fig. 8.17 shows the influence of parameter ψ on the initial value of hardening modulus for each successive loading and unloading elasto-plastic stress paths of a cyclic test. The figure includes the three above examples and two additional simulated tests with ψ equal to 20 and 25. As parameter ψ increases, the value of plastic modulus at a certain cycle increases and its variation with the number of cycles is less marked. In this example, for ψ less than 20, the value of H at the beginning of each loading or unloading cycle does not change with the number of cycles, while for higher values (e.g. 30) the dependency of H with respect to the number of cycles is evident.

This feature affects the model response in the stress-strain plane. In the case of a low value of parameter ψ, the plastic stiffness does not change significantly with the number of cycles. Thus, the stress-strain loops are all similar, without hardening associated to the number of cycles. This in turn causes the accumulated strain to increase linearly with the number of cycles. On the contrary, a higher value of ψ produces a non-linear response, with large plastic strain during the first cycles and a progressive reduction with the number of cycles, associated to a stiffer response (cyclic hardening). The trend of accumulation is expected to be non-linear, with a decreasing rate of accumulation (logarithmic trend).

It is also possible that the value of the hardening modulus decreases with the number of cycles (the so-called cyclic softening – Dafalias & Popov, 1975). This happens when the surface is progressively shrinking with the number of cycles, and distance b is decreasing accordingly. In such case and with a sufficiently high value of parameter ψ, the loops become wider with the number of cycles and the accumulated axial strain increases with a progressively increasing (exponential) rate of accumulation, eventually leading to cyclic failure.

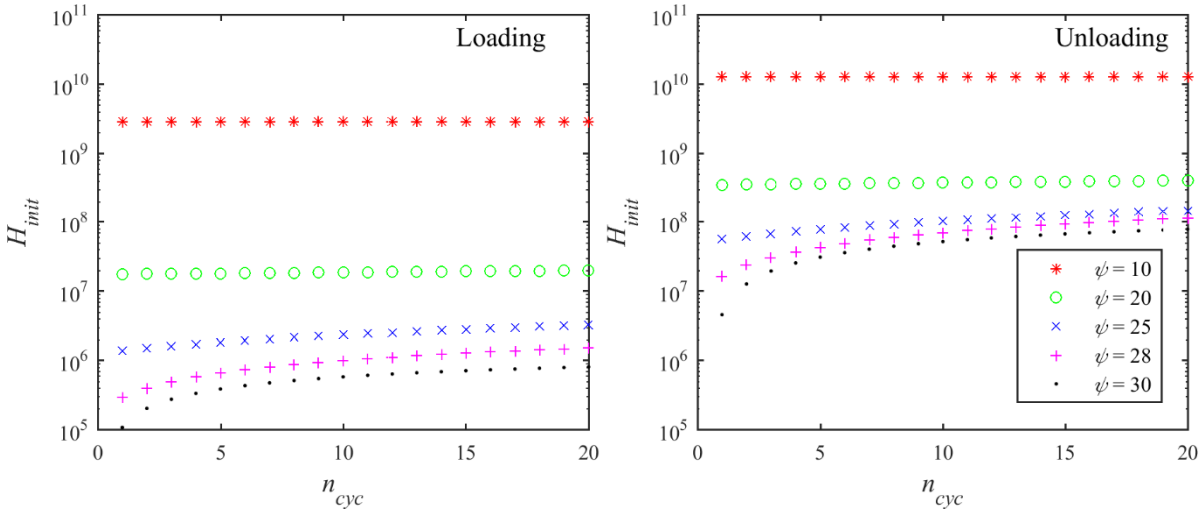

Fig. 8.17 – Hardening modulus at the initial point of a loading or unloading stress path vs. number of cycles

As stated above, parameter ψ also regulates the non-linearity within a single loading (or unloading) path, i.e. the slope of the curves in the semi-logarithmic $(H - q)$ plane. Fig. 8.18 shows the ratio of the hardening modulus at the beginning of a stress path (loading or unloading) to the corresponding value at the end of the same path. The ratio generally decreases with the number of cycles for the loading paths and increases for the unloading paths, until the ratio stabilizes to a constant value, specific for each value of the parameter. The higher is the parameter, the greater is the value of the ratio. Hence, increasing values of parameter ψ lead not only to an increased non-linearity among different cycles, but also within each single loading or unloading stress path.

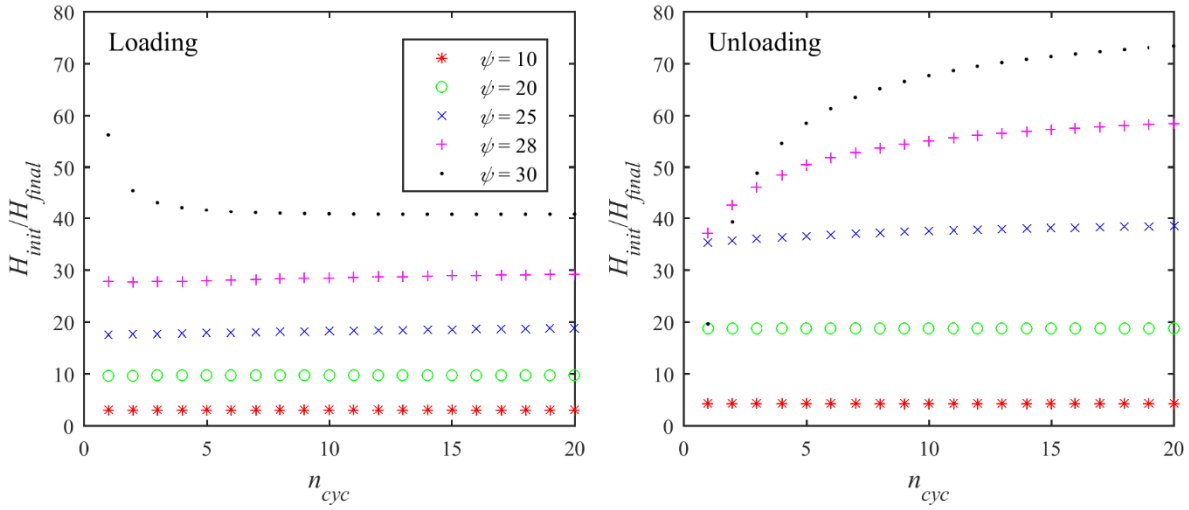

Fig. 8.18 – Ratio of the hardening modulus at the initial to the final point of the loading path vs. number of cycles

Another important feature controlled by parameter ψ is the ratio of the hardening modulus at the beginning of a generic unloading path to the corresponding value at the beginning of the loading path in the same cycle. This ratio is important because the overall accumulation at the end of a cycle depends on the sum of the two contributions of plastic strain developed during loading and during unloading (opposite in sign in the case of the axial strain). In Fig. 8.19, the variation of this ratio with the number of cycles and for different values of parameter ψ is reported.

One can see that the ratio is higher for higher values of ψ and its variation with number of cycles more marked. If the value of parameter ψ is less than a lower limit value, the ratio is less than one, meaning that the hardening modulus during a cycle is higher during unloading than during loading. Thus, soil response is stiffer during unloading than during loading. Such situation leads to a positive plastic axial strain during loading, inferior in absolute values to the corresponding negative strain during unloading. Therefore, the overall accumulation of axial strain during a loading-unloading cycle would be negative (i.e. the specimen height would progressively increase during cyclic loading) despite the compressive deviatoric cyclic stress applied. Such outcome would have no physical meaning and it shall be avoided by selecting an adequate value of parameter ψ.

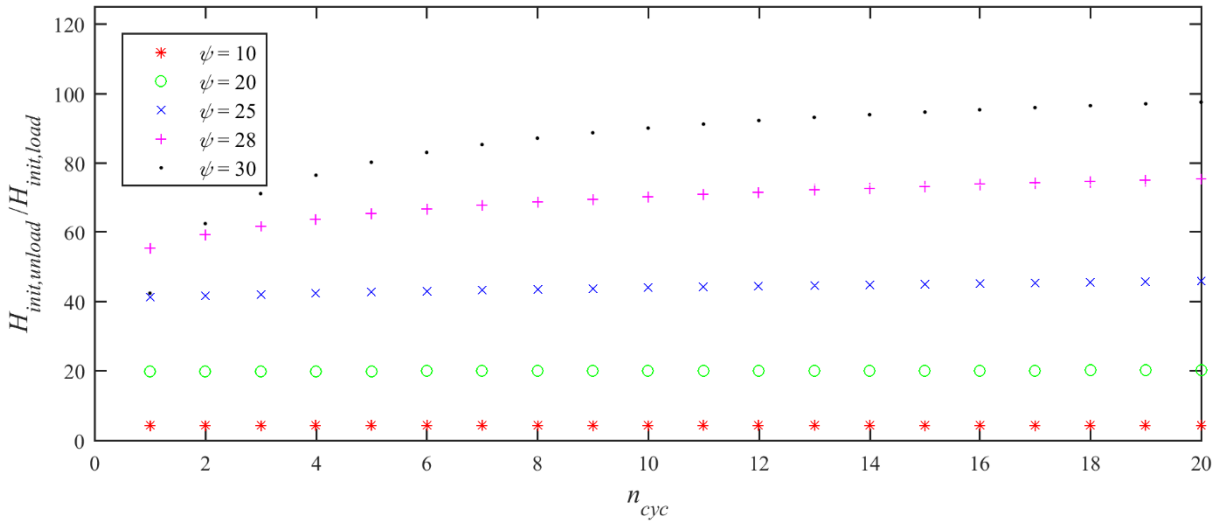

Fig. 8.19 – Ratio of the hardening modulus at the initial point of the loading path over the initial point of the unloading path

On the contrary, for high values of parameter ψ, high ratios of the hardening moduli at unloading/loading are expected, leading to a plastic stiffness during unloading much higher than during loading. Above a certain value of parameter ψ, the plastic stiffness during unloading is so elevated that the plastic strain increment is almost nil and the behaviour during unloading is almost purely elastic. An example of such case is reported in Fig. 8.20, where ψ = 100. This type of output is similar to that obtained in Dafalias & Hermann (1982) model, which is formulated in the framework of bounding plasticity without kinematic hardening. In such model, plastic strain are only predicted during loading, with a perfectly elastic unloading.

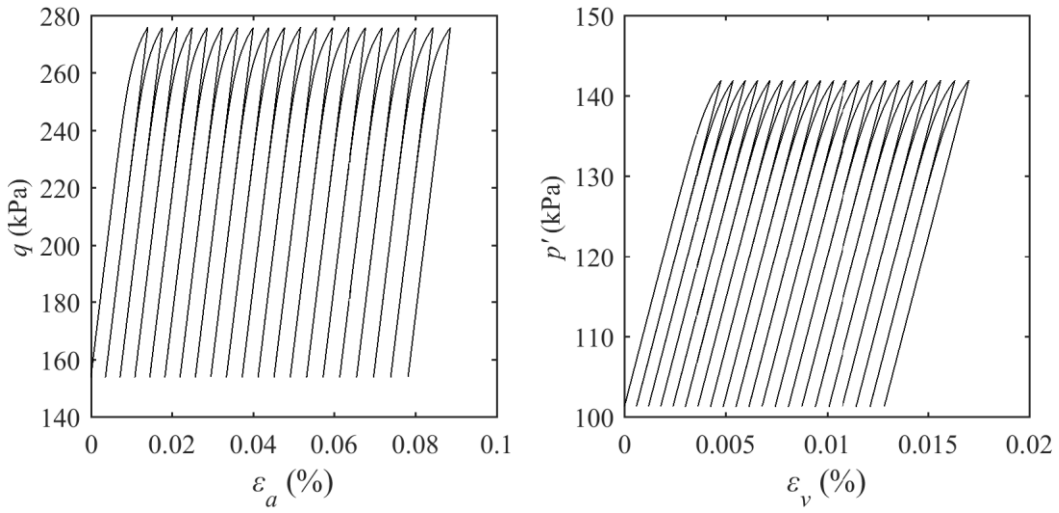

Fig. 8.20 – Model response with a high value of parameter ψ

Thus, parameter ψ regulates four relevant aspects of the model response:

- Variation of the hardening modulus during loading (within a cycle);
- Variation of the hardening modulus during unloading;
- Variation of the hardening modulus with the number of cycles (cyclic hardening);
- Ratio between hardening moduli during loading and unloading (in the same cycle).

As seen, parameter ψ also influence the absolute value of the hardening modulus (H decreases for increasing ψ), but this linear effect can be compensated simply by increasing the value of the linear parameter B, which causes the curves in the $(H - q)$ plane to shift upwards or downwards in the vertical direction.

The multiple effects regulated by parameter ψ makes the model less flexible: during the calibration process, a value of ψ that accommodates one of the four characteristics reported above can be inadequate for the others. Thus, the value of ψ should be a compromise between the best-fit values for each of the four reported features.

An example of such issue is seen during the calibration of the model against cyclic tests, as will be illustrated in the following sections. Parameter ψ is calibrated by comparing the model output and the experimental results; it is seen that, to achieve the fast cyclic hardening observed in experimental results (Chapter 5), parameter ψ shall be very high, in order to make the dependence of hardening modulus H from the distance b strongly non-linear. On the other hand, such an elevated value of parameter ψ leads to the reproduction of cyclic loops similar to those reported in Fig. 8.20, with an elasto-plastic behaviour in loading followed by an almost purely elastic unloading response. This output conflicts with the experimentally observed behaviour: examining the hysteretic stress-strain loops retrieved from test results, one can see that the unloading part is elasto-plastic (as well as the loading part) and not purely elastic. Thus, the model cannot reproduce correctly at the same time the shape of the stress-strain loops and the accumulation of permanent strain with the number of cycles.

8.2.3. PARAMETRIC ANALYSIS IN CYCLIC DRAINED TRIAXIAL TESTS

As explained in the precedent section, it is not possible to find a set of parameters that fit the hysteretic stress-strain behaviour and the overall strain accumulation at the end of a large number of cycles. In the

present work, it was preferred to search a set of parameters that would best fit the long-term accumulation of plastic strain with the number of cycles. In fact, given the high number of loading cycles, it would be difficult to analyse the model response through a million of hysteretic cyclic loops. The accumulated strain at the end of each cycle is a more concise indicator of the model performance and it is more useful in a practical approach, where the expected accumulated settlement at a certain number of loading cycles shall be predicted. For these reasons, the model response will be analysed in the plane of the accumulated stress vs. number of cycles, through a number of simulated tests with one million cycles, varying in turn one parameter and keeping the others fix. In each test, the cyclic loops have the shape showed in Fig. 8.20, with elasto-plastic loading and quasi-elastic unloading, as explained.

A parametric study was performed on a series of simulated uncemented cyclic drained triaxial tests with initial specific volume v_i = 1.75 and confining pressure of 40 kPa. In all the simulations performed, the limits of the deviatoric stress q are low compared to the ultimate deviatoric stress for the same test conditions, in order to ensure that a minimum distance between the surfaces is kept. Some parameters are fixed in this analysis, namely the parameters determined by Rios et al. (2016) for the shape of the surfaces and the critical state framework (Table 8.7). The elastic moduli were fixed as well, because they were determined experimentally in the precedent chapters from the tests and do not need to be calibrated.

Table 8.7 - Conventional model parameters (Rios et al., 2016)

Constitutive model parameters	
κ	0.0097
λ	0.112
M	1.4
N	2.352
$\bar{n}$	2.2
r	3.7

In these conditions, the effect of different values of kinematic parameters R, B, ψ, on the response of an unstructured soil specimen was studied. Then, the parameters were all maintained fixed and the soil response under different levels of confining pressure was studied.

8.2.3.1. PARAMETER ψ

In the aforementioned conditions and by fixing R = 0.06 and B = 18.55, seven cyclic tests were simulated with six different values of ψ: 300, 500, 750, 1000, 1500, 2000, and 2500. The results are reported in Fig. 8.21 in terms of accumulated axial and volumetric strain vs. number of cycles.

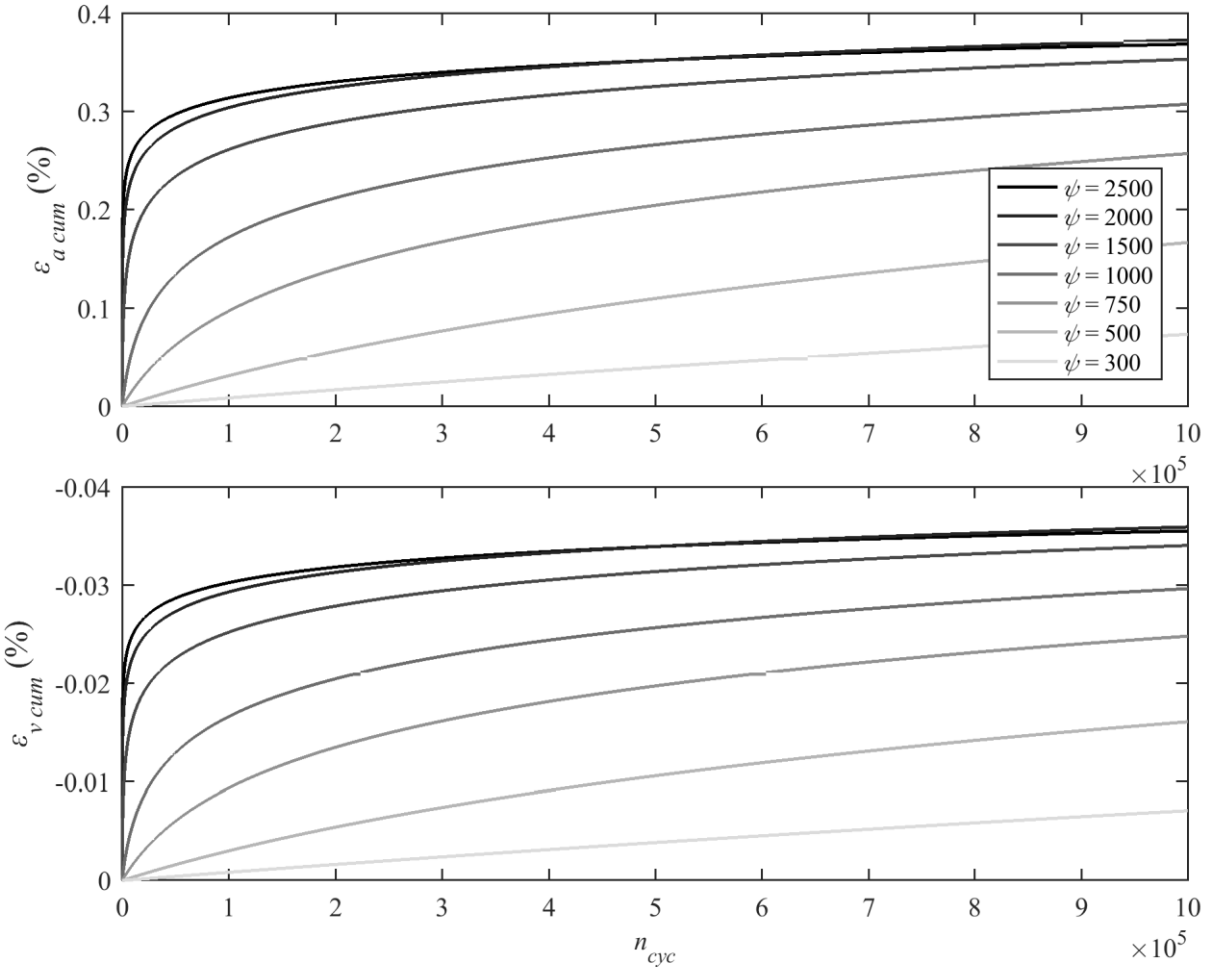

Fig. 8.21 – Set of simulated cyclic triaxial tests: effect of parameter ψ on axial and volumetric accumulated strain

As expected, the results show a strong influence of the parameter on the shape of the curves: increasing values of ψ result in higher accumulation during the first cycles followed by a lower rate of accumulation in the subsequent cycles. On the contrary, if ψ decreases, the trend of accumulation tends to become linear, as observed in the precedent section.

A negative volumetric strain accumulation is observed: this behaviour is consistent with the dilative behaviour of the material, which is tested under low confinement. Further simulated tests with higher confining pressures will be presented in the following sections.

Since the shape of these curves seems to be logarithmic, it is interesting to observe the same results in semi-logarithmic scale (Fig. 8.22).

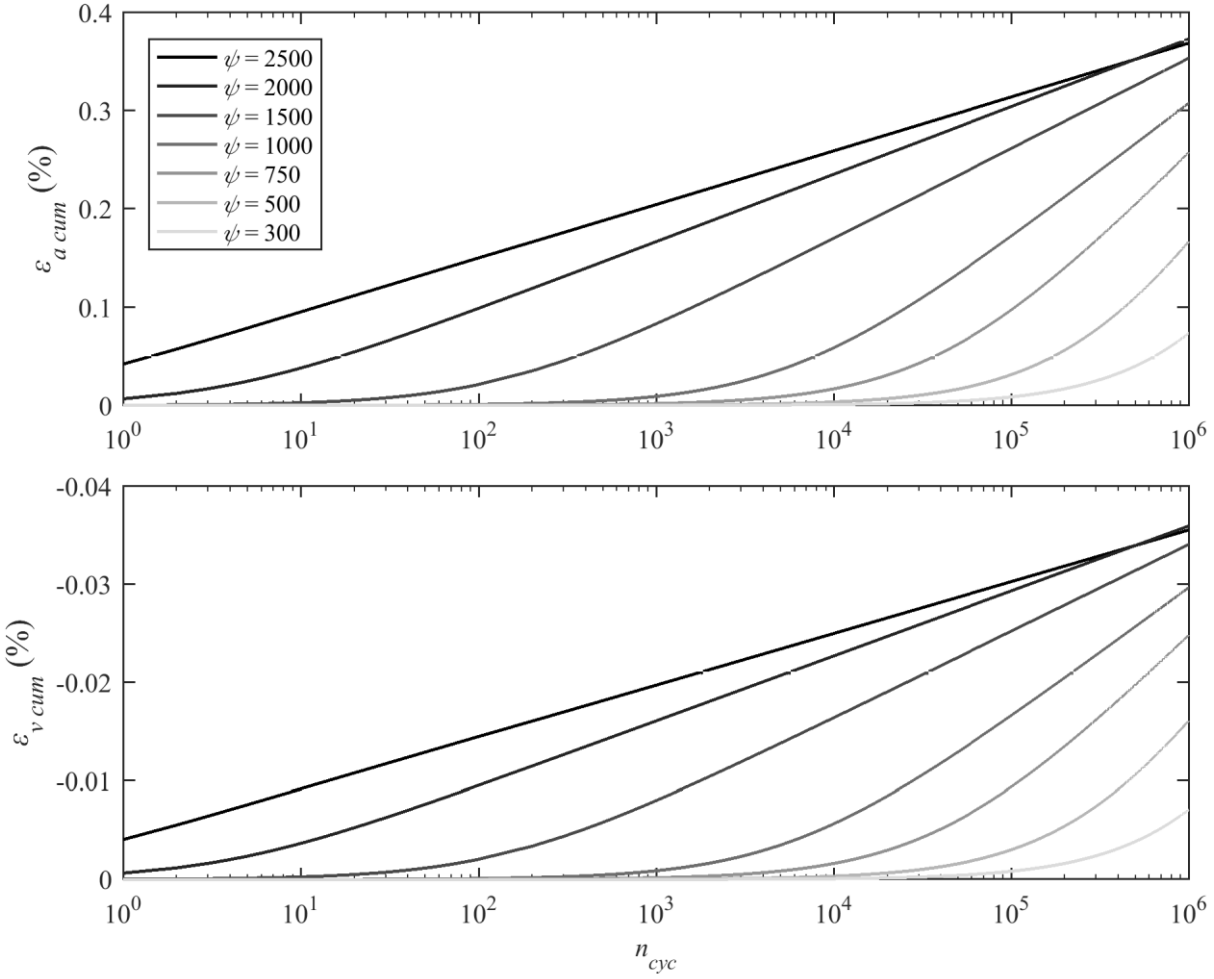

Fig. 8.22 – Set of simulated cyclic triaxial tests: effect of parameter ψ on axial and volumetric accumulated strain (semi-log scale)

Two trends can be highlighted, following the scheme proposed in Fig. 8.23.

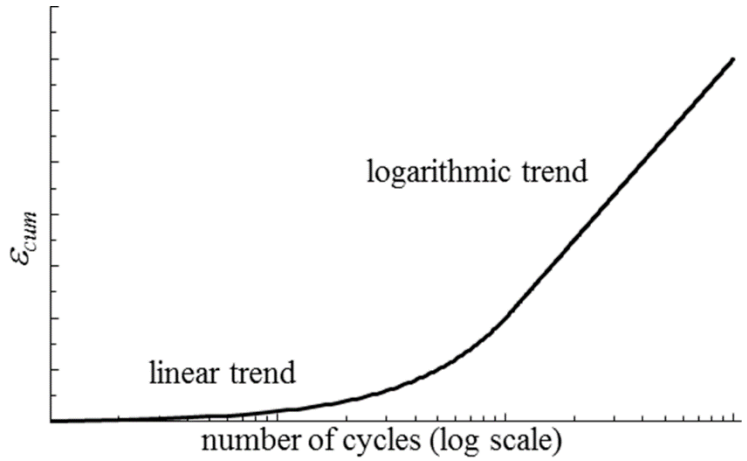

Fig. 8.23 – Scheme for the interpretation of the model output

The first part is characterised by a linear accumulation of the strain with the number of cycles, while in the second part the rate of accumulation is logarithmic. The linearity of the first part is confirmed in Fig.

8.24, where the detail of the first 100 cycles of the tests presented in Fig. 8.21 are reported. The vertical scale is different for each graph in order to report all the curves in the same figure. The linearity of the curves is shown for the simulations with low parameter ψ (for the presented case less than 2000). For higher values, a logarithmic trend is observed from the beginning of the simulated test. The semilogarithmic scale is more convenient to represent the long-term accumulation of the plastic strain and will be preferred hereafter in the modelling of the tests' results.

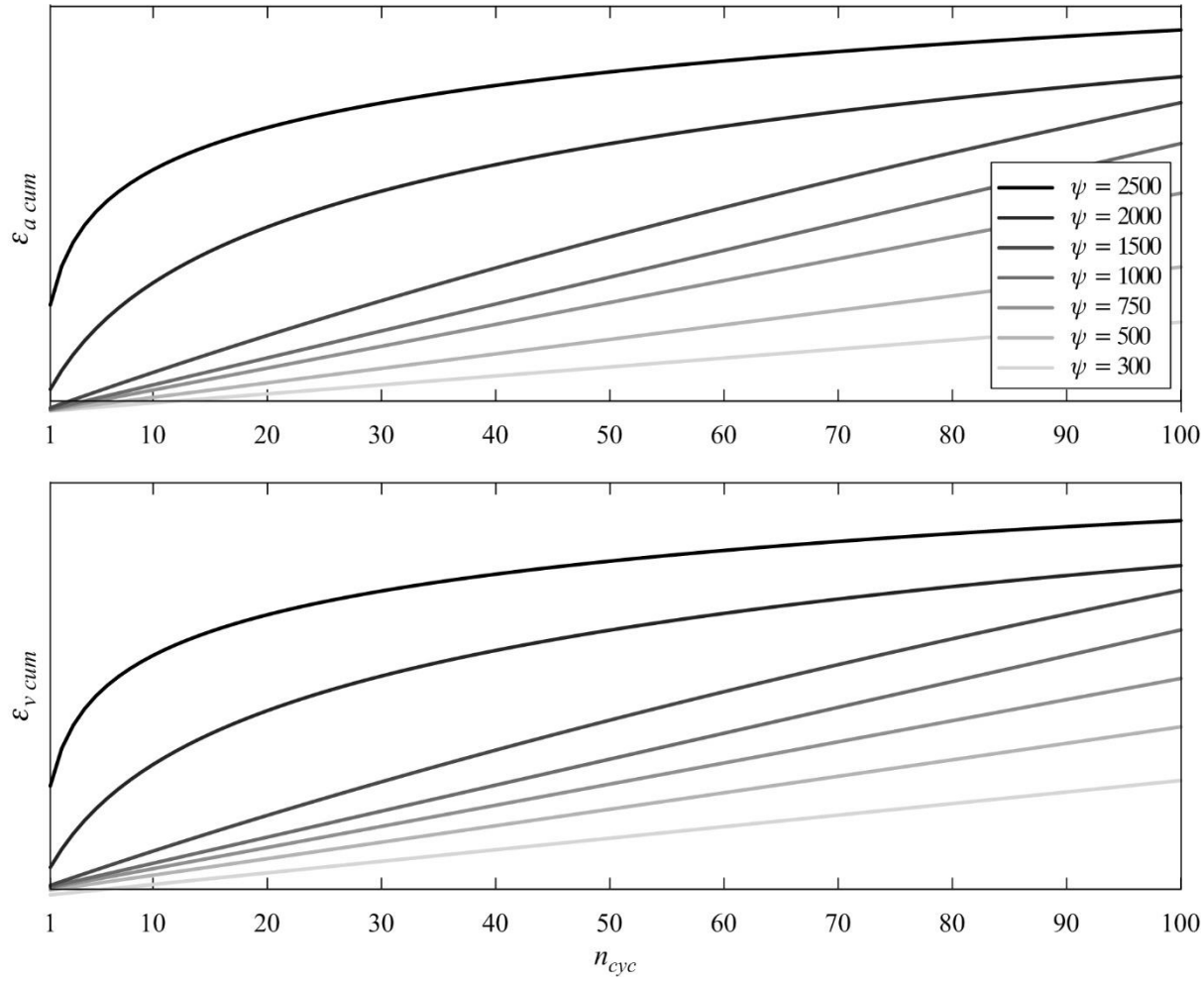

Fig. 8.24 - Set of simulated cyclic triaxial tests: detail of the first 100 cycles of the results. Axial and volumetric accumulated strain (vertical axis scale is different for each curve)

Parameter ψ governs the number of cycles at which the transition from linear to logarithmic trend occurs. Higher values of ψ lead to a decrease of the number of cycles at which the switch occurs. This is a very convenient feature of the model, since both linear and logarithmic trends are very commonly observed in long duration cyclic loading tests. Thus, by varying ψ, one can adapt the model to the observed behaviour of the soil. It is also possible to reproduce only one of the two trends by choosing an appropriate value for the parameter: for conveniently high values of ψ, only the logarithmic trend is observed (see the simulation with ψ = 2500). On the other hand, a low value of ψ leads to a linear trend without logarithmic part (ψ = 300). Intermediate values show the two trends in the same simulated test.

Moreover, this parameter determines the rates of accumulation of both trends: by increasing ψ, the rate of accumulation of the linear part increases while the rate of the logarithmic part decreases. In this way,

parameter ψ regulates the shape of the curves: a higher value of the parameter results in a higher accumulation rate in the first cycles and lower rate in the long term.

8.2.3.2. PARAMETER *R*

This parameter governs the size of the bubble, regulating the amplitude of the true elastic domain and determining the boundary between the purely elastic and elasto-plastic domain. Since R does not influence the hardening moduli, it is expected to have a linear effect on the accumulation curves, i.e. to affect only the level of the accumulated strain at a certain number of cycles but not the shape of the curves.

Five simulated tests were performed with R equal to 0.03, 0.04, 0.05, and 0.06. The remaining parameters are fixed as B = 18.55 and ψ = 500.

The results, reported in Fig. 8.25, show that the variation of R preserves the shape of the strain accumulation curves but affects the magnitude of the strain accumulation at a given cycle. The slope of the logarithmic increment is constant, while the strain accumulation decreases for increasing values of R. Also in this case, the linear and logarithmic trends are observed, in accordance to the scheme of Fig. 8.23.

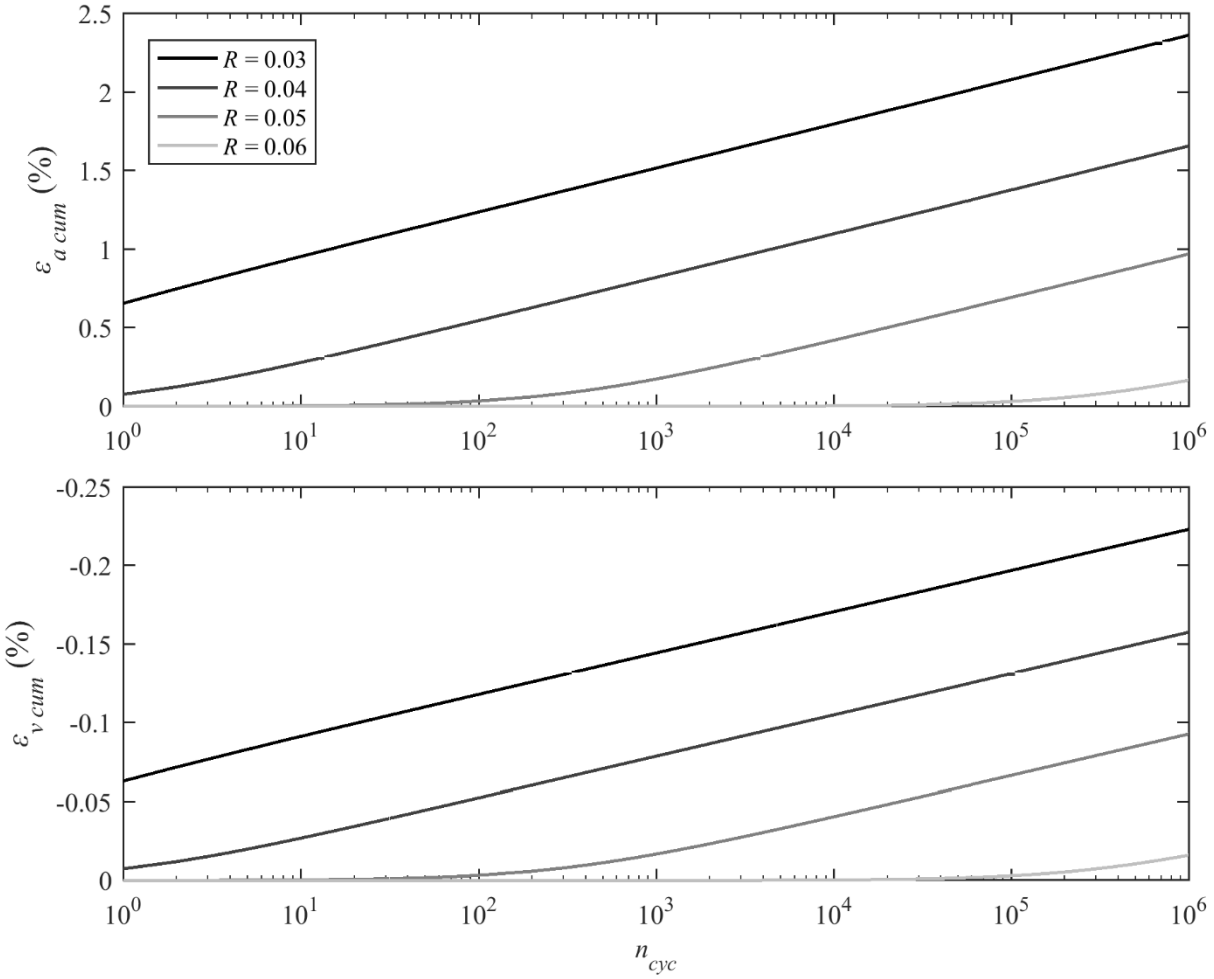

Fig. 8.25 – Set of simulated cyclic triaxial tests: effect of parameter R on axial and volumetric accumulated strain

The range of values of parameter R is limited by the amplitude of the stress path: if R is greater than a certain value (0.06 in the example presented), the cyclic stress-path will be entirely enclosed in the elastic domain. This leads to a perfectly elastic behaviour with no observed plastic strain increments. Thus, an upper limit for parameter R exists for each test, depending on the load range of the cyclic stress path.

8.2.3.3. PARAMETER B

This parameter affects the kinematic hardening modulus, H'. When the model is applied to a low-stress cyclic test, distance b between surfaces is high, thus the kinematic modulus is much greater than the isotropic modulus. This means that kinematic and total hardening modulus are almost coincident in the referred conditions. Therefore, B influences the whole hardening modulus. Consequently, parameter B has the same effect of parameter R: its variation produces a higher or lower strain accumulation but the shape of the curves is not influenced by this parameter. The simulated tests reported in Fig. 8.26 confirm this behaviour. The figure is referred to B equal to 18, 18.2, 18.28, 18.37, 18.45, 18.55, and 18.6. Parameter R is 0.06 and ψ is 500. The other parameters are reported in Table 8.7.

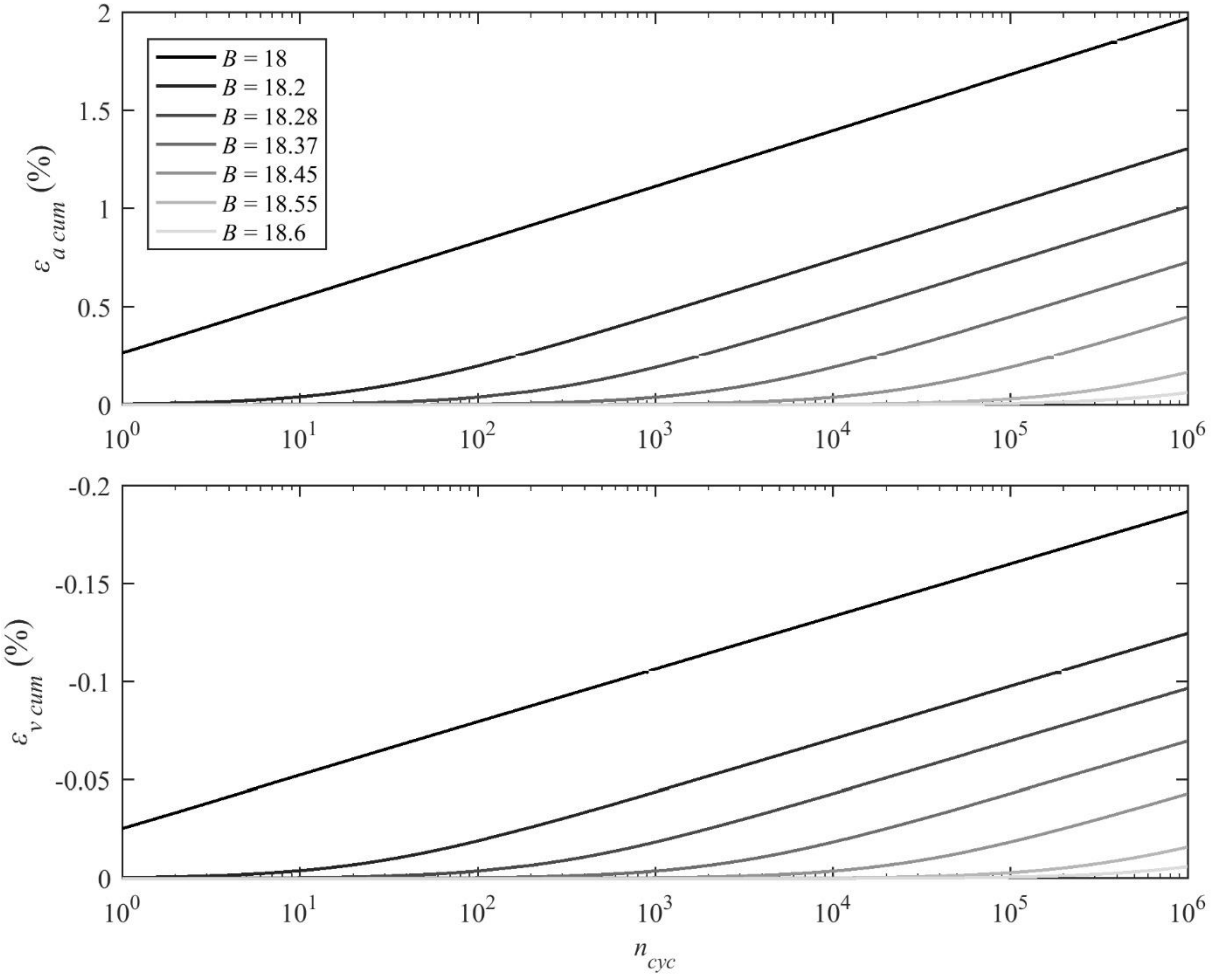

Fig. 8.26 – Set of simulated cyclic triaxial tests: effect of parameter B on axial and volumetric accumulated strain

As parameter B increases, the accumulation of axial and volumetric strain decreases. In this case, there is not an upper bound as for parameter R and this allows fitting the model results also to small strain

accumulations. On the other hand, parameter B has a lower bound (dependent on the stress levels and on the model parameters) imposed by the expression of the kinematic hardening modulus. From this expression (6.13), it can be seen that the quantity in brackets shall be greater than 1, because it is the basis of the exponent $\psi \gg 1$:

$$B\frac{b}{b_{max}} > 1 \tag{8.7}$$

Thus, parameter B shall not be lower than an inferior limit B_{lim}:

$$B_{lim} > \frac{1}{b/b_{max}} \tag{8.8}$$

Otherwise the value of the term in parenthesis is less than 1. A number less than unity, elevated to a high positive exponent produces a very small number, conversely to a base higher than 1. Thus, if the value changes (for effect of the change in b) from a value slightly higher than 1 to a value slightly less than 1, the kinematic hardening modulus drops suddenly to a much smaller value, causing numerical instability and possible sudden failure. The minimum value of B to avoid such situation depends on the value of the normalized distance b/b_{max}, which in turn depends on the stress conditions and initial parameters of the test. For example, in the test with B = 18.2 reported in Fig. 8.26, the normalized distance has a minimum value throughout the test approximately equal to 0.092 (this value can be very different from one test to another). Thus, the minimum value for the parameter B not causing instability in this test (not known a priori) is B_{lim} = 1/0.092 = 10.9. For higher values of B, the base of the exponent ψ (in this example ψ = 500) is higher than 1. If lower values are adopted, during the test the base of the exponent will assume a range of values including values higher than 1 and values less than 1 (because the normalized distance changes continuously during the test). This in turns produces major fluctuations in the value of the plastic modulus, since a small variation in the base (say between 0.99 and 1.01) causes high discrepancies when elevated to a high esponent (from 0.99^{500} to 1.01^{500}). Thus, such situation shall be avoided by selecting a value of B that guarantees only values of the base greater than 1. This selection shall be done by a trial and error procedure, because the minimum value of the normalized distance depends on the imposed stress and on the model parameters (including B) and cannot be known a priori.

8.2.3.4. Effect of confining pressure

The confining pressure at which the test is performed influences the direction of the plastic strain increment vector, according to the flow rule. When the confining pressure is low, the stress path intersects the yield surface in the dilatant side of the stress domain in the loading and unloading stress paths. This leads to negative volumetric plastic strain increments as shown in the precedent sections, in which the confining pressure of 40 kPa is much smaller than the isotropic yield stress (300 kPa).

As reported in 6.4, the yield surface tends to occupy a position so the configuration in Fig. 6.8 is reproduced. In particular, condition (6.67) is verified. This is verified during loading and unloading in a cyclic test. Thus, for a drained triaxial stress path, the confining pressure influences the value of effective stress ratio η'_U on the reference surface and, consequently of η'_α on the yield surface. The lower is the confinement, the higher are the two effective stress ratios. Since this parameter in turn determines the flow rule, it determines whether the volumetric strain tendency is dilative or compressive. Hence, the level of confinement determines the volumetric response of the test, similarly to what happens in single surface isotropic models, while simulating monotonic tests.

In the case of the tests reported in the precedent sections, the confining pressure of 40 kPa is low in comparison with the size of the reference surface (300 kPa). For the effect of the translation rule, this

corresponds to a high value of the stress ratio on the kinematic yield surface and thus a corresponding dilative behaviour (in loading and unloading). For increasing values of confinements, the stress ratios referred to the reference and yield surface decrease simultaneously, producing a compressive response for an adequate level of confining pressure. This explains the negative sign of the accumulated volumetric plastic strain observed in the precedent figures.

For progressively increasing values of confining pressures, the yield position adjust accordingly and the effective stress ratios of the yielding points during loading and unloading progressively decrease. For a certain confinement, the stress path will intersect the yield surface in the compressive side during loading and in the dilative side during unloading. As referred earlier, the resulting sign of the volumetric strain depends on the weights of the two concurrent components. If new tests are performed, each with a higher value of confining pressure, the stress path will intersects the yield surface in the compressive side during loading and unloading, resulting in compressive overall volumetric strain at the end of each cycle.

Two simulated tests are reported in Fig. 8.27, where the confining pressure is 250 kPa (relatively high, comparatively to an isotropic yield stress of 300 kPa) and the constants presented in Table 8.7 are maintained. Two values of parameter ψ were adopted, in order to show that this parameter has no influence on the volumetric tendency (i.e. the sign) of the model response, but only on the shape and magnitude of the accumulation curves. The volumetric strain accumulation is positive as expected (axial strain is also positive).

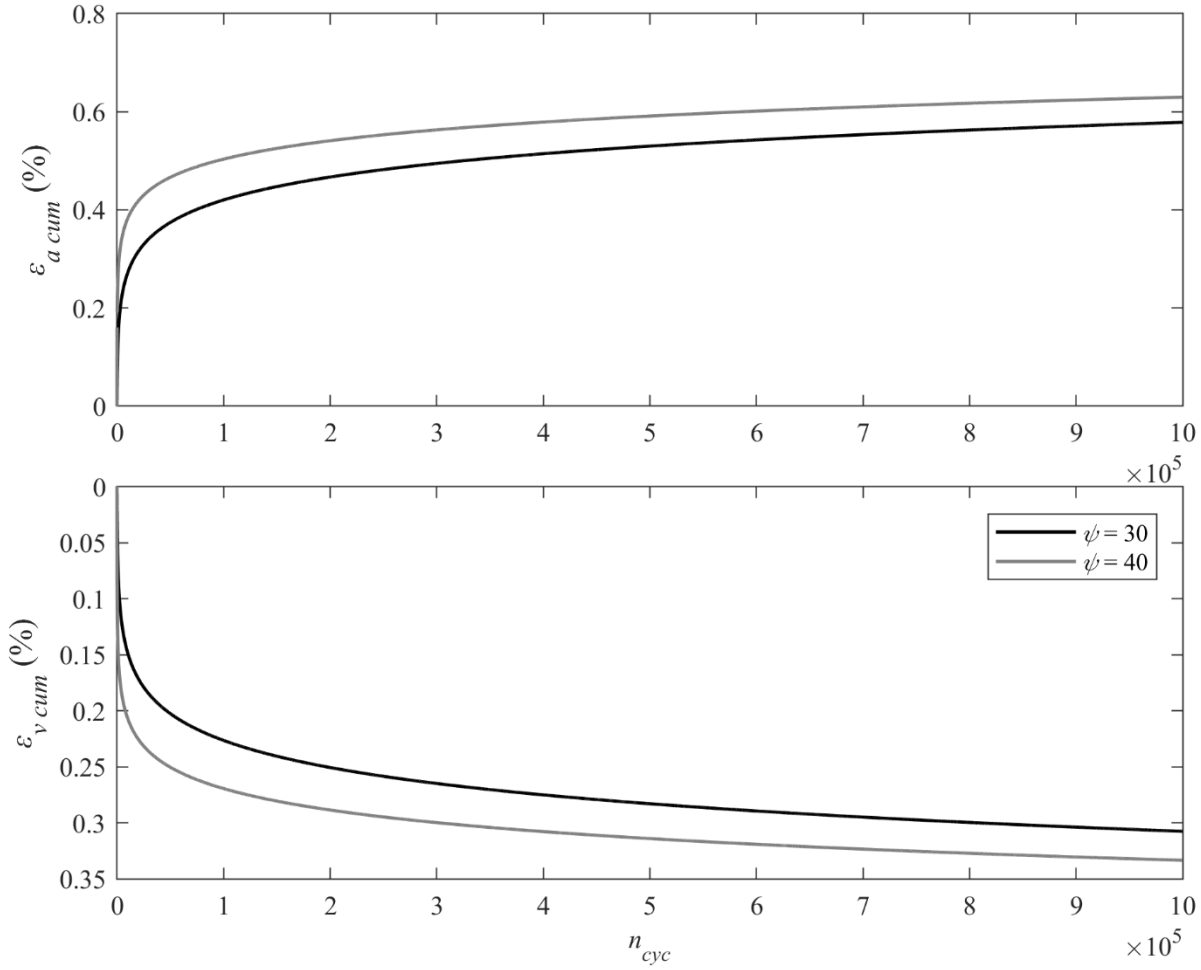

Fig. 8.27 – Simulated tests for σ'_c = 250 kPa

Finally, when the confining pressure is at an intermediate value, the sign of the volumetric plastic increments is positive during loading and negative during unloading and the overall accumulation depends on which of the two competing contributions prevails. The simulated tests (Fig. 8.28) show that, depending on the confining pressure, the volumetric strain accumulation can be positive or negative. Nevertheless, in either case an equilibrium point is eventually reached, at which the components of the volumetric plastic strain increment during loading and unloading are equal and have opposite signs. Thus, the accumulation of volumetric strain remains constant (no further accumulation of volumetric strain is observed after this point). When this happens, the yield surface does not change in size and the corresponding axial strain accumulation increases linearly with the number of cycles.

In the figure, the confining pressure in one test is slightly higher than in the other and this distinguishes the two initial volumetric strain accumulations, which become opposite, while the accumulated axial strain is positive in the two cases, as expected.

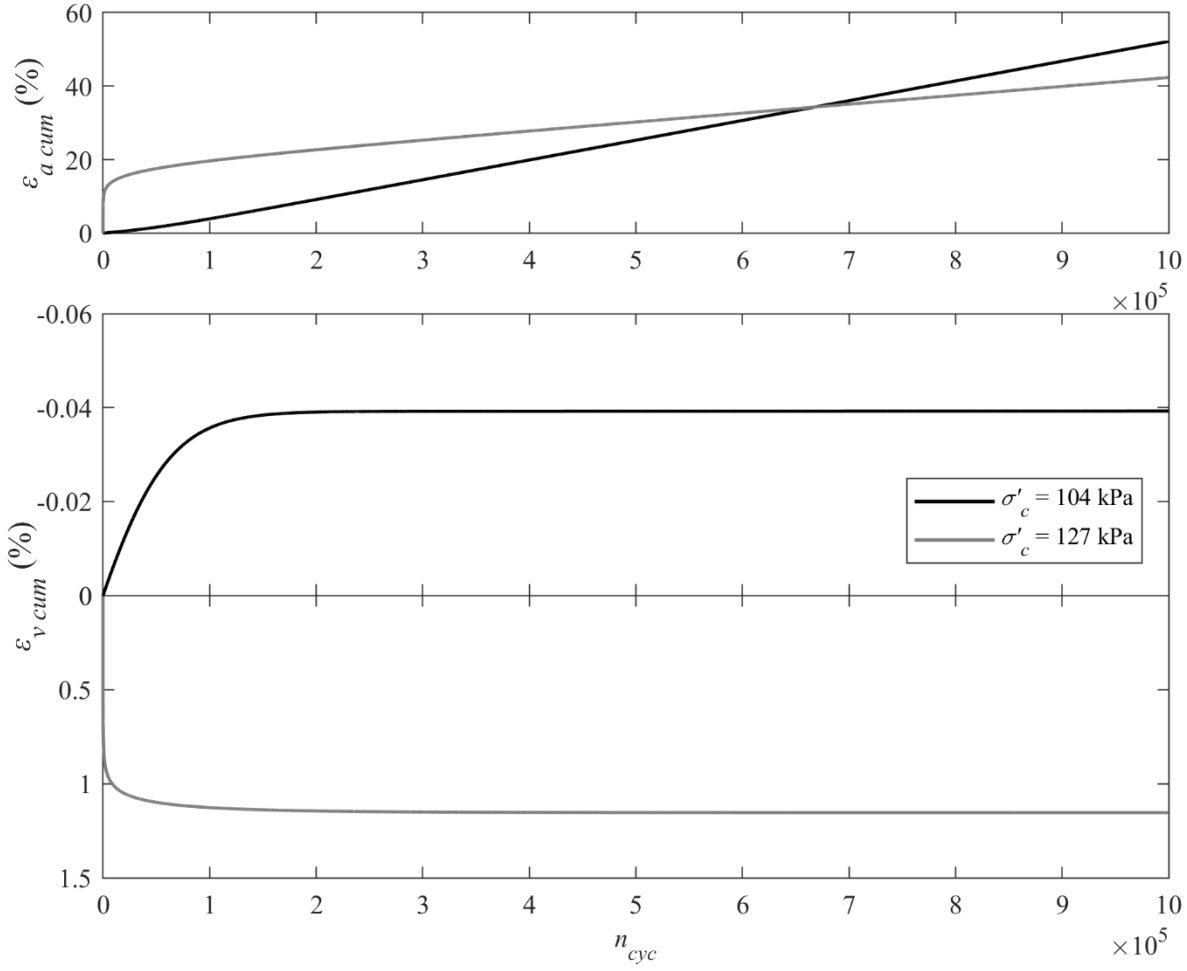

Fig. 8.28 –Test with similar confining pressures (σ'_c = 104 and 127 kPa) and opposite volumetric strain accumulation (positive and negative sides of vertical axis in different scales)

8.3. MODELLING CYCLIC TRIAXIAL TESTS

The aim of the present section is to calibrate the model against the long-term cyclic triaxial tests described in Chapter 5. The calibration performed against monotonic tests in section 8.1 is taken as a

starting point to model the more complex cyclic tests. Cyclic tests present extra features not present in monotonic tests, such as the stress-strain loops observed in the experimental results and the complex accumulation curves representing the increase in permanent axial and volumetric strain with the number of loading cycles.

As illustrated in the precedent sections, the features of the model do not allow the correct reproduction of both the stress-strain loops and the accumulation curves using a single set of parameters. Since in the present section the model is calibrated against long-term cyclic behaviour, attention is focused on the accumulation curves rather than on the hysteretic stress-strain loops.

The four state parameters referring to the nine soil-cement mixtures submitted to the 24 drained and the 3 undrained triaxial tests were initialized as illustrated in section 8.1. The state parameters are:

- initial size for the uncemented soil;
- initial level of bonding;
- initial tensile strength;
- initial position of the yield surface.

The results of the process (along with the index properties of the specimens) are reported in Table 8.8. As illustrated in the precedent sections, the determination of the bonding state variables is possible only after having selected the parameters regulating the shape of the reference surface (M, r, and $\bar{n}$). In the present process, the same shape parameters determined in sections 8.1.2 and 8.1.3 for monotonic tests were used (M = 1.4; $\bar{n}$ = 2.2; r = 3.7). The initial coordinates of the yield surface apex are calculated using expression (8.3) and are not reported in table, as their value depends on model parameter R.

Table 8.8 – Initial state variables and index properties for cyclic triaxial tests

Name	v_i	C	$n/C_{iv}^{0.21}$	p'_{0unc_i} (kPa)	p'_{0i} (kPa)	b_0	p'_{ti} (kPa)
0%_e1	1.75	0	-	353	353	0	0
3%_e1	1.75	3	39.6	353	2150	5.0	270.9
5%_e1	1.75	5	35.7	353	3193	7.9	465.4
7%_e1	1.75	7	33.3	353	4212	10.7	663.6
0%_e2	1.60	0	-	1527	1527	0	0
3%_e2	1.60	3	33.7	1527	5068	2.3	502.9
5%_e2	1.60	5	30.7	1527	6895	3.4	846.8
7%_e2	1.60	7	28.5	1527	9002	4.8	1267.4
3%_e3	1.65	3	36	937	3614	2.8	385.5

8.3.1. UNCEMENTED TESTS

Similarly to the monotonic case, the calibration of the kinematic parameters started from the uncemented tests, as these require less parameters. All the parameters were initially taken equal to those used for the monotonic tests and reported in Table 8.1, Table 8.2, and Table 8.3, and Rowe flow rule was adopted also in this case. This group of parameters was used to perform simulated tests and the outcome proved that not all the values are adequate for reproducing cyclic tests. In particular, parameters regulating the kinematic hardening properties of the model need to be set to very different values. The value set for

parameter R in monotonic tests (0.8) would correspond to a large purely elastic domain that includes completely the small cyclic stress paths applied in the cyclic tests. In such configuration, after the first loading cycle, the stress path would no longer intersect the surface (i.e. no yielding would be observed) and the successive unloading-reloading paths would be purely elastic, without plastic strain development.

For the reasons expressed in the precedent sections, parameter ψ shall assume a high value to reproduce the rapid cyclic hardening observed in cyclic tests. A small value was used for monotonic tests, because the non-linearity is produced by the great variation of distance b between the beginning and the end of the stress path. Conversely, in cyclic tests such a low value produces an almost linear accumulation of plastic strain with the number of cycles, while a strong non-linearity is observed in the experimental results. This is due to the small extension of the stress paths, which leads to small variations of b between successive cycles. Moreover, as previously illustrated, a low value of parameter ψ in cyclic tests can lead to a soil response stiffer during loading than during unloading and, consequently, to undesirable negative strain accumulation.

Finally, the value of parameter B previously determined shall be increased in order to obtain an adequate value of hardening modulus. In the example of Fig. 8.29, the model was calibrated against test TC_0%_e1_s1. The parameters used for monotonic tests were kept, except for the three aforementioned parameters, which were calibrated using the procedure described in section 8.1.4. The new values are reported in Table 8.9.

Table 8.9 – Kinematic hardening parameters for test TC_0%_e1_s1

R	B	ψ
0.02	7.58	5000

Parameter R is smaller than the value adopted in monotonic tests, while parameters B and ψ are substantially higher. The new values of B and ψ respond to the need of obtaining higher values of the plastic modulus H and a stronger dependence on distance b.

Model output shows a fair agreement with experimental results in the axial strain accumulation. The results are coincident in the first 10 cycles and in the interval from 10^5 to one million cycles, with a small error in the intermediate cycles; the logarithmic rate of accumulation observed in the experimental results is consistent with the simulated test.

Volumetric strain accumulation is not at all reproduced by the model. Experimental results in volumetric strain variation is more complex than the axial accumulation: a compressive behaviour is followed by a change in the sense of accumulation and a successive dilative behaviour.

This pattern reveals a kind of elastoplastic evolutive behaviour, which the model is unable to reproduce. Indeed, as explained in the previous sections, if the yield surface is initially located in a position for which the translation vector is not parallel to the stress increment vector, the surface rapidly shifts to a position that accommodates this requirement. This shift is proved to happen within a few loading-unloading cycles. If the initial coordinates of the apex are determined with the same criterion used in monotonic tests (equations (8.3)), the bubble apex shifts towards the positive direction of the p' axis and the volumetric strain switches from compressive to dilative within the first two cycles. This behaviour is not consistent with the experimental results, where the change in the volumetric accumulation tendency occurs after thousands of cycles.

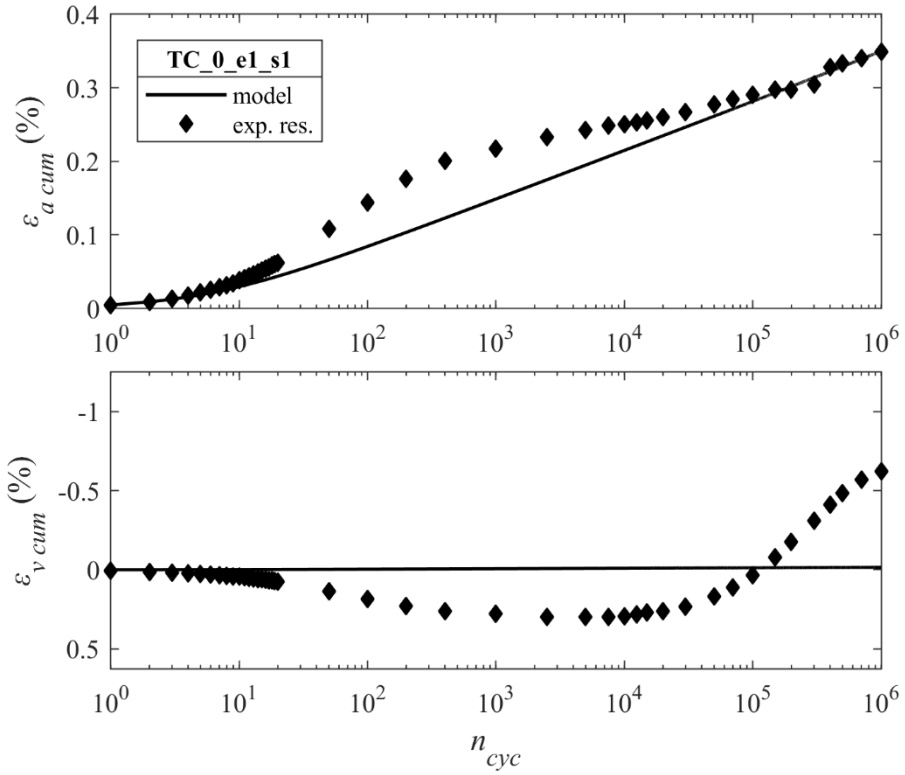

Fig. 8.29 – Model calibration against drained cyclic test TC_0%_e1_s1: axial and volumetric strain accumulation vs. number of cycles

The accumulation of volumetric strain predicted by the model is much smaller than the one observed in experimental results. Thus, Rowe flow rule does not seem to be adequate for the cyclic case. It is possible to reduce the value of parameter B (and consequently the hardening modulus H) and obtain a larger volumetric strain, closer to the real experimental value. Nevertheless, such option would produce a very high axial strain.

Yu flow rule was tentatively adopted as an alternative to Rowe flow rule. Such formulation incorporates an adjusting parameter m that allows to control the dilatancy (i.e. the incremental volumetric over distortional plastic strain ratio) for a given stress ratio. In the present case, a higher dilatancy than in the former case is required. As described in Chapter 6, dilatancy increases for decreasing values of parameter m. On the other hand, if parameter m is less than 1, the domain that is controlled by the flow rule reduces when values of this parameter decrease below one. That is, when values of parameter m lower than 1 are selected, the compatibility of this condition must be checked at each stress increment during the test. Even if the smallest allowable value of m is selected (m = 0.49), the dilatancy does not increase considerably with respect to Rowe's dilatancy. In Fig. 8.30, the output obtained with Yu flow rule is shown. Even though accumulated volumetric strain is higher than in the precedent simulation, it remains considerably smaller than in the experimental results.

While the results in monotonic loading are correct, the flow rules fail in correctly representing the ratio between the two components of the plastic strain vector. It is possible that both the flow rule explored (Rowe and Yu) are not adequate to reproduce the soil dilatancy during unloading. Both rules were developed from experimental data relative to monotonic compressive loading (with positive deviatoric stress) or tensile unloading (with negative deviatoric stress). In the case of a cyclic test, the unloading part is performed with a positive value of deviatoric stress. It is possible that in such situation, the flow rule has a specific formulation that may be suitable to these experimental results, since unloading in the

positive deviatoric plane was considered as a purely elastic unloading in the classic single-surface framework.

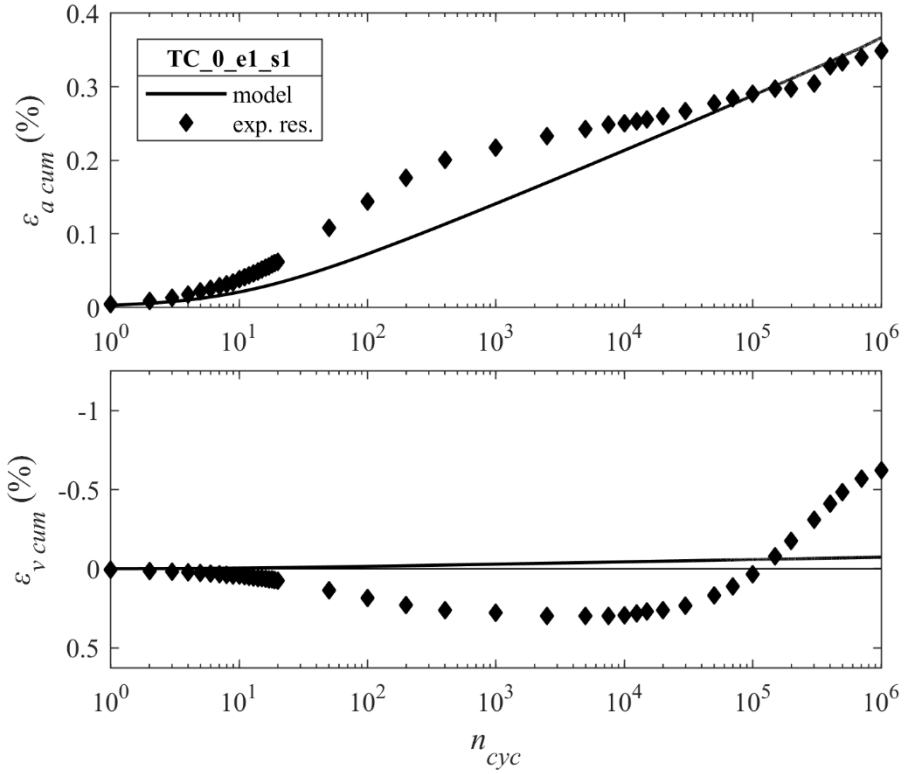

Fig. 8.30 – Model calibration against drained cyclic test TC_0%_e1_s1 using Yu flow rule

It is important to notice that kinematic hardening parameters used to calibrate the model with Rowe flow rule are no longer valid when Yu flow rule is applied. The results of Fig. 8.30 were found using the parameters reported in Table 8.10.

Table 8.10 – Kinematic hardening parameters for test TC_0%_e1_s1 using Yu flow rule

R	B	ψ	m
0.02	7.5	1000	0.49

The calibration of the subsequent tests showed the impossibility of finding a unique set of values for the three parameters reported in Table 8.9 or in Table 8.10. In fact, each test requires a specific set of parameters to produce a good agreement at least in the axial component of the plastic strain accumulation (similar to that shown in Fig. 8.29 and in Fig. 8.30). Moreover, the sets of values adopted vary considerably between different tests. Thus, it was impossible to correlate the values of the parameters in the different tests to some physical property of the specimen or some testing conditions. The values of the parameters retrieved for all the tests are resumed in Table 8.11, taking the void ratio as reference, and the relative accumulation curves reported in Annex 6.

As shown in the table, the values of the kinematic hardening parameters vary considerably from test to test. The value of parameter R has been maintained constant, because its variation had the only effect of increasing or decreasing the accumulated strain linearly, but not the shape of the accumulation vs. number of cycles curve (due to the low loading range of the cycles).

Table 8.11 – Parameters for the calibration of the uncemented tests

	s1			s2			s3		
e	R	B	ψ	R	B	ψ	R	B	ψ
e1	0.02	7.578	5000	0.02	2.875	-1100	0.02	2.2563	-1650
e2	0.02	26.9	450	0.02	4.275	-2300	0.02	5.5238	-20000

The values determined for test TC_0%_e1_s1 are not suitable for test TC_0%_e1_s2. In fact, it was observed that, for the latter test, any positive value of ψ would produce negative values of accumulated axial strain. Further analysis of the results showed that, for the particular stress levels imposed in this test, the length of vector $\boldsymbol{\beta}$ in the loading phase is longer than in the unloading phase, as shown in Fig. 8.31:

$$\|\boldsymbol{\beta}_{load}\| > \|\boldsymbol{\beta}_{unl}\| \tag{8.9}$$

This in turns causes distance b to be higher in loading than in unloading. In fact, the angles θ_β between $\boldsymbol{\beta}$ and the normalized outward normal vector $\boldsymbol{n_f}$ are similar in loading and unloading; thus, the value of the scalar product is mainly influenced by the magnitude of $\boldsymbol{\beta}$. Therefore, the kinematic hardening modulus is higher during loading than during unloading (e.g. the soil is stiffer in loading than in unloading), and the resulting accumulated axial strain is negative. Such negative accumulation is observed for any positive value of parameter ψ, for the reasons herein explained.

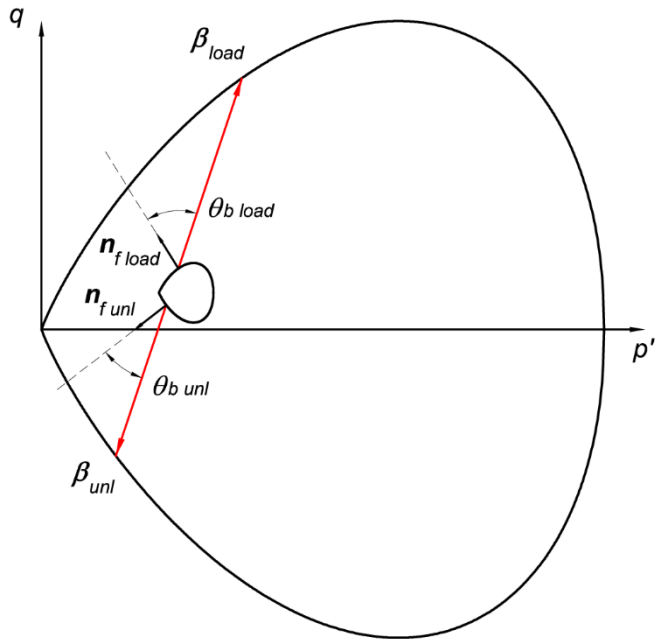

Fig. 8.31 – Initial configuration of test TC_0%_e1_s2 with vector $\boldsymbol{\beta}$ in loading and unloading

An example of calibration of test TC_0%_e1_s2 is reported in Fig. 8.32 and Fig. 8.33, where similar parameters to test TC_0%_e1_s1 are adopted (Table 8.12).

Table 8.12 – First set of parameters used for calibrating test TC_0%_e1_s2

R	B	ψ
0.02	3	5000

In Fig. 8.32, where the first 20 cycles are shown, one can observe that the loading part of the cycles is almost purely elastic, while the unloading part presents a clear plastic component of strain. As a result, the accumulation of axial strain is negative. Such result was confirmed by many other simulations conducted with different positive values of ψ in the range from 0 to 10000, confirming this behaviour.

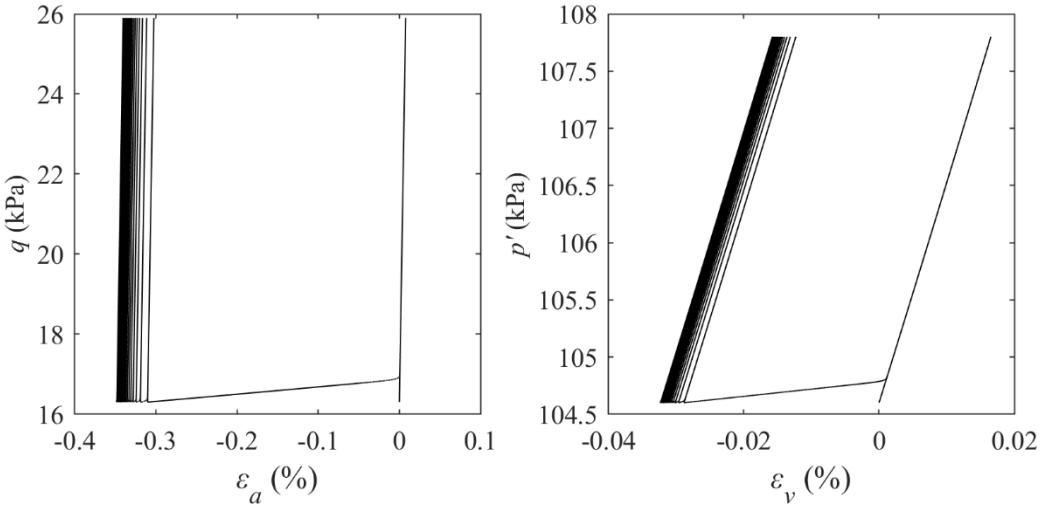

Fig. 8.32 – Stress strain loops for test TC_0%_e1_s2 with positive parameter ψ (first 20 cycles)

In order to obtain a positive axial accumulation, a negative value of ψ should be adopted. In fact, the expression of the kinematic hardening modulus H', reported in (6.13), shows that the modulus depends on the term:

$$\left(\frac{b}{b_{max}}\right)^{\psi} \tag{8.10}$$

Adopting a negative value of the exponent ψ is equivalent to consider a positive exponent and a reciprocal ratio:

$$\left(\frac{b}{b_{max}}\right)^{-|\psi|} = \left(\frac{b_{max}}{b}\right)^{|\psi|} \tag{8.11}$$

Thus, if $b_{load} > b_{unl}$ and ψ is negative, the kinematic hardening modulus is less in loading than in unloading, as required. Hence, the values reported in Table 8.11 were adopted for test TC_0%_e1_s2, leading to the results reported in Fig. 8.34 and Fig. 8.35.

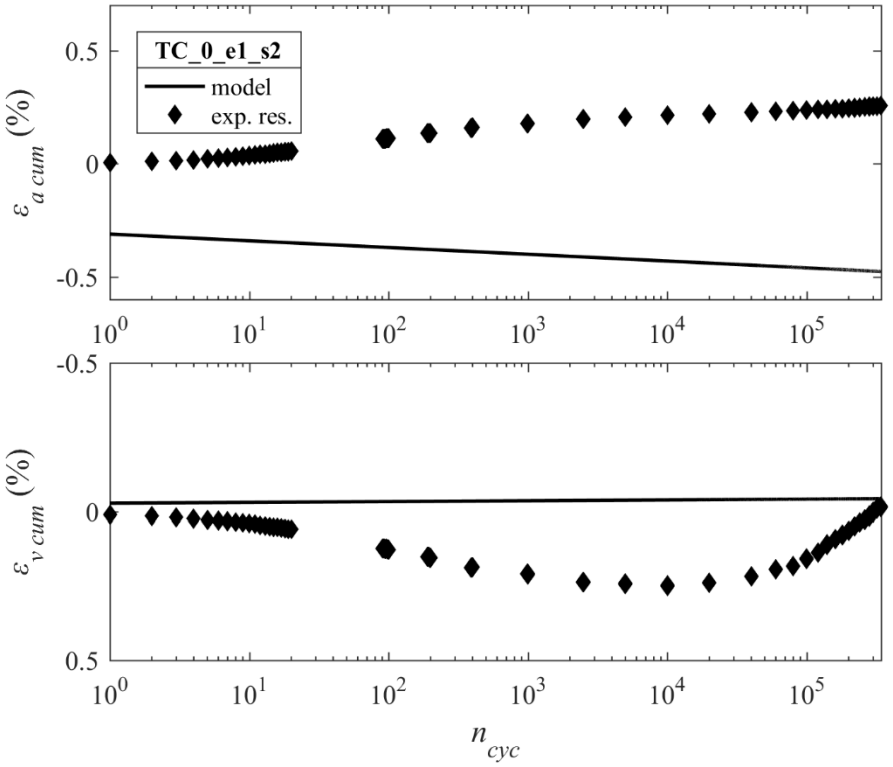

Fig. 8.33 – Accumulation curves for test TC_0%_e1_s2 with positive parameter ψ

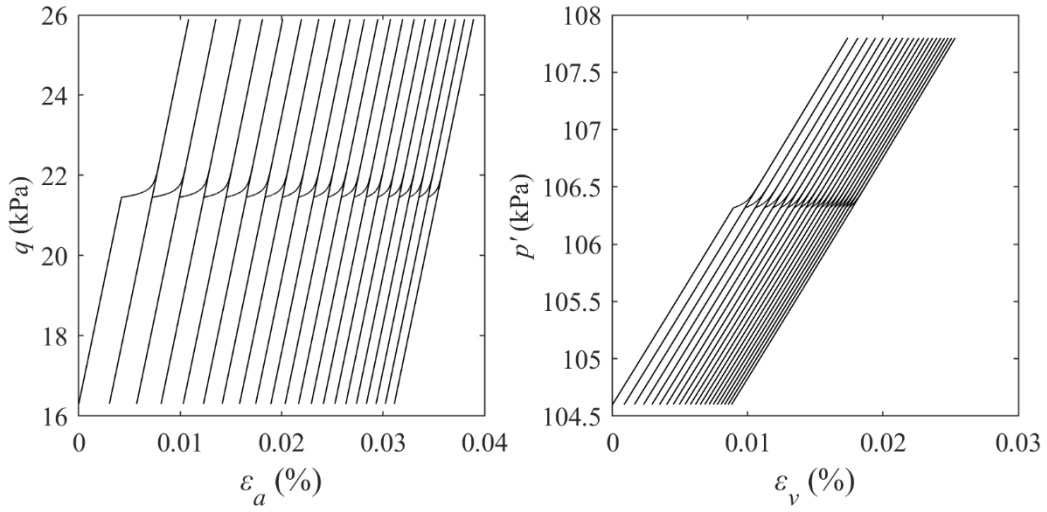

Fig. 8.34 – Stress strain loops for test TC_0%_e1_s2 with negative parameter ψ (first 20 cycles)

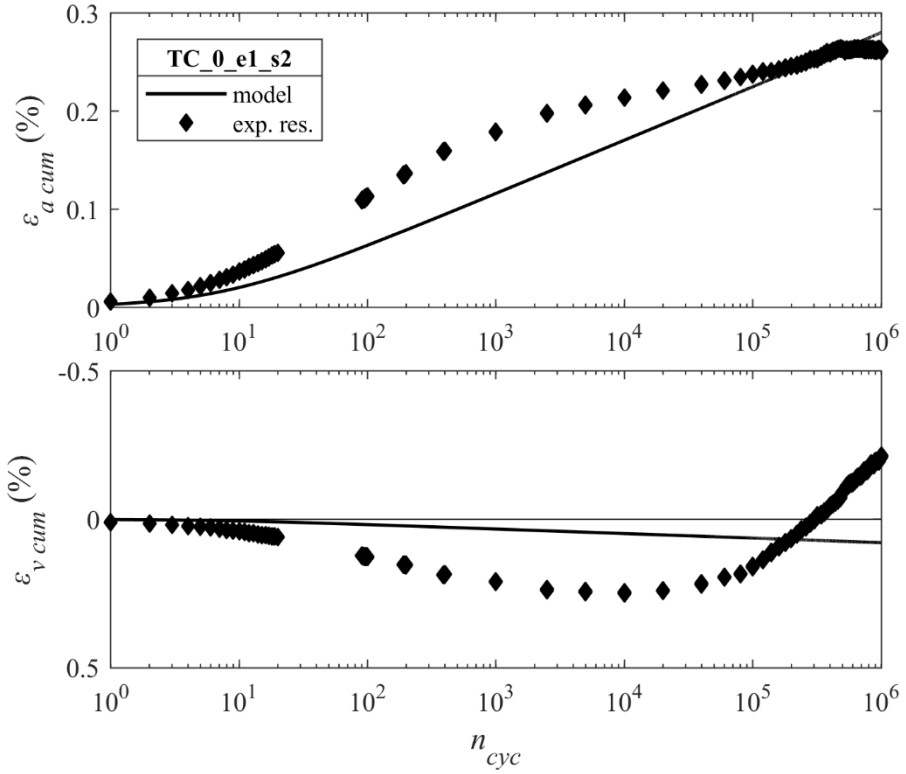

Fig. 8.35 – Accumulation curves for test TC_0%_e1_s2 with negative parameter ψ

The accumulated axial strain is positive. The selected parameters allow for a fair accuracy in the reproduction of the experimental results, similarly to test TC_0%_e1_s1. Also in this case, the volumetric accumulated strain predicted by the model is lower than the strain observed in the experimental results. Moreover, the volumetric tendency is compressive throughout the test, without the observed switch from compression to dilatant behaviour. The reproduction of the stress-strain loops in the case of a negative value of parameter ψ is not accurate. As shown in Fig. 8.34, the loading part is constituted by an elastic domain followed by an elasto-plastic phase, as usual; nevertheless, this last part of the domain presents a very low stiffness at the onset of yielding, followed by a progressive hardening with the increment of axial load. This is a consequence of the negative value of ψ, which causes kinematic hardening modulus to be inversely proportional to distance b. In the case of positive parameter ψ, the stress-strain loops assume the shape reported in the example in Fig. 8.20. In that case, the shape is much closer to the experimental results, with the elasto-plastic domain presenting a progressive softening after the onset of plastic strain.

Of course, in the present case the adoption of a negative ψ is necessary to obtain a positive accumulation of axial strain with the cycles. As previously referred, it is not possible to find a value for parameter ψ that guarantees the correct reproduction of the accumulation curves and the stress-strain loops. As explained in the previous sections, priority is given to the reproduction of the accumulation curves rather than the stress-strain curves.

Similarly to test TC_0%_e1_s1, also in this case Yu flow rule was applied as an alternative to Rowe flow rule. Also in this case, the adopted parameters are different from the set selected for the precedent calibration, as shown in Table 8.13. Parameter ψ is negative also in this case. The resulting accumulation curves are presented in Fig. 8.36.

Table 8.13 – Kinematic hardening parameters for test TC_0%_e1_s2 using Yu flow rule

R	B	ψ	m
0.02	3.05	-200	0.3

The output of the axial accumulation is similar to the precedent one, obtained using Rowe flow rule, while the reproduction of volumetric accumulation improves considerably. The agreement is very good in the first 10000 cycles, while diverging after this limit, because of the specific change in accumulation observed in experimental tests, this being the novel finding of this experimental study.

The adjusting parameter for Yu flow rule (m) was set equal to 0.3, less than the value adopted in TC_0%_e1_s1 (0.49). As previously explained, the less is the value of m, the higher is the volumetric plastic strain increment. As referred in Chapter 6, Yu flow rule is not defined on the entire stress plane when $m < 1$. In the case of test TC_0%_e1_s2, the maximum effective stress ratio η'_α reached during the test is less than in test TC_0%_e1_s1. Thus, the value of m can be inferior to the latter simulated case. The value of 0.3 cannot be used in that precedent test because it would violate the domain of existence of the flow rule. Thus, the need of having a low value of m contrasts with the necessity to guarantee that the condition of existence is met. This is a clear limitation of this flow rule.

The remaining uncemented tests confirmed the need for different sets of parameters (for Rowe and for Yu flow rules), and the need for a negative value of ψ in the majority of the cases, as resumed in Table 8.11. The results of the strain accumulation curves for these tests are reported in Annex 6. They show a good agreement in the axial accumulation strain and a volumetric accumulation inferior to the accumulation observed in laboratory tests.

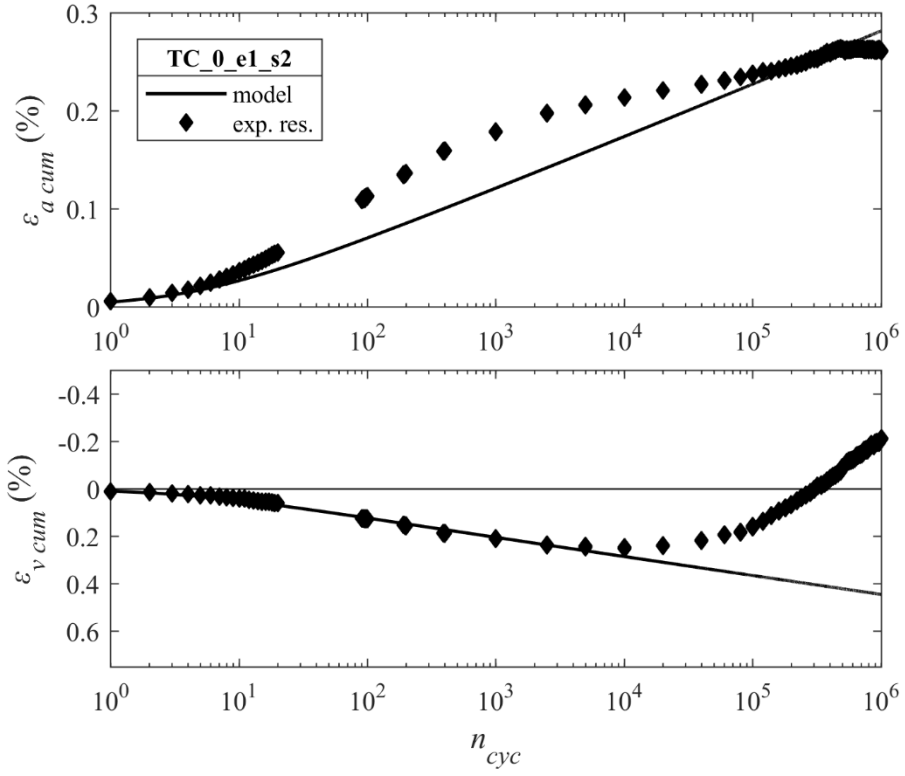

Fig. 8.36 – Accumulation curves for test TC_0%_e1_s2 with negative parameter ψ and Yu flow rule

8.3.2. CEMENTED TESTS

The calibration of cemented tests would follow the same staged approach used in the monotonic tests (paragraph 8.1): using the kinematic parameters determined for the uncemented soils, in the present section only the destructuration parameters would be implemented. Nevertheless, as explained in the precedent section, it was not possible to determine a single set of kinematic parameters. Thus, it is difficult to determine the destructuration parameters for cemented tests.

In Table 8.14, two different sets of kinematic and destructuration parameters are presented. In the set reported in first row, the rate of destructuration is approximately zero. In the second row, a higher value of destructuration is imposed. The value of ψ and B are higher in the second case, while R is constant. The results of the simulations performed with the two sets show a very similar trend in the two cases (Fig. 8.37 and Fig. 8.38). The increased accumulation due to the higher rate of destructuration is compensated in the second case by a higher kinematic hardening modulus, which results in an increased stiffness of the uncemented component of the soil. Thus, it is not possible to distinguish the concurrent contributions represented by the loss of bonding on one hand, and the cyclic stiffening of the uncemented component of the soil, on the other hand.

Table 8.14 – Two different sets of kinematic hardening and destructuration parameters for test TC_3%_e1_s1 using Rowe flow rule

R	B	ψ	b_1	b_2
0.02	9.139	8000	1e-4	1e-4
0.02	9.146	13000	10	10

A tentative calibration of the kinematic hardening parameters of the cemented soil was performed in the hypothesis that the destructuration parameters are nil ($b_1 = b_2$ = 1e-4 as in the precedent case). Such attempt was performed in the hypothesis that the strong structure of the artificial cement suffer negligible loss during the small-stress tests performed. The results of the calibration, reported in Annex 6 (parameters adopted are reported in Tables A.0 to A.0), do not show a consistent set of kinematic parameters. In some tests (e.g. TC_3%_e2_s1), the accumulation of the axial and volumetric strain with the number of cycles presents a progressively increasing rate with the number of cycles, i.e. the stiffness decreases with the number of cycles and the rate of accumulation is exponential, and ultimately failure. It was noted that this behaviour is no dependent on the set of kinematic parameter selected.

A detailed analysis revealed that, for the stress state applied in those tests, even though the surfaces are expanding with the number of cycles, distance b is decreasing. As explained in Chapter 6, this behaviour occurs because the length of vector $\boldsymbol{\beta}$ is increasing, but the angle θ_β between this vector and the normalized normal vector $\boldsymbol{n_f}$ is also increasing. Since b is the scalar product of the two vectors, the effect is in certain cases a reduction of this variable. Thus, H' in turn decreases with the number of cycles, leading to increasing incremental accumulated strain and failure. For this reason, the only solution was to select low values of the kinematic parameters, which result in a linear accumulation of the axial and volumetric strain. This outcome is not adequate, since the experimental results show less than linear (logarithmic) accumulation of permanent strain with the number of cycles.

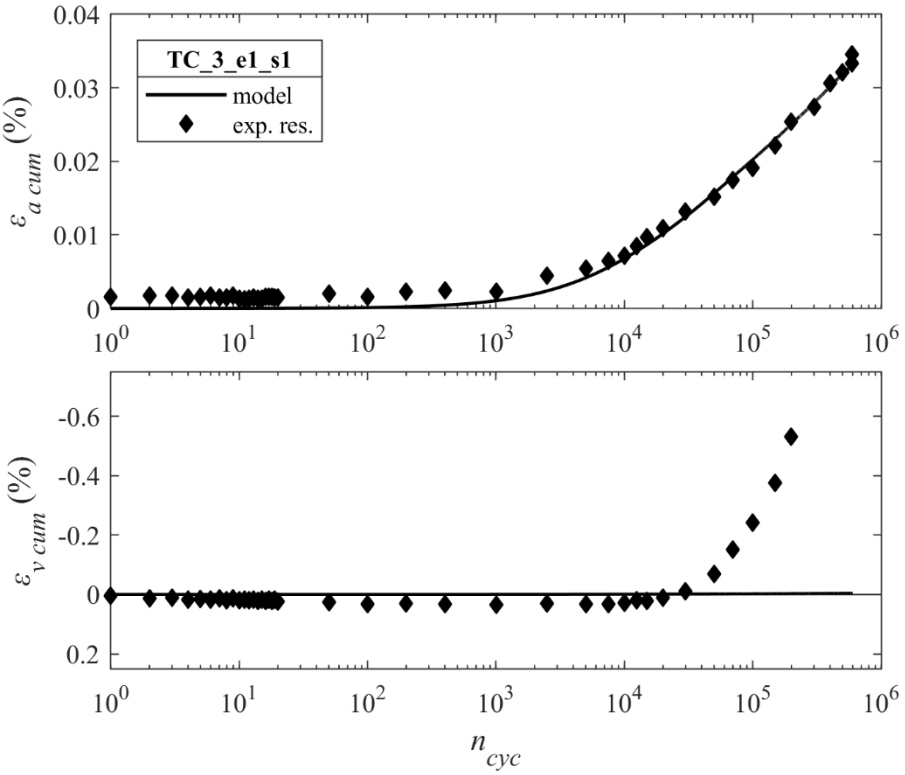

Fig. 8.37 – Accumulation curves for test TC_3%_e1_s1 with low value of destructuration parameters

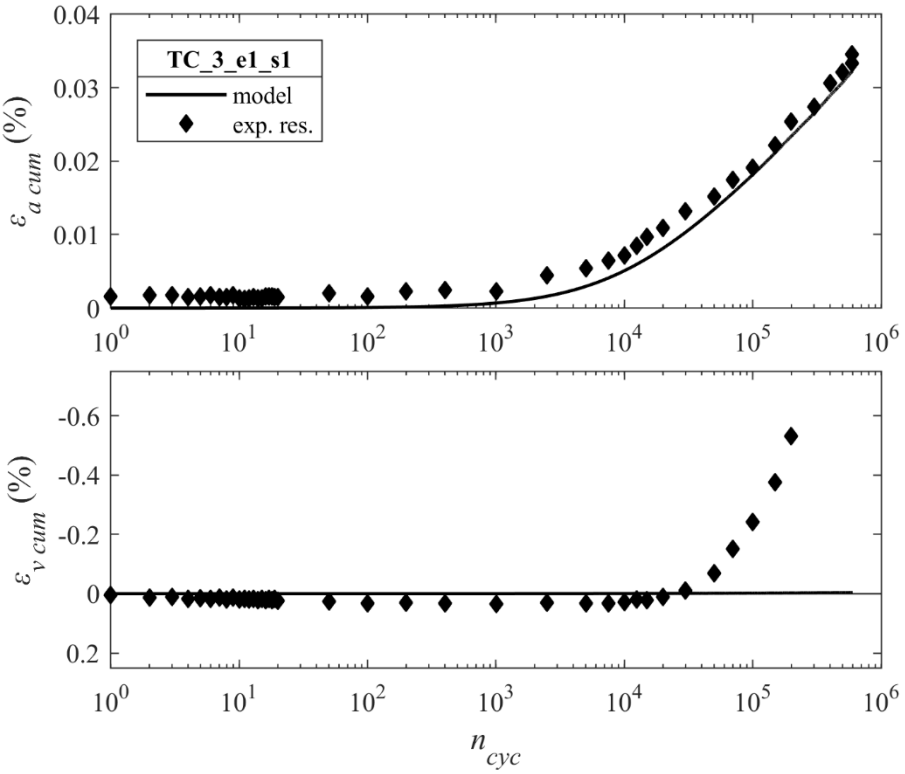

Fig. 8.38 – Accumulation curves for test TC_3%_e1_s1 with higher value of destructuration parameters

8.4. MODEL: PROPOSALS FOR MINOR MODEL MODIFICATIONS

The model performance in cyclic test is not completely satisfactory. Even though a reasonable agreement is found between the calculated and observed axial strain accumulation with number of cycles, it was not possible to determine a unique set of kinematic hardening parameters. A great variability is observed between tests with different stress conditions. It was not possible to determine an average value of each parameter or infer a regression law that could link their values in different tests. Moreover, the model cannot reproduce the complex behaviour observed in the volumetric strain accumulation.

In this section, some tentative modifications to the original model are proposed in order to overcome or reduce these problems. The proposed modifications are implemented in a hierarchical approach. As explained in the previous chapters, the new features should complement the existing model without modifying it. The original formulation can be restored by settings specific parameters of the new features.

8.4.1. MODEL PITFALLS: PROBLEMS WITH CURRENT MODEL

The problems with the current model, which were illustrated in the previous sections, are here summarised and more thoroughly explained in detail. Three main issues are outlined.

8.4.1.1. CYCLIC HARDENING

As outlined in 8.2.2, parameters B and ψ regulate three specific features of the stress-strain response of the model:

- Variation in plastic stiffness during loading (within a cycle);
- Variation in plastic stiffness during unloading (within a cycle);
- Cyclic hardening, i.e. rate of stiffness variation between successive cycles.

As outlined, a high value of ψ leads to a fast increase of stiffness with the number of cycles, which is in agreement to the observed experimental behaviour. Nevertheless, in such configuration, the stiffness of the unloading part of single hysteretic cycles is much higher than the stiffness of the loading part. The resulting hysteretic loops in the stress-strain plane present a practically elastic unloading part, since the plastic strain increment is negligible (see Fig. 8.20).

On the other hand, low values of ψ result in more realistic shapes of the stress-strain loops (as in Fig. 8.12), but the cyclic hardening is very slow, leading to a nearly linear accumulation of strain with the number of cycles, which contradicts the logarithmic trend observed in experimental data. Thus, the variation of stiffness within a stress-strain loop and from loop to loop in different loading cycles are not simultaneously reproducible with only two parameters. It is possible that the stiffness during loading and unloading is dependent on specific parameters that are not correlated to each other.

Thus, a tentative solution to this problem is to define two different sets of parameters B and ψ for loading and unloading, as explained in the next section.

8.4.1.2. DEFINITION OF DISTANCE BETWEEN SURFACES

The formulation (6.16) of distance b between surfaces causes two problems:

- there are particular stress states in the positive q semiplan (compression) for which the distance between surfaces during loading is higher than the corresponding distance during unloading:

$$b_{load} > b_{unl} \text{ with } q > 0 \tag{8.12}$$

  This, in turn, implies that the kinematic hardening modulus (and consequently the overall hardening modulus, since the kinematic modulus is the predominant component) is higher in loading than in unloading. This corresponds to a soil cycled under compressive deviatoric stress, which is stiffer during loading than during unloading. It is evident that this situation has no physical meaning, as it results into a negative accumulation of axial load in a soil submitted to deviatoric compression stress;
- as explained in section 8.3.2, for particular stress states, even though the surfaces are expanding with the number of cycles, distance b is decreasing. In fact, although the length of vector $\boldsymbol{\beta}$ is increasing, the scalar product $(\boldsymbol{\beta} \cdot \boldsymbol{n_f}/\|\boldsymbol{n_f}\|)$, from which b originates, is decreasing as an effect of the increasing angle θ_β between the two vectors. This situation typically occurs in low confined tests on cemented soil. This effect has been observed in many simulated tests. In such cases, the reduction of scalar b with the number of cycles causes kinematic modulus H' to decrease as well, leading to an increasing rate of accumulated strain (i.e. exponential strain accumulation with cycles) and rapid failure. Such behaviour is not expected and it is undesirable when surfaces are expanding and vector $\boldsymbol{\beta}$ is progressively increasing.

A slight modification in the definition of b is proposed in section 8.4.2 to mitigate these problems.

8.4.1.3. CHANGE IN VOLUMETRIC ACCUMULATION SIGN

Finally, as already mentioned, the experimental results relative to the volumetric strain accumulation present a change in the sense of accumulation from a compressive to a dilative behaviour, which is not reproduced with the current model. Such behaviour corresponds to a change of the sign of the isotropic hardening modulus H_0 from positive to negative. This could be obtained by setting the initial position of the yield surface in a zone in which H_0 is positive, and then take advantage of the observed shift of the surface (Fig. 8.10) to reach a domain of negative isotropic hardening. The shift of the surface would correspond to a change in the sign of the modulus.

Attempts in this sense have been made; nevertheless, as already explained, the shift of the surface to the configuration of Fig. 8.10 occurs in a very short number of cycles, while the experimental results suggest that this process takes tens of thousands cycles.

8.4.2. IMPLEMENTING THE NEW FEATURES

To solve the issues identified in the precedent section concerning the regulation of the soil stiffness, the definition of distance b, and the prediction of the volumetric accumulated strain, the following modifications were implemented in the model.

In the present thesis, these modifications are only applied in a preliminary way. A more extensive research on this topic can possibly be the object of future research.

8.4.2.1. INTERPOLATING PARAMETERS

As explained in the precedent section, the two interpolating parameters are not sufficient to reproduce correctly the stress-strain loops and the accumulation of permanent strain with the number of cycles.

Thus, two different sets of interpolating parameters are defined for the loading and for the unloading part of a cycle:

$$\begin{aligned} \dot{q} > 0&: (B_{load}, \psi_{load}) \\ \dot{q} < 0&: (B_{unl}, \psi_{unl}) \end{aligned} \tag{8.13}$$

With this formulation, the stiffness of the loading and unloading part of a cycle can be regulated separately. This allows having different initial stiffness and different rate of increase of stiffness with the number of cycles, with an increased accuracy in the model response. On the other hand, the number of parameters to be calibrated is increased with respect to the precedent formulation. A possible topic for future developments can be the search for a law relating the values of the parameters during loading and unloading.

It is worth noting that the original formulation is restored if the same values are selected for B and ψ in the loading and unloading domain.

8.4.2.2. DEFINITION OF DISTANCE *b*

The two problems highlighted in the precedent section are solved if, in the definition expressed in (6.16), the vector of the outward normal to the yield surface is considered without normalization:

$$b_{new} = \boldsymbol{\beta} \cdot \boldsymbol{n_f} \tag{8.14}$$

In this new formulation, the value of the distance depends not only on the magnitude of $\boldsymbol{\beta}$ and on the angle between the vectors, but also on the magnitude of the outward normal $\boldsymbol{n_f}$, that is, on the value of the first derivatives of the yield surface. The magnitude of the vector increases for increasing values of the effective stress ratio referred to the yield surface apex, η'_α, as schematically shown in Fig. 8.39.

In a drained cyclic test, the stress path intersects the yield surface in a value of η'_α which, during loading, is less than the corresponding value during unloading (in absolute value):

$$\eta'_{\alpha\, load} < \left|\eta'_{\alpha\, unl}\right| \tag{8.15}$$

Consequently, the magnitude of the normal vector is greater during unloading than during loading:

$$\left\|\boldsymbol{n_{f\ load}}\right\| < \left\|\boldsymbol{n_{f\ unl}}\right\| \tag{8.16}$$

This contributes to increase the distance b during unloading with respect to the loading part. This reduces the undesirable situation in which b is higher during loading than during unloading when the deviatoric stress is compressive.

Moreover, this formulation solves also the second problem highlighted in 8.4.1.2. In fact, when the apex of the yield surface shift progressively towards higher values of mean effective stress (i.e. the yield surface shift right in the stress plane) and the angle θ_β between vectors increases, the magnitude of $\boldsymbol{n_f}$ increases accordingly. The overall effect is that the scalar product (i.e. scalar b) increases, as required. This behaviour has been verified in many simulations performed with the numerical implementation of the model.

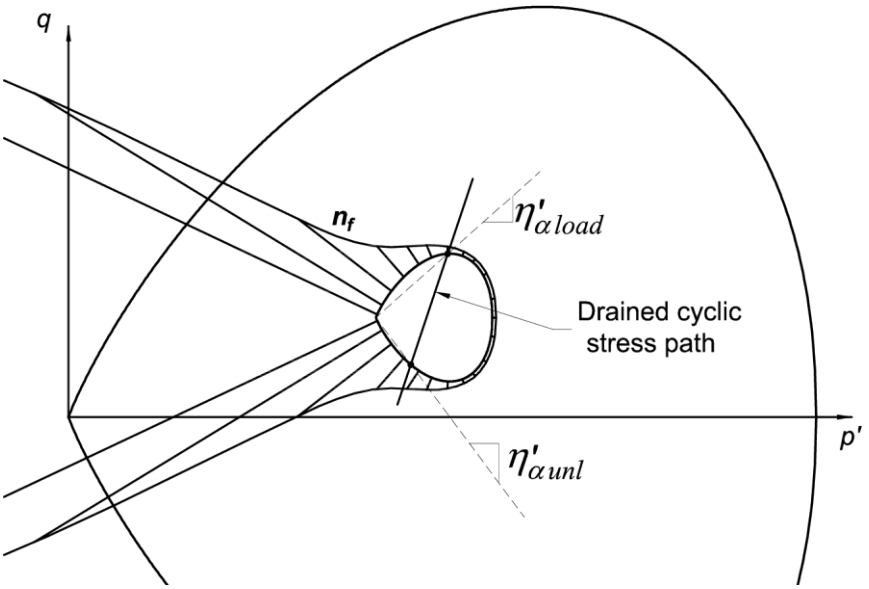

Fig. 8.39 – Normal vector to the yield surface not normalized and a drained cyclic stress path

In order to preserve the original formulation of the model, expression (8.14) can be rewritten as follows:

$$b = \boldsymbol{\beta} \cdot \frac{\boldsymbol{n_f}}{\|\boldsymbol{n_f}\|^{\zeta}} \tag{8.17}$$

Where the new parameter ζ is equal to 0 or 1. In the first case, the new formulation is implemented; in the second case, the original formulation is restored.

8.4.2.3. DEFINITION OF THE TRANSLATION VECTOR $\boldsymbol{\beta}$

The observed change in the sign of the accumulated volumetric strain from compressive to dilatant tendency is interpreted as the change of the isotropic hardening modulus H_0 from a positive to a negative value. As illustrated in section 6.1.6, H_0 is positive when the stress path intersects the yield surface in a point with an effective stress ratio referred to the apex of the bubble (η'_α) lower than the parameter M (such domain in classic, one-surface models, corresponds to the wet side of critical state). Conversely, a condition in which $\eta'_\alpha > M$ (which would corresponds to the dry side of critical state) is associated to a negative isotropic hardening modulus and dilatancy. It is reasonable to admit that, at the beginning of the shearing phase of a drained isotropically consolidated (monotonic or cyclic) triaxial test, the stress path intersects the yield surface in a point with low effective stress path. In fact, in the isotropic compression prior the application of deviatoric shear, the stress path is a horizontal line on the p' axis, starting near the origin of the $p' - q$ plane and developing in the direction of an increasing mean effective stress, as shown in Fig. 6.10. During this initial phase, the stress path intersects the yield surface and this is dragged along with the stress point. Thus, at the beginning of the shearing phase, it is reasonable to admit that the stress point intersects the yield surface in the point A, shown in Fig. 6.10, which is associated to a positive value of the isotropic hardening modulus. This position does not satisfy the condition of parallelism between translation vector and stress increment (configuration illustrated in section 6.4). Thus, during successive loading-unloading cycles, the horizontal coordinate of the surface apex, p'_α, increases progressively (i.e. the yield surface shifts towards the right), and the stress path intersects the surface at increasing values of effective stress ratio, η'_α. At a certain point and depending on the level of confinement imposed (as explained in 8.2.3.4), the yielding point crosses the border

between the domain of positive hardening modulus and the domain in which the modulus is negative. Hence, the change in tendency in the accumulated volumetric strain observed in the experimental results is reproduced by the model.

In the current formulation, this shift is excessively fast (example in Fig. 8.10). For this reason, the definition of vector $\boldsymbol{\beta}$ was altered. When the translation vector is not parallel to the stress increment, vector $\boldsymbol{\beta}$ can be decomposed in a component parallel to the stress increment vector ($\boldsymbol{\beta}_{par}$) and a normal component ($\boldsymbol{\beta}_{norm}$) (see Fig. 6.9). The latter component is responsible for the shift of the yield surface and it reduces to zero when this shift occurs. Thus, in order to decrease the shift velocity, $\boldsymbol{\beta}_{norm}$ is multiplied by an adimensional constant scalar parameter μ, ranging between 0 and 1:

$$\boldsymbol{\beta}_{norm\,new} = \mu \boldsymbol{\beta}_{norm} \tag{8.18}$$

The effect of the new parameter on vector $\boldsymbol{\beta}$ is shown in Fig. 8.40a.

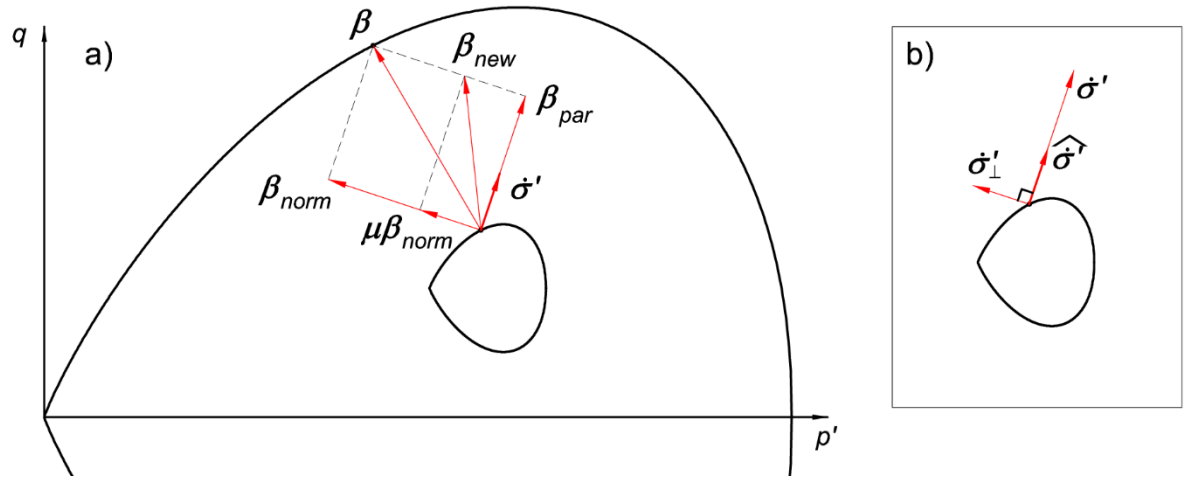

Fig. 8.40 – a) Definition of the new vector $\boldsymbol{\beta}$; b) Definition of the parallel and normal unit vectors to the stress increment vector

To compute the components of the new vector, it is necessary to calculate the parallel and normal components of the original $\boldsymbol{\beta}$ vector. For a drained triaxial stress path, vector $\dot{\boldsymbol{\sigma}}'$ is inclined at a slope $s = 3$ in the $p' - q$ stress plane. The direction of the stress increment vector can be written normalizing the vector by its length, obtaining the unit vector $\hat{\dot{\boldsymbol{\sigma}}}'$:

$$\hat{\dot{\boldsymbol{\sigma}}}' = \frac{\dot{\boldsymbol{\sigma}}'}{\|\dot{\boldsymbol{\sigma}}'\|} = \begin{pmatrix} \frac{1}{\sqrt{10}} \\ \frac{3}{\sqrt{10}} \end{pmatrix} \tag{8.19}$$

which is a unit vector with slope equal to 3 in the stress plane (Fig. 8.40b).

The unit vector perpendicular to this vector is:

$$\dot{\boldsymbol{\sigma}}'_{\perp} = \begin{pmatrix} -\frac{3}{\sqrt{10}} \\ \frac{1}{\sqrt{10}} \end{pmatrix} \tag{8.20}$$

Thus, the parallel and normal components of vector $\boldsymbol{\beta}$ to the stress increment in the original formulation are written as:

$$\boldsymbol{\beta}_{par} = (\boldsymbol{\beta} \cdot \hat{\boldsymbol{\sigma}}')\hat{\boldsymbol{\sigma}}' = \left(\frac{1}{\sqrt{10}}\beta_{p'} + \frac{3}{\sqrt{10}}\beta_q\right)\hat{\boldsymbol{\sigma}}' = \left(\frac{1}{\sqrt{10}}\beta_{p'} + \frac{3}{\sqrt{10}}\beta_q\right)\begin{pmatrix}\frac{1}{\sqrt{10}}\\ \frac{3}{\sqrt{10}}\end{pmatrix} = \\ = \frac{1}{10}(\beta_{p'} + 3\beta_q)\begin{pmatrix}1\\ 3\end{pmatrix} \tag{8.21}$$

and:

$$\boldsymbol{\beta}_{norm} = (\boldsymbol{\beta} \cdot \dot{\boldsymbol{\sigma}}'_{\perp})\dot{\boldsymbol{\sigma}}'_{\perp} = \left(-\frac{3}{\sqrt{10}}\beta_{p'} + \frac{1}{\sqrt{10}}\beta_q\right)\dot{\boldsymbol{\sigma}}'_{\perp} = \\ = \left(-\frac{3}{\sqrt{10}}\beta_{p'} + \frac{1}{\sqrt{10}}\beta_q\right)\begin{pmatrix}-\frac{3}{\sqrt{10}}\\ \frac{1}{\sqrt{10}}\end{pmatrix} = \frac{1}{10}(3\beta_{p'} - \beta_q)\begin{pmatrix}3\\ -1\end{pmatrix} \tag{8.22}$$

where $\beta_{p'}$ and β_q are the components of vector $\boldsymbol{\beta}$ in the stress plane, expressed in (6.14) for uncemented soils and in (6.61) for cemented soils. Following the new formulation, the parallel component remains unaltered while the normal component is multiplied by the new parameter μ:

$$\boldsymbol{\beta}_{norm\ new} = \frac{\mu}{10}(3\beta_{p'} - \beta_q)\begin{pmatrix}3\\ -1\end{pmatrix} \tag{8.23}$$

By composing the two components $\boldsymbol{\beta}_{par}$ and $\boldsymbol{\beta}_{norm\ new}$, one obtains the expression of the modified vector $\boldsymbol{\beta}_{new}$ in the p' and q components:

$$\boldsymbol{\beta}_{new} = \boldsymbol{\beta}_{par} + \boldsymbol{\beta}_{norm\ new} = \begin{pmatrix}\frac{1}{10}(\beta_{p'} + 3\beta_q) + \frac{3}{10}\mu(3\beta_{p'} - \beta_q)\\ \frac{3}{10}(\beta_{p'} + 3\beta_q) - \frac{1}{10}\mu(3\beta_{p'} - \beta_q)\end{pmatrix} = \\ = \frac{1}{10}\begin{pmatrix}(9\mu + 1)\beta_{p'} - 3(\mu - 1)\beta_q\\ 3(1 - \mu)\beta_{p'} + (\mu + 9)\beta_q\end{pmatrix} \tag{8.24}$$

It is easy to verify that, by replacing the value of parameter μ to 1 in the above expression, the original formulation of $\boldsymbol{\beta}$ is restored.

8.4.2.4. MODEL IMPLEMENTATION

The new formulation has been implemented in a MATLAB® script and validated through several simulated tests. An example is reported in Fig. 8.41, where a drained cyclic triaxial test with one million cycles has been simulated. The cyclic stress path initially intersects the yield surface in a point with an effective stress ratio η'_{α} close to zero. A value of μ = 2.5e-5 was selected for the new parameter. It can be seen that the shift of the bubble towards the position that satisfies condition (6.66) is much slower than in the original formulation (example shown in Fig. 8.10). In the case illustrated, the shifting process takes around 30000 cycles, instead of the 2 cycles observed in the original formulation. This new behaviour produces a different output in terms of accumulated strain with number of cycles, as shown in the following section.

In the more general case of an undrained stress path or a drained stress path with variable confining pressure, the slope of the stress increment vector in the stress plane is a generic quantity s (constant or variable). The unit stress increment vector and the corresponding normal vector are written as:

$$\hat{\dot{\boldsymbol{\sigma}}}' = \frac{\dot{\boldsymbol{\sigma}}'}{\|\dot{\boldsymbol{\sigma}}'\|} = \begin{pmatrix} \frac{1}{\sqrt{1+s^2}} \\ \frac{s}{\sqrt{1+s^2}} \end{pmatrix} \tag{8.25}$$

$$\dot{\boldsymbol{\sigma}}'_{\perp} = \begin{pmatrix} -\frac{s}{\sqrt{1+s^2}} \\ \frac{1}{\sqrt{1+s^2}} \end{pmatrix} \tag{8.26}$$

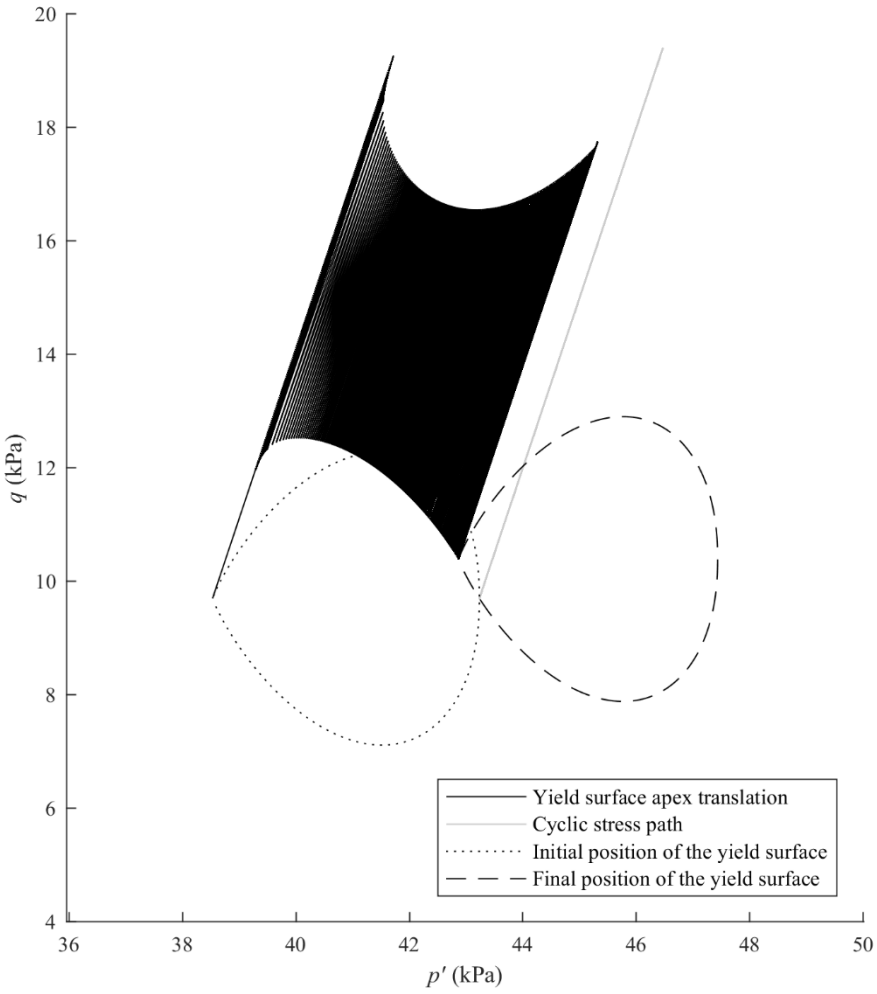

Fig. 8.41 – Shift of the yield surface towards the position of equilibrium in the modified formulation

Which represents a generalization of expressions (8.19) and (8.20). By following the same procedure, one obtains the expression of the new vector $\boldsymbol{\beta}$ in the stress space:

$$\boldsymbol{\beta}_{new} = \frac{1}{1+s^2} \begin{pmatrix} (1+\mu s^2)\beta_{p'} - s(\mu-1)\beta_q \\ \\ s(1-\mu)\beta_{p'} + (\mu+s^2)\beta_q \end{pmatrix} \tag{8.27}$$

In the case of a vertical stress path, for example the initial part of an undrained stress path or a constant p' stress path, the value of the slope s assumes an infinite value. To avoid numerical problems in the implementation, the limit value of the vector in the case of $s \to \infty$ is calculated:

$$\boldsymbol{\beta}_{new\_vert} = \lim_{s\to\infty} \boldsymbol{\beta}_{new} = \begin{pmatrix} \frac{\mu s^2}{s^2}\beta_{p'} \\ \frac{s^2}{s^2}\beta_q \end{pmatrix} = \begin{pmatrix} \mu\beta_{p'} \\ \beta_q \end{pmatrix} \tag{8.28}$$

This result is geometrically coherent: if the stress increment is vertical, the parallel component of $\boldsymbol{\beta}$ coincides with the component along the q axis and the component normal to $\dot{\boldsymbol{\sigma}}'$ coincides with the component of $\boldsymbol{\beta}$ along p' (Fig. 8.42). In the numerical implementation, it is necessary to define this last expression when the stress increment is vertical.

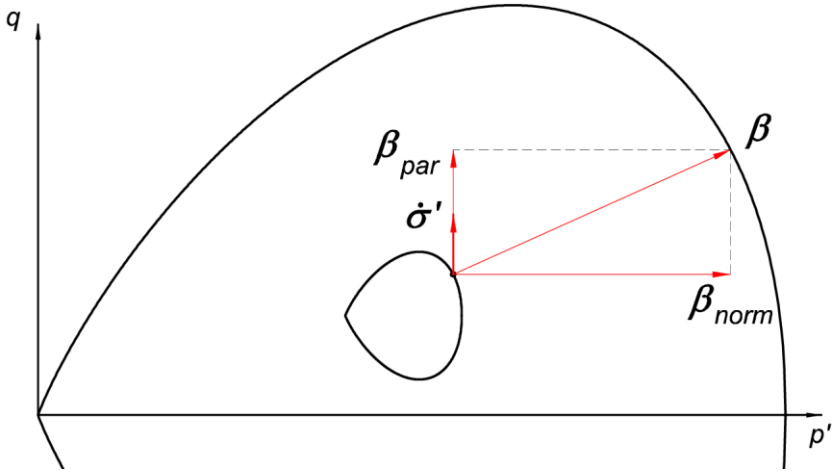

Fig. 8.42 – Components of vector $\boldsymbol{\beta}$ in the case of vertical stress increment

In conclusion, the model has been modified by adding four new parameters. The original formulation is not lost and can be restored by selecting the following values for the new parameters:

$$\begin{cases} B_{unl} = B_{load} = B \\ \psi_{unl} = \psi_{load} = \psi \\ \zeta = 1 \\ \mu = 1 \end{cases} \tag{8.29}$$

8.4.3. TESTING THE MODIFIED MODEL

8.4.3.1. DRAINED UNCEMENTED TESTS

The modified parameters has been applied to test TC_0%_e1_s1. It is important to note that this study was performed as a preliminary stage and further analyses should be executed in future works. As explained in the previous section, the yield surface was initially positioned in a configuration similar to that shown in Fig. 8.41, that is, an initial small value of η'_α. The parameters of the new formulation were determined with a heuristic method; Yu flow rule was adopted. Thus, seven parameters shall be calibrated, as reported in Table 8.15. Additionally, it shall be $\zeta = 0$, as explained in the precedent section. The results of the simulated test, reported in Fig. 8.43, shows a good agreement with the experimental results. In particular, the change in volumetric strain accumulation from compressive to

dilative tendency is reproduced by the modified model, thanks to the shift of the yield surface in the stress plane from the compressive to the dilative side, as explained in detail in the precedent sections.

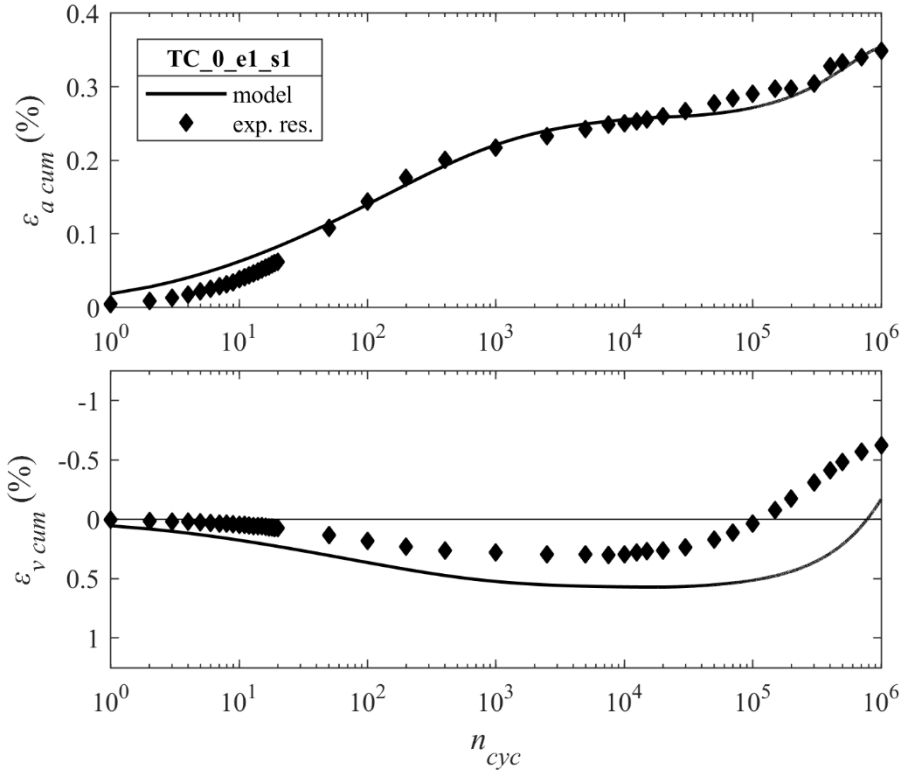

Fig. 8.43 – Performance of the modified model with test TC_0%_e1_s1

Table 8.15 – Model parameters for test TC_0%_e1_s1 in the modified formulation

R	B_{load}	B_{unl}	ψ_{load}	ψ_{unl}	μ	m
0.015	3.2	3.2	4.5	1.78	2.5e-5	1.8

Parameter μ regulates the velocity of the shift, and consequently the number of cycles at which the sign the incremental volumetric strain changes from positive to negative. Thus, this parameter was regulated with a trial and error process until the switch point observed in the simulated curve and in experimental data corresponded. Parameters B and ψ were initially considered equal in loading and unloading and their values successively modified in order to accommodate the model output to the experimental curve.

In the presented case, it was possible to keep parameters B equals in loading and unloading (B_{load}=B_{unl}), while calibrated parameters ψ are different. It was noted that parameter ψ_{load} has a marked influence on the shape of the first part of the axial accumulated strain curve (up to 10^3-10^4 cycles) while ψ_{unl} regulates the second part.

It can be seen that the values of parameters ψ are much smaller than in the original version of the model, which brings to more stable behaviour of the model response (a value of the exponent ψ = 5000 was adopted for the same test in the original model). This is due to the progressive shift of the bubble, which leads to a continuous change in the yielding point with the number of cycles. This in turn causes a progressive change in magnitude and direction of vector $\boldsymbol{\beta}$ and in the first derivatives of yield surface and plastic potential with the number of cycles.

This change is reflected in a correspondent variation of the stiffness (or compliance) matrix, thus leading to a non-linear response. In the original model, the configuration of the relative position of the yield surface and the stress point evolves very slowly; thus, the only way to variate the stiffness matrix is by imposing a very strong variation of the kinematic hardening modulus with a small variation of the distance b, i.e. selecting a very high value of its exponent ψ.

The stress-strain loops associated to the test reported in Fig. 8.43 present a similar shape of the example shown in Fig. 8.20, relative to the original formulation of the model. Thus, the representation of the stress-strain loops is not improved in the modified implementation of the model. Nevertheless, the representation of the accumulation curves presents some improvements, in spite of an increased complexity of the calibration process.

The model was applied to test TC_0%_e1_s2, with the parameters reported in Table 8.16. Parameters R, ψ_{load}, and μ were kept equal to the precedent test. The remaining were changed to ensure a good concordance between the simulated axial strain accumulation and the experimental results, as expressed in the curves in Fig. 8.44. Although the parameters are not equal to the precedent case, the differences between the two calibrations with the modified formulation are less pronounced than the variations in parameters between different tests with the original formulation.

Table 8.16 – Model parameters for test TC_0%_e1_s2 in the modified formulation

R	B_{load}	B_{unl}	ψ_{load}	ψ_{unl}	μ	m
0.015	4	2.01	4.5	2.44	2.5e-5	1.5

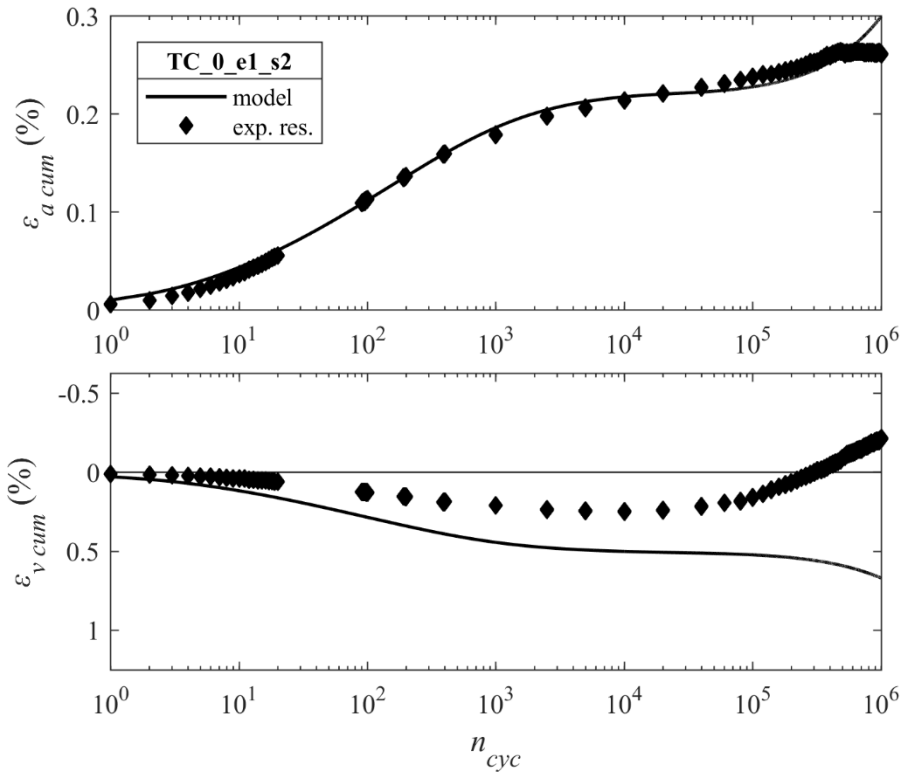

Fig. 8.44 – Performance of the modified model with test TC_0%_e1_s2

Conversely to the original formulation, in this case there is not need to adopt negative values for the exponents ψ. A common set of parameters for all the tests could be tentatively derived in future works. Fig. 8.44 shows that in this case no change in volumetric accumulation is observed; in fact, the tendency is compressive (positive accumulation) throughout the test. The analysis of the model output reveals that the yield surface has completed its shift without crossing the limit separating the compressive and the dilatant side of the yield surface. Thus, the change in volumetric strain accumulation in this case cannot be reproduced by any specific set of parameters. Possible alterative strategies would be the definition of a new flow rule or the definition of a higher value of the isotropic yield stress σ'_y. In the last case, the value of the effective stress ratio η'_α at the end of the surface shift would be higher (in loading and unloading) and the dilatant domain could be reached. It is important to remember that the definition of yield pressure σ'_y is affected by high uncertainty, thus the determined value can be different from the real value.

8.4.3.2. DRAINED AND UNDRAINED CEMENTED TESTS

A cemented test was tentatively calibrated (TC_3%_e1_s1 - Table 8.17 and Fig. 8.45). The parameters are different from the uncemented tests (the destructuration parameters were taken equal to 1e-4 also in this case). The volumetric strain shows a change in behaviour from compressive to dilatant (the second graph of Fig. 8.45 is reported in Fig. 8.46 at an increased vertical scale), even though the predicted strain is lower than the accumulation observed in laboratory test. Such switch in volumetric tendency is observed also in undrained specimens in the sense of accumulation of pore pressure (Fig. 8.47).

The present study on the performance of this modified version of the model is not complete and should be object of future works.

Table 8.17 – Model parameters for test TC_3%_e1_s1 in the modified formulation

R	B_{load}	B_{unl}	ψ_{load}	ψ_{unl}	μ	m
0.005	0.5	15	2	0.2	1e-6	1.8

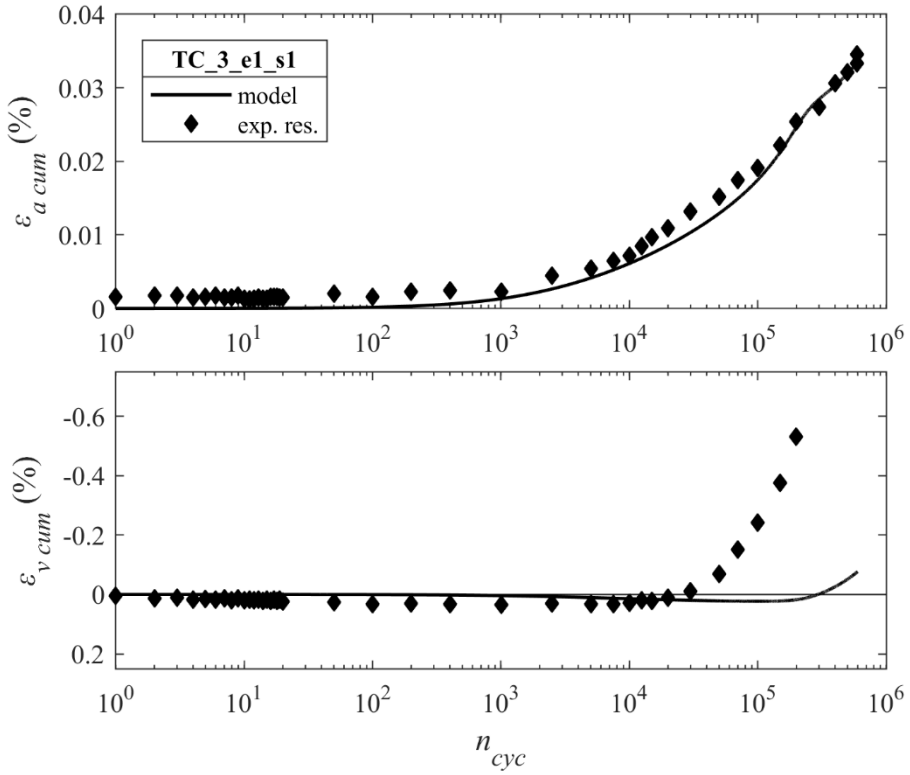

Fig. 8.45 – Performance of the modified model with test TC_3%_e1_s1

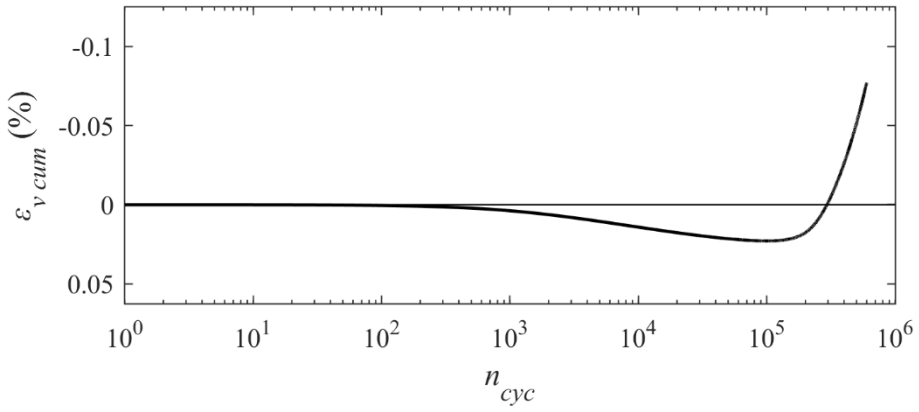

Fig. 8.46 – Performance of the modified model with test TC_3%_e1_s1: detail of the volumetric strain accumulation

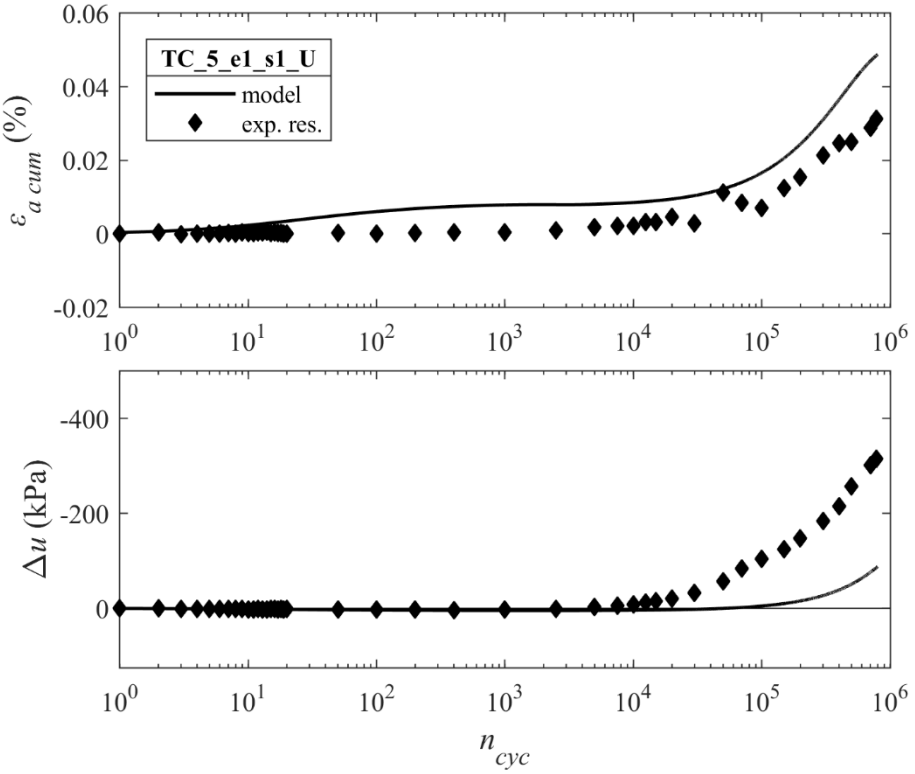

Fig. 8.47 – Performance of the modified model with undrained test TC_5%_e1_s1_U

8.5. CONCLUSIONS

In the present chapter, the proposed model performance was assessed and tentatively calibrated. The process involved increasing complexity, starting from the simpler monotonic tests to the more complex cyclic tests, from uncemented to cemented soil.

The comparison performed between the proposed model and an existing implementation from Rios et al. (2016) of a single-surface, isotropic hardening CASM-n model (Yu, 2007), showed the advantages of the present implementation for modelling uncemented and cemented soils. Taking advantage of the similarities of the two models, the value of the common parameters were taken equal to Rios et al. (2016) model. The remaining parameters were divided in groups representing specific characteristics of the model, and a staged approach was followed in the calibration. The new model was tested on the same tests used for the previous model. The comparison between the results showed that the two models have the same response in the large-stress domain, but different behaviour in the small strain domain. Such outcome allows validating the present model, because the large strain behaviour is mostly regulated by the reference surface, which corresponds to the yield surface of the one-surface model. Thus, a similar behaviour in the large-strain domain (corresponding to the near-yielding and post-yielding domain of the one-surface approach) is expected. The small strain domain showed an increased accuracy of the present two-surface model, which is capable to reproduce more correctly the early non-linearity showed by the soil. On the contrary, the single surface approach presents a large domain of elasticity, which does not represent well the soil behaviour in small-strain conditions, even if a non-linear elastic law is adopted.

The model response in long duration low-stress cyclic tests was analysed. Attention was particularly focused on the influence of parameter ψ on the kinematic hardening modulus and, in turn, on the shape

of the stress-strain loops and the accumulation of permanent strain with the number of cycles. It was shown that this single parameter cannot reproduce correctly both the aspects of the cyclic loading; thus, in the following calibration process, priority was given in the accurate reproduction of the accumulation curves rather than the cyclic hysteretic loops.

The calibration of the performed tests showed that the axial strain accumulation of each test is well reproduced only if a specific set of kinematic hardening parameters is selected for each test. The calibration process showed the necessity of adopting parameters of opposite sign in tests performed with different confining pressures. This shows the impossibility of having a single set of parameters with the present formulation of the model.

A modified version of the model was presented in order to deal with the pitfalls highlighted in the calibration of the cyclic tests. In the implementation of the modified model, special care was taken to preserve the original formulation of the model, which is not lost and can be recovered by selecting specific values of the new parameters. In this sense, the modified version can be regarded as an extension or a more general version of the original formulation. The new formulation was implemented in order to eliminate some evident pitfalls of the model, such as the negative accumulation of axial strain in compressive deviatoric cyclic stress.

The analysis of the modified model is, at present, at a preliminary stage. Although a unique set of parameters was not determined, a step towards a more stable (less sensitive to parameter variation) response of the model was proposed. The parameters vary less from one test to another than in the first version. The major pitfalls highlighted in the original formulation were eliminated. The volumetric response was improved, with the correct reproduction of the change of volumetric strain from compressive to dilatant behaviour. The modified formulation should be further studied to tentatively found a unique set of parameters.

Chapter 9.

CONCLUSIONS

9.1. CONCLUSIONS

The present work was focused on the study of the long-term cyclic response of a remoulded silty-sand, originated from residual soils of Porto granitic formation, compacted and artificially cemented. As such, three main aspects were covered:

- soil cementation;
- static and cyclic loads;
- long-term loading conditions.

The literature review presented in Chapter 2 showed that the three characteristics were studied in previous works. Nevertheless, few studies are found in which the three aspects are simultaneously addressed. Moreover, the problem was approached from two different aspects, starting independently but converging and integrating each other: an experimental study and an analytical-numerical approach.

Three main goals were outlined for the present work in Chapter 1, dealing with the need of a complete and consistent experimental study, in order to define a complete mechanical characterization of the soil, and establish the bases for the implementation and validation of an original constitutive model that can reproduce the obtained experimental results described later in the thesis.

The characteristics related to the structure of the cemented soils were assessed in experimental tests. The gain in structure with the curing time was observed in repeated dynamic tests. The dependence of the bonding level from an adjusted porosity/cement ratio that has been adopted in different works in FEUP was confirmed in the non-destructive and destructive static tests. This ratio was used as an indexing parameter in previous works conducted on the same soil in static and monotonic conditions and it proved capable of joining in a unique framework the two concurrent basic variables of a cemented soil: initial void ratio and cement content. Soil stiffness and strength characteristics are expected to improve with decreasing values of the first and increasing values of the second variable; hence the idea of expressing them in a single parameter. As shown in precedent works, also in this case the ratio showed a good correlation with strength and stiffness characteristics of the soil-cement mixtures.

An extensive testing programme was conducted over 27 specimens of artificially cemented silty-sand, moulded in distinct state conditions: 9 different moulding points including four different cementation levels (including uncemented specimens) and three different initial void ratios. More than one test was performed for each specimen, including non-destructive dynamic tests, unconfined monotonic tests up to failure, and long-term cyclic triaxial tests with low to moderate stress levels. The tests performed

before and after cyclic tests (wave propagation tests with velocity measurements of shear/distortional and compression seismic waves and unconfined compression tests) allowed to understand the evolution of the mechanical parameters of cemented soil during curing, on one side, and when stabilisation of bonding was reached after the induction of long cyclic loading. As a part of the integrated approach between experimental and theoretical research highlighted above, it should be noted that the tensile strength due to cementation was derived from the elemental (uniaxial compression) tests and was used as the base of the subsequent options for the initialization of the constitutive model.

Long-term cyclic triaxial tests represent the core of the experimental part of this work. Twenty-four (24) specimens were submitted to drained tests, while three (3) were tested undrained. Eight samples of cemented mixtures were prepared to be cyclically tested under three different confining pressures, in a total of 24 drained triaxial tests. The applied cyclic stress was selected to guarantee that the tests were performed within the so-called "small-strain" domain of the material (a domain far from the ultimate envelope of the material). The results of the drained tests show that the accumulation rate of axial and volumetric strain decreases with the number of loading cycles, but does not stabilize despite the large duration of this cycling, even considering the low intensity of deviatoric stress applied. The undrained tests confirmed this tendency in the axial accumulation and in the pore pressure variation.

In all the tests, the trend of accumulation of the axial strain with the number of cycles is mostly logarithmic. Noticeably, an inflection point is observed at a certain number of cycles (dependent on the bonding level of the particles of the specimen, in turn related to the adjusted porosity/cement ratio) after which the rate of accumulation – still logarithmic – changes.

This change of cyclic long term behaviour becomes higher for the cemented specimens and lower for the uncemented specimens. This result evidences the role of cementation: the admixture becomes stiffer but more brittle due to the progressive degradation of the particle bonds with the accumulation of permanent strain. Drained tests performed with different confining pressures show that an increase of confining pressure, which is associated to a more ductile response in uncemented specimens, has a negative effect on cemented specimens, since it accelerates the destructuration process leading to higher accumulation of axial strain.

The volumetric strain accumulation shows a complex behaviour. Many precedent studies published on uncemented and cemented soils under cyclic loading only present the results relative to the axial strain accumulation, neglecting the volumetric strain accumulation; thus, a comparison with other results cannot be substantially discussed. The results show some similarities with the behaviour of a monotonically compressed soil: an initial compression is observed in all the specimens; then, the accumulation trend switches to a dilatant behaviour, which is more evident in less confined specimens (as observed in monotonic tests) and less pronounced in those confined with higher pressures. In some tests, a double switch is observed, with a double change in the sign of accumulation rate with the number of loading cycles. Consistently, the undrained tests, being confined under a low confining pressure, show a negative pore pressure variation, which corresponds to a dilatant tendency. The pore pressure variation observed in undrained tests shows a trend similar (corresponding) to the volumetric strain accumulation in drained tests: an initial part with small positive variation in pore pressure is followed by a sudden increase in negative variation, confirming the increased rigidity and fragility provided by the cementation.

This experimental work showed the importance of performing experimental investigations with a very high number of loading cycles (at least 500000) to recognise the main properties of the cyclic behaviour of a cemented soil. The data retrieved showed that, even with a low value of the deviatoric stress, cyclic strain accumulation evolves up to 1 million cycles, and possibly even beyond this limit. Furthermore, it

is very important (although it implies increasing complexity in the equipment facilities) to assure an accurate acquisition of the volumetric variation during the tests, since volumetric strain accumulation is an important feature of the cyclic behaviour of cemented and uncemented soils that should not be neglected in experimental studies.

A novel elasto-plastic model is proposed (Panico et al., 2018), based on the framework of bounding plasticity and equipped with a bonding variable and destructuration law, with the aim of modelling the observed behaviour of the cemented soil in long term cyclic loading conditions. The model was conceived following the principles of the hierarchical modelling (Desai et al., 1986), in which each new feature expands the model capabilities without overriding the precedent features. The model presents a kinematically hardening yield surface translating inside a larger reference surface. The two surfaces have the shape of CASM model yield surface (Yu, 1998); the translation rule follows the model of Al Tabbaa & Muir Wood (1989), where the yield surface translation is parallel to a vector linking the stress point on the yield surface with the conjugate point on the reference surface. The translation rule and a non-associated flow rule (Rowe or Yu – typical of granular materials) are harmonized with a consistency condition. This uncemented formulation is completed with the proposed model for cemented soils developed by Gens & Nova (1993).

The model is described in the uncemented formulation and in the cemented formulation. The translation of the yield surface was analysed in detail, revealing that the surface tends towards a specific configuration relatively to the stress state (shown in Fig. 6.8). This position satisfied the requirement that the translation vector is parallel to the stress increment vector (expression (6.66)). If this condition is not satisfied, the yield surface shift perpendicularly to the stress increment vector, until the parallelism with this vector is restored. This behaviour was shown analytically with geometrical considerations in section 6.4 and it was confirmed in the simulations that were developed under the numerical implementation, whose results were presented in section 8.2.1. This behaviour becomes very important when long-term cyclic tests shall be calibrated, because it shows that the initial position of the yield surface does not influence the long-term response of the material. In fact, the shift towards the referred position occurs within few loading cycles. Thus, tests with different initial positions of the yield surface will only differ for the very first cycles. If a cyclic test with hundreds of thousands of cycles shall be performed, the difference is negligible.

A general analytical solution for the constitutive equations of the model could not be found. Nevertheless, some partial closed-form solutions for particular cases with special stress path and simplified hypotheses were determined. The solution were referred to the model for uncemented soils, in purely kinematic and mixed hardening conditions. In all the cases reported, the first derivatives of yield surface and plastic potential were constant during the loading process, due to the particular conditions selected for the tests. In such conditions, the expression of the governing equations were simplified and their integration was possible. The analytical solutions were compared against a numerical solution based on an explicit substepping algorithm with a numerical integration method and error control. The comparison between the two outputs showed a good concordance, contributing to the model validation. Particular attention shall be made for the stress paths intersecting the yield surface in its apex, $\boldsymbol{\alpha}$; in such case, the first derivatives of the surface are not defined, causing numerical problems. For this reason, if such a test shall be modelled, the shape of the yield surface around the apex should be redefined. In any case, for isotropically consolidated cyclic triaxial tests (drained or undrained), or for monotonic isotropic tests such problem does not arise.

The number of model parameters to be calibrated suggests to group them in subsets related to specific features of the model. A subset of parameters regulates the critical state characteristics, a subset is referred to the purely elastic behaviour, another to the bounding plasticity framework, etc. In this way,

a staged approach can be applied (Rios et al., 2016), calibrating each subset of parameters and activating subsequently the other features with the corresponding groups of parameters, which can then be calibrated.

Thus, the model was initially calibrated against monotonic triaxial tests. This choice had a double purpose: on one hand, the kinematic hardening parameters had a small influence on the large-strain response of the model; thus, attention could be focused on the calibration of the critical state parameters. On the other hand, a similar one-surface model (Rios et al., 2016) was already implemented and calibrated against the same set of triaxial test. Such model presents a single isotropically hardening yield surface, of the same shape of the reference surface of the model presented in this thesis. Thus, this comparison of the output of the two models allowed to validate the present model. In fact, in the large-strain domain, when the yield and the reference surface intersect at a common normal, the response of the two models ought to be very similar. The results of the analyses confirmed this prediction, thus validating the present implementation. As for the small-strain behaviour, the present model presents a better performance than the single-surface model. This result confirms again the validity of the model.

Model performance in the long-term cyclic loading has not been as successfull as it was for monotonic triaxial tests. Modelling cyclic tests with such a high number of cycles using a theoretical model is a difficult task. In fact, in the examples present in literature, either empirical or semi-empirical models are used to model long-term cyclic tests; or the number of cycles modelled with rational frameworks is very reduced, normally under 100. Nevertheless, a good capability of the present model to reproduce the accumulation of axial strain with the number of cycles is observed if a specific set of kinematic hardening parameters is selected for each test. Some pitfalls of the model were outlined during the calibration process. For example, in specific loading conditions, a compressive deviatoric cyclic test would produce negative accumulation of axial strain independently of the selected parameters. Another example is the mentioned rapid shift of the yield surface during cyclic loading. Even though the experimental evidence suggests that such shift is beneficial for the model performance (in order to model the observed change in volumetric accumulated strain with the number of cycles from compressive to dilative behaviour), the rapidity of the process is too high to produce a reasonable response.

For these reasons, some modifications to the original formulation of the model were implemented (without losing the original formulation). These improvements are the outcome of the experience accumulated from the use of the original formulation, with the model pitfalls that became evident after a long learning process. The modifications included the definition of distinct kinematic hardening parameters for loading and unloading; the definition of a new distance b between surfaces; and the addition of a new parameter in the definition of the translation vector $\boldsymbol{\beta}$.

The modifications herein resumed conclude the present work and cannot simply replace the original formulation, as they are the possible answer to the model drawbacks that are intrinsic and not dependent on the particular parameters selected. Such suggestions seem to contribute to a better performance of the model, as resulted in a preliminary analysis. The negative axial strain accumulation under compressive variable load is no longer observed, and the switch in volumetric tendency is represented, at least qualitatively. Additionally, the observed soil softening in the case of expanding surfaces was eliminated. The model parameters are not constant for all the tests, but their variation is much smoother than in the original formulation and a possible interpolation can be attempted in future works. Nevertheless, the number of requested parameters is higher than the considered original model and a direct relation between some of them and physical characteristics of the material, directly measurable in laboratory tests, is not evident at present.

9.2. FUTURE DEVELOPMENTS

The conclusions drawn in the precedent section highlighted some open questions in the performed work, related to the experimental plan, to the definition of the constitutive model, and to its numerical implementation.

The long-term cyclic triaxial test programme was extensive and included different void ratios, cement contents, and confining pressures. The goal was to explore different regions in the p'-q-v space. Although a large number of tests were performed, the number of the considered variables did not allow to obtain a broad range of variation in each of them. Specifically, applying three different confinements had the main goal of studying the dilative(group s1), compressive (s3), and intermediate (s2) regions within the normalized bounding surface. The results of the volumetric tests showed that the dilative (s1) and the intermediate (s2) regions were explored in the cyclic tests. The less confined (s1) tests showed a clear dilatant behaviour, while the tests subjected to intermediate confining pressure (s2) showed a mixed behaviour, with a change between negative and positive accumulation of volumetric strain. Nevertheless, the tests with higher confinement (s3) did not always show a clear compressive behaviour, although they tend towards larger compressive strain than the tests of the second group. To tentatively seek for a purely compressive response, new tests conducted on the same type of soil investigated in this work could be performed with a ratio of the applied confining stress over the respective isotropic yield stress higher than the value (0.5) applied in tests "s3".

Moreover, it would be of interest to perform also tests with different stress path than the conventional drained triaxial stress path. In fact, as referred in Chapter 8 relatively to the framework of bounding surface plasticity, conventional drained triaxial stress paths intersect the yield surface at a stress ratio (relative to the yield surface apex) higher (in absolute value) during unloading than during loading. Thus, in conventional drained cyclic triaxial tests, the value of dilatancy is different during loading and unloading. Due to the low amplitude of the deviatoric stress applied, it is cumbersome to distinguish the effects of the loading and unloading part of each cycle, which can be very different. Indeed, they can be opposite, with a compressive parcel during loading and a dilative behaviour during unloading. The weight of the two parcels on the resulting behaviour is unknown. Thus, the accumulation of volumetric strain observed is the sum of two different contributions (in loading and unloading) which cannot be clearly distinguished. In a low-stress undrained cyclic test, the direction of the stress path is approximately parallel to the q axis (in the $p' - q$ stress plane), because the development of excess pore water pressure in a cycle is much smaller than the deviatoric stress variation. Thus, the stress ratio is similar in loading and unloading and, consequently, the value of dilatancy (in absolute value) should be similar in the two cases. Thus, the individual contribution of the loading and unloading part on the volumetric strain at each cycle should be equal to half the total strain at the end of each cycle. For the same reason, additional drained tests could be performed in constant p' stress conditions.

The new tests should also include two-way symmetric tests (with applied deviatoric stress $q_{min} = -q_{max}$). This would be useful for two reasons:

- the distance from the reference surface would be the same during loading and unloading. This, together with the constant p' (or undrained) stress path would possibly help to clearly highlight and distinguish the contributions of the loading and unloading parts and possibly to better define an experimental expression of the kinematic hardening modulus (this topic is further detailed hereafter);
- it would allow to have stress paths with higher amplitude, still respecting the requirement of being far from the bounding surface envelope. This would ease the analysis of the results, as it would be easier to differentiate disturbances from the real trends.

For what concerns the formulation of the constitutive model, it is worth noting that the parameters related to the kinematic hardening modulus lack some physical meaning, that is, they cannot be identified by direct relations obtained in specific laboratory tests. This makes the calibration process difficult. Additionally, the experimental results show that the formulation of kinematic hardening modulus H' can be improved. In fact, H' only depends on the normalized distance b/b_{max}. The tests were designed specifically with a constant minimum and maximum distance of the stress path from the boundary surface. The results show a great difference in the accumulated axial plastic strain between the uncemented and cemented soils, which is not dependent on cementation, since cementation was considered through an enlarged surface size. Thus, a dependence on the cementation should be introduced in the expression of H'.

The flow rules commonly used in monotonic loading (Rowe and Yu flow rule) showed a poor performance in cyclic stresses, leading to a smaller than expected volumetric strain accumulation. This is probably because these flow rules were determined either in monotonic compression loading or in tension loading, while, in the case of cyclic loading, the deviatoric stress is decreasing but positive during unloading.

For addressing these problems, further cyclic tests should be performed, as explained above, with higher load amplitudes and loading paths symmetric to the p' axis. In this way, the unloading-reloading cycles would be better defined and the variation of the kinematic hardening modulus would be better outlined. At the same time, the unloading part of the cycles would potentially reveal the true shape of the flow rule. Basing on the results of these tests (that should be performed on different soil-cement mixtures, including uncemented), the expression of the kinematic hardening modulus and/or the flow rule could be tentatively changed, in order to find a better fitting to the experimental evidence.

The modifications proposed for the model showed the potentiality of a new formulation for the translation rule. The parameter adopted in this case could not be the most suitable, and the definition of different parameters (still having the same effect of slowing the shift of the yield surface towards the equilibrium position) should be explored.

For what concerns the numerical implementation of the model, the implementation of an improved version of the model in a finite element code would be very valuable to test the model in a boundary condition problem, such as an embankment or a foundation soil. In order to achieve this goal, an implicit numerical resolution algorithm should be implemented. In the present work, the discretization of the problem was performed through two substepping (second and fifth order) algorithms. As explained in Chapter 7, substepping is an explicit algorithm, which is simple and reliable in the particular stress conditions studied, that is, stress-driven cyclic or strain-driven monotonic axisymmetric stress conditions. In such case, although the consistency condition is not necessarily respected, the problem is stable enough to be solved in a reasonable number of intervals (i.e. in a reasonable computational time). Nevertheless, in order to implement the mode in a finite element code, its formulation should be extended to the general stress space and an implicit algorithm should be implemented, such as the return algorithm. After this method is implemented, the model could be applied to a finite element code by recurring to a comercial software that allows for the implementation of user-defined model.

REFERENCES

Airey, D.W. & Fahey, M. (1991). *Cyclic response of calcareous soil from the north-west shelf of Australia*. Géotechnique, 41(1), 101-121.

Al-Tabbaa, A. (1987). *Permeability and stress-strain response of speswhite kaolin*. Ph.D. Thesis, University of Cambridge, UK.

Al-Tabbaa, A. & Muir Wood, D. (1989). *An experimentally based 'bubble' model for clay*. Proc. of 3rd Int. Symp. on Numerical Models in Geomechanics (NUMOG 3) (S. Pietruszczak & G.N. Pande, eds.), 8-11 May 1989, Niagara Falls, Canada, 91-99, Elsevier Applied Science, London.

Allen Marr, W. & Christian, J.T. (1981). *Permanent displacement due to cyclic wave loading*. Journal of Geotechnical Engineering Division, ASCE, 107(GT8), 1129-1149.

Allotey, N. & El Naggar, M.H. (2005). *Cyclic soil degradation/hardening models: a critique*. Proc. of 16th Int. Conf. on Soil Mechanics and Geotechnical Engineering, 11-16 September 2005, Osaka, 785-790, MillPress Science Publishers, Rotterdam.

Amaral, M.F. (2012). *Modelling and characterization of the dynamic and cyclic behaviour of soil-cement admixtures to apply in transport infrastructures*. Ph.D. Thesis, University of Porto, Portugal (in Portuguese).

Amaral, M.F., Rios, S., & Viana da Fonseca, A. (2012). *Yielding in the isotropic compression of Porto silty sand*. Acta Geotechnica Slovenica, 9(1), 31-45.

ASTM (1995). *D 2938: Standard Test Method for Unconfined Compressive Strength of Intact Rock Core Specimens*. American Society for Testing Materials, USA.

ASTM (1998). *D 2487-98: Standard practice for classification of soils and engineering purposes (Unified Classification System)*. American Society for Testing Materials, USA.

Astrom, K. & Hagglund, T. (1995). *PID controllers: theory, design, and tuning*. Research Triangle Park, NC: Instrument society of America.

Bardet, J.P. (1986). *Bounding surface plasticity model for sands*. Journal of Engineering Mechanics, 112(11), 1198-1217.

Barksdale, R. D. (1972). *Laboratory Evaluation of Rutting in Base Course Materials*. Proc. 3rd Int. Conf. on Structural Design of Asphalt Pavements, 11-15 September 1972, London, UK, 161-174.

Bassani, M., Khosravifar, S., Goulias, D.G., & Schwartz, C.W. (2015). *Long-term resilient and permanent deformation behaviour of Controlled Low-Strength Materials for pavement applications*. Transportation Geotechnics, 2, 108-118.

Been, K. & Jefferies, M.G. (1985). *A state parameter for sands*. Géotechnique, 35(2), 99-112.

Bishop, A.W. & Henkel, D.J. (1957). *The measurement of soil properties in the triaxial test*. Edward Arnold Publishers, London.

Borja, R.I. (1991). *Cam-clay plasticity, part II: Implicit integration of constitutive equations based on nonlinear elastic stress prediction*. Computer Methods in Applied Mechanics and Engineering, 88, 225-240

Borja, R.I. & Lee, S.R. (1990). *Cam-clay plasticity, part I: Implicit integration of constitutive relations*. Computer Methods in Applied Mechanics and Engineering, 78, 49-72.

Butcher, J.C. (1965). *On the attainable order of Runge-Kutta methods*. Mathematics of Computation, 19(91), 408-417.

Carol, I., Rizzi, E., & Willam, K. (2001). *On the formulation of anisotropic elastic degradation. I. Theory based on a pseudologarithmic damage tensor rate*. International Journal of Solids and Structures, 38(4), 491-518.

Carter, J.P., Johnston, I.W., Fahey, M., Chapman, G.A., Novello, E.A., & Kaggwa, W.S. (1988). Triaxial testing of North Rankine calcarenite. Proc. Int. Conf. on Engineering for Calcareous Sediments, (Jewell, R.J. & Khorshid, M.S., eds.), 15-18 March 1988, Perth, Australia, 2, 515-530, Balkema, Rotterdam.

Carter, J.P., Airey, D.W., & Fahey, M. (1999). *A review of laboratory testing of calcareous soils*. Engineering for calcareous sediments: Proc. of 2nd Int. Conf. on Engineering for Calcareous Sediments (K.A. Al-Shafei ed.), 21-24 February 1999, Bahrain, 2, 401-431, Balkema, Rotterdam.

CEN (1994). *EN 196-1: Methods of testing cement - Part 1: Determination of strength*. Brussels, Belgium.

CEN (2000). *EN 197-1: Cement - Part 1: Composition, specifications and conformity criteria for common cements*. Brussels, Belgium.

CEN (2003a). *EN 13286-41: Unbound and hydraulically bound mixtures - Part 41: Test method for the determination of the compressive strength of hydraulically bound mixtures*. Brussels, Belgium.

CEN (2003b). *EN 13286-43: Unbound and hydraulically bound mixtures - Part 43: Test method for the determination of the modulus of elasticity of hydraulically bound mixtures*. Brussels, Belgium.

CEN (2004). *EN 13286-7: Unbound and hydraulically bound mixtures - Part 7: Cyclic load triaxial test for unbound mixtures*. Brussels, Belgium.

Clough, G.W., Sitar, N., Bachus, R.C., & Rad, N.S. (1981). *Cemented sands under static loading*. Journal of the Geotechnical Engineering Division, 107(6), 799-817.

Clough, G.W., Iwabuchi, J., Rad, N.S., & Kuppusamy, T. (1989). *Influence of cementation on liquefaction of sands*. Journal of Geotechnical Engineering, 115(8), 1102-1117.

Consoli, N.C., Foppa, D., Festugato, L., & Heineck, K.S. (2007). *Key parameters for strength control of artificially cemented soils*. Journal of Geotechnical and Geoenvironmental Engineering, ASCE, 133(2), 197-205.

Consoli, N.C., Viana da Fonseca, A., Cruz, R.C., & Heineck, K. (2009). *Fundamental Parameters for the Stiffness and Strength Control of Artificially Cemented Sand*. Journal of Geotechnical and Geoenvironmental Engineering, 135(9), 1347-1353.

Consoli, N.C., Cruz, R., Floss, M., & Festugato, L. (2010). *Parameters Controlling Tensile and Compressive Strength of Artificially Cemented Sand*. Journal of Geotechnical and Geoenvironmental Engineering, ASCE, 136(5), 759-763.

Consoli, N.C., Viana da Fonseca, A., Silva, S.R., Cruz, R.C., & Fonini, A. (2012). *Parameters controlling stiffness and strength of artificially cemented soils*. Géotechnique, 62(2), 177-183.

Coop, M. & Atkinson, J. (1993). *The mechanics of cemented carbonate sands*. Géotechnique, 43(1), 53-67.

Cordebois, J.P. & Sidoroff, F. (1982). *Endommagement anisotrope en élasticité et plasticité*. Journal de Mécanique Théorique et Appliqueé, Numéro Spécial, 45-60.

Corti, R., Diambra, A., Muir Wood, D., Escribano, D., & Nash, D. (2016). *Memory Surface Hardening Model for Granular Soils under Repeated Loading Conditions*. Journal of Engineering Mechanics, 142(12), 04016102.

Costa, C. (2008). *Development of a monitoring system for control of triaxial tests of soils*. M.Sc. thesis, University of Porto, Portugal (in Portuguese).

Cuccovillo, T. & Coop, M. R. (1993). *The influence of bond strength on the mechanics of carbonate soft rocks*. Geotechnical Engineering of Hard soils - Soft Rocks: Proc. of an International Symposium under the auspices of the ISSMFE (Anagnostopoulos et al., eds.), 20-23 September 1993, Athens, 485-494, Balkema, Rotterdam.

Cuccovillo, T. & Coop, M.R. (1997). *Yielding and pre-failure deformation of structured sands*. Géotechnique, 47(3), 491-508.

Cuccovillo, T. & Coop, M.R. (1999). *On the mechanics of structured sands*. Géotechnique, 49(6), 741-760.

Cuellar, V., Bazant, Z. P., Krizek, R. J., & Silver, M. (1977). *Densification and hysteresis of sand under cyclic shear*. Journal of Geotechnical and Geoenvironmental Engineering, ASCE, 103(GT5), 399-416.

Dafalias, Y.F. & Popov, E.P. (1975). *A model of nonlinearly hardening materials for complex loading*. Acta Mechanica, 21(3), 173-192.

Dafalias, Y.F. & Herrmann, L.R. (1982). Bounding surface formulation of plasticity. In *Soil Mechanics - Transient and Cyclic Loads* (Pande & Zienkiewicz, eds.), 253-282, Wiley, Chichester, UK.

Dawson, A., Kolisoja, P., & Vuorimies, N. (2005). *Permanent Deformation Behaviour of Low Volume Roads in the Northern Periphery Areas*. Proceedings of the 7th International Conference on Bearing Capacity of Roads, Railways and Airfields, 27-29 June 2005, Trondheim, Norway (CD-ROM).

Desai, C.S., Somasundaram, S., & Frantziskonis, G. (1986). *A hierarchical approach for constitutive modelling of geologic materials*. International Journal for Numerical and Analytical Methods in Geomechanics, 10(3), 225-257.

Ding, Y., Huang, W., Sheng, D., & Sloan, S.W. (2015). *Numerical study on finite element implementation of hypoplastic models*. Computers and Geotechnics, 68, 78-90.

England, R. (1969). *Error estimates for Runge-Kutta type solutions to systems of ordinary differential equations*. Computer Journal, 12, 166-170.

Ferreira, C., Viana da Fonseca, A., & Nash, D. (2011). *Shear wave velocities for sample quality assessment on a residual soil*. Soils and Foundations, 51(4), 683–692.

Fu, Z., Chen, S., & Peng, C. (2014). *Modeling Cyclic Behavior of Rockfill Materials in a Framework of Generalized Plasticity*. International Journal of Geomechanics, 14(2), 191-204.

Gajo, A., & Muir Wood, M. (1999a). *Severn–Trent sand: a kinematic-hardening constitutive model: the q–p formulation*. Géotechnique, 49(5), 595-614.

Gajo, A. & Muir Wood, D. (1999b). *A kinematic hardening constitutive model for sands: the multiaxial formulation*. International Journal for Numerical and Analytical Methods in Geomechanics, 23, 925-965.

Gens, A. & Nova, R. (1993). *Conceptual bases for a constitutive model for bonded soils and weak rocks*. Geotechnical Engineering of Hard soils - Soft Rocks: Proc. of an International Symposium under the

auspices of the ISSMFE (Anagnostopoulos et al., eds), 20-23 September 1993, Athens, 485-494, Balkema, Rotterdam.

Gens, A. & Potts, D.M. (1988). *Critical state models in computational geomechanics*. Engineering Computations, 5, 178-197.

Gens, A., Vaunat, J., & Garitte, B. (2005). *Elastoplastic modeling of hard soils and soft rocks: formulation and application*. Proc. 8th Int. Conf. on Computational Plasticity (COMPLAS 2005), 5-7 September 2005, Barcelona (CD-ROM).

Gens, A., Vaunat, J., Garitte, B., & Wileveau, Y. (2007). *In situ behaviour of a stiff layered clay subject to thermal loading: observations and interpretation*. Géotechnique 57 (2), 207–228.

Ghorbani, J., Nazem, M., & Carter, J.P. (2016). *Numerical modelling of multiphase flow in unsaturated deforming porous media*. Computers and Geotechnics, 71, 195-206.

Gomes Correia, A. (2004). *Evaluation of mechanical properties of unbound granular materials for pavement and rail tracks*. Geotechnics in Pavement and Railway Design and Construction: Proc. Int. Seminar on Geotechnics and Railway Design and Construction (Gomes Correia & Loizos, eds.), 16-17 December 2004, Athens, Greece, 35-60, Millpress, Rotterdam.

González, N. (2011). *Development of a family of constitutive models for geotechnical applications*. Ph.D. Thesis, Universitat Politècnica de Catalunya (UPC), Barcelona.

Goto, S., Tatsuoka, F., Shibuya, S., Kim, Y.-S., & Sato, T. (1991). *A simple gauge for local small strain measurements in the laboratory*. Soils and Foundations, 31(1), 169-180.

Grammatikopoulou, A., Zdravkovic, L., & Potts, D.M. (2006). *General formulation of two kinematic hardening constitutive models with a smooth elastoplastic transition*. International Journal of Geomechanics, 6(5), 291-302.

Hashiguchi, K. (1985). *Two and three surface models of plasticity*. Proc. 5th Int. Conf. on Numerical Methods in Geomechanics (Kawamoto & Itikawa, eds), 1-5 April 1985, Nagoya, 125-134, Balkema, Rotterdam.

Head, K.H. (1982). *Manual of soil laboratory testing*. Pentech Press Limited, London.

Iwan W.D. (1967). *On a class of models for the yielding behaviour of continuous and composite systems*. Journal of Applied Mechanics, ASME, 34(3), 612-617.

Jardine, R.J. (1992). *Some observations on the kinematic nature of soil stiffness*. Soils and Foundations, 32(2), 111–124.

Jardine, R.J. (1995). *One perspective on the pre-failure deformation characteristics of some geomaterials*. Proc. of Int. Symp. on Pre-Failure Deformation Characteristics of Geomaterials (Shibuya, Mitachi, & Miura, eds.), 12-14 September 1994, Sapporo, Japan, 855-885, Balkema, Rotterdam.

Jardine, R.J., Potts, D.M., Fourie, A.B., & Burland J.B. (1986). *Studies of the influence of nonlinear stress-strain characteristics in soil-structure interaction*. Géotechnique, 36(3), 377-396.

Kan, M., Taiebat, H., & Khalili, N. (2014). *Simplified Mapping Rule for Bounding Surface Simulation of Complex Loading Paths in Granular Materials*. International Journal of Geomechanics, 14(2), 239-253.

Krieg, R.D. (1975). *A practical two-surface plasticity theory*. Journal of Applied Mechanics, 42, 641-646.

Ladd, R.S. (1978). *Preparing tests specimens using undercompaction*. Geotechnical Testing Journal, 1(1), 16-23.

Lade, P.V. (2016). *Triaxial testing of soils*. Wiley, Chichester, UK.

Lekarp, F., & Dawson, A. (1998). *Modelling permanent deformation behaviour of unbound granular materials*. Construction and building materials, 12(1), 9-18.

Lekarp, F., Isacsson, U., & Dawson, A. (2000). *State of the Art. II: Permanent Strain Response of Unbound Aggregates*. Journal of Transportation Engineering, 126(1), 76-83.

Leroueil, S., High, D.W. (2003). Behaviour and properties of natural soils and soft rocks. In *Characterization and Engineering Properties of Natural Soils* (Tan et al., eds.), 29-254, Swets and Zeitlinger, Lisse.

Leroueil, S. & Vaughan, A. (1990). *The general and congruent effects of structure in natural soils and weak rocks*. Géotechnique, 40(3), 467-438.

LNEC (1972). *E 264: Soil-Cement Mixtures. Compression Test*. National Laboratory for Civil Engineering (LNEC). Lisbon, Portugal (in Portuguese).

Malandraki, V. & Toll, D.G. (1996). *The definition of yield for bonded materials*. Geotechnical Geological Engineering, 14(1), 67-82.

Manzari, M. T., & Dafalias, Y. F. (1997). *A critical state two-surface plasticity model for sands*. Geotechnique, 47(2), 255-272.

Mitchell, J.K. (1976). *Fundamentals of Soil Behavior*. Wiley, New York.

Morgan, J.R. & Williams, A.F. (1970). Repeated loads on cement-stabilized sand. Proc. 5th Conf. of the Australian Road Research Board, Canberra, Australia. 5(6), 5-16.

Mróz, Z. (1967). *On the description of anisotropic work hardening*. Journal of the Mechanics and physics of Solids, 15, 163-175.

Mróz, Z., Norris, V.A., & Zienkiewicz, O.C. (1978). *An anisotropic hardening model for soils and its application to cyclic loading*. International Journal for Numerical and Analytical Methods in Geomechanics, 2(3), 203-221.

Mróz, Z., Norris, V.A., Zienkiewicz, O.C. (1979). *Application of an anisotropic hardening model in the analysis of elasto-plastic deformation of soils*. Géotechnique, 29(1), 1-34.

Muir Wood, D. (1990). *Soil Behaviour and Critical State Soil Mechanics*. Cambridge University Press.

Muir Wood, D. (2004). *Geotechnical modelling*. Spoon Press, London.

Ni, J., Indraratna, B., Geng, X., Carter, J., & Chen, Y. (2015). *Model of Soft Soils under Cyclic Loading*. International Journal of Geomechanics, 15(4), 04014067.

Niemunis, A., Wichtmann, T., & Triantafyllidis, T. (2004). *Explicit accumulation model for cyclic loading.* Cyclic behaviour of soils and liquefaction phenomena: Proc. of CBS04, March/April 2004, Bochum, Germany, 65-76, Balkema, Rotterdam.

Nnadi, G. N., & Mitchell, R. J. (1991). *Behaviour of cemented sandfills under repeated loadings*. Canadian Geotechnical Journal, 28(5), 746-752.

Nova, R. (1988). *Sinfonietta classica: an exercise on classical soil modelling*. Proc. of Int. Workshop on Constitutive Equations for Granular Non-Cohesive Soils (Saada & Bianchini, eds.), 22-24 July 1987, Cleveland, Ohio, 501-520, Balkema, Rotterdam.

Nova, R., & Muir Wood, D. (1979). *A constitutive model for sand in triaxial compression*. International Journal for Numerical and Analytical Methods in Geomechanics, 3(3), 255-278.

Oka, F., Yashima, A., Tateishi, A., Taguchi, Y., & Yamashita, S. (1999). *A cyclic elasto-plastic constitutive model for sand considering a plastic-strain dependence of the shear modulus*. Géotechnique, 49(5), 661-680.

Panico, F. & Viana da Fonseca, A. (2016a). *Experimental study of the long term cyclic behaviour of artificially cemented Porto silty-sand*. A Geotecnia e os Desafios Societais: Proc. of 15th Portuguese National Geotechnical Congress (15CNG) (M. Matos Fernandes et al., eds.), 20-23 June 2016, Porto, Portugal (e-book) (in Portuguese).

Panico, F. & Viana da Fonseca, A. (2016b). *Long Term Cyclic Response of a Soil-Cement Mixture: Experimental Study and Modelling*. Procedia Engineering, 143, 178-186.

Panico, F., Viana da Fonseca, A., & Vaunat, J. (2018). *Modelling the small strain behaviour of a cemented silty sand with bounding plasticity*. Numerical Methods in Geotechnical Engineering IX: Proc. of 9th European Conf. on Numerical Methods in Geotechnical Engineering (NUMGE 2018) (A.S. Cardoso et al., eds.), 25-27 June 2018, Porto, Portugal, 1, 289-297, Taylor & Francis Group, London.

Pasten, C. (2013). *Geomaterials subjected to repetitive loading: implications on energy systems*. Ph.D. Thesis, Georgia Institute of Technology, USA.

Pasten, C., Shin, H., & Santamarina, J. C. (2013). *Long-term foundation response to repetitive loading*. Journal of Geotechnical and Geoenvironmental Engineering, 140(4), 04013036.

Paute, J.-L., Hornych, P., & Benaben, J.-P. (1996). *Repeated load triaxial testing of granular materials in the French Network of Laboratories des Ponts et Chaussées*. Flexible pavements: Proc. of European Symp. EUROFLEX 93 (Gomes Correia ed.), 20-22 September 1993, Lisbon, Portugal, 53-64, Balkema, Rotterdam.

Potts, D.M. & Ganendra, D. (1994). *Evaluation of substepping and implicit stress point algorithms*. Computer Methods in Applied Mechanics and Engineering, 119, 341-354.

Potts, D.M. & Gens, A. (1985). *A critical assessment of methods of correcting for drift from the yield surface in elasto-plastic finite element analysis*. International Journal for Numerical and Analytical Methods in Geomechanics, 9(2), 149-159.

Potts, D.M. & Zdravkovic, L. (1999). *Finite Element Analysis in Geotechnical Engineering: Theory*. Thomas Telford Publishing, London.

Prager, W (1949). *Recent developments of the mathematical theory of plasticity*. Journal of Applied Physics, 20(3), 235-241.

Prager, W (1955). *The theory of plasticity - a survey of recent achievements*. Proc. Inst. Mech. Eng., London, 3-19.

Puppala, A.J., Saride, S., & Chomtid, S. (2009). *Experimental and Modeling Studies of Permanent Strains of Subgrade Soils*. Journal of Geotechnical and Geoenvironmental Engineering, 135(10), 1379–1389.

Puppala, A.J., Saride, S., & Williammee, R. (2012). *Sustainable Reuse of Limestone Quarry Fines and RAP in Pavement Base/Subbase Layers*. Journal of Materials in Civil Engineering, 24(4), 418-429.

Qadimi, A. & Coop, M. (2007). *The undrained cyclic behaviour of a carbonate sand*. Géotechnique, 57(9), 739-750.

Rios, S. (2011). *A general framework for the geomechanical characterisation of artificially cemented soil*. Ph.D. Thesis, University of Porto, Portugal.

Rios, S., Viana da Fonseca, A., & Baudet, B.A. (2012). *The Effect of the Porosity/Cement Ratio on the Compression of Cemented Soil*. Journal of Geotechnical and Geoenvironmental Engineering, 138(11), 1422-1426.

Rios, S., Viana da Fonseca, A., & Baudet, B.A. (2014). *On the shearing behaviour of an artificially cemented soil*. Acta Geotechnica, 9(2), 215-226.

Rios, S., Ciantia, M., Gonzalez, N., Arroyo, M., & Viana da Fonseca, A. (2016). *Simplifying calibration of bonded elasto-plastic models*. Computers and Geotechnics, 73, 100-108.

Roscoe, K.H., Schofield, A.N., & Wroth, C.P. (1958). *On the yielding of soils*. Géotechnique, 8(1), 22-52.

Roscoe, K.H. & Burland, J.B. (1968). On the generalized stress-strain behaviour of 'wet' clay. In *Engineering Plasticity*, 535-609, Cambridge University Press.

Rouainia, M. & Muir Wood, D. (2000). *A kinematic hardening constitutive model for natural clays with loss of structure*. Géotechnique, 50(2), 153-164.

Rouainia, M. & Muir Wood, D. (2001). *Implicit numerical integration for a kinematic hardening soil plasticity model*. International Journal for Numerical and Analytical Methods in Geomechanics, 25, 1305-1325.

Rowe, P.W. (1962). *The stress-dilatancy relation for static equilibrium of an assembly of particles in contact*. Proceedings of the Royal Society A: Mathematical, Physical and Engineering Sciences, 269(1339), 500-527.

Sarra, S.A. (2003). *The Method of Characteristics & Conservation Laws*. Journal of Online Mathematics and its Applications, 3, http://www.maa.org/press/periodicals/loci/joma/the-method-of-characteristics-conservation-laws.

Sawicki, A., & Swidzinski, W. (1989). *Mechanics of a sandy subsoil subjected to cyclic loadings*. International Journal for Numerical and Analytical Methods in Geomechanics, 13(5), 511-529.

Schofield, A.N. & Wroth, C.P. (1968). *Critical State Soil Mechanics*. McGraw-Hill, New York.

Sharma, S. (2004). *Characterisation of cyclic behaviour of calcite cemented calcareous soils*. Ph.D. Thesis, the University of Western Australia, Perth.

Sharma, S. & Fahey, M. (2003a). *Evaluation of cyclic shear strength of two cemented calcareous soils*. Journal of Geotechnical and Geoenvironmental Engineering, 129(7), 608-618.

Sharma, S. & Fahey, M. (2003b). *Degradation of Stiffness of Cemented Calcareous Soil in Cyclic Triaxial Tests*. Journal of Geotechnical and Geoenvironmental Engineering, 129(7), 619-629.

Silver, M.L., & Seed, H.B. (1971). *Volume Changes in Sands during Cyclic Loading*. Journal of the Soil Mechanics and Foundations Division, ASCE, 97(SM9), 1171-1182.

Skempton, A.W. (1954). *The pore pressure coefficients, A and B*. Géotechnique, 4(4), 143-147.

Sloan, S.W. (1987). *Substepping schemes for numerical integration of elasto-plastic stress-strain relations*. International Journal for Numerical Methods in Engineering, 24, 893-911.

Sloan, S.W., Abbo, A.J., & Sheng, D. (2001). *Refined explicit integration of elasto-plastic models with automatic error control*. Engineering Computations, 18, 121-154.

Stallebrass, S.E. & Taylor, R.N. (1997). *The development and evaluation of a constitutive model for the prediction of ground movements in overconsolidated clay*. Géotechnique, 47(2), 235-253.

Tonni, L., Cola, S., & Pastor, M. (2006). *A Generalized Plasticity approach for describing the behaviour of silty soils forming the Venetian lagoon basin*. Proceedings of 6th European Conference on Numerical Methods in Geotechnical Engineering (Schweiger ed.), 6-8 September 2006, Graz, 93-99, Taylor & Francis, London.

Vaunat, J. & Gens, A. (2003). *Numerical modelling of an excavation in a hard soil/soft rock formation using a coupled damage/plasticity model*. Proc. 7th Int. Conf. on Computational Plasticity (COMPLAS 2003), 7-10 April 2003, Barcelona (CD-ROM).

Viana da Fonseca, A. (1996). *Geomechanics in Residual Soils from Porto Granite. Criteria for the Design of Shallow Foundations*. Ph.D. Thesis, University of Porto, Portugal (in Portuguese).

Viana da Fonseca, A. (2003). Characterising and deriving engineering properties of a saprolitic soil from granite, in Porto. In *Characterization and Engineering Properties of Natural Soils* (Tan et al., eds.), 1341-1378, Swets and Zeitlinger, Lisse.

Viana da Fonseca, A., & Coutinho, R.Q. (2008). *Characterization of residual soils*. Geotechnical and Geophysical Site Characterization: Proc. 3rd Int .Conf. on Site Characterization (ISC'3) (Huang & Mayne, eds.), 1-4 April 2008, Taipei, Taiwan, 195-248, Taylor & Francis, London.

Viana da Fonseca, A., Carvalho, J., Ferreira, C., Santos, J.A., Almeida, F., Pereira, E., Feliciano, J., Grade, J., & Oliveira, A. (2006). *Characterization of a profile of residual soil from granite combining geological, geophysical and mechanical testing techniques*. Geotechnical and Geological Engineering, 24(5), 1307-1348.

Viana da Fonseca, A., Caberlon Cruz, R., & Consoli, N. (2009a). *Strength properties of sandy soil-cement admixtures*. Geotechnical and Geological Engineering, 27(6), 681-686.

Viana da Fonseca, A., Ferreira, C., & Fahey, M. (2009b). *A framework interpreting bender element tests, combining time-domain and frequency-domain methods*. Geotechnical Testing Journal, 32(2), 1-17.

Viana da Fonseca, A., Rios, S., & Cruz, N. (2010). *Geotechnical characterization by in situ and lab tests to the back-analysis of a supported excavation in Metro do Porto*. Geotechnical and Geological Engineering, 28(3), 251-264.

Viana da Fonseca, A., Rios, S., Amaral, M.F., & Panico, F. (2013a). *Fatigue Cyclic Tests on Artificially Cemented Soil*. Geotechnical Testing Journal, 36(2), 1-9.

Viana da Fonseca, A., Rios, S., Amaral, M.F. (2013b). *Structural anisotropy by static compaction*. Engineering geology, 154, 89-97.

Viana da Fonseca, A., Amaral, M. F, Panico, F., & Rios, S. (2014). *Indexation of dynamic and static geomechanical properties of a cemented aggregate for transportation engineering*. Transportation Geotechnics, 1(1), 31-44.

Wang, G., & Xie, Y. (2014). *Modified bounding surface hypoplasticity model for sands under cyclic loading*. Journal of Engineering Mechanics, 140(1), 91-101.

Werkmeister, S., Dawson, A. R., & Wellner, F. (2005). *Permanent deformation behaviour of granular materials*. Road Materials and Pavement Design, 6(1), 31-51.

Wichtmann, T., Niemunis, A., & Triantafyllidis, Th. (2005). *Strain accumulation in sand due to cyclic loading: drained triaxial tests*. Soil Dynamics and Earthquake Engineering, 25, 967-979.

Wichtmann, T., Niemunis, A., & Triantafyllidis, Th. (2010). *On the ''elastic'' stiffness in a high-cycle accumulation model for sand: a comparison of drained and undrained cyclic triaxial tests*. Canadian Geotechnical Journal, 47(7), 791-805.

Wichtmann, T. & Triantafyllidis, T. (2012). Behaviour of granular soils under environmentally induced cyclic loads. In *Mechanical behaviour of soils under environmentally induced cyclic loads* (Di Prisco & Muir Wood, eds.), 1-136, Springer, Vienna.

Wissman, J.W. & Hauck, C. (1983). *Efficient elasto-plastic finite element analysis with higher order stress point algorithms*. Computers and Structures, 17, 89-95.

Yeoh, C.K. & Airey, D. (1994). *Undrained Cyclic Loading of a Cemented Sand*. Prefailure Deformation of Geomaterials: Proc. Int. Symp. on Pre-Failure Deformation Characteristics of Geomaterials (Shibuya et al., eds.), 12-14 September 1994, Sapporo, Japan, 1, 95-100, Balkema, Rotterdam.

Yeoh, C.K. & Airey, D. (1998). *Drained cyclic response of an artificially cemented calcareous sand*. The Geotechnics of Hard Soils - soft Rocks: Proc. of 2nd Int. Symp. on Hard Soils, Soft Rocks, 12-14 October 1998, Naples, Italy, 2, 935-942, Balkema, Rotterdam.

Youd, T.L. (1972). *Compaction of sands by repeated shear straining*. Journal of Soil Mechanics & Foundations Division, ASCE, 98(SM7), 709-725.

Yu, H.S. (1998). *CASM: A Unified state parameter model for clay and sand*. International Journal for Numerical and Analytical Methods in Geomechanics, 22, 621-653.

Yu, H.S. (2006). *Plasticity and Geotechnics*. Springer Publishers, New York.

Yu, H.S., Khong, C., & Wang, J (2007a). *A unified plasticity model for cyclic behaviour of clay and sand*. Mechanics Research Communications, 34(2), 97-114.

Yu, H.S., Tan, S. M., & Schnaid, F. (2007b). *A critical state framework for modelling bonded geomaterials*. Geomechanics and Geoengineering, 2(1), 61-74.

Zhao, M. M. & Airey, D. W. (1992). *Fatigue testing of an artificially cemented calcareous sand*. Proc. of 2nd Int. Offshore and Polar Engineering Conference (ISOPE-92),14-19 June 1992, San Francisco, USA, 1, 424-429, International Society of Offshore and Polar Engineers.

Zhao, M.M., Huang, J.T. & Airey, D.W. (1992). *Fatigue failure for a cemented sand*. Proc. of 6th Australia-New Zealand Conference on Geomechanics, 3-7 February 1992, Christchurch, New Zealand, 1, 401-405, The New Zealand Geomechanics Society.

Zytynski, M., Randolph, M.F., Nova, R., & Wroth, C.P. (1978). On modelling the unloading-reloading behaviour of soils. International Journal for Numerical and Analytical Methods in Geomechanics, 2, 87-94.

ANNEX 1: ELEMENTS OF TENSOR ANALYSIS AND ELEMENTS OF CLASSIC ELASTOPLASTICITY THEORY

Basic relations

Total and effective stresses:

$$\sigma' = \sigma - u \tag{A.1}$$

Mean effective stress and deviatoric stress in axisymmetric conditions:

$$p' = \frac{\sigma_1' + 2\sigma_3'}{3} = \frac{\sigma_a' + 2\sigma_r'}{3} \tag{A.2}$$

$$q = \sigma_1' - \sigma_3' = \sigma_a' - \sigma_r' \ (= \sigma_1 - \sigma_3 = \sigma_a - \sigma_r) \tag{A.3}$$

Volumetric and distortional strain in axisymmetric conditions:

$$\varepsilon_v = \varepsilon_1 + 2\varepsilon_3 = \varepsilon_a + 2\varepsilon_r \tag{A.4}$$

$$\varepsilon_s = \frac{2}{3}(\varepsilon_1 - \varepsilon_3) = \frac{2}{3}(\varepsilon_a - \varepsilon_r) \tag{A.5}$$

Tensor analysis

INDEX NOTATION AND DEFINITION OF TENSOR

In tensor notation, indexes are used in combination with the letter representing the quantity under examination. One defines symbols of the first order, those symbols with a single index. They are written as follows:

$$a_i \tag{A.6}$$

in the three-dimensional Euclidean space (E^3), for each symbol of the first order, three elements correspond. Therefore index i can assume integer values between 1 and 3; the three elements ai will denote the component of the vector $\boldsymbol{a}$.

Second-order symbols are characterized by two indexes and are usually represented as follows:

$$a_{ij} \text{ or } A_{ij} \tag{A.7}$$

in the space E^3, for each symbol of the second order, 3^2 elements correspond:

$$\begin{pmatrix} A_{11} & A_{12} & A_{13} \\ A_{21} & A_{22} & A_{23} \\ A_{31} & A_{32} & A_{33} \end{pmatrix} \tag{A.8}$$

If a planar problem is considered, the space is two-dimensional (E^2) and the tensor has 2^2 elements:

$$\begin{pmatrix} A_{11} & A_{12} \\ A_{21} & A_{22} \end{pmatrix} \tag{A.9}$$

These values ordered in a square matrix represent the components of a second-order tensor, **T**. In general, a symbol of the n^{th} order is characterized by *n* indexes and it defines the components of a tensor of the n^{th} order, having 3*n* components. For example, a third-order symbol is written as follows:

$$A_{ijk} \tag{A.10}$$

and in the space E^3 it defines a third-order tensor, constituted by 33 elements ordered in a cubic matrix. A fourth-order symbol is written as follows:

$$A_{ijhk} \tag{A.11}$$

and defines a fourth-order tensor, constituted by 34 elements ordered in a 4-dimensional cubic matrix. Following this definition, a vector can be regarded as a first-order tensor and a scalar as a tensor of the order 0. It is common to refer to a second-order tensor simply as "tensor" without any further specification.

TENSOR AS A LINEAR OPERATOR

Mathematically, a tensor of the second order can be regarded as a linear operator between vector fields. This means that the components of a second order tensor represent the coefficients of a linear relationship between the components of the vectors. Thus, given two vectors $\boldsymbol{a}$ and $\boldsymbol{b}$ in the space E^3, a linear relationship between their components can be written using a convenient tensor **T** of components T_{ij}:

$$b_i = \sum_{j=1}^{3} T_{ij} a_j \quad \text{for } i = 1..3 \tag{A.12}$$

Similarly, in a space E^2 is:

$$b_i = \sum_{j=1}^{2} T_{ij} a_j \quad \text{for } i = 1..2 \tag{A.13}$$

It should be noted that the linearity of this expressions is not dependent on the reference system chosen, and this property of invariance makes the tensor an entity suitable for representing physical quantities.

In a general way, a tensor of the n^{th} order is a linear operator between two tensor fields. A very well known example is the elastic constitutive relation, linking the stress tensor with the strain tensor:

$$T_{ij} = \sum_{h=1}^{3} \sum_{k=1}^{3} D_{ijhk} E_{hk} \tag{A.14}$$

where the fourth order tensor **D** is the stiffness tensor and **T** and **E** are the stress and strain tensors (described in detail in the next sections).

A tensor field is a region of space in which a tensor is assigned at every instant time t to each material point. Although **T** and **E** are commonly referred to as tensors, they are tensor fields, since they are defined for each point of a continuum.

EINSTEIN NOTATION AND OPERATIONS

The last two expressions could be written in a simpler manner using the Einstein summation convention (or Einstein notation). According to this notation, when an index variable appears twice in a symbol or in a term formed by many symbols, it implies summation of that term over all the values of the index. The following examples explain the meaning of the notation (in a E^3 space):

$$\begin{aligned} T_{ii} &= T_{11} + T_{22} + T_{33} \\ T_{ij} a_j &= T_{i1} a_1 + T_{i2} a_2 + T_{i3} a_3 \end{aligned} \tag{A.15}$$

Thus, the following relationship:

$$a_i = b_i + c_i \tag{A.16}$$

corresponds to a system of three equations and:

$$A_{ij} = B_{ij} + C_{ij} \tag{A.17}$$

corresponds to a system of nine equations. Equations (A.12) and (A.14) can thus be rewritten simply as:

$$b_i = T_{ij} a_j \tag{A.18}$$

$$T_{ij} = D_{ijhk} E_{hk} \tag{A.19}$$

And, in a space E^3, they represent a system of 3 and 9 equations, respectively. In E^2, the equations reduce to 2 and 4, respectively.

Kronecker delta

When writing relations between vectors or tensors in index notation, Kronecker delta δ_{ij} is often used. It assumes the value 1 if $i = j$ and 0 if $i \neq j$ and its use is illustrated in the examples below:

$$\begin{aligned} a_i \delta_{ik} &= a_k \\ b_{hl} \delta_{lk} &= b_{hk} \end{aligned} \tag{A.20}$$

Throughout the present dissertation, Einstein notation is implicitly used and the stress and strain spaces are always assumed to be E^2 or E^3 Euclidian spaces.

Scalar product

Scalar product or dot product or inner product of two vectors $\boldsymbol{a}$ and $\boldsymbol{b}$ is given by:

$$\boldsymbol{a} \cdot \boldsymbol{b} = a_i b_i \tag{A.21}$$

which represents a scalar quantity, given by the sum of the products of the corresponding elements of each vector.

Scalar product induces the definition of norm of a vector $\boldsymbol{a}$ as the following non-negative scalar value:

$$\|\boldsymbol{a}\| = \boldsymbol{a} \cdot \boldsymbol{a} = a_i a_i \tag{A.22}$$

The norm of a vector geometrically corresponds to the length of the vector.

Dot product between a second-order tensor and a vector corresponds to a vector:

$$\boldsymbol{c} = \mathbf{A} \cdot \mathbf{b} = \left(A_{ij} b_j\right) \tag{A.23}$$

The dot product of two second-order tensors **A** and **B**, denoted by **AB** or $\mathbf{A} \cdot \mathbf{B}$, results in a second-order tensor **C**:

$$\mathbf{C} = \mathbf{A} \cdot \mathbf{B} = \left(A_{ik} B_{kj}\right) \tag{A.24}$$

This operation corresponds to the usual matrix product.

In general, the scalar product between a tensor of order n and a tensor of order m gives a tensor of order d:

$$d = n + m - 2 \tag{A.25}$$

Frobenius inner product

Frobenius inner product of two second-order tensors **A** and **B** is given by:

$$\mathbf{A}:\mathbf{B} = A_{ij}B_{ij} \tag{A.26}$$

that represents a scalar quantity, given by the sum of the products of the 9 corresponding elements of each matrix. The scalar product of a fourth-order tensor (**C**) and a second-order tensor (**D**) gives a second-order tensor **E** defined as follows:

$$\mathbf{E} = \mathbf{C}:\mathbf{D} = \left(C_{ijhk}D_{hk}\right) \tag{A.27}$$

This definition allows rewriting equation (A.19) as follows:

$$\mathbf{T} = \mathbf{D}:\mathbf{E} \tag{A.28}$$

Tensor product

Tensor product (or outer product) between a tensor **A** of order n and a tensor **B** of order m produces a tensor **C** of order $(n+m)$ whose components are the products of the components of the original tensors. In the case of two second-order tensors, tensor **C** is a fouth-order tensor defined as follows:

$$\mathbf{C} = \left(C_{ijhk}\right) = \mathbf{A} \otimes \mathbf{B} = \left(A_{ij}B_{hk}\right) \tag{A.29}$$

Trace and determinant

Trace of a second-order tensor is defined as the sum of the elements of the principal diagonal:

$$\operatorname{tr}\mathbf{A} = \operatorname{tr}\begin{pmatrix} A_{11} & A_{12} & A_{13} \\ A_{21} & A_{22} & A_{23} \\ A_{31} & A_{32} & A_{33} \end{pmatrix} = A_{11} + A_{22} + A_{33} \tag{A.30}$$

Determinant of a second-order tensor is defined as determinant of the matrix of the components. In space E^2:

$$\det\mathbf{A} = \det\begin{pmatrix} A_{11} & A_{12} \\ A_{21} & A_{22} \end{pmatrix} = A_{11}A_{22} - A_{21}A_{12} \tag{A.31}$$

In space E^3:

$$\begin{aligned} \det\mathbf{A} = \det\begin{pmatrix} A_{11} & A_{12} & A_{13} \\ A_{21} & A_{22} & A_{23} \\ A_{31} & A_{32} & A_{33} \end{pmatrix} = \\ = A_{11}A_{22}A_{33} - A_{11}A_{23}A_{32} - A_{12}A_{21}A_{33} + A_{12}A_{23}A_{31} + \\ + A_{13}A_{21}A_{32} - A_{13}A_{22}A_{31} \end{aligned} \tag{A.32}$$

Inverse and transpose

The inverse of a second-order tensor **A** is a tensor $\mathbf{A}^{-1}$ such that:

$$\mathbf{A}\,\mathbf{A}^{-1} = \mathbf{I} = \mathbf{A}^{-1}\,\mathbf{A} \tag{A.33}$$

Where **I** is the identity tensor of the same order.

A second-order tensor is symmetric if it is equal to its transpose, that is, if the matrix does not change when writing its columns as the rows of the new matrix.

TENSOR FUNCTIONS

Tensor functions are functions whose expressions depend on the components of one or more tensors (of any order). Depending on its output, a tensor function can be scalar-valued, vector-valued or tensor-valued. A scalar-valued tensor function has the following general form:

$$\phi = \phi(t, \boldsymbol{a}, \mathbf{B}, \dots) \tag{A.34}$$

that is, the function depends on one or more scalar (e.g. time t), vector or tensor variables and gives in output a scalar value ϕ. Two examples of scalar-valued tensor are yield function f and plastic potential g.

Vector and tensor-valued functions have similar expressions but give as output a vector and a tensor, respectively:

$$\boldsymbol{u} = \boldsymbol{u}(t, \boldsymbol{a}, \mathbf{B}, \dots) \tag{A.35}$$

$$\mathbf{A} = \mathbf{A}(t, \boldsymbol{a}, \mathbf{B}, \dots) \tag{A.36}$$

First time derivatives

The first time derivatives of ϕ, $\boldsymbol{u}$, and $\mathbf{A}$ are:

$$\dot{\phi} = \frac{\partial \phi}{\partial t} \tag{A.37}$$

$$\dot{\boldsymbol{u}} = \frac{\partial \boldsymbol{u}}{\partial t} = \left(\frac{\partial u_i}{\partial t}\right) \tag{A.38}$$

$$\dot{\mathbf{A}} = \frac{\partial \mathbf{A}}{\partial t} = \left(\frac{\partial A_{ij}}{\partial t}\right) \tag{A.39}$$

The constitutive relations (scalar, vector and tensor-valued) presented in this dissertation are all time-independent. This could lead to the conclusion that all the time derivatives are nil. Nevertheless, the values of these functions vary with time (e.g. stress and strain tensors components change as external load and/or displacement are applied). In this sense, time derivatives represent the infinitesimal increment of that function rather than the rate of change. Hence, time derivatives have meaning if time is regarded as a parameter ordering the events rather than a variable of the functions. For example, the derivatives $\dot{\boldsymbol{\sigma}}$ and $\dot{\boldsymbol{\varepsilon}}$ have to be regarded as stress and strain increments, respectively.

Differential and gradient of a scalar-valued function

For a scalar-valued tensor function $\phi(\mathbf{A})$ of a tensor variable $\mathbf{A}$, the exact differential $d\phi$ is:

$$d\phi = \frac{\partial \phi(\mathbf{A})}{\partial \mathbf{A}} \cdot \dot{\mathbf{A}} = \frac{\partial \phi}{\partial A_{ij}} \dot{A}_{ij} \tag{A.40}$$

The differential represents the change in the function as its variables change of an infinitesimal. For a scalar-valued function dependent from vector and tensor variables $\phi(\boldsymbol{u}, \mathbf{A})$, the total differential is:

$$d\phi = \frac{\partial \phi(\boldsymbol{u}, \mathbf{A})}{\partial \boldsymbol{u}} \cdot \dot{\boldsymbol{u}} + \frac{\partial \phi(\boldsymbol{u}, \mathbf{A})}{\partial \mathbf{A}} \cdot \dot{\mathbf{A}} \tag{A.41}$$

The gradient of a function of a vector variable $\phi(\boldsymbol{u})$ is a vector:

$$grad(\phi) = \frac{\partial \phi(\boldsymbol{u})}{\partial \boldsymbol{u}} = \left(\frac{\partial \phi}{\partial u_i}\right) \tag{A.42}$$

In this case, the gradient represents the direction of the steepest slope of the function in each point and the value of that slope. The direction of the gradient at each point is normal to the contour line of the function at that point.

The gradient of a function of a tensor variable $\phi(\mathbf{A})$ is a second-order tensor:

$$grad(\phi) = \frac{\partial \phi(\mathbf{A})}{\partial \mathbf{A}} = \left(\frac{\partial \phi}{\partial A_{ij}}\right) \tag{A.43}$$

STRESS TENSOR

The two most important second-order symmetric tensors in continuum mechanics are the stress tensor and the infinitesimal strain tensor. They are two tensor fields as they are defined for each point of a region.

The stress tensor (also known as Cauchy stress tensor) is usually expressed in the following engineering notation:

$$\boldsymbol{\sigma} = (\sigma_{ij}) = \begin{pmatrix} \sigma_{11} & \sigma_{12} & \sigma_{13} \\ \sigma_{21} & \sigma_{22} & \sigma_{23} \\ \sigma_{31} & \sigma_{32} & \sigma_{33} \end{pmatrix} = \begin{pmatrix} \sigma_x & \tau_{xy} & \tau_{xz} \\ \tau_{yx} & \sigma_y & \tau_{yz} \\ \tau_{zx} & \tau_{zy} & \sigma_z \end{pmatrix} \tag{A.44}$$

where the components indicated with the symbol σ are referred to the normal stress and the components indicated with τ to the shear stress in the elementary volume considered. The convention commonly used in soil mechanics considers normal compression stresses as positive.

Principal directions and principal stress space

For each material point in the stress tensor field, it is possible to define a local reference system for which the shear components are nil. The axes of this system are called principal directions of stress and the planes perpendicular to them are the principal planes of stress. Mathematically, the principal directions correspond to the eigenvectors of the stress tensor. The eigenvalues associated to the eigenvectors represent the principal stresses. The symmetry of tensor $\boldsymbol{\sigma}$ ensures that the three eigenvalues are always real. The shape of the stress tensor in the principal directions reference system is the following:

$$\boldsymbol{\sigma} = (\sigma_{ij}) = \begin{pmatrix} \sigma_1 & 0 & 0 \\ \sigma_{21} & \sigma_2 & 0 \\ 0 & 0 & \sigma_3 \end{pmatrix} \tag{A.45}$$

in which $\sigma_1 \geq \sigma_2 \geq \sigma_3$ are the principal stresses. It is important to note that the state of stress in a point in this reference system is fully described by only three components. They can be regarded as the components of a vector in a three-dimensional space called the principal stress space. In this space, the state of stress in a point and its evolution in time (stress-path) can be represented as vectors (vector $\boldsymbol{\sigma}$

and the above-mentioned stress first time derivative $\dot{\boldsymbol{\sigma}}$). A scalar-valued tensor function can be represented as a set of curves in this space, whose gradient is the outward normal vector.

Stress invariants and decomposition of the stress tensor

In any reference system adopted, there are three scalar quantities associated to the stress tensor that are invariant. They are called stress invariants and are defined as follows:

$$I_1 = \mathrm{tr}\,\boldsymbol{\sigma} = \sigma_{ii} = \sigma_x + \sigma_y + \sigma_z = \sigma_1 + \sigma_2 + \sigma_3 \tag{A.46}$$

$$\begin{aligned} I_2 = \frac{1}{2}[(\mathrm{tr}\,\boldsymbol{\sigma})^2 - \mathrm{tr}(\boldsymbol{\sigma}^2)] = \frac{1}{2}\left(\sigma_{ii}\sigma_{jj} - \sigma_{ij}\sigma_{ij}\right) = \\ = \sigma_x\sigma_y + \sigma_y\sigma_z + \sigma_x\sigma_z - \tau_{xy}^2 - \tau_{xz}^2 - \tau_{yz}^2 = \\ = \sigma_1\sigma_2 + \sigma_2\sigma_3 + \sigma_1\sigma_3 \end{aligned} \tag{A.47}$$

$$I_3 = \det\boldsymbol{\sigma} = \sigma_x\sigma_y\sigma_z + 2\tau_{xy}\tau_{yz}\tau_{xz} - \sigma_z\tau_{xy}^2 - \sigma_x\tau_{yz}^2 - \sigma_y\tau_{xz}^2 = \sigma_1\sigma_2\sigma_3 \tag{A.48}$$

The three invariants are related to physical properties that are constant, regardless the reference system used.

The stress tensor can be decomposed in an isotropic part, called volumetric stress tensor, and in a deviatoric part, called stress deviator tensor. In an isotropic elastic material, the first component is responsible of the volume variation, while the second component causes variation in shape.

The volumetric stress tensor is defined as follows:

$$\boldsymbol{\sigma}_p = \begin{pmatrix} p & 0 & 0 \\ 0 & p & 0 \\ 0 & 0 & p \end{pmatrix} = \left(\delta_{ij}p\right) \tag{A.49}$$

where p is the mean stress, which in turn is related to the first invariant of the stress tensor:

$$p = \frac{1}{3}\sigma_{ii} = \frac{I_1}{3} \tag{A.50}$$

The deviatoric stress tensor **s** and it is calculated as the difference between the stress tensor and the volumetric stress tensor:

$$\mathbf{s} = \left(s_{ij}\right) = \left(\sigma_{ij} - \delta_{ij}p\right) = \begin{pmatrix} \sigma_x - p & \tau_{xy} & \tau_{xz} \\ \tau_{yx} & \sigma_y - p & \tau_{yz} \\ \tau_{zx} & \tau_{zy} & \sigma_z - p \end{pmatrix} = \begin{pmatrix} s_x & \tau_{xy} & \tau_{xz} \\ \tau_{yx} & s_y & \tau_{yz} \\ \tau_{zx} & \tau_{zy} & s_z \end{pmatrix} \tag{A.51}$$

It can be easily demonstrated that the principal directions of tensor **s** (s_1, s_2, s_3) are the same as stress tensor **σ**. As for stress tensor, also **s** has three stress invariants:

$$J_1 = 0 \tag{A.52}$$

$$J_2 = \frac{1}{2}(\mathbf{s}\cdot\mathbf{s}) = \frac{1}{2}(s_1^2 + s_2^2 + s_3^2) \tag{A.53}$$

$$J_3 = \det\mathbf{s} = s_1 s_2 s_3 \tag{A.54}$$

Alternative expressions of J_2 are:

$$\begin{aligned} J_2 = \frac{1}{6}\left[\left(\sigma_x - \sigma_y\right)^2 + \left(\sigma_y - \sigma_z\right)^2 + (\sigma_z - \sigma_x)^2 + \tau_{xy}^2 + \tau_{yz}^2 + \tau_{zx}^2\right] = \\ = \frac{1}{6}[(\sigma_1 - \sigma_2)^2 + (\sigma_2 - \sigma_3)^2 + (\sigma_3 - \sigma_1)^2] \end{aligned} \tag{A.55}$$

Two important variables linked to the deviatoric stress invariants are deviatoric stress (q) and Lode's angle (θ), defined as follows:

$$q = \sqrt{3J_2} \tag{A.56}$$

$$\theta = \frac{1}{3}\sin^{-1}\left[-\frac{3\sqrt{3}\,J_3}{2\,J_2^{3/2}}\right] \tag{A.57}$$

Another parameter commonly used is stress ratio η:

$$\eta = q/p \tag{A.58}$$

The geometric meaning of the stress variables p, q, and θ is illustrated in Fig. A.1, in which a generic point P (σ_1, σ_2, σ_3) is represented in the principal stress space. Vector OP can be decomposed in the direction of the space diagonal ON and in the perpendicular direction NP. The magnitude of the two components are $\sqrt{3}p$ and $\sqrt{2/3}q$, respectively. Considering the plane containing P and perpendicular to the space diagonal (plane ABC in Fig. A.2), Lode's angle is the angle formed by directions ND and NP, measured starting from ND. For an isotropic material (i.e. a material that has the same properties in all directions), it is only sufficient to describe material behaviour within a Lode's angle included between -30º and 30º. In the remaining 5 sectors of the deviatoric plane, the same behaviour is repeated, following a radial symmetry. In a transversely isotropic material, behaviour shall be indicated in half the extension of the deviatoric plane (e.g. a Lode's angle between -30º and 150º), and the behaviour presents an axial symmetry about the axis that is normal to the plane of isotropy.

Thus, the stress tensor in this space reduces to a vector, simplifying the mathematical manipulation. The state of stress in a point is univocally individuated by the three variables p, q, and θ, that have the advantage of remaining constant regardless the reference system adopted and that are expression of two distinct components of the stress: isotropic and deviatoric. Many existing models assume an independent constitutive response of the two components: volumetric strain is associated to the isotropic component of stress and distortional strain depends only on the deviatoric component.

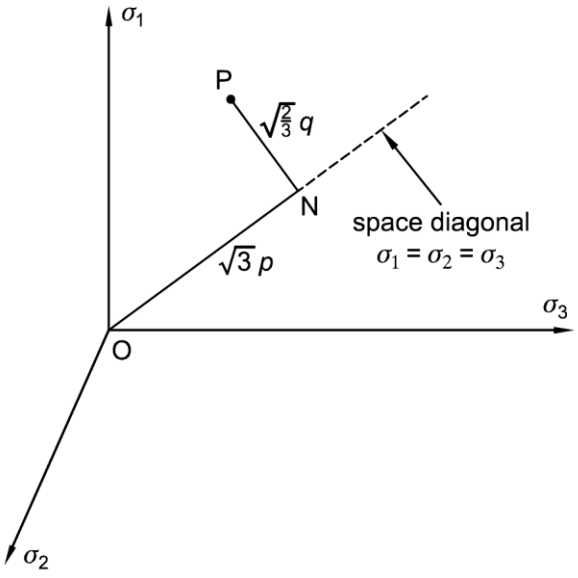

Fig. A.1 – Principal stress space: definition of mean and deviatoric stress

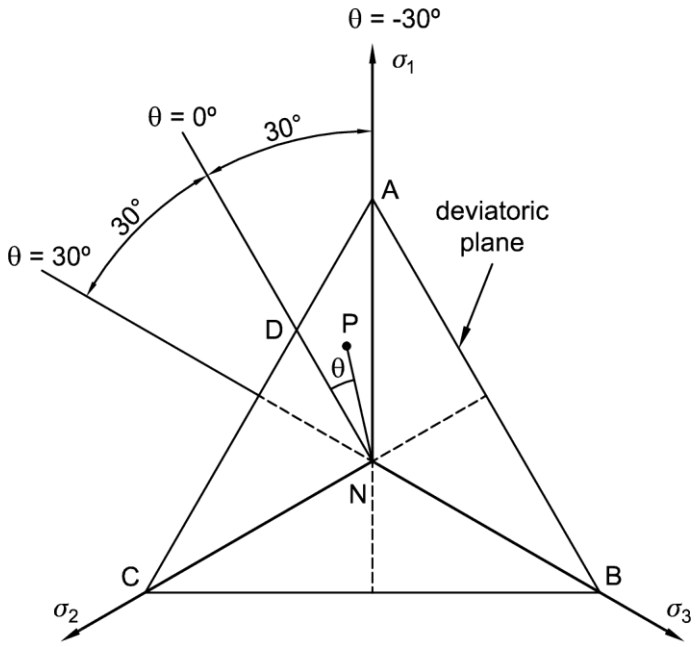

Fig. A.2 – Principal stress space: deviatoric plane view

Total and effective stress

The principle of effective stress states that, for a saturated soil, deformation is controlled by the effective stress rather than the total stress tensor. This principle is considered axiomatic in all the models presented in this dissertation, which are conceived for saturated soils.

Given a total stress tensor $\boldsymbol{\sigma}$ and a pore water pressure u, the effective stress tensor $\boldsymbol{\sigma}'$ is given by:

$$\boldsymbol{\sigma}' = \boldsymbol{\sigma} - u\mathbf{I} = \left(\sigma_{ij} - u\delta_{ij}\right) \tag{A.59}$$

Pore pressure only affects normal stress and not the shear stress. Thus, the distinction between total and effective stress only affects the isotropic part of the stress tensor and his related quantities and will not affect the deviatoric part:

$$p' = \frac{1}{3}\sigma'_{ii} \tag{A.60}$$

$$\eta' = q/p' \tag{A.61}$$

The values of $\mathbf{s}$, q, and θ, remain the same and are never written with the prime symbol.

Stress tensor in axisymmetric conditions

One particular state of stress is called axisymmetric condition. In this configuration of stress, two principal stresses are equal (usually $\sigma'_1 > \sigma'_2 = \sigma'_3$). This is the case of triaxial tests and oedometer tests; thus, this state is very important in laboratory practice. In these tests, σ'_1 is commonly identified withc the stress in the vertical direction and it is also noted as σ'_a (referring to the axis of a cylindrical specimen). The two equal horizontal stress components σ'_2 and σ'_3 are noted as σ'_r. In the principal stress

space, axisymmetric conditions identify a plane containing the axis σ_1' and the space diagonal (Fig. A.3). Lode's angle is constant (θ = -30º) and the stress state is determined by the two variable p' and q, which assume the following form:

$$p' = \frac{\sigma_1' + 2\sigma_3'}{3} = \frac{\sigma_a' + 2\sigma_r'}{3} \tag{A.62}$$

$$q = \sigma_1' - \sigma_3' = \sigma_a' - \sigma_r' \tag{A.63}$$

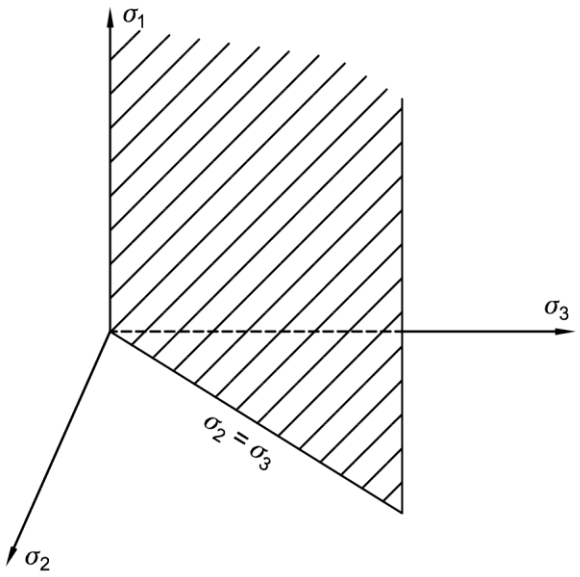

Fig. A.3 – Axisymmetric plane

Stress state and stress path can be represented in the (p', q) plane instead of a three dimensional space.

The deviatoric stress tensor becomes:

STRAIN TENSOR

The infinitesimal strain tensor is usually expressed in engineering notation as follows:

$$\boldsymbol{\varepsilon} = (\varepsilon_{ij}) = \begin{pmatrix} \varepsilon_{11} & \varepsilon_{12} & \varepsilon_{13} \\ \varepsilon_{21} & \varepsilon_{22} & \varepsilon_{23} \\ \varepsilon_{31} & \varepsilon_{32} & \varepsilon_{33} \end{pmatrix} = \begin{pmatrix} \varepsilon_x & \frac{1}{2}\gamma_{xy} & \frac{1}{2}\gamma_{xz} \\ \frac{1}{2}\gamma_{yx} & \varepsilon_y & \frac{1}{2}\gamma_{yz} \\ \frac{1}{2}\gamma_{zx} & \frac{1}{2}\gamma_{zy} & \varepsilon_z \end{pmatrix} \tag{A.64}$$

where the components denoted with ε are normal strains and those indicated with γ are shear strains. The first are associated to a change of size of the element and the second to a change in shape (i.e. angular strain). All the considerations made for the stress tensor can be extended to the strain tensor. The isotropic part of the strain is linked to the volume change:

$$\boldsymbol{\varepsilon}_{\mathrm{v}} = \begin{pmatrix} \varepsilon_v & 0 & 0 \\ 0 & \varepsilon_v & 0 \\ 0 & 0 & \varepsilon_v \end{pmatrix} \tag{A.65}$$

where ε_v is the volumetric strain:

$$\varepsilon_v = \varepsilon_{ii} = \varepsilon_x + \varepsilon_y + \varepsilon_z \tag{A.66}$$

which corresponds to the first invariant of the strain tensor. The deviatoric component of the tensor (strain deviator tensor) is:

$$\mathbf{e} = \left(\varepsilon_{ij} - \frac{1}{3}\varepsilon_v \delta_{ij}\right) = \begin{pmatrix} \varepsilon_x - \frac{\varepsilon_v}{3} & \frac{1}{2}\gamma_{xy} & \frac{1}{2}\gamma_{xz} \\ \frac{1}{2}\gamma_{yx} & \varepsilon_y - \frac{\varepsilon_v}{3} & \frac{1}{2}\gamma_{yz} \\ \frac{1}{2}\gamma_{zx} & \frac{1}{2}\gamma_{zy} & \varepsilon_z - \frac{\varepsilon_v}{3} \end{pmatrix} \tag{A.67}$$

Three principal directions and three principal strains ε_1, ε_2, ε_3 exist in each point of the continuum. It can be shown that the principal directions of the strain and stress tensor coincide. Thus, the principal strain space coincides with the principal stress space and the principal axes can be superposed. Strain tensor and strain increment tensor $\dot{\boldsymbol{\varepsilon}}$ reduce to vectors in the principal strain space.

The distortional strain ε_s is proportional to the second invariant of the strain deviator and is equal to

$$\varepsilon_s = \sqrt{\frac{2}{3}\mathbf{e}:\mathbf{e}} = \frac{1}{\sqrt{3}}\sqrt{(\varepsilon_1 - \varepsilon_2)^2 + (\varepsilon_2 - \varepsilon_3)^2 + (\varepsilon_3 - \varepsilon_1)^2} \tag{A.68}$$

In axisymmetric conditions ($\varepsilon_1 = \varepsilon_a$; $\varepsilon_2 = \varepsilon_3 = \varepsilon_r$) the two components of strain become:

$$\varepsilon_v = \varepsilon_1 + 2\varepsilon_3 = \varepsilon_a + 2\varepsilon_r \tag{A.69}$$

$$\varepsilon_s = \frac{2}{3}(\varepsilon_1 - \varepsilon_3) = \frac{2}{3}(\varepsilon_a - \varepsilon_r) \tag{A.70}$$

As stated before, volumetric strain increment is the effect of the application of the isotropic part of the stress p' and distortional strain is the effect of the deviatoric component q. Thus, the elementary work done by the effective stress in changing the volume and shape of a unit element of soil is:

$$\dot{W} = \sigma_1'\dot{\varepsilon}_1 + \sigma_2'\dot{\varepsilon}_2 + \sigma_3'\dot{\varepsilon}_3 = p'\dot{\varepsilon}_v + q\dot{\varepsilon}_s \tag{A.71}$$

In this relation, each addendum is composed by the product of a stress and a strain factor that are said to be work conjugate.

Elasto-plastic constitutive relations

Constitutive relations establish a dependency between the stress and strain tensors that depends on the nature of the material. The behaviour of any material is very complex and particularly that of a soil. For this reason, any constitutive law has a validity restrained to a particular phase of the loading process and under particular hypotheses.

ELASTIC MODEL

This model is the simplest one and proposes a relationship between stress and strain increments in which only elastic (reversible) strain is produced:

$$\dot{\boldsymbol{\sigma}}' = \mathbf{D}:\dot{\boldsymbol{\varepsilon}} = \left(\dot{\sigma}_{ij}'\right) = \left(D_{ijhk}\dot{\varepsilon}_{hk}\right) \tag{A.72}$$

D is the fourth-order stiffness tensor, constituted by 81 elements. Because of the symmetry of the stress and strain tensors, only 21 elements are independent. In the case of an isotropic material, the independent

elements are two: Young's modulus, E, and Poisson's ratio, ν. Equation (A.72) can be inverted obtaining:

$$\dot{\boldsymbol{\varepsilon}} = \mathbf{C}\colon \dot{\boldsymbol{\sigma}}' \tag{A.73}$$

where $\mathbf{C}$ is the compliance tensor, which is the inverse of stiffness tensor. In the principal stress space, $\mathbf{D}$ and $\mathbf{C}$ reduce to second-order tensors.

Elastic models are linear if the stiffness and compliance tensors are constant; otherwise, they are non-linear. In this case, the tensors can be functions of the state of stress and/or strain.

Young's modulus and Poisson's ratio can be converted in two different moduli that have a great importance in soil mechanics. These are the effective bulk modulus K' and the shear modulus G:

$$K' = \frac{E}{3(1-2\nu)} \tag{A.74}$$

$$G = \frac{E}{2(1+\nu)} \tag{A.75}$$

These moduli allow linking the stress and strain in their volumetric and deviatoric components in a decoupled response described as follows:

$$\dot{p}' = K'\dot{\varepsilon}_v \tag{A.76}$$

$$\dot{q} = 3G\dot{\varepsilon}_s \tag{A.77}$$

Many soils are not isotropic materials as they present an initial anisotropy due to the sedimentary process and stress history. Since many soils are deposited over areas of large lateral extent and the symmetry of deposition is essentially vertical, they present a horizontal isotropic plane and a vertical axis of symmetry. This is called transverse isotropy or cross anisotropy and the stiffness tensor is fully described by 5 independent elastic moduli: E_v and E_h are Young's moduli in the vertical and horizontal directions, respectively; G_{vh} is the shear modulus in a vertical plane. Poisson's ratios ν_{hh} and ν_{vh} relate to the lateral strains that occur in the horizontal direction orthogonal to a horizontal direction of compression and a vertical direction of compression, respectively.

ELASTIC-HARDENING PLASTIC MODELS

The elastic model is only valid until the stress state reaches a threshold above which strain is not entirely recovered and an irrecoverable (plastic) part of it remains when the stress causing it is removed.

The simplest model to describe plasticity is the elastic-perfectly plastic model, in which the stiffness is constant throughout the elastic phase and steadily falls to zero when the plastic threshold is reached, while the stress level remains constant. Indefinite plastic strains will develop after this point, thus the incipient plasticization coincide with failure. An example of this model is Mohr-Coulomb model.

In an elasto-plastic model with hardening plasticity, a plastic strain increment is associated to a positive or negative variation of the stress, which corresponds to positive hardening or negative hardening (softening), respectively.

In such models, the material shows an elastic behaviour until a boundary (yield surface) is reached in the stress space. After this threshold is reached, elastic and plastic strains develop simultaneously and the stress varies. This hardening process is governed by the hardening modulus (H), which links the stress increment with the plastic component of the strain increment. Upon unloading, soil response is

purely elastic, indicating an expansion of the yield domain. If the strain level is increased indefinitely, elastic and plastic strain will continue to develop until constant stress is reached (H = 0).

The structure of an elastic-hardening plastic model is constituted by four main features:

- Elastic behaviour: When behaviour of the soil is fully elastic, the constitutive relation is the same seen in the precedent section:

$$\dot{\boldsymbol{\sigma}}' = \mathbf{D}^e : \dot{\boldsymbol{\varepsilon}}^e \tag{A.78}$$

  with the superscript e specifying that the stiffness matrix refers to the elastic moduli and that the strain tensor refers to elastic deformations;
- Yield criterion: this criterion defines a boundary surface (yield surface) in the stress space that represents the limit between the elastic region and elastic-plastic behaviour;
- Flow rule: it describes the increment of plastic deformation through the definition of a plastic potential;
- Hardening rule: The hardening rule links the change in size of the yield surface with the magnitude of the plastic strain and hence provides a link between the yield surface and the flow rule expressions.

Yield surface or yield locus (f) is a closed domain in the stress space. The behaviour of the material is elastic if the stress state $\boldsymbol{\sigma}'$ lies inside this domain:

$$f(\boldsymbol{\sigma}', \boldsymbol{h}) \leq 0 \tag{A.79}$$

The yield surface is usually defined in the principal stress space, since it can be represented as a geometric closed surface in a Euclidian space. In axisymmetric conditions, it is usually defined in the (p', q) plane as a closed curve. In this expression, $\boldsymbol{h}$ is a vector containing n constitutive parameters The determination of these parameters, as well as the determination of function f, can be obtained through experimental results and/or theoretical considerations. Parameters $\boldsymbol{h}$ are called hidden variables, since they do not appear explicitly in the equilibrium equations linking the internal stress and the external loads. They are also called hardening parameters as they govern the hardening process.

When plastic strain occurs (i.e. when yield is reached), the surface can evolve in two ways: it can expand without changing its shape or it can move rigidly. The first case is called isotropic hardening while the second is kinematic hardening.

In strain-hardening models, parameters $\boldsymbol{h}$ depends on the plastic strain $\left(\varepsilon_{rs}^p\right)$:

$$f = f\left(\boldsymbol{\sigma}', \boldsymbol{h}(\varepsilon_{rs}^p)\right) \tag{A.80}$$

In stress-hardening models, they depend on stress.

When the stress state lays on the yield surface (i.e. $f(\boldsymbol{\sigma}', \boldsymbol{h})$ = 0), two situations can occur:

- if the stress increment vector $\dot{\sigma}'$ is directed inwards the yield surface, the stress state comes back into the elastic domain and no plastic deformation occurs;
- if the direction of $\dot{\sigma}'$ is outwards the yield surface, elastic and plastic strains are expected. Constitutive equations are written as:

$$\dot{\boldsymbol{\varepsilon}} = (\dot{\boldsymbol{\varepsilon}}^e + \dot{\boldsymbol{\varepsilon}}^p) = (\mathbf{C}^e + \mathbf{C}^p) : \dot{\boldsymbol{\sigma}}' = \mathbf{C}^{ep} : \dot{\boldsymbol{\sigma}}' \tag{A.81}$$

An elastic-plastic compliance tensor links strain and stress; it is constituted by the usual elastic component and by a plastic component $\mathbf{C}^p$. Experimental evidence shows that the direction of the plastic strain increment depends on the state of stress and not on the stress increment. This means that $\dot{\boldsymbol{\sigma}}'$ influences the magnitude of $\dot{\boldsymbol{\varepsilon}}^p$ but not its direction, which depends on the stress state $\boldsymbol{\sigma}'$ only. Thus, it

is possible to define a scalar function in the stress space called plastic potential $g = g(\boldsymbol{\sigma}')$. The plastic strain increment is related to the gradient of the plastic potential through the following flow rule:

$$\dot{\varepsilon}_{ij}^{p} = \dot{\Lambda}\frac{\partial g}{\partial \sigma_{ij}} \tag{A.82}$$

where $\dot{\Lambda}$ is a scalar non-negative parameter called plastic multiplier. This relation implies that the vector of plastic strain increment is always normal to the surface defined by the plastic potential function and directed outwards it.

Prager's consistency condition (1949) states that the stress state remains on the yield surface when plastic strains are generated. If the stress state were outside the yield surface, there would be plastic strains also in the unloading phase. This rule is expressed mathematically by the condition that the total differential of f is equal to zero:

$$df = \frac{\partial f}{\partial \sigma_{ij}}\dot{\sigma}_{ij} + \frac{\partial f}{\partial h_k}\frac{\partial h_k}{\partial \varepsilon_{rs}^{p}}\dot{\varepsilon}_{rs}^{p} = 0 \tag{A.83}$$

Combining relations (A.82) and (A.83), it is possible to determine the plastic multiplier $\dot{\Lambda}$:

$$\dot{\Lambda} = \frac{1}{H}\frac{\partial f}{\partial \sigma_{ij}}\dot{\sigma}_{ij} \tag{A.84}$$

Where:

$$H = -\frac{\partial f}{\partial h_k}\frac{\partial h_k}{\partial \varepsilon_{rs}^{p}}\frac{\partial g}{\partial \sigma_{rs}} \tag{A.85}$$

is the hardening modulus. Finally, $\dot{\boldsymbol{\varepsilon}}^{p}$ is determined:

$$\dot{\varepsilon}_{rs}^{p} = \frac{1}{H}\frac{\partial g}{\partial \sigma_{rs}}\frac{\partial f}{\partial \sigma_{ij}}\dot{\sigma}_{ij} \tag{A.86}$$

By comparing this relation with (A.81), the tensor of plastic compliance is:

$$C_{rsij}^{p} = \frac{1}{H}\frac{\partial g}{\partial \sigma_{rs}}\frac{\partial f}{\partial \sigma_{ij}} \tag{A.87}$$

The same procedure is valid if the constitutive relations are expressed in terms of the stiffness tensor:

$$\dot{\boldsymbol{\sigma}}' = \mathbf{D}^{ep} : \dot{\boldsymbol{\varepsilon}} \tag{A.88}$$

Where $\mathbf{D}^{ep}$ is the elasto-plastic stiffness tensor. This tensor can be determined by rewriting the above expression as follows:

$$\dot{\boldsymbol{\sigma}}' = \mathbf{D}^{e} : \dot{\boldsymbol{\varepsilon}}^{e} = \mathbf{D}^{e} : (\dot{\boldsymbol{\varepsilon}} - \dot{\boldsymbol{\varepsilon}}^{p}) = \mathbf{D}^{e} : \left(\dot{\boldsymbol{\varepsilon}} - \dot{\Lambda}\frac{\partial g}{\partial \boldsymbol{\sigma}'}\right) \tag{A.89}$$

Applying consistency condition (A.83), one obtains the plastic multiplier:

$$\dot{\Lambda} = \frac{\frac{\partial f}{\partial \boldsymbol{\sigma}'} : \mathbf{D}^{e} : \dot{\boldsymbol{\varepsilon}}}{H + \frac{\partial f}{\partial \boldsymbol{\sigma}'} : \mathbf{D}^{e} : \frac{\partial g}{\partial \boldsymbol{\sigma}'}} \tag{A.90}$$

and, consequently, the tensor is:

$$\mathbf{D}^{ep} = \mathbf{D}^{e} - \frac{\left(\mathbf{D}^{e} : \frac{\partial g}{\partial \boldsymbol{\sigma}'}\right) \otimes \left(\frac{\partial f}{\partial \boldsymbol{\sigma}'} : \mathbf{D}^{e}\right)}{H + \frac{\partial f}{\partial \boldsymbol{\sigma}'} : \mathbf{D}^{e} : \frac{\partial g}{\partial \boldsymbol{\sigma}'}} \tag{A.91}$$

Where the expression of the hardening modulus is equal to (A.85).

In the principal stress space, the fourth-order tensor reduce to second-order tensors and the second-order tensors reduce to vectors. Thus, in the above expressions, tensor product and Frobenius product can be substituted by the usual scalar product between matrix and vector and between vectors.

In metal plasticity, it is usually assumed the existence of a normality rule that states $g = f$. This means that the yield surface and the plastic potential are coincident. In soil mechanics, this is not true in general but it can be assumed for a particular soil if experimental evidence suggests that the deviation from normality is not very large. In this case, the flow rule is called an associated flow rule; otherwise, it is called non-associated.

ANNEX 2: FIRST DERIVATIVES OF YIELD SURFACE AND PLASTIC POTENTIALS FOR THE MODEL

The first derivatives of yield surface (6.36) are:

$$\begin{cases} \dfrac{\partial f}{\partial p'} = -\dfrac{\bar{n}}{p' - p'_\alpha}\left(\dfrac{|q - q_\alpha|}{M(p' - p'_\alpha)}\right)^{\bar{n}} + \dfrac{1}{(p' - p'_\alpha)\ln r} \\ \dfrac{\partial f}{\partial q} = \dfrac{\bar{n}}{q - q_\alpha}\left(\dfrac{|q - q_\alpha|}{M(p' - p'_\alpha)}\right)^{\bar{n}} \\ \dfrac{\partial f}{\partial p'_0} = -\dfrac{1}{p'_0 \ln r} \\ \dfrac{\partial f}{\partial p'_\alpha} = -\dfrac{\partial f}{\partial p'} \\ \dfrac{\partial f}{\partial q_\alpha} = -\dfrac{\partial f}{\partial q} \end{cases} \tag{A.92}$$

The first derivatives of the plastic potential surface for Rowe's (1962) flow rule (6.29) are:

$$\begin{cases} \dfrac{\partial g}{\partial p'} = 27\,\dfrac{M(p' - p'_\alpha) - |q - q_\alpha|}{[3(p' - p'_\alpha) + 2|q - q_\alpha|][3(p' - p'_\alpha) - |q - q_\alpha|]} \\ \dfrac{\partial g}{\partial q} = 3\,\dfrac{(3M + 9)(p' - p'_\alpha) - 2M|q - q_\alpha|}{[3(p' - p'_\alpha) + 2|q - q_\alpha|][3(p' - p'_\alpha) - |q - q_\alpha|]}\,\mathrm{sgn}(q - q_\alpha) \end{cases} \tag{A.93}$$

The first derivatives of the plastic potential surface for Yu's (2006) flow rule (6.31) are:

$$\begin{cases} \dfrac{\partial g}{\partial p'} = \dfrac{\bar{n}\,(1 - m)}{(p' - p'_\alpha)\left[1 + (m - 1)\left(\dfrac{|q - q_\alpha|}{M(p' - p'_\alpha)}\right)^{n}\right]}\left[\left(\dfrac{|q - q_\alpha|}{M(p' - p'_\alpha)}\right)^{\bar{n}} - 1\right] \\ \dfrac{\partial g}{\partial q} = \dfrac{\bar{n}\,m\,(m - 1)}{|q - q_\alpha|\left[1 + (m - 1)\left(\dfrac{|q - q_\alpha|}{M(p' - p'_\alpha)}\right)^{\bar{n}}\right]}\left(\dfrac{|q - q_\alpha|}{M(p' - p'_\alpha)}\right)^{\bar{n}}\mathrm{sgn}(q - q_\alpha) \end{cases} \tag{A.94}$$

where sgn is the signum function.

These derivatives can be applied to one-surface CASM model by taking $p'_\alpha = q_\alpha = 0$.

ANNEX 3: DERIVATION OF PLASTIC POTENTIALS

In the following annex, the integration process of Rowe (1962) and Yu (2006) flow rules is described. This process leads to the determination of the plastic potential functions in both cases. These expressions are already available in literature (Yu, 2006). Nevertheless, the process of integration led to a better understanding of the relation between the flow rule and the plastic potential that the mere observation of the initial and final equations could not reveal. In particular, the process was performed to answer to the following two questions:

- In Rowe flow rule, the flow rule is defined over the whole stress space. Nevertheless, the plastic potential is only defined for $\eta' < 3$. Why this difference?
- In Yu flow rule, the flow rule is univocally defined for any positive value of parameter m. Nevertheless, the plastic potential behaves differently depending on whether m is less or greater than 1. Additionally, if m = 1, the plastic potential expression reduces to g = 0.

The integration is performed in the hypothesis that the flow rules are centred in the origin of the stress plane, as in CASM flow rule. The results are then extended to the model presented in this thesis, by translating the coordinates from the origin of the stress plane to the apex of the yield surface.

Rowe flow rule

Flow rule is:

$$\frac{\dot{\varepsilon}_v^p}{\dot{\varepsilon}_s^p} = \frac{9(M-\eta')}{9+3M-2M\eta'} \tag{A.95}$$

Where η' is the stress ratio q/p' and M is the slope of the critical state line in the (p', q) plane.

Remembering that the plastic strain increments are related to the first derivatives of the plastic potential $g(p', q)$, the above expression can be rewritten as follows:

$$\frac{\dot{\varepsilon}_v^p}{\dot{\varepsilon}_s^p} = \frac{\partial g(p',q)\big/\partial p'}{\partial g(p',q)\big/\partial q} = \frac{9(M-\eta')}{9+3M-2M\eta'} \tag{A.96}$$

This relation is a partial differential equation, which needs a boundary condition to be fully determined, i.e. a function must be specified on a boundary of the region were the solution is defined. It is convenient to identify the boundary plane with the isotropic plane (i.e. plane (p',0)) since in this plane only volumetric strain occurs and the incremental relation between stress and strain increments is well known:

$$\dot{\varepsilon}_v^p = \frac{\lambda-\kappa}{v_i}\frac{\dot{p}'}{p'} \tag{A.97}$$

Moreover, the usual relation between plastic strain and plastic potential is valid:

$$\frac{\partial \varepsilon_v^p}{\partial \Lambda} = \frac{\partial g}{\partial p'} \tag{A.98}$$

With geometrical consideration, it is easy to demonstrate that in this monodimensional case, the plastic multiplier $\partial\Lambda$ coincides with the increment of the isotropic stress $\partial p'$. Thus, combining the two precedent relations, one obtains:

$$\frac{\partial \varepsilon_v^p}{\partial p'} = \frac{\partial g}{\partial p'} = \frac{\lambda-\kappa}{v_i}\frac{1}{p'} \tag{A.99}$$

And, integrating:

$$g(p',0) = \ln\frac{p'}{\xi} \tag{A.100}$$

Where ξ is an arbitrary constant that regulates the size of the curve.

This condition, combined with equation (A.96), gives a unique solution for the problem.

The right-hand term of equation (A.96) is only dependent on the effective stress ratio η'. Thus, it is convenient to change the variables of the left-hand term from (p', q) to (p', η'). To perform such a change, the new variables shall be written as functions of the old ones and the Jacobian matrix shall be calculated:

$$\begin{cases} p'(p',q) = p' \\ \\ \eta'(p',q) = {}^{q}/_{p'} \end{cases} \tag{A.101}$$

$$\mathbf{J} = \begin{pmatrix} \dfrac{\partial p'}{\partial p'} = 1 & \dfrac{\partial p'}{\partial q} = 0 \\ \\ \dfrac{\partial \eta'}{\partial p'} = -\dfrac{q}{p'^2} & \dfrac{\partial \eta'}{\partial q} = \dfrac{1}{p'} \end{pmatrix} \tag{A.102}$$

Thus, the first derivatives of g can be expressed as functions of the new variables using the chain rule as follows:

$$\begin{gathered} \frac{\partial g(p',q)}{\partial p'} = \frac{\partial g}{\partial p'}\frac{\partial p'}{\partial p'} + \frac{\partial g}{\partial \eta'}\frac{\partial \eta'}{\partial p'} = \frac{\partial g}{\partial p'} - \frac{q}{p'^2}\frac{\partial g}{\partial \eta'} = \frac{\partial g}{\partial p'} - \frac{\eta'}{p'}\frac{\partial g}{\partial \eta'} \\ \\ \frac{\partial g(p',q)}{\partial q} = \frac{\partial g}{\partial p'}\frac{\partial p'}{\partial q} + \frac{\partial g}{\partial \eta'}\frac{\partial \eta'}{\partial q} = \frac{1}{p'}\frac{\partial g}{\partial \eta'} \end{gathered} \tag{A.103}$$

and equation (A.96) becomes:

$$\frac{\dfrac{\partial g}{\partial p'} - \dfrac{\eta'}{p'}\dfrac{\partial g}{\partial \eta'}}{\dfrac{1}{p'}\dfrac{\partial g}{\partial \eta'}} = p'\frac{\dfrac{\partial g}{\partial p'}}{\dfrac{\partial g}{\partial \eta'}} - \eta' = \frac{9(M-\eta')}{9+3M-2M\eta'} \tag{A.104}$$

Rearranging the expression one obtains:

$$\frac{g_{p'}}{g_{\eta'}} = \frac{9(M-\eta')}{p'(9+3M-2M\eta')} + \frac{\eta'}{p'} \tag{A.105}$$

Where $g_{p'}$ and $g_{\eta'}$ are the first derivatives of g in p' and q, respectively. With some algebraic steps, the above expression can be rewritten as:

$$\frac{g_{p'}}{g_{\eta'}} = \frac{-2M(\eta'-3)\left(\eta'+\frac{3}{2}\right)}{p'(9+3M-2M\eta')} \tag{A.106}$$

and finally:

$$p'\frac{(9+3M-2M\eta')}{\left(\eta'+\frac{3}{2}\right)}\,g_{p'} + 2M(\eta'-3)\,g_{\eta'} = 0 \tag{A.107}$$

This expression has the following general form:

$$a(p',\eta')\, g_{p'} + b(p',\eta')\, g_{\eta'} = 0 \tag{A.108}$$

which is a first-order, linear, homogeneous, partial differential equation. This type of equation can be solved with the so-called method of characteristics, which is a well-established mathematical procedure described in numerous works (e.g. Sarra, 2003). This method consists in rewriting the above expression using a new variable t, so that the partial differential equation is transformed into an ordinary differential equation:

$$\frac{\partial g}{\partial t} = \frac{\partial p'}{\partial t}\, g_{p'} + \frac{\partial \eta'}{\partial t}\, g_{\eta'} = a(p',\eta') g_{p'} + b(p',\eta') g_{\eta'} = 0 \tag{A.109}$$

Thus, the partial differential equation is reduced to the following system of ordinary differential equations:

$$\begin{aligned} &I) \quad \frac{\partial p'}{\partial t} = p' \frac{(9 + 3M - 2M\eta')}{\left(\eta' + \frac{3}{2}\right)} \\ &II) \quad \frac{\partial \eta'}{\partial t} = 2M(\eta' - 3) \\ &III) \quad \frac{\partial g}{\partial t} = 0 \end{aligned} \tag{A.110}$$

To solve the system, it is convenient to start by integrating equation II, which is a first-order, linear differential equation only dependent on η'. The solution, obtained with the usual procedure, is:

$$\eta(t) = 3(1 - e^{2Mt}) \tag{A.111}$$

Where the constant of integration was found by setting $\eta(0) = 0$ (Sarra, 2003).

Substituting expression (A.111) into (A.110- I) and separating the variables, one obtains:

$$\frac{dp'}{p'} = 2\, \frac{9 - 3M + 6Me^{2Mt}}{3 - 2e^{2Mt}}\, dt \tag{A.112}$$

and the two terms can be integrated separately. The left-hand term is:

$$\int \frac{dp'}{p'} = \ln \frac{p'}{C} \tag{A.113}$$

Where C is the constant of integration. To integrate the right-hand term, it is convenient to change variable as follows:

$$\begin{aligned} e^{2Mt} &= s \\ dt &= \frac{1}{2Ms}\, ds \end{aligned} \tag{A.114}$$

obtaining:

$$\int 2\, \frac{9 - 3M + 6Me^{2Mt}}{3 - 2e^{2Mt}}\, dt = \frac{1}{M} \int \frac{3 - M + 2Ms}{s(3 - 2s)}\, ds \tag{A.115}$$

Integrating the above expression using partial fraction decomposition method and restoring the precedent variable, one obtains:

$$\frac{1}{M} \int \frac{3 - M + 2Ms}{s(3 - 2s)}\, ds = \frac{3 - M}{3M}\, \ln \left| \frac{e^{2Mt}}{3 - 2e^{2Mt}} \right| - \ln|3 - 2e^{2Mt}| \tag{A.116}$$

It is worth noting that the terms in absolute values appear by solving integrals of the following type:

$$\int \frac{A}{f(x)}dx = A\ \frac{\ln|f(x)|}{\partial f/\partial x} \tag{A.117}$$

Where $f(x)$ is a generic function of the first order and A is a constant.

Combining the solutions obtained in (A.113) and (A.115), equation (A.110- I) results in:

$$p'(t) = C\ \exp\left(\frac{3-M}{3M}\ \ln\left|\frac{e^{2Mt}}{3-2e^{2Mt}}\right| -\ \ln|3-2e^{2Mt}|\right) \tag{A.118}$$

where exp indicates the exponential function. The constant of integration C will be successively determined by substituting in equation (A.110- III). Before solving the third equation, one must join equations I and II in order to eliminate variable t, which is no longer needed. From equation (A.111) one obtains:

$$e^{2Mt} = 1 - \frac{\eta'}{3} \tag{A.119}$$

Substituting this result in expression (A.118), one obtains the expression of p' as a function of η':

$$p' = C\ \exp\left(\frac{3-M}{3M}\ \ln\left|\frac{1-\frac{\eta'}{3}}{3-2\left(1-\frac{\eta'}{3}\right)}\right| -\ \ln\left|3-2\left(1-\frac{\eta'}{3}\right)\right|\right) \tag{A.120}$$

The solution of equation (A.110- III) is a generic term independent from t. To determine this constant, the method of characteristics (Sarra, 2003) prescribes the substitution of constant C from (A.120) in the boundary condition (A.100):

$$g(t) = g(C,0) = \ln\frac{C}{\xi} \tag{A.121}$$

Isolating constant C in (A.120), substituting into (A.121), and rearranging the terms, one obtains the expression of plastic potential g as a function of p' and η':

$$g(p',\eta') = 3M\ \ln\frac{p'}{\xi} - (3-M)\ \ln|3-\eta'| + (3+2M)\ \ln|2\eta'+3| \tag{A.122}$$

Fig. A.4 shows this family of curves in the stress plane $(p'-q)$. A discontinuity is observed for η' = 3 (red line) that separates two different domains with two different families of curves.

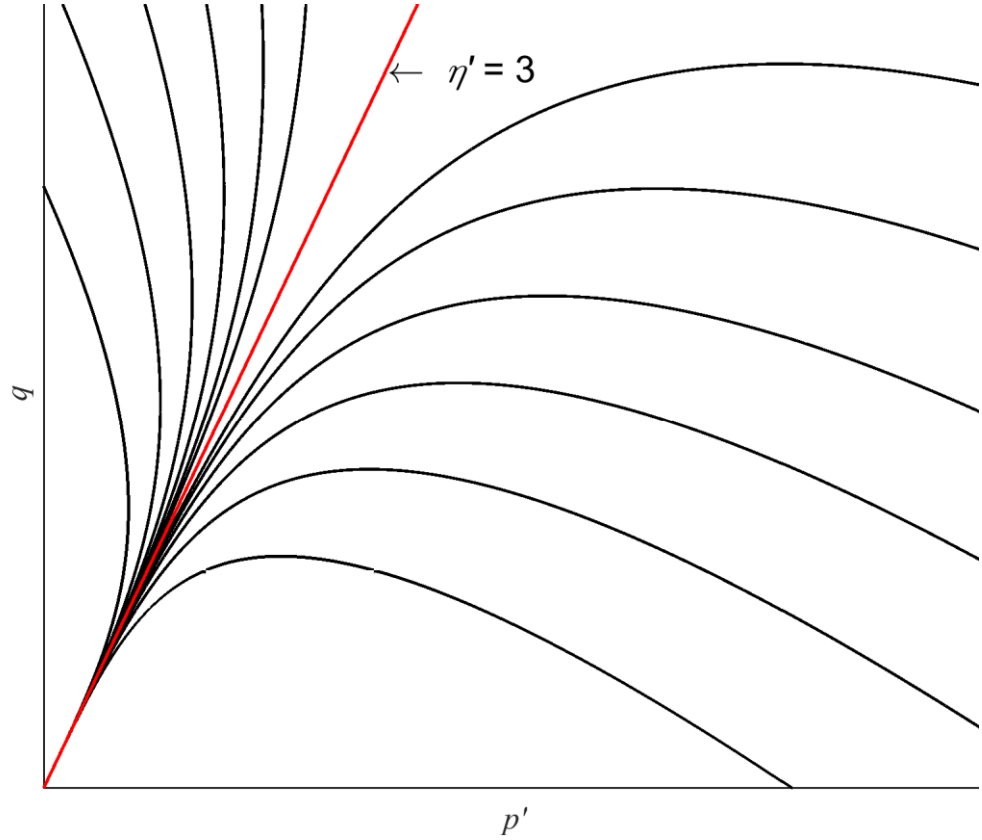

Fig. A.4 – Plastic potential curves derived from Rowe flow rule

This can cause numerical problems when the stress path crosses the discontinuity, because the plastic potential is not defined for $\eta' = 3$. Moreover, plastic potential surface is supposed to be continuous and convex. Thus, when Rowe flow rule is used, it is necessary to prescribe the condition:

$$\eta' < 3 \tag{A.123}$$

This is equivalent to rewrite expression (A.122) as follows:

$$g(p', \eta') = 3M \ln\frac{p'}{\xi} - (3 - M)\ln(3 - \eta') + (3 + 2M)\ln(2\eta' + 3) \tag{A.124}$$

which is the expression usually reported in literature (e.g. Yu, 2006). This expression implies that the effective stress ratio is less than 3, otherwise the plastic potential is not defined. This condition is always respected when conventional monotonic compression triaxial tests with constant confinement are considered and a single-surface model is adopted. In such case, the condition is always satisfied. In the case of the model presented in this thesis, the coordinates shall be centred in the yield surface apex (p'_α, q_α):

$$g = 3M \ln\frac{p' - p'_\alpha}{\xi} + (3 + 2M)\ln(2|\eta'_\alpha| + 3) - (3 - M)\ln(3 - |\eta'_\alpha|) \tag{A.125}$$

Where η'_α is the effective stress ratio referred to the apex of the yield surface. In this case, the condition of existence becomes:

$$|\eta'_\alpha| < 3 \tag{A.126}$$

The condition is represented in Fig. 6.3, along with the plastic potential curves. It is evident that the limit value can be exceeded, especially during the unloading phase in a low-confined drained test. Thus, in the application of the model, this condition must be checked throughout the test.

Yu flow rule

Flow rule is:

$$\frac{\dot{\varepsilon}_v^p}{\dot{\varepsilon}_s^p} = \frac{M^{\bar{n}} - \eta'^{\bar{n}}}{m\,\eta'^{\bar{n}-1}} \tag{A.127}$$

As in the precedent case, the boundary condition (A.100) is considered. Operating the same change in variables (expressions (A.101) and (A.102)), one obtains:

$$mp'g_{p'} - \frac{M^{\bar{n}} + (m-1)\eta'^{\bar{n}}}{\eta'^{\bar{n}-1}}\, g_{\eta'} = 0 \tag{A.128}$$

Using the method of characteristics, the equation is transformed into the following system of ordinary differential equations:

$$\begin{aligned} I)\ & \begin{cases} \dfrac{\partial p'}{\partial t} = mp' \end{cases} \\ II)\ & \begin{cases} \dfrac{\partial \eta'}{\partial t} = -\dfrac{M^{\bar{n}} + (m-1)\eta'^{\bar{n}}}{\eta'^{\bar{n}-1}} \end{cases} \\ III)\ & \begin{cases} \dfrac{\partial g}{\partial t} = 0 \end{cases} \end{aligned} \tag{A.129}$$

In this case, the solution depends on the value of parameter m. In fact, two different solutions are found for $m = 1$ and $m \neq 1$.

SOLUTION FOR m = 1

Solution of equation I is:

$$p'(t) = C\, e^t \tag{A.130}$$

Equation II reduces to:

$$\frac{\partial \eta'}{\partial t} = -\frac{M^{\bar{n}}}{\eta'^{\bar{n}-1}} \tag{A.131}$$

Which can be solved separating the variables and imposing $\eta'(0) = 0$:

$$\eta'(t) = M\,(-\bar{n}t)^{1/\bar{n}} \tag{A.132}$$

Isolating variable t from this equation and substituting in (A.130):

$$p' = C \exp\left[-\frac{1}{\bar{n}}\left(\frac{\eta'}{M}\right)^{\bar{n}}\right] \tag{A.133}$$

Finally, isolating constant C and substituting in (A.121):

$$g(p', \eta') = \ln\frac{p'}{\xi} + \frac{1}{\bar{n}}\left(\frac{\eta'}{M}\right)^{\bar{n}} \tag{A.134}$$

SOLUTION FOR $m \neq 1$

Solution of equation I is:

$$p'(t) = C\, e^{mt} \tag{A.135}$$

Equation II can be rewritten as:

$$\frac{\partial \eta'}{\partial t} = -(M^{\bar{n}}\, \eta'^{1-\bar{n}} + (m-1)\, \eta') \tag{A.136}$$

This is a Bernoulli differential equation, whose solution strategy is well established. Setting also in this case $\eta'(0) = 0$ and solving one obtains:

$$\eta'(t) = M \sqrt[\bar{n}]{\frac{1}{m-1}\left[\exp(-\bar{n}(m-1)t) - 1\right]} \tag{A.137}$$

Following the usual procedure, equations (A.135) and (A.137) are combined:

$$p'(t) = C \left[(m-1)\left(\frac{\eta'}{M}\right)^{\bar{n}} + 1\right]^{-\frac{m}{\bar{n}(m-1)}} \tag{A.138}$$

and the plastic potential function is obtained:

$$g(p', \eta') = \ln\frac{p'}{\xi} + \frac{m}{\bar{n}(m-1)} \ln\left[1 + (m-1)\left(\frac{\eta'}{M}\right)^{\bar{n}}\right] \tag{A.139}$$

Rearranging the terms, the following equivalent expression is obtained:

$$g(p', \eta') = \bar{n}(m-1) \ln\frac{p'}{\xi} + m \ln\left[1 + (m-1)\left(\frac{\eta'}{M}\right)^{\bar{n}}\right] \tag{A.140}$$

Although the expression is reported in this last form by the author (Yu, 2006), it is preferable to use expression (A.139). In fact, the first derivatives $\partial g/\partial p'$ and $\partial g/\partial \eta'$ calculated using expression (A.140) (corresponding to the direction of the plastic strain increment vector) change whether is $m < 1$ or $m > 1$. Using expression (A.139), the derivatives do not depend on m. Additionally, these expressions are equal to the derivatives calculated in the precedent case ($m = 1$) (expression (A.134)). Thus, expression (A.139) has a more general validity.

DOMAIN OF EXISTENCE

The domain of validity of the flow rule is determined by the condition that the argument of the logarithm must be positive. Two cases are outlined, depending on the value of parameter m. If $m > 1$, the argument of the logarithm is positive for any value of p'. Plotting a family of plastic potential curves (Fig. A.5), one can see that in this case the curves are defined on the entire stress plane without discontinuities. This characteristic makes Yu flow rule with $m > 1$ very suitable to be applied in a kinematic hardening model, were the effective stress ratio referred to the apex of the yield surface can be very high. The same domain is valid for $m = 1$: in this case equation (A.134) applies, which is defined in the whole stress space.

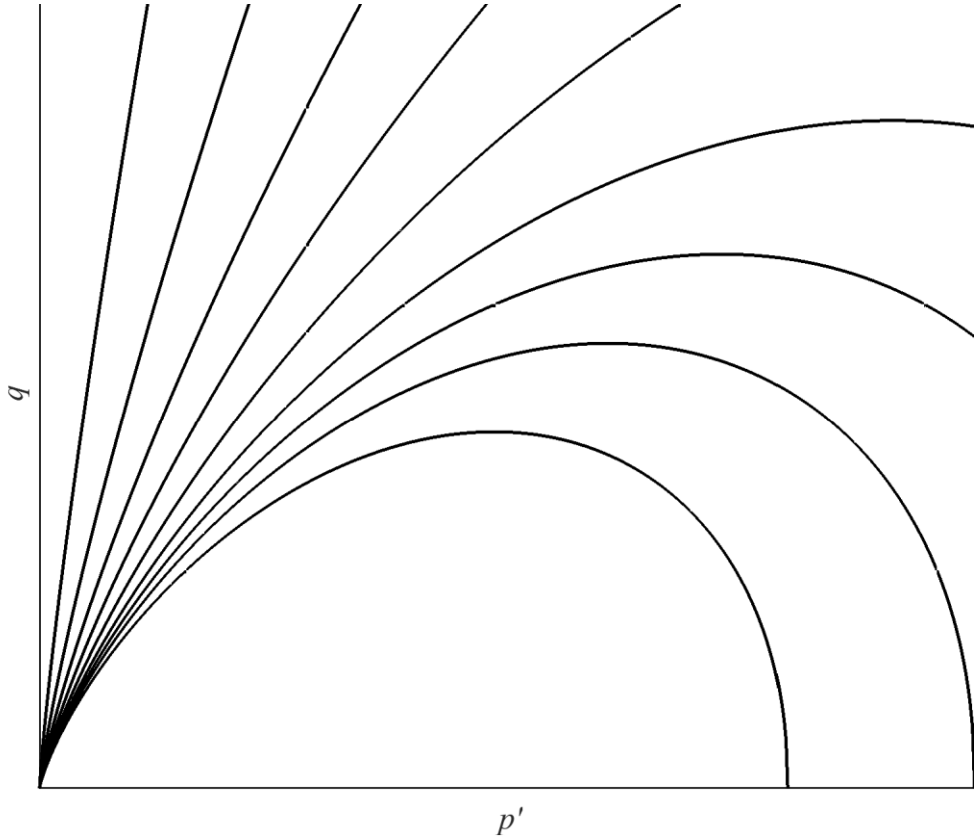

Fig. A.5 – Plastic potential curves derived from Yu flow rule ($m \geq 1$)

If $m < 1$, the condition of positivity of the argument of the logarithmic leads to the following condition:

$$\eta' < M \sqrt[\bar{n}]{\frac{1}{1-m}} \tag{A.141}$$

This condition corresponds to a straight line in the $(p' - q)$ stress plane that shall not be crossed (Fig. A.6). The inclination of this limit line decreases (i.e. the domain of definition restrains) for decreasing values of the parameter m.

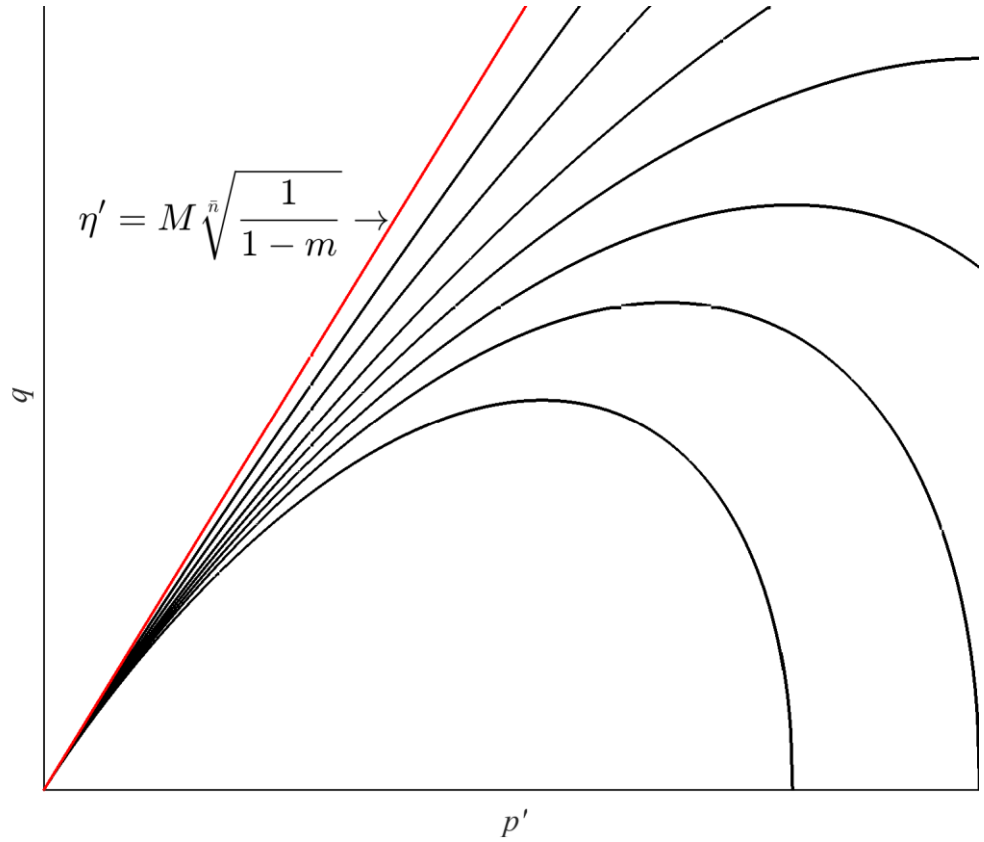

Fig. A.6 – Plastic potential curves derived from Yu flow rule ($m < 1$)

The condition of existence must be verified at any time during its application. In the case of the kinematically hardening formulation, the condition is referred to the apex of the yield surface and it is mirrored about the horizontal axis of the surface:

$$|\eta'_\alpha| < M\sqrt[\bar{n}]{\frac{1}{1-m}} \tag{A.142}$$

The condition and the potential surfaces are plotted in Fig. 6.5.

ANNEX 4: ANALYTICAL SOLUTIONS FOR SIMPLIFIED CONDITIONS

Solutions for purely kinematic hardening

ISOTROPIC LOADING

This case refers to the configuration in Fig. 6.10. Since the isotropic modulus is nil, surface size p_0' is a constant. An associative flow rule is considered in this case for simplicity.

The first derivatives of yield surface f (relations (A.92)) calculated in the isotropic yielding point Y = (p', 0) are:

$$\begin{cases} \left(\dfrac{\partial f}{\partial p'}\right)_{\mathrm{Y}} = \dfrac{1}{(p' - p'_\alpha)\ln r} \\ \left(\dfrac{\partial f}{\partial q}\right)_{\mathrm{Y}} = 0 \\ \left(\dfrac{\partial f}{\partial p'_0}\right)_{\mathrm{Y}} = -\dfrac{1}{p'_0 \ln r} \end{cases} \tag{A.143}$$

Substituting the coordinated of yielding point Y in the expression of the yield surface (6.2), and in the hypothesis that $q_\alpha = 0$ (apex of the yield surface is on the p' axis), one obtains:

$$p' - p'_\alpha = R p'_0 \tag{A.144}$$

which allows to rewrite the first of the (A.143) as a constant:

$$\left(\frac{\partial f}{\partial p'}\right)_{\mathrm{Y}} = \frac{1}{R p'_0 \ln r} \tag{A.145}$$

Vector $\boldsymbol{\beta}$ joining the yielding point with the conjugate point of the reference surface is:

$$\boldsymbol{\beta} = \begin{pmatrix} p'_0 - p' \\ 0 \end{pmatrix} \tag{A.146}$$

The normalized outward normal $\left(\boldsymbol{n_f}/\|\boldsymbol{n_f}\|\right)$ in the yielding point is (1, 0). The scalar product between the two vectors gives the scalar b:

$$b = p'_0 - p' \tag{A.147}$$

It is now possible to calculate the kinematic hardening modulus H' by substituting expressions (A.147) and (6.18) into (6.13):

$$H' = \frac{v_i}{\lambda - \kappa}\left(B\,\frac{p'_0 - p'}{b_{max}}\right)^{\psi} p_0'^{3} \tag{A.148}$$

In the above expression, the only variable term is p'. Since H_0 is nil, H' represents the total hardening modulus H. Substituting expressions (A.145) and (A.148) in the first of the (6.23) and remembering that $g = f$, one obtains:

$$\dot{\varepsilon}_v^p = \frac{1}{H'}\left(\frac{\partial f}{\partial p'}\right)_{\mathrm{Y}}^2 \dot{p}' = \frac{\lambda - \kappa}{v_i}\,\frac{(b_{max})^{\psi}}{B^{\psi} R^2 {p'_0}^5 (\ln r)^2}\,(p'_0 - p')^{-\psi}\,\dot{p}' \tag{A.149}$$

The integration of the above expression between the initial and final points of the stress path follows two different methods depending on the value of exponent ψ. If ψ = 1, the equation reduces to:

$$\int_A^B \dot{\varepsilon}_v^p = \frac{\lambda-\kappa}{v_i}\,\frac{b_{max}}{B^\psi R^2 {p'_0}^5\,(\ln r)^2}\int_{p'_{min}}^{p'_{max}}\frac{\dot{p}'}{(p'_0-p')} \tag{A.150}$$

resulting in:

$$\Delta\varepsilon_{vAB}^p = -\frac{\lambda-\kappa}{v_i}\,\frac{b_{max}}{BR^2 {p'_0}^5\,(\ln r)^2}\ln\frac{p'_0-p'_{max}}{p'_0-p'_{min}} \tag{A.151}$$

If $\psi \neq 1$, it is:

$$\int_A^B \dot{\varepsilon}_v^p = \frac{\lambda-\kappa}{v_i}\,\frac{(b_{max})^\psi}{B^\psi R^2 {p'_0}^5\,(\ln r)^2}\int_{p'_{min}}^{p'_{max}}(p'_0-p')^{-\psi}\,\dot{p}' \tag{A.152}$$

resulting in an exponential relation:

$$\Delta\varepsilon_{vAB}^p = -\frac{\lambda-\kappa}{v_i}\,\frac{(b_{max})^\psi}{B^\psi R^2 {p'_0}^5\,(\ln r)^2(1-\psi)}\left[(p'_0-p'_{max})^{1-\psi}-(p'_0-p'_{min})^{1-\psi}\right] \tag{A.153}$$

Total volumetric strain is obtained adding elastic and plastic volumetric strain:

$$\Delta\varepsilon_{vAB} = \Delta\varepsilon_{vAB}^e + \Delta\varepsilon_{vAB}^p \tag{A.154}$$

Elastic strain is determined through the usual relation:

$$\Delta\varepsilon_{vAB}^e = \frac{1}{K'}\,(p'_{max}-p'_{min}) \tag{A.155}$$

CONSTANT P' STRESS PATH

The configuration of this case is reported in Fig. 6.12. Rowe flow rule is adopted.

The coordinates of the yielding point Y_{load} at a given stress state during loading are calculated by imposing that the first derivative of the yield surface in p' is nil (first of the (A.92)): $(\partial f/\partial p')_{Y_{load}} = 0$. Combining this condition with the expression of the yield surface ($f = 0$), it results:

$$\begin{cases} p'_{Y_{load}} = p'_\alpha + \dfrac{R\,p'_0}{\sqrt[\bar{n}]{\exp(1)}} \\ q_{Y_{load}} = q_\alpha + \dfrac{MR\,p'_0}{\sqrt[\bar{n}]{\exp(1)\,\bar{n}\ln r}} \end{cases} \tag{A.156}$$

During unloading, yielding point is point Y_{unl}. Using the condition on the derivative and the yield surface, the coordinates are determined:

$$\begin{cases} p'_{Y_{unl}} = p'_\alpha + \dfrac{R\,p'_0}{\sqrt[\bar{n}]{\exp(1)}} \\ q_{Y_{unl}} = q_\alpha - \dfrac{MR\,p'_0}{\sqrt[\bar{n}]{\exp(1)\,\bar{n}\ln r}} \end{cases} \tag{A.157}$$

The first derivatives of f calculated these points are:

$$\begin{cases} \left(\frac{\partial f}{\partial p'}\right)_{\mathrm{Y}_{load}} = \left(\frac{\partial f}{\partial p'}\right)_{\mathrm{Y}_{unl}} = 0 \\ \left(\frac{\partial f}{\partial q}\right)_{\mathrm{Y}_{load}} = -\left(\frac{\partial f}{\partial q}\right)_{\mathrm{Y}_{unl}} = \frac{\sqrt[\bar{n}]{\exp(1)\,\bar{n}\ln r}}{MR\,p'_0\ln r} \\ \left(\frac{\partial f}{\partial p'_0}\right)_{\mathrm{Y}_{load}} = \left(\frac{\partial f}{\partial p'_0}\right)_{\mathrm{Y}_{unl}} = -\frac{1}{p'_0\ln r} \end{cases} \tag{A.158}$$

The first derivatives of plastic potential g in the same points are:

$$\begin{cases} \left(\frac{\partial g}{\partial p'}\right)_{\mathrm{Y}_{load}} = \left(\frac{\partial g}{\partial p'}\right)_{\mathrm{Y}_{unl}} = \frac{27}{Rp'_0}\,\frac{M\sqrt[\bar{n}]{\exp(1)\,\bar{n}\ln r}\,(\sqrt[\bar{n}]{\bar{n}\ln r}-1)}{\left[3\sqrt[\bar{n}]{\bar{n}\ln r}+2M\right]\left[3\sqrt[\bar{n}]{\bar{n}\ln r}-M\right]} \\ \left(\frac{\partial g}{\partial q}\right)_{\mathrm{Y}_{load}} = -\left(\frac{\partial g}{\partial q}\right)_{\mathrm{Y}_{unl}} = \frac{3}{Rp'_0}\,\frac{\sqrt[\bar{n}]{\exp(1)\,\bar{n}\ln r}\left[(3M+9)\sqrt[\bar{n}]{\bar{n}\ln r}-2M^2\right)\right]}{\left[3\sqrt[\bar{n}]{\bar{n}\ln r}+2M\right]\left[3\sqrt[\bar{n}]{\bar{n}\ln r}-M\right]} \end{cases} \tag{A.159}$$

All the derivatives are constant quantities.

Vector $\boldsymbol{\beta}$ joining yielding point and the conjugate point of the outer surface is:

$$\boldsymbol{\beta_{load}} = \begin{pmatrix} 0 \\ \frac{M\,p'_0}{\sqrt[\bar{n}]{\exp(1)\,\bar{n}\ln r}} - q \end{pmatrix} \tag{A.160}$$

during loading and

$$\boldsymbol{\beta_{unl}} = \begin{pmatrix} 0 \\ -\frac{M\,p'_0}{\sqrt[\bar{n}]{\exp(1)\,\bar{n}\ln r}} - q \end{pmatrix} \tag{A.161}$$

during unloading. The normalized outward normal $\left(\boldsymbol{n_f}/\left\|\boldsymbol{n_f}\right\|\right)$ is (0, ±1) during loading and unloading, respectively. The scalar product between the two vectors gives the scalar b during loading and unloading:

$$\underset{unl}{b_{load}} = \frac{M\,p'_0}{\sqrt[\bar{n}]{\exp(1)\,\bar{n}\ln r}} \mp q \tag{A.162}$$

It is now possible to calculate kinematic hardening modulus H' by substituting expressions (A.162) and (6.18) into (6.13):

$$H'_{\underset{unl}{load}} = \frac{v_i}{\lambda-\kappa}\left[\frac{B}{b_{max}}\left(\frac{M\,p'_0}{\sqrt[\bar{n}]{\exp(1)\,\bar{n}\ln r}} \mp q\right)\right]^{\psi} p_0'^3 \tag{A.163}$$

where the only variable term is q. Substituting expressions (A.158), (A.159), and (A.163) in the (6.23), one obtains the volumetric plastic strain:

$$\dot{\varepsilon}^p_{v\ \underset{unl}{load}} = \frac{1}{H'_{\underset{unload}{load}}}\left(\frac{\partial g}{\partial p'}\right)_{\underset{\mathrm{Y}_{unl}}{\mathrm{Y}_{load}}}\left(\frac{\partial f}{\partial q}\right)_{\underset{\mathrm{Y}_{unl}}{\mathrm{Y}_{load}}}\dot{q} = \pm K_p\left(\frac{M\,p'_0}{\sqrt[\bar{n}]{\exp(1)\,\bar{n}\ln r}} \mp q\right)^{-\psi}\dot{q} \tag{A.164}$$

Where constant K_p is:

$$K_p = \frac{\lambda-\kappa}{v_i}\left(\frac{\partial g}{\partial p'}\right)_{\mathrm{Y}_{load}}\left(\frac{\partial f}{\partial q}\right)_{\mathrm{Y}_{load}}\frac{1}{p_0'^3}\left(\frac{b_{max}}{B}\right)^{\psi} \tag{A.165}$$

Deviatoric plastic strain is:

$$\dot{\varepsilon}_{s\ \ unl}^{p\ load} = \dot{\varepsilon}_{v\ \ unl}^{p\ load} \left(\frac{\partial g}{\partial q}\right)_{\substack{Y_{load} \\ Y_{unl}}} / \left(\frac{\partial g}{\partial p'}\right)_{\substack{Y_{load} \\ Y_{unl}}} \tag{A.166}$$

Observing Fig. 6.12, one can observe that the loading path is delimited between q_{min} and q_{max}; stresses q_{Yl} and q_{Yu} correspond to the yielding points during loading and unloading, respectively. During loading, the stress path is elastic in the interval between q_{min} and q_{Yl} and elasto-plastic between q_{Yl} and q_{max}. During unloading, stress path is elastic between q_{max} and q_{Yu} and elasto-plastic between q_{Yu} and q_{min}. Equations (A.164) and (A.166), which are referred solely to the plastic component of the strain, shall be integrated in the correct interval. The initial yielding points at the beginning of loading and unloading are determined geometrically:

$$\begin{cases} q_{\mathrm{Yl}} = q_i + \dfrac{2MR\ p_0'}{\sqrt[\bar{n}]{\exp(1)\ \bar{n} \ln r}} \\ q_{\mathrm{Yu}} = q_f - \dfrac{2MR\ p_0'}{\sqrt[\bar{n}]{\exp(1)\ \bar{n} \ln r}} \end{cases} \tag{A.167}$$

Therefore, the integration of the (A.164) during loading is:

$$\int_A^B \dot{\varepsilon}_v^p = K_p \int_{q_{\mathrm{Yl}}}^{q_{\max}} \left(\frac{M\ p_0'}{\sqrt[\bar{n}]{\exp(1)\ \bar{n} \ln r}} - q\right)^{-\psi} \dot{q} \tag{A.168}$$

During unloading it is:

$$\int_B^A \dot{\varepsilon}_v^p = -K_p \int_{q_{\min}}^{q_{\mathrm{Yu}}} \left(\frac{M\ p_0'}{\sqrt[\bar{n}]{\exp(1)\ \bar{n} \ln r}} + q\right)^{-\psi} \dot{q} \tag{A.169}$$

For $\psi \neq 1$, the resulting plastic volumetric strain during loading is:

$$\Delta\varepsilon_{vAB}^p = C_p \left[\left(\frac{Mp_0'}{\sqrt[n]{\exp(1) \cdot \bar{n} \cdot \ln r}} - q_{max}\right)^{1-\psi} - \left(\frac{Mp_0'}{\sqrt[n]{\exp(1) \cdot \bar{n} \cdot \ln r}} - q_{Yl}\right)^{1-\psi}\right] \tag{A.170}$$

During unloading, it is:

$$\Delta\varepsilon_{vBA}^p = C_p \left[\left(\frac{Mp_0'}{\sqrt[n]{\exp(1) \cdot \bar{n} \cdot \ln r}} + q_{min}\right)^{1-\psi} - \left(\frac{Mp_0'}{\sqrt[n]{\exp(1) \cdot \bar{n} \cdot \ln r}} + q_{Yu}\right)^{1-\psi}\right] \tag{A.171}$$

And the new constant C_p is:

$$C_p = -\frac{K_p}{(1-\psi)} \tag{A.172}$$

If $\psi = 1$, the result during loading is:

$$\Delta\varepsilon_{vAB}^p = C_p \ln \frac{Mp_0' - \sqrt[n]{\exp(1) \cdot \bar{n} \cdot \ln r}\ q_{max}}{Mp_0' - \sqrt[n]{\exp(1) \cdot \bar{n} \cdot \ln r}\ q_{Yl}} \tag{A.173}$$

During unloading it is:

$$\Delta\varepsilon_{vBA}^p = C_p \ln \frac{Mp_0' + \sqrt[n]{\exp(1) \cdot \bar{n} \cdot \ln r}\ q_{min}}{Mp_0' + \sqrt[n]{\exp(1) \cdot \bar{n} \cdot \ln r}\ q_{Yu}} \tag{A.174}$$

And:

$$C_p = -K_p \tag{A.175}$$

The accumulated volumetric plastic strain in a loading-unloading cycle is:

$$\Delta\varepsilon_{vABA}^{p} = \Delta\varepsilon_{vAB}^{p} + \Delta\varepsilon_{vBA}^{p} \tag{A.176}$$

The plastic accumulated volumetric strain coincides with the total volumetric strain, because the elastic part is nil at the end of each cycle since the initial and final stresses coincide and the elastic law is considered linear. The accumulated strain at the end of n_{cyc} loading-unloading cycles is:

$$\varepsilon_{v\,cum} = n_{cyc}\Delta\varepsilon_{vABA}^{p} \tag{A.177}$$

DRAINED TRIAXIAL STRESS PATH WITH CONSTANT EFFECTIVE CONFINING PRESSURE

Referring to the scheme in Fig. 6.14 and remembering that U and Y (during loading and unloading, respectively) are conjugate points, the following relations apply:

$$\begin{cases} \dfrac{p'_{\mathrm{Y}} - p'_{\alpha}}{R} = p'_{\mathrm{U}} \\ \dfrac{q_{\mathrm{Y}} - q_{\alpha}}{R} = q_{\mathrm{U}} \end{cases} \tag{A.178}$$

All the coordinates are intended to be followed by the subscript "*load*" or "*unl*" depending whether the stress is increasing or decreasing (loading or unloading). Using these relations, the first derivatives of f and g in the yielding point can be written as follows:

$$\begin{cases} \left(\dfrac{\partial f}{\partial p'}\right)_{\mathrm{Y}} = -\dfrac{n}{Rp'_{\mathrm{U}}}\left(\dfrac{|q_{\mathrm{U}}|}{Mp'_{\mathrm{U}}}\right)^{n} + \dfrac{1}{Rp'_{\mathrm{U}}\ln r} \\ \left(\dfrac{\partial f}{\partial q}\right)_{\mathrm{Y}} = \dfrac{n}{Rq_{\mathrm{U}}}\left(\dfrac{|q_{\mathrm{U}}|}{Mp'_{\mathrm{U}}}\right)^{n} \\ \left(\dfrac{\partial f}{\partial p'_{0}}\right)_{\mathrm{Y}} = -\dfrac{1}{p'_{0}\ln r} \end{cases} \tag{A.179}$$

$$\begin{cases} \left(\dfrac{\partial g}{\partial p'}\right)_{\mathrm{Y}} = \dfrac{27}{R}\,\dfrac{Mp'_{\mathrm{U}} - |q_{\mathrm{U}}|}{[3p'_{\mathrm{U}} + 2|q_{\mathrm{U}}|][3p'_{\mathrm{U}} - |q_{\mathrm{U}}|]} \\ \left(\dfrac{\partial g}{\partial q}\right)_{\mathrm{Y}} = \dfrac{3}{R}\,\dfrac{(3M+9)p'_{\mathrm{U}} - 2M|q_{\mathrm{U}}|}{[3p'_{\mathrm{U}} + 2|q_{\mathrm{U}}|][3p'_{\mathrm{U}} - |q_{\mathrm{U}}|]}\,\mathrm{sgn}(q_{\mathrm{U}}) \end{cases} \tag{A.180}$$

Since point U is constant during loading or unloading, these expressions are constant during loading and during unloading. Coordinates of point U (during loading and unloading, respectively) are calculated as the intercept point between the extension of the stress path (which is a straight line inclined at a constant slope s) and the reference surface:

$$\begin{cases} \left(\dfrac{|q_{\mathrm{U}}|}{Mp'_{\mathrm{U}}}\right)^{n} + \dfrac{1}{\ln r}\ln\dfrac{p'_{\mathrm{U}}}{p'_{0}} = 0 \\ q_{\mathrm{U}} = s(p'_{\mathrm{U}} - p'_{\mathrm{c}}) \end{cases} \tag{A.181}$$

In conventional triaxial tests, s = 3. In order to determine the coordinates of ultimate point U, the stress path can be expressed in a parametric form:

$$p'_{\mathrm{U}} = \sigma'_{\mathrm{c}} + x_{TX} \tag{A.182}$$

Parameter x_{TX} is the unknown variable that shall be determined. Substituting this expression in the equation of the reference surface, one obtains:

$$\left(\frac{s|x_{TX}|}{M(\sigma_c'+x)}\right)^n+\frac{1}{\ln r}\ln\frac{(\sigma_c'+x_{TX})}{p_0'}=0 \tag{A.183}$$

This equation does not have a closed-form solution and it shall be solved iteratively (e.g. with bisection method) to determine the two solutions $x_{TX1,2}$ corresponding to U_{load} and U_{unl}.

Vector $\boldsymbol{\beta}$, joining the yielding point on the yield surface and the conjugate point of the reference surface, is:

$$\boldsymbol{\beta}=\begin{pmatrix}p_{\mathrm{U}}'-p'\\ q_{\mathrm{U}}-q\end{pmatrix}=\begin{pmatrix}p_{\mathrm{U}}'-p'\\ s(p_{\mathrm{U}}'-p')\end{pmatrix} \tag{A.184}$$

The normalized outward normal $\boldsymbol{n_f}/\|\boldsymbol{n_f}\|$ is calculated using the first derivatives of f (expressions (A.92)):

$$\frac{\boldsymbol{n_f}}{\|\boldsymbol{n_f}\|}=\frac{1}{\sqrt{\left(\frac{\partial f}{\partial p'}\right)_{\mathrm{Y}}^2+\left(\frac{\partial f}{\partial q}\right)_{\mathrm{Y}}^2}}\begin{bmatrix}\left(\frac{\partial f}{\partial p'}\right)_{\mathrm{Y}}\\ \\ \left(\frac{\partial f}{\partial q}\right)_{\mathrm{Y}}\end{bmatrix} \tag{A.185}$$

Since the derivatives are constant during loading and unloading, the vector is constant. The scalar product between $\boldsymbol{\beta}$ and $\boldsymbol{n_f}/\|\boldsymbol{n_f}\|$ results in the scalar b:

$$b=(n_{p'}+sn_q)(p_{\mathrm{U}}'-p') \tag{A.186}$$

Where $n_{p''}$ and n_q are the components of the normalized vector $\boldsymbol{n_f}$ in the p' and q directions, respectively.

Kinematic hardening modulus H' is:

$$H'_{\substack{load\\unl}}=\frac{v_i}{\lambda-\kappa}\left[\frac{B}{b_{max}}(n_{p'}+sn_q)(p_{\mathrm{U}}'-p')\right]^{\psi}p_0'^3 \tag{A.187}$$

where the only variable term is p'. Substituting all the calculated terms in the constitutive relations, one obtains:

$$\begin{aligned}\dot{\varepsilon}_v^p&=\frac{1}{H'}\left[\left(\frac{\partial g}{\partial p'}\right)_{\mathrm{Y}}\left(\frac{\partial f}{\partial p'}\right)_{\mathrm{Y}}\dot{p}'+\left(\frac{\partial g}{\partial p'}\right)_{\mathrm{Y}}\left(\frac{\partial f}{\partial q}\right)_{\mathrm{Y}}\dot{q}\right]=\frac{1}{H'}\left(\frac{\partial g}{\partial p'}\right)_{\mathrm{Y}}\left[\left(\frac{\partial f}{\partial p'}\right)_{\mathrm{Y}}+s\left(\frac{\partial f}{\partial q}\right)_{\mathrm{Y}}\right]\dot{p}'=\\&=\frac{\lambda-\kappa}{v_i}\left(\frac{\partial g}{\partial p'}\right)_{\mathrm{Y}}\left[\left(\frac{\partial f}{\partial p'}\right)_{\mathrm{Y}}+s\left(\frac{\partial f}{\partial q}\right)_{\mathrm{Y}}\right]\frac{1}{p_0'^3}\left(\frac{b_{max}}{B}\right)^{\psi}\left[(n_{p'}+s\,n_q)(p_{\mathrm{U}}'-p')\right]^{-\psi}\dot{p}'\end{aligned} \tag{A.188}$$

This value is referred to the loading or unloading phase, respectively, depending on whether the terms are referred to loading or unloading.

If ψ = 1, the integral of the equation in the loading path AB is:

$$\begin{aligned}\dot{\varepsilon}_{v\mathrm{AB}}^p=&-\frac{\lambda-\kappa}{v_i}\left(\frac{\partial g}{\partial p'}\right)_{\mathrm{Y}_{load}}\left[\left(\frac{\partial f}{\partial p'}\right)_{\mathrm{Y}_{load}}+s\left(\frac{\partial f}{\partial q}\right)_{\mathrm{Y}_{load}}\right]\frac{1}{p_0'^3}\frac{b_{max}}{B}\frac{1}{n_{p'_{load}}+s\,n_{q_{load}}}\\&\ln\left[\frac{\left(n_{p'_{load}}+s\,n_{q_{load}}\right)\left(p'_{\mathrm{U}_{load}}-p'_f\right)}{\left(n_{p'_{load}}+s\,n_{q_{load}}\right)\left(p'_{\mathrm{U}_{load}}-p'_{\mathrm{Y}_{load}}\right)}\right]\end{aligned} \tag{A.189}$$

Applying this result to the cyclic stress load ABA illustrated in Fig. 6.14, and imposing n_{cyc} cycles, one obtains:

$$\varepsilon_v^p = n_{cyc}\left(K_{load}\ \ln\frac{p'_{\mathrm{U}_{load}} - p'_f}{p'_{\mathrm{U}_{load}} - p'_{\mathrm{Y}_{load}}} + K_{unl}\ \ln\frac{p'_{\mathrm{U}_{unl}} - p'_i}{p'_{\mathrm{U}_{unl}} - p'_{\mathrm{Y}_{unl}}}\right) \tag{A.190}$$

where K_{load} and K_{unl} are the following constants:

$$\begin{aligned} K_{load} &= -\frac{\lambda-\kappa}{v_i\ p_0'^3}\frac{b_{max}}{B}\left(\frac{\partial g}{\partial p'}\right)_{\mathrm{Y}_{load}}\left[\left(\frac{\partial f}{\partial p'}\right)_{\mathrm{Y}_{load}} + s\left(\frac{\partial f}{\partial q}\right)_{\mathrm{Y}_{load}}\right]\frac{1}{n_{p'_{load}} + s\ n_{q_{load}}} \\ K_{unl} &= -\frac{\lambda-\kappa}{v_i\ p_0'^3}\frac{b_{max}}{B}\left(\frac{\partial g}{\partial p'}\right)_{\mathrm{Y}_{unl}}\left[\left(\frac{\partial f}{\partial p'}\right)_{\mathrm{Y}_{unl}} + s\left(\frac{\partial f}{\partial q}\right)_{\mathrm{Y}_{unl}}\right]\frac{1}{n_{p'_{unl}} + s\ n_{q_{unl}}} \end{aligned} \tag{A.191}$$

Yielding points $p'_{\mathrm{Y}_{load}}$ and $p'_{\mathrm{Y}_{unl}}$ are calculated geometrically considering that these points are conjugate with the ultimate points on the reference surface calculated above:

$$\begin{aligned} p'_{\mathrm{Y}_{load}} &= p'_i + R\left(p'_{\mathrm{U}_{load}} - p'_{\mathrm{U}_{unl}}\right) \\ p'_{\mathrm{Y}_{unl}} &= p'_f - R\left(p'_{\mathrm{U}_{load}} - p'_{\mathrm{U}_{unl}}\right) \end{aligned} \tag{A.192}$$

If $\psi \neq 1$, the solution of the (A.188) during loading is:

$$\begin{aligned} \dot{\varepsilon}_{v\mathrm{AB}}^p &= -\frac{\lambda-\kappa}{v_i\ p_0'^3}\left(\frac{\partial g}{\partial p'}\right)_{\mathrm{Y}}\left[\left(\frac{\partial f}{\partial p'}\right)_{\mathrm{Y}} + s\left(\frac{\partial f}{\partial q}\right)_{\mathrm{Y}}\right]\left(\frac{b_{max}}{B}\right)^{\psi}\frac{1}{1-\psi}\frac{1}{n_{p'_{load}} + s\ n_{q_{load}}} \\ &\left\{\left[\left(n_{p'_{load}} + s\ n_{q_{load}}\right)\left(p'_{\mathrm{U}} - p'_f\right)\right]^{1-\psi} - \left[\left(n_{p'_{load}} + s\ n_{q_{load}}\right)\left(p'_{\mathrm{U}} - p'_{\mathrm{Y}_{load}}\right)\right]^{1-\psi}\right\} \end{aligned} \tag{A.193}$$

As in the precedent case, this result is extended to the complete cycle ABA, which is repeated n_{cyc} times:

$$\dot{\varepsilon}_v^p = n_{cyc}\left[K_{load}\left(\left|p'_{\mathrm{U}} - p'_f\right|^{1-\psi} - \left|p'_{\mathrm{U}} - p'_{\mathrm{Y}_{load}}\right|^{1-\psi}\right) + K_{unl}\left(\left|p'_{\mathrm{U}} - p'_i\right|^{1-\psi} - \left|p'_{\mathrm{U}} - p'_{\mathrm{Y}_{unl}}\right|^{1-\psi}\right)\right] \tag{A.194}$$

And the constants are:

$$\begin{aligned} K_{load} &= -\frac{\lambda-\kappa}{v_i\ p_0'^3}\left(\frac{b_{max}}{B}\right)^{\psi}\frac{1}{1-\psi}\left(\frac{\partial g}{\partial p'}\right)_{\mathrm{Y}_{load}}\left[\left(\frac{\partial f}{\partial p'}\right)_{\mathrm{Y}_{load}} + s\left(\frac{\partial f}{\partial q}\right)_{\mathrm{Y}_{load}}\right]\frac{\left|n_{p'_{load}} + s\ n_{q_{load}}\right|^{1-\psi}}{n_{p'_{load}} + s\ n_{q_{load}}} \\ K_{unl} &= -\frac{\lambda-\kappa}{v_i\ p_0'^3}\left(\frac{b_{max}}{B}\right)^{\psi}\frac{1}{1-\psi}\left(\frac{\partial g}{\partial p'}\right)_{\mathrm{Y}_{unl}}\left[\left(\frac{\partial f}{\partial p'}\right)_{\mathrm{Y}_{unl}} + s\left(\frac{\partial f}{\partial q}\right)_{\mathrm{Y}_{unl}}\right]\frac{\left|n_{p'_{unl}} + s\ n_{q_{unl}}\right|^{1-\psi}}{n_{p'_{unl}} + s\ n_{q_{unl}}} \end{aligned} \tag{A.195}$$

Yield points are the same expressed in (A.192).

Distortional strain is computed using the flow rule expression (A.166).

Solutions for mixed hardening

CONSTANT EFFECTIVE STRESS RATIO STRESS PATH

The generic yielding point (point Y) is determined as the intersection between the yield surface (6.2) and the stress path (6.88):

$$\begin{cases} p'_{\mathrm{Y}} = p'_\alpha + R\left(\frac{1}{r}\right)^{(\bar{\eta}/M)^{\bar{n}}} p'_0 \\ q_{\mathrm{Y}} = q_\alpha + \bar{\eta}\ R\left(\frac{1}{r}\right)^{(\bar{\eta}/M)^{\bar{n}}} p'_0 \end{cases} \tag{A.196}$$

These expressions can be rewritten as follows:

$$\begin{cases} \dfrac{p'_{\mathrm{Y}} - p'_{\alpha}}{R} = k_M \, p'_0 \\ \dfrac{q_{\mathrm{Y}} - q_{\alpha}}{R} = \bar{\eta} \, k_M \, p'_0 \end{cases} \tag{A.197}$$

where k_M is a constant depending on the shape of the yield surface and on the slope of the stress path:

$$k_M = \left(\frac{1}{r}\right)^{(\bar{\eta}/M)^{\bar{n}}} \tag{A.198}$$

The first derivatives of yield surface f calculated in the yield point Y are:

$$\begin{cases} \left(\dfrac{\partial f}{\partial p'}\right)_{\mathrm{Y}} = \dfrac{1}{R \, k_M \, p'_0}\left[-\bar{n}\left(\dfrac{|\bar{\eta}|}{M}\right)^{\bar{n}} + \dfrac{1}{\ln r}\right] \\ \left(\dfrac{\partial f}{\partial q}\right)_{\mathrm{Y}} = \dfrac{\bar{n}}{R \, \bar{\eta} \, k_M \, p'_0}\left(\dfrac{|\bar{\eta}|}{M}\right)^{\bar{n}} \\ \left(\dfrac{\partial f}{\partial p'_0}\right)_{\mathrm{Y}} = -\dfrac{1}{p'_0 \ln r} \end{cases} \tag{A.199}$$

The partial derivatives of Rowe plastic potential (expressions (A.93) become:

$$\begin{cases} \left(\dfrac{\partial g}{\partial p'}\right)_{\mathrm{Y}} = \dfrac{27}{R \, k_M \, p'_0} \dfrac{M - |\bar{\eta}|}{[3 + 2|\bar{\eta}|]\,[3 - |\bar{\eta}|]} \\ \left(\dfrac{\partial g}{\partial q}\right)_{\mathrm{Y}} = \dfrac{3}{R \, k_M \, p'_0} \dfrac{(3M + 9) - 2M|\bar{\eta}|}{[3 + 2|\bar{\eta}|]\,[3 - |\bar{\eta}|]} \operatorname{sgn}(\bar{\eta}) \end{cases} \tag{A.200}$$

It is worth noting that all the partial derivatives are only dependent on p'_0 and not on the stress state.

Vector $\boldsymbol{\beta}$ joining points Y and U is:

$$\boldsymbol{\beta} = \begin{pmatrix} \dfrac{p'_{\mathrm{Y}} - p'_{\alpha}}{R} - p' \\ \dfrac{q_{\mathrm{Y}} - q_{\alpha}}{R} - q \end{pmatrix} = \begin{pmatrix} k_M \, p'_0 - p' \\ \bar{\eta}\,(k_M \, p'_0 - p') \end{pmatrix} \tag{A.201}$$

As expected, vector $\boldsymbol{\beta}$ is parallel to the stress path.

The normalized outward normal in Y is given by the first derivatives of f:

$$\begin{aligned} \frac{\boldsymbol{n_f}}{\|\boldsymbol{n_f}\|} &= \frac{1}{\sqrt{\left(\dfrac{\partial f}{\partial p'}\right)^2_{\mathrm{Y}} + \left(\dfrac{\partial f}{\partial q}\right)^2_{\mathrm{Y}}}} \begin{pmatrix} \left(\dfrac{\partial f}{\partial p'}\right)_{\mathrm{Y}} \\ \left(\dfrac{\partial f}{\partial q}\right)_{\mathrm{Y}} \end{pmatrix} = \\ &= \frac{1}{\sqrt{\left[-\bar{n}\left(\dfrac{|\bar{\eta}|}{M}\right)^{n} + \dfrac{1}{\ln r}\right]^2 + \left[\dfrac{\bar{n}}{\bar{\eta}}\left(\dfrac{|\bar{\eta}|}{M}\right)^{\bar{n}}\right]^2}} \begin{pmatrix} -\bar{n}\left(\dfrac{|\bar{\eta}|}{M}\right)^{n} + \dfrac{1}{\ln r} \\ \dfrac{\bar{n}}{\bar{\eta}}\left(\dfrac{|\bar{\eta}|}{M}\right)^{n} \end{pmatrix} \end{aligned} \tag{A.202}$$

which is a constant as expected. From the scalar product of these vectors, variable b is determined:

$$b = (k_M\, p'_0 - p')(n_{p'} + \bar{\eta}\, n_q) \tag{A.203}$$

Where $n_{p'}$ and n_q are the constant components of the normalized outward normal vector in the p' and q directions, respectively.

It is possible to calculate the kinematic hardening modulus H' by substituting expressions (A.203) and (6.18) into (6.13):

$$H' = k_{H'} \left(k_M - \frac{p'}{p'_0} \right)^{\psi} p_0'^3 \tag{A.204}$$

where constant $k_{H'}$ is:

$$k_{H'} = \frac{v_i}{\lambda - \kappa} \left(B\, \frac{n_{p'} + \bar{\eta}\, n_q}{(1-R)\, \max\left(\frac{2M}{\sqrt[n]{\exp(1)\, \bar{n} \ln r}}, 1 \right)} \right)^{\psi} \tag{A.205}$$

Similarly, isotropic hardening modulus H_0 is calculated by substituting the last of the (A.199) and the first of the (A.200) into (6.12):

$$H_0 = \frac{k_{H_0}}{p'_0} \tag{A.206}$$

where the constant k_{H_0} is:

$$k_{H_0} = \frac{27\, v_i}{(\lambda - \kappa)\, R\, k_M \ln r}\, \frac{M - |\bar{\eta}|}{[3 + 2|\bar{\eta}|]\, [3 - |\bar{\eta}|]} \tag{A.207}$$

The total hardening modulus is:

$$H = k_{H'} \left(k_M - \frac{p'}{p'_0} \right)^{\Psi} p_0'^3 + \frac{k_{H_0}}{p'_0} \tag{A.208}$$

Since vector $\boldsymbol{\beta}$ is parallel to the stress increment vector, equation (6.77) is valid. Thus, translation rule assumes the form of the following differential equation:

$$\dot{p}'_\alpha = \frac{H'}{H} \dot{p}' \tag{A.209}$$

Since H' and H are only dependent on p'_0, it is convenient to operate a change of variables from p'_α to p'_0. From the first of the (A.197), one can find p'_0 as a function of p' and p'_α:

$$p'_0 = \frac{p' - p'_\alpha}{R k_M} \tag{A.210}$$

Differentiating this expression, one obtains:

$$\dot{p}'_0 = \frac{\dot{p}' - \dot{p}'_\alpha}{R k_M} \tag{A.211}$$

By rearranging this expression and substituting it in (A.209), one obtains the following equation:

$$\frac{\dot{p}'}{\dot{p}'_0} = R k_M \frac{H}{H_0} = R k_M \left(1 + \frac{H'}{H_0} \right) = R k_M + R k_M \frac{k_{H'}}{k_{H_0}} \left(k_M - \frac{p'}{p'_0} \right)^{\psi} p_0'^4 \tag{A.212}$$

which is an inhomogeneous first-order nonlinear ordinary differential equation with variable coefficients. Its boundary condition is:

$$p'(p'_{0i}) = p'_{\mathrm{A}} \tag{A.213}$$

where p'_{0i} and p'_{A} are the values of p'_0 and p' at the beginning of yielding.

The general solution of this problem appears hard to find. As written above, two particular solutions where found for ψ = 1 and ψ = 4. The equation can be rewritten in the following form:

$$\frac{\dot{p}'}{\dot{p}'_0} = Rk_M + Rk_M \frac{k_{H'}}{k_{H_0}} (k_M\, p'_0 - p')^{\psi}\, {p'_0}^{4-\psi} \tag{A.214}$$

The following substitution is performed:

$$z = (k_M\, p'_0 - p')^{\psi} \tag{A.215}$$

By rearranging and differentiating one obtains:

$$\dot{p}' = k_M - \frac{1}{\psi}\, z^{\left(\frac{1-\psi}{\psi}\right)}\, \dot{z} \tag{A.216}$$

Thus, equation (A.214) can be rewritten as follows:

$$\frac{\dot{z}}{\dot{p}'_0} = -R\, k_M\, \psi\, \frac{k_{H'}}{k_{H_0}}\, {p'_0}^{(4-\psi)}\, z^{\left(\frac{2\psi-1}{\psi}\right)} + k_M\, (1 - \mathrm{R})\, \psi\, z^{\left(\frac{\psi-1}{\psi}\right)} \tag{A.217}$$

One can see that, for ψ = 1, the equation becomes linear in z:

$$\frac{\dot{z}}{\dot{p}'_0} = -Rk_M \frac{k_{H'}}{k_{H_0}}\, {p'_0}^{3}\, z + k_M\, (1 - \mathrm{R}) \tag{A.218}$$

and can be solved with the usual formula, leading to the solution :

$$\begin{aligned} p' = k_M p'_0 - (k_M p'_{0i} - p'_{\mathrm{A}}) \exp\left[\frac{1}{4} Rk_M \frac{k_{H'}}{k_{H_0}} (p'^4_{0i} - p'^4_0)\right] - k_M\, (1 - \\ - R) \exp\left(-\frac{1}{4} Rk_M \frac{k_{H'}}{k_{H_0}} p'^4_0\right) \int_{p'_{0i}}^{p'_0} \exp\left(\frac{1}{4} Rk_M \frac{k_{H'}}{k_{H_0}} p'^4_0\right) dp'_0 \end{aligned} \tag{A.219}$$

For ψ = 4, equation (A.214) becomes:

$$\frac{\dot{p}'}{\dot{p}'_0} = Rk_M + Rk_M \frac{k_{H'}}{k_{H_0}} (k_M\, p'_0 - p')^4 \tag{A.220}$$

In this case, the following substitution is operated:

$$\begin{aligned} z &= k_M\, p'_0 - p' \\ \dot{p}' &= k_M - \dot{z} \end{aligned} \tag{A.221}$$

obtaining:

$$\frac{\dot{z}}{\dot{p}'_0} = k_M \left(1 - \mathrm{R} - \mathrm{R} \frac{k_{H'}}{k_{H_0}} \mathrm{z}^4\right) \tag{A.222}$$

which is a separable differential equation:

$$\int_{z_i}^{z} \frac{\dot{z}}{(1 - \mathrm{R}) - \mathrm{R} \frac{k_{H'}}{k_{H_0}} \mathrm{z}^4} = \int_{p'_{0i}}^{p'_0} k_M\, \dot{p}'_0 \tag{A.223}$$

where

$$z_i = k_M\, p'_{0i} - p'_{\mathrm{A}} \tag{A.224}$$

The integration of the left-hand member depends on the sign of the constants in the denominator. Quantities R and (1-R) are always positive; constant $k_{H'}$ is also always positive, since it is the coefficient of the kinematic hardening modulus H'. Constant k_{H_0} can be positive or negative depending on whether the stress path is in the wet ($\bar{\eta} < M$) or dry ($\bar{\eta} > M$) side of the critical state. In the first case, the denominator is of the type $(|a| - |b|\, z^4)$; in the second it is $(|a| + |b|\, z^4)$, leading to two different polynomial decompositions and thus two different solutions. In both cases it is impossible to separate the variables, leading to an implicit function of p' and p'_0. In the wet side of critical state, solution is:

$$\begin{aligned}
&\frac{1}{4\,(1-R)^{3/4}\,\sqrt[4]{R\;k_{H'}/k_{H_0}}}\left[\ln\left(\frac{\sqrt[4]{R\;k_{H'}/k_{H_0}}\;(k_M\,p'_0 - p') + \sqrt[4]{1-R}}{\sqrt[4]{R\;k_{H'}/k_{H_0}}\;(k_M\,p'_0 - p') - \sqrt[4]{1-R}}\right) + \right.\\
&\quad + 2\,\mathrm{atan}\left(\sqrt[4]{\frac{R}{1-R}\,\frac{k_{H'}}{k_{H_0}}}\;(k_M\,p'_0 - p')\right) -\\
&\quad - \ln\left(\frac{\sqrt[4]{R\;k_{H'}/k_{H_0}}\;(k_M\,p'_{0i} - p'_{\mathrm{A}}) + \sqrt[4]{1-R}}{\sqrt[4]{R\;k_{H'}/k_{H_0}}\;(k_M\,p'_{0i} - p'_{\mathrm{A}}) - \sqrt[4]{1-R}}\right) -\\
&\quad \left. - 2\,\mathrm{atan}\left(\sqrt[4]{\frac{R}{1-R}\,\frac{k_{H'}}{k_{H_0}}}\;(k_M\,p'_{0i} - p'_{\mathrm{A}})\right)\right] - k_M(\,p'_0 - \,p'_{0i}) = 0
\end{aligned} \tag{A.225}$$

For the dry side, the solution is:

$$\begin{aligned}
&\frac{1}{4\sqrt{2}\,(1-R)^{\frac{3}{4}}\,\sqrt[4]{R\;k_{H'}/|k_{H_0}|}}\\
&\left[\ln\left(\frac{\sqrt{R\;k_{H'}/|k_{H_0}|}\;(k_M\,p'_0 - p')^2 + \sqrt{2}\,\sqrt[4]{R(1-R)\;k_{H'}/|k_{H_0}|} + \sqrt{1-R}}{\sqrt{R\;k_{H'}/|k_{H_0}|}\;(k_M\,p'_0 - p')^2 - \sqrt{2}\,\sqrt[4]{R(1-R)\;k_{H'}/|k_{H_0}|} + \sqrt{1-R}}\right) -\right.\\
&- 2\,\mathrm{atan}\left(1 - \sqrt{2}\,\sqrt[4]{\frac{R}{1-R}\,\frac{k_{H'}}{|k_{H_0}|}}\;(k_M\,p'_0 - p')\right) +\\
&+ 2\,\mathrm{atan}\left(1 + \sqrt{2}\,\sqrt[4]{\frac{R}{1-R}\,\frac{k_{H'}}{|k_{H_0}|}}\;(k_M\,p'_0 - p')\right) -\\
&- \ln\left(\frac{\sqrt{R\;k_{H'}/|k_{H_0}|}\;(k_M\,p'_{0i} - p'_{\mathrm{A}})^2 + \sqrt{2}\,\sqrt[4]{R(1-R)\,k_{H'}/|k_{H_0}|} + \sqrt{1-R}}{\sqrt{R\;k_{H'}/|k_{H_0}|}\;(k_M\,p'_{0i} - p'_{\mathrm{A}})^2 - \sqrt{2}\,\sqrt[4]{R(1-R)\,k_{H'}/|k_{H_0}|} + \sqrt{1-R}}\right) +\\
&+ 2\,\mathrm{atan}\left(1 - \sqrt{2}\,\sqrt[4]{\frac{R}{1-R}\,\frac{k_{H'}}{|k_{H_0}|}}\;(k_M\,p'_{0i} - p'_{\mathrm{A}})\right) -\\
&\left. - 2\,\mathrm{atan}\left(1 + \sqrt{2}\,\sqrt[4]{\frac{R}{1-R}\,\frac{k_{H'}}{|k_{H_0}|}}\;(k_M\,p'_{0i} - p'_{\mathrm{A}})\right)\right] - k_M(\,p'_0 - \,p'_{0i}) = 0
\end{aligned} \tag{A.226}$$

ANNEX 5: MODEL IMPLEMENTATION IN MATLAB®

Stress-driven cyclic triaxial tests

```
%Bubble CASM model in drained conditions for cyclic loading
%TC_5%_e1_s1
fclose all; clearvars;
[~, name] = system('hostname');
%Model parameters
k = 0.0097; l = 0.112; N = 2.352; M = 1.4;
r = 3.7; n = 2.2; m = 1.5; omega = 0; theta = 2.5e-5;
pti = 264.4471; b0 = 4.2189; b1 = 3; b2 = b1;
R_v = 0.015;
Y_v_1 = 4.5;
Y_v_2 = 2.1;
dilatancy = 2; %1- Rowe; - Yu
normalize = 0; %1- normal vector (ort) to the yield surface is normalized
in the determination of scalar b; 0- ort is not normalized

%Initial stress point and preconsolidation point
qi = 84; sigma_c = 40; pinit = sigma_c+qi/3;  vi = 1.733; p0_unc_i =
exp((N-vi)/(l-k));
p0i = p0_unc_i*(1+b0);
K = 9.75e4*(1+sqrt((p0i-p0_unc_i-pti)/pinit));
G = 3*K*(1-2*0.3)/(2*(1+0.3));
B_v_1 = 3.2*(1+sqrt((p0i-p0_unc_i-pti)/pinit)); %3.2
B_v_2 = 2.8*(1+sqrt((p0i-p0_unc_i-pti)/pinit)); %2.8

%Defining number of cycles, loading path and load increment
n_cyc = 6e5;
ratio = 3; %dq/dp
qf = 168; pf = pinit + (qf-qi)/ratio; %final stress point
Dq_el = 0.03; %elastic load increment
SSTOL = 1e-12;
YTOL = 1;

%Define output type
output_type = 2; %0 = only 1st and last point of each cycle; 1 = complete
output; 2 = complete output of selected cycles

fil = 50; %max num of points plotted in half cycle

sel_cycles = [1:20 41:50 91:100 191:200 391:400 991:1000 9991:10000  ...
    19991:20000 39991:40000 59991:60000 79991:80000 99991:100000 ...
    199991:200000 299991:300000 399991:400000 499991:500000 599991:600000
...
    699991:700000 799991:800000 899991:900000 999991:1000000];

if output_type == 1 && n_cyc > 20,
    input('Warning! Complete output selected. Output file may be very
large');
end;

%Choose if mail is sent
mail = 0; %1-send e-mail; 0- do not send
```

```
mailmessage =
cell(1,numel(R_v)*numel(B_v_1)*numel(B_v_2)*numel(Y_v_1)*numel(Y_v_2));

%Preallocation
preall = 50000;
p = zeros(1,preall); q = zeros(1,preall); p_alfa = zeros(1,preall);
q_alfa = zeros(1,preall); p0 = zeros(1,preall); p0_unc = zeros(1,preall);
pt = zeros(1,preall); X = zeros(1,preall); H0 = zeros(1,preall); Hb =
zeros(1,preall);
H_prime = zeros(1,preall); H = zeros(1,preall); b = zeros(1,preall);
b_max = zeros(1,preall); beta = zeros(2,preall); ort = zeros(2,preall);
S = zeros(1,preall); D = zeros(1,preall); dF_dp = zeros(1,preall);
dF_dq = zeros(1,preall); dF_dp_alfa = zeros(1,preall); dF_dq_alfa =
zeros(1,preall);
dF_dp0 = zeros(1,preall); dp0_dp0_unc = zeros(1,preall); dp0_dX =
zeros(1,preall);
dX_dl = zeros(1,preall); dG_dp = zeros(1,preall); dG_dq = zeros(1,preall);
d_eps_p_v = zeros(1,preall); d_eps_p_s = zeros(1,preall);
dv_ep = zeros(1,preall); d_v_e = zeros(1,preall); v = zeros(1,preall);
d_eps_e_v = zeros(1,preall); d_eps_v = zeros(1,preall); eps_e_v =
zeros(1,preall);
eps_p_v = zeros(1,preall); eps_v = zeros(1,preall); d_eps_e_s =
zeros(1,preall);
d_eps_s = zeros(1,preall); eps_e_s = zeros(1,preall); eps_p_s =
zeros(1,preall);
eps_s = zeros(1,preall); eps_a = zeros(1,preall); eps_r = zeros(1,preall);
plas = zeros(1,preall); filenum = 0;

for i_R = 1:numel(R_v),
    for i_B_1 = 1:numel(B_v_1),
        for i_B_2 = 1:numel(B_v_2),
            for i_Y_1 = 1:numel(Y_v_1),
                for i_Y_2 = 1:numel(Y_v_2),

                    %start to measure elapsed time
                    tic

                    filenum = filenum+1;
                    flag_print = 0;
                    %Model parameters input
                    R = R_v(i_R); B = [B_v_1(i_B_1) B_v_2(i_B_2)]; Y =
[Y_v_1(i_Y_1) Y_v_2(i_Y_2)];

                    %Initial Centre of the bubble
                    %calculating ultimate point with bisection method
                    P_try = -pti;
                    P_a = pf; Q_a = qf;
                    Q_try = qi + ratio*(P_try-pinit);
                    F_ref = 1;
                    P_bis = (P_try+P_a)/2;
                    Q_bis = (Q_try+Q_a)/2;

                    while abs(F_ref) > 1e-13,     %tolerance
                        P_bis = (P_try+P_a)/2;
                        Q_bis = (Q_try+Q_a)/2;
                        F_ref = (abs(Q_bis)/(M*(P_bis+pti)))^n +
1/log(r)*log((P_bis+pti)/p0i);
                        if F_ref < 0,
```

```
                        P_a = P_bis;
                        Q_a = Q_bis;
                    else
                        P_try = P_bis;
                        Q_try = Q_bis;
                    end;
                end;

                pU_inf = P_bis;
                qU_inf = Q_bis;

%                 %centre that gives sigma_y=sigma_c
%                 p_alfa_i = pinit - R*(pU_inf+pti);
%                 q_alfa_i = qi - R*qU_inf;

                %centre that gives sigma_y=(p0,0)
                p_alfa_i = 1.001*(pinit - R*p0i); %1.004
                q_alfa_i = qi;

                disp(['Current parameters are: R= ', num2str(R), ...
                    '; Y= ', num2str(Y(1), '%g'), ',', num2str(Y(2),
'%g'), ...
                    '; B= ', num2str(B(1), '%g'), ',', num2str(B(2),
'%g')]);

                %output file
                fnformat = ['TC_v8_D_R_', num2str(R, '%g'), ...
                    '_Y_', num2str(Y(1), '%g'), ',', num2str(Y(2),
'%g'), ...
                    '_B_', num2str(B(1), '%g'), ',', num2str(B(2),
'%g'), ...
                    '_o_', num2str(omega), '_M_', num2str(M), '_n_',
...
                    num2str(n), '_r_', num2str(r), '_k_', num2str(k),
...
                    '_l_', num2str(l), '_center_', num2str(p_alfa_i),
...
                    ',', num2str(q_alfa_i), '_b0_', num2str(b0),
'_b1_', ...
                    num2str(b1, '%g'), '_b2_', num2str(b2, '%g'), ...
                    '_pti_', num2str(pti), '_theta_', num2str(theta,
'%g')];

                switch dilatancy
                    case 1
                        filename = [fnformat, '_RW.csv'];
                    case 2
                        filename = [fnformat, '_m_', num2str(m),
'_YU.csv'];
                    otherwise
                        error('Wrong input!');
                end;

                JAY = fopen('j.csv', 'w+');
                OUTPUT = fopen(filename, 'w+');
                while OUTPUT == -1 || JAY == -1,
```

```
                        disp('Output file already open. Please close file
and press ENTER to continue');
                        input(' ');
                        JAY = fopen('j.csv', 'w');
                        OUTPUT = fopen(filename, 'w');
                    end;

                    header = ['cycle,eps_a_cum,eps_v_cum,eps_s_cum,v,p0,'
...
                    'pt,p_alfa,q_alfa,p,q,H0,H_prime,Hb,S,dF_dp,dF_dq,' ...
                    'dF_dp0,dp0_dp0_unc,dp0_dX,dX_dl,dG_dp,dG_dq,D,beta_x,'
...
                    'beta_y,norm_x,norm_y,b,b_max,b_dash,cresc,plas\r\n'];

                    fprintf(OUTPUT, header);
                    fprintf(JAY,
'cycle,j_max,norm(E_eps_max),DT_max,DT_min,i_plas,cresc\r\n');
                    ncols = numel(strfind(header, ',')) + 1;
                    format = ['%g', repmat(',%g', 1, ncols-1), '\r\n'];
%use ',%.7g' for more decimal points
                    fprintf(OUTPUT, format, 0, 0, 0, 0, vi, p0i, pti, ...
                    p_alfa_i, q_alfa_i, pinit, qi, ...
                    [], [], [], [], [], [], [], [], [], [], ...
                    [], [], [], [], [], [], [], [], [], ...
                    b0, 0, 0);

                    %initializing variables
                    %stress variables
                    p0_prec = p0i;
                    p0_unc_prec = p0_unc_i; pt_prec = pti;
                    p_alfa_prec = p_alfa_i; q_alfa_prec = q_alfa_i;
                    p0(1) = p0i; p0_unc(1) = p0_unc_i; pt(1) = pti;
                    p_alfa(1) = p_alfa_i; q_alfa(1) = q_alfa_i;

                    %volume/pore pressure variables
                    %volumetric strain
                    v(1) = vi;
                    v_prec = vi; eps_v_prec = 0;
                    eps_e_v_prec = 0; eps_p_v_prec = 0;

                    %distortional strain
                    eps_s_prec = 0; eps_e_s_prec = 0; eps_p_s_prec = 0;

                    %hardening variables
                    H_prime_prec = 0; H0_prec = 0; Hb_prec = 0; H_prec = 0;
S_prec = 0;
                    beta_prec = [0 0]; ort_prec = [0 0]; b_prec = 0;
                    b_max_prec = 0; D_prec = 0;
                    dF_dp_prec = 0; dF_dq_prec = 0; dF_dp_alfa_prec = 0;
                    dF_dq_alfa_prec = 0; dF_dp0_prec = 0;
                    dp0_dp0_unc_prec = 0; dp0_dX_prec = 0; dX_dl_prec = 0;
                    dG_dp_prec = 0; dG_dq_prec = 0;

                    %bonding variable
                    X_prec = 0;

                    %system variables
```

```
                    err = 0; warn1 = 0; flag = 0;

                    %-----------Starting calculation-----------------------
--------------------
                    for cyc = 1:n_cyc; %cycle loop

                        if err ~= 0, break; end;

                        if cyc <= 1000 || mod(cyc, 1000) == 0 || cyc ==
n_cyc,
                            disp(['Processing cycle ', int2str(cyc), ' of
', int2str(n_cyc), '...']);
                        end;

                        if cyc == 4,
                            disp('');
                        end;

                        for cresc = 1:2, %cresc = 1 -> loading, cresc = 2 -
> unloading
                            %calculating yield point
                            tol_Y = 1e-11;
                            p_ab = [pinit pf];
                            q_ab = [qi qf];
                            f_A =
f_yield_f(p_ab(1),q_ab(1),p_alfa_prec,q_alfa_prec,p0_prec,M,n,r,R);
                            f_B =
f_yield_f(p_ab(2),q_ab(2),p_alfa_prec,q_alfa_prec,p0_prec,M,n,r,R);

                            if p_ab(1) < p_alfa_prec, %check if the first
point is within the domain of existence
                                p_ab(1) = p_alfa_prec;
                                q_ab(1) = 3*(p_alfa_prec-sigma_c);
                                f_A = 100;
                            end;

                            if (cresc == 1 && f_B > tol_Y) || (cresc == 2
&& f_A > tol_Y), %elasto-plastic SP

                                p_bis = mean(p_ab);
                                q_bis = mean(q_ab);
                                f_bis =
f_yield_f(p_bis,q_bis,p_alfa_prec,q_alfa_prec,p0_prec,M,n,r,R);

                                while abs(f_bis) > tol_Y,     %tolerance
                                    if f_bis < 0,
                                        p_ab(cresc) = p_bis;
                                        q_ab(cresc) = q_bis;
                                    else
                                        p_ab(3-cresc) = p_bis;
                                        q_ab(3-cresc) = q_bis;
                                    end;
                                    p_bis = mean(p_ab);
                                    q_bis = mean(q_ab);
                                    f_bis =
f_yield_f(p_bis,q_bis,p_alfa_prec,q_alfa_prec,p0_prec,M,n,r,R);
                                end;
```

```
                                p_y = p_bis; q_y = q_bis; %yielding point
                            else
                                err = 1; %fully elastic stress path
                            end;

                            if err ~= 0, continue; end;
                            p_ab = [pinit pf];
                            q_ab = [qi qf];
                            n_int_el = max(2,ceil(abs(q_y-
q_ab(cresc))/Dq_el));

                            q_el = linspace(q_ab(cresc), q_y, n_int_el);
                            p_el = (q_el-qi)/ratio + pinit;
                            p(1:numel(p_el)) = p_el;
                            q(1:numel(q_el)) = q_el;


%eeeeeeeeeeeeeeeeeeeeeeeeeeeeeeeeeeeeeeeeeeeeeeeeeeeeeeeeeeeeeeeeeeeeeeeeeeee
                            %ELASTIC DOMAIN
                            ind = 1:numel(q_el);
                            p0(ind) = p0_prec; p0_unc(ind) = p0_unc_prec;
pt(ind) = pt_prec;
                            p_alfa(ind) = p_alfa_prec; q_alfa(ind) =
q_alfa_prec;
                            H0(ind) = H0_prec; H_prime(ind) = H_prime_prec;
Hb(ind) = Hb_prec;
                            H(ind) = H_prec; X(ind) = X_prec; S(ind) =
S_prec; D(ind) = D_prec;
                            beta(1,ind) = beta_prec(1); beta(2,ind) =
beta_prec(2);
                            ort(1,ind) = ort_prec(1); ort(2,ind) =
ort_prec(2);
                            b(ind) = b_prec; b_max(ind) = b_max_prec;
                            dF_dp(ind) = dF_dp_prec; dF_dq(ind) =
dF_dq_prec;
                            dF_dp_alfa(ind) = dF_dp_alfa_prec;
                            dF_dq_alfa(ind) = dF_dq_alfa_prec;
                            dF_dp0(ind) = dF_dp0_prec;
                            dp0_dp0_unc(ind) = dp0_dp0_unc_prec;
                            dp0_dX(ind) = dp0_dX_prec; dX_dl(ind) =
dX_dl_prec;
                            dG_dp(ind) = dG_dp_prec; dG_dq(ind) =
dG_dq_prec;


                            %volumetric strain
                            d_v_e(ind) = [0 -vi/K*diff(p(ind))];
                            v(ind) = v_prec + cumsum(d_v_e(ind));
                            d_eps_e_v(ind) = -d_v_e(ind)./vi;
                            d_eps_p_v(ind) = 0;
                            d_eps_v(ind) = d_eps_e_v(ind) + d_eps_p_v(ind);
                            if cresc == 1,
                                eps_e_v_prec = 0;
                            end;
                            eps_e_v(ind) = eps_e_v_prec +
cumsum(d_eps_e_v(ind));
                            eps_p_v(ind) = eps_p_v_prec +
cumsum(d_eps_p_v(ind));
                            eps_v(ind) = eps_v_prec + cumsum(d_eps_v(ind));
```

```
                            %distortional strain
                            d_eps_e_s(ind) = [0 diff(q_el)/(3*G)];
                            d_eps_p_s(ind) = 0;
                            d_eps_s(ind) = d_eps_e_s(ind) + d_eps_p_s(ind);
                            if cresc == 1,
                                eps_e_s_prec = 0;
                            end;
                            eps_e_s(ind) = eps_e_s_prec +
cumsum(d_eps_e_s(ind));
                            eps_p_s(ind) = eps_p_s_prec +
cumsum(d_eps_p_s(ind));
                            eps_s(ind) = eps_s_prec + cumsum(d_eps_s(ind));

                            %axial strain
                            eps_a(ind) = eps_s(ind) + eps_v(ind)/3;

                            %radial strain
                            eps_r(ind) = eps_v(ind)/3 - eps_s(ind)/2;

                            plas(ind) = 1;

%eeeeeeeeeeeeeeeeeeeeeeeeeeeeeeeeeeeeeeeeeeeeeeeeeeeeeeeeeeeeeeeeeeeeeeeeee


%pppppppppppppppppppppppppppppppppppppppppppppppppppppppppppppppppppppppppp
                            %ELASTOPLASTIC DOMAIN
                            T = 0;
                            DT = 0.1;
                            i = numel(q_el);
                            j_max = 0;
                            DT_max = 0;
                            DT_min = 0.1;
                            if cresc == 1,
                                Dp_s = pf - p_y;
                                Dq_s = qf - q_y;
                            else
                                Dp_s = pinit - p_y;
                                Dq_s = qi - q_y;
                            end;

                            while T < 1, %cycle on load increments
                                %initialize variables
                                i = i+1;
                                j = 0;
                                E = [SSTOL SSTOL];
                                E_eps_max = 0;
                                F_err = 2*YTOL;
                                plas(i) = 2;

                                %initializing variables of the next cycle
                                pinit_ss = p(i-1);
                                qi_ss = q(i-1);
                                p_alfa_i_ss = p_alfa(i-1);
                                q_alfa_i_ss = q_alfa(i-1);
                                p0_i_ss = p0(i-1);
                                p0_unc_i_ss = p0(i-1)/(1+b0*exp(-X(i-1)));
                                pt_i_ss = pti*exp(-X(i-1));
                                X_i_ss = X(i-1);
```

```
                                %hhhhhhhhhhhhhhhhhhhhhhhh substepping
hhhhhhhhhhhhhhhhhhhhhhhhhhhhhhhh
                                while norm(E) > SSTOL || abs(F_err) > YTOL
|| isreal(F_err) == 0,
                                    if err ~= 0, break; end;
                                    j = j+1;
                                    Dp_ss = DT*Dp_s;
                                    Dq_ss = DT*Dq_s;

                                    if j == 10000 || (j > 10 && T < 1 && DT
< 1e-50),
                                        err = 2;
                                    end;

                                    %+++++++ FIRST ITERATION +++++++
                                    %first derivatives of F
                                    dF_dp_i_ss =
dF_dp_f(pinit_ss,qi_ss,p_alfa_i_ss,q_alfa_i_ss,M,n,r);
                                    dF_dq_i_ss =
dF_dq_f(pinit_ss,qi_ss,p_alfa_i_ss,q_alfa_i_ss,M,n);
                                    if qi_ss == q_alfa_i_ss,
                                        dF_dq_i_ss = 0;
                                    end;
                                    dF_dp_alfa_i_ss = -dF_dp_i_ss;
                                    dF_dq_alfa_i_ss = -dF_dq_i_ss;
                                    dF_dp0_i_ss =  -1/(p0_i_ss*log(r));

                                    %first derivatives of G (depending on
flow rule)
                                    switch dilatancy
                                        case 1 %Bubble Rowe flow rule
                                            dG_dp_i_ss = 27*(M.*(pinit_ss-
p_alfa_i_ss)-abs(qi_ss-q_alfa_i_ss))/ ...
                                                ((2*abs(qi_ss-
q_alfa_i_ss)+3*(pinit_ss-p_alfa_i_ss))*(3*(pinit_ss-p_alfa_i_ss)-abs(qi_ss-
q_alfa_i_ss)));
                                            dG_dq_i_ss =
3*((3*M+9)*(pinit_ss-p_alfa_i_ss)-2*M*abs(qi_ss-q_alfa_i_ss))/ ...
                                                ((3*(pinit_ss-
p_alfa_i_ss)+2*abs(qi_ss-q_alfa_i_ss))*(3*(pinit_ss-p_alfa_i_ss)-abs(qi_ss-
q_alfa_i_ss)))* ...
                                                    sign(qi_ss-q_alfa_i_ss);

                                        case 2 %Bubble General CASM flow
rule
                                            dG_dp_i_ss = (1-(abs(qi_ss-
q_alfa_i_ss)/(M*(pinit_ss-p_alfa_i_ss)))^n)/ ...
                                                ((pinit_ss-
p_alfa_i_ss)*(1+(abs(qi_ss-q_alfa_i_ss)/(M*(pinit_ss-p_alfa_i_ss)))^n*(m-
1)));
                                            dG_dq_i_ss = m*(abs(qi_ss-
q_alfa_i_ss)/(pinit_ss-p_alfa_i_ss))^(n-1)/ ...
                                                (M^n*(pinit_ss-
p_alfa_i_ss)*(1+(abs(qi_ss-q_alfa_i_ss)/(M*(pinit_ss-p_alfa_i_ss)))^n*(m-
1)))* ...
                                                    sign(qi_ss-q_alfa_i_ss);
                                    end;
```

```
                                    %first derivatives of bonding
                                    dp0_dp0_unc_i_ss = 1 + b0*exp(-X_i_ss);
                                    dp0_dX_i_ss = -p0_unc_i_ss*b0*exp(-
X_i_ss);
                                    dX_dl_i_ss =
b1*abs(dG_dp_i_ss)+b2*abs(dG_dq_i_ss);

                                    %isotropic hardening modulus H0
                                    H0_i_ss = -
dF_dp0_i_ss*dp0_dp0_unc_i_ss*vi/(1-k)*p0_unc_i_ss* ...
                                        (dG_dp_i_ss+omega*dG_dq_i_ss);

                                    %beta, n, b, bmax
                                    beta_i_ss_original = [(pinit_ss-
p_alfa_i_ss)/R-(pinit_ss+pt_i_ss) ...
                                        (qi_ss-q_alfa_i_ss)/R-qi_ss];

                                    beta_i_ss = 1/10*
[(9*theta+1)*beta_i_ss_original(1)-3*(theta-1)*beta_i_ss_original(2) ...
                                        -3*(theta-
1)*beta_i_ss_original(1)+(theta+9)*beta_i_ss_original(2)];

                                    ort_i_ss =
(1/sqrt(dF_dp_i_ss^2+dF_dq_i_ss^2))^normalize* ...
                                        [dF_dp_i_ss dF_dq_i_ss];

                                    b_i_ss = beta_i_ss*ort_i_ss';
                                    b_max_i_ss = max(p0_i_ss*(1-R), ...
                                        2*M*p0_i_ss*(1-
R)/(exp(1)*n*log(r))^(1/n));

                                    %kinematic hardening modulus H'
                                    H_prime_i_ss =
(B(cresc)*b_i_ss/b_max_i_ss)^Y(cresc)*vi/(1-k)*p0_i_ss^3;

                                    if H_prime_i_ss == inf, %try to
rearrange expression of H' if this is infinite
                                        H_prime_i_ss = ((vi/(1-
k)*p0_i_ss^3)^(1/Y(cresc))*B(cresc)*b_i_ss/b_max_i_ss)^Y(cresc);
                                    end;

                                    %bonding hardening modulus Hb
                                    Hb_i_ss = -
dF_dp0_i_ss*dp0_dX_i_ss*dX_dl_i_ss;

                                    %total hardening modulus H
                                    H_i_ss = H0_i_ss + Hb_i_ss +
H_prime_i_ss;

                                    %matrix of plastic compliance
                                    Cp_i_ss = 1/H_i_ss* ...
                                        [ dG_dp_i_ss*dF_dp_i_ss ...
                                        dG_dp_i_ss*dF_dq_i_ss; ...
                                        dG_dq_i_ss*dF_dp_i_ss ...
                                        dG_dq_i_ss*dF_dq_i_ss ];
```

```
                                    if abs(H_i_ss) == inf,
                                        Cp_i_ss = zeros(2);
                                    end;

                                    %strain values (1st iteration)
                                    D_eps_p_v_1 = Cp_i_ss(1,:)*[Dp_ss
Dq_ss]';
                                    D_eps_p_s_1 = Cp_i_ss(2,:)*[Dp_ss
Dq_ss]';

                                    %scalar S
                                    if H_i_ss == inf,
                                        S_i_ss = -(dF_dp_i_ss*Dp_ss+ ...
                                            dF_dq_i_ss*Dq_ss)/ ...
                                            (dF_dp_alfa_i_ss*beta_i_ss(1)+
...
                                            dF_dq_alfa_i_ss*beta_i_ss(2));
                                    else
                                        S_i_ss = -(dF_dp_i_ss*Dp_ss+ ...
                                            dF_dq_i_ss*Dq_ss)/ ...
                                            (dF_dp_alfa_i_ss*beta_i_ss(1)+
...
                                            dF_dq_alfa_i_ss*beta_i_ss(2))/
...
                                            H_i_ss*H_prime_i_ss;
                                    end;

                                    %hardening parameters (1st iteration)
                                    Dp0_unc_1 = vi/(1-k)*p0_unc_i_ss* ...
                                        (D_eps_p_v_1+omega*D_eps_p_s_1);
                                    DX_1 =
b1*abs(D_eps_p_v_1)+b2*abs(D_eps_p_s_1);
                                    Dp_alfa_1 = S_i_ss*beta_i_ss(1);
                                    Dq_alfa_1 = S_i_ss*beta_i_ss(2);


                                    %+++++++ SECOND ITERATION +++++++
                                    p_f_ss = pinit_ss + Dp_ss;
                                    q_f_ss = qi_ss + Dq_ss;
                                    p0_unc_f_ss = p0_unc_i_ss + Dp0_unc_1;
                                    X_f_ss = X_i_ss + DX_1;
                                    p0_f_ss = p0_unc_f_ss*(1+b0*exp(-
X_f_ss));
                                    pt_f_ss = pti*exp(-X_f_ss);
                                    p_alfa_f_ss = p_alfa_i_ss + Dp_alfa_1;
                                    q_alfa_f_ss = q_alfa_i_ss + Dq_alfa_1;

                                    %first derivatives of F
                                    dF_dp_f_ss =
dF_dp_f(p_f_ss,q_f_ss,p_alfa_f_ss,q_alfa_f_ss,M,n,r);
                                    dF_dq_f_ss =
dF_dq_f(p_f_ss,q_f_ss,p_alfa_f_ss,q_alfa_f_ss,M,n);
                                    if q_f_ss == q_alfa_f_ss,
                                        dF_dq_f_ss = 0;
                                    end;
                                    dF_dp_alfa_f_ss = -dF_dp_f_ss;
```

```
                                    dF_dq_alfa_f_ss = -dF_dq_f_ss;
                                    dF_dp0_f_ss =  -1/(p0_f_ss*log(r));

                                    if isreal(dF_dp_f_ss) == 0,
                                        DT = 0.5*DT;
                                        continue;
                                    end;

                                    %first derivatives of G (depending on
flow rule)
                                    switch dilatancy
                                        case 1 %Bubble Rowe flow rule
                                            dG_dp_f_ss = 27*(M.*(p_f_ss-
p_alfa_f_ss)-abs(q_f_ss-q_alfa_f_ss))/ ...
                                                ((2*abs(q_f_ss-
q_alfa_f_ss)+3*(p_f_ss-p_alfa_f_ss))*(3*(p_f_ss-p_alfa_f_ss)-abs(q_f_ss-
q_alfa_f_ss)));
                                            dG_dq_f_ss =
3*((3*M+9)*(p_f_ss-p_alfa_f_ss)-2*M*abs(q_f_ss-q_alfa_f_ss))/ ...
                                                ((3*(p_f_ss-
p_alfa_f_ss)+2*abs(q_f_ss-q_alfa_f_ss))*(3*(p_f_ss-p_alfa_f_ss)-abs(q_f_ss-
q_alfa_f_ss)))* ...
                                                    sign(q_f_ss-q_alfa_f_ss);

                                        case 2 %Bubble General CASM flow
rule
                                            dG_dp_f_ss = (1-(abs(q_f_ss-
q_alfa_f_ss)/(M*(p_f_ss-p_alfa_f_ss)))^n)/ ...
                                                ((p_f_ss-
p_alfa_f_ss)*(1+(abs(q_f_ss-q_alfa_f_ss)/(M*(p_f_ss-p_alfa_f_ss)))^n*(m-
1)));
                                            dG_dq_f_ss = m*(abs(q_f_ss-
q_alfa_f_ss)/(p_f_ss-p_alfa_f_ss))^(n-1)/ ...
                                                (M^n*(p_f_ss-
p_alfa_f_ss)*(1+(abs(q_f_ss-q_alfa_f_ss)/(M*(p_f_ss-p_alfa_f_ss)))^n*(m-
1)))* ...
                                                    sign(q_f_ss-q_alfa_f_ss);
                                    end;

                                    %first derivatives of bonding
                                    dp0_dp0_unc_f_ss = 1 + b0*exp(-X_f_ss);
                                    dp0_dX_f_ss = -p0_unc_f_ss*b0*exp(-
X_f_ss);
                                    dX_dl_f_ss =
b1*abs(dG_dp_f_ss)+b2*abs(dG_dq_f_ss);

                                    %isotropic hardening modulus H0
                                    H0_f_ss = -
dF_dp0_f_ss*dp0_dp0_unc_f_ss*vi/(1-k)*p0_unc_f_ss* ...
                                        (dG_dp_f_ss+omega*dG_dq_f_ss);

                                    %beta, n, b, bmax
                                    beta_f_ss_original = [(p_f_ss-
p_alfa_f_ss)/R-(p_f_ss+pt_f_ss) ...
                                        (q_f_ss-q_alfa_f_ss)/R-q_f_ss];
```

```
                                    beta_f_ss = 1/10*
[(9*theta+1)*beta_f_ss_original(1)-3*(theta-1)*beta_f_ss_original(2) ...
                                        -3*(theta-
1)*beta_f_ss_original(1)+(theta+9)*beta_f_ss_original(2)];

                                    ort_f_ss =
(1/sqrt(dF_dp_f_ss^2+dF_dq_f_ss^2))^normalize* ...
                                        [dF_dp_f_ss dF_dq_f_ss];

                                    b_f_ss = beta_f_ss*ort_f_ss';
                                    b_max_f_ss = max(p0_f_ss*(1-R), ...
                                        2*M*p0_f_ss*(1-
R)/(exp(1)*n*log(r))^(1/n));

                                    %kinematic hardening modulus H'
                                    H_prime_f_ss =
(B(cresc)*b_f_ss/b_max_f_ss)^Y(cresc)*vi/(1-k)*p0_f_ss^3;

                                    if H_prime_f_ss == inf, %try to
rearrange expression of H' if this is infinite
                                        H_prime_f_ss = ((vi/(1-
k)*p0_f_ss^3)^(1/Y(cresc))*B(cresc)*b_f_ss/b_max_f_ss)^Y(cresc);
                                    end;

                                    %bonding hardening modulus Hb
                                    Hb_f_ss = -
dF_dp0_f_ss*dp0_dX_f_ss*dX_dl_f_ss;

                                    %total hardening modulus H
                                    H_f_ss = H0_f_ss + Hb_f_ss +
H_prime_f_ss;

                                    %matrix of plastic compliance
                                    Cp_f_ss = 1/H_f_ss* ...
                                        [ dG_dp_f_ss*dF_dp_f_ss ...
                                        dG_dp_f_ss*dF_dq_f_ss; ...
                                        dG_dq_f_ss*dF_dp_f_ss ...
                                        dG_dq_f_ss*dF_dq_f_ss ];

                                    if abs(H_f_ss) == inf,
                                        Cp_f_ss = zeros(2);
                                    end;

                                    %strain values (2st iteration)
                                    D_eps_p_v_2 = Cp_f_ss(1,:)*[Dp_ss
Dq_ss]';
                                    D_eps_p_s_2 = Cp_f_ss(2,:)*[Dp_ss
Dq_ss]';

                                    %scalar S
                                    if H_f_ss == inf,
                                        S_f_ss = -(dF_dp_f_ss*Dp_ss+ ...
                                            dF_dq_f_ss*Dq_ss)/ ...
                                            (dF_dp_alfa_f_ss*beta_f_ss(1)+
...
                                            dF_dq_alfa_f_ss*beta_f_ss(2));
                                    else
```

```
                                        S_f_ss = -(dF_dp_f_ss*Dp_ss+ ...
                                            dF_dq_f_ss*Dq_ss)/ ...
                                            (dF_dp_alfa_f_ss*beta_f_ss(1)+
...
                                            dF_dq_alfa_f_ss*beta_f_ss(2))/
...
                                            H_f_ss*H_prime_f_ss;
                                    end;

                                    %hardening parameters (2st iteration)
                                    Dp0_unc_2 = vi/(1-k)*p0_unc_f_ss* ...
                                        (D_eps_p_v_2+omega*D_eps_p_s_2);
                                    DX_2 =
b1*abs(D_eps_p_v_2)+b2*abs(D_eps_p_s_2);
                                    Dp_alfa_2 = S_f_ss*beta_f_ss(1);
                                    Dq_alfa_2 = S_f_ss*beta_f_ss(2);

                                    %+++++++ AVERAGE +++++++
                                    D_eps_p_v_ss =
1/2*(D_eps_p_v_1+D_eps_p_v_2);
                                    D_eps_p_s_ss =
1/2*(D_eps_p_s_1+D_eps_p_s_2);
                                    Dp0_unc_ss = 1/2*(Dp0_unc_1+Dp0_unc_2);
                                    DX_ss =1/2*(DX_1+DX_2);
                                    Dp_alfa_ss = 1/2*(Dp_alfa_1+Dp_alfa_2);
                                    Dq_alfa_ss = 1/2*(Dq_alfa_1+Dq_alfa_2);

                                    %+++++++ ERRORS +++++++
                                    E = 1/2*[D_eps_p_v_2-D_eps_p_v_1
                                        D_eps_p_s_2-D_eps_p_s_1];

                                    F_err = (abs(q_f_ss-(q_alfa(i-1) +
Dq_alfa_ss))/(M*(p_f_ss-(p_alfa(i-1) + Dp_alfa_ss))))^n + ...
                                    1/log(r)*log((p_f_ss-(p_alfa(i-1) +
Dp_alfa_ss))/(R*((p0_unc(i-1) + Dp0_unc_ss)*(1+b0*exp(-(X(i-1)+DX_ss))))));

                                    %+++++++ UPDATING VARIABLES FOR NEXT
SUBSTEP/ITERATION +++++++
                                    if norm(E) < SSTOL && abs(F_err) <
YTOL,
                                        T = T + DT; %T next substep
                                    end;

                                    beta_corr =
min(0.8*sqrt(SSTOL/norm(E)),0.8*sqrt(YTOL/abs(F_err)));
                                    beta_corr = max(beta_corr, 0.1);
                                    beta_corr = min(beta_corr, 2);

                                    DT = beta_corr*DT; %DT for next ss or
next iteration of the current ss
                                    if T+DT > 1, %if T next ss + DT next ss
is >1
                                        DT = 1-T;
                                    end;
                                end;
                                %hhhhhhhhhhhhhhhhhhhhhhh substepping
hhhhhhhhhhhhhhhhhhhhhhhhhhhhhh
```

```
                                if err ~= 0, break; end;
                                %writing new variables
                                p(i) = p(i-1) + Dp_ss;
                                q(i) = q(i-1) + Dq_ss;
                                p0_unc(i) = p0_unc(i-1) + Dp0_unc_ss;
                                X(i) = X(i-1) + DX_ss;
                                p0(i) = p0_unc(i)*(1+b0*exp(-X(i)));
                                pt(i) = pti*exp(-X(i));
                                p_alfa(i) = p_alfa(i-1) + Dp_alfa_ss;
                                q_alfa(i) = q_alfa(i-1) + Dq_alfa_ss;
                                d_eps_p_v(i) = D_eps_p_v_ss;
                                d_eps_p_s(i) = D_eps_p_s_ss;
                                dF_dp(i) = 1/2*(dF_dp_i_ss+dF_dp_f_ss);
                                dF_dq(i) = 1/2*(dF_dq_i_ss+dF_dq_f_ss);
                                dF_dp_alfa(i) =
1/2*(dF_dp_alfa_i_ss+dF_dp_alfa_f_ss);
                                dF_dq_alfa(i) =
1/2*(dF_dq_alfa_i_ss+dF_dq_alfa_f_ss);
                                dF_dp0(i) = 1/2*(dF_dp0_i_ss+dF_dp0_f_ss);
                                dp0_dp0_unc(i) =
1/2*(dp0_dp0_unc_i_ss+dp0_dp0_unc_f_ss);
                                dp0_dX(i) = 1/2*(dp0_dX_i_ss+dp0_dX_f_ss);
                                dX_dl(i) = 1/2*(dX_dl_i_ss+dX_dl_f_ss);
                                dG_dp(i) = 1/2*(dG_dp_i_ss+dG_dp_i_ss);
                                dG_dq(i) = 1/2*(dG_dq_i_ss+dG_dq_i_ss);
                                H(i) = 1/2*(H_i_ss+H_f_ss);
                                if H(i) <= 0,
                                    err = 4;
                                    break;
                                end;
                                H0(i) = 1/2*(H0_i_ss+H0_f_ss);
                                H_prime(i) =
1/2*(H_prime_i_ss+H_prime_f_ss);
                                Hb(i) = 1/2*(Hb_i_ss+Hb_f_ss);
                                beta(:,i) = 1/2.*(beta_i_ss'+beta_f_ss');
                                ort(:,i) = 1/2.*(ort_i_ss'+ort_f_ss');
                                b(i) = 1/2*(b_i_ss+b_f_ss);
                                b_max(i) = 1/2*(b_max_i_ss+b_max_f_ss);
                                S(i) = 1/2*(S_i_ss+S_f_ss);

                                %volumetric strain/pore pressure
                                d_v_e(i) = -vi/K*(p(i)-p(i-1));
                                dv_ep(i) = d_v_e(i) - d_eps_p_v(i)*vi;
                                v(i) = v(i-1) + dv_ep(i);
                                d_eps_e_v(i) = -d_v_e(i)/vi;
                                d_eps_v(i) = d_eps_e_v(i) + d_eps_p_v(i);
                                eps_e_v(i) = eps_e_v(i-1) + d_eps_e_v(i);
                                eps_p_v(i) = eps_p_v(i-1) + d_eps_p_v(i);
                                eps_v(i) = eps_e_v(i) + eps_p_v(i);

                                %distortional strain
                                d_eps_e_s(i) = (q(i)-q(i-1))/(3*G);
                                d_eps_s(i) = d_eps_e_s(i) + d_eps_p_s(i);
                                eps_e_s(i) = eps_e_s(i-1) + d_eps_e_s(i);
                                eps_p_s(i) = eps_p_s(i-1) + d_eps_p_s(i);
                                eps_s(i) = eps_e_s(i) + eps_p_s(i);

                                %dilatancy
```

```
                                D(i) = d_eps_p_v(i)/d_eps_p_s(i);

                                %axial strain
                                eps_a(i) = eps_s(i) + eps_v(i)/3;

                                %radial strain
                                eps_r(i) = eps_v(i)/3 - eps_s(i)/2;

                                %check for errors
                                if isnan(p0(i)) == 1 || isreal(p0(i)) == 0,
                                    err = 3; %p0 is not real
                                end;
                                if err ~= 0, break; end;

                                if dilatancy == 2 && ...
                                        m < 1 && ...
                                        abs(q(i)-q_alfa(i))/(p(i)-
p_alfa(i)) > M*(1-m)^(-1/n)|| ...
                                        dilatancy == 1 && ...
                                        abs(q(i)-q_alfa(i))/(p(i)-
p_alfa(i)) > 3,
                                    warn1 = 1;
                                end;

                                %control variables
                                j_max = max(j, j_max);
                                E_eps_max = max(E_eps_max, norm(E));
                                if T < 1, %excluding last step, in which
DT=0
                                    DT_max = max(DT_max, DT);
                                    DT_min = min(DT_min, DT);
                                end;
                            end;

%pppppppppppppppppppppppppppppppppppppppppppppppppppppppppppppppppppppppppp
                            if mod(cyc(1), 100) == 0 || cyc(1) <= 1000,
%writes cycles 1-1000 and one each 100 after that
                                fprintf(JAY, '%u,%u,%g,%g,%g,%u,%u\r\n',
...
                                    [cyc j_max E_eps_max DT_max DT_min i-
numel(q_el) cresc]);
                            end;

%                             if cyc > 10 && abs(eps_s_prec + eps_v_prec/3)
< 1e-15,
%                                 err = 5;
%                             end;

%                             if cyc > 10 && (eps_s_prec + eps_v_prec/3) <
-1e-3,
%                                 err = 6;
%                             end;

                            if cyc > 10 && (eps_s_prec + eps_v_prec/3) >
0.05,
                                err = 7;
                            end;
```

```
                        %check for errors
                        if err ~= 0, break; end;

                        %saving last value of each vector
                        %stress parameters
                        p0_prec = p0(i);
                        p0_unc_prec = p0_unc(i); pt_prec = pt(i);
                        p_alfa_prec = p_alfa(i); q_alfa_prec =
q_alfa(i);

                        %volumetric strain
                        v_prec = v(i); eps_e_v_prec = eps_e_v(i);
                        eps_p_v_prec = eps_p_v(i); eps_v_prec =
eps_v(i);

                        %distortional strain
                        eps_e_s_prec = eps_e_s(i);
                        eps_p_s_prec = eps_p_s(i); eps_s_prec =
eps_s(i);

                        %hardening parameters
                        H_prime_prec = H_prime(i); H0_prec = H0(i);
                        Hb_prec = Hb(i); H_prec = H(i);
                        S_prec = S(i); beta_prec = beta(:,i);
                        ort_prec = ort(:,i); b_prec = b(i); b_max_prec
= b_max(i);
                        D_prec = D(i);
                        dF_dp_prec = dF_dp(i); dF_dq_prec = dF_dq(i);
                        dF_dp_alfa_prec = dF_dp_alfa(i);
                        dF_dq_alfa_prec = dF_dq_alfa(i); dF_dp0_prec =
dF_dp0(i);
                        dp0_dp0_unc_prec = dp0_dp0_unc(i);
                        dp0_dX_prec = dp0_dX(i); dX_dl_prec = dX_dl(i);
                        dG_dp_prec = dG_dp(i); dG_dq_prec = dG_dq(i);

                        %bonding variable
                        X_prec = X(i);

                        %output matrix
                        out = [repmat(cyc, 1, i); eps_a(1:i);
eps_v(1:i);
                            eps_s(1:i); v(1:i); p0(1:i); pt(1:i);
p_alfa(1:i);
                            q_alfa(1:i); p(1:i); q(1:i); H0(1:i);
                            H_prime(1:i); Hb(1:i); S(1:i); dF_dp(1:i);
                            dF_dq(1:i); dF_dp0(1:i); dp0_dp0_unc(1:i);
                            dp0_dX(1:i); dX_dl(1:i); dG_dp(1:i);
dG_dq(1:i);
                            D(1:i); beta(1,1:i); beta(2,1:i);
ort(1,1:i);
                            ort(2,1:i); b(1:i); b_max(1:i); b0*exp(-
X(1:i));
                            repmat(cresc, 1, i); plas(1:i)];

                        %write to file
                        switch output_type,
```

```
                                    case 0
                                        if mod(out(1), 100) == 0 || out(1) <=
100, %first 100 cycles and 1 every 100 cycles after that
                                            fprintf(OUTPUT, format,
out(1:size(out,1), end)); %only prints last point of each cycle;
                                        end;
                                    case 1
                                        if mod(out(1), 100) == 0 || out(1) <=
100, %first 100 cycles and 1 out of 100 cycles after that
                                            if size(out,2) < fil, %if the
output points are less than the user defined filter, the program prints all
the point of the matrix
                                                fprintf(OUTPUT, format, out);
%complete output (all points of the cycles);
                                            else %if the output points are more
than the user defined filter, the filter is applied to reduce the output
size
                                                fprintf(OUTPUT, format,
out(:,round(linspace(cresc,size(out,2),fil)))); %cresc -> this way it
eliminates the first line of the unloading part (which is equal to the last
line of the loading)
                                            end;
                                        end;
                                    case 2
                                        if ismember(out(1), sel_cycles),
%selective output (all points of selected cycles and first and last point
of cycles 1-100 and each 100);
                                            if size(out,2) < fil, %if number of
points in the semi-cycle is less than the user defined filter, print all
the points
                                                fprintf(OUTPUT, format, out);
                                            else %if number of points in the
semi-cycle is greater than the user defined filter, apply filter
                                                if i-numel(q_el) > fil/2, %if
number of points of the plastic part is > fil/2, then print fil/2 points
from the elastic part and fil/2 from the plastic
                                                    fprintf(OUTPUT, format,
out(:,[round(linspace(2,numel(q_el),fil/2))
round(linspace(numel(q_el)+1,size(out,2),fil/2))]));
                                                else %if number of points of
the plastic part is < fil/2, then print all the points of the plastic part
and the necessary points of the elastic part to reach a total number of fil
points
                                                    fprintf(OUTPUT, format,
out(:,[round(linspace(2,numel(q_el),(fil-(i-numel(q_el)))))
round(linspace(numel(q_el)+1,size(out,2),(i-numel(q_el))))]));
                                                end;
                                            end;
                                        else
                                            if mod(out(1), 100) == 0 || out(1)
<= 100, %first 100 cycles and 1 out of 100 cycles after that
                                                fprintf(OUTPUT, format,
out(1:size(out,1), end)); %only prints last point of each cycle;
                                            end;
                                        end;
                                end;
                            end; %cresc loop

                            if warn1 == 1 && flag == 0,
```

```
                            disp ('Warning! Stress ratio exceeds plastic
potential existence domain');
                            flag = 1;
                        end;

                        if cyc > 9 && (mod(cyc,10^floor(log10(cyc))) == 0
|| cyc == n_cyc),
                            Print_results_real_time_cem;
                            flag_print = flag_print + 1;
                        end;

                        if strcmp(name(1:end-1),'User-PC'),
                            if flag_print > 0 && mod(cyc,1000) == 0,
                                pause(0.1);
                            end;
                        end;

                        %check for errors
                        if err ~= 0, break; end;
                    end; %cycle loop
                    %-----------Ending calculation-------------------------
--------------------

                    %close output file
                    fclose('all');

                    if flag_print > 0,
                        hold off;
                    end;

                    %Display error or warning messages and close the
execution
                    if err == 1,
                        disp('Stopped: stress-path is fully elastic');
                    elseif err == 2,
                        disp('Error: Iteration does not converge');
                    elseif err == 3,
                        disp('Error: p0 is not a number');
                    elseif err == 4,
                        disp('Stopped: Specimen failure');
                    elseif err == 5,
                        disp('Error: Cumulated strain is zero');
                    elseif err == 6,
                        disp('Error: Cumulated axial strain is negative');
                    elseif err == 7,
                        disp('Error: Cumulated axial strain is too high');
                    end;

                    if warn1 == 1,
                        disp ('Warning! Stress ratio exceeds plastic
potential existence domain');
                    end;

                    %Display ok message and elapsed time
                    disp(['Created file: ', filename]);
                    mailmessage{1,filenum} = ['Created file: ', filename, '
(', num2str(cyc, '%g'), ' cycles)' 10];
```

```
                    toc
                    disp(' ');

                end; %Y2 loop
            end; %Y1 loop
        end; %B2 loop
    end; %B1 loop
end; %R loop

if mail == 1,
    myaddress = 'miomatlab@gmail.com';
    mypassword = '**********';

    setpref('Internet','E_mail',myaddress);
    setpref('Internet','SMTP_Server','smtp.gmail.com');
    setpref('Internet','SMTP_Username',myaddress);
    setpref('Internet','SMTP_Password',mypassword);

    props = java.lang.System.getProperties;
    props.setProperty('mail.smtp.auth','true');
    props.setProperty('mail.smtp.socketFactory.class', ...
        'javax.net.ssl.SSLSocketFactory');
    props.setProperty('mail.smtp.socketFactory.port','465');

    [~, name] = system('hostname');
    name = name(1:end-1);
    subj = ['Matlab has finished on ', name];
    regexprep(subj,'\r\n|\n|\r','');
    sendmail('fabrizio.paf@gmail.com', subj, mailmessage);
end;
beep;
if err == 0,
    clearvars;
end
```

Strain-driven monotonic triaxial tests

```
%Bubble CASM model in drained conditions for cyclic loading
%TC_5%_e1_s1
fclose all; clearvars;
[~, name] = system('hostname');
%Model parameters
k = 0.0097; l = 0.112; N = 2.352; M = 1.4; K = 9.75e3; G = 4.5e3;% K =
9.75e5; G = 4.5e5;
r = 3.7; n = 2.2; m = 2; omega = 0; theta = 1;%e-5;
pti = 0; b0 = 0; b1 = 0; b2 = b1; %X0 = 2.1312; b0=exp(X0)-1
R_v = 0.01;
B_v_1 = 5e-13;
B_v_2 = B_v_1;
Y_v_1 = 0.5;
Y_v_2 = Y_v_1;
dilatancy = 1; %1- Rowe; - Yu
normalize = 1; %1- normal vector (ort) to the yield surface is normalized
in the determination of scalar b; 0- ort is not normalized

%Initial stress point and preconsolidation point
```

```
qi = 0; sigma_c = 100; pinit = sigma_c+qi/3;  vi = 1.6; p0_unc_i = exp((N-
vi)/(1-k));
p0i = p0_unc_i*(1+b0);
D_e = [K, 0; 0, 3*G];

%loading path and load increment
ratio = 3; %dq/dp
eps_a_f = 0.2;
Dq_el = 0.01; %elastic load increment
SSTOL = 1e-9;
YTOL = 10;

%Define output type
fil = 2000; %max num of points plotted in half cycle

%Choose if mail is sent
mail = 0; %1-send e-mail; 0- do not send
mailmessage =
cell(1,numel(R_v)*numel(B_v_1)*numel(B_v_2)*numel(Y_v_1)*numel(Y_v_2));

%preparing flags
num_flag = max(10,ceil(eps_a_f/0.01));
flag2(1:num_flag) = 0;
values_fl(1:num_flag) = 0;
for fl = 1:num_flag,
    values_fl(fl) = round(eps_a_f*fl/num_flag*100)/100;
end;

%Preallocation
preall = 20000;
p = zeros(1,preall); q = zeros(1,preall); p_alfa = zeros(1,preall);
q_alfa = zeros(1,preall); p0 = zeros(1,preall); p0_unc = zeros(1,preall);
pt = zeros(1,preall); X = zeros(1,preall); H0 = zeros(1,preall); Hb =
zeros(1,preall);
H_prime = zeros(1,preall); H = zeros(1,preall); b = zeros(1,preall);
b_max = zeros(1,preall); beta = zeros(2,preall); ort = zeros(2,preall);
S = zeros(1,preall); Dil = zeros(1,preall); dF_dp = zeros(1,preall);
dF_dq = zeros(1,preall); dF_dp_alfa = zeros(1,preall); dF_dq_alfa =
zeros(1,preall);
dF_dp0 = zeros(1,preall); dp0_dp0_unc = zeros(1,preall); dp0_dX =
zeros(1,preall);
dX_dl = zeros(1,preall); dG_dp = zeros(1,preall); dG_dq = zeros(1,preall);
d_eps_p_v = zeros(1,preall); d_eps_p_s = zeros(1,preall);
dv_ep = zeros(1,preall); d_v_e = zeros(1,preall); v = zeros(1,preall);
d_eps_e_v = zeros(1,preall); d_eps_v = zeros(1,preall);
eps_v = zeros(1,preall); d_eps_e_s = zeros(1,preall);
d_eps_s = zeros(1,preall); eps_e_s = zeros(1,preall); eps_p_s =
zeros(1,preall);
eps_s = zeros(1,preall); eps_a = zeros(1,preall); eps_r = zeros(1,preall);
plas = zeros(1,preall); filenum = 0;

for i_R = 1:numel(R_v),
    for i_B_1 = 1:numel(B_v_1),
        for i_B_2 = 1:numel(B_v_2),
            for i_Y_1 = 1:numel(Y_v_1),
                for i_Y_2 = 1:numel(Y_v_2),
```

```
                    %start to measure elapsed time
                    tic

                    filenum = filenum+1;
                    flag_print = 0;
                    %Model parameters input
                    R = R_v(i_R); B = [B_v_1(i_B_1) B_v_2(i_B_2)]; Y =
[Y_v_1(i_Y_1) Y_v_2(i_Y_2)];

                    %Initial Centre of the bubble
                    %calculating ultimate point with bisection method
                    P_try = -pti;
                    P_a = pinit; Q_a = qi;
                    Q_try = qi + ratio*(P_try-pinit);
                    F_ref = 1;
                    P_bis = (P_try+P_a)/2;
                    Q_bis = (Q_try+Q_a)/2;

                    while abs(F_ref) > 1e-13,     %tolerance
                        P_bis = (P_try+P_a)/2;
                        Q_bis = (Q_try+Q_a)/2;
                        F_ref = (abs(Q_bis)/(M*(P_bis+pti)))^n +
1/log(r)*log((P_bis+pti)/p0i);
                        if F_ref < 0,
                            P_a = P_bis;
                            Q_a = Q_bis;
                        else
                            P_try = P_bis;
                            Q_try = Q_bis;
                        end;
                    end;

                    pU_inf = P_bis;
                    qU_inf = Q_bis;

                    %centre that gives sigma_y=sigma_c
                    p_alfa_i = pinit - R*(pU_inf+pti);
                    q_alfa_i = qi - R*qU_inf;

                    %                   %centre that gives sigma_y=(p0,0)
                    %                   p_alfa_i = 1.00*(pinit - R*p0i);
%1.004
                    %                   q_alfa_i = qi;

                    disp(['Current parameters are: R= ', num2str(R), ...
                        '; Y= ', num2str(Y(1), '%g'), ',', num2str(Y(2),
'%g'), ...
                        '; B= ', num2str(B(1), '%g'), ',', num2str(B(2),
'%g')]);

                    %output file
                    fnformat = ['TX_bubble_CASM_v1_1_', 'drain', '_R_',
num2str(R, '%g'), ...
                        '_Y_', num2str(Y(1), '%g'), ',', num2str(Y(2),
'%g'), ...
                        '_B_', num2str(B(1), '%g'), ',', num2str(B(2),
'%g'), ...
```

```
                        '_o_', num2str(omega), '_M_', num2str(M), '_n_',
...
                        num2str(n), '_r_', num2str(r), '_k_', num2str(k),
...
                        '_l_', num2str(l), '_center_', num2str(p_alfa_i),
...
                        ',', num2str(q_alfa_i), '_b0_', num2str(b0),
'_b1_', ...
                        num2str(b1, '%g'), '_b2_', num2str(b2, '%g'), ...
                        '_pti_', num2str(pti), '_theta_', num2str(theta,
'%g'), ...
                        '_K_', num2str(K, '%g'), '_G_', num2str(G, '%g')];

                    switch dilatancy
                        case 1
                            filename = [fnformat, '_Rowe.csv'];
                        case 2
                            filename = [fnformat, '_m_', num2str(m),
'_Gen_CASM.csv'];
                        otherwise
                            error('Wrong input!');
                    end;

                    JAY = fopen('j.csv', 'w+');
                    OUTPUT = fopen(filename, 'w+');
                    while OUTPUT == -1 || JAY == -1,
                        disp('Output file already open. Please close file
and press ENTER to continue');
                        input(' ');
                        JAY = fopen('j.csv', 'w');
                        OUTPUT = fopen(filename, 'w');
                    end;

                    header = ['eps_a_cum,eps_v_cum,eps_s_cum,v,p0,' ...
                        'pt,p_alfa,q_alfa,p,q,H0,H_prime,Hb,S,dF_dp,dF_dq,'
...

'dF_dp0,dp0_dp0_unc,dp0_dX,dX_dl,dG_dp,dG_dq,D,beta_x,' ...
                        'beta_y,norm_x,norm_y,b,b_max,b_dash,plas\r\n'];

                    fprintf(OUTPUT, header);
                    fprintf(JAY,
'j_max,norm(E_eps_max),DT_max,DT_min,i_plas\r\n');
                    ncols = numel(strfind(header, ',')) + 1;
                    format = ['%g', repmat(',%g', 1, ncols-1), '\r\n'];
%use ',%.7g' for more decimal points
                    fprintf(OUTPUT, format, 0, 0, 0, vi, p0i, pti, ...
                        p_alfa_i, q_alfa_i, pinit, qi, ...
                        [], [], [], [], [], [], [], [], [], [], ...
                        [], [], [], [], [], [], [], [], [], ...
                        b0, 0);

                    %initializing variables
                    %stress variables
                    p0_prec = p0i;
                    p0_unc_prec = p0_unc_i; pt_prec = pti;
                    p_alfa_prec = p_alfa_i; q_alfa_prec = q_alfa_i;
                    p0(1) = p0i; p0_unc(1) = p0_unc_i; pt(1) = pti;
```

```
                    p_alfa(1) = p_alfa_i; q_alfa(1) = q_alfa_i;

                    %volume/pore pressure variables
                    %volumetric strain
                    v(1) = vi;
                    v_prec = vi;

                    %distortional strain
                    eps_s_prec = 0; eps_e_s_prec = 0; eps_p_s_prec = 0;

                    %hardening variables
                    H_prime_prec = 0; H0_prec = 0; Hb_prec = 0; H_prec = 0;
S_prec = 0;
                    beta_prec = [0 0]; ort_prec = [0 0]; b_prec = 0;
                    b_max_prec = 0; D_prec = 0;
                    dF_dp_prec = 0; dF_dq_prec = 0; dF_dp_alfa_prec = 0;
                    dF_dq_alfa_prec = 0; dF_dp0_prec = 0;
                    dp0_dp0_unc_prec = 0; dp0_dX_prec = 0; dX_dl_prec = 0;
                    dG_dp_prec = 0; dG_dq_prec = 0;

                    %bonding variable
                    X_prec = 0;

                    %system variables
                    err = 0; warn1 = 0; flag = 0;

                    %-----------Starting calculation-----------------------
---------------------

                    if err ~= 0, break; end;

                    %                     if cyc <= 1000 || mod(cyc, 1000)
== 0 || cyc == n_cyc,
                    %                         disp(['Processing cycle ',
int2str(cyc), ' of ', int2str(n_cyc), '...']);
                    %                     end;

                    %calculating yield point
                    tol_Y = 1e-10;
                    p_try = R*p0_prec + p_alfa_prec;
                    q_try = qi + ratio*(p_try-pinit);
                    p_ab = [pinit p_try];
                    q_ab = [qi q_try];
                    f_A =
f_yield_f(p_ab(1),q_ab(1),p_alfa_prec,q_alfa_prec,p0_prec,M,n,r,R);
                    f_B =
f_yield_f(p_ab(2),q_ab(2),p_alfa_prec,q_alfa_prec,p0_prec,M,n,r,R);

                    if p_ab(1) < p_alfa_prec, %check if the first point is
within the domain of existence
                        p_ab(1) = p_alfa_prec;
                        q_ab(1) = 3*(p_alfa_prec-sigma_c);
                        f_A = 100;
                    end;

                    if f_B > tol_Y, %elasto-plastic SP
```

```
                        p_bis = mean(p_ab);
                        q_bis = mean(q_ab);
                        f_bis =
f_yield_f(p_bis,q_bis,p_alfa_prec,q_alfa_prec,p0_prec,M,n,r,R);

                        while abs(f_bis) > tol_Y,     %tolerance
                            if f_bis < 0,
                                p_ab(1) = p_bis;
                                q_ab(1) = q_bis;
                            else
                                p_ab(2) = p_bis;
                                q_ab(2) = q_bis;
                            end;
                            p_bis = mean(p_ab);
                            q_bis = mean(q_ab);
                            f_bis =
f_yield_f(p_bis,q_bis,p_alfa_prec,q_alfa_prec,p0_prec,M,n,r,R);
                        end;
                        p_y = p_bis; q_y = q_bis; %yielding point
                    else
                        err = 1; %fully elastic stress path
                    end;

                    if err ~= 0, continue; end;

                    n_int_el = max(2,ceil(abs(q_y-qi)/Dq_el));
                    q_el = linspace(qi, q_y, n_int_el);
                    p_el = (q_el-qi)/ratio + pinit;
                    p(1:numel(p_el)) = p_el;
                    q(1:numel(q_el)) = q_el;


%eeeeeeeeeeeeeeeeeeeeeeeeeeeeeeeeeeeeeeeeeeeeeeeeeeeeeeeeeeeeeeeeeeeeeeeeeeee
                    %ELASTIC DOMAIN
                    ind = 1:numel(q_el);
                    p0(ind) = p0_prec; p0_unc(ind) = p0_unc_prec; pt(ind) =
pt_prec;
                    p_alfa(ind) = p_alfa_prec; q_alfa(ind) = q_alfa_prec;
                    H0(ind) = H0_prec; H_prime(ind) = H_prime_prec; Hb(ind)
= Hb_prec;
                    H(ind) = H_prec; X(ind) = X_prec; S(ind) = S_prec;
Dil(ind) = D_prec;
                    beta(1,ind) = beta_prec(1); beta(2,ind) = beta_prec(2);
                    ort(1,ind) = ort_prec(1); ort(2,ind) = ort_prec(2);
                    b(ind) = b_prec; b_max(ind) = b_max_prec;
                    dF_dp(ind) = dF_dp_prec; dF_dq(ind) = dF_dq_prec;
                    dF_dp_alfa(ind) = dF_dp_alfa_prec;
                    dF_dq_alfa(ind) = dF_dq_alfa_prec;
                    dF_dp0(ind) = dF_dp0_prec;
                    dp0_dp0_unc(ind) = dp0_dp0_unc_prec;
                    dp0_dX(ind) = dp0_dX_prec; dX_dl(ind) = dX_dl_prec;
                    dG_dp(ind) = dG_dp_prec; dG_dq(ind) = dG_dq_prec;

                    %volumetric strain
                    d_v_e(ind) = [0 -vi/K*diff(p(ind))];
                    v(ind) = v_prec + cumsum(d_v_e(ind));
                    d_eps_e_v(ind) = -d_v_e(ind)./vi;
```

```
                    d_eps_p_v(ind) = 0;
                    d_eps_v(ind) = d_eps_e_v(ind) + d_eps_p_v(ind);
                    eps_v(ind) = cumsum(d_eps_v(ind));

                    %distortional strain
                    d_eps_e_s(ind) = [0 diff(q_el)/(3*G)];
                    d_eps_p_s(ind) = 0;
                    d_eps_s(ind) = d_eps_e_s(ind) + d_eps_p_s(ind);
                    eps_e_s(ind) = eps_e_s_prec + cumsum(d_eps_e_s(ind));
                    eps_p_s(ind) = eps_p_s_prec + cumsum(d_eps_p_s(ind));
                    eps_s(ind) = eps_s_prec + cumsum(d_eps_s(ind));

                    %axial strain
                    eps_a(ind) = eps_s(ind) + eps_v(ind)/3;

                    %radial strain
                    eps_r(ind) = eps_v(ind)/3 - eps_s(ind)/2;

                    plas(ind) = 1;

%eeeeeeeeeeeeeeeeeeeeeeeeeeeeeeeeeeeeeeeeeeeeeeeeeeeeeeeeeeeeeeeeeeeeeeeeeee


%ppppppppppppppppppppppppppppppppppppppppppppppppppppppppppppppppppppppppppp
                    %ELASTOPLASTIC DOMAIN
                    T = 0;
                    DT = 1;
                    i = numel(q_el);
                    j_max = 0;
                    DT_max = 0;
                    DT_min = 1;
                    D_eps_a_s = eps_a_f - eps_a(ind(end));

                    %                      while mod(i-
numel(q_el),10000)~=0,
                    while T < 1 && DT > 1e-9 && err == 0, %cycle on load
increments
                        %initialize variables
                        i = i+1;

                        if mod(i,preall) == 0,
                            p(numel(p)+1:numel(p)+preall) =
zeros(1,preall);
                            q(numel(q)+1:numel(q)+preall) =
zeros(1,preall);
                            p_alfa(numel(p_alfa)+1:numel(p_alfa)+preall) =
zeros(1,preall);
                            q_alfa(numel(q_alfa)+1:numel(q_alfa)+preall) =
zeros(1,preall);
                            p0(numel(p0)+1:numel(p0)+preall) =
zeros(1,preall);
                            p0_unc(numel(p0_unc)+1:numel(p0_unc)+preall) =
zeros(1,preall);
                            pt(numel(pt)+1:numel(pt)+preall) =
zeros(1,preall);
                            X(numel(X)+1:numel(X)+preall) =
zeros(1,preall);
```

```
                            H0(numel(H0)+1:numel(H0)+preall) =
zeros(1,preall);
                            Hb(numel(Hb)+1:numel(Hb)+preall) =
zeros(1,preall);
                            H_prime(numel(H_prime)+1:numel(H_prime)+preall)
= zeros(1,preall);
                            H(numel(H)+1:numel(H)+preall) =
zeros(1,preall);
                            b(numel(b)+1:numel(b)+preall) =
zeros(1,preall);
                            b_max(numel(b_max)+1:numel(b_max)+preall) =
zeros(1,preall);
                            beta(:,size(beta,2)+1:size(beta,2)+preall) =
zeros(2,preall);
                            ort(:,size(ort,2)+1:size(ort,2)+preall) =
zeros(2,preall);
                            S(numel(S)+1:numel(S)+preall) =
zeros(1,preall);
                            Dil(numel(Dil)+1:numel(Dil)+preall) =
zeros(1,preall);
                            dF_dp(numel(dF_dp)+1:numel(dF_dp)+preall) =
zeros(1,preall);
                            dF_dq(numel(dF_dq)+1:numel(dF_dq)+preall) =
zeros(1,preall);

dF_dp_alfa(numel(dF_dp_alfa)+1:numel(dF_dp_alfa)+preall) = zeros(1,preall);

dF_dq_alfa(numel(dF_dq_alfa)+1:numel(dF_dq_alfa)+preall) = zeros(1,preall);
                            dF_dp0(numel(dF_dp0)+1:numel(dF_dp0)+preall) =
zeros(1,preall);

dp0_dp0_unc(numel(dp0_dp0_unc)+1:numel(dp0_dp0_unc)+preall) =
zeros(1,preall);
                            dp0_dX(numel(dp0_dX)+1:numel(dp0_dX)+preall) =
zeros(1,preall);
                            dX_dl(numel(dX_dl)+1:numel(dX_dl)+preall) =
zeros(1,preall);
                            dG_dp(numel(dG_dp)+1:numel(dG_dp)+preall) =
zeros(1,preall);
                            dG_dq(numel(dG_dq)+1:numel(dG_dq)+preall) =
zeros(1,preall);

d_eps_p_v(numel(d_eps_p_v)+1:numel(d_eps_p_v)+preall) = zeros(1,preall);

d_eps_p_s(numel(d_eps_p_s)+1:numel(d_eps_p_s)+preall) = zeros(1,preall);
                            dv_ep(numel(dv_ep)+1:numel(dv_ep)+preall) =
zeros(1,preall);
                            d_v_e(numel(d_v_e)+1:numel(d_v_e)+preall) =
zeros(1,preall);
                            v(numel(v)+1:numel(v)+preall) =
zeros(1,preall);

d_eps_e_v(numel(d_eps_e_v)+1:numel(d_eps_e_v)+preall) = zeros(1,preall);
                            d_eps_v(numel(d_eps_v)+1:numel(d_eps_v)+preall)
= zeros(1,preall);
                            eps_v(numel(eps_v)+1:numel(eps_v)+preall) =
zeros(1,preall);

d_eps_e_s(numel(d_eps_e_s)+1:numel(d_eps_e_s)+preall) = zeros(1,preall);
```

```
                            d_eps_s(numel(d_eps_s)+1:numel(d_eps_s)+preall)
= zeros(1,preall);
                            eps_e_s(numel(eps_e_s)+1:numel(eps_e_s)+preall)
= zeros(1,preall);
                            eps_p_s(numel(eps_p_s)+1:numel(eps_p_s)+preall)
= zeros(1,preall);
                            eps_s(numel(eps_s)+1:numel(eps_s)+preall) =
zeros(1,preall);
                            eps_a(numel(eps_a)+1:numel(eps_a)+preall) =
zeros(1,preall);
                            eps_r(numel(eps_r)+1:numel(eps_r)+preall) =
zeros(1,preall);
                            plas(numel(plas)+1:numel(plas)+preall) =
zeros(1,preall);
                        end;

                        j = 0;
                        R_err = 1.1*SSTOL;
                        R_eps_max = 0;
                        F_err = 2*YTOL;
                        plas(i) = 2;

                        %initializing variables of the next cycle
                        pinit_ss = p(i-1);
                        qi_ss = q(i-1);
                        p_alfa_i_ss = p_alfa(i-1);
                        q_alfa_i_ss = q_alfa(i-1);
                        p0_i_ss = p0(i-1);
                        p0_unc_i_ss = p0(i-1)/(1+b0*exp(-X(i-1)));
                        pt_i_ss = pti*exp(-X(i-1));
                        X_i_ss = X(i-1);

                        %hhhhhhhhhhhhhhhhhhhhhhhh substepping
hhhhhhhhhhhhhhhhhhhhhhhhhhhhhhhh
                        while abs(R_err) > SSTOL || isreal(R_err) == 0,% ||
abs(F_err) > YTOL,
                            if err ~= 0, break; end;
                            j = j+1;
                            D_eps_a_ss = DT*D_eps_a_s;

                            if j == 10000 || (T < 1 && DT < 1e-9),
                                err = 2; break;
                            end;

                            %+++++++ FIRST ITERATION +++++++
                            %first derivatives of F
                            dF_dp_i_ss =
dF_dp_f(pinit_ss,qi_ss,p_alfa_i_ss,q_alfa_i_ss,M,n,r);
                            dF_dq_i_ss =
dF_dq_f(pinit_ss,qi_ss,p_alfa_i_ss,q_alfa_i_ss,M,n);
                            if qi_ss == q_alfa_i_ss,
                                dF_dq_i_ss = 0;
                            end;
                            F_prime_i_ss = [dF_dp_i_ss; ...
                                dF_dq_i_ss];
                            dF_dp_alfa_i_ss = -dF_dp_i_ss;
                            dF_dq_alfa_i_ss = -dF_dq_i_ss;
                            dF_dp0_i_ss =  -1/(p0_i_ss*log(r));
```

```
                            %first derivatives of G (depending on flow
rule)
                            switch dilatancy
                                case 1 %Bubble Rowe flow rule
                                    dG_dp_i_ss = 27*(M.*(pinit_ss-
p_alfa_i_ss)-abs(qi_ss-q_alfa_i_ss))/ ...
                                        ((2*abs(qi_ss-
q_alfa_i_ss)+3*(pinit_ss-p_alfa_i_ss))*(3*(pinit_ss-p_alfa_i_ss)-abs(qi_ss-
q_alfa_i_ss)));
                                    dG_dq_i_ss = 3*((3*M+9)*(pinit_ss-
p_alfa_i_ss)-2*M*abs(qi_ss-q_alfa_i_ss))/ ...
                                        ((3*(pinit_ss-
p_alfa_i_ss)+2*abs(qi_ss-q_alfa_i_ss))*(3*(pinit_ss-p_alfa_i_ss)-abs(qi_ss-
q_alfa_i_ss)))* ...
                                        sign(qi_ss-q_alfa_i_ss);

                                case 2 %Bubble General CASM flow rule
                                    dG_dp_i_ss = (1-(abs(qi_ss-
q_alfa_i_ss)/(M*(pinit_ss-p_alfa_i_ss)))^n)/ ...
                                        ((pinit_ss-
p_alfa_i_ss)*(1+(abs(qi_ss-q_alfa_i_ss)/(M*(pinit_ss-p_alfa_i_ss)))^n*(m-
1)));
                                    dG_dq_i_ss = m*(abs(qi_ss-
q_alfa_i_ss)/(pinit_ss-p_alfa_i_ss))^(n-1)/ ...
                                        (M^n*(pinit_ss-
p_alfa_i_ss)*(1+(abs(qi_ss-q_alfa_i_ss)/(M*(pinit_ss-p_alfa_i_ss)))^n*(m-
1)))* ...
                                        sign(qi_ss-q_alfa_i_ss);
                            end;

                            G_prime_i_ss = [dG_dp_i_ss; dG_dq_i_ss];

                            %first derivatives of bonding
                            dp0_dp0_unc_i_ss = 1 + b0*exp(-X_i_ss);
                            dp0_dX_i_ss = -p0_unc_i_ss*b0*exp(-X_i_ss);
                            dX_dl_i_ss =
b1*abs(dG_dp_i_ss)+b2*abs(dG_dq_i_ss);

                            %isotropic hardening modulus H0
                            H0_i_ss = -dF_dp0_i_ss*dp0_dp0_unc_i_ss*vi/(1-
k)*p0_unc_i_ss* ...
                                (dG_dp_i_ss+omega*dG_dq_i_ss);

                            %beta, n, b, bmax
                            beta_i_ss_original = [(pinit_ss-p_alfa_i_ss)/R-
(pinit_ss+pt_i_ss) ...
                                (qi_ss-q_alfa_i_ss)/R-qi_ss];

                            beta_i_ss = 1/10*
[(9*theta+1)*beta_i_ss_original(1)-3*(theta-1)*beta_i_ss_original(2) ...
                                -3*(theta-
1)*beta_i_ss_original(1)+(theta+9)*beta_i_ss_original(2)];

                            ort_i_ss =
(1/sqrt(dF_dp_i_ss^2+dF_dq_i_ss^2))^normalize* ...
                                [dF_dp_i_ss dF_dq_i_ss];
```

```
                            b_i_ss = beta_i_ss*ort_i_ss';
                            b_max_i_ss = max(p0_i_ss*(1-R), ...
                                2*M*p0_i_ss*(1-R)/(exp(1)*n*log(r))^(1/n));

                            %kinematic hardening modulus H'
                            H_prime_i_ss =
(B(1)*b_i_ss/b_max_i_ss)^Y(1)*vi/(1-k)*p0_i_ss^3;

                            if H_prime_i_ss == inf, %try to rearrange
expression of H' if this is infinite
                                H_prime_i_ss = ((vi/(1-
k)*p0_i_ss^3)^(1/Y(1))*B(1)*b_i_ss/b_max_i_ss)^Y(1);
                            end;

                            %bonding hardening modulus Hb
                            Hb_i_ss = -dF_dp0_i_ss*dp0_dX_i_ss*dX_dl_i_ss;

                            %total hardening modulus H
                            H_i_ss = H0_i_ss + Hb_i_ss + H_prime_i_ss;

                            %stiffness matrix
                            D_ep_i_ss = D_e -
D_e*G_prime_i_ss*F_prime_i_ss'*D_e/ ...
                                (H_i_ss+F_prime_i_ss'*D_e*G_prime_i_ss);

                            %strain values (1st iteration)
                            Dq_1 = 9*det(D_ep_i_ss)/ ...
                                (9*D_ep_i_ss(1,1)-3*D_ep_i_ss(1,2)- ...

3*D_ep_i_ss(2,1)+D_ep_i_ss(2,2))*D_eps_a_ss;
                            Dp_1 = Dq_1/ratio;
                            D_eps_v_1 = 3*(D_ep_i_ss(2,2)-
3*D_ep_i_ss(1,2))/ ...
                                (9*D_ep_i_ss(1,1)-3*D_ep_i_ss(1,2)- ...

3*D_ep_i_ss(2,1)+D_ep_i_ss(2,2))*D_eps_a_ss;
                            D_eps_s_1 = D_eps_a_ss - D_eps_v_1/3;

                            D_eps_p_v_1 = D_eps_v_1 - Dp_1/K;
                            D_eps_p_s_1 = D_eps_s_1 - Dq_1/(3*G);

                            %scalar S
                            if H_i_ss == inf,
                                S_i_ss = -(dF_dp_i_ss*Dp_1+ ...
                                    dF_dq_i_ss*Dq_1)/ ...
                                    (dF_dp_alfa_i_ss*beta_i_ss(1)+ ...
                                    dF_dq_alfa_i_ss*beta_i_ss(2));
                            else
                                S_i_ss = -(dF_dp_i_ss*Dp_1+ ...
                                    dF_dq_i_ss*Dq_1)/ ...
                                    (dF_dp_alfa_i_ss*beta_i_ss(1)+ ...
                                    dF_dq_alfa_i_ss*beta_i_ss(2))/ ...
                                    H_i_ss*H_prime_i_ss;
                            end;

                            %hardening parameters (1st iteration)
```

```
                            Dp0_unc_1 = vi/(1-k)*p0_unc_i_ss* ...
                                (D_eps_p_v_1+omega*D_eps_p_s_1);
                            DX_1 =
b1*abs(D_eps_p_v_1)+b2*abs(D_eps_p_s_1);
                            Dp_alfa_1 = S_i_ss*beta_i_ss(1);
                            Dq_alfa_1 = S_i_ss*beta_i_ss(2);


                            %+++++++ SECOND ITERATION +++++++
                            p_f_ss = pinit_ss + Dp_1;
                            q_f_ss = qi_ss + Dq_1;
                            p0_unc_f_ss = p0_unc_i_ss + Dp0_unc_1;
                            X_f_ss = X_i_ss + DX_1;
                            p0_f_ss = p0_unc_f_ss*(1+b0*exp(-X_f_ss));
                            pt_f_ss = pti*exp(-X_f_ss);
                            p_alfa_f_ss = p_alfa_i_ss + Dp_alfa_1;
                            q_alfa_f_ss = q_alfa_i_ss + Dq_alfa_1;

                            %first derivatives of F
                            dF_dp_f_ss =
dF_dp_f(p_f_ss,q_f_ss,p_alfa_f_ss,q_alfa_f_ss,M,n,r);
                            dF_dq_f_ss =
dF_dq_f(p_f_ss,q_f_ss,p_alfa_f_ss,q_alfa_f_ss,M,n);
                            if q_f_ss == q_alfa_f_ss,
                                dF_dq_f_ss = 0;
                            end;
                            F_prime_f_ss = [dF_dp_f_ss; ...
                                dF_dq_f_ss];
                            dF_dp_alfa_f_ss = -dF_dp_f_ss;
                            dF_dq_alfa_f_ss = -dF_dq_f_ss;
                            dF_dp0_f_ss =  -1/(p0_f_ss*log(r));

                            if isreal(dF_dp_f_ss) == 0,
                                DT = 0.5*DT;
                                continue;
                            end;

                            %first derivatives of G (depending on flow
rule)
                            switch dilatancy
                                case 1 %Bubble Rowe flow rule
                                    dG_dp_f_ss = 27*(M.*(p_f_ss-
p_alfa_f_ss)-abs(q_f_ss-q_alfa_f_ss))/ ...
                                        ((2*abs(q_f_ss-
q_alfa_f_ss)+3*(p_f_ss-p_alfa_f_ss))*(3*(p_f_ss-p_alfa_f_ss)-abs(q_f_ss-
q_alfa_f_ss)));
                                    dG_dq_f_ss = 3*((3*M+9)*(p_f_ss-
p_alfa_f_ss)-2*M*abs(q_f_ss-q_alfa_f_ss))/ ...
                                        ((3*(p_f_ss-
p_alfa_f_ss)+2*abs(q_f_ss-q_alfa_f_ss))*(3*(p_f_ss-p_alfa_f_ss)-abs(q_f_ss-
q_alfa_f_ss)))* ...
                                        sign(q_f_ss-q_alfa_f_ss);

                                case 2 %Bubble General CASM flow rule
                                    dG_dp_f_ss = (1-(abs(q_f_ss-
q_alfa_f_ss)/(M*(p_f_ss-p_alfa_f_ss)))^n)/ ...
```

```
                                        ((p_f_ss-
p_alfa_f_ss)*(1+(abs(q_f_ss-q_alfa_f_ss)/(M*(p_f_ss-p_alfa_f_ss)))^n*(m-
1)));
                                    dG_dq_f_ss = m*(abs(q_f_ss-
q_alfa_f_ss)/(p_f_ss-p_alfa_f_ss))^(n-1)/ ...
                                        (M^n*(p_f_ss-
p_alfa_f_ss)*(1+(abs(q_f_ss-q_alfa_f_ss)/(M*(p_f_ss-p_alfa_f_ss)))^n*(m-
1)))* ...
                                        sign(q_f_ss-q_alfa_f_ss);
                                end;

                                G_prime_f_ss = [dG_dp_f_ss; dG_dq_f_ss];

                                %first derivatives of bonding
                                dp0_dp0_unc_f_ss = 1 + b0*exp(-X_f_ss);
                                dp0_dX_f_ss = -p0_unc_f_ss*b0*exp(-X_f_ss);
                                dX_dl_f_ss =
b1*abs(dG_dp_f_ss)+b2*abs(dG_dq_f_ss);

                                %isotropic hardening modulus H0
                                H0_f_ss = -dF_dp0_f_ss*dp0_dp0_unc_f_ss*vi/(1-
k)*p0_unc_f_ss* ...
                                    (dG_dp_f_ss+omega*dG_dq_f_ss);

                                %beta, n, b, bmax
                                beta_f_ss_original = [(p_f_ss-p_alfa_f_ss)/R-
(p_f_ss+pt_f_ss) ...
                                    (q_f_ss-q_alfa_f_ss)/R-q_f_ss];

                                beta_f_ss = 1/10*
[(9*theta+1)*beta_f_ss_original(1)-3*(theta-1)*beta_f_ss_original(2) ...
                                    -3*(theta-
1)*beta_f_ss_original(1)+(theta+9)*beta_f_ss_original(2)];

                                ort_f_ss =
(1/sqrt(dF_dp_f_ss^2+dF_dq_f_ss^2))^normalize* ...
                                    [dF_dp_f_ss dF_dq_f_ss];

                                b_f_ss = beta_f_ss*ort_f_ss';
                                b_max_f_ss = max(p0_f_ss*(1-R), ...
                                    2*M*p0_f_ss*(1-R)/(exp(1)*n*log(r))^(1/n));

                                %kinematic hardening modulus H'
                                H_prime_f_ss =
(B(1)*b_f_ss/b_max_f_ss)^Y(1)*vi/(1-k)*p0_f_ss^3;

                                if H_prime_f_ss == inf, %try to rearrange
expression of H' if this is infinite
                                    H_prime_f_ss = ((vi/(1-
k)*p0_f_ss^3)^(1/Y(1))*B(1)*b_f_ss/b_max_f_ss)^Y(1);
                                end;

                                %bonding hardening modulus Hb
                                Hb_f_ss = -dF_dp0_f_ss*dp0_dX_f_ss*dX_dl_f_ss;

                                %total hardening modulus H
                                H_f_ss = H0_f_ss + Hb_f_ss + H_prime_f_ss;
```

```
                            %stiffness matrix
                            D_ep_f_ss = D_e -
D_e*G_prime_f_ss*F_prime_f_ss'*D_e/ ...
                                (H_f_ss+F_prime_f_ss'*D_e*G_prime_f_ss);

                            %strain values (2st iteration)
                            Dq_2 = 9*det(D_ep_f_ss)/ ...
                                (9*D_ep_f_ss(1,1)-3*D_ep_f_ss(1,2)- ...

3*D_ep_f_ss(2,1)+D_ep_f_ss(2,2))*D_eps_a_ss;
                            Dp_2 = Dq_2/ratio;
                            D_eps_v_2 = 3*(D_ep_f_ss(2,2)-
3*D_ep_f_ss(1,2))/ ...
                                (9*D_ep_f_ss(1,1)-3*D_ep_f_ss(1,2)- ...

3*D_ep_f_ss(2,1)+D_ep_f_ss(2,2))*D_eps_a_ss;
                            D_eps_s_2 = D_eps_a_ss - D_eps_v_2/3;

                            D_eps_p_v_2 = D_eps_v_2 - Dp_2/K;
                            D_eps_p_s_2 = D_eps_s_2 - Dq_2/(3*G);

                            %scalar S
                            if H_f_ss == inf,
                                S_f_ss = -(dF_dp_f_ss*Dp_2+ ...
                                    dF_dq_f_ss*Dq_2)/ ...
                                    (dF_dp_alfa_f_ss*beta_f_ss(1)+ ...
                                    dF_dq_alfa_f_ss*beta_f_ss(2));
                            else
                                S_f_ss = -(dF_dp_f_ss*Dp_2+ ...
                                    dF_dq_f_ss*Dq_2)/ ...
                                    (dF_dp_alfa_f_ss*beta_f_ss(1)+ ...
                                    dF_dq_alfa_f_ss*beta_f_ss(2))/ ...
                                    H_f_ss*H_prime_f_ss;
                            end;

                            %hardening parameters (2st iteration)
                            Dp0_unc_2 = vi/(1-k)*p0_unc_f_ss* ...
                                (D_eps_p_v_2+omega*D_eps_p_s_2);
                            DX_2 =
b1*abs(D_eps_p_v_2)+b2*abs(D_eps_p_s_2);
                            Dp_alfa_2 = S_f_ss*beta_f_ss(1);
                            Dq_alfa_2 = S_f_ss*beta_f_ss(2);

                            %+++++++ AVERAGE +++++++
                            D_eps_v_ss = 1/2*(D_eps_v_1+D_eps_v_2);
                            D_eps_s_ss = 1/2*(D_eps_s_1+D_eps_s_2);
                            Dp0_unc_ss = 1/2*(Dp0_unc_1+Dp0_unc_2);
                            DX_ss = 1/2*(DX_1+DX_2);
                            Dp_alfa_ss = 1/2*(Dp_alfa_1+Dp_alfa_2);
                            Dq_alfa_ss = 1/2*(Dq_alfa_1+Dq_alfa_2);
                            Dp_ss = 1/2*(Dp_1+Dp_2);
                            Dq_ss = 1/2*(Dq_1+Dq_2);

                            %+++++++ ERRORS +++++++
                            E = 1/2*(Dq_2-Dq_1);
                            R_err = E/(q(i-1)+Dq_ss);
```

```
                            F_err = (abs(q_f_ss-(q_alfa(i-1) +
Dq_alfa_ss))/(M*(p_f_ss-(p_alfa(i-1) + Dp_alfa_ss))))^n + ...
                                1/log(r)*log((p_f_ss-(p_alfa(i-1) +
Dp_alfa_ss))/(R*((p0_unc(i-1) + Dp0_unc_ss)*(1+b0*exp(-(X(i-1)+DX_ss))))));

                            %+++++++ UPDATING VARIABLES FOR NEXT
SUBSTEP/ITERATION +++++++
                            if abs(R_err) < SSTOL && isreal(R_err),% &&
abs(F_err) < YTOL,
                                T = T + DT; %T next substep
                            end;

                            beta_corr = 0.8*sqrt(SSTOL/abs(R_err));
%min(0.8*sqrt(SSTOL/R_err),0.8*sqrt(YTOL/abs(F_err)));
                            beta_corr = max(beta_corr, 0.1);
                            beta_corr = min(beta_corr, 2);

                            if isreal(R_err) == 0,
                                beta_corr = 0.5;
                            end;

                            DT = beta_corr*DT; %DT for next ss or next
iteration of the current ss
                            if T+DT > 1, %if T next ss + DT next ss is >1
                                DT = 1-T;
                            end;
                            %                                   if err ~= 0,
return; end;
                        end;
                        %hhhhhhhhhhhhhhhhhhhhhhhh substepping
hhhhhhhhhhhhhhhhhhhhhhhhhhhhhh



                        %writing new variables
                        p(i) = p(i-1) + Dp_ss;
                        q(i) = q(i-1) + Dq_ss;
                        p0_unc(i) = p0_unc(i-1) + Dp0_unc_ss;
                        X(i) = X(i-1) + DX_ss;
                        p0(i) = p0_unc(i)*(1+b0*exp(-X(i)));
                        pt(i) = pti*exp(-X(i));
                        p_alfa(i) = p_alfa(i-1) + Dp_alfa_ss;
                        q_alfa(i) = q_alfa(i-1) + Dq_alfa_ss;
                        d_eps_v(i) = D_eps_v_ss;
                        d_eps_s(i) = D_eps_s_ss;
                        d_eps_p_v(i) = 1/2*(D_eps_p_v_1+D_eps_p_v_2);
                        d_eps_p_s(i) = 1/2*(D_eps_p_s_1+D_eps_p_s_2);
                        dF_dp(i) = 1/2*(dF_dp_i_ss+dF_dp_f_ss);
                        dF_dq(i) = 1/2*(dF_dq_i_ss+dF_dq_f_ss);
                        dF_dp_alfa(i) =
1/2*(dF_dp_alfa_i_ss+dF_dp_alfa_f_ss);
                        dF_dq_alfa(i) =
1/2*(dF_dq_alfa_i_ss+dF_dq_alfa_f_ss);
                        dF_dp0(i) = 1/2*(dF_dp0_i_ss+dF_dp0_f_ss);
                        dp0_dp0_unc(i) =
1/2*(dp0_dp0_unc_i_ss+dp0_dp0_unc_f_ss);
                        dp0_dX(i) = 1/2*(dp0_dX_i_ss+dp0_dX_f_ss);
```

```
                        dX_dl(i) = 1/2*(dX_dl_i_ss+dX_dl_f_ss);
                        dG_dp(i) = 1/2*(dG_dp_i_ss+dG_dp_i_ss);
                        dG_dq(i) = 1/2*(dG_dq_i_ss+dG_dq_i_ss);
                        H(i) = 1/2*(H_i_ss+H_f_ss);
                        H0(i) = 1/2*(H0_i_ss+H0_f_ss);
                        H_prime(i) = 1/2*(H_prime_i_ss+H_prime_f_ss);
                        Hb(i) = 1/2*(Hb_i_ss+Hb_f_ss);
                        beta(:,i) = 1/2.*(beta_i_ss'+beta_f_ss');
                        ort(:,i) = 1/2.*(ort_i_ss'+ort_f_ss');
                        b(i) = 1/2*(b_i_ss+b_f_ss);
                        b_max(i) = 1/2*(b_max_i_ss+b_max_f_ss);
                        S(i) = 1/2*(S_i_ss+S_f_ss);

                        %volumetric strain/pore pressure
                        dv_ep(i) = -d_eps_v(i)*vi;
                        v(i) = v(i-1) + dv_ep(i);
                        eps_v(i) = eps_v(i-1) + d_eps_v(i);

                        %distortional strain
                        eps_s(i) = eps_s(i-1) + d_eps_s(i);

                        %dilatancy
                        Dil(i) = d_eps_p_v(i)/d_eps_p_s(i);

                        %axial strain
                        eps_a(i) = eps_a(i-1) + D_eps_a_ss;

                        %radial strain
                        eps_r(i) = eps_v(i)/3 - eps_s(i)/2;

                        %check for errors
                        if isnan(p0(i)) == 1 || isreal(p0(i)) == 0,
                            err = 3; %p0 is not real
                        end;
                        %                               if err ~= 0, return;
end;

                        if dilatancy == 2 && ...
                                m < 1 && ...
                                abs(q(i)-q_alfa(i))/(p(i)-p_alfa(i)) >
M*(1-m)^(-1/n)|| ...
                                dilatancy == 1 && ...
                                abs(q(i)-q_alfa(i))/(p(i)-p_alfa(i)) > 3,
                            warn1 = 1;
                        end;

                        %control variables
                        j_max = max(j, j_max);
                        R_eps_max = max(R_eps_max, abs(R_err));
                        if T < 1, %excluding last step, in which DT=0
                            DT_max = max(DT_max, DT);
                            DT_min = min(DT_min, DT);
                        end;
                        fprintf(JAY, '%u,%g,%g,%g,%u\r\n', ...
                            [j_max R_eps_max DT_max DT_min i-numel(q_el)]);

                        posit_fl = find((values_fl/eps_a(i)) > 1, 1);
```

```
                        if posit_fl > 1,
                            message = ['Axial strain = ',
num2str(values_fl(posit_fl-1)*100), '% ...'];
                        end;

                        if posit_fl > 1,
                            if flag2(posit_fl-1)==0,
                                disp(message);
                                flag2(posit_fl-1)=1;
                            end;
                        end;

                    end;

%ppppppppppppppppppppppppppppppppppppppppppppppppppppppppppppppppppppppppppp


                    %                      if cyc > 10 && abs(eps_s_prec +
eps_v_prec/3) < 1e-15,
                    %                          err = 5;
                    %                      end;
                    %
                    %                      if cyc > 10 && (eps_s_prec +
eps_v_prec/3) < -1e-3,
                    %                          err = 6;
                    %                      end;
                    %
                    %                      if cyc > 10 && (eps_s_prec +
eps_v_prec/3) > 0.05,
                    %                          err = 7;
                    %                      end;

                    %check for errors
                    %                          if err ~= 0, break; end;

                    %                          %saving last value of each
vector
                    %                          %stress parameters
                    %                          p0_prec = p0(i);
                    %                          p0_unc_prec = p0_unc(i);
pt_prec = pt(i);
                    %                          p_alfa_prec = p_alfa(i);
q_alfa_prec = q_alfa(i);

                    %                          %volumetric strain
                    %                          v_prec = v(i);

                    %                          %distortional strain
                    %                          eps_e_s_prec = eps_e_s(i);
                    %                          eps_p_s_prec = eps_p_s(i);
eps_s_prec = eps_s(i);

                    %                          %hardening parameters
                    %                          H_prime_prec = H_prime(i);
H0_prec = H0(i);
```

```
                    %                           Hb_prec = Hb(i); H_prec =
H(i);
                    %                           S_prec = S(i); beta_prec =
beta(:,i);
                    %                           ort_prec = ort(:,i); b_prec =
b(i); b_max_prec = b_max(i);
                    %                           D_prec = Dil(i);
                    %                           dF_dp_prec = dF_dp(i);
dF_dq_prec = dF_dq(i);
                    %                           dF_dp_alfa_prec =
dF_dp_alfa(i);
                    %                           dF_dq_alfa_prec =
dF_dq_alfa(i); dF_dp0_prec = dF_dp0(i);
                    %                           dp0_dp0_unc_prec =
dp0_dp0_unc(i);
                    %                           dp0_dX_prec = dp0_dX(i);
dX_dl_prec = dX_dl(i);
                    %                           dG_dp_prec = dG_dp(i);
dG_dq_prec = dG_dq(i);

                    %                           %bonding variable
                    %                           X_prec = X(i);

                    %output matrix
                    out = [eps_a(1:i); eps_v(1:i);
                        eps_s(1:i); v(1:i); p0(1:i); pt(1:i); p_alfa(1:i);
                        q_alfa(1:i); p(1:i); q(1:i); H0(1:i);
                        H_prime(1:i); Hb(1:i); S(1:i); dF_dp(1:i);
                        dF_dq(1:i); dF_dp0(1:i); dp0_dp0_unc(1:i);
                        dp0_dX(1:i); dX_dl(1:i); dG_dp(1:i); dG_dq(1:i);
                        Dil(1:i); beta(1,1:i); beta(2,1:i); ort(1,1:i);
                        ort(2,1:i); b(1:i); b_max(1:i); b0*exp(-X(1:i));
                        plas(1:i)];

                    %write to file

                    if size(out,2) < fil, %if number of points in the semi-
cycle is less than the user defined filter, print all the points
                        fprintf(OUTPUT, format, out);
                    else %if number of points in the semi-cycle is greater
than the user defined filter, apply filter
                        %print all the points of the plastic part and the
necessary points of the elastic part to reach a total number of fil points
                        fprintf(OUTPUT, format, out(:,[1:numel(q_el)
round(linspace(numel(q_el)+1,size(out,2),fil))]));
                    end;


                    if warn1 == 1 && flag == 0,
                        disp ('Warning! Stress ratio exceeds plastic
potential existence domain');
                        flag = 1;
                    end;

                    %                           if cyc > 9 &&
(mod(cyc,10^floor(log10(cyc))) == 0 || cyc == n_cyc),
```

```
                    %
Print_results_real_time_cem;
                    %                               flag_print = flag_print +
1;
                    %                           end;

                    %                           if strcmp(name(1:end-
1),'User-PC'),
                    %                               if flag_print > 0 &&
mod(cyc,1000) == 0,
                    %                                   pause(0.1);
                    %                               end;
                    %                           end;

                    %check for errors
                    %                           if err ~= 0, break; end;
                    %                       end; %printing block
                    %-----------Ending calculation-------------------------
--------------------

                    %close output file
                    fclose('all');

                    if flag_print > 0,
                        hold off;
                    end;

                    %Display error or warning messages and close the
execution
                    if err == 1,
                        disp('Stopped: stress-path is fully elastic');
                    elseif err == 2,
                        disp('Error: Iteration does not converge');
                    elseif err == 3,
                        disp('Error: p0 is not a number');
                    elseif err == 5,
                        disp('Error: Cumulated strain is zero');
                    elseif err == 6,
                        disp('Error: Cumulated axial strain is negative');
                    elseif err == 7,
                        disp('Error: Cumulated axial strain is too high');
                    end;

                    if warn1 == 1,
                        disp ('Warning! Stress ratio exceeds plastic
potential existence domain');
                    end;

                    %Display ok message and elapsed time
                    disp(['Created file: ', filename]);
                    mailmessage{1,filenum} = ['Created file: ', filename,
10];


                    toc
                    disp(' ');

                end; %Y2 loop
```

```
            end; %Y1 loop
        end; %B2 loop
    end; %B1 loop
end; %R loop

if mail == 1,
    myaddress = 'miomatlab@gmail.com';
    mypassword = '*********';

    setpref('Internet','E_mail',myaddress);
    setpref('Internet','SMTP_Server','smtp.gmail.com');
    setpref('Internet','SMTP_Username',myaddress);
    setpref('Internet','SMTP_Password',mypassword);

    props = java.lang.System.getProperties;
    props.setProperty('mail.smtp.auth','true');
    props.setProperty('mail.smtp.socketFactory.class', ...
        'javax.net.ssl.SSLSocketFactory');
    props.setProperty('mail.smtp.socketFactory.port','465');

    [~, name] = system('hostname');
    name = name(1:end-1);
    subj = ['Matlab has finished on ', name];
    regexprep(subj,'\r\n|\n|\r','');
    sendmail('fabrizio.paf@gmail.com', subj, mailmessage);
end;
beep;
if err == 0,
    %     clearvars;
end
```

ANNEX 6: RESULTS FOR THE CALIBRATED MODEL

Table A.1 – Calibration of drained tests with Rowe flow rule

C	e_i	s1			s2			s3		
		R	B	ψ	R	B	ψ	R	B	ψ
0	e1	0.02	7.578	5000	0.02	2.875	-1100	0.02	2.256	-1650
	e2	0.02	26.9	450	0.02	4.275	-2300	0.02	5.524	-20000
3	e1	0.02	9.139	8000	0.02	2.779	-3000	0.02	2.097	-3000
	e2	0.02	4	35	0.02	2.262	-750	0.02	2.125	280
5	e1	0.02	4.55	30	0.02	2.107	-9000	0.02	2.208	900
	e2	0.02	3.3	35	0.02	2.065	-5000	0.02	2.155	2300
7	e1	0.02	3.3	35	0.02	2.204	-9000	0.02	2.213	550
	e2	0.02	3.21	-950	0.02	2.55	-70	0.02	3.052	1000

$b_1 = b_2$ = 1e-4 for all the cemented tests

Table A.2 – Calibration of undrained tests with Rowe flow rule

C	e_i	s1		
		R	B	ψ
3	e3	0.02	7.36	500
5	e1	0.02	8.07	650
7	e2	0.02	8.985	1500

$b_1 = b_2$ = 1e-4 for all tests

Table A.3 – Calibration of drained tests with Yu flow rule

C	e_i	s1				s2				s3			
		R	B	ψ	m	R	B	ψ	m	R	B	ψ	m
0	e1	0.02	7.5	1000	0.49	0.02	3.045	-200	0.3	0.02	2.313	-390	0.49
	e2	0.02	24.65	130	0.68	0.02	4.405	-500	0.49	0.02	5.448	-3500	0.49
3	e1	0.02	9.088	2000	0.55								

$b_1 = b_2$ = 1e-4 for the cemented test

Uncemented specimens

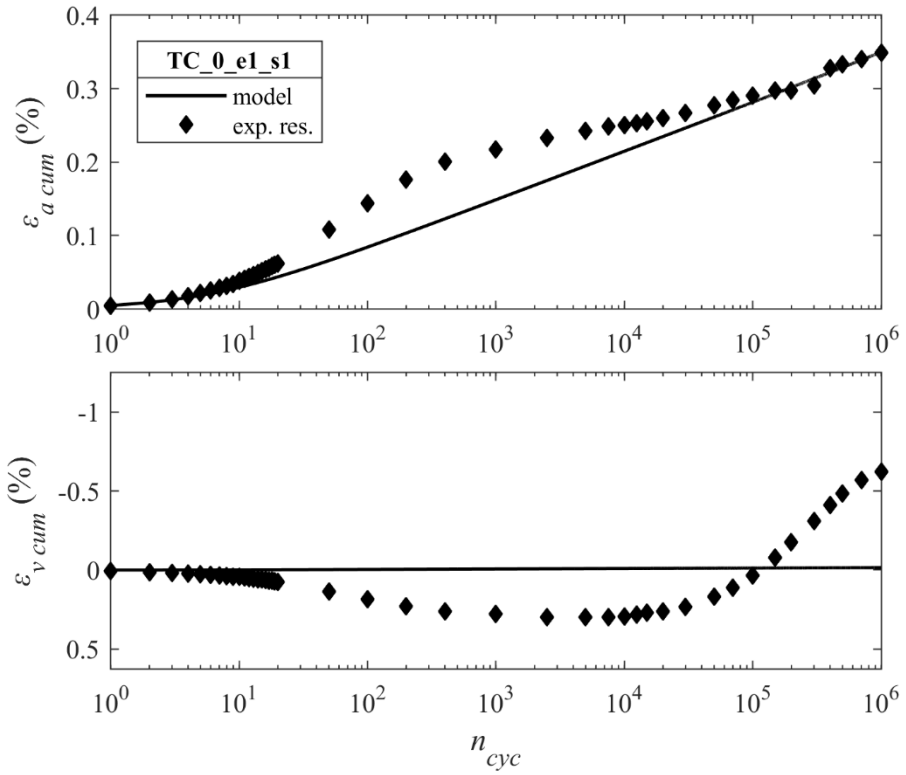

Fig. A.7 – TC_0%_e1_s1: Rowe flow rule

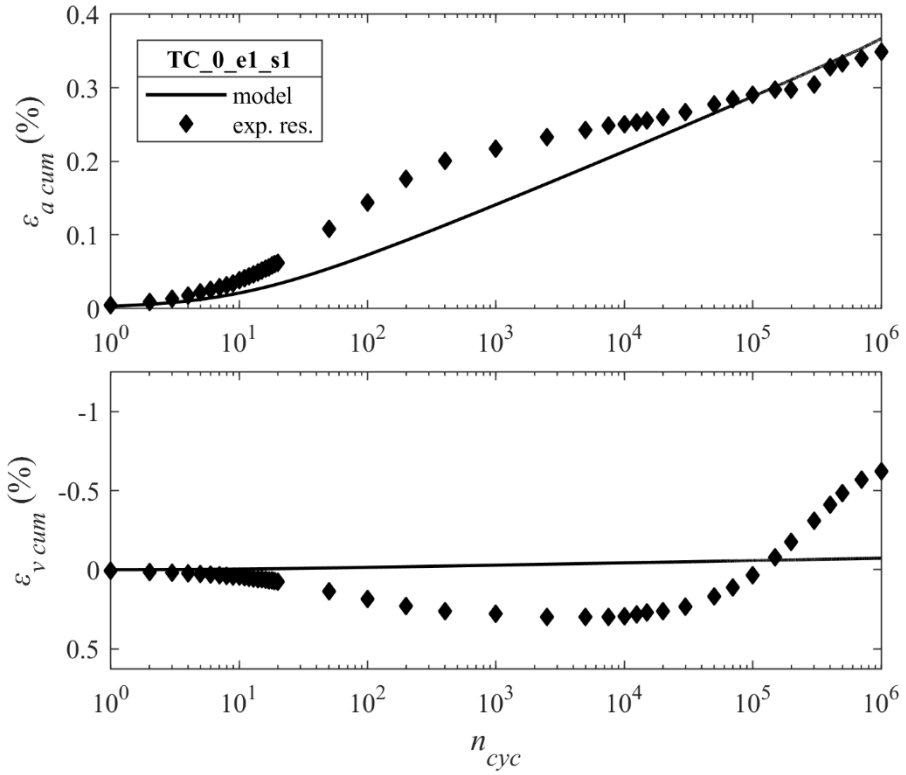

Fig. A.8 – TC_0%_e1_s1: Yu flow rule

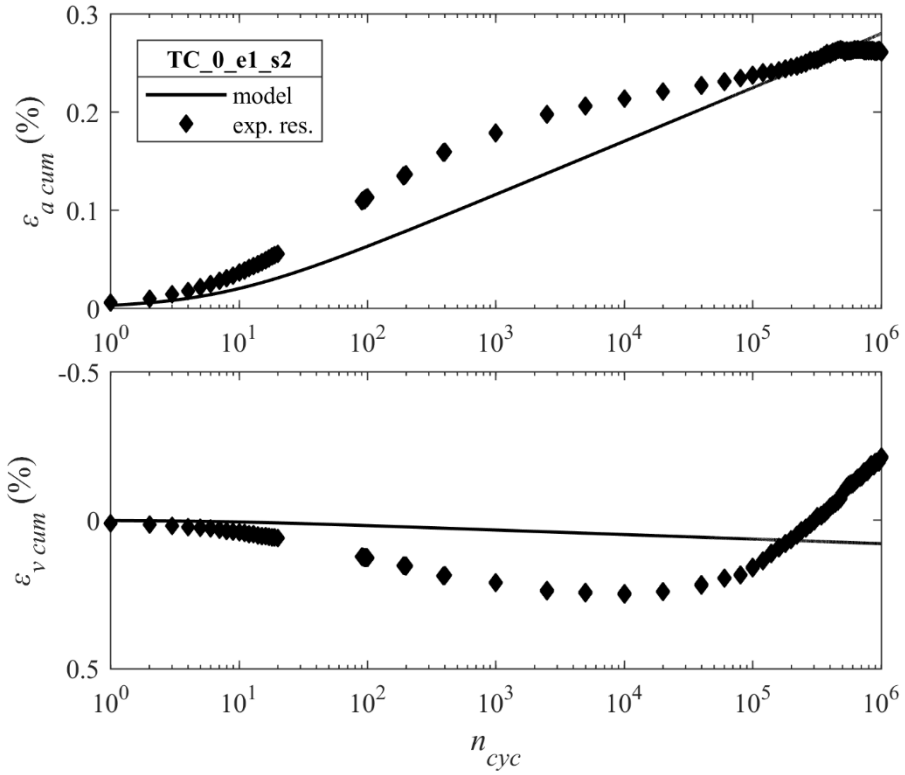

Fig. A.9 – TC_0%_e1_s2: Rowe flow rule

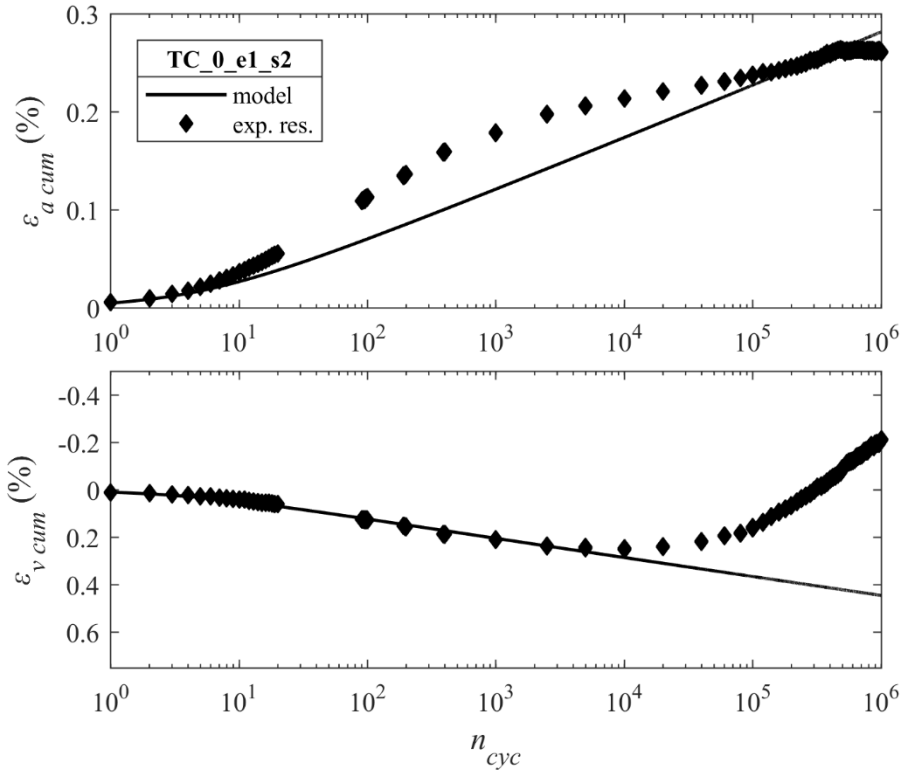

Fig. A.10 – TC_0%_e1_s2: Yu flow rule

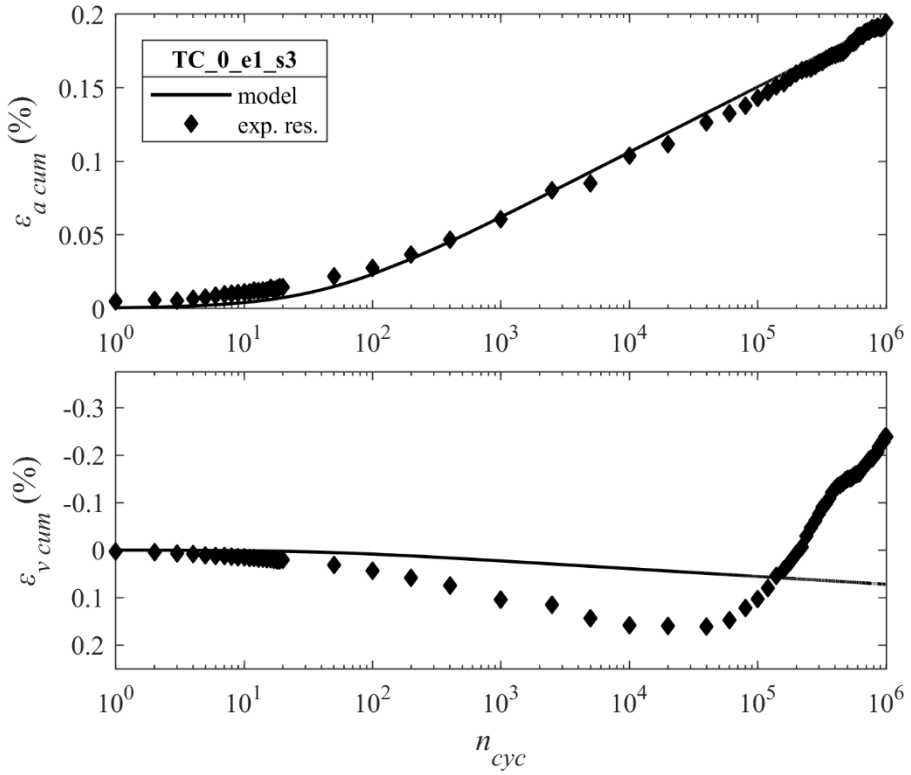

Fig. A.11 – TC_0%_e1_s3: Rowe flow rule

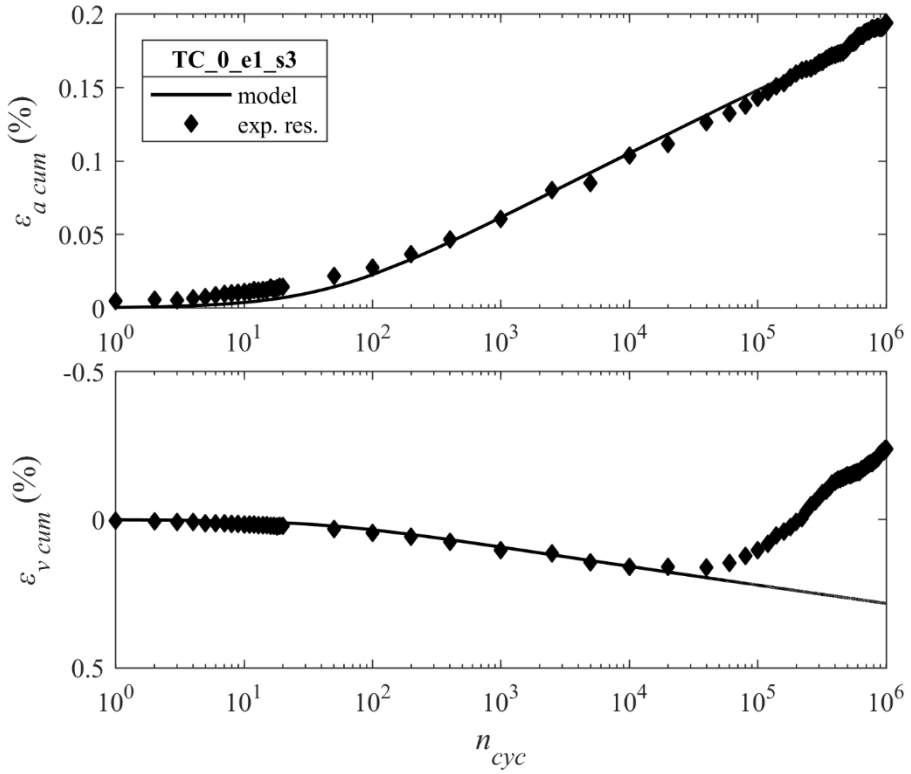

Fig. A.12 – TC_0%_e1_s3: Yu flow rule

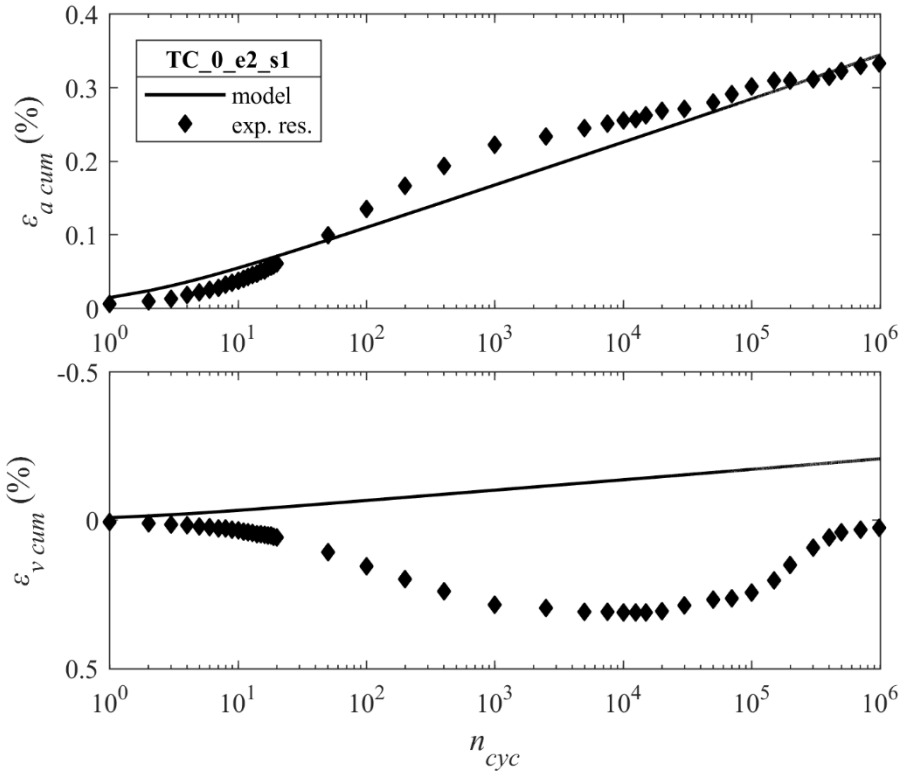

Fig. A.13 – TC_0%_e2_s1: Rowe flow rule

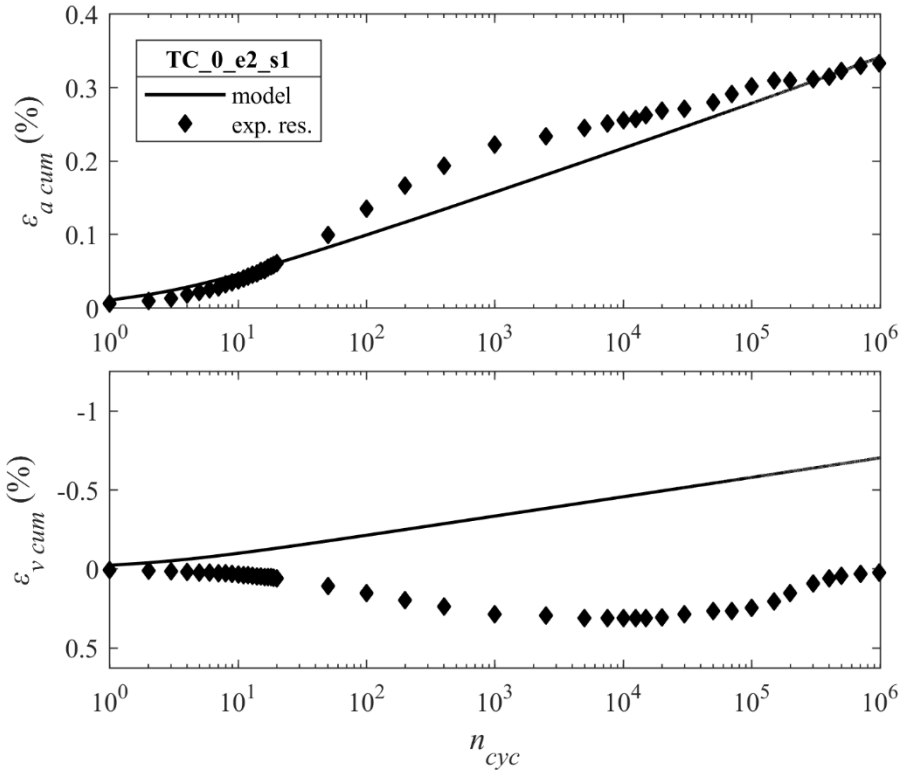

Fig. A.14 – TC_0%_e2_s1: Yu flow rule

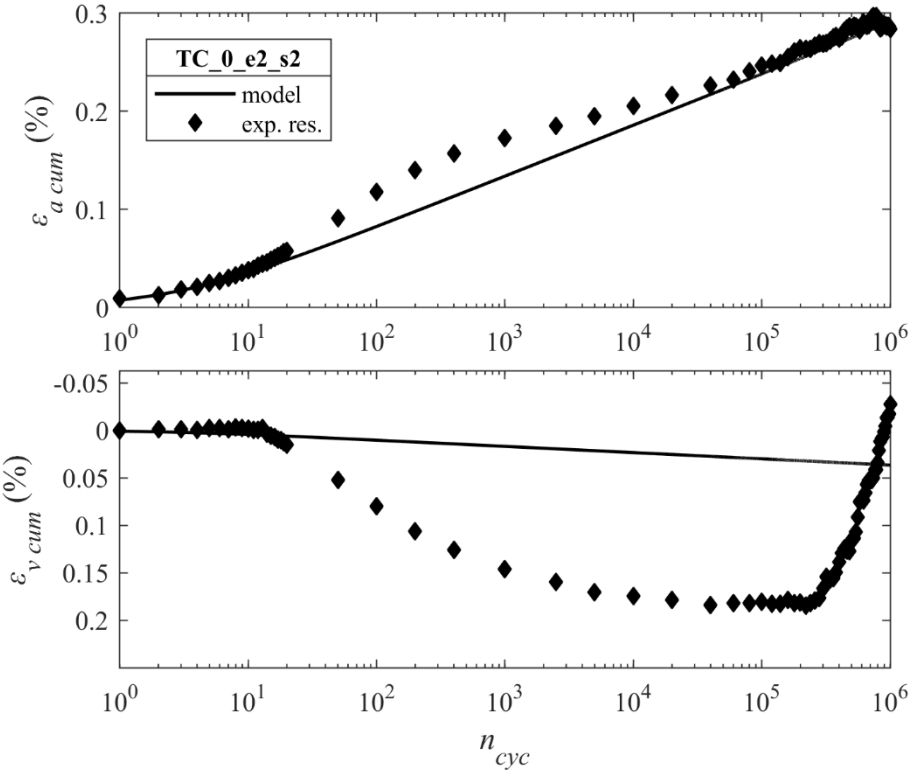

Fig. A.15 – TC_0%_e2_s2: Rowe flow rule

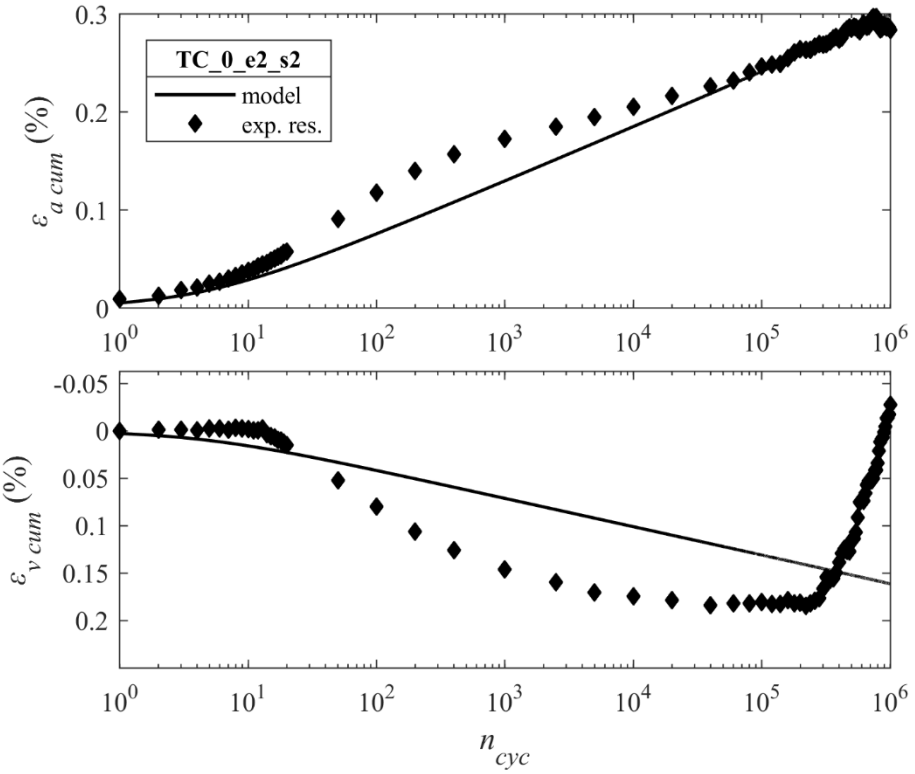

Fig. A.16 – TC_0%_e2_s2: Yu flow rule

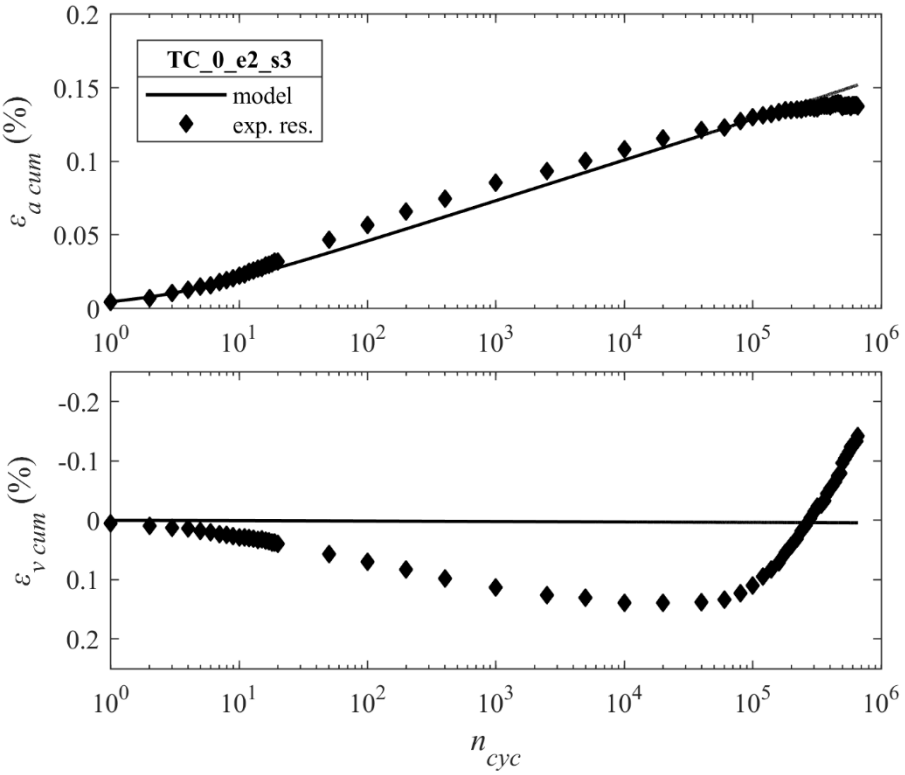

Fig. A.17 – TC_0%_e2_s3: Rowe flow rule

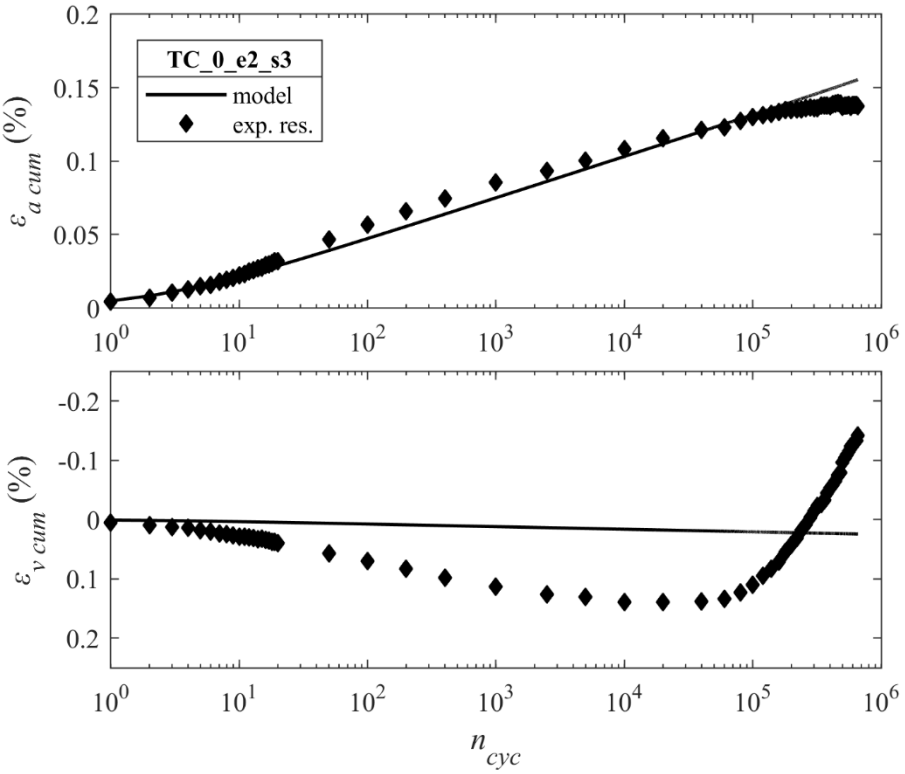

Fig. A.18 – TC_0%_e2_s3: Yu flow rule

3% cement specimens

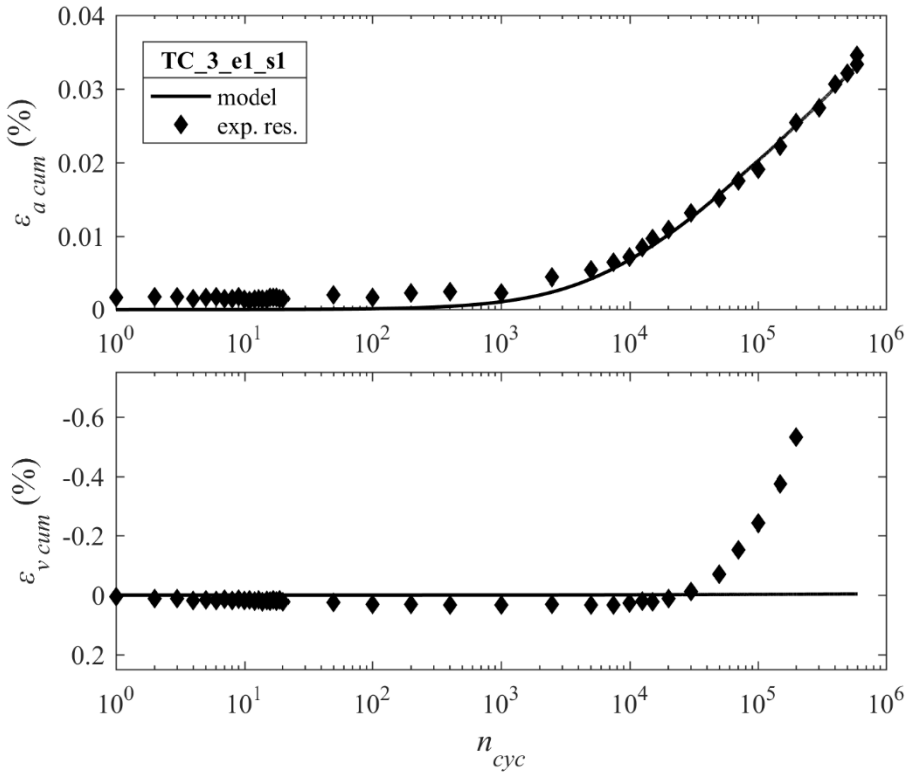

Fig. A.19 – TC_3%_e1_s1: Rowe flow rule

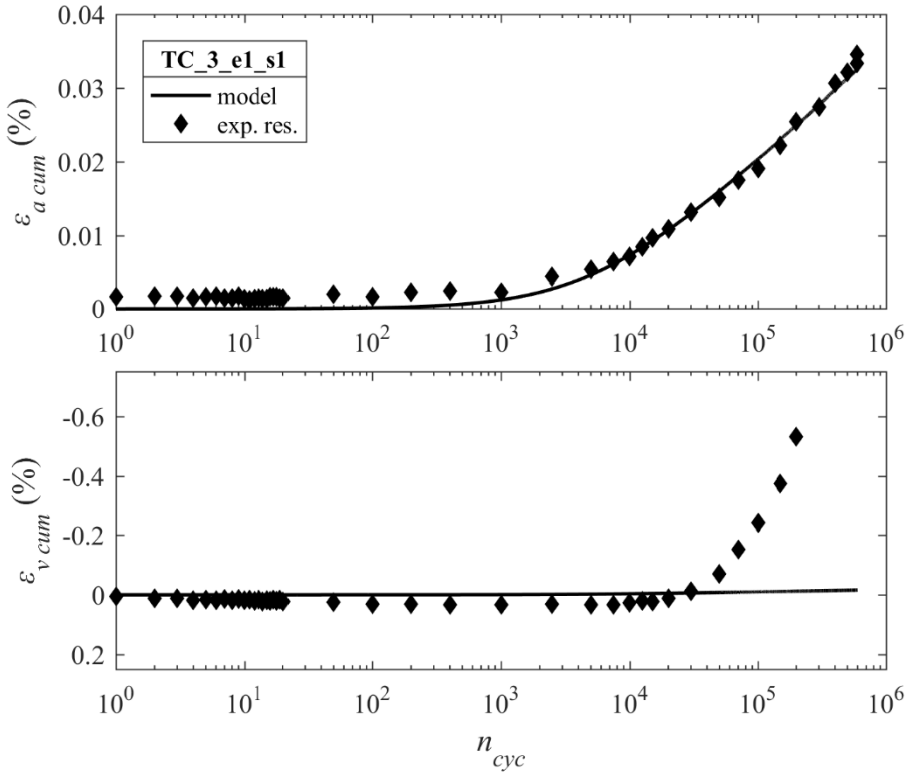

Fig. A.20 – TC_3%_e1_s1: Yu flow rule

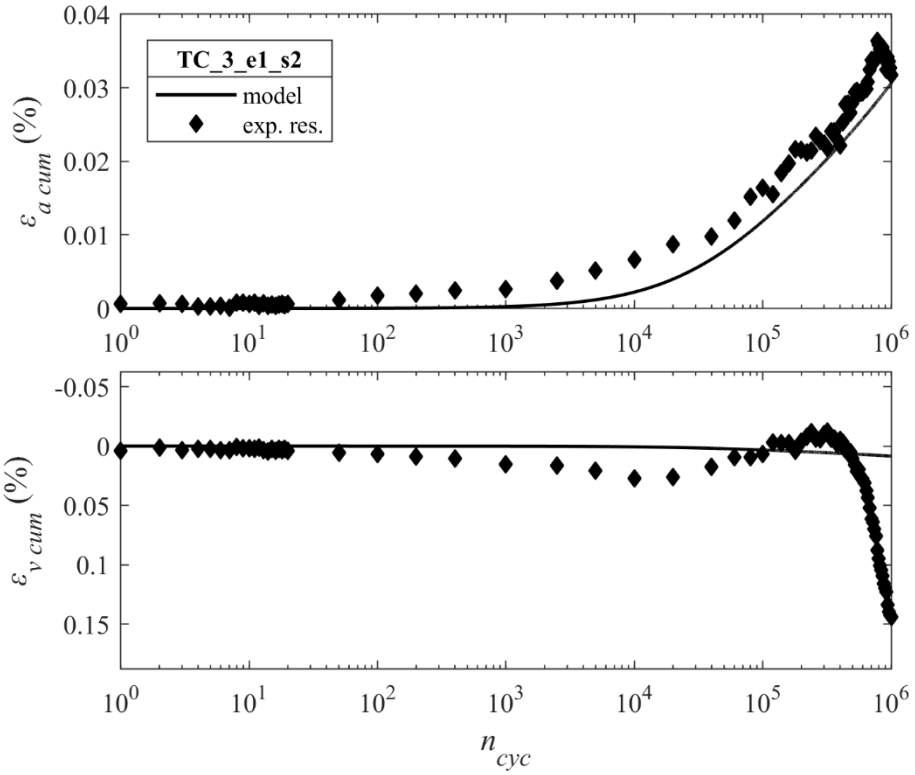

Fig. A.21 – TC_3%_e1_s2: Rowe flow rule

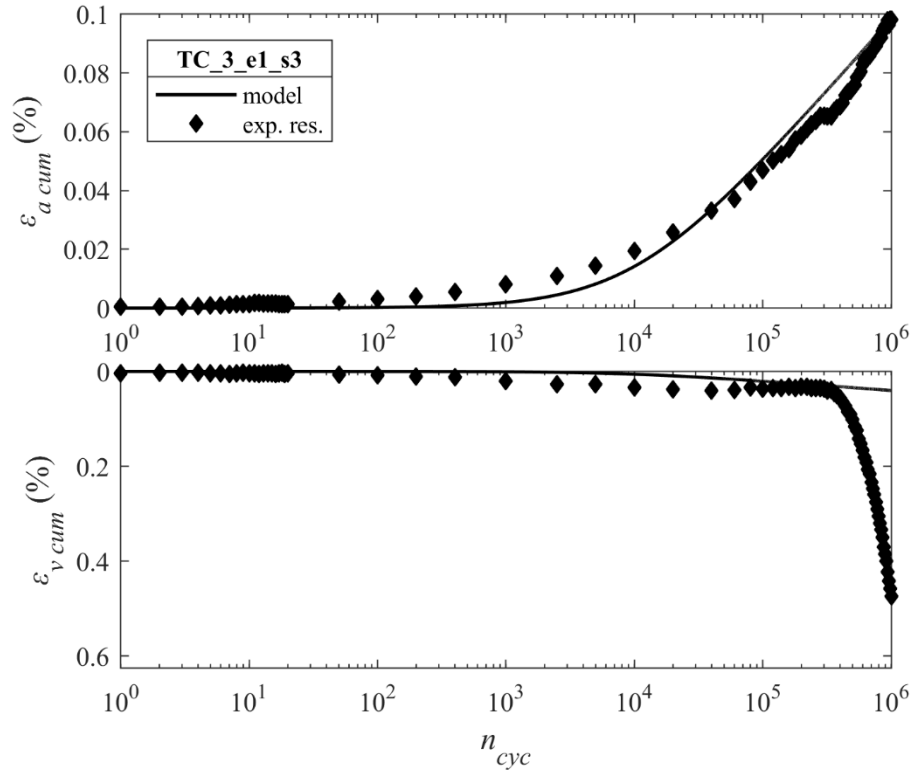

Fig. A.22 – TC_3%_e1_s3: Rowe flow rule

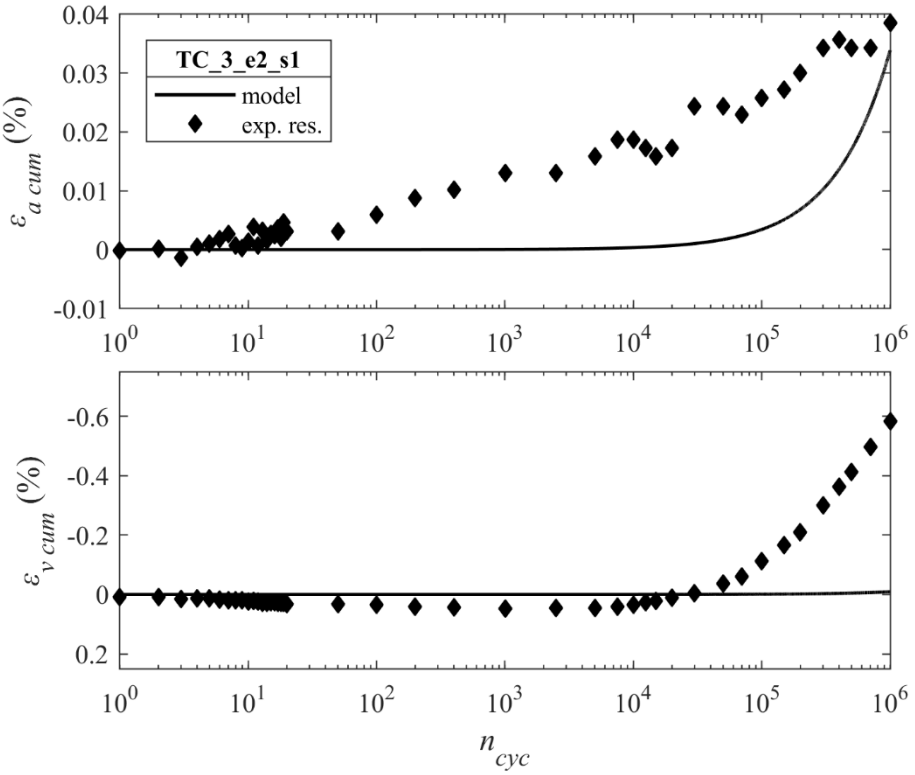

Fig. A.23 – TC_3%_e2_s1: Rowe flow rule

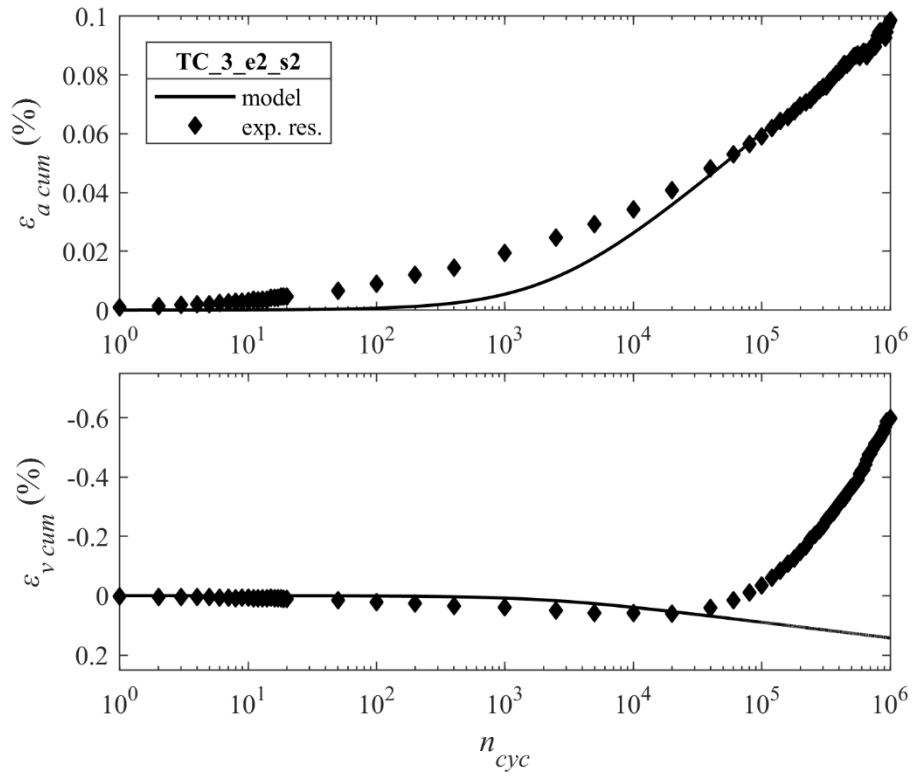

Fig. A.24 – TC_3%_e2_s2: Rowe flow rule

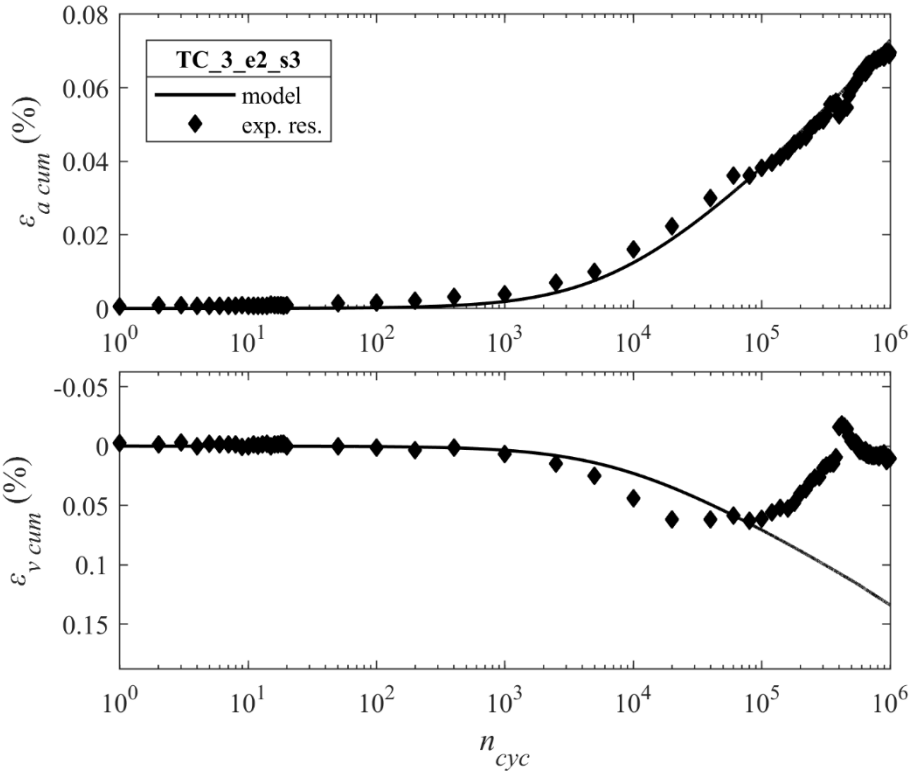

Fig. A.25 – TC_3%_e2_s3: Rowe flow rule

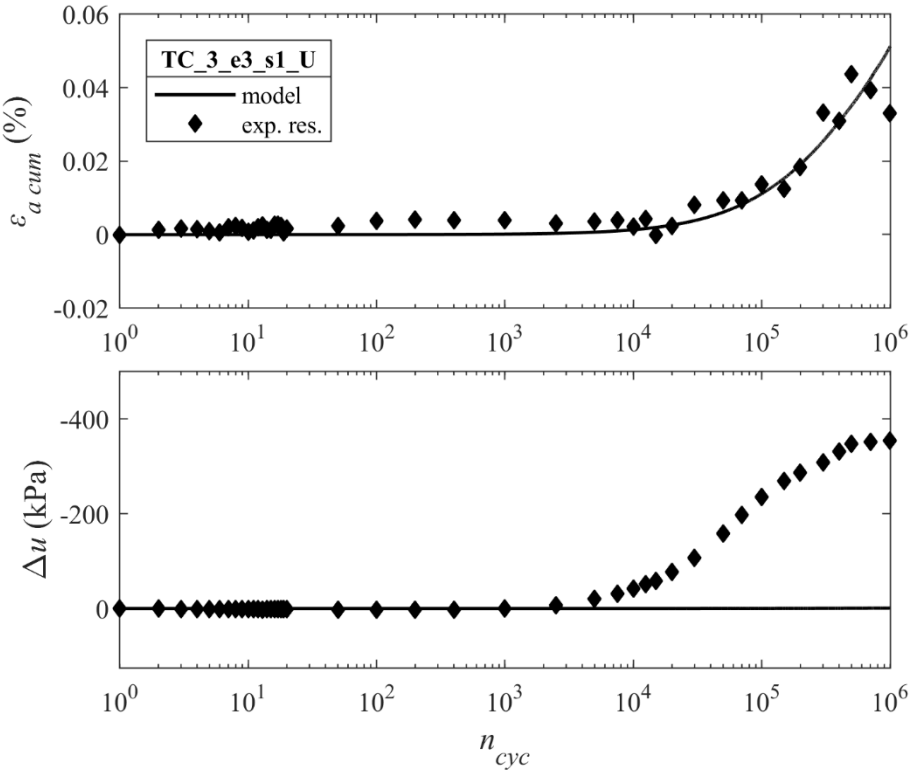

Fig. A.26 – TC_3%_e3_s1_U: Rowe flow rule

5% cement specimens

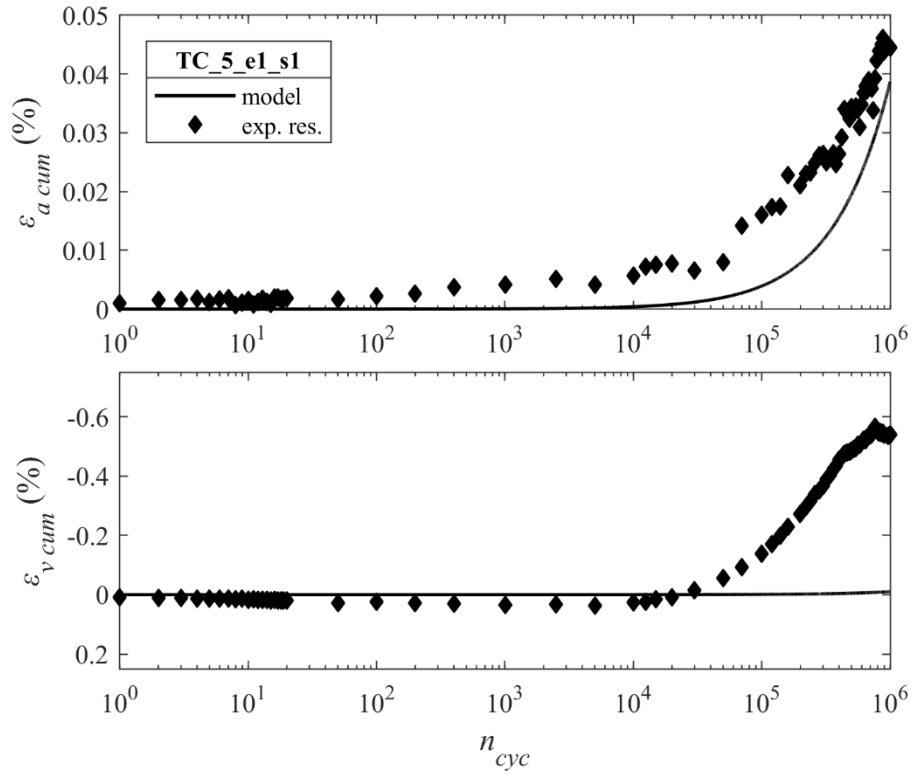

Fig. A.27 – TC_5%_e1_s1: Rowe flow rule

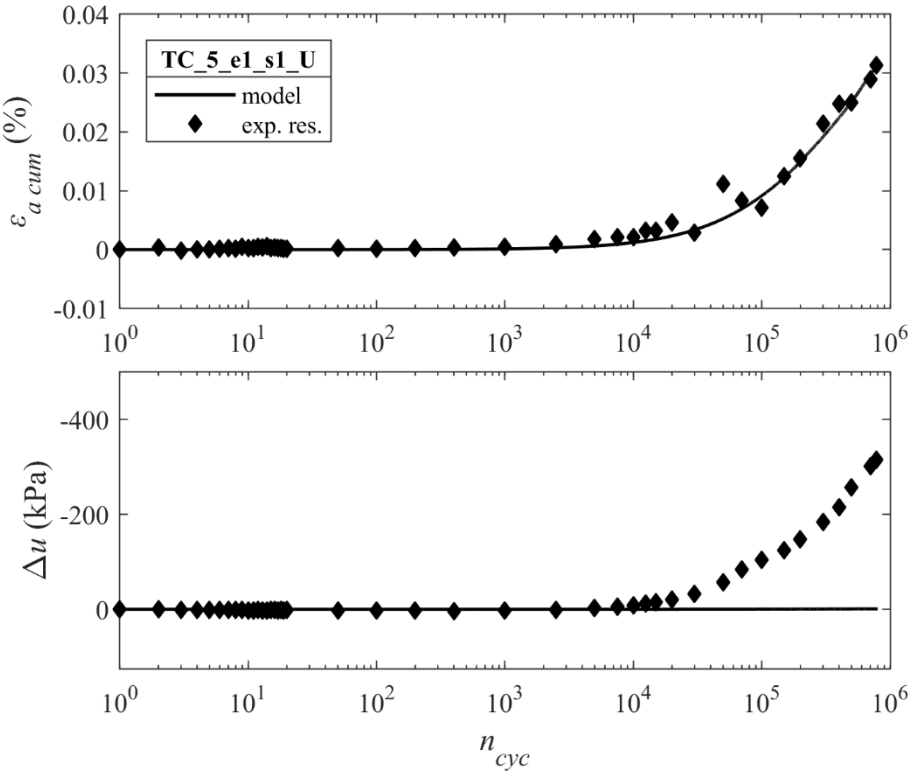

Fig. A.28 – TC_5%_e1_s1_U: Rowe flow rule

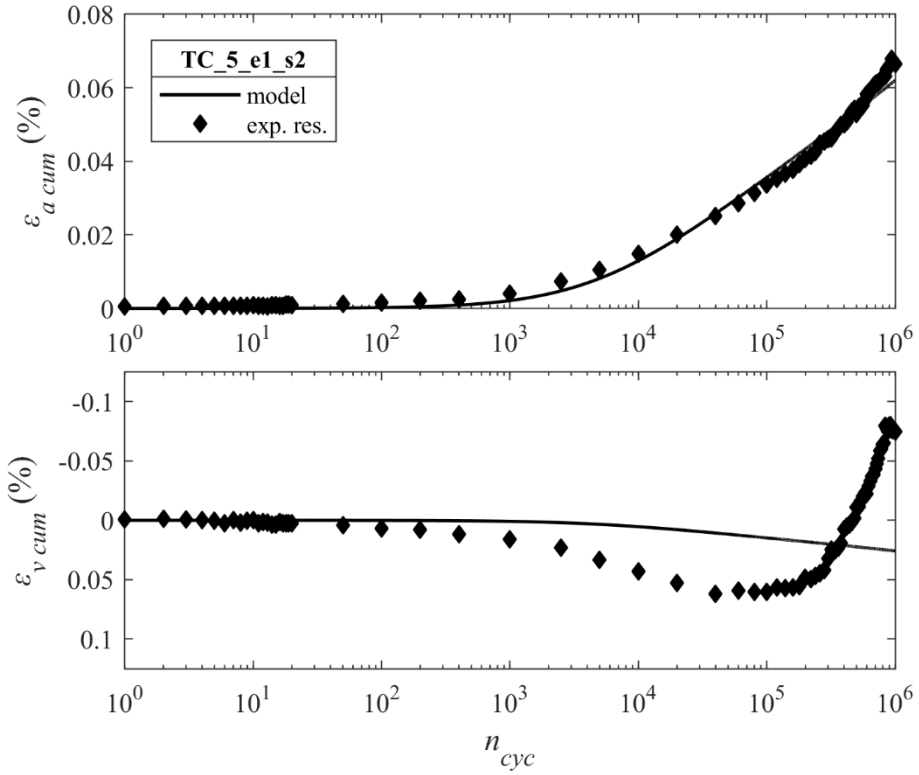

Fig. A.29 – TC_5%_e1_s2: Rowe flow rule

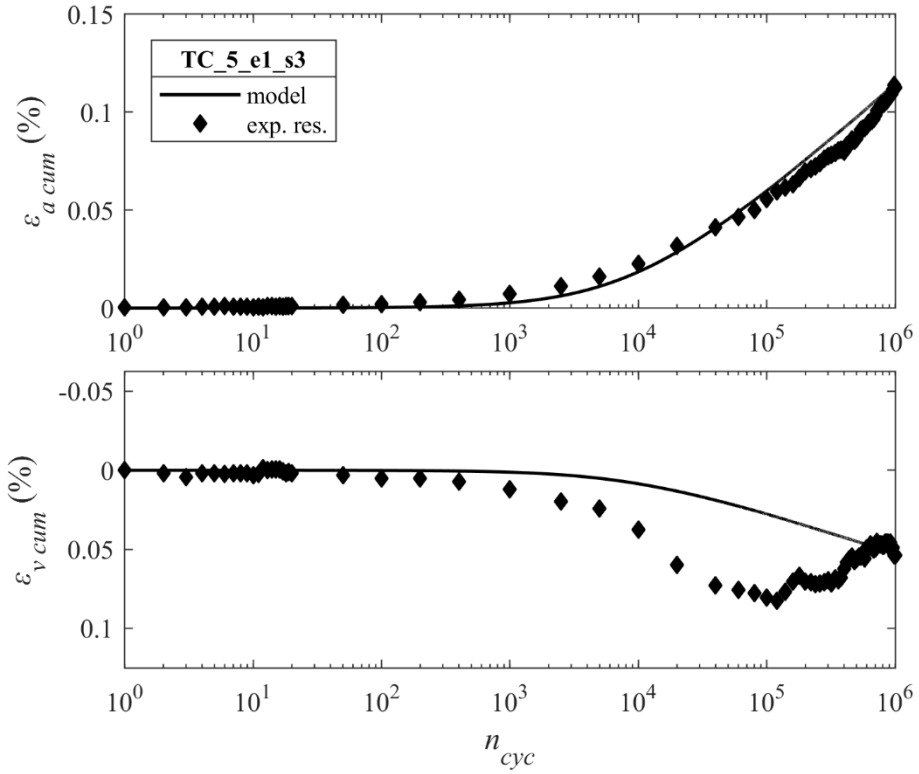

Fig. A.30 – TC_5%_e1_s3: Rowe flow rule

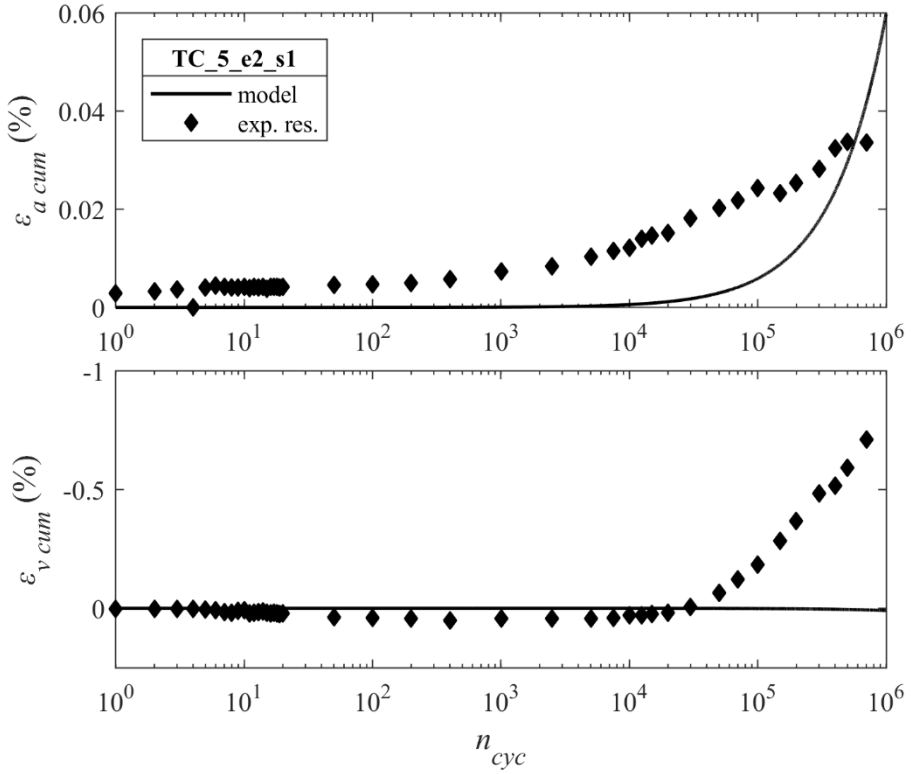

Fig. A.31 – TC_5%_e2_s1: Rowe flow rule

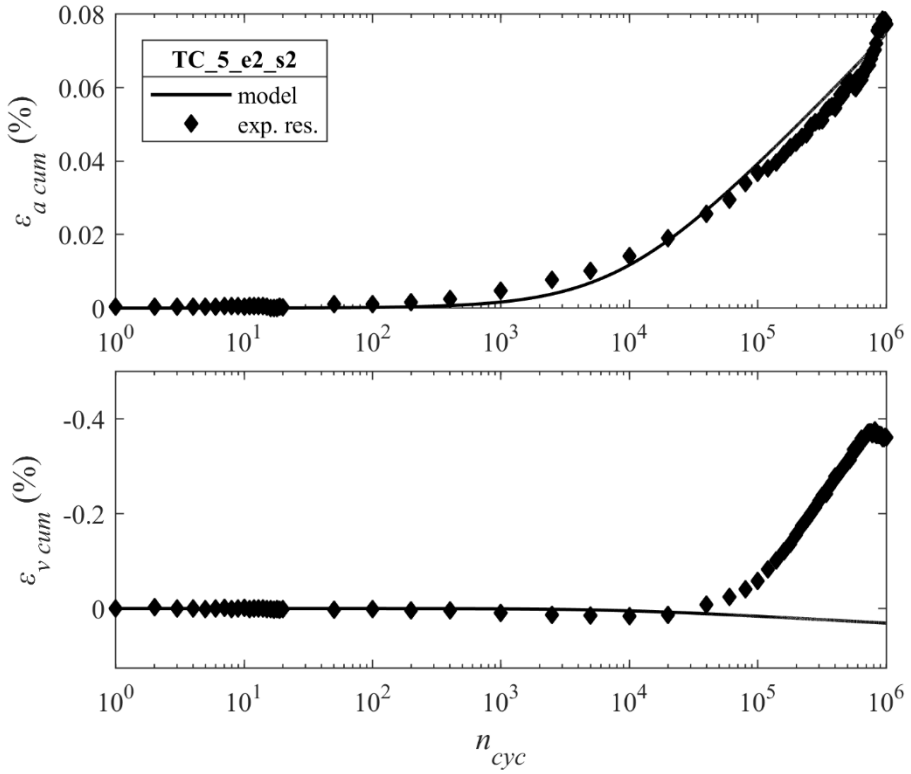

Fig. A.32 – TC_5%_e2_s2: Rowe flow rule

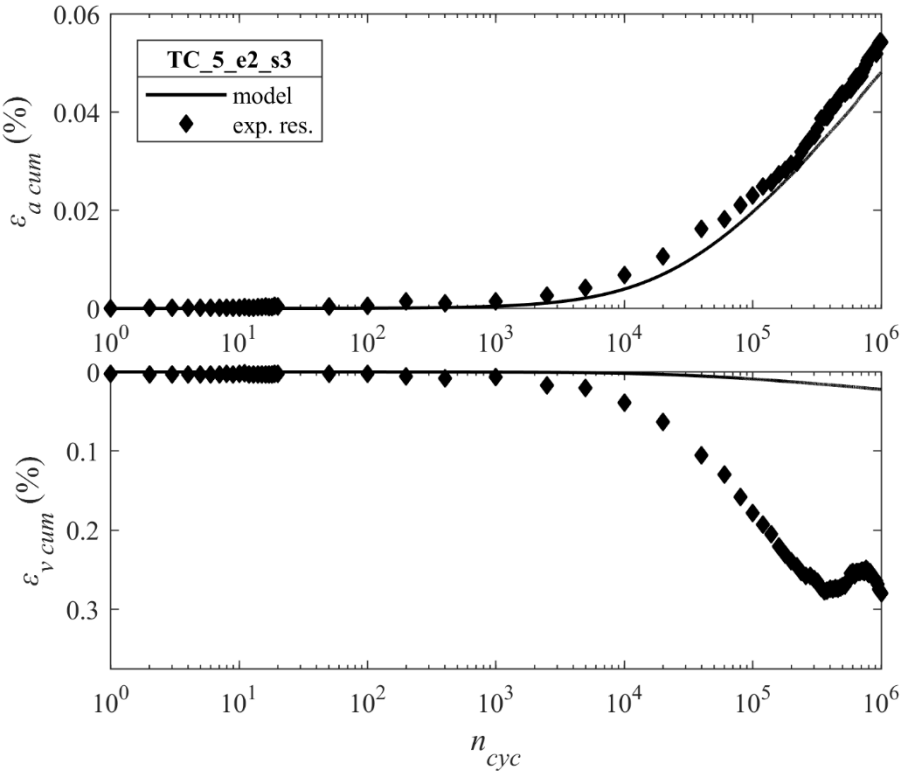

Fig. A.33 – TC_5%_e2_s3: Rowe flow rule

7% cement specimens

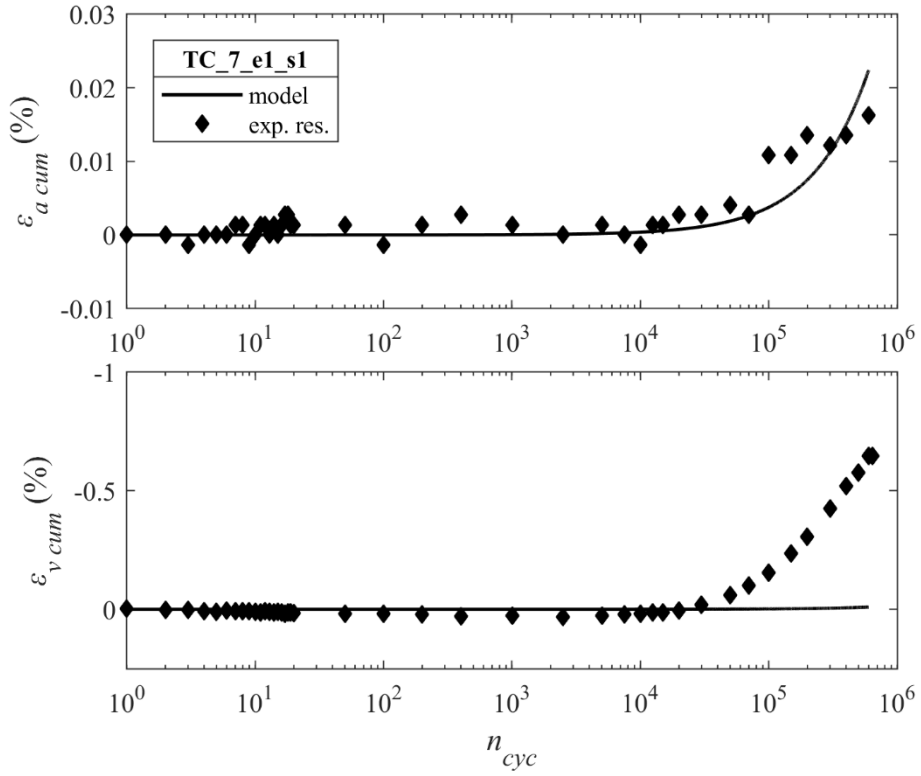

Fig. A.34 – TC_7%_e1_s1: Rowe flow rule

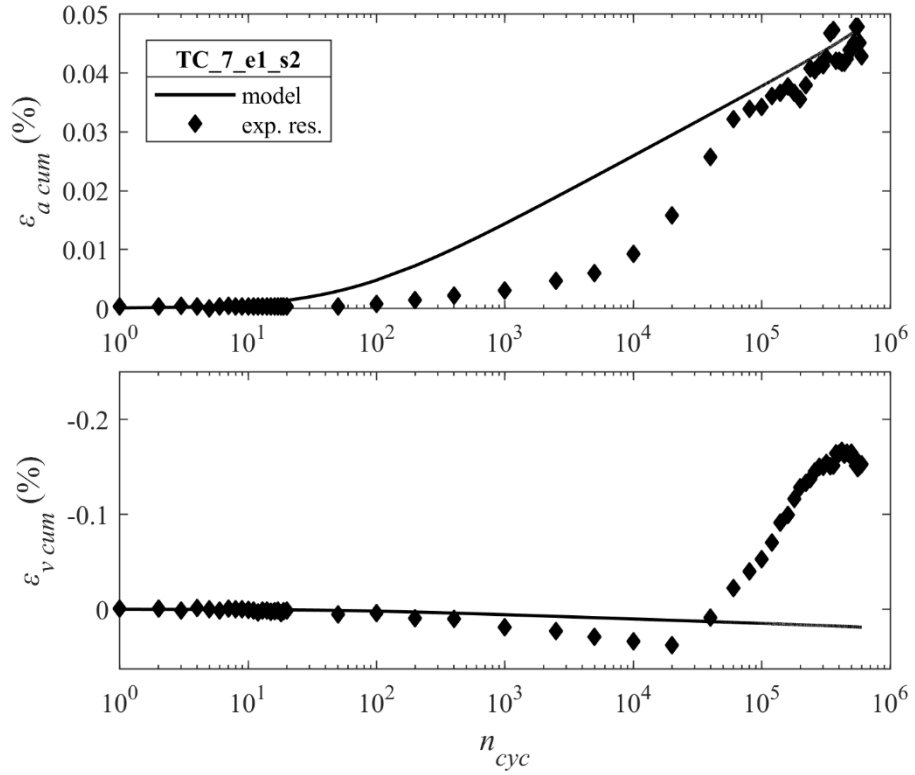

Fig. A.35 – TC_7%_e1_s2: Rowe flow rule

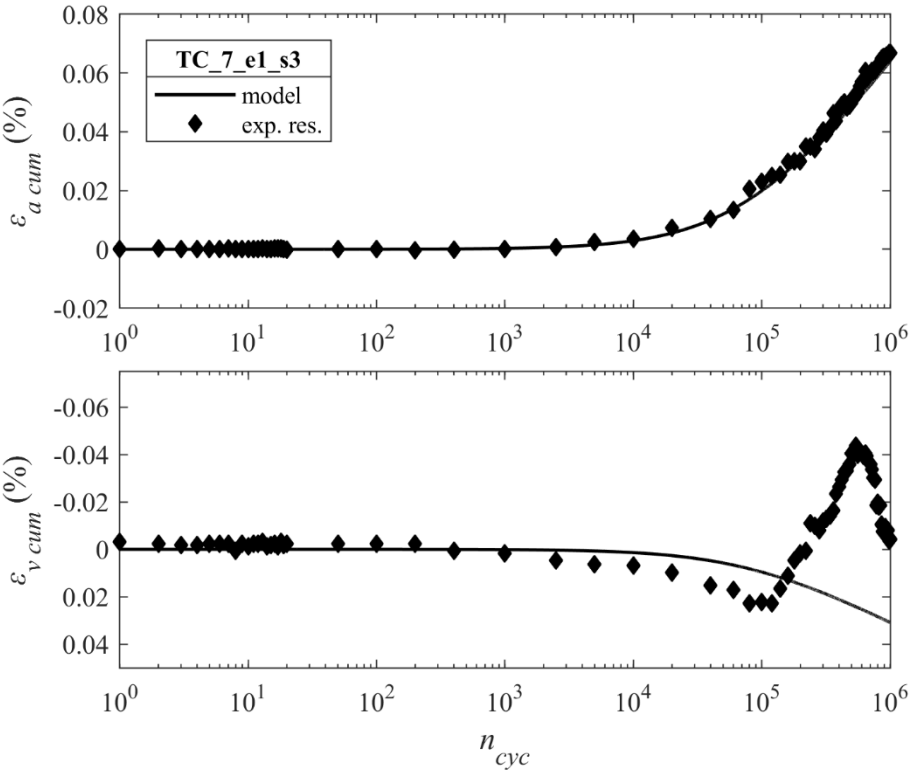

Fig. A.36 – TC_7%_e1_s3: Rowe flow rule

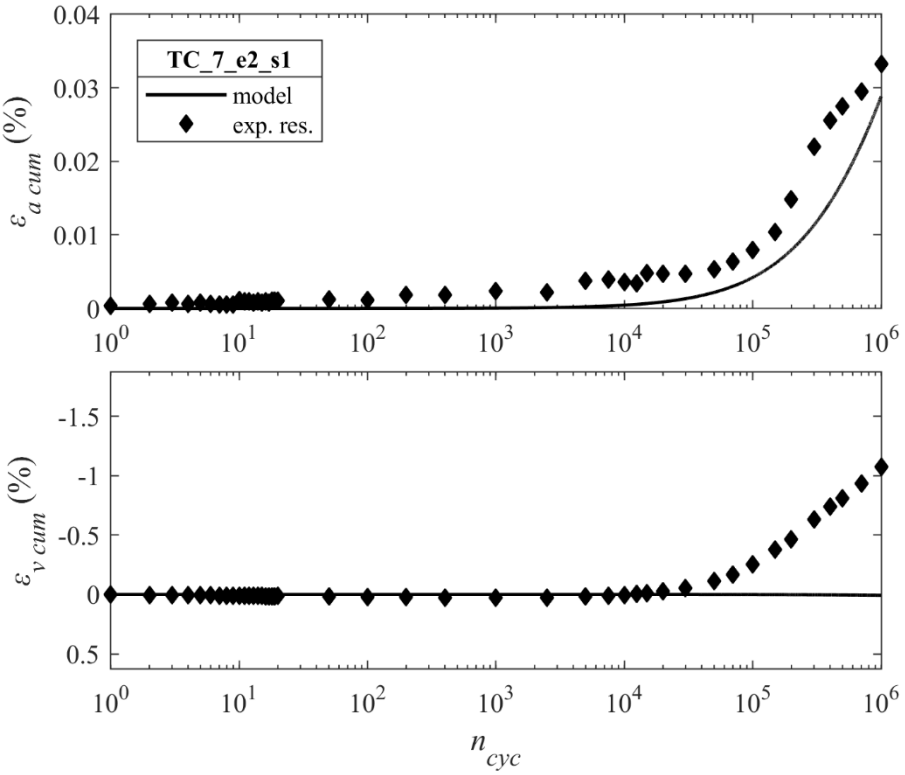

Fig. A.37 – TC_7%_e2_s1: Rowe flow rule

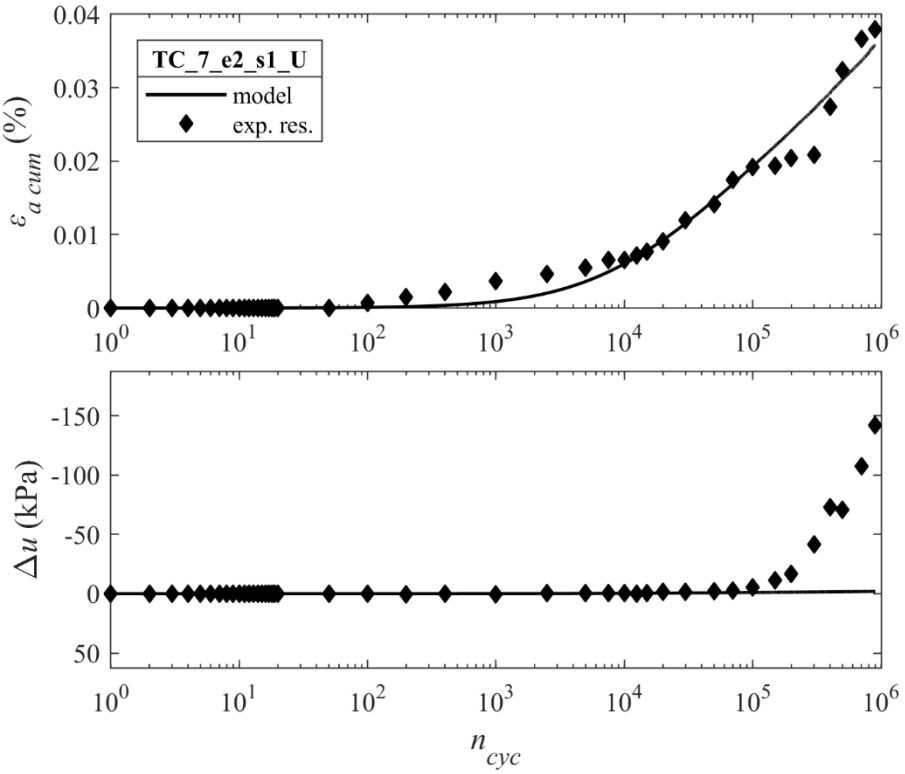

Fig. A.38 – TC_7%_e2_s1_U: Rowe flow rule

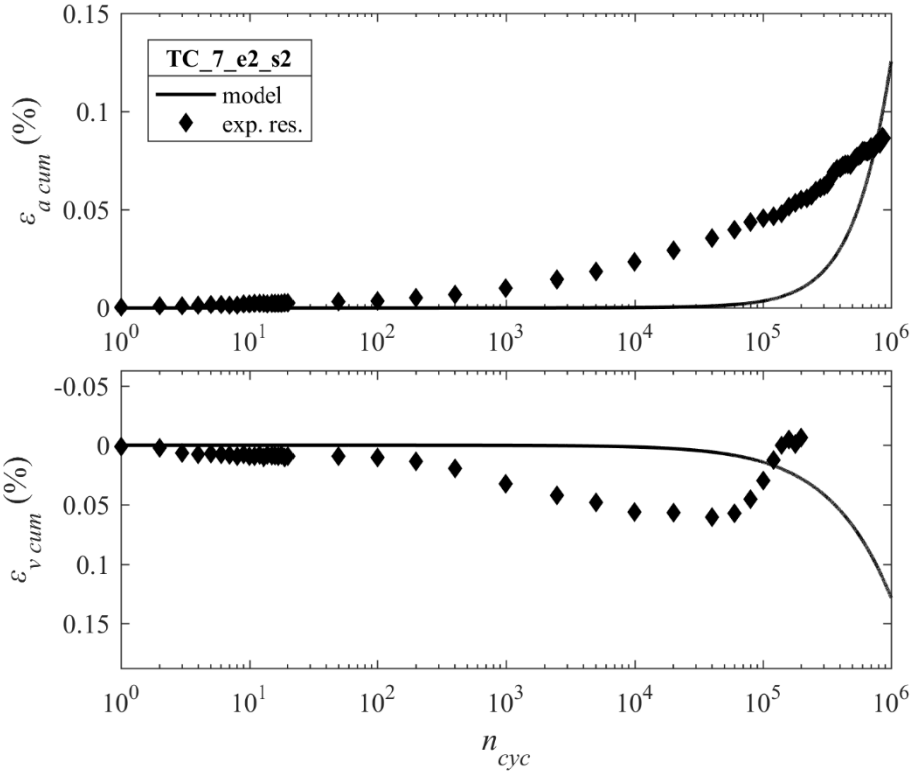

Fig. A.39 – TC_7%_e2_s2: Rowe flow rule

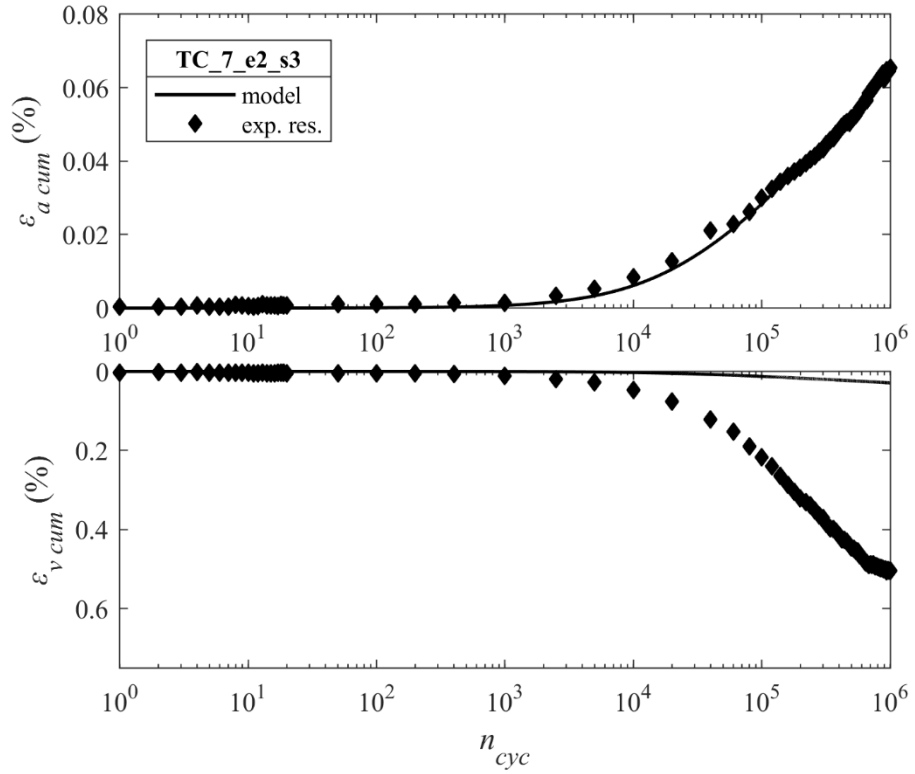

Fig. A.40 – TC_7%_e2_s3: Rowe flow rule